Revista Mexicana de Ingeniería Química

Academia Mexicana de Investigación y Docencia en Ingeniería Química, A.C.

Volumen 24, Número 3, Septiembre-Diciembre 2025

ISSN 1665-2738

Revista Mexicana de Ingeniería Química

Publicación de la Academia Mexicana de Investigación y Docencia en Ingeniería Química, A.C.

La Revista Mexicana de Ingeniería Química publica artículos de investigación originales, con el fin de promover la rápida divulgación de investigaciones significantes en las varias disciplinas que abarca la Ingeniería Química y sus interfaces con otras disciplinas de la Ingeniería. Los temas incluidos son: Termodinámica, Catálisis y Reactores, Control, Simulación, Seguridad, Diseño de Procesos, Biotecnología, Tecnología de Alimentos, Ingeniería Ambiental, Cinética de Materiales, Matemáticas Aplicadas, y Educación.

Revista Mexicana de Ingeniería Química

CONTENIDO

Volumen (Volume) 24, número (number) 3, 2025

IA25620 Treatment of brackish sardine processing wastewater employing an integrated anaerobic/anoxic/aerobic fixed-bed reactor

C.D. Loreto-Muñoz, C. Gastelum-Rosas, G. López-Avilés, M. Plascencia-Jatomea, F.J. Almendariz-Tapia

IA25621 Effect of operational parameters in electrocoagulation for the removal of phosphorus, nitrates, and ammoniacal nitrogen from water

G.A. Tamayo-Roman, S. Enciso-Sáenz, J.H. Castañon-González, J.J. Villalobos-Maldonado

IA25694 Chemical, physical, and energetic characterization of biochar produced via sugarcane bagasse pyrolysis

O. Sánchez-Castillo, M.G. Vizcarra-Mendoza, C. Martínez-Vera, S.A. Gómez-Torres, E. Rojas-García

IA25642 Aromatic hydrocarbons in mangrove areas in Tabasco: Preliminary studies

I. Fuentes-Domínguez, L. L. Vázquez-Vázquez, C. M. Morales-Bautista, Y. Y. Solís-Pérez, J. A. González-Garrido, M. E. Ojeda-Morales

IE25590 Using a composite coating (Cu/(TiO2) + (SiO2)/ Al2O2)to increase the efficiency of photovoltaic panels

R.khatir, K.kessairi, N.sellami, A.fidjah

Mat25638 Influence of the retardant additive on the compressive strength of concrete

S. Vishkulli, M. Hoxhaj, S. Vito, I. Boci

Proc25626 Alternative activated carbon method for recovery of gold from thiosulfate solutions

J. Bautista-Hernández, J. L. Valenzuela-García, J. R. Parga-Torres, M. A. Encinas-Romero, G. Tiburcio-Munive, G. Martínez-Ballesteros

Proc25627 Zinc solvent extraction from waste electronic card leaching solutions

E.G. Sustaita-Martínez, J.L. Valenzuela-García, G. Martínez-Ballesteros, B. Valdez-Salas, M.M. Salazar-Campoy, G. López-Aviles

Indizado en/Indexed in:

- **Chemical Abstracts;**
- **Thomson Reuters (*Science Citation Index Expanded, also known as SciSearch®; Chemistry Citation Index®; Journal Citation Reports, Science Edition*);**
- **Periódica;**
- **Latindex;**
- **Redalyc;**
- **Scopus**

RMIQ pertenece al Índice de Revistas Mexicanas de Investigación Científica y Tecnológica del CONACyT
RMIQ belongs to the Mexican Journals Index of Scientific and Technological Research of CONACyT

Vol. 24, No. 3 (2025)

Suscripciones
Envíe giro postal o cheque a nombre de la Academia Mexicana de Investigación y Docencia en Ingeniería Química, A.C. a:

Dr. Tomás Viveros García
Universidad Autónoma Metropolitana-Iztapalapa
Depto. de I. P. H., Area de Ing. Química
Edificio T-160, Av. San Rafael Atlixco No. 186, Vicentina. Tel. (55) 58044600
e-mail: tvig@xanum.uam.mx

Suscripción anual / Annual subscription

Personal	$160 USD
Estudiantes / Students	$80 USD
Institucional / Institutional	$540 USD

El envío de la revista se efectúa por correo ordinario
(Shipping is made by standard mail)

Portada: Tulips
Autora de la portada: Jessica Sánchez Vargas
Año: 2025.
Medidas: 1200x1600 pixeles (31.8 x 42.3 cm aproximado)
Técnica: fotografía digital

Indizado en/ Indexed in: Chemical Abstracts; Thomson Reuters (*Science Citation Index Expanded, also known as SciSearch®; Chemistry Citation Index®; Journal Citation Reports / Science Edition*); **Periódica; Latindex; Scopus; Redalyc**.

RMIQ pertenece al Índice de Revistas Mexicanas de Investigación Científica y Tecnológica del CONACYT

REVISTA MEXICANA DE INGENIERIA QUIMICA, Volumen 24, Número 3, Año 2025, septiembre-diciembre de 2025, es una publicación cuatrimestral editada por la Universidad Autónoma Metropolitana a través de la Unidad Iztapalapa, División de Ciencias Básicas e Ingeniería, Departamento de Ingeniería de Procesos e Hidráulica. Prolongación Canal de Miramontes 3855, Col. Ex-Hacienda San Juan de Dios, Delegación Tlalpan, C.P. 14387, México, D.F. y Av. San Rafael Atlixco No. 186. Col. La Vicentina, Iztapalapa. C.P. 09340. México, D.F. Tel. 58044600. Página electrónica de la revista: www.rmiq.org; dirección electrónica: amidiq@xanum.uam.mx. Editor Responsable: Dr. Tomás Viveros García. Certificado de Reserva de Derechos al Uso Exclusivo de Título No. 04-2012-101810590800-102, ISSN 1665-2738, ambos otorgados por el Instituto Nacional del Derecho de Autor. Certificado de Licitud de Título número 12238 y Certificado de Licitud de Contenido número 8891, ambos otorgados por la Comisión Calificadora de Publicaciones y Revistas Ilustradas de la Secretaría de Gobernación. Impresa por Impresos América, Avenida Hidalgo Número 46, Col. San Vicente Chicoloapan, Municipio de Chicoloapan, Estado de México, C.P. 56370, teléfono 0445522814012. Este número se terminó de imprimir en México, D.F. el 1 de diciembre de 2024, con un tiraje de 500 ejemplares.

Vol. 24, No. 3(2025) Alim25592
Revista Mexicana de Ingeniería Química

Development and characterization of antimicrobial bilayer biodegradable films from wheat flour and biopolymers for food packaging

Desarrollo y caracterización de películas biodegradables bicapa con actividad antimicrobiana a partir de harina de trigo y biopolímeros para empaques de alimentos

R.E. González-Cuello[1], J.A. Gómez-Salazar[2], R. Ortega-Toro[1‡]
[1]Professor University of Cartagena, Food Engineering Department, Food Packaging and Shelf-Life research group (FP&SL), Cartagena de Indias D.T. y C., 130015, Colombia;
[2]Profesor Departamento de Alimentos, División de Ciencias de la Vida, Universidad de Guanajuato, Campus Irapuato-Salamanca, C.P.36500 Irapuato, Guanajuato, México.
Sent date: May 16, 2025; Accepted: August 30, 2025

Abstract
This study focuses on the development and characterization of biodegradable bilayer films with antimicrobial properties (against *Bacillus cereus*) formed from wheat flour (WF) monolayers assembled with polycaprolactone (PCL) or Mater-Bi (MB). Monolayer films were made by compression molding, and bilayer films were obtained by bonding a wheat flour layer with a PCL or Mater-Bilayer, incorporating potassium sorbate (PS) and citric acid (CA) as antimicrobial agents at the interface. Film properties were evaluated, including color, gloss, thickness, opacity, internal transmittance, moisture content, water solubility, water absorption capacity, water contact angle, water vapor permeability, mechanical properties, and antimicrobial activity. The results showed that the bilayers with PCL and Mater-Bi offer a better barrier and lower solubility than the wheat flour monolayers and, in turn, show moderate stresses and deformations, with higher elastic moduli, especially in the $B_{WF\text{-}CA\text{-}MB}$ bilayer, which has the highest elastic modulus (174.5 MPa). Also, the inclusion of antimicrobial agents and the combination of varied materials significantly influence the properties of the films, highlighting the antimicrobial effectiveness against *Bacillus cereus*. The study concludes the films offer a sustainable alternative to conventional plastics, improving food safety and extending shelf life in food packaging combining sustainability with functionality. However, additional studies using real food matrices are required to confirm their impact on food safety and product shelf-life extension.
Keywords: Biodegradable packaging, Bilayer films, Wheat flour, Polycaprolactone (PCL), Mater Bi, Antimicrobial activity, *Bacillus cereus*.

Resumen
Este estudio se centra en el desarrollo y la caracterización de películas biodegradables bilaminares con propiedades antimicrobianas (contra *Bacillus cereus*), formadas a partir de monoláminas de harina de trigo (WF) ensambladas con Policaprolactona (PCL) o Mater-Bi (MB). Las películas monolaminares se elaboraron mediante moldeo por compresión, y las películas bilaminares se obtuvieron uniendo una capa de harina de trigo con una de PCL o Mater-Bi, incorporando sorbato de potasio (PS) y ácido cítrico (CA) como agentes antimicrobianos en la interfaz. Se evaluaron diversas propiedades de las películas, incluyendo color, brillo, espesor, opacidad, transmitancia interna, contenido de humedad, solubilidad en agua, capacidad de absorción de agua, ángulo de contacto con el agua, permeabilidad al vapor de agua, propiedades mecánicas y actividad antimicrobiana. Los resultados mostraron que las películas bilaminares con PCL y Mater-Bi ofrecen una mejor barrera y menor solubilidad que las monoláminas de harina de trigo, y presentan esfuerzos y deformaciones moderados, con módulos elásticos más altos, especialmente en la película bilaminar $B_{WF\text{-}CA\text{-}MB}$, que presentó el mayor módulo elástico (174.5 MPa). Asimismo, la inclusión de agentes antimicrobianos y la combinación de distintos materiales influyen significativamente en las propiedades de las películas, destacándose la efectividad antimicrobiana frente a *Bacillus cereus*. El estudio concluye que estas películas representan una alternativa sostenible a los plásticos convencionales, mejorando la seguridad alimentaria y prolongando la vida útil de los productos envasados, al combinar sostenibilidad y funcionalidad. Sin embargo, se requieren estudios adicionales utilizando matrices alimentarias reales para confirmar su impacto en la inocuidad y el tiempo de conservación de los alimentos.
Palabras clave: Envases biodegradables, Películas bilaminares, Harina de trigo, Policaprolactona (PCL), Mater-Bi, Actividad antimicrobiana, *Bacillus cereus*.

‡*Corresponding author. E-mail*: rortegap1@unicartagena.edu.co;
https://doi.org/10.24275/rmiq/Alim25592
ISSN:1665-2738, *issn-e*: 2395-8472

1 Introduction

The search for sustainable solutions has encouraged the development of biodegradable materials, especially in packaging. Biodegradable films, capable of decomposing into natural components through biological processes, have attracted considerable attention in recent research (Moshood *et al*., 2022). Wheat flour has emerged as a promising resource due to its availability, low cost, non-toxicity, and properties (Wang *et al*., 2022). Composed of starch (78-82%) and gluten (8-16%) (Hong *et al*., 2021; Guo *et al*., 2020), wheat flour is among the most abundant sources used as thermoplastic materials for food packaging. However, its use faces challenges related to mechanical and barrier properties (Drakos *et al*., 2018; Dong *et al*., 2022).

Bilayer films have been developed combining wheat flour monolayers with monolayers of biodegradable polymers such as poly(ε-caprolactone) (PCL) and Mater-Bi to overcome these limitations. These combinations improve mechanical and barrier properties and allow the incorporation of antimicrobial agents, such as potassium sorbate, which inhibit microbial growth, prolonging the shelf life of packaged products (Alzate *et al*., 2021; Cheng *et al*., 2024). Furthermore, using citric acid as a linking agent improves the compatibility between the layers, favoring interactions and increasing the cohesion and stability of the bilayer structure (Loukri *et al*., 2024). Integrating natural and synthetic components in these films presents an innovative and sustainable solution for the packaging industry (Avila *et al*., 2022).

Furthermore, the environmental benefits of using renewable resources such as wheat flour and biodegradable polymers contribute to reducing the carbon footprint associated with traditional packaging solutions (Singh *et al*., 2021; Stoica *et al*., 2024). This innovative strategy underlines the potential of developing sustainable packaging materials that meet the growing demand for eco-friendly alternatives in the food industry. On the one hand, using wheat flour as a raw material for manufacturing biodegradable films presents multiple benefits. Firstly, wheat flour is an abundant and low-cost by-product derived from the food industry, making it an economically viable option. Its global availability allows for the reduction of dependence on non-renewable resources, contributing to sustainability. (Stoica *et al*., 2024; Suárez-Castillo *et al*., 2024) Furthermore, wheat flour is rich in carbohydrates, mainly starch, which provides valuable functional properties such as forming films and acting as a binding agent in the film matrix (Wang *et al*., 2022; Petaloti *et al*., 2024).

On the other hand, biodegradable polymers such as polycaprolactone (PCL) and Mater-Bi offer significant advantages in terms of sustainability. PCL, for example, is an aliphatic polymer that decomposes quickly under ambient and non-toxic conditions, minimizing its environmental impact (Thakur *et al*., 2021). Mater-Bi, a biodegradable polymer based on renewable raw materials, decomposes efficiently, and has a favorable environmental profile (Aldas *et al*., 2021). Together, these materials improve the mechanical and barrier properties of films and favor the reduction of plastic waste, offering a sustainable alternative in the packaging industry. The combination of these ingredients allows the creation of packaging solutions that are functional and environmentally friendly and contribute to a circular economy where materials are reused and valued throughout their life cycle.

This study aims to develop bilayer films composed of wheat flour-based monolayers assembled with monolayers of PCL or Mater-Bi, with a focus on evaluating their antimicrobial properties against *Bacillus cereus*, which were assessed exclusively against *Bacillus cereus*.

2 Materials and methods

2.1 Materials

The materials used in this research were carefully selected for their specific properties. The wheat flour, with a humidity of 11.9 % and a composition of total carbohydrates 73 %, protein 12 %, fat 1.4 %, and ash 1.7 %, was purchased from local chain stores in Cartagena. Polycaprolactone (PCL) (average~Mn 80000; density 1.145~g/mL~at 25~°C) was obtained from Sigma-Aldrich and Merck in Bogotá, Colombia, and the Mater-Bi (EF05B, density 1.28 g/cm^3 at 23 °C) was purchased from Novamont, Italy. Glycerol, citric acid, potassium sorbate broths, and microbiological agars, crucial for the process, were supplied by PANREAC, also in Bogotá, Colombia.

2.1.1 Preparation of monolayer films

Monolayer films were fabricated from wheat flour, Mater-Bi, and polycaprolactone (PCL) by compression molding method with previous studies (Moreno-Ricardo *et al*., 2024).

To prepare the wheat flour film, a 4:1 ratio of wheat flour and water was taken; glycerol was additionally incorporated as a plasticizing agent in 25 % of the flour. Then, the ingredients were mixed until a homogeneous mass was obtained and left to rest for 24 h. After this, small portions of 13 g were taken to form the film. These portions were placed in a hydraulic press at a temperature of 120 °C and subjected to pressures from 0 to 100 bar for approximately 2 minutes for each pressure.

Table 1. Mass fractions of the formulations studied (M: monolayers; B: bilayers; WF: wheat flour; PCL: polycaprolactone; MB: Mater-Bi; PS: potassium sorbate; CA: citric acid).

Formulations	WF	PCL	MB	PS	CA
M_{WF}	1	0	0	0	0
M_{PCL}	0	1	0	0	0
M_{MB}	0	0	1	0	0
$B_{WF\text{-}PS\text{-}PCL}$	0.813	0.125	0	0.063	0
$B_{WF\text{-}PS\text{-}MB}$	0.813	0	0.125	0.063	0
$B_{WF\text{-}CA\text{-}PCL}$	0.813	0.125	0	0	0.063
$B_{WF\text{-}CA\text{-}MB}$	0.813	0	0.125	0	0.063

Regarding the preparation of the monolayer PCL and Mater-Bi films, 2 g of each material were weighed. These materials were pressed in the hydraulic press at temperatures of 85 °C for the PCL and 150 °C for the Mater-Bi, with pressures from 0 to 100 bar for approximately 1 minute for each pressure used.

2.2 *Preparation of bilayer films*

The films were obtained following methodologies previously established by other studies (Ortega-Toro, *et al*., 2016). To form the bilayer film, a layer of wheat flour film and a layer of PCL and Mater-Bi were joined at 130 °C and 100 bar pressures for 1 minute. Additionally, antimicrobial agents (potassium sorbate and citric acid) were placed directly at the interface during the assembly of the wheat flour and PCL or Mater-Bilayers. All films were conditioned in desiccators with supersaturated sodium bromide solutions (56% RH) until characterization. Table 1 shows the mass fractions of the studied formulations using a full factorial 2×2 design for the bilayer films, along with additional treatments (controls).

2.2.1 *Characterization of the films*

2.2.1.1 Color

The color was measured with a colorimeter that provided CIE Lab* coordinates, hue angle (h), and chroma or saturation (c). The CIE Lab* coordinates indicate the luminosity on the vertical axis and the orientation towards the color's red, green, blue, and yellow on the horizontal axes (Rivera-Leiva *et al*., 2022). Based on this, the color change was determined by comparing the color of the sample with that of a reference sample. In the case of the bilayer films, color measurements were performed on both sides of the films. Based on this, the color change was determined by comparing the color of the sample with that of a reference sample. The color difference in each coordinate (ΔL, Δb, and Δa) was calculated to do this. The total color difference ΔE^* was calculated using equation (1).

$$\Delta E^* = \sqrt{\Delta L^2 + \Delta b^2 + \Delta a^2} \quad (1)$$

2.2.1.2 Glow

The gloss was measured at an angle of incidence of 60° according to the ASTM D523 standard procedure, using a gloss meter with a flat surface (3NH YG268 multi-angle gloss meter, Minolta, Langenhagen, Germany). Nine films were evaluated, and three readings were taken from each sample. The results were expressed in gloss units (GU).

2.2.1.3 Thickness

The thickness was determined by using a digital micrometer (TL268 TOP EU). Seven random measurements were made of the films, and their average value and standard deviation were recorded.

2.2.1.4 Film opacity

A spectrophotometer (BIOBASE BK-UV1900) was used (Mohammed *et al*., 2023). The films were cut into strips (1 × 3 cm) and affixed to the inner wall of the cuvette for measurement. Opacity was determined using Equation (2):

$$Opacity = \frac{Absorbance\ (600nm)}{Thickness\ (mm)} \quad (2)$$

2.2.1.5 Internal transmittance

For internal transmittance analysis, a spectrophotometer and quartz cells were used. 1 x 3 cm films were introduced into the quartz cells and, subsequently, absorbance data in the UV-visible range (200-800 nm) were obtained. This range was chosen as it covers the wavelengths relevant to the study of internal transmittance (Ortega-Toro *et al*., 2016).

2.2.1.6 Moisture content

The 2x2cm films were dried in a natural convection muffle at 60 °C, maintaining continuous heating until reaching a constant weight. The percentage of humidity was determined using equation (3). Mean values were calculated by averaging three repetitions for each formulation.

$$\%\ Moisture = \frac{W_h - W_s}{W_s} \times 100\% \quad (3)$$

The terms are defined as follows: W_h(Weight hydrated): Weight of the film before drying; W_s (Weight solid): Weight of the film after drying.

2.2.1.7 Water solubility

The films were immersed in distilled water at a ratio of 1:10 (Film: Water) for 48 h. The samples were then dried for 24 h in a natural convection oven at 60 °C to remove free water. Subsequently, they were placed in a desiccator with a saturated sodium bromide (NaBr) solution (RH = 58 %, T = 25 °C) for two weeks to remove bound water. Finally, the percentage of solubility of the films was calculated based on their initial and final weights. This procedure was repeated three times for each formulation and the arithmetic mean obtained was reported (Acevedo-Puello *et al*., 2023).

2.2.1.8 Accumulated water loss and gain

The methodology proposed by Collazo-Bigliardi *et al* (2019) was followed with some adjustments. First, the films were cut into 2x2 cm dimensions and placed in a desiccator with lithium bromide, generating a relative humidity of 6.4% at room temperature. The weight of the films was recorded every 24 h until constant weight (72 h), considering it as well as the weight of the dry film. Next, the films were transferred to a desiccator with a saturated solution of potassium sulfate (97.3 % relative humidity) and weighed every 24 h until the weight was almost constant (72 h), said weight being considered as the wet weight. Finally, graphs representing the accumulated loss or gain of the different formulations were constructed. Each value is the accumulated weight loss or gain in each time interval (Equations 4 and 5). This procedure was performed in triplicate for each formulation.

$$Cumulative\ weight\ loss = P_W - P_t \quad (4)$$

$$Cumulative\ weight\ gain = P_D - P_t \quad (5)$$

P_W = Wet weight of the films
P_t = Weight of the films in the time interval
P_D: Dry weight of the films

2.2.1.9 Contact angle in water

The contact angle was determined as follows: a film sample was placed on a horizontal surface with a white background, and subsequently, a drop of water (with dye) or oil was deposited on the surface of the film. The image was captured with a digital camera after 30 seconds, maintaining a constant distance of 20 cm between the water or oil drop and the camera lens. Finally, the captured image was analyzed using Goniotrans software. In the case of bilayer films, measurements were performed independently on each side due to potential differences in composition and surface behavior. This procedure was performed in triplicate for each formulation, and the average value was reported (Acevedo-Puello *et al*., 2023).

2.2.1.10 Water vapor permeability

The determination was conducted using a gravimetric method following the procedure established in ASTM E96-95, with some modifications. Specific parameters were adjusted to create a humidity gradient from 53 % RH to 100 % at 25 °C. Films without physical defects were selected for water vapor permeability (WVP) testing. Payne permeation cups containing distilled water were used, exposing one side of the film to 100 % RH. These cups and the films were placed in humidity-controlled cabinets at 25 °C, with the relative humidity of the cabinet (53 %) being maintained by supersaturated sodium bromide solutions.

Furthermore, to facilitate the practical use of the films in products with high water activity, the free surface of the film during its elaboration was exposed to a lower relative humidity. The breakers with the films were weighed periodically using a precision analytical balance (0.0001 g). Once the measurements reached a steady state, the water vapor transmission rate (WVTR) was calculated by analyzing the slope of the regression curve and plotting weight loss versus time. This value was then divided by the area of the film. The entire test was performed three times, and the reported results include the average value and the corresponding standard deviation (Muñoz-Suarez *et al*., 2024).

2.2.1.11 Mechanical properties

The fundamental mechanical properties of the analyzed films, including elastic modulus (EM), tensile strength (TS), and elongation (E), were evaluated under controlled conditions of 50 ± 5% relative humidity and 23 ± 2 °C, in accordance with standardized procedures (ASTM D882). The test was performed using a texture analyzer (TX-700 TEXTURE ANALYZER) equipped with a 500 N load cell, operating at a speed of 50 mm/min. The film samples measured 1 mm × 100 mm, with a clamping.

2.2.1.12 Microstructure

The microstructural analysis of the cross-sections of the films was conducted using a scanning electron microscope (JSM-5910, JEOL Ltd., Tokyo, Japan). The film samples were stored in desiccators containing P_2O_5 for two weeks to ensure the absence of water in the samples. Film pieces measuring 0.5 cm^2, were cryofractured, mounted on copper stubs, gold-coated, and examined using an accelerating voltage of 10 kV. Conversely, optical microscopy was performed to analyses the surface of the films. Samples measuring 2 cm^2 were taken to examine their surface using an optical microscope (ZEISS model 415500-1800-000)

at a magnification of 10×. Prior to analysis, the films were conditioned at a relative humidity of 53% and a temperature of 25 °C for one week (Gómez-Contreras *et al*., 2023).

2.2.1.13 Antimicrobial activity against *Bacillus cereus*

The methodology was implemented to evaluate the antimicrobial activity (Aguirre *et al*., 2013), using the agar disc diffusion technique against *Bacillus cereus*, the only microorganism evaluated in this study. Mueller Hinton agar was used as the culture medium, and the bacterium was inoculated by surface seeding. Subsequently, small portions of the films (incorporated with potassium sorbate) were placed around the Petri dish. The plates were incubated at 37 °C for 48 h. After the incubation period, the antimicrobial activity of each material was evaluated by observing the formation of inhibition zones and measuring their diameters in millimeters.

2.3 Statistical analysis

Data analysis was carried out through an ANOVA analysis of variance. The significant differences ($p<0.05$) were evaluated using the Tukey test between the analyses conducted on the different samples. Statistical analyses were performed with Statgraphics Centurion XVI software (Manugistics Corp., Rockville, MD, USA).

3 Results and discussion

3.1 Characterization of the films

3.1.1 Color

Table 2 shows the gloss measurements at 60°, the color parameters (L*, a*, b*, C, h), and the color change (ΔE) value of the formulations. It is observed that the formulations present significant variations in gloss, color, and color change (ΔE). M_{PCL} (pure PCL) has the highest gloss (14.6), indicating a smooth and shiny surface, while M_{MB} (pure Mater-Bi) shows a low gloss (6.0), suggesting a more matte surface. Blends with wheat flour show notable differences between their layers: in $B_{WF\text{-}PS\text{-}PCL}$ and $B_{WF\text{-}PS\text{-}MB}$, the flour layers have a significantly lower gloss than the PCL or Mater-Bi layers. Regarding luminosity (L*), it varies significantly between the formulations, being higher in the pure formulations of M_{PCL} (88.1) and M_{MB} (85.2), which indicates transparent and reflective surfaces. In bilayers that include wheat flour, the lightness is lower, especially in the flour layers, suggesting a darkening effect due to the flour (L* between 76.6 and 79.8). The PCL and Mater-Bi layers in these films maintain a high luminosity, showing that they are brighter than the flour layers. In previous studies, a luminosity close to 90 was reported for M_{PCL} (Gürler *et al*., 2023) and 89 for M_{MB} (Aldas *et al*., 2021), which is consistent with the results obtained in this analysis.

Table 2. Mean values ± standard deviation (SD) is reported of the brightness (GU) and color parameters (luminosity (L*), red/green (a*), yellow/blue (b*), chromaticity (C), and hue angle (h, °) of the films studied. The layer in which the determination is made is indicated in parentheses.

Formulation	Brightness at 60°	Color parameters					ΔE
		L*	a*	b*	C	h	
M_{WF}	14.1±0.7^{ab}	31.1±0.3^{e}	-5.1±0.1^{h}	3.3±0.1^{e}	6.3±0.4^{e}	158.8±0.6^{a}	-
M_{PCL}	14.6±0.8^{a}	88.1±0.3^{a}	-0.3±0.01^{f}	0.6±0.02^{f}	0.9±0.01^{f}	109.2±0.5^{b}	-
M_{MB}	6.0±0.8^{cd}	85.2±0.8^{b}	3.2±0.3^{b}	15.9±0.5^{c}	16.4±0.8^{c}	78.8±0.7^{c}	-
$B_{WF\text{-}PS\text{-}PCL}$ (WF Layer)	5.1±0.4^{d}	77.2±0.6^{d}	-0.9±0.01^{g}	12.7±0.3^{d}	12.8±0.2^{d}	94.1±0.1^{d}	47.3±0.8^{d}
$B_{WF\text{-}PS\text{-}PCL}$ (PCL layer)	13.1±0.4^{b}	77.6±0.4^{d}	-0.9±0.06^{g}	13.2±0.7^{d}	13.1±0.6^{d}	94.0±0.3^{c}	16.41±0.9^{e}
$B_{WF\text{-}PS\text{-}MB}$ (WF layer)	3.8±0.7^{e}	76.6±0.1^{d}	4.8±0.2^{a}	24.7±0.06^{a}	25.2±0.04^{a}	78.8±0.5^{d}	51.4±0.4^{b}
$B_{WF\text{-}PS\text{-}MB}$ (MB layer)	12.7±0.8^{b}	83.6±0.4^{b}	0.3±0.04^{e}	13.1±0.1^{d}	13.1±0.2^{d}	91.6±4.0^{c}	4.4±0.4^{f}
$B_{WF\text{-}CA\text{-}PCL}$ (WF layer)	6.5±0.8^{c}	77.9±0.8^{cd}	-0.5±0.2^{f}	13.1±0.1^{d}	13.4±0.2^{d}	91.6±4.0^{c}	16.1±0.5^{e}
$B_{WF\text{-}CA\text{-}PCL}$ (PCL layer)	14.1±0.7^{ab}	78.8±0.9^{cd}	-0.4±0.02^{f}	12.5±0.7^{d}	12.5±0.8^{d}	91.5±1.1^{c}	48.8±0.5^{c}
$B_{WF\text{-}CA\text{-}MB}$ (WF layer)	5.5±0.8^{cd}	79.8±1.2^{c}	2.4±0.4^{c}	20.8±1.1^{b}	21.1±1.1^{b}	80.73±1.0^{d}	55.4±0.5^{a}
$B_{WF\text{-}CA\text{-}MB}$ (MB layer)	13.7±0.5^{ab}	83.0±1.2^{b}	1.5±0.06^{d}	12.8±0.5^{d}	12.9±0.5^{d}	82.1±1.9^{d}	4.3±0.4^{f}

Different superscript letters in the columns indicate significant differences between the formulations ($p < 0.05$).

Table 3. Mean values ± standard deviation (SD) is reported for thickness (μm), water vapor permeability (WVP, g·mm/kPa·h·m^2), solubility (Sw, g solubilized film/g initial film), moisture content (Xw, g of water/g dry film), and water absorption capacity (Abw, g of dry film/g wet film) of the films studied.

Formulation	Thickness (μm)	WVP	Sw	Abw	Xw
M_{WF}	248.3±0.02^{f}	1.7±0.08^{a}	0.9±0.02^{a}	0.30±0.02^{a}	0.147±0.031^{a}
M_{PCL}	377.7±0.03^{d}	0.3±0.06^{e}	0.008±0.002^{f}	0.11±0.02^{c}	0.034±0.005^{d}
M_{MB}	308.0±0.03^{e}	0.7±0.02^{d}	0.07±0.051^{e}	0.07±0.04^{c}	0.051±0.010^{c}
$B_{WF\text{-}PS\text{-}PCL}$	526.6±0.03^{b}	1.1±0.04^{c}	0.52±0.02^{b}	0.19±0.05^{b}	0.087±0.015^{b}
$B_{WF\text{-}PS\text{-}MB}$	598.0±0.03^{a}	1.3±0.04^{b}	0.84±0.05^{a}	0.20±0.02^{b}	0.081±0.012^{b}
$B_{WF\text{-}CA\text{-}PCL}$	395.3±0.02^{c}	1.1±0.08^{c}	0.15±0.02^{d}	0.18±0.04^{b}	0.071±0.013^{bc}
$B_{WF\text{-}CA\text{-}MB}$	379.9±0.03^{d}	0.8±0.02^{d}	0.36±0.03^{c}	0.20±0.04^{b}	0.065±0.014^{bc}

Different superscript letters in the columns indicate significant differences between the formulations ($p < 0.05$).

Color parameters also varied, with M_{WF} showing greener, less saturated tones, while those with Mater-Bi tended to have more yellow, saturated tones. Differences in color change (ΔE) suggest significant variations in color consistency between formulations. The monolayers (M) showed more uniform gloss and color characteristics defined by the single material. At the same time, the bilayers had more significant variability in gloss and luminosity but with notable chromatic uniformity in the Mater-Bi layers., evidenced by color change (ΔE) values less than 5, which implies that color variations in these layers are insignificant and difficult to detect visually.

3.1.2 Barrier properties

The studied formulations exhibited significant differences in thickness, water vapor permeability (WVP), solubility (Sw), moisture content (Xw), and water absorption capacity (Abw), as shown in Table 3. These variations reflect important distinctions in the physical and functional properties of the films, which are critical for assessing their suitability in packaging applications. The M_{WF} formulation (monolayers composed exclusively of wheat flour) displayed the lowest thickness but showed limited performance, exhibiting the highest values of WVP and solubility. These results suggest that M_{WF} films allow moisture to pass through rapidly, potentially compromising the protection of moisture-sensitive products. Reported WVP values for wheat flour-based films typically range from 1.6 to 2 g/m^2·day, in agreement with the findings of this study (Wang et al., 2022). In contrast, the M_{PCL} formulation showed lower water vapor permeability, indicating superior barrier performance. This improvement is attributed to the hydrophobic nature of poly(ε-caprolactone) (PCL), which reduces both moisture transmission and film solubility, thereby enhancing the protection of packaged food. Meanwhile, the $B_{WF\text{-}PS\text{-}MB}$ formulation, noted for its greater thickness, presented intermediate WVP values but high solubility. This suggests that, although it functions as a moderate moisture barrier, its elevated solubility may compromise structural integrity during prolonged storage. Overall, the bilayer films incorporating PCL and Mater-Bi demonstrated superior barrier properties and lower solubility compared to wheat flour monolayers. This enhanced performance results from the complementary characteristics of the polymers: Mater-Bi, a biodegradable polymer, contributes to mechanical strength and reduced permeability, while PCL improves flexibility and mitigates solubility issues. Collectively, the results highlight the potential of these bilayer formulations to provide effective moisture control while maintaining the structural integrity necessary to extend the shelf life of packaged food products.

3.1.3 Accumulated weight loss and gain from the films

Figure 1 illustrates the accumulated water weight loss of the film formulations over time, providing insight into their dehydration behaviour. As anticipated, the hydrophilic formulations exhibited the highest weight loss due to greater initial hydration levels. Notably, the M_{WF} monolayers showed prominent water loss. In contrast, the M_{PCL} and M_{MB} monolayers retained moisture more effectively, as these materials display lower water affinity. The bilayer films demonstrated intermediate weight loss overall. Among the bilayers, those incorporating monolayers of Mater-Bi lost more moisture compared to those with PCL monolayers, which is consistent with Mater-Bi's greater water affinity than PCL. The addition of citric acid and potassium sorbate at the interface did not significantly influence this property.

In the wheat flour-containing formulations, the hydrophilic nature of starch and gluten likely facilitates water absorption, potentially explaining the observed weight loss, especially in the early stages of the experiment. Additionally, the gradual release of antimicrobial agents such as potassium sorbate and citric acid from the film interfaces could contribute to weight reduction. These water-soluble compounds may migrate to the surface and evaporate or leach under humid conditions (Xu & Li, 2023).

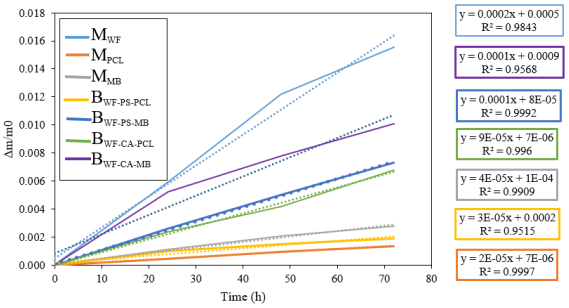

Figure 1. Cumulative weight loss of the films studied, stored at room temperature (25 °C).

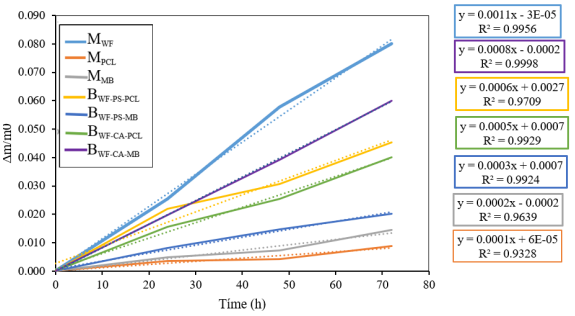

Figure 2. The cumulative weight gain of the films studied was stored at room temperature (25 °C).

Figure 2 shows the accumulated weight gain due to water absorption in the different film formulations. The monolayer made from wheat flour exhibited the highest moisture uptake, a behavior consistent with the hydrophilic nature of starch and gluten present in its composition. In contrast, the PCL monolayer showed the lowest water absorption, followed by the Mater-Bi monolayers. The bilayer films displayed intermediate values between the tested monolayers, highlighting the complementarity of the layers that compose them. This design strategy aims to combine contrasting properties: a hydrophilic layer (wheat flour) and another with lower water affinity (PCL or Mater-Bi). This distinctive feature imparts a balanced moisture response to the developed films, potentially expanding their range of applications in food packaging.

On the other hand, the coefficients of determination (R^2) of both graphs were significantly high, indicating an excellent fit of the data to the proposed linear models. A high R^2 value suggests that a considerable proportion of the variability in the data is explained by the model, implying that the selected independent variables have a significant impact on the dependent variable (Carmona-Cantillo *et al.,* 2025).

3.1.4 Internal transmittance and opacity

Figure 3 shows the UV-Vis transmittance spectra for the monolayers and bilayers studied. Significant variations in transmittance are observed between the different formulations, indicating differences in light absorption, probably due to the chemical composition

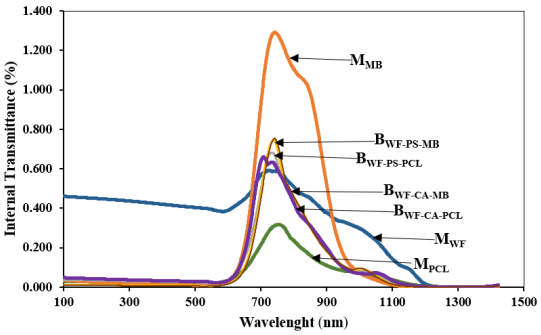

Figure 3. UV-Vis internal transmittance spectra of the different treatments.

and internal structure of the materials. M_{MB} shows a more remarkable ability to allow light to pass through, which could be desirable for applications where transparency is required, while M_{PCL} is the opaquest compared to the others. Furthermore, the other formulations have intermediate UV-Vis transmittance values. This suggests that combinations of wheat flour with additives such as sorbate and citric acid, together with biopolymers (PCL or Mater-Bi), result in materials with optical properties that fall between the high opacity of M_{PCL} and high transparency from M_{MB}. These intermediate values indicate a balance in light transmission, which can be helpful for applications requiring a moderate level of transparency or light protection. This is especially important as continuous exposure to light, particularly ultraviolet light, can compromise food quality as ultraviolet light triggers photolysis and photooxidation reactions, which generate reactive oxygen and free radicals. These compounds result in unpleasant odors and flavors, reduced nutritional value, discoloration, and generally accelerated food degradation (Ezati *et al*., 2023; Nurfani *et al*., 2021).

The opacity data presented in Figure 4 complement the UV-Vis transmittance results discussed previously. The M_{MB} formulation, which exhibited the highest transmittance peak in Figure 3, also shows the highest opacity value (6.4) in Figure 4. This apparent contradiction may be attributed to internal light scattering within the film matrix rather than surface absorption. Conversely, the M_{PCL} formulation, which showed the lowest transmittance peak, also presents a high opacity value (5.5), confirming its opaquer nature. These findings suggest that both materials limit light transmission, although likely through different optical mechanisms.

The optical properties of the films, including color and brightness (Table 1), as well as opacity (Figure 4), are complemented by representative images that allow for the correlation between numerical data and visual appearance. The M_{WF} formulation, composed exclusively of wheat flour, exhibited the lowest brightness value (14.1 ± 0.7) and a reduced L* parameter (31.1 ± 0.3), indicating a darker, matte, and

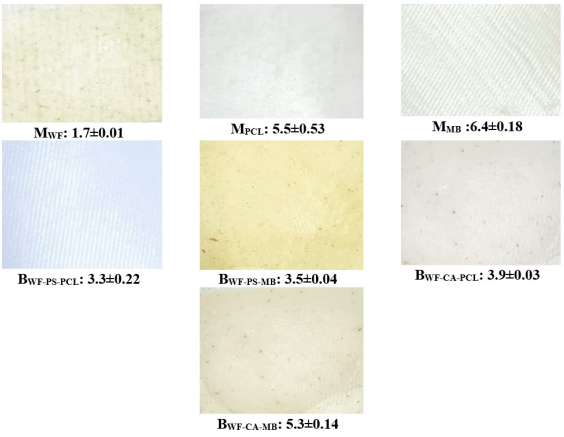

Figure 4. Film appearances from photographs and mean values and standard deviation of the opacity of the monolayer and bilayer films studied. In the bilayers, the PCL or Mater-Bi layer is observed respectively.

less uniform surface. It also showed the lowest opacity (1.7), corresponding to a clearer and more translucent appearance. In contrast, the monolayer films made of PCL and Mater-Bi (M_{PCL} and M_{MB}) displayed higher opacity values (5.5 and 6.4, respectively), along with increased lightness (L* values between 77 and 83), resulting in brighter, more reflective, and less transparent surfaces. The bilayer formulations exhibited intermediate values in both opacity and color, modulated by the combination of biopolymers and additives. Films containing citric acid ($B_{WF\text{-}CA\text{-}MB}$: 5.3 and $B_{WF\text{-}CA\text{-}PCL}$: 3.9) were opaquer than those containing potassium sorbate ($B_{WF\text{-}PS\text{-}PCL}$: 3.3 and $B_{WF\text{-}PS\text{-}MB}$: 3.5). These results demonstrate that the incorporation of wheat flour, PCL, Mater-Bi, and additives allows for the adjustment of the films' optical properties an essential feature for designing packaging materials with varying levels of transparency or light protection, depending on the specific requirements of the product (Drakos *et al*., 2018).

3.1.5 Contact angle

Table 4 shows the values of the contact angle with water and oil indicating the hydrophobicity (CAw) and lipophobicity (CAo) of the films, respectively. Hydrophobicity refers to the ability of a surface to repel water, while lipophobicity is the ability to repel oils. The results showed values less than 90°, which indicates that the films are hydrophilic (CAw) or oleophilic (CAo). This ability to attract water is due to the hydrophilic nature of the starch in wheat flour, which contains hydroxyl groups. These groups form hydrogen bonds with water, making the surface more prone to wetting (Ribero-Sanches *et al*., 2021; Wei *et al*., 2016). These results demonstrate that the contact angle is affected by surface roughness, inhomogeneity, and particle shape and size, where the contact angle values of hydrophilic materials generally decrease with

Table 4. Mean values ± standard deviation (SD) is reported of the contact angle in water (CAw, °) and contact angle in oil (CAo, °) of the monolayer and bilayer films (both sides) studied. The layer in which the determination is made is indicated in parentheses.

Formulations	CAw	CAo
M_{WF}	58.6 ± 1.5^{c}	32.3 ± 2.5^{a}
M_{PCL}	63.0 ± 1.7^{b}	10.3 ± 0.5^{f}
M_{MB}	69.3 ± 2.3^{a}	14.3 ± 1.1^{e}
$B_{WF\text{-}PS\text{-}PCL}$ (WF Layer)	43.3 ± 1.5^{f}	32.2 ± 2.08^{a}
$B_{WF\text{-}PS\text{-}PCL}$ (PCL layer)	58.7 ± 1.5^{c}	16.0 ± 1.0^{de}
$B_{WF\text{-}PS\text{-}MB}$ (WF layer)	52.3 ± 2.1^{de}	22.7 ± 0.6^{c}
$B_{WF\text{-}PS\text{-}MB}$ (MB layer)	67.3 ± 2.0^{ab}	14.7 ± 0.6^{e}
$B_{WF\text{-}CA\text{-}PCL}$ (WF layer)	49.7 ± 2.3^{e}	27.3 ± 0.5^{b}
$B_{WF\text{-}CA\text{-}PCL}$ (PCL layer)	58.6 ± 1.5^{c}	10.6 ± 1.5^{f}
$B_{WF\text{-}CA\text{-}MB}$ (WF layer)	55.3 ± 1.1^{d}	29.6 ± 1.5^{a}
$B_{WF\text{-}CA\text{-}MB}$ (MB layer)	64.7 ± 1.5^{b}	17.3 ± 1.3^{d}

Different superscript letters in columns indicate significant differences between formulations ($p < 0.05$).

increasing roughness of the surface (Gu *et al*., 2016; Balan *et al*., 2021).

The films show more significant variability regarding lipophobicity since M_{PCL} films and bilayers with PCL layers have the lowest contact angles, indicating greater lipophilicity. At the same time, formulations with wheat flour and additives (such as $B_{WF\text{-}CA\text{-}PCL}$ and $B_{WF\text{-}CA\text{-}MB}$) present higher oil contact angles, indicating more oil resistance. These differences show that the composition and structure of the films influence their interaction with liquids, which is crucial in determining their use in specific applications requiring water or oil resistance.

3.1.6 Mechanical properties

The values of the mechanical properties are shown in Table 5 and Figure 5. In general, significant variations are observed in terms of stress (TS), strain (E), and elastic modulus (EM). M_{MB} presents the highest stress (32 MPa) and an intermediate strain (350%), indicating a solid but flexible film. M_{PCL} has the highest strain (1067%), suggesting high elasticity but with lower stress than M_{MB}.

Table 5. Mean values ± standard deviation (SD) is reported for the mechanical parameters: elongation at break (E, %), tensile strength (TS, MPa), and elastic modulus (EM, MPa) of the films studied.

Formulations	TS (Mpa)	E (%)	EM (Mpa)
M_{WF}	7.6 ± 0.2^{d}	140 ± 2^{c}	27.2 ± 1.6^{f}
M_{PCL}	22 ± 2^{b}	1067 ± 22^{a}	314 ± 5^{a}
M_{MB}	32 ± 3^{a}	350 ± 5^{b}	275 ± 3^{b}
$B_{WF-PS-PCL}$	7.5 ± 0.5^{d}	90 ± 2^{d}	114.5 ± 1.5^{e}
$B_{WF-PS-MB}$	6.2 ± 0.2^{e}	140 ± 5^{c}	153.5 ± 1.4^{d}
$B_{WF-CA-PCL}$	11.1 ± 0.3^{c}	120 ± 2^{c}	106.1 ± 0.4^{e}
$B_{WF-CA-MB}$	11.5 ± 0.2^{c}	140 ± 2^{c}	174.5 ± 0.71^{c}

Different superscript letters in columns indicate significant differences between formulations ($p < 0.05$).

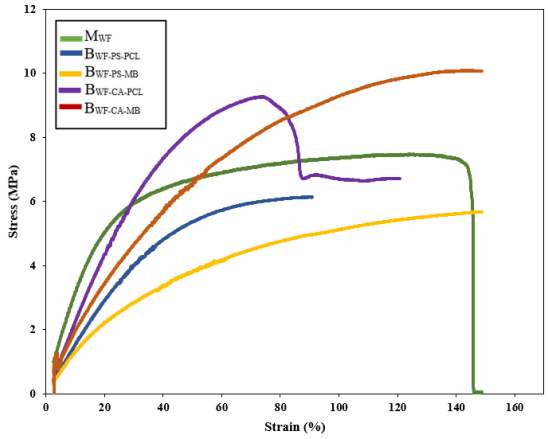

Figure 5. Stress (σ) - deformation (ε) curves of the films studied.

Regarding the bilayers, the bilayer formulations (B_{WF}) with PCL and Mater-Bi show moderate stress and deformations, with higher elastic modulus, especially in $B_{WF\text{-}CA\text{-}MB}$, which has the highest elastic modulus (174.5 MPa), indicating greater rigidity. This suggests that $B_{WF\text{-}CA\text{-}MB}$ could be suitable for applications where a rigid film is required. On the other hand, M_{WF}, with its low values in all parameters, suggests a more brittle and less flexible film, which may not be suitable for certain packaging needs.

As was expected, the WF monolayers exhibited inferior mechanical properties compared to PCL or Mater-Bi. However, when assembled into bilayers, the elastic modulus was significantly improved in all cases, along with tensile strength in those containing citric acid, though deformation capacity remained with no remarkable improvement. These findings are significant, as they illustrate how material properties can be enhanced through a straightforward methodology. The addition of citric acid at the interface appears to further improve these parameters, potentially due to a cross-linking effect exerted by this compound (Sapuła *et al.*, 2023).

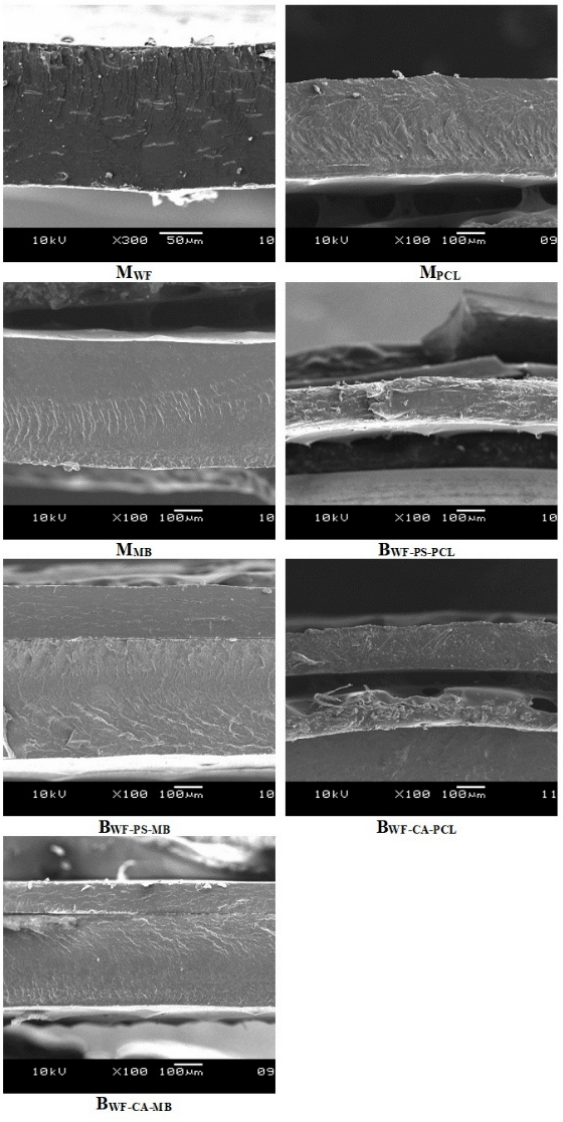

Figure 6. Cross-section SEM micrographs of the studied films.

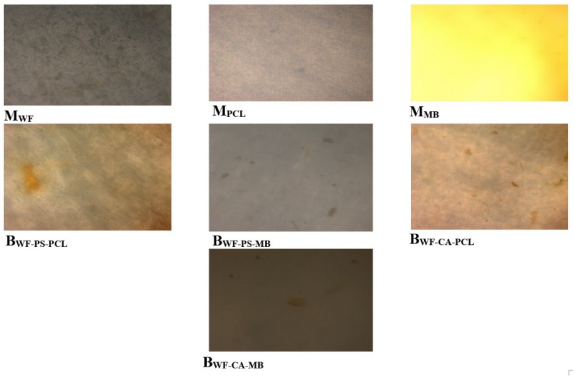

Figure 7. Surface optical micrographs (10X) of the biodegradable films studied. In the bilayers, the PCL or Mater-Bi layer is observed respectively.

3.1.7 Microstructure of the studied films

Figure 6 shows the cross-section of the mono- and bilayers analyzed by SEM. In the monolayers, the cross-sections exhibit some deformations caused by cryofracture. This is particularly evident in the cross-section of M_{PCL}, as polycaprolactone, which has an exceptionally low glass transition temperature (-61.9 °C) (Ortega-Toro *et al*., 2016), demonstrated greater resistance to cryofracture with liquid nitrogen. This same characteristic led to the detachment of bilayers containing PCL during cryofracture, both in the presence of potassium sorbate and citric acid. In contrast, the bilayers containing Mater-Bi exhibited good adhesion, as observed in both $B_{WF\text{-}PS\text{-}MB}$ and $B_{WF\text{-}CA\text{-}MB}$. This is a positive indicator for the development of bilayer materials composed of wheat flour and Mater-Bi, using citric acid and potassium sorbate as interfacial agents, as interfacial adhesion was maintained even under extremely low temperatures and mechanical stress (cryofracture conditions in the SEM technique).

Figure 7 presents optical micrographs taken at 10X magnification showing the surface of the studied biodegradable films. These micrographs allow us to observe the differences in each type of film's texture, structure, and possible surface defects.

Figure 8 presents 2.5D surface optical micrographs at 10× magnification, illustrating the topography and texture of the analyzed biodegradable films. These images reveal significant differences in surface roughness and homogeneity among the various formulations. The monolayer M_{MB} exhibits the smoothest and most homogeneous surface, suggesting high compatibility among its components. In contrast, formulations containing wheat flour, such as M_{WF}, display greater surface roughness, possibly due to the presence of particles of varying sizes, such as non-gelatinized starch, proteins (gluten), and fibers. Regarding bilayer films, $B_{WF\text{-}CA\text{-}MB}$ and $B_{WF\text{-}PS\text{-}PCL}$ demonstrate greater interfacial homogeneity, which may be attributed to the plasticizing and compatibilizing effects of citric acid (CA) and potassium sorbate (PS). These compounds may diffuse into the Mater-Bi and PCL layers during thermal pressing, promoting better integration between layers and reducing interfacial roughness. Such microstructural differences directly influence the films' physical properties, affecting characteristics such as adhesion, permeability, and mechanical performance. This highlights the relevance of surface morphology in the design of biodegradable materials for packaging applications.

M_{MB} presents the smoothest and most homogeneous surface compared to all, while formulations that include wheat flour usually show greater heterogeneity in texture. This finding is significant in the field of materials science as it provides insights into the surface properties of biodegradable films. In addition, M_{WF} presents a roughness that may be related to the presence of particles of varied sizes such as non-gelatinized starch, proteins such as gluten, and fibers (Balan *et al*., 2021).

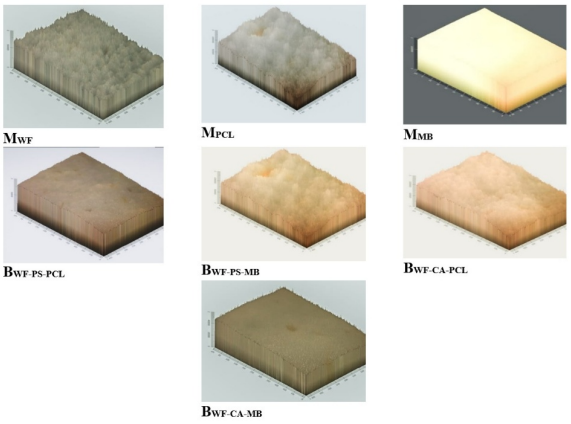

Figure 8. 2.5D (10X) surface optical micrographs of the biodegradable films studied. In the bilayers, the surface of the wheat flour monolayer is observed.

It is worth mentioning that the $B_{WF\text{-}PS\text{-}PCL}$ and $B_{WF\text{-}CA\text{-}MB}$ combinations presented greater homogeneity between the bilayers; this may be because wheat flour provides heterogeneity due to its granular structure and its combination with citric acid or potassium sorbate. It mitigates this effect since it acts as a plasticizer that helps improve the dispersion and integration of the components. The particles of different sizes may be related to non-gelatinized starch and proteins such as gluten and fibers.

3.1.8 Antimicrobial activity against Bacillus cereus

Figure 9 shows the inhibition zones of bilayer films based on wheat flour and Mater-Bi incorporated with 10% potassium sorbate against *Bacillus cereus*. Specifically, the image corresponds to the $B_{WF\text{-}PS\text{-}MB}$ film, where a clear zone is observed around the sample, indicating the inhibition of Bacillus cereus growth due to the presence of potassium sorbate. This suggests that the compound plays a significant role in microbial inhibition. The inhibition zones observed in this experiment reflect the effectiveness of the films in preventing bacterial growth, measured by the diameter of the areas where microbial proliferation was suppressed. Potassium sorbate is a preservative with antimicrobial properties (Kowalczyk *et al*., 2020), primarily used to inhibit the growth of bacteria, fungi, and yeasts (Marínez-Tenorio *et al*., 2024; Martins *et al*., 2022). Similar studies have demonstrated that incorporating 10% and 2.5% potassium sorbate into wheat gluten films plasticized with glycerol can inhibit the growth of *Aspergillus niger* and *Fusarium incarnatum*, respectively. In that study, the wheat gluten films released a significant amount of potassium sorbate when in contact with an absorbent medium, such as agar

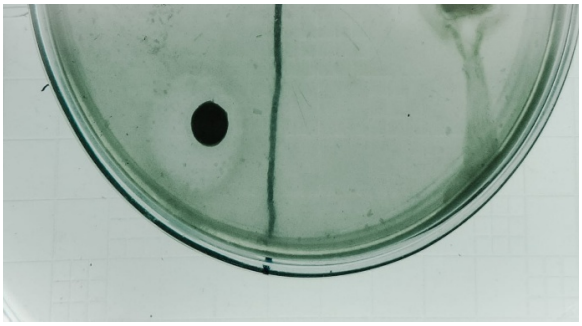

Figure 9. Inhibition zones of bilayer films based on wheat flour and Mater-Bi incorporated with 10% potassium sorbate against the bacteria *Bacillus cereus*.

Table 6. Mean values ± standard deviation (SD) is reported of the inhibition diameters against *Bacillus cereus* of the studied bilayers.

Optimal formulations	Inhibition diameter (mm)
$B_{WF\text{-}PS\text{-}PCL}$	6.0±1.4[a]
$B_{WF\text{-}PS\text{-}MB}$	5.5±0.2[a]

Different superscript letters in the columns indicate significant differences between the formulations ($p < 0.05$).

solution. This indicates that, with further development and optimization, these films could be applied as active edible packaging materials, capable of releasing the antimicrobial agent into food to help prevent the proliferation of microorganisms (Türe *et al*., 2012).

Table 6 presents the inhibition diameter values of the bilayer films studied. The results of the antimicrobial activity against *Bacillus cereus* indicate that the evaluated films exhibited a certain capacity to inhibit the growth of this microorganism, although to a limited extent. In particular, the $B_{WF\text{-}PS\text{-}PCL}$ formulation showed a larger inhibition diameter than $B_{WF\text{-}PS\text{-}MB}$. Therefore, $B_{WF\text{-}PS\text{-}PCL}$ was slightly more effective in stopping the bacteria's growth than $B_{WF\text{-}PS\text{-}MB}$. However, the higher standard deviation for $B_{WF\text{-}PS\text{-}PCL}$ suggests more variability in the measure of the inhibition zone with this formulation. In contrast, the low standard deviation of $B_{WF\text{-}PS\text{-}MB}$ indicates that the results were more uniform and consistent. On the other hand, the observed inhibition zones are relatively small, indicating that the films have a limited capacity to combat *Bacillus cereus* on the red arrow.

Conclusions

In conclusion, the study demonstrates that bilayer films made with PCL and Mater-Bi, combined with wheat flour and antimicrobial agents, present improved properties compared to wheat flour monolayers. These bilayers offer a better water vapor barrier, lower solubility and higher gloss, and more excellent color uniformity, making them more suitable for applications in biodegradable food packaging. The incorporation of PCL and Mater-Bi not only improves the functionality of the films by providing higher opacity and strength but also contributes to their potential as sustainable alternatives in the packaging industry. Therefore, these formulations represent a promising option for combining sustainability and food preservation efficacy. Future applications may include packaging for perishable goods, where enhanced barrier properties and antimicrobial activity can effectively preserve food quality. Overall, this research paves the way for innovative, eco-friendly solutions in food packaging that marry sustainability with functionality.

Funding

This research was funded by Universidad de Cartagena, Strengthening Project Act 048-2023.

Acknowledgements

Special thanks to engineer Diana Paola Carmona for her support in conducting this work.

References

Acevedo-Puello, V., Figueroa-López, K.J. and Ortega-Toro, R. (2023). Gelatin-based hydrogels containing microcrystalline and nanocrystalline cellulose as moisture absorbers for food packaging applications. *Journal of Composites Science 7(8)*, 337. https://doi.org/10.3390/jcs7080337

Aguirre, A., Borneo, R. and León, A.E. (2013). Antimicrobial, mechanical and barrier properties of triticale protein films incorporated with oregano essential oil. *Food Bioscience 1*, 2–9. https://doi.org/10.1016/j.fbio.2012.12.001

Aldas, M., Pavon, C., Ferri, J. M., Arrieta, M. P., and López-Martínez, J. (2021). Films based on Mater-Bi® compatibilized with pine resin derivatives: optical, barrier, and disintegration properties. *Polymers,* 13(9), 1506. https://doi.org/10.3390/polym13091506

Alzate, P., Gerschenson, L., and Flores, S. (2021). Study of the performance of particles based on modified starches containing potassium sorbate and incorporated into biodegradable films: Physicochemical characterization and antimicrobial action. *Chem, 3*(2), 658–671. https://doi.org/10.3390/chemistry3020046

ASTM International. *Standard Test Method for Specular Gloss*. 1999;523–89.

Avila, L.B., Pinto, D., Silva, L.F.O., de Farias, B.S., Moraes, C.C., Da Rosa, G.S. and Dotto, G. (2022). Antimicrobial bilayer film based on chitosan/electrospun zein fiber loaded with jaboticaba peel extract for food packaging applications. *Polymers 14(24)*, 5457. https://doi.org/10.3390/polym14245457

Balan, G.C., Paulo, A.F.S., Correa, L.G., Alvim. I.D., Ueno, C.T., Coelho, A.R., Stroher, G.R., Yamashita, F., Sakanaka, L.S. and Shirai, M.A. (2021). Production of wheat flour/PBAT active films incorporated with oregano oil microparticles and its application in fresh pastry conservation. *Food and Bioprocess Technology 14(8)*, 1587–99. https://doi.org/10.1007/s11947-021-02659-2

Carmona-Cantillo, D., López-Padilla, A., & Ortega-Toro, R. (2025b). Innovation in Biodegradable Composites: Wheat Flour and *Hermetia illucens* Larvae Flour Biocomposites Enhanced with Cellulose Nanocrystals. *Journal of Composites Science* 2025, Vol. 9, Page 249, 9(5), 249. https://doi.org/10.3390/JCS9050249

Cheng, S., Yin, C., Li, K., Liu, Z., Pan, Q., Zuo, X., Guo, A. and Ma, H. (2024). Preparation and characterization of probiotic *Bacillus velezensis* 906 metabolites /potassium sorbate/ polyvinyl alcohol antimicrobial blend film. *Food Bioscience 61*, 104633. https://doi.org/10.1016/j.fbio.2024.104633

Collazo-Bigliardi, S., Ortega-Toro, R. and Chiralt, A. (2019). Improving properties of thermoplastic starch films by incorporating active extracts and cellulose fibres isolated from rice or coffee husk. *Food Packaging and Shelf Life 22*, 100383. https://doi.org/10.1016/j.fpsl.2019.100383

Dong, M., Tian, L., Li, J., Jia, J., Dong, Y., Tu, Y., Liu, X., Tan, C. and Duan, X. (2022). Improving physicochemical properties of edible wheat gluten protein films with proteins, polysaccharides and organic acid. *LWT 154*, 112868. https://doi.org/10.1016/j.lwt.2021.112868

Drakos, A., Pelava, E. and Evageliou, V. (2018). Properties of flour films as affected by the flour's source and particle size. *Food Research International 107*, 551–8. https://doi.org/10.1016/j.foodres.2018.03.005

Ezati, P., Khan, A., Priyadarshi, R., Bhattacharya, T., Tammina, S.K. and Rhim, J.W. (2023) Biopolymer-based UV protection functional films for food packaging. *Food Hydrocolloids 142*, 108771. https://doi.org/10.1016/j.foodhyd.2023.108771

Gómez-Contreras, P., Hernández-Fernández, J. and Ortega-Toro, R. (2023). Obtención y caracterización de colágeno del pez de agua dulce *Prochilodus magdalenae*: aplicación en películas biodegradables. *Información Tecnológica 34(2)*, 89–98. https://doi.org/10.1016/j.ijbiomac.2021.10.075

Gu, H., Wang, C., Gong, S., Mei, Y., Li, H. and Ma, W. (2016) Investigation on contact angle measurement methods and wettability transition of porous surfaces. *Surface and Coatings Technology 292*, 72–7. https://doi.org/10.1016/j.surfcoat.2016.03.014

Guo, L., Fang, F., Zhang, Y., Xu, D., Xu, X. and Jin, Z. (2020). Effect of glutathione on gelatinization and retrogradation of wheat flour and starch. *Journal of Cereal Science 95*, 103061. https://doi.org/10.1016/j.jcs.2020.103061

Gürler, N., Pekdemir, M.E., Torğut, G. and Kök, M. (2023). Binary PCL–waste photopolymer blends for biodegradable food packaging applications. *Journal of Molecular Structure 1279*, 134990. https://doi.org/10.1016/j.molstruc.2023.134990

Hong, J., An, D., Wang, M., Liu, C., Buckow, R., Li, L., Zheng, X. and Bian, K. (2021). Wheat noodles enriched with A-type and/or B-type wheat starch: physical, thermal and textural properties of dough sheet and noodle samples from different noodle-making process. *International Journal of Food Science & Technology 56(6)*, 3111–22. https://doi.org/10.1111/ijfs.14954

Kowalczyk, D., Kordowska-Wiater, M., Karaś, M., Zięba, E., Mężyńska, M. and Wiącek, A.E. (2020). Release kinetics and antimicrobial properties of the potassium sorbate-loaded edible films made from pullulan, gelatin and their blends. *Food Hydrocolloids 101*, 105539. https://doi.org/10.1016/j.foodhyd.2019.105539

Loukri, A., Kyriakoudi, A., Oliinychenko, Y., Stratakos, A.C., Lazaridou, A. and Mourtzinos, I. (2024). Preparation and characterization of chitosan-citric acid edible films loaded with Cornelian cherry pomace extract as active packaging materials. *Food Hydrocolloids 150*, 109687. https://doi.org/10.1016/j.foodhyd.2023.109687

Martínez-Tenorio, Y., Ramírez-Corona, N., Jiménez-Munguía M.T., López-Malo, A. and Mani-López, E. (2024). Development of antifungal packaging from low-density polyethylene with essential oil of oregano and potassium sorbate. *Packaging Technology and Science 37(7)*, 641–53. https://doi.org/10.1002/pts.2813

Martins, M.P., de Sousa, R.S., Dagostin, J.L.A., Franco, T.S; de Muñiz, G.I.B. and Masson, M.L. (2022). Impact of clove essential oil and potassium sorbate incorporation on cassava starch-based films reinforced peach palm cellulose nanofibrils. *Journal of Food Processing and Preservation 46(10)*, e16867. https://doi.org/10.1111/jfpp.16867

Mohammed, A.A.B.A., Hasan, Z, Omran A.A., Elfaghi, A.M., Ali, Y.H., Akeel, N.A.A., Ilyas, R.A. and Sapuan, S.M. (2023). Effect of sugar palm fibers on the properties of blended wheat starch/polyvinyl alcohol (PVA) -based biocomposite films. *Journal of Materials Research and Technology 24*, 1043–55. https://doi.org/10.1016/j.jmrt.2023.02.027

Moreno-Ricardo, M.A., Gómez-Contreras, P., González-Delgado, Á.D., Hernández-Fernández, J. and Ortega-Toro, R. (2024). Development of films based on chitosan, gelatin and collagen extracted from bocachico scales (*Prochilodus magdalenae*). *Heliyon 10(3)*, e25194. https://doi.org/10.1016/j.heliyon.2024.e25194

Moshood, T.D., Nawanir, G., Mahmud, F., Mohamad, F., Ahmad, M.H. and AbdulGhani, A. (2022). Sustainability of biodegradable plastics: new problem or solution to solve the global plastic pollution? *Current Research in Green and Sustainable Chemistry 5*, 100273. https://doi.org/10.1016/j.crgsc.2022.100273

Muñoz-Suarez, A. M., Cortés-Rodríguez, M., & Ortega-Toro, R. (2024). Biodegradable films based on tilapia collagen (Oreochromis sp): improvement of properties with PLA and PCL bilayers with potential use in sustainable food packaging. *Revista Mexicana de Ingeniera Química,* 23(3). https://doi.org/10.24275/rmiq/Alim24326

Nurfani, E., Lailani, A., Kesuma, W.A.P., Anrokhi, M.S., Kadja, G.T.M. and Rozana, M. (2021). UV sensitivity enhancement in Fe-doped ZnO films grown by ultrafast spray pyrolysis. *Optical Materials 112*, 110768. https://doi.org/10.1016/j.optmat.2020.110768

Ortega-Toro, R., Collazo-Bigliardi, S., Talens, P. and Chiralt, A. (2016). Influence of citric acid on the properties and stability of starch-polycaprolactone based films. *Journal of Applied Polymer Science 133(2)*. https://doi.org/10.1002/app.42220

Ortega-Toro, R., Santagata, G., Gomez, G., Cerruti, P., Talens, P., Chiralt, A. and Malinconico, M. (2016). Enhancement of interfacial adhesion between starch and grafted poly(ε-caprolactone). *Carbohydrate Polymers 147*, 16-27. https://doi.org/10.1016/j.carbpol.2016.03.070

Petaloti, A.I., Makri, S., and Achilias, D.S. (2024). Bioactive edible gel films based on wheat flour and glucose for food packaging applications. *Gels 10(2)*, 105. https://doi.org/10.3390/gels10020105

Ribeiro-Sanches, M.A., Camelo-Silva, C., Tussolini, L., Tussolini, M., Zambiazi, R.C. and Becker-Pertuzatti, P. (2021). Development, characterization and optimization of biopolymers films based on starch and flour from jabuticaba (*Myrciaria cauliflora*) peel. *Food Chemistry 343*, 128430. https://doi.org/10.1016/j.foodchem.2020.128430

Rivera Leiva, A.F., Hernández-Fernández, J. and Ortega-Toro, R. (2022). Active films based on starch and wheat gluten (*Triticum vulgare*) for shelf-life extension of carrots. *Polymers 14(23)*, 5077. https://doi.org/10.3390/polym14235077

Sapuła, P., Bialik-Wąs, K., & Malarz, K. (2023). Are Natural Compounds a Promising Alternative to Synthetic Cross-Linking Agents in the Preparation of Hydrogels? *Pharmaceutics 2023, Vol. 15, Page 253*, *15*(1), 253. https://doi.org/10.3390/PHARMACEUTICS1501025

Shen, G., Yu, G., Wu, H., Li, S., Hou, X., Li, M., Li, Q., Liu, X., Zhou, M., Chen, A. and Zhang, Z. (2021). Incorporation of lipids into wheat bran cellulose/wheat gluten composite film improves its water resistance properties. *Membranes*, *12(1)*, 18. https://doi.org/10.3390/membranes12010018

Singh, R., Sharma, R., Shaqib, M., Sarkar, A., and Chauhan, K.D. Biodegradable polymers as packaging materials. (2021). In *Biopolymers and their industrial applications*. Pp. 245-259. Elsevier. https://doi.org/10.1016/B978-0-12-819240-5.00010-9

Stoica, M., Bichescu, C.I., Crețu, C. M., Dragomir, M., Ivan, A.S., Podaru, G.M., ... and Stuparu-Crețu, M. (2024). Review of bio-based biodegradable

Polymers: smart solutions for sustainable food packaging. *Foods 13(19)*, 3027. https://doi.org/10.3390/foods13193027

Suárez-Castillo, G. M., Salcedo-Guadalupe, J. G., Contreras-Lozano, K. P., Rangel-Pérez, M. G., Cervera-Ricardo, M. A., & Figueroa-Flórez, J. A. (2024). Increase in the degree of substitution of cassava starches by dual modification processes. *Revista Mexicana de Ingeniera Quimica*, 23(3). https://doi.org/10.24275/RMIQ/POLY24303

Thakur, M., Majid, I., Hussain, S. and Nanda, V. (2021). Poly (ε-caprolactone): a potential polymer for biodegradable food packaging applications. *Packaging Technology and Science 34(8)*, 449-461. https://doi.org/10.1002/pts.2572

Türe, H., Gällstedt M. and Hedenqvist, M.S. (2012). Antimicrobial compression-moulded wheat gluten films containing potassium sorbate. *Food Research International 45(1)*, 109–15. https://doi.org/10.1016/j.foodres.2011.10.012

Wang, J., Sun, X., Xu, X., Sun, Q., Li, M., Wang, Y. and Xie, F. (2022). Wheat flour-based edible films: effect of gluten on the rheological properties, structure, and film characteristics. *International Journal of Molecular Sciences 23 (19)*, 11668. https://doi.org/10.3390/ijms231911668

Wei, B., Sun, B., Zhang, B., Long, J., Chen, L. and Tian, Y. (2016). Synthesis, characterization and hydrophobicity of silylated starch nanocrystal. *Carbohydrate Polymers 136*, 1203–8. https://doi.org/10.1016/j.carbpol.2015.10.025

Xu, J., & Li, Y. (2023). Wheat glutenbased coatings and films: preparation, properties, and applications. *Journal of Food Science*, *88*(2), 582–594. https://doi.org/10.1111/1750-3841.16454;WGROUP:STRING:PUBLICATION

Vol. 24, No. 3(2025) Alim25628
Revista Mexicana de Ingeniería Química

Impact of modulation of solar irradiance on spinach drying and its effects on bioactive compounds and quality

Impacto de la modulación de la irradiancia solar en el secado de espinacas y sus efectos sobre los compuestos bioactivos y la calidad

D.P. García-Moreira[1]*, I. Moreno[1], L. Delgadillo-Ruiz[2], E. C. López-Vidaña[3]*
[1]Unidad Académica de Ciencia y Tecnología de la Luz y la Materia, Universidad Autónoma de Zacatecas, 98160, Zacatecas, Mexico.
[2]Unidad Académica de Ciencias Biológicas, Autónoma de Zacatecas, 98000, Zacatecas, Mexico
[3]CONAHCYT-Centro de Investigación en Materiales Avanzados S.C., Calle CIMAV 110, Ejido Arroyo Seco, 34147, Durango, Mexico.
Sent date: July 11, 2025; Accepted: october 7, 2025

Abstract
This study investigated spinach's drying kinetics, colorimetric degradation, Antioxidant Capacity and Total Phenolic Content using two solar dryers: Cylindrical Solar Dryer and a novel Solar Dryer with Dynamic Irradiance Control. The parameters monitored were moisture content, temperature, relative humidity, solar irradiance, and CIELa*b* color coordinates. The Solar Dryer with Dynamic Irradiance Control achieved a final moisture content of 0.030 g H_2O/g d.m. in 220 minutes, while the Cylindrical Solar Dryer reached equilibrium in 160 minutes. The Solar Dryer with Dynamic Irradiance Control exhibited a maximum drying rate of 0.1346 g H_2O/g d.m. min^{-1} and demonstrated superior control over drying conditions, mitigating thermal losses and preserving color quality. The Cylindrical Solar Dryer showed faster drying but greater color degradation, particularly in the b* coordinate. Chemical analyses revealed that SDIC-dried spinach retained significantly higher antioxidant activity (1686.34 ± 42.98 μmol Eq Trolox/g d.w. by ABTS) compared to CSD (1419.00 ± 50.79), despite CSD showing elevated total phenolics (62.541 ± 1.76 mg GAE/100 g) likely due to oxidative degradation. These findings highlight SDIC's potential to balance drying efficiency with phytochemical preservation in photosensitive crops. These findings highlight the potential of the Solar Dryer with Dynamic Irradiance Control for preserving the quality of photosensitive crops like spinach, offering a sustainable solution for food preservation in semi-arid regions.
Keywords: Food Colorimetry, Solar Drying, Solar Irradiance modulator, Spinach drying, PDLC applied in solar drying.

Resumen
Este estudio investigó la cinética de secado, la degradación colorimétrica, la capacidad antioxidante y el contenido fenólico de las espinacas utilizando dos secadores solares: Secador Solar Cilíndrico y un novedoso Secador Solar con Control Dinámico de Irradiancia. Los parámetros monitoreados fueron el contenido de humedad, la temperatura, la humedad relativa, la irradiancia solar y las coordenadas de color CIELa*b*. El secador solar con control dinámico de la irradiancia alcanzó un contenido final de humedad de 0,030 g H_2O/g d.m. en 220 minutos, mientras que el secador solar cilíndrico alcanzó el equilibrio en 160 minutos. El Secador Solar con Control Dinámico de la Irradiancia exhibió una velocidad de secado máxima de 0,1346 g H_2O/g d.m. min-¹ y demostró un control superior sobre las condiciones de secado, mitigando las pérdidas térmicas y preservando la calidad del color. El secador solar cilíndrico mostró un secado más rápido pero una mayor degradación del color, especialmente en la coordenada b* (verde). Los análisis químicos revelaron que las espinacas secadas con SDIC conservaban una actividad antioxidante significativamente mayor (1686,34 ± 42,98 μmol Eq Trolox/g p.c. por ABTS) en comparación con las secadas con CSD (1419,00 ± 50,79), a pesar de que el CSD mostraba unos fenoles totales elevados (62,541 ± 1,76 mg GAE/100 g) probablemente debido a la degradación oxidativa. Estos resultados demuestran el potencial del SDIC para equilibrar la eficacia del secado con la conservación de los fitoquímicos en cultivos fotosensibles. Estos resultados muestran el potencial del secador solar con control dinámico de la irradiancia para preservar la calidad de cultivos fotosensibles como las espinacas, ofreciendo una solución sostenible para la conservación de alimentos en regiones semiáridas.
Palabras clave: Colorimetría de alimentos, Secado solar, Modulador de irradiancia solar, Secado de espinacas, PDLC aplicado en secado solar.

*Corresponding author. *E-mail*: erick.lopez@cimav.edu.mx;
https://doi.org/10.24275/rmiq/Alim25628
ISSN:1665-2738, *issn-e*: 2395-8472

1 Introduction

Drying is critical for preserving food, reducing post-harvest losses, and extending shelf life. Traditional drying methods, such as sun and hot air often lead to significant color quality degradation, particularly in photosensitive crops like spinach (Guiné, 2018). Spinach (*Spinacia oleracea L.*) is a global widely consumed leafy vegetable, with global production reaching 65.8 million tons in 2023, of which Mexico contributed 40,924 tons (FAOSTAT, 2024). When the harvest is high, farmers have to sell produce at very low prices on the day of harvest because the high moisture content of fresh vegetables can lead to rapid deterioration of product quality, including microbiota growth. As a result, farmers suffer large losses. However, these losses can be reduced by drying the material to a safe moisture content, which can be achieved by advanced processing techniques (Nahar, 2009). In addition, dried products have the advantage of reducing packaging, shipping, and storage costs due to weight and volume reduction. Food drying is a complex process involving mass and energy transfer in the system. Drying is considered one of the most energy-intensive processes in industrial conversion processes due to the interaction between water molecules and the biopolymer matrix and the increased enthalpy of vaporization when the moisture content of the product is low. Therefore, various physicochemical and structural changes of thermal origin occur during drying, which often negatively affects the final product quality (Vargas, Kapoor, Nemzer, & Feng, 2022).

Over the years, various drying techniques have been developed and tested to enhance quality retention of the dried product and improve drying efficiency. Among different drying technologies, hot air drying, spray drying, freeze drying, and that can deliver significantly improved quality have often been investigated for the selection of the right drying method for a target product concerning product quality, production costs, and recently, process sustainability and low carbon footprint.

The spinach (*Spinacia oleracea L.*), is leave from the family Chenopodiaceae and is consumed around the world for its important nutritional composition. Spinach array of phytonutrients and bioactive compounds like β-carotene, lutein, zeaxanthin, ascorbic acid, flavonoids, andpolyphenols (Manzoor, *et al*., 2020). Spinach is commonly used as raw material for the development of different products, so a drying process that maintains its properties and quality results in a quality final product since the quality of the ingredients is essential for the result. Examples of this are Waseem *et al*. (2021), who investigated the physicochemical and bread-making features of drying spinach (Waseed, *et al*., 2021) and Galla *et al*. (2017), who developed Biscuits by spinach powder (Galla, Pamidighantam, Karakala, Gurusiddaiah, & Akula, 2017).

However, the drying process always impacts the quality of dried product; in the case of solar drying, green products, such as leaves, are degraded in color as they are exposed to sunlight for a long duration (Aravindh & Sreekumar, 2015). Notwithstanding Visual inspection is the first step in food selection. Consumers use color to make rapid judgments about a product's freshness, sensory properties (e.g., flavor intensity), and overall acceptability before purchase or consumption (Spence , 2015). Mulokozi and Svanber (2003) studied the effect of Open Sun-Drying and Solar Cabinet Drying on Green Leafy Vegetables, and they found that the amount of all-trans-β-carotene in traditionally treated vegetables was highly reduced by open-sun drying. In contrast, significantly higher retentions were obtained in solar-dried vegetables (Mulokozi & Svanber , 2003). Pal and Acedo Jr studied drying tomato, onion, cabbage, and spinach in a simple solar dryer with a rotary chimney and a tunnel type with a transparent polyethylene cover and black polyethylene cover, and they concluded that the black polyethylene cover was effective in maintaining the green color of dried spinach. However, the vitamin C content as nutritional indicator decreased in the dried products (Pal & Acedo Jr, 2022). Vargas *et al*. (2022) studied the color change in spinach dried in different drying methods: hot air drying, freeze drying and refractance window drying. They concluded that the drying method could have a highly important effect on chemical content and the type of vegetable and species. The color results showed that hot air drying decreased the Luminosity more than other methods. However, hot air drying was the method that did not traverse its b*-coordinate to the yellow color, as did the other methods mentioned above (Vargas, Kapoor, Nemzer, & Feng, 2022).

Traditional solar drying systems often struggle to preserve the quality of photosensitive crops such as spinach due to uncontrolled solar irradiance and uneven drying conditions. While simple covers can reduce light exposure, a dynamic control system offers a more flexible and potentially precise solution. It can be tuned to an optimal irradiance level for different products and adjusted throughout the day to compensate for changing solar intensity, something a static cover cannot do. To overcome these challenges, this study proposes a novel Solar Dryer with Dynamic Irradiation Control (SDIC), with propose to regulate irradiance levels and ensure consistent drying conditions, thereby minimizing quality degradation. The primary objective of this research is to explore the drying characteristics of spinach leaves under controlled solar drying conditions, with a focus on developing drying curves, quantifying colorimetric degradation, and analyzing the influence of solar irradiation intensity. Two solar

drying systems are employed: the SDIC, which utilizes a PDLC film capable of adjusting its transmittance based on input voltage to limit irradiance to 700 W/m^2, and a Cylindrical Solar Dryer (CSD), both maintained at a constant temperature of 50 °C. By systematically evaluating the effects of drying parameters on the quality and photosensitivity of spinach leaves, this study seeks to advance the optimization of solar drying systems for high-value agricultural products.

2 Materials and methods

2.1 Raw material

Spinach (*Spinacia oleracea L.*) was obtained from a local market in Guadalupe, Zacatecas, Mexico, in May 2024. The leaves were washed with 0.05% chlorinated water and stored at 20 °C for a day before experimentation. Before drying, its initial moisture content was determined using a moisture analyzer (Ohaus MB25) at 105 °C. The initial properties of the spinach are summarized in Table 1.

Table 1. Initial properties of spinach.

Initial properties	
Moisture content	3.69 g H_2O / g d.m.
Color Parameter	
L	38.50
a*	-8.61
b*	9.79
Total absorbic content	48.49 mg/100 g FW

2.2 Description of the solar dryers

The experiments were realized in two solar dryers: The Solar Dryer with Dynamic Irradiation Control (SDIC) and Cylindrical Solar Dryer (CSD). The SDIC is designed to regulate heat and sunlight entering its drying chamber using a smart film (PDLC film) and a control mechanism. The CSD shares similar structural features with the SDIC but cannot control solar radiation. Both dryers consist of a horizontally mounted transparent acrylic cylinder measuring 0.8 meters in length, 0.45 meters in diameter, and 0.006 meters in thickness. Each unit is equipped with DC 12V fans, 0.08 meters in diameter, operating at 4000 RPM, installed at the front and rear air openings. The internal drying chamber has a volume of 0.001800 cubic meters, and the system includes two racks arranged across six levels of trays, offering a total drying area of 0.5544 square meters. These designs are depicted in Figure 1.

Figure 1. SDIC (left side) and CSD (right side).

2.3 Moisture content

For the drying experiments, approximately 300 grams of spinach were distributed across each of the four trays in both SDIC and CSD. The weight of the samples was recorded at 20-minute intervals until the change in weight was less than 0.2 grams over that period, indicating that the final moisture content under the specified drying conditions had been achieved. The moisture content was calculated using the following formula (Zhu & Shen, 2014):

$$M_{db} = \frac{W_w}{W_d} \tag{1}$$

where M_{db} is the moisture content on dry basis, expressed as the ratio of water mass (W_w) to the weight of dry material (W_d).

2.4 Drying rate

The drying rate represents the rate at which moisture is extracted or eliminated from the product at a specific moment. This parameter is defined as (Wang, Li, Emam Hassanien, Wang, & Yang, 2018):

$$Dr(t) = -\frac{dMc(t)}{dt} \tag{2}$$

2.5 Color change

During the drying process of spinach, the drying color parameters were registered every 20 minutes. The measuring instrument was a CR30 colorimeter manufactured by Hangzhou Zhongse Technology Co., Ltd., which was calibrated in the CIELa*b* color space, expressed in L (light-dark), a* (red-green) and b* (yellow-blue). Also, to visually record color changes during the drying process, photographs were taken with a camera Nikon D5100 at the same lighting level and distance from the camera in box light to maintain the same color perception as possible. Hue and Chroma

were calculated following the equations:

$$Hue = \tan^{-1}\left(\frac{b*}{a*}\right) \quad (3)$$

$$Chroma = \sqrt{\left(a*^2 + b*^2\right)} \quad (4)$$

The color difference ΔE of the randomly selected samples was calculated using the following equation.

$$\Delta E = \sqrt{(\Delta L*)^2 + (\Delta a*)^2 + (\Delta b*)^2} \quad (5)$$

Where, $\Delta L^*= L*_o - L*_f$, $\Delta a^* = a*_o - a*_f$ and $\Delta b^*= b*_o - b*_f$, comparing color parameters between raw ($_o$) and dried sample ($_f$).

2.6 Antioxidant capacity by ABTS method and DPPH

Following the protocol outlined by García-Moreira *et al*. (2025), an ABTS solution was prepared at a concentration of 2 mM. The radical cation was generated by reacting this solution with potassium persulfate at 70 mM. The resulting ABTS solution was then diluted using a phosphate buffer (pH 7) until its absorbance reached 0.700 ± 0.02 at a wavelength of 734 nm. Subsequently, 10 μL of papaya residue extract was added to 990 μL of the ABTS working solution. After an incubation period of six minutes at ambient temperature, the absorbance was recorded to evaluate antioxidant activity (García-Moreira, López-Vidaña, Moreno, & Delgadillo-Ruiz, 2025). A solution of Trolox in absolute methanol in the range of 0 to 0.0008 μM was used to obtain calibration curves. The absorbance was measured at 630 nm in an Elisa microplate reader (Termo Scientific). Results were expressed as TEAC (Trolox equivalent activity (μM/100 g sample fresh weight of sample) (Álvarez - Parrilla, De la Rosa, Martínez, & González, 2007).

For DPPH, a solution of DPPH (SIGMA) was prepared in reagent grade methanol with absorbance equal to one (1.00 A) at 480 nm. To 20 μL of each sample 280 μL of the prepared DPPH solution was added and after 30 min in the dark the absorbance at 480 nm was measured in an ultraviolet visible spectrophotometer (Chew and Lim, 2008). For the calibration curve, Trolox solution was used from which seven concentrations from 0 to 0.0008 μM in absolute methanol were prepared. Expressed as TEAC (Trolox equivalent capacity) (Chew, Lim, Omar, & Khoo, 2008).

2.7 Total phenolic content

Total flavonoids were determined based on the method of Zhishen *et al*. (1999). In a microcentrifuge tube, 100 μL of the extracts were mixed with 40 μL of distilled water, then 30 μL of 5% NaNO3 were added and left to react for five minutes. Subsequently, 30 μL of 10% AlCl3 was added. The mixture was left to react for 6 min and then 200 μL of 1 N NaOH was added. Then 240 μL of distilled water was added and 300 μL of this mixture was transferred to the Elisa plate. The absorbance was measured at 510 nm in an Elisa microplate reader (Termo Scientific). Catechin in 80% methanol was used to obtain calibration curves in the range of 0 to 0.6 mg/mL. Results were expressed in mg/mL (Zhishen , Mengcheng, & Jianming, 1999).

2.8 Tannin content

According to the method of Amarowicz and Pegg (2006), 50 μL of each extract was placed in triplicate on a polystyrene Elisa plate. Afterwards, 250 μL of the prepared HCI 8% and vanillin 1% (1:1) mixed solution was added in 50 μL at a time to complete 250 μL. For the blank, a solution of 50 μL of methanol plus 250 μL of 4% HCI was prepared. A calibration curve for catechin in absolute methanol was prepared at concentrations of 0.8, 0.6, 0.4, 0.2, 0.1 mg/mL. The assay was read at 492 nm. The results were expressed as mg/mL (Amarowicz & Pegg, 2008).

2.9 Operating conditions

Both dryers operated at a constant temperature of 50 °C and were equipped with DC 12V fans (4000 RPM) to ensure uniform airflow. Approximately 300 grams of spinach leaves were evenly distributed across four trays in each dryer, with sample weights recorded at 20-minute intervals. Color parameters (L, a*, b*) were measured every 20 minutes using a CR30 colorimeter, and visual documentation was performed with a Nikon D5100 camera under consistent lighting. Under typical regional solar conditions, the experiments took place in May 2024 in Zacatecas, Mexico (22.785835, -102.616187).

A paired experimental design was employed. The drying experiments for each dryer (SDIC and CSD) were conducted simultaneously on the same day using spinach from the same batch to ensure direct comparability under identical external environmental conditions. This single, paired run was performed with all measurements (drying kinetics, color, bioactive compounds) conducted in triplicate (n=3). This approach is standard for initial comparative studies of novel drying systems. We acknowledge that replication across multiple days is a recommended step for future validation and scaling.

The temperature, solar irradiance, and relative humidity were measured every 5 minutes by the control system in both dryers. A portable meteorological system also recorded the environmental conditions and placed next to solar dryers every 5 minutes.

Figure 2. Drying experiment of spinach.

3 Results and discussion

The drying process was conducted at a constant temperature of 50 °C in both dryers with an exhaust fan. The SDIC maintained an irradiance level of 700 W/m^2, while the CSD operated under unrestricted solar irradiation. The irradiance was limited to 700 W/m^2 in the SDIC as this value represents a high but sub-maximal solar irradiance level common in semi-arid regions like Zacatecas. The goal was to evaluate the dryer's performance under a high-stress scenario that is still below peak radiation levels (which can exceed 1000 W/m^2). Figure 2 illustrates the experimental setup.

3.1 *Moisture ratio and drying rate*

During drying, the environment temperatures ranged from 30.6 to 33.3 °C and solar radiation from 1038 to 666 W/m^2. Relative humidity remained between 22 and 18 %, and wind speeds of up to 3 m/s were maintained (Figure 3).

The drying process in the SDIC dryer (Figure 4b) took 220 minutes (12:25 to 16:05 h), with an initial moisture content of 3.6 g H_2O / g d.m., until reaching a final moisture content of 0.030 g H_2O / g d.m. During this process, a maximum drying rate of 0.1346 g H_2O / g d.m. min^{-1} was presented in the first time interval, where the moisture content had a drop to 0.07 g H_2O / g d.m. The drying conditions that were presented during the process were a maximum solar irradiance of 710 W/m^2. and a minimum of 500 W/m^2; the relative humidity between ranged from 20 - 40 %. When the relative humidity increases, the air velocity of the exhaust fan increases due to the control system commands the fan to increase speed depending on the signal it receives from the temperature and relative humidity sensor, and the speed of the exhaust fan continues to oscillate according to the temperature of the hot and humid air inside the drying cabin (Figure 4a). Yamakage *et al.* (2021) reported a similar drying time, 210 minutes, where they dried spinach under hot air drying at 50 °C, and with a pretreatment of a pulsed electric field with that of hot water.

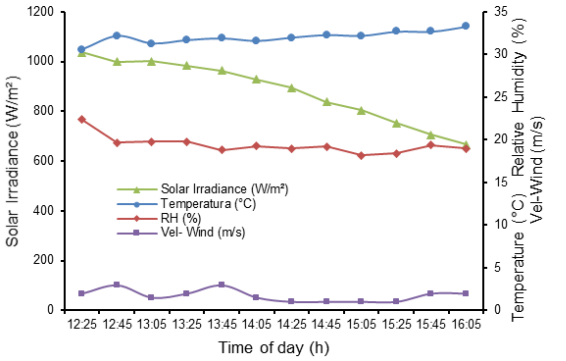

Figure 3. Environmental conditions during the drying process.

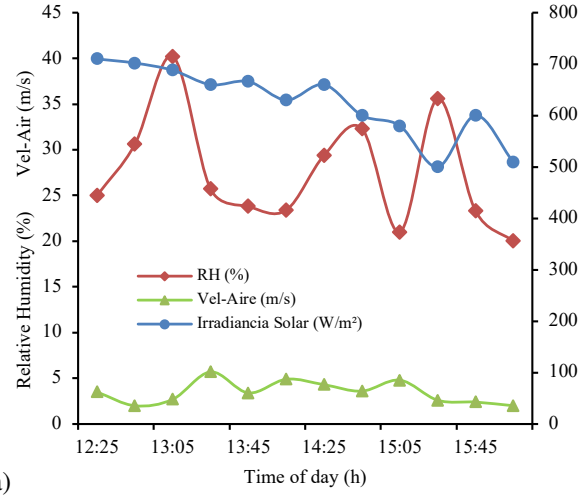

a)

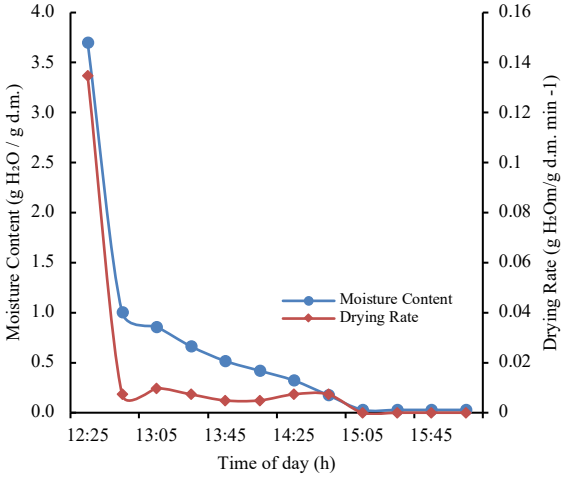

b)

Figure 4. a) Drying conditions and b) Drying kinetics and Drying Rate in SDIC.

In the case of CSD (Figure 5a), the spinach reached equilibrium after 150 minutes (12:25 to 15:05 h), one hour before than SDIC. In its drying conditions, the maximum irradiance inside the cabin was 1002 W/m^2, relative humidities of 18 - 51 %, and an exhaust air velocity of 2 - 7.7 m/s. The peak in relative humidity is since after the fast drop in the moisture content of the spinach, the moisture in the hot air increased, the exhaust fan played a critical role in regulating internal

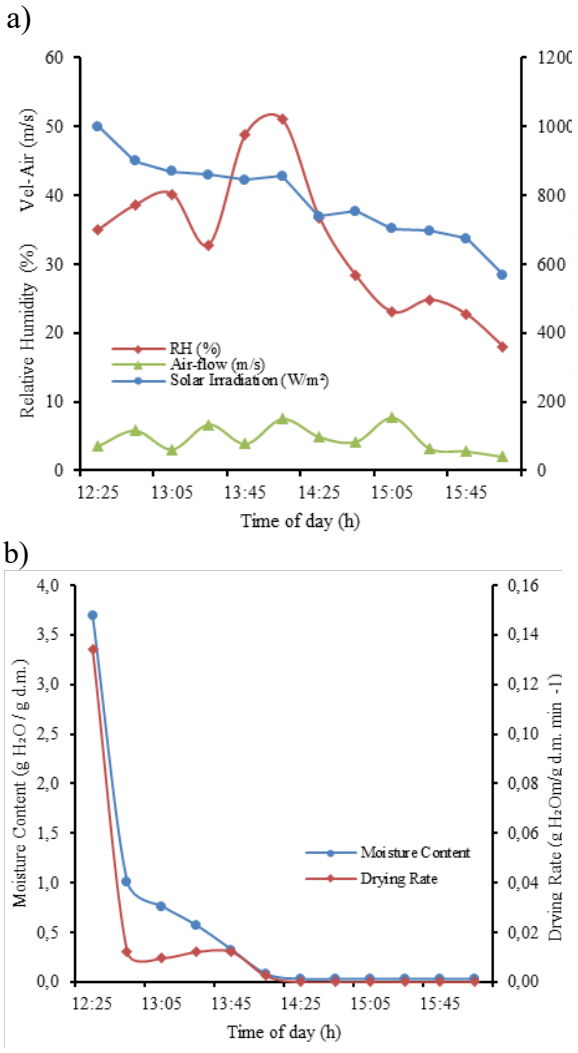

Figure 5. a) Drying conditions and b) Drying kinetics and Drying Rate in CSD.

humidity levels by expelling hot and humid air from the drying chamber. To achieve optimal drying conditions, the air velocity of the exhaust fan was adjusted based on real-time sensor data (Figure 5b).

3.2 *Color change*

In most green fruits and vegetables, color degradation after harvest is manifested by chlorophyll loss and synthesis of carotenoid pigments, resulting in progressive change from green to brown (Krokida, Tsami, & Maroulis, 1998). Color is a crucial organoleptic characteristic that directly influence the consumer choice (Gutiérrez-Martínez, *et al*., 2024). The color degradation that occurred during the drying process is shown in Table 1. In this, we can observe that the cylindrical solar dryer shows a decrease in the green color because the b* coordinate decreased by 8 units (Table 2). However, the luminosity decreases by 3 units, so it does not show a darkening. The solar dryer with dynamic irradiance control presented a decrease in the b* coordinate of 6 units, so it is perceived to maintain part of its characteristic green color. On the other hand, the luminosity decreased by 10 units, showing darkening because the drying process was longer than the cylindrical solar dryer.

Despite this, it has been shown in previous studies that when spinach is subjected to a thermal process it presents a decrease in all its colorimetric parameters, especially in the b* coordinate (Vargas, Kapoor, Nemzer, & Feng, 2022). Moreover, even more, it is affected when it is exposed to solar radiation, this is also exposed in the study of Mulokozi and Svanberg, where they dried spinach under different methods, including solar drying and sun drying, and showed that the greatest degradation of spinach properties was under the sun drying process (Mulokozi & Svanber , 2003). Thus, this confirms the importance of regulating solar irradiance in food.

Table 2. Color shift during the drying process.

SDIC							CSD					
Time	L	a*	b*	Δ*E*	Hue	Chroma	L	a*	b*	Δ*E*	Hue	Chroma
12:25	38.5	-8.6	9.7	0	-48.6	13	44.5	-10.8	17.1	0	20.3	-57.7
12:45	39.6	-5.5	12.7	4.4	-66.5	13.9	43.9	-7.1	15.7	4	17.3	-65.7
13:05	40.1	-4	10.9	5	-69.8	11.6	49	-7	20.8	6.9	22	-71.4
13:25	42.5	-5.7	13.9	6.5	-67.7	15	47.9	-5,9	17.9	5.9	18.8	-71.6
13:45	36.2	-4.1	11.4	5.2	-70	12.1	50.2	-0.4	16.5	11.9	16.5	-88.5
14:05	42.8	-2.9	13.7	8.2	-78.1	14	47.8	-0.2	13.8	11.6	13.8	-89
14:25	32	-1.5	8	9.7	-79.3	8.1	51.6	0	14	13.3	14	89.9
14:45	29.1	-0.4	4.4	13.4	-83.8	4.4	40.5	4	9.6	17.2	10.4	67
15:05	28.6	0.9	3.4	15.1	74.7	3.5	45.8	1.4	11.4	13.5	11.5	83
15:25	27.8	-1	3.8	14.3	-75.4	3.9						
15:45	30.9	-1.7	4.9	11.3	-70.4	5.2						
16:05	29.9	1.3	5.2	13.9	75.6	5.3						

Yamakage *et al*. (2021) quantified the color change in spinach drying at 50 °C, and with the drying parameters controlled, they found 5.1 units of Color Difference, keeping its characteristic green color due to they got +0.35 difference in –a* coordinate to the final color (Yamakage, *et al*., 2021). Kaur *et al*. (2007) dried spinach by sun drying and decreased 12 units in L coordinate, 6.25 in a* coordinate, and 8 in b* coordinate. These results are similar to CSD due to the drying being under full solar irradiance, a different case in SDIC, where it was only 6 units for b* (Kaur, Kaur, Oberoi, Gill, & Sogi, 2008).

The SDIC samples exhibited a notable evolution in both hue angle and chroma over the extraction time. Initially, the hue angle was negative, indicating a dominant greenish-yellow character (a* < 0, b* > 0), with values ranging from approximately -48.67° to -83.80°. This was followed by a distinct shift towards positive values (74.76° to 75.60°), signifying a transition to a reddish-yellow hue as extraction progressed. Concurrently, chroma values, representing color saturation, demonstrated a general decreasing trend from a maximum of 15.07 to a minimum of 3.58. This indicates a gradual loss of color intensity and a movement towards a duller, less saturated appearance, likely attributable to the continued leaching of compounds and potential oxidation throughout the extended brewing period.

The CSD samples displayed a more pronounced and consistent chromatic shift compared to SDIC. The hue angle began strongly negative (-57.73°), confirming a green-yellow profile, and progressed rapidly towards neutral and then positive values, culminating at 83.01° and 67.05° in the later stages. This clear progression reflects a significant reduction in greenness (a* moving from highly negative to positive) and a strengthening of yellowness and redness. Chroma values for CSD started higher than SDIC (reaching 22.03) but showed a marked and steady decline over time to a final value of 11.51, indicating a substantial loss of color vibrancy. This suggests that the steeping process initially extracts highly saturated compounds, which then degrade or precipitate, leading to a significant fading of color intensity as the contact time increases.

Figure 6 illustrates the shift in color coordinates for spinach dried using SDIC and CSD methods, measured in the CIELa*b* color space. The SDIC method maintained higher L values (lightness) and showed a slower shift in a* values towards positive (greenness loss) compared to CSD. In contrast, CSD exhibited a faster decrease in L and a more rapid shift in a* to positive values, indicating faster darkening and greenness degradation. Overall, the CIELAB data quantitatively demonstrates that SDIC facilitates better color preservation in dried spinach than CSD, evidenced by superior retention of lightness and greenness attributes over the drying period. The non-

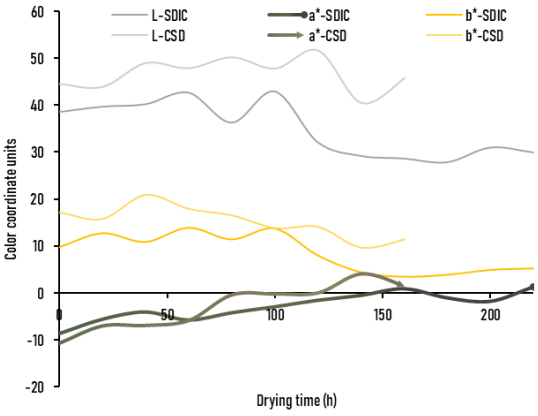

Figure 6. Color coordinate shift.

monotonic behavior of L* is a known phenomenon in food drying. The initial increase can be caused by light-scattering from surface moisture loss or migration of compounds, while subsequent darkening is due to Maillard reaction and pigment concentration.

The total color difference (ΔE) provides a comprehensive metric for evaluating overall visual change, effectively overcoming the inherent variability in the initial color of the biological samples. A higher ΔE value indicates a more pronounced deviation from the original fresh state. Throughout the drying process, the CSD samples consistently exhibited higher ΔE values compared to the SDIC samples (e.g., 17.2 vs. 13.4 at 14:45 h). This significant difference demonstrates that spinach dried under uncontrolled, full irradiance underwent a more drastic and visually apparent color transformation.

The accelerated rate of ΔE increase in the CSD correlates with its higher operating irradiance and temperature, which drive faster degradation of chlorophyll and promote non-enzymatic browning reactions. Conversely, the SDIC's regulated irradiance resulted in a slower, more controlled increase in ΔE, confirming its superior efficacy in minimizing overall visual degradation and better preserving the spinach's original color characteristics.

Figure 7 visually represents the color degradation of spinach leaves during solar drying using two distinct methods: CSD and SDIC. The figure displays photographs of spinach leaves at various intervals, ranging from 12:25 to 16:05, documenting the progressive color change throughout the drying process. A color bar in (b) provides a visual gradient of the color evolution under the SDIC method. Across both drying methods, a clear visual shift from a vibrant green to a less intense, more brownish, or yellowish hue is evident as drying time increases. This figure illustrates the dynamic nature of color degradation in spinach under solar drying and facilitates a visual comparison of the color preservation efficacy of the CSD and SDIC techniques.

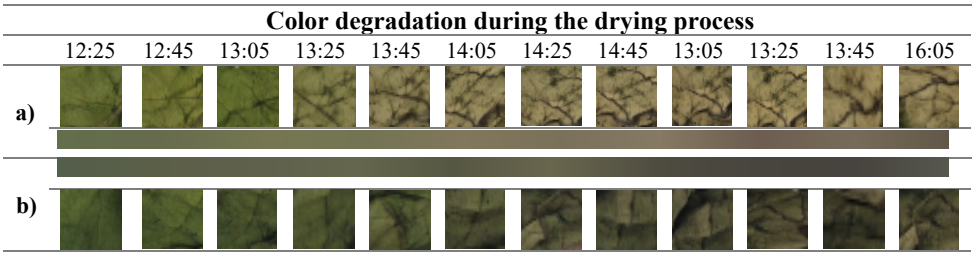

NOTE* a): Spinach dried in CSD; b) Spinach dried in SDIC.

Figure 7. Color degradation during the drying process.

Table 3. TEAC/g, ABTS, and DPPH antioxidant activity values obtained from dried spinach in SDIC and CSD.

Method	ABTS (μmol Eq Trolox/g d.w.)	DPPH (μmol Eq Trolox/g d.w.)	TEAC/g
SDIC	1686.34 ± 42.98	89.292 ± 0.667	0.575 ± 0.005
CSD	1419.00 ± 50.79	82.033 ± 3.663	0.458 ± 0.030

NOTE* Data expressed as average standard deviation (n = 3).

Table 4.Phenols, Flavonoids and Tannins content values obtained from dried spinach in SDIC and CSD.

Method	Total phenols (mg gallic acid equivalent/100 g sample ±DE)	Flavonoids content (mg/mL ± DE)	Tannins content (mg/mL ± DE)
SDIC	39.774 ± 0.70	0.066 ± 0.007	6.574 ± 0.446
CSD	62.541 ± 1.76	0.202 ± 0.014	14.965 ± 2.450

NOTE* Data expressed as average standard deviation (n = 3).

3.3 Antioxidant capacity and phenolic content

The antioxidant capacity and phenolic composition of spinach dried under the two solar drying systems (SDIC and CSD) revealed significant differences, highlighting the impact of irradiance control on phytochemical preservation (Table 3).

The SDIC dried spinach exhibited superior antioxidant activity, with 1686.34 ± 42.98 μmol Eq Trolox/g d.w. (ABTS) and 89.292 ± 0.667 μmol Eq Trolox/g d.w. (DPPH), compared to CSD (1419.00 ± 50.79 ABTS; 82.033 ± 3.663 DPPH). This aligns with the SDIC's controlled irradiance (max 700 W/m^2), which likely mitigated thermal degradation of antioxidants. The TEAC/g values (SDIC: 0.575 ± 0.005; CSD: 0.458 ± 0.030) further confirm that dynamic irradiance regulation helps preserve free radical-scavenging capacity.

Uncontrolled solar exposure in CSD may accelerate oxidative reactions, degrading heat-sensitive antioxidants (e.g., ascorbic acid, polyphenols). The PDLC film in SDIC reduces UV/visible light-induced oxidation, consistent with studies linking lower irradiance to higher antioxidant retention.

3.4 Total flavonoids and tannin content

Total flavonoids and Tannin content are presented in the Table 4, where the CSD showed higher total phenolics (62.541 ± 1.76 mg GAE/100 g) and flavonoids (0.202 ± 0.014 mg/mL) than SDIC (39.774 ± 0.70 mg GAE/100 g; 0.066 ± 0.007 mg/mL). Tannins followed a similar pattern (CSD: 14.965 ± 2.450 mg/mL; SDIC: 6.574 ± 0.446 mg/mL).

Prolonged thermal stress in CSD (despite faster drying) may rupture cell walls, releasing bound phenolics. However, this could also indicate advanced Maillard reactions or oxidation, as suggested by the browning observed in CSD samples.

The higher tannin content in CSD suggests greater polymerization of flavonoids into condensed tannins under intense irradiance, which may reduce bioactive availability despite higher measured quantities.

Conclusions

This study investigated spinach leaves' drying kinetics and colorimetric degradation using two solar drying systems: Solar Dryer with Dynamic Irradiation Control (SDIC) and a Cylindrical Solar Dryer (CSD). The results demonstrated that both dryers effectively reduced the moisture content of spinach to safe

levels due to the average temperature, with the CSD achieving equilibrium faster (160 minutes) than the SDIC (220 minutes). However, the SDIC exhibited superior control over drying conditions, maintaining a consistent irradiance and mitigating thermal losses, which resulted in a more uniform drying process.

Our preliminary results show a promising trend towards better color retention and colorimetric analysis revealed significant differences in color degradation between the two dryers. The CSD, operating under unrestricted solar irradiation, showed a pronounced decrease in the b* coordinate (greenness), indicating a loss of chlorophyll and a shift toward yellow-brown hues. In contrast, the SDIC, with its controlled irradiance, preserved more of the spinach's green color but exhibited greater darkening (reduced L values), with Irradiance controlled drying, but the high natural variability of samples and solar radiation (transient nature) requires a more robust analysis to confirm this statistically. These findings underscore the importance of regulating solar irradiance to minimize color degradation, a critical factor in maintaining dried spinach's visual and market quality.

Despite lower phenolic levels, SDIC preserved functional antioxidants better, aligning with its color protection (higher b* retention). Emphasize that quality (bioactivity) matters more than quantity (total phenolics).

The SDIC minimized color degradation and preserved functional antioxidant capacity, as shown by 19% higher ABTS values compared to CSD. Notably, the elevated phenolic content in CSD samples (57% higher than SDIC) may reflect oxidative by products rather than bioactive availability, given the concurrent browning and reduced antioxidant efficacy. This underscores the importance of irradiance control in maintaining not only visual appeal but also nutritional value.

A limitation of this study is the confounding effect of drying time and irradiance level, as the SDIC process took longer. Future studies with controlled laboratory settings should aim to isolate these variables to definitively attribute the observed effects solely to irradiance modulation

The study also highlighted solar drying systems' environmental and operational advantages, particularly in semi-arid regions like Zacatecas, Mexico, where solar energy is abundant. The SDIC's ability to regulate internal conditions makes it a promising technology for preserving the quality of photosensitive crops like spinach, while the CSD offers a simpler, faster alternative for applications where color retention is less critical.

This research provides valuable insights into optimizing solar drying systems for leafy vegetables. The SDIC's controlled drying environment balances drying efficiency and quality preservation, making it suitable for high-value agricultural products. Future studies could further explore integrating hybrid drying technologies or advanced control systems to enhance the quality and efficiency of solar-dried spinach, contributing to sustainable food preservation practices in resource-limited settings.

Acknowledgements

The authors wish to thank Professor J. R. Irigoyen-Campuzano for his professional advice on statistical analysis, which enhanced the interpretation and validity of our experimental results.

References

Guiné, R. P. (2018). The Drying of Foods and Its Effect on the. *International Journal of Food Engineering Physical-Chemical, Sensorial and Nutritional Properties, 4*(2), 93-100.

Álvarez - Parrilla, E., De la Rosa, L. A., Martínez, N. R., & González, G. A. (2007). Total phenols and antioxidant activity of commercial and wild mushrooms from chihuahua, Mexico fenoles totalesy capacidad antioxidante de hongos comercialesy silvestres De Chihuahua, México. *CYTA-Journal of Food, 5*(5), 329-334.

Amarowicz, R., & Pegg, R. B. (2008). Legumes as a source of natural antioxidants. *European Journal of Lipid Science and Technology, 110*(10), 865-878.

Aravindh, M. A., & Sreekumar, A. (2015). Solar drying—a sustainable way of food processing. In *Energy sustainability through green energy* (pp. 27-46). Sharma: Springer India.

Benzie, I. F., & Strain, J. J. (1996). The ferric reducing ability of plasma (FRAP) as a measure of "antioxidant power": The FRAP assay. *Analytical Biochemistry, 239*(1), 70-76.

Chew, Y. L., Lim, Y. Y., Omar, M., & Khoo, K. S. (2008). Antioxidant activity of three edible seaweeds from two areas in South East Asia. *LWT-Food Science and Technology, 41*(6), 1067-1072.FAOSTAT. (2024, December 20). *Food Agriculture Organization of the United Nations*. Retrieved January 21, 2025, from https://www.fao.org/faostat/en/#data/QCL

Galla, N. R., Pamidighantam, P. R., Karakala, B., Gurusiddaiah, M. R., & Akula, S. (2017). Nutritional, textural and sensory qualitu of biscuits supplemented with spinach (Spinacia oleracea L.). *International Journal of Gastronomy and Food Science, 7*, 20-26.

García-Moreira, D. P., López-Vidaña, E. C., Moreno, I., & Delgadillo-Ruiz, L. (2025). Impact of Spectral Irradiance Control on Bioactive Compounds and Color Preservation in Solar Dried Papaya. *Processes, 13*, 2311.

García-Moreira, D. P., Moreno, I., Irigoyen-Campuzano, J., Martín-Domínguez, I., García-Valladares, O., & López-Vidaña, E. C. (2024). Effect of convective drying on color, water activity, and browning index of peach slices. *Revista Mexicana de Ingeniería Química, 23*(1).

Gutiérrez-Martínez, S., Hernández-Varela, J., Chanona-Pérez, J., Méndez-Méndez, J., González-Martínez, H., Perea-Flores, M., . . González-Victoriano, L. (2024). Study of drying, thermal, shrinkage, and color kinetics using digital and thermographic imaging of potato slices under real-time convective drying. *Revista Mexicana de Ingeniería Química, 23*(3), Alim24322.

Kaur, A., Kaur, D., Oberoi, D., Gill, B., & Sogi, D. (2008). Effect of dehydration on physicochemical properties of mustard, mint and spinach. *Journal of Food Processing and Preservation, 32*, 103-116.

Krokida, M. K., Tsami, E., & Maroulis, Z. B. (1998). Kinetics on color changes during drying of some fruits and vegetables. *Drying Technology: An International Journal, 3*(5), 667-685.

Manzoor, M. F., Ahmed, Z., Ahmad, N., Aadil, R. M., Rahaman, A., Roobab, U., . . . Siddeeg, A. (2020). Novelprocessing techniques and spinach juice: Quality and safety im-provements. *Journal of Food Science, 85*(4), 1018-1026.

Mulokozi , G., & Svanber , U. (2003). Effect of Traditional Open Sun-Drying and Solar Cabinet Drying on Carotene Content and Vitamin A Activity of Green Leafy Vegetables. *Plant Foods for Human Nutrition, 58*(3), 1-15.

Nahar, N. M. (2009). Processing of vegetables in solar dryer in arid areas. *International Solar Food Processing Conference.* Indore, India.Pal, A. A., & Acedo Jr, A. L. (2022). Quality profile of different vegetables dried using simple solardryers. *Int. J. Postharvest Technology and Innovation, 8*(4), 313-327.

S., G., Brat, P., Alter, P., & Amiot, J. (2005). Rapid determination of polyphenols and vitamin C in plant-derived products. *Journal of Agricultural and Food Chemistry, 53*, 1370-1373.Spence , C. (2015). On the psychological impact of food colour. *Flavour, 4*(21). doi: https://doi.org/10.1186/s13411-015-0031-3

Vargas, L., Kapoor, R., Nemzer, B., & Feng, H. (2022). Application of different drying methods for evaluation of phytochemical content and physical properties of broccoli, kale, and spinach. *LWT, 155*, 112892.

Wang, W., Li, M., Emam Hassanien, R. H., Wang, Y., & Yang, L. (2018). Thermal performance of indirect forced convection solar dryer and kinetics analysis of mango. *Applied Thermal Engineering, 134*, 310-321.

Waseed, M., Akhtar, S., Manzoor, M. F., Mirani, A. A., Ali, Z., Ismail, T., . . . Karrar, E. (2021). Nutritional characterization and food value addition properties of dehydrated spinach powder. *Food Sci Nutr, 9*, 1213-1221.

Yamakage, K., Yamada, T., Takahashi, K., Takaki, K., Komuro, M., Sasaki, K., . . . Orikasa, T. (2021). Impact of pre-treatment with pulsed electric field on drying rate and changes in spinach quality during hot air drying. *Innovative Food Science and Emerging Technologies, 68*, 102615.

Zhishen , J., Mengcheng, T., & Jianming, W. (1999). The determination of flavonoid contents in mulberry and their scavenging effects on superoxide radicals. *Food Chemistry, 64*, 555-559.

Zhu, A., & Shen, X. (2014). The model and mass transfer characteristics of convection drying on peach slices. *International Journal of Heat and Mass Transfer, 72*, 345-351.

Vol. 24, No. 3(2025) Alim25633
Revista Mexicana de Ingeniería Química

Calcium carbonate addition decreases the *in vitro* starch digestibility of wheat bread

Adición de carbonato de calcio disminuye la digestibilidad *in vitro* de pan de trigo

L. Acosta-Domínguez[1], R.M. Mata-Ramirez[1], E.J. Vernon-Carter[2], J. Alvarez-Ramirez[2], A. Garcia-Hernandez[1], C.A. Roldan-Cruz[3], S. Garcia-Diaz[4]*

[1]Facultad de Ciencias Químicas. Universidad Veracruzana-Región Xalapa. Gonzalo Aguirre- Beltrán, s/n, Zona Universitaria, Xalapa, Veracruz 91090 México.

[2]División de Ciencias Básicas e Ingeniería. Universidad Autónoma Metropolitana, Unidad Iztapalapa. AP 55-534. Iztapalapa, CDMX, 09340 México.

[3]Facultad de Nutrición. Universidad Veracruzana-Región Veracruz. Calle Carmen Serdán 5, Salvador Díaz Mirón, Veracruz, Veracruz, 91700 México

[4]Facultad de Ciencias Químicas. Universidad Veracruzana-Región Veracruz. Bv. Adolfo Ruíz Cortines 455, Costa Verde, 94294 Veracruz, Ver., México.

Sent date: July 18, 2025; Accepted: October 28, 2025

Abstract

The objective was to prepare white bread with decreased starch digestibility via the incorporation of small amounts of calcium carbonate. The addition of calcium carbonate increased the pH, decreased the titratable acidity and increased the soluble protein content. FTIR analysis showed that calcium carbonate increased the structured water content and modified the protein secondary structure by increasing coils and β-sheet. The short-range ordered and hydrated starch structures determined by FTIR increased, which was seen as indicative of the formation of crosslinked starch networks. The *in vitro* starch digestibility indicated that the calcium carbonate decreased the rapidly digestible and slowly digestible starch fractions by about 33 and 10%, respectively while increasing the resistant starch fraction by about 160% relative to the control bread. Principal component analysis revealed the existent relation between the reduced starch digestibility linked to the formation of ordered starch structures mediated by calcium crosslinking, which limited the binding of amylolytic enzymes to the starch chains.

Keywords: White bread, calcium carbonate, FTIR, *in vitro* digestibility.

Resumen

El objetivo fue preparar pan blanco con digestibilidad de almidón disminuida vía la incorporación de pequeñas cantidades de carbonato de calcio. La adición de carbonato de calcio aumentó el pH, disminuyó la acidez titulable e incrementó el contenido de la proteína soluble. Los análisis FTIR mostraron que el carbonato de calcio aumentó el contenido de agua estructurada y modificó la estructura secundaria de la proteína incrementando las conformaciones de espiral y β-láminas. Asimismo, se incrementaron las estructuras hidratadas y ordenadas a corto alcance del almidón, las cuales fueron vistas como indicativo de la formación de redes de almidón entrecruzadas. La digestibilidad *in vitro* del almidón indicó que el carbonato de calcio disminuyó las fracciones del almidón rápida y lentamente digerible en alrededor de 33 y 10%, respectivamente mientras se aumentaron las fracciones de almidón resistente en alrededor del 160% relativamente al pan control. El análisis de componentes principales reveló la relación existente entre la digestibilidad del almidón ligada a la formación de las estructuras ordenadas de almidón mediado por el entrecruzamiento con el calcio lo cual limitó el enlace de las enzimas amilolíticas con las cadenas de almidón.

Palabras clave: Pan blanco, carbonato de calcio, FTIR, digestibilidad *in vitro*.

*Corresponding author. *E-mail*: samgarcia@uv.mx;
https://doi.org/10.24275/rmiq/Alim25633
ISSN:1665-2738, *issn-e*: 2395-8472

1 Introduction

Bread is considered a staple food highly consumed in the world. Bread production techniques are quite diverse depending on cultural traditions, although all bread recipes comprise cereal flour, water and a leavening agent as the main ingredients (Sluimer, 2005). Bread is a significant source of nutrients for the human diet, providing carbohydrates, proteins and minerals. In particular, the high starch content of bread contributes to the energy requirements for human physical activity. However, excessive consumption of starchy food products combined with a sedentary lifestyle has been linked to unhealthy conditions known as metabolic syndrome (Miao *et al*., 2015). Starch in common white bread can exhibit high digestion rates with the consequent production and absorption of glucose in the small intestine (Meraz *et al*., 2022). Sub-utilized glucose in the blood is transformed and stored in adipose tissue as emulsified lipids, leading eventually to health problems related to metabolic syndrome diseases (Pradham, 2007). In this regard, there is strong motivation to modify the ingredients and methods for bread production to reduce starch digestibility. According to Scazzina *et al*. (2009) sourdough fermented bread gives glycemic responses lower than bread leavened with *S. cerevisiae*. Reshmi et al. (2017) reported that white bread combined with 20% fresh and 5% dry pomelo segments presented higher levels of resistant starch fractions (3.97-10.96%) and low predicted glycemic index (62.97-53.13%). It was postulated that naringin was responsible for the reduced starch digestibility via the inhibition of the binding capacity of hydrolyzing enzymes. Sardabi *et al*. (2021) used Moringa peregrina seed husk as a source of dietary fiber to reduce the starch digestibility in wheat bread. Whitney and Simsek (2017) showed that whole wheat bread exhibited decreased starch digestibility in comparison with white bread. Korompokis *et al*. (2021) determined that the addition of maltogenic amylase decreased the starch digestibility of white bread. Ge *et al*. (2021) showed that bread supplemented with 20% pumpkin flour had reduced starch digestibility by about 55.4% as compared to 69.9% for the non-supplemented bread. The decreased digestibility was explained by the enhanced digesta viscosity by the fiber added and the presence of compact gel networks hindering the contact between starch granules and α-amylase. Bajka *et al*. (2021) found that the incorporation of cellular legume powder can reduce by about 40% the *in vivo* glycemic index without compromising the bread quality. The aforementioned approaches for decreasing starch digestibility rely on the addition of an edible fiber source that acts as an obstruction for amylolytic enzymes. In the present work, we explored the incorporation of calcium carbonate as the calcium source in bread preparation. The hypothesis is that calcium could act as a crosslinking agent of starch chains, promoting the formation of a starch molecular organization that offers increased resistance to the action of amylolytic enzymes and, consequently, decreases starch digestibility. These actions are particularly relevant in the context of addressing metabolic syndrome-related disorders, which represent a growing concern in global nutrition and public health strategies. Calcium is commonly used as a crosslinking agent for biopolymers, including alginate, guar gum and starch (Giz *et al*., 2020; George & Abraham, 2007; Liu *et al*., 2016). Also, calcium has been used as a nutritional additive in bread preparation (Salinas *et al*., 2016; Alsuhaibani, 2018) without appreciable deleterious drawbacks to the sensorial and textural bread characteristics. One expects that the addition of small amounts of calcium carbonate may lead to marked reductions in the enzymatic hydrolysis of bread starch.

2 Materials and methods

2.1 Materials

Commercial wheat flour (Tres Estrellas®, CDMX, Mexico; 73 g carbohydrates, 11 g protein, 1 g lipids, 2 g dietary fiber and 0.0016 g ash per 100 g of flour dry basis), salt, sugar salt, baking dry yeast (TradiPan, CDMX, Mexico) were purchased at a local market (Comercial Mexicana, Veracruz, Mexico). Calcium carbonate used in all experiments were of analytical grade (Sigma-Aldrich, St. Louis, Mo, US).

2.2 Bread preparation

The bread recipe consisted of wheat flour (187.37 g), water (109.42 g), yeast (2.74 g), NaCl (1.82 g), sugar (3.65 g) and $CaCO_3$ (0.0, 0.82, 1.64 or 2.46 g). This study aims to analyze the effect of calcium carbonate on the biopolymers present in bread, considering starch as the primary component affected. Accordingly, the amount of calcium used was calculated based on the starch content. The starch content was estimated by considering starch as the primary carbohydrate in wheat flour. According to the manufacturer, this corresponds to 73 g of starch per 100 g of flour, so that 100 g of starch is equivalent to 136.99 g of wheat flour. The amount of calcium represented 0.0, 0.7, 1.4 and 2.1 g $CaCO_3$/100 g starch. The breads were coded as B_0, B_1, B_2 and B_3, respectively. The preparation of the bread was conducted by mixing the ingredients with the help of a SP-800-J Laboratory Spiral Mixer (Grupo Alpha Simet, Queretaro, Mexico). The wheat flour, yeast, salt, sugar and $CaCO_3$ were put into a mixing bowl and water at 30 °C was added. The ingredients

were mixed at low speed until a homogeneous mix was achieved (5 min). Then the mix was kneaded for 15 min. Subsequently, the mass was transferred to an aluminum mold (20 × 10 × 10 cm) covered with waxed paper and placed in the mechanical convection incubator (BEING Scientific, model BIF-35, Shangai, China) for 2 hours at 35 ºC. Then, the obtained dough was placed in a conventional convection oven (Rational AG, Landsberg, Germany) adjusting temperature at 200º C and 20% relative humidity for 25 minutes. The bread was allowed to reach room temperature and finally stored in hermetic Ziploc bags (4 ºC).

2.3 Methods

Moisture (925.10), ashes (923.03), and titratable acidity (942.15) were analyzed using the official methods instituted by the Association of Official Analytical Chemists (AOAC, 2000). The pH was precise analytically by a digital pH meter (MP220, Mettler, Toledo; AACC method 02-52.01). The soluble protein content was analyzed using the Bradford technique with bovine serum albumin as standard. SEM analysis of the bread crumb was carried out in a JEOL-JMS-7600F microscope with the LM mode at 15 kV accelerating voltage (Akishima, Japan). Samples were fixed on a carbon sample holder with a double-sided sticky tape. were coated in with gold with a thin film sputtering unit (model Desk V, Denton Vacuum) (Ramos-Villacob *et al.*, 2024). Fourier transform infrared (FTIR) spectroscopy was conducted at 20 °C using a equipped FTIR-ATR spectrophotometer (Spectrum 100, Perkin-Elmer, Waltham, MA, USA). All spectra were analyzed following the procedure described by Morales-Huerta *et al.* (2025), using Gaussian and Lorentzian fitting functions implemented in Fortran for spectral deconvolution. *In vitro* starch digestibility was performed with the methodology proposed by Englyst *et al.* (1992). The following discontinuous exponential model was used to explore the presence of multi-phase hydrolysis kinetics (Bello-Perez *et al.*, 2019):

$$X(t) = X_{\infty} + X_{fast}\exp\left(-k_{H,fast}t\right) + X_{slow}\exp\left(-k_{H,slow}t\right) \quad (1)$$

Here, $X(t)$ is the starch concentration at time t, X_{∞} is the residual starch for long times (i.e., indigestible starch), $k_{H,fast}$ and $k_{H,slow}$ are the hydrolysis rate constants for fast and slow kinetics, and X_{fast} and X_{slow} are the concentrations of the fast and slow digestible starch in the initial sample. The model (1) assumed that the starch is composed of three fractions. Two fractions that can be digested, although with different rate, and a third fraction that cannot be hydrolyzed under the amylolytic digestion conditions of the experimental run. For $t = 0$, one has

$$X_0 = X_{\infty} + X_{fast} + X_{slow} \quad (2)$$

This means that the parameters X_{∞}, X_{fast} and X_{slow} are not mutually independent. For a given initial concentration X_0, the parameters of the model (1) were estimated by least-squares fitting of the hydrolysis kinetics data subjected to the constraint (2). The estimation of digestible starch fractions of the bread variations was done as described by Godoy-Ramírez *et al.* (2024); namely, the rapidly digestible starch (RDS) and the slowly digestible starch (SDS) were established as the digested starch after first 20 min and 20-120 min, respectively. Finally, the resistant starch (RS) was taken as the starch that was not digested after 120 min.

2.4 Data analysis

Experimental runs were carried out in triplicate. ANOVA and Tukey's test were conducted with the Statgraphics 7 software (Statistical Graphics Corp. Manugistics Inc., Cambridge, MA). Statistically significance difference was taken when $p<0.05$. A principal component analysis (PCA) was conducted to assess the multi-variate effect of the calcium carbonate in the bread response variables.

3 Results and discussion

The pH of the control white bread without $CaCO_3$ (B_0) was about 5.32, and increased to 6.08, 6.43 and 6.54 for breads B_1, B_2 and B_3 (Table 1). Yeast produced acids during the fermentation process, leading to a slightly acidic medium. Calcium carbonate acted as a neutralizer for the acid medium resulting from the dough leavening.

Table 1. Characteristics of the white bread variations with different calcium content.

Bread	pH	Titratable acidity (%)	Moisture content (%)	Ashes (%)	Soluble protein (%)
B_0	5.32 ± 0.03^{d}	0.42 ± 0.01^{a}	41.37 ± 0.63^{b}	2.66 ± 0.01^{a}	4.34 ± 0.04^{d}
B_1	6.08 ± 0.02^{c}	0.37 ± 0.01^{b}	42.92 ± 0.69^{ab}	2.81 ± 0.02^{b}	8.27 ± 0.05^{c}
B_2	6.43 ± 0.02^{b}	0.35 ± 0.01^{c}	43.88 ± 0.77^{a}	2.93 ± 0.02^{bc}	11.52 ± 0.05^{b}
B_3	6.54 ± 0.02^{a}	0.33 ± 0.01^{d}	43.96 ± 0.77^{a}	2.98 ± 0.02^{c}	12.63 ± 0.05^{a}

Values are reported as means ± standard deviation. Column with different lower-case letters in columns indicate significant differences ($p < 0.05$). B_0 = control; B_1 = 0.7, B_2 = 1.4 and B_3 = 2.1 g $CaCO_3$/100 g starch.

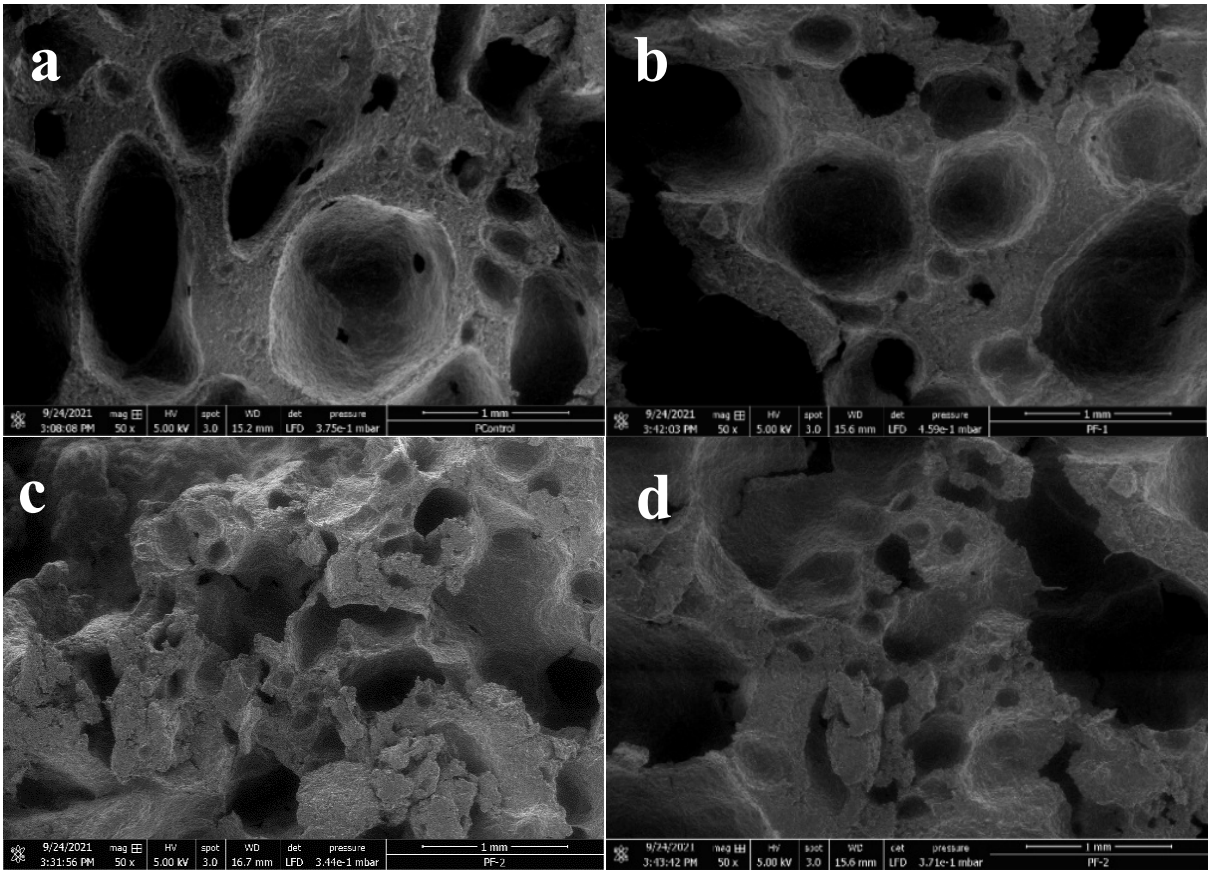

Figure 1. SEM images (50×) from the crumb of the bread variations. a) B_0 = control, b) B_1 = 0.7, c) B_2 = 1.4, d) B_3 = 2.1 g $CaCO_3$/100 g starch.

The effect was also reflected in the titratable acidity, which decreased from about 0.42 mg NaOH 0.1 N/g for B_0 to 0.33 mg NaOH 0.1 N/g for B_3. The moisture content exhibited a slight increase with the calcium carbonate addition, from 41.37% to 43.96 for B_3. Ashes also increased as a consequence of the calcium addition. The most visible variation was exhibited by the soluble protein, which increased from 4.34% for B_0 to 12.63% for B_3. Ono *et al*. (1993) reported that protein solubility increases with the pH, which is in line with the correlation ($\rho = 0.87$) between the pH and protein solubility shown in Table 1.

3.1 Morphology

Figure S1 presents images of bread slices for the control and the bread with the three different levels of calcium carbonate content. The crumb morphology of the control bread (B_0) was homogeneous, and the shape was regular. The calcium carbonate addition produced bread with a heterogeneous distribution of crumb pores and channels. Large pores can be observed in the crumb of B_2 and B_3. Besides, the slice shape was less regular with some fractures discernible in the crust. SEM micrographs offer a more detailed view of the crumb morphology (Figure 1). The high homogeneity of the pore distribution was confirmed for B_0 (Figure 1.a). Starch granules covered by gelatinized starch chains formed a complex 3D network with irregular caves and pores. The sample B_1 exhibited morphology similar to that of the control sample, although with the presence of large fractures (Figure 1.b). The further addition of calcium carbonate produced a less homogeneous crumb morphology (figures 1.c and 1.d) with larger fractures and pores. This suggests that calcium carbonate produced bread with an irregular 3D network formed by starch and proteins. Similar results were found recently by Garcia-Hernandez *et al*. (2022) who reported that baking powder produced less heterogeneous bread morphologies with slightly increased moisture content than bread made with regular yeast as a leavening agent.

3.2 FTIR analysis

Figure 2.a shows the FTIR spectrum of the bread variations in the range 4000-800 cm^{-1} where some salient bands were highlighted. The broad signal at 3600-3000 cm^{-1} corresponds to the hydroxyl group OH linked to the interactions between water and biopolymers (e.g., proteins and starch). The peak at 2950 cm^{-1} is associated to the CH and CH_2 aliphatic

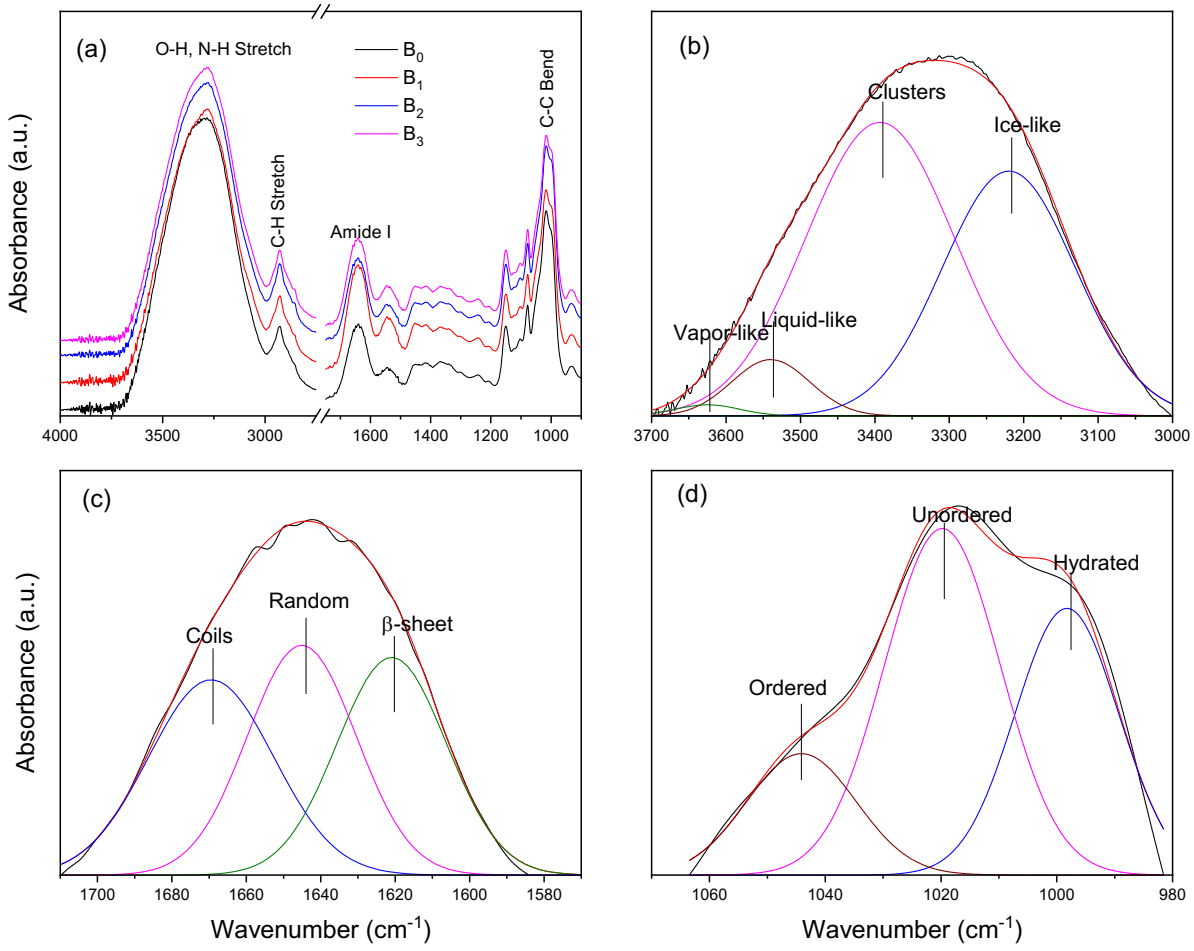

Figure 2. (a) FTIR spectrum for the different bread variations (B_0, B_1, B_2 and B_3). Prominent bands were highlighted, including the OH stretching, the Amide I and the fingerprint starch bands. The subsequent panels illustrate the numerical deconvolution of the FTIR spectrum: (b) the OH stretching band, (c) the Amide I band, and (d) the starch fingerprint region. B_0 = control, B_1 = 0.7, B_2 = 1.4, B_3 = 2.1 g $CaCO_3$/100 g starch.

groups of lipids. The band in the range 1700-1600 cm^{-1} indicate the C=O stretching of the Amide I linked to the bread proteins. The sharp peak at about 1025 cm^{-1} is attributed to the bread carbohydrates, mainly starch.

Figure 2.b shows that the hydroxyl band can be approximated by four Gaussian functions obtained by numerical deconvolution. These findings have been related to the structure of water forming polymeric hydrogels, and can be identified as non-freezing, freezing bound and free water (Vasylieva *et al*., 2018). Free water does not interact with the polymer molecules. Freezing-bound water interacts weakly with biopolymer, and non-freezing-bound water interacts with polymeric chains by forming hydrogen bonds (Goda *et al*., 2006). Water interactions at low wavenumber (i.e., at low-energy levels) reflect strong hydrogen bonds. Water vibrations at high wavenumber (i.e., high-energy levels) can be ascribed to water-water interactions (De Ninno & De Francesco, 2018). Figure S2.b shows that the water structure in the bread is dominated by low-energy vibrations linked to clusters and ice-like structures. Figure 3.a presents the variation of the water structure distribution for the different bread variations. The liquid-like water had significant ($p < 0.05$) variations with the addition of calcium carbonate, which is in line with the small variations of the moisture content shown in Table 1. In contrast, the content of water clusters decreased, and the ice-like water increased with the calcium carbonate content, suggesting that calcium improved the extent of the OH bonds via maybe crosslinking effects. A conceptual illustration of the proposed mechanism is provided in Supplementary Figure S3. Figure 2.c shows that an accurate fitting of the experimental FTIR spectrum in the Amide I region can be achieved by three Gaussian functions. The three individual peaks can be assigned to coils (~1670 cm^{-1}), random (~1642 cm^{-1}) and β-sheets (~1618 cm^{-1}) (Dong *et al*., 1990). These three configurations have a similar relative contribution to the protein secondary structure. Figure 3.b presents the effect of the calcium carbonate on the protein secondary structure of the white bread. Coils decreased with the calcium addition, from about 34% to about 30%. Such decrease was accompanied by an increase in random

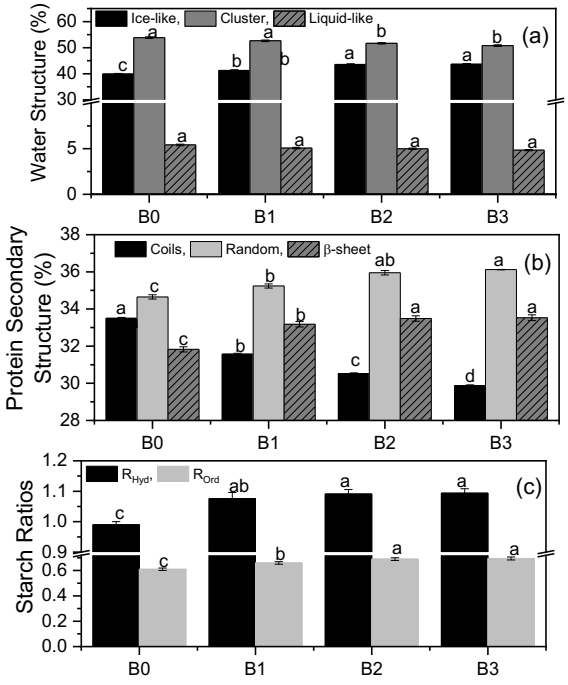

Figure 3. Percentage changes of (a) the water structure components, (b) protein secondary structure and (c) the starch structure ratios for the different bread variations. B_0 = control, B_1 = 0.7, B_2 = 1.4, B_3 = 2.1 g $CaCO_3$/100 g starch. The small letters above bars denote statistically significant differences.

and β-sheet structures. In particular, β-sheets have been linked to the elasticity of gluten, and hence of the wheat dough and bread (Saadi *et al*., 2022).

Figure 2.d shows the graphical deconvolution of the starch backbones in the range 1100-950 cm^1. The spectrum in this region can be approximated by three Gaussian peaks linked to hydrated (~995 cm^{-1}), amorphous (~1022 cm^{-1}) and short-range ordered (~1047 cm^{-1}) starch structures (van Soest *et al*., 1995). Rather than the magnitude of individual peaks, the ratios R_{hyd}=995/1022 and R_{ord}=1047/1022 obtained from the deconvoluted Gaussian function areas are considered to represent the contents of hydrated and short-range ordered structures as compared with amorphous ones. Figure 3.c presents the starch ratios for the different bread formulations. The addition of calcium carbonate led to a significant ($p<0.05$) increase in the FTIR ratios R_{hyd} and R_{ord}. That is, the calcium increased the relative content of the hydrated and short-range ordered starch structures, which can be seen as an insight into the binding of the calcium in the starch chains. It has been postulated that covalent bonds are involved in the calcium-starch interactions (Chatakanonda et al., 2000). FTIR analysis has indicated that linkages are likely to occur between carbons of sugar rings, resulting in the crosslinking of two or more starch chains to give non-regular space networks (Liu et al., 2014). Cornejo-Villegas *et al*. (2018) have postulated that van der Waals interactions might be involved in the interaction of Ca^{2+} ions and starch chains. The increased ratio 1047/1022 is probably indicating the increase of ordering as induced by cross-linking and van der Waals effects.

3.3 In vitro starch digestibility

Figure S2 presents the *in vitro* starch hydrolysis for the control bread (B_0) and the bread added with calcium carbonate (B_1 and B_2). The addition of calcium carbonate decreased the starch hydrolysis after 120 min, from about 95% for B_0 to about 82 and 70% for B_1 and B_2, respectively. The continuous lines in Figure S3 denote the least-squares fitting by Eq. (2) and the estimated parameters are presented in Table 2. It is noted that the transition time t_{tr} is higher than zero, meaning that the digestograms exhibited a two-phase behavior. The first phase for times $t < t_{tr}$ corresponds to a fast hydrolysis rate, and the second phase for times $t > t_{tr}$ corresponds to a slow hydrolysis rate. This transition time increased with the calcium addition, from 16.44 min for B_0 to about 31.98 for B_2. Both the fast and slow hydrolysis rates decreased with the calcium addition. In particular, the fast hydrolysis rate showed a strong decrease from 18.13×10^{-2} 1/min for the control bread B_0 to 3.16×10^{-2} 1/min for B_2. The slow hydrolysis rate showed only a slight decrease with the calcium addition, from 4.37×10^{-2} 1/min for B_0 to 2.91×10^{-2} 1/min for B_2. The decrease in the hydrolysis rate was reflected in the distribution of the digestible starch fractions. The RDS fractions showed a marked decrease from about 25.19% for the control bread B_0 to 17.31% for bread B_2. The SDS fraction showed a similar trend. In contrast, the RS increased from 12.49% for B_0 to about 32.19% for B_2. In this context, certain compounds such as polyphenols may enhance resistant starch (RS) content to a greater extent. Kwaśny *et al*. (2022) reported RS increases exceeding 300 %; however, they also noted that polyphenols can significantly alter the organoleptic properties of food, including color, astringency, and bitterness. Moreover, other compounds are known to promote RS formation, although their effectiveness depends on the type of fiber and the processing conditions applied and (Koksel *et al*., 2025). These results showed that the addition of calcium carbonate had an important impact on starch digestibility by reducing the hydrolysis rate and limiting starch hydrolysis. It was postulated that calcium-mediated cross-linking leads to compact 3D networks, limiting the accessibility of enzymes for binding with starch chains (Roldan-Cruz *et al*., 2020).

Table 2. Estimated parameters of the kinetics model Eq. (1) and the digestible starch fraction according with the classification by Englyst *et al*. (1992).

Bread	$k_{fast} \times 10^2$ (1/min)	$k_{slow} \times 10^2$ (1/min)	RDS (%)	SDS (%)	RS (%)
B_0	1.62 ± 0.05^a	1.57 ± 0.04^a	25.19 ± 1.16^a	62.32 ± 0.63^a	12.49 ± 0.43^d
B_1	1.30 ± 0.02^c	1.24 ± 0.03^b	20.98 ± 0.33^b	57.60 ± 0.69^b	21.42 ± 0.69^c
B_2	1.46 ± 0.02^c	0.79 ± 0.02^c	17.31 ± 0.24^c	51.50 ± 0.77^c	31.19 ± 0.77^b
B_3	1.61 ± 0.03^b	0.71 ± 0.02^c	16.51 ± 0.17^c	48.12 ± 0.64^{cd}	35.37 ± 0.77^a

Values are reported as means ± standard deviation. Column with different lower-case letters in columns indicate significant differences ($p < 0.05$). B_0 = control, B_1 = 0.7, B_2 = 1.4 and B_3 = 2.1 g $CaCO_3$/100 g starch.

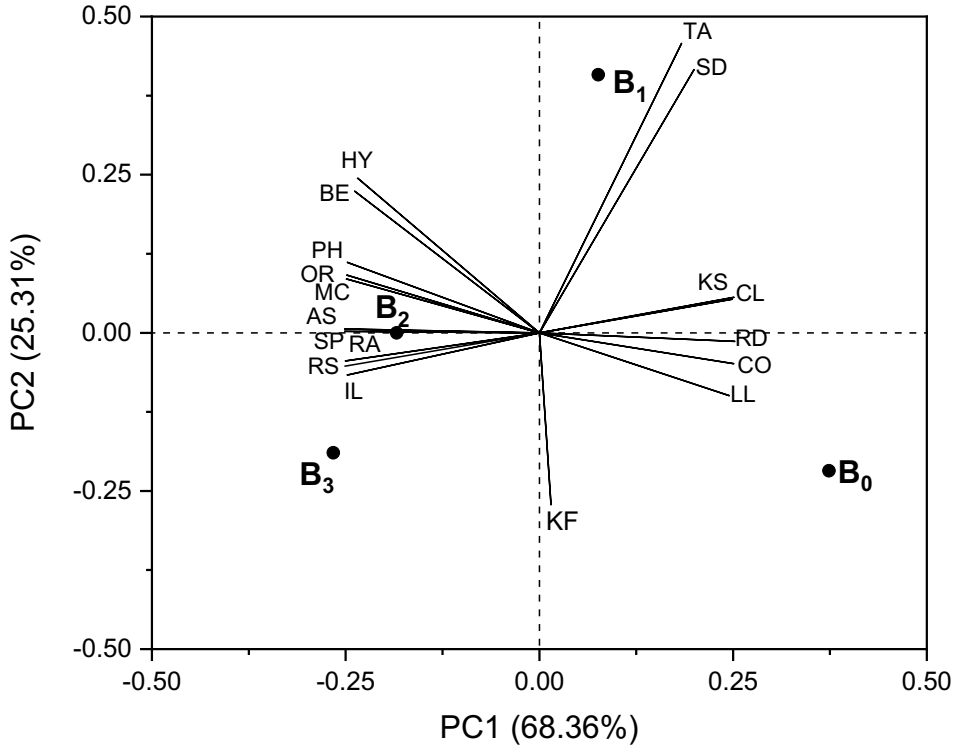

Figure 4. Bi-plot of the principal component analysis (PCA) results for the 19 response variables of the three bread variations. B_0 = control; B_1 = 0.7; B_2 = 1.4, B_3 = 2.1 g $CaCO_3$/100 g starch.

3.4 Principal component analysis (PCA)

The following set of 19 response variables was considered for PCA: pH (PH), moisture content (MC), titratable acidity (TA), ashes (AS), soluble protein (SP), ice-like (IL), clusters (CL), liquid-like (LL) water structures, coils (CO), random (RA) and β-sheet (BE) protein structures, hydrated R_{hyd} (HY) and short-range ordered R_{ord} (SO) starch structures, fast hydrolysis rate (KF), slow hydrolysis rate (KS), RDS (RD), SDS (SD) and RS (RS). The letters in parenthesis correspond to the acronyms used for denoting the response variables in a score bi-plot (Figure 4). The first and second principal components accounted for 68.36 and 25.31% of the total variability. The response variables were aggregated about two clusters, with one in the negative part of PC1 and the other in the positive part of PC1. The RDS and SDS fractions are aligned with the hydrolysis rates (KS and KF), and also with the titratable acidity (TA). This is not surprising since acids contribute to the hydrolysis of the starch chains. Interestingly, the RS fraction is aligned with the transition time (TT) from fast to slow hydrolysis rate, the pH, the soluble protein (SP), and the hydrated (HY) and short-range ordered (OR) starch structures. The alignment with SP might be indicating that soluble protein promoted the formation of complexes with the starch chains, decreasing in this the ability of the amylolytic enzymes to breakdown the starch chains. Lin *et al*. (2020) showed that proteins promote the formation of ordered starch structures that mitigate starch digestibility. The increase of starch ordered structures was reflected by the 1047/1022 FTIR ratio R_{ord}. The protein secondary structure (CO, RA and BE) and the water structure (IL, CL and LL) showed poor

alignment with the starch digestibility, suggesting that the water and protein structures played only a minor role in the *in vitro* digestibility of the bread starch.

Conclusions

This work studied the effect of adding calcium carbonate in the *in vitro* starch digestibility of white bread. The main conclusion is that small amounts of calcium carbonate addition to wheat bread led to a marked decrease in the *in vitro* starch digestibility. The effect was ascribed to the formation of a starch network mediated by calcium-mediated cross-linking, which limits the action of amylolytic enzymes. Calcium carbonate addition is a simple, viable and inexpensive technique to obtain white bread with reduced starch digestibility.

References

AACC International. Approved Methods of Analysis. Method 02-52.01. Hydrogen-Ion Activity (pH). Method 44-15.02. Electrometric Method; St. Paul, MN, U.S.A., 999.

Alsuhaibani, A. (2018). Rheological and nutritional properties and sensory evaluation of bread fortified with natural sources of calcium. *Journal of Food Quality*, 2018, 8308361. https://doi.org/10.1155/2018/8308361

AOAC (2000) *Official Methods of Analysis*. 17th Edition. The Association of Official Analytical Chemists, Gaithersburg, MD, USA.

Bajka, B. H., Pinto, A. M., Ahn-Jarvis, *et al*. (2021). The impact of replacing wheat flour with cellular legume powder on starch bioaccessibility, glycaemic response and bread roll quality: A double-blind randomised controlled trial in healthy participants. *Food Hydrocolloids*, 114, 106565. https://doi.org/10.1016/j.foodhyd.2020.106565

Bello-Perez, L. A., Agama-Acevedo, E., Garcia-Valle, D. E., & Alvarez-Ramirez, J. (2019). A multiscale kinetics model for the analysis of starch amylolysis. *International journal of biological macromolecules*, 122, 405-409. http://doi.org/10.1016/j.ijbiomac.2018.10.161

Chatakanonda, P., Varavinit, S. & Chinachoti, P. (2000). Effect of crosslinking on thermal and microscopic transitions of rice starch. *LWT-Food Science and Technology*, 33, 276-284. https://doi.org/10.1006/fstl.2000.0662

Cornejo-Villegas, M. D. L. Á., Rincón-Londoño, N., Real-López, D. & Rodríguez-García, M. E. (2018). Effect of Ca^{2+} ions on the pasting, morphological, structural, vibrational, and mechanical properties of corn starch–water system. *Journal of Cereal Science*, 79, 174-182. https://doi.org/10.1016/j.jcs.2017.10.003

De Ninno, A. & De Francesco, M. (2018). ATR-FTIR study of the isosbestic point in water solution of electrolytes. *Chemical Physics*, 513, 266-272. https://doi.org/10.1016/j.chemphys.2018.08.018

Dong, A., Huang, P. & Caughey, W. S. (1990). Protein secondary structures in water from second-derivative amide I infrared spectra. *Biochemistry*, 29, 3303-3308. https://doi.org/10.1021/bi00465a022

Englyst, H. N., Kingman, S. M. & Cummings, J. H. (1992). Classification and measurement of nutritionally important starch fractions. *European Journal of Clinical Nutrition*, 46, S33-50. PMID: 1330528

Garcia-Hernandez, A., Roldan-Cruz, C., Vernon-Carter, E. J. & Alvarez-Ramirez, J. (2022). Effects of leavening agent and time on bread texture and *in vitro* starch digestibility. *Journal of Food Science and Technology*, 59, 1922-1930. https://doi.org/10.1007/s13197-021-05206-1

Ge, F., Wu, P. & Chen, X. D. (2021). Evolutions of rheology, microstructure and starch hydrolysis of pumpkin-enriched bread during simulated gastrointestinal digestion. *International Journal of Food Science & Technology*, 56, 6000-6010. https://doi.org/10.1111/ijfs.15273

George, M. & Abraham, T. E. (2007). pH sensitive alginate–guar gum hydrogel for the controlled delivery of protein drugs. *International Journal of Pharmaceutics*, 335, 123-129. https://doi.org/10.1016/j.ijpharm.2006.11.009

Giz, A. S., Berberoglu, M., Bener, S., Aydelik-Ayazoglu, S., Bayraktar, H., Alaca, B. E., & Catalgil-Giz, H. (2020). A detailed investigation of the effect of calcium crosslinking and glycerol plasticizing on the physical properties of alginate films. *International Journal of Biological Macromolecules*, 148, 49-55. https://doi.org/10.1016/j.ijbiomac.2020.01.103

Goda, T., Watanabe, J., Takai, M. & Ishihara, K. (2006). Water structure and improved mechanical properties of phospholipid polymer hydrogel with phosphorylcholine centered intermolecular cross-linker. *Polymer*, 47, 1390-1396. https://doi.org/10.1016/j.polymer.2005.12.04

Godoy-Ramírez, A., Rodríguez-Huezo, M. E., Lara-Corona, V.H., Vernon_Carter, E.J., & Alvarez-Ramirez, J. (2024). Wheat bread supplemented with potato peel flour: color, molecular organization, texture. *Revista Mexicana de Ingeniería Química*, 23, Alim24201. https://doi.org/10.24275/rmiq/Alim24201

Koksel, H., Samray, M. N., Masatcioglu, T. M., & Koksel, F. (2025). Quality of resistant starch-enriched breadcrumbs extrudates. *Cereal Chemistry*, *102*(2), 364-376. https://doi.org/10.1002/cche.10863

Kwaśny, D., Borczak, B., Sikora, M., & Kapusta-Duch, J. (2022). Preliminary study on the influence of the polyphenols of different groups on the digestibility of wheat starch, measured by the content of resistant starch. *Applied Sciences*, *12*(21), 10859. https://doi.org/10.3390/app122110859

Korompokis, K., Deleu, L. J., De Brier, N. & Delcour, J. A. (2021). Investigation of starch functionality and digestibility in white wheat bread produced from a recipe containing added maltogenic amylase or amylomaltase. *Food Chemistry*, 362, 130203. https://doi.org/10.1016/j.foodchem.2021.130203

Lin, L., Yang, H., Chi, C. & Ma, X. (2020). Effect of protein types on structure and digestibility of starch-protein-lipids complexes. *LWT*, 134, 110175. https://doi.org/10.1016/j.lwt.2020.110175

Liu, H., Guan, Y., Wei, D., Gao, C., Yang, H. & Yang, L. (2016). Reinforcement of injectable calcium phosphate cement by gelatinized starches. *Journal of Biomedical Materials Research Part B: Applied Biomaterials*, 104, 615-625. https://doi.org/10.1002/jbm.b.33434

Liu, J., Wang, B., Lin, L., Zhang, J., Liu, W., Xie, J. & Ding, Y. (2014). Functional, physicochemical properties and structure of cross-linked oxidized maize starch. *Food Hydrocolloids*, 36, 45-52. https://doi.org/10.1016/j.foodhyd.2013.08.013

Meraz, M., Vernon-Carter, E. J., Bello-Perez, L. A. & Alvarez-Ramirez, J. (2022). Mathematical modeling of gastrointestinal starch digestion-blood glucose-insulin interactions. *Biomedical Signal Processing and Control*, 77, 103812. https://doi.org/10.1016/j.bspc.2022.103812

Miao, M., Jiang, B., Cui, S. W., Zhang, T. & Jin, Z. (2015). Slowly digestible starch—A review. *Critical Reviews in Food Science and Nutrition*, 55, 1642-1657. https://doi.org/10.1080/10408398.2012.704434

Morales-Huerta, A., Vernon-Carter, E. J., Alvarez-Ramirez, J., & Román-Guerrero, A. (2025). Effect of microwave dry-heat treatment of wheat flour in the *in vitro* digestibility of bread starch. *International Journal of Biological Macromolecules*, 144392. https://doi.org/10.1016/j.ijbiomac.2025.144392

Ono, T., Katho, S. & Mothizuki, K. (1993). Influences of calcium and pH on protein solubility in soybean milk. *Bioscience, Biotechnology, and Biochemistry*, 57, 24-28. https://doi.org/10.1271/bbb.57.24

Pradhan, A. (2007). Obesity, metabolic syndrome, and type 2 diabetes: inflammatory basis of glucose metabolic disorders. *Nutrition Reviews*, 65(suppl_3), S152-S156. https://doi.org/10.1111/j.1753-4887.2007.tb00354.x

Ramos-Villacob, V., Figueroa-Flórez, J. G., Salcedo-Mendoza, J. E., Hernández-Ruidíaz, J. E., Romero-Verbel, L. A. (2024). Development of modified cassava starches by ultrasound-assisted amylose/lauric acid. *Revista Mexicana de Ingeniería Química*, 23, Alim24109.

https://doi.org/10.24275/rmiq/Alim24109

Reshmi, S. K., Sudha, M. L. & Shashirekha, M. N. (2017). Starch digestibility and predicted glycemic index in the bread fortified with pomelo (Citrus maxima) fruit segments. *Food Chemistry*, 237, 957-965. https://doi.org/10.1016/j.foodchem.2017.05.138

Roldan-Cruz, C., Garcia-Diaz, S., Garcia-Hernandez, A., Alvarez-Ramirez, J. & Vernon-Carter, E. J. (2020). Microstructural changes and *in vitro* digestibility of maize starch treated with different calcium compounds used in nixtamalization processes. *Starch - Stärke*, 72, 1900303. https://doi.org/10.1002/star.201900303

Saadi, S., Saari, N., Ghazali, H. M., Abdulkarim, S. M., Hamid, A. A. & Anwar, F. (2022). Gluten proteins: Enzymatic modification, functional and therapeutic properties. *Journal of Proteomics*, 251, 104395. https://doi.org/10.1016/j.jprot.2021.104395

Salinas, M. V., Zuleta, A., Ronayne, P. & Puppo, M. C. (2016). Wheat bread enriched with organic calcium salts and inulin. A bread quality study. *Journal of Food Science and Technology*, 53, 491-500. https://doi.org/10.1007/s13197-015-2008-8

Sardabi, F., Azizi, M. H., Gavlighi, H. A. & Rashidinejad, A. (2021). The effect of Moringa peregrina seed husk on the *in vitro* starch digestibility, microstructure, and quality of white wheat bread. *LWT*, 136, 110332. https://doi.org/10.1016/j.lwt.2020.110332

Scazzina, F., Del Rio, D., Pellegrini, N. & Brighenti, F. (2009). Sourdough bread: Starch digestibility and postprandial glycemic response. *Journal of Cereal Science*, 49, 419-421. https://doi.org/10.1016/j.jcs.2008.12.008

Sluimer, P., 2005. *Principles of Breadmaking: Functionality of Raw Materials and Process Steps*. American Association of Cereal Chemists, St. Paul.

Whitney, K. & Simsek, S. (2017). Reduced gelatinization, hydrolysis, and digestibility in whole wheat bread in comparison to white bread. *Cereal Chemistry*, 94, 991-1000. https://doi.org/10.1094/CCHEM-05-17-0116-R

van Soest, J. J., Tournois, H., de Wit, D. & Vliegenthart, J. F. (1995). Short-range structure in (partially) crystalline potato starch determined with attenuated total reflectance Fourier-transform IR spectroscopy. *Carbohydrate Research*, 279, 201-214. https://doi.org/10.1016/0008-6215(95)00270-7

Vasylieva, A., Doroshenko, I., Vaskivskyi, Y., Chernolevska, Y. & Pogorelov, V. (2018). FTIR study of condensed water structure. *Journal of Molecular Structure*, 1167, 232-238. https://doi.org/10.1016/j.molstruc.2018.05.002

Vol. 24, No. 3(2025) Bio25514
Revista Mexicana de Ingeniería Química

Biotic and abiotic interactions during the decomposition of *Sargassum* spp. from the Mexican Caribbean

Interacciones bióticas y abióticas durante la degradación de *Sargassum* spp. del caribe mexicano

J.A. Domínguez-Maldonado [1], R. Tapia-Tussell [2]*, E. Olguin-Maciel [2], K.J. Azcorra-May [2], E. Sauri-Duch[3], G. Rivera-Muñoz[3], G. Lizama-Uc[3], S. E. Solís-Pereira[3]*

[1]Dirección de Gestión Tecnológica, Centro de Investigación Científica de Yucatán A. C. Calle 43 No. 130 x 32 y 34, Chuburná de Hidalgo; CP 97205, Mérida, Yucatán, México.

[2]Unidad de energía Renovable del Centro de Investigación Científica de Yucatán A. C. Carretera Sierra Papacal Chuburná Puerto Km 5, c.p. 97302 Mérida, Yucatán, México.

[3] Departamento de Química y de ingeniería bioquímica, Tecnológico Nacional de México /IT de Mérida, Av., Tecnológico Km 4.5 S/N 97118 Mérida Yucatán, México.

Sent date: January 27, 2025; Accepted: August 5, 2025

Abstract

A study was conducted to examine decomposition process of *Sargassum* spp., using 1.25-liter conical reactors. This study used a multifaceted approach to analyze the roles of biotic and abiotic factors in the degradation process. The aim of this study was to identify the physicochemical changes in *Sargassum* spp. To this end, the structural composition of the biomass was analyzed during a period of 150 day. Additionally, the production of leachate and biogas during sargassum natural degradation process was measured, and the structural changes in microbial communities were evaluated. This study explored the relationship between biogas production and the microorganisms in sargassum, as well as their potential biotechnological applications. The results of this study indicated the presence of *Thermofilum* and *Methanopyrus* microorganisms during the initial degradation stage (0-30 days). These microorganisms are marine archaea that primarily generate greenhouse gases through their metabolic byproducts, including hydrogen sulfide and methane. This observation is particularly salient during the initial stages of degradation when gas production is particularly prolific. A comprehensive understanding of these foundational principles can facilitate the development of effective management strategies for the management of *Sargassum* spp., which could subsequently lead to the creation of a biotechnological tool to produce high value-added compounds, such as biogas, and fertilizers.

Keywords: *Sargassum* spp, sargassum decomposition, biotic interactions, abiotic interactions, Caribbean sargassum.

Resumen

Se realizó un estudio para examinar el proceso de descomposición de *Sargassum* spp. utilizando reactores cónicos de 1,25 litros. Este estudio utilizó un enfoque multifacético para analizar el papel de los factores bióticos y abióticos en el proceso de degradación. El objetivo fue identificar los cambios fisicoquímicos en el *Sargassum* spp. Para ello, se analizó la composición estructural de la biomasa durante un periodo de 150 días. Además, se midió la producción de lixiviado y biogás durante el proceso de degradación natural del sargassum y se evaluaron los cambios espaciotemporales de las comunidades microbianas. Este estudio exploró la relación entre la producción de biogás y los microorganismos del sargassum, así como sus potenciales aplicaciones biotecnológicas. Los resultados indicaron la presencia de microorganismos *Thermofilum* y *Methanopyrus* durante la etapa inicial de degradación (0-30 días). Estos microorganismos son Arqueas marinas que generan principalmente gases de efecto invernadero a través de sus subproductos metabólicos, incluidos el sulfuro de hidrógeno y el metano. Esto es especialmente relevante durante las fases iniciales de la degradación, cuando la producción de gases es prolífica. Una estudio de este proceso podría facilitar el desarrollo de estrategias de gestión eficaces para el *Sargassum* spp., lo que posteriormente podría conducir a la creación de herramientas biotecnológicas para la obtención de productos de alto valor añadido, como biogás y fertilizantes.

Palabras clave: *Sargassum* spp, Degradación de sargazo, interacciones bióticas, Interacciones abióticas, Sargazo del caribe.

*Corresponding author. *E-mail*: sara.sp@merida.tecnm.mx, rtapia@cicy.mx;
https://doi.org/10.24275/rmiq/Bio25514
ISSN:1665-2738, *issn-e*: 2395-8472

1 Introduction

During the last decade, excessive amounts of pelagic *Sargassum* spp. have arrived in the Caribbean, causing severe environmental damage and economic consequences for the tourism industries of several Caribbean countries (Chávez *et al*., 2020; Vázquez-Delfín *et al*., 2021). However, the long-term impacts of this phenomenon have not been fully measured or evaluated, as they could potentially lead to future changes in the Caribbean coastal zone, including alterations in pH, dissolved oxygen levels, and turbidity (Álvarez-Rocha, 2022). It is imperative to consider the possibility of an increase in nitrogen levels over time in the groundwater of the Yucatan Peninsula, as this could have significant environmental and economic consequences. This increase can be attributed to leachate production during biomass degradation (García-Sánchez et al., 2020; Leal-bautista *et al*., 2024; John J. Milledge & Harvey, 2016b). These alterations could persist since sargassum quantities appear to increase annually. In 2019, (Wang *et al*., 2019) estimated 20 million tons of macroalgae in the Atlantic and referred to it as the "Great Sargassum Belt". Several research have demonstrated that these massive amounts of seaweed contain toxic metals. These metals are accumulated during biomass trajectory and life cycle. This accumulation is due its hyperaccumulating nature (Leal-bautista et al., 2024; Olguin *et al*., 2022; Rodríguez-Martínez *et al*., 2020b).

A key feature of *Sargassum* spp. is its structural composition, which is mostly constituted by polymers such as fucoidan. These polymers are an integral part of the structure of organism and contain sulfate groups that can constitute a significant proportion of its weight, ranging from 5% to 38% depending on the season (Lim & Wan Aida, 2017). The sulfur content in sargassum is relevant because it transforms into hydrogen sulfide during degradation. Devault *et al*., (2021) and John James Milledge *et al*., (2020) have reported that this chemical compound induces toxicological effects when people are exposed to sargassum at concentrations between 0 and 10 ppm (Resiere *et al*., 2020). Recent reports have documented the production of hydrogen sulfide due to sargassum degradation on beaches, with concentrations reaching up to 5 ppm (Rodríguez-Martínez *et al*., 2024). However, the magnitude of the problem and the role of hydrogen sulfide production in confinement sites are not established.

A confinement site is a location designated for the disposal of sargassum; it often lacks security, accurate management and organization. These sites receive the substantial volumes of sargassum removed from beaches, over extended periods from months to years. Within these sites, the algae decomposes due to temperature and humidity levels, resulting in the generation of large volumes of gases and leachates (Olguin *et al*., 2022).

The structure-function relationship of the carbohydrates varies by species (Takagi *et al*., 2018). Their degradation depends on alginate dissolution, although other reactive compounds also impact their biological degradation (Robledo & Vázquez-Delfín, 2019). Recent reports indicate that these macroalgae contain significant amounts of lignin (Alzate-Gaviria *et al*., 2020; Ardalan *et al*., 2018; Thompson *et al*., 2019). The conversion of lignin fractions into biofuels and other high value-added products remains a challenge for researchers due to the heterogeneity and complex structure of the polymer (Ponnusamy et al., 2019).

During the sargassum degradation process, the production of leachates and organic particles causes the phenomenon of brown tides. These events have been observed to cause a decrease in light penetration, oxygen levels, and pH. This, also causes an increase in temperature, sulfide levels, and organic matter and nutrient loads (López-Contreras *et al*., 2021). The leachates produced during this process create conditions analogous to eutrophication and may contain heavy metals (Antonio-martínez *et al*., 2020). Discharging sargassum leachates into the sea or in inadequate land deposits can contribute to toxic metal contamination of groundwater (Rodríguez-Martínez *et al*., 2020). The Yucatan Peninsula and the Mexican Caribbean are particularly vulnerable due to the prevalence of karst soil. This has prompted early warnings regarding leachates, that can percolate into the soil and reach the groundwater systems in the area(Estrada Medina, 2019). Additionally, the decomposition of pelagic sargassum has been found to affect coral species, leading to their partial or complete death (Antonio-Martínez *et al*., 2020). Bacteria are considered a vital component in the degradation process of sargassum due to their environmental adaptability and biochemical versatility. The diversity of microorganisms found on and within macroalgae is referred as the "microbiome" and includes bacteria, archaea, eukaryotic protists, fungi, and viruses(Egan *et al*., 2017). A recent study analyzed the bacterial community structure of *Sargassum horneri* drifting in the Yellow Sea (Mei *et al*., 2019). Consistent with the findings of other studies on macroalgae, Mei *et al*. (2019), demonstrated genus-level variations in bacterial composition between surrounding water and drifting algae, as well as in nearshore seaweeds. This indicates that community composition might differ based on geographical location. In a similar study, Torralba *et al*. (2017) found that sargassum complexes of two dominant surface-drifting species, *S. natans* and *S. fluitans*, in the Gulf of Mexico were associated with microbial communities dominated by the families Rhodobacteraceae and Saprospiraceae (Torralba *et al*., 2017). Additionally, Serebryakova *et*

al. (2018) studied the bacterial diversity of pelagic sargassum by analyzing 16S rRNA gene sequences associated with the benthic species *Sargassum muticum*. They found that the microbial community was primarily composed of Proteobacteria, Bacteroidetes, and Actinobacteria (Serebryakova *et al*., 2018). Determining the structure of microbial communities is difficult due to its dependence on the type of macroalgae and its seasonality. The microbiome associated with macroalgae is influenced by various biotic factors, such as algal growth and the production of metabolites by the macroalgae, as well as the composition of the surrounding seawater microbial community. Abiotic factors including temperature, and, pH, salinity, and oxygen availability affect microbial community, wave activity, and nutrient levels in seawater also play a role (Egan *et al*., 2017). Furthermore, bacteria have been observed to associate specifically with certain species of macroalgae and even with specific parts of the alga. Although the mechanisms underlying this specificity have not been fully elucidated, some associated ecological functions have been demonstrated. Specifically, chemical reaction mechanisms can be clearly attributed to algae or their epibionts. In many cases, these mechanisms can trigger the biosynthesis of bioactive compounds (Goecke *et al*., 2010). Other changes in the community may be associated with season, location, environmental stress, and macroalgae-specific regions (Egan *et al*. 2017). Given the scarcity of research on degradation in macroalgae in this region of the Caribbean, the objective of this work was to study some of the biotic and abiotic processes involved in the decomposition of *Sargassum* spp. To this end, the physicochemical characteristics of *Sargassum* spp., were assessed before and after 150 days of degradation. The volume of leachates and biogas produced during the natural degradation process were also measured. Additionally, the structural changes in microbial communities present in *Sargassum* spp. leachates over 150 days of natural degradation were determined and their relationship to the structural changes undergone by *Sargassum* was established. This information is relevant for developing effective management strategies for *Sargassum* spp., which could lead to the establishment of a biotechnological approach to produce high value-added products.

2 Materials and methods

2.1 *Sargassum spp. collection site*

Sargassum samples were collected in September 2020 along the coast of Benito Juárez (21°4'04.1 "N,86°46'33 "W) in Quintana Roo, Mexico, using a fishing net. The fresh sargassum was preserved with its leachates in plastic bags on ice. Upon arrival in the laboratory, the pelagic sargassum was separated from seagrass vegetation, such as *Thalassia testudinum* and *Syringodium filiforme*, as well as from epibionts. A portion of the collected sargassum was used for initial characterization, while another portion was employed for the environmental degradation experiment.

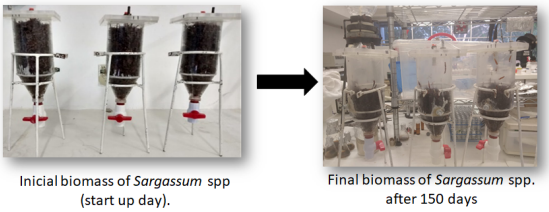

Fig. 1. Reactors used for the natural degradation of *Sargassum* spp.

2.2 *Natural degradation of sargassum*

The study of the natural degradation of *Sargassum* spp. was carried out as follows: Initially, 300 g of fresh *Sargassum* spp. biomass was weighed using a Torrey digital balance. Subsequently, the material was placed in three 1,250-mL conical reactors with the natural humidity of the macroalgae, i.e., in triplicate (see Figure 1). The reactors were maintained at a room temperature of 28 ± 2 °C for a duration of 150 days. To prevent evaporation while enabling gas exchange, the reactors were sealed.

2.3 *Characterization of the raw material*

2.3.1 *Determination of lignin in Sargassum spp*

The NREL/TP-510-42618 protocol was employed to quantify the lignin content (Sluiter, *et al*., 2008).

2.3.2 *Elemental analysis of Sargassum spp*

Elemental analysis (C, H, N, and S) was performed using a Thermo-Scientific Flash 2000 (Waltham, MA, USA) on a dried, ground, and sieved sargassum sample with 80 mesh. Approximately three to four milligrams of the sample were placed in tin containers (ThermoScientific) and 10 milligrams of vanadium pentoxide (V_2O_5) (ThermoScientific) were used as the catalyst for the sulfur peak. Each sample was analyzed in triplicate.

2.3.3 *Leachates*

The leachate produced by the degradation of sargassum biomass were collected at 0, 30, 60, 90, and 150 days and quantified.

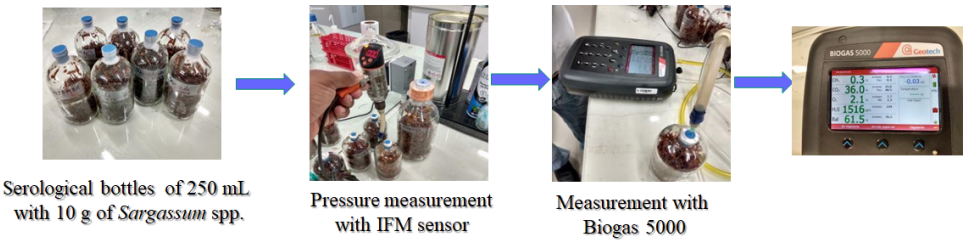

Fig. 2 Determination of greenhouse gases.

The natural moisture of the biomass was maintained as it was collected in the field, without adding more water. This approach was adopted to replicate decomposition processes occurring in beaches, confinement sites or landfills. The reactors were sealed to prevent evaporation of water from the sargassum biomass and the entry of dust. The leachates were analyzed for pH, temperature, conductivity, and salinity.

2.3.4 Determination of greenhouse gases

A biogas analyzer (Fonotest Biogas 5000) was used to measure the gases. For this purpose, ten grams of fresh sargassum were placed in 250 milliliters serological bottles (see Figure 2). To maintain anaerobic conditions, the bottles were capped with sealed septa, and the pressure was monitored using an IFM digital pressure sensor (model PN2596). This sensor was coupled to a needle capable of penetrating the septa to measure the pressure (see Figure 2). Quantification of the gases was carried out every two days; during this period, the compounds H_2 S, CH_4 and CO_2 were identified as greenhouse gasses produced by the sargassum.

2.4 DNA and metagenomic analysis

The microbial consortium was isolated as follows: First, 1 mL of sargassum leachate was inoculated into a Petri dish containing an SBM (Screening Bacteria Medium 523, Sigma-Aldrich®) culture medium. Then, the inoculum was distributed evenly across the surface of the media using an inoculation loop. The dishes were incubated in dark at 35 °C for 48 hours. This process was repeated for each leachate collection after 30, 60, 90, and 150 days.

DNA was isolated from each sample using a ZymoBIOMICSTM DNA miniprep Kit (Zymo Research, Irvine, CA, USA). The genomic DNA samples were then subjected to sequencing on the Illumina MiSeq platform (Macrogen). The library preparation was carried out using Herculase II Fusion DNA polymerase Nextera XT Index Kit V2 and the sequencing was performed by single end (SE x 300bp) with four biological samples, each with duplicates. The primers used to amplify the 16S rRNA genes from bacteria and archaea were 341F and 805R.

The raw reads were analyzed using the Galaxy platform (https://usegalaxy.org), where a quality control analysis was performed with FASTQC. The sequences were entered into Trim Galore to remove adapters (PHRED: 20, MINLEN: 50 bp). Finally, Trimmomatic (Bolger et al., 2014), was used to remove low quality sequences (SLIDINGWINDOW:4:20, MINLEN: 50 bp).

Taxonomic assignment was performed on the Galaxy platform using the Kraken2 program (Wood & Salzberg, 2014) with the single-end option. A comparison was then conducted using the Greengenes2 2022.10 database with the parameters configured by the program: k-mer-len: 35, minimizer-len: 31, minimizer-spaces: 6, load-factor: 0.7.

3 Results and discussion

3.1 Sargassum spp. characterization

The characterization of *Sargassum* spp. was conducted at the beginning and end of the 150-day experiment, which was focused on the natural degradation of the macroalgae. These parameters are essential for evaluating the environmental impact of this macroalga. Analyzing microbial metabolism during the degradation process provided critical insights that facilitated the development of management strategies. This analysis determined the degradation time in the environment and identified current deposition sites.

A comprehensive characterization of sargassum was conducted; as shown in Table 1, in which, relative humidity, total ash content, and lignin content were presented, the values can vary among different *Sargassum* species, location and temporality (Ardalan *et al*., 2018; Bikker *et al*., 2016; Borines *et al*., 2013; Rabemanolontsoa & Saka, 2013). The analysis showed that pelagic sargassum has unique characteristics, it has a low relative humidity content when ground and dried., contrasting with the findings reported by other authors, such as Biswas *et al*. 2017, who documented higher values (13.5%) for brown algae *Sargassum terrarium* (Biswas *et al*., 2017). However, the authors do not specify the time when the biomass was collected, where it was collected from (offshore or on the beach), or the

method used to grind and dry the sample.

These factors are important when comparing moisture and ash results because the season and the locality where the seaweed was collected can influence sargassum characterization results. Several studies have noted that the ash, moisture, and mineral content can vary depending on the season in which the seaweed was collected (Antúnez-Argüelles *et al*., 2020; John James Milledge *et al*., 2020; Oliveira *et al*., 2015; Saldarriaga-Hernandez *et al*., 2021). The particle size is another factor that influences this process, as it has been observed that screening with a fine mesh can affect water absorption in the sample. For instance, Ali and Bahadar subjected the *Sargassum* spp., to a drying process involving dry air for a period of four hours. Thereafter, they proceeded to grind and screen the material, reducing its size to bellow 0.4 mm, obtaining a moisture content of 9.8 ± 1.1 wt% for this macroalgae (Ali & Bahadar, 2017).

The results of this study also indicate a high lignin content (Table 1), suggesting the adaptability of the macroalgae as they undergo changes from the Atlantic Ocean to the Mexican Caribbean. A histological staining method was used by Alzate *et al*, (2020), to characterized complex polyphenolic compounds in *Sargassum* spp. This work established a foundational framework for enhancing the comprehension of the architecture and arrangement of heteropolymers within the cell wall of these macroalgae. It also explored the potential factors that may contribute to this phenomenon, focusing on the abiotic stresses, such as UV radiation and high temperatures, which are adverse conditions generated by climate change (Alzate-Gaviria *et al*., 2020).

One of the most descriptive analyses of sargassum biomass is the organic elemental analysis (C, N, H and S), since it provides insight into the composition of the biomass. Through elemental analysis of dry sargassum, the following concentrations were obtained: carbon concentration of 32.47%, a hydrogen concentration of 4.8%, a sulfur concentration of 0.91%, and a nitrogen concentration of 1.005% (see Table 2).

The carbon content of the samples was observed to range from 30.63% to 33.72%, this is consistent with the findings reported in other studies of brown algae. Biswas *et al*. (2017) found that the carbon content of the macroalgae *Sargassum tenerrimum* ranged from 30 to 32%, respectively. However, the nitrogen content is noteworthy for its lower values compared to those reported by Milledge *et al*. (2020), in which nitrogen levels were found up to 1.71% for sargassum in the Caribbean. Regarding sulfur content, the values were higher compared with other authors.

The nitrogen-carbon ratio was around 30, indicating a nitrogen deficiency for the composting context, for which the recommended is 10 to 20. However to initiate microbial growth, the ratio must be between 20 and 30 carbon atoms per nitrogen atom (Méndez *et al*., 2011).

Table 1. *Sargassum* spp. characterization.

Material	% Residual moisture	% Ash	% lignin	Reference
Sargassum tenerrimum	13.5	23.2	ND	(Biswas *et al*., 2017)
Sargassum sp	11.16 ±0.01	26.19 ± 0.07	less than 1	(Borines *et al*., 2013)
Ulva lactuca	ND	17.30	6.90	(Bikker *et al*., 2016)
Sargassum sp	ND	17.10	6.0	(Rabemanolontsoa & Saka, 2013)
Sargassum angustifolium	ND	35.5-43.8	11.8-25.8	(Ardalan *et al*., 2018)
Sargassum sp	ND	ND	4.60	(Oliveira *et al*., 2015)
Macroalgae consortium	ND	23.1	24.1	(Antúnez-Argüelles *et al*., 2020)
***Sargassum* spp.**	**5.06 ±0.5**	**24.48 ±1.75**	**30.14**	**This study**

Table 2. Elemental analysis of *Sargassum* spp.

Day 0	N (%)	C (%)	H (%)	S (%)
Reactor 1	1.21	30.62	4.87	1
Reactor 2	0.55	33.72	5.02	0.78
Reactor 3	1.24	33.06	4.71	0.95
Mean	1	32.5	4.87	0.91
Standard deviation	0.39	1.63	0.155	0.115
Day 150	N (%)	C (%)	H (%)	S (%)
Reactor 1	2.53	23.27	2.44	1.63
Reactor 2	2.98	23.39	2.58	1.77
Reactor 3	2.76	23.33	2.51	1.7
Mean	2.76	23.3	2.51	1.7
Standard deviation	0.225	0.06	0.07	0.07

Table 3. Comparative analysis of the elemental composition of different sargassum studies.

Sample	C (%)	H (%)	N (%)	S (%)	C/N	Reference
Sargassum spp	**33.159**	**4.784**	**1.173**	**0.962**	**28.269**	**This study**
S. fluitans, y natans	27.41	3.13	1.71	0.21	16.029	Milledge (2020)
Sargassum spp.	25.35	3.81	1.37	N.D	18.504	Ali and Bahadar (2017)
Sargassum spp.	27.5	4.16	1.21	0.82	22.727	Thompson et al. (2020)
Sargassum spp	27.68	2.72	1.64	ND	16.878	Nielsen (2021)

N. D.; Not detected.

As shown in Table 2, the increase in nitrogen content may be due the activity of the cyanobacteria found in the macroalgae. Numerous studies have shown that marine epiphytic bacteria are a significant source of fixed nitrogen for algae (Goecke *et al*., 2010). Several epiphytic cyanobacteria (*Calothrix* sp., *Anabaena*/*Dolichospermun* sp. and *Phormidium* sp.) that fix nitrogen and supply it to *Codium* species (Chlorophyta) have been identified in certain areas. Another nitrogen-fixing species, *Dichothrix fucicola*, has been observed in association with *Sargassum natans* and *S. fluitans* in the Sargasso Sea and Gulf Stream (Goecke *et al*. 2010). This phenomenon may have arisen during the degradation of *Sargassum* spp.

As illustrated in Table 3, this study presents a comparative analysis of the elemental compositions of various sargassum studies. This analysis reveals that the consortium in question has the highest Sulphur content, compared with findings from other researchers.

The C/N ratio is a crucial factor in determining the suitability of macroalgae for biogas production. It is important to note that this ratio can vary significantly based on nutrient viability. For example, studies have shown that the average C/N ratio in the deep open ocean is 47, whereas in shallower neritic waters is 27. However, no significant differences were observed between the C/N ratios of *S. fluitans* and *S. natans* (Milledge *et al*., 2020). Although elemental determinations of macroalgae are not a common practice, recent studies have revealed signs of nitrogen deficiency in macroalgae, with the C/N ratio displaying seasonal fluctuations (Nielsen *et al*., 2021). A study on *Sargassum muticum* revealed that summer samples had a C/N ratio closer to optimal levels reported in the literature, while spring samples exhibited deficiency. This finding is particularly relevant in the context of anaerobic digestion, where the rapid consumption of carbon leads to the accumulation of volatile fatty acids (VFA) (Thompson *et al*., 2020). Excess of nitrogen in the substrate promotes ammonia formation, which is toxic for various groups of bacteria at high concentrations, thereby reducing the potential of substrate for methane production.

3.2 Leachates

The leachates generated after 150 days from the *Sargassum* spp. inside the conical bottom reactor were 0.302 ± 0.02 L/kg. Approximately, 50% of the initial biomass was lost, likely due to the loss of water and organic compounds from the cell walls, including alginates, fucoidans, proteins, and lipids. These substances are degraded by the enzymatic system of microorganisms (Alderkamp *et al*., 2007; Morrissey et al., 2021). The highest volume of leachate (25 mL) was collected on day 30, while the lowest volume (7 mL) was collected at the end of the 150 days. This phenomenon can be attributed to the natural process of *Sargassum* spp. losing water and organic matter over time, as discussed by Antúnez-Argüelles *et al* 2020 and Alzate-Gaviria *et al*, 2020. The recalcitrance of compounds such as lignin results in their greater resistance to degradation.

Research on leachate generation during algal decomposition, particularly in the Mexican Caribbean, is limited. Currently, there is a lack of data on the volume of leachate produced by this macroalgae during decomposition. Milledge and Harvey (2016) used ensiling as a conservation technique for *Sargassum muticum* and observed leachate generation of 7.8% w/w after 60 days(Milledge & Harvey, 2016a). Subsequently, Antonio-Martínez *et al*. (2020) examined the impact of leachate on coral larvae, reporting a leachate generation time of 3.5 days in 0.4 x 0.4 x 1 m tanks, yielding a leachate volume of 6.6 L/kg of biomass. However, these studies were not conducted over an extended period, nor did they examine leachate production of other species of macroalgae. Therefore, this study is the first to investigate the mechanisms of sargassum degradation by microbial communities and their influence on leachate production. Understanding the structure of microbial communities during sargassum degradation can provide valuable information for establishing confinement sites and determining the subsequent treatment of this macroalgae. Previous studies have documented that the algae removed from beaches are disposed of in areas that are not adequately prepared to prevent leachates from reaching the aquifer (Rodríguez-Martínez *et al*., 2020).

3.3 Summary of the initial and final characterization of environmental degradation of Sargassum spp

After 150 days of *Sargassum* spp. degradation, the characterization parameters were evaluated again, as shown in Table 4. The table provides an overview of the parameters measured during the degradation process. It reveals that the initial mass loss was 146 g, corresponding to 48.46% of the original weight. By the end of the 150-days period, a total of 90.83 milliliters of leachates had been produced, representing 30.28% of the initial weight. This calculation assumes that the density of the leachates is equivalent to that of water (1 g/cm^3). This data indicates a significant decrease in moisture content within the macroalgae tissue, which was 30.28% when considering the loss of water exclusively attributable to the production of leachates over the 150-day period. Other studies have indicated that leachate generation varies depending on the collection site (Leal et al., 2024). The *Sargassum* spp. consortium was reported to generate 58 milliliters of leachate, which was designated as leachate per se. This consortium was collected at sea, similar to the present study. However, this study focused on the leachate generated by the decomposition of the macroalgae. A notable finding is the loss of carbon, as evidenced by a 9.2% reduction in total carbon content compared to the initial level. This was followed by a decline in hydrogen content, from 4.87% to 2.51%. These changes may be attributed to the loss of organic structures, as indicated by a decrease in lignin from 30.13% to 12.14%. This decline suggests a loss of approximately half of the initial biomass. Regarding the nitrogen and sulfur content, there was an increase from 1% to 2.76% for nitrogen and from 0.9% to 1.7% for sulfur, respectively.

3.4 Microbial diversity in leachates

More than 250 genera were identified with OTUs during the degradation of *Sargassum* spp. at room temperature. However, as shown in Figure 3, the composition of these genera changed over time; the composition of the leachates also changed significantly over time. Initially, *Thermophilum* dominated, accounting for 84% of the relative abundance, it was followed by *Methanopyrus* (9%), *Hydrogenophilus* (3%), and *Thermoproteus* and *Thermoplasma* (1% each). After 30 days, a major shift occurred, with *Fischerella* and *Hydrogenophilus* becoming the dominant genera, accounting for 60% and 26%, respectively. Conversely, the least abundant genera were *Mycobacterium*, *Thermophilum*, and *Thermoproteus*, with only 1% of the relative abundance.

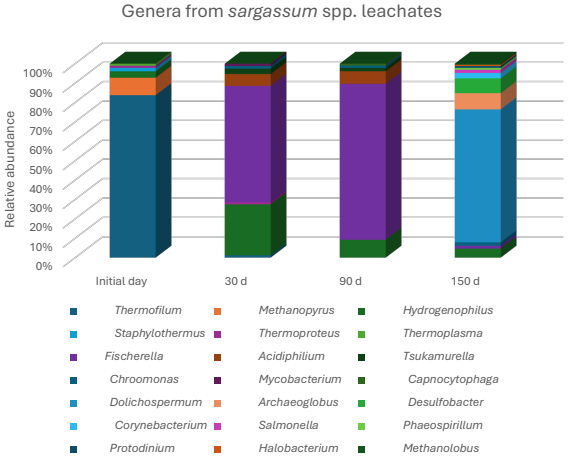

Fig. 3 Microbial communities present in *Sargassum* spp.

Table 4. Summary of the initial and final characterization of environmental degradation of *Sargassum* spp from Caribbean.

Parameter	Initial (Day 0)	Final (Day 150)	Difference
Mass (g)	300	154.6	146
Leacheates (mL)	0	90.83	-90.83
C (%)	32.47	23.27	9.2
H (%)	4.87	2.51	2.36
S (%)	0.91	1.7	-0.79
N (%)	1	2.76	-1.76
Moisture (%)	86.15	55.87	30.28
Ash (%)	24.48	26.34	-1.86
Lignin (%)	30.137	17.99	12.147
Conductivity	100mS	100mS	0
pH	7.6	8.2	0.6

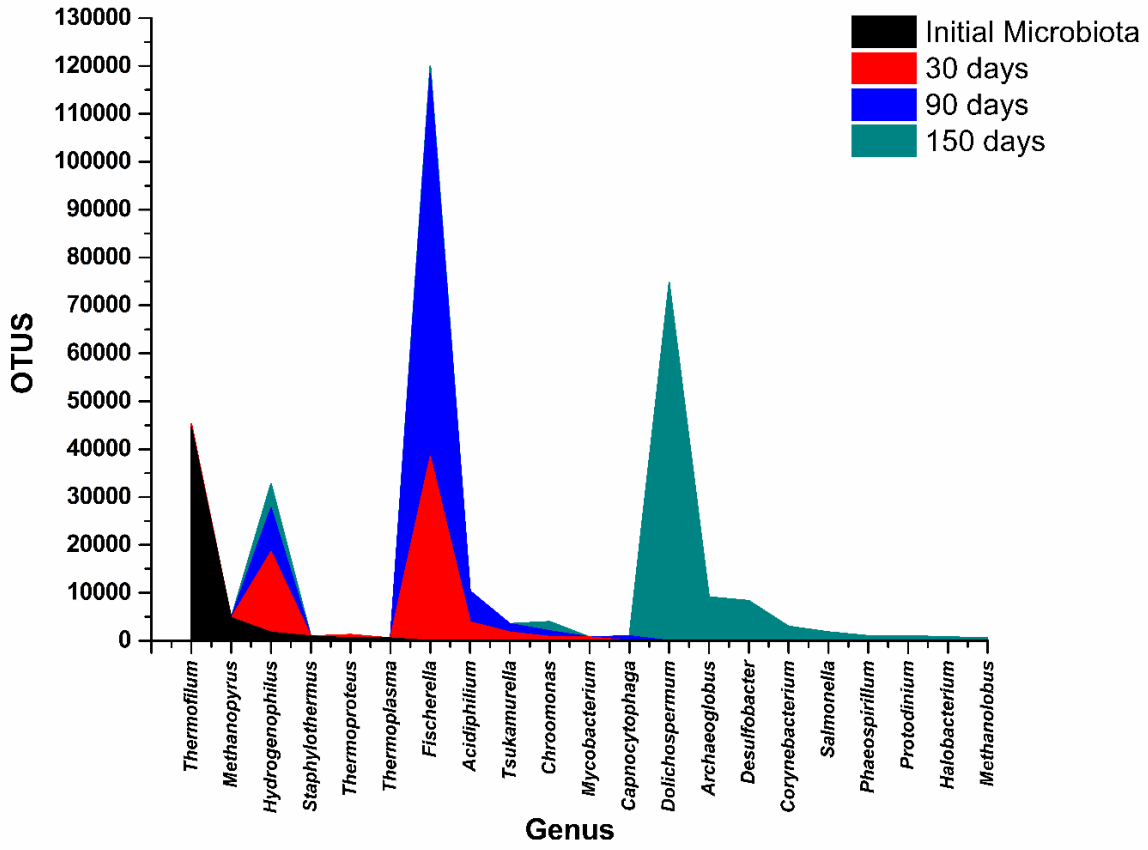

Fig. 4 Relative abundance over time of the main genera presents in *Sargassum* spp leachates.

Figure 4 illustrates that the genera *Methanopyrus* and *Thermofilum*, which are hyperthermophiles, belong to the phyla *Euryarchaeota* and *Crenarchaeota*, respectively, and were the most abundant at the beginning. These microorganisms are also the most abundant in oceans. Thus, it is hypothesized that they were found in the fresh leachates of *Sargassum* spp. which were collected from the sea at the beginning of the experiment. Methanopyrus metabolism has been linked to methane production from algal biomass, as documented for other *Euryarchaeota* microorganisms (Hervé *et al*., 2021). These genera play a pivotal role in degradating *Sargassum* spp. and the producing leachate, since they utilize macroalgal polysaccharides (Devault *et al*., 2021). *Methanopyrus* has been observed to capture carbon dioxide and hydrogen in its metabolic processes and produce methane. Additionally, *Thermofilum*, a sulfur-dependent anaerobic heterotroph (Fenner, 2008), has been implicated in the degradation of sulfur-containing polymers, such as fucoidan. These organisms produce methane and hydrogen sulfide when degrading *Sargassum* spp., either on beaches or at storage sites. Consequently, these organisms are present at the onset of leachate collection.

As shown in Figure 4, the most prevalent genera (*Thermofilum, Fischerella,* and *Dolichospermum*) are represented by black, blue, and green, respectively. A less abundant red peak is followed by *Hydrogenophilus, Methanopyrus,* and *Desulphobacter* as the second most prevalent genera, corresponding to a time between zero and 30 days. Subsequent analysis of the abundance of these genera over time revealed *Thermofilum* and *Methanopyrus* as the most prevalent in the initial phase. It is noteworthy that these genera are known to metabolize sulfur and hydrogen, suggesting a potential role in the degradation of sulfur-containing sugars, such as fucoidan, which are characteristic of brown algae

(Egan *et al*., 2017). This observation aligns with the onset of sargassum degradation, suggesting a possible link between the abundance of these genera and the initiation of this ecological process.

The genera *Hydrogenophilus* and *Fischerella* were the most prevalent after 90 days, while *Dolichospermum* and *Desulfobacter* dominated until the end of the 150 days. Figure 4 illustrates the predominance of *Methanopyrus* and *Thermofilum*, which are hyperthermophiles microorganisms classified within the *Euryarchaeota* and *Crenarchaeota* phyla, respectively. The cyanobacteria found in the sargassum leachates at 150 days are likely to be related to their decomposition, as they normally, like other photosynthetic organisms, require nutrients such as nitrogen and phosphorus for their growth, causing massive growth under favorable conditions such as high temperature and nutrient availability.

3.5 Greenhouse gas production

Figure 5 shows the production of greenhouse gasses during the degradation of *Sargassum spp*. Methane (CH_4), hydrogen sulfide (H_2S) and carbon dioxide (CO_2) were analyzed for 35 days until no pressure measurements could be taken in the 250 ml serological bottles. The results show that during the *Sargassum spp.* degradation, carbon dioxide and hydrogen sulfide were the most abundant reaching values of 28 and 0.4% respectively, compared to methane at 35 °C. These results indicate that the microorganisms present in the biomass are more active at warmer temperatures. As observed in Figure 4, greenhouse gases production occurs during the first 10 days of decomposition with microorganisms endemic to sargassum. It is worth mentioning that hydrogen sulfide is striking because it is the most dangerous gas produced during this process. Figure 5 shows that more than 4,400 ppm is produced for every 10 grams of sargassum in a 250-milliliters volume under anaerobic conditions. Thus, the fresh biomass that accumulates on the Caribbean beaches will contribute large amounts of greenhouse gases. The greenhouse gas concentrations obtained in this study are higher than those reported by other authors. For example, Rodríguez-Martínez *et al*., (2024) reported 10 ppm H_2S in degraded sargassum on the beach. While, Resiere *et al*., (2020) studied the effects of this gas on sargassum workers, indicating effects at 10 ppm and above. Our results are higher as we conducted the measurement in a fully enclosed, controlled environment that favors anaerobic digestion. Consequently, this maximizes the potential damage caused by *Sargassum* decomposition.

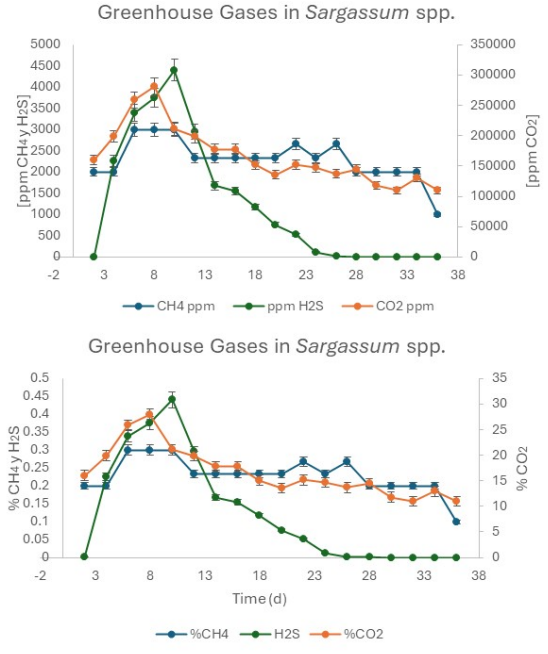

Fig. 5 Determination of greenhouse gases in *Sargassum* spp.

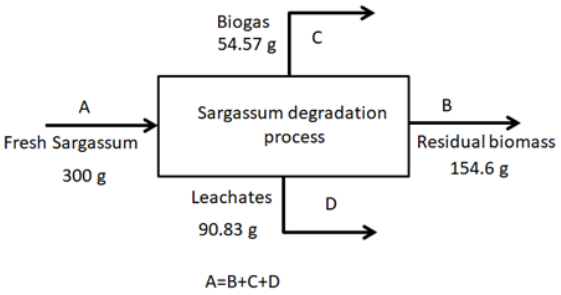

Fig. 6 General balance of degraded sargassum biomass.

The highest gas production occurs during the initial days of degradation. This finding is supported by our metagenomic analysis. During the initial stage of degradation, the most active microbial communities were the *Thermofilum* and *Methanopyrus* genera. These sulphate-reducing bacteria are responsible of the degradation of the consortium, since they use sulfur polymers to produce the gases.

By conducting a general balance of the biomass consortium (see Figure 6), we can obtain valuable information for estimating future sargassum upwelling damage. Starting from an initial biomass of 300 grams, it was found that the production of leachates and gases is dependent on the present microbial community. After 150 days, it was found that 18.2% of the biomass had transformed into gases and water evaporation, while 30.27% had degraded as leachate. For instance, in the case of the great Atlantic Sargassum belt (Wang *et al* 2019), it was estimate that of the 20 million tons of sargassum calculated in 2018, 18.2% by weight into gases and water evaporation and the degradation of 30.27% as leachate after 150 days. It can be extrapolated that the degradation of sargassum in the Atlantic Ocean results in the production of approximately 6 million tons of leachates and 3.63 million tons of greenhouse gases. This situation is problematic, and it is necessary to find new applications for the biomass that reaches the Mexican Caribbean. In 2022, the Mexican Navy reported that 52,647 tons of sargassum were collected in Quintana Roo, Mexico. This suggests that approximately 15,936.24 tons of leachate and a substantial amount of greenhouse gases were produced, depending on the anaerobic conditions that can form in the sargassum piles that reach the Caribbean Sea. The issue of greenhouse gas and heavy metal production, as a result of leachates and brown tides, represents a grave environmental concern in the Mexican Caribbean region, as previously highlighted.

The description of this biodiversity provides a basis for understanding the role that microbial communities play in the degradation of sargassum. As previously documented, epiphytic communities associated with sargassum decomposition have been reported in both marine and terrestrial ecosystems (Hervé *et al*., 2021). However, a more comprehensive understanding of

the functionality of phycosphere is imperative, as it appears that the degradation of sargassum is influenced not only by microorganisms but also by a variety of environmental factors that were not thoroughly addressed in this study. This work serves as an approximation to the complex reality of the degradation of this macroalgae. It is evident that microorganisms play a significant role in the production of greenhouse gases and leachates. However, further research is required to explore the decomposition process in marine and terrestrial environments in greater depth. It is imperative to consider the elevated temperature that is generated in the sargassum compost once it has reached the beach, as well as the parameters in the sea, including the salinity, oxygen content, epiphytic organisms of the macroalgae, and those that are associated with the phycospere.

Conclusions

This study examined the natural degradation of a consortium of *Sargassum* spp. 150 days to investigate the structural and physical changes that occur during degradation. The study identified spatiotemporal changes in the microbial communities involved in the degradation of pelagic sargassum. After 150 days, the macroalgae exhibited a 29% loss in carbon content, which was attributed to the loss of carbon structures resulting from the production of leachates and greenhouse gases. Conversely, there was a significant increase in nitrogen content, modifying the C/N ratio due to nitrogen capture by the cyanobacteria group. Among the changes observed in the microbial community, Archaea belonging to the genera *Thermofilum* and *Methanopyrus* were identified in the initial stages of degradation (0-30 days). These archaea are capable of reducing sulfate and have been identified as the primary producers of greenhouse gases.

The populations of *Thermofilum* and *Acidiphilum* have been identified as key factors in the depolymerization of macroalgae. These genera were detected following a 30-day degradation period, suggesting their role as primary agents responsible for this form of degradation. This process enables the release of organic compounds, as well as leachates and heavy metals, which can have a detrimental effect on water bodies. The production of greenhouse gases approaches 5,000 ppm of H_2S, exceeding the regulatory limits established for this gas. Meanwhile, CO_2 and methane levels decline over time. Although the production of these gases is substantial, it pales in comparison to H_2S given its status as the most hazardous gas for the environment and human health. The above findings are highly relevant for the management of sargassum and the implementation of new policies for managing this macroalgae. This is a significant issue for the Mexican government, as these types of studies will help to make the management of marine resources more efficient and effective.

Acknowledgements

The authors would like to thank the TecNM 20185.24-P project, and IQ. Alberto Cortes, for his support in molecular biology techniques, Tanit Toledano Thompsom for the conservation of the microbial communities and technical support provided.

References

A. Sluiter, B. Hames, R. Ruiz, C. S., Slui, J., & ter, D. Templeton, and D. C. (2008). Determination of Structural Carbohydrates and Lignin in Biomass: Laboratory Analytical Procedure (LAP). *Technical Report NREL/ TP -510 -42618*, *January*, 1–15.

Alderkamp, A., Rijssel, M. Van, & Bolhuis, H. (2007). *Characterization of marine bacteria and the activity of their enzyme systems involved in degradation of the algal storage glucan laminarin*. *59*, 108–117. https://doi.org/10.1111/j.1574-6941.2006.00219.x

Ali, I., & Bahadar, A. (2017). Red Sea seaweed (*Sargassum* spp.) pyrolysis and its devolatilization kinetics. *Algal Research*, *21*(January 2019), 89–97. https://doi.org/10.1016/j.algal.2016.11.011

Álvarez-Rocha, M., & Ortegón-Aznar, I. (2022). Can the *Sargassum* sp. drift influence on cover and morphology of Syringodium filiforme (Cymodoceaceae) in the Mexican Caribbean? *Hidrobiologica*, *32*(1), 51–58. https://doi.org/10.24275/uam/izt/dcbs/hidro/2022v32n1/Alvarez

Alzate-Gaviria, L., Domínguez-Maldonado, J., Chablé-Villacís, R., Olguin-Maciel, E., Leal-Bautista, R. M., Canché-Escamilla, G., Caballero-Vázquez, A., Hernández-Zepeda, C., Barredo-Pool, F. A., & Tapia-Tussell, R. (2020). Presence of Polyphenols Complex Aromatic "Lignin" in *Sargassum* spp. from Mexican Caribbean. *Journal of Marine Science and Engineering*, *9*(1), 6. https://doi.org/10.3390/jmse9010006

Antonio-Martínez, F., Henaut, Y., Vega-Zepeda, A., Cerón-Flores, A. I., Raigoza-Figueras, R., Cetz-Navarro, N. P., & Espinoza-Avalos, J. (2020).

Leachate effects of pelagic Sargassum spp. on larval swimming behavior of the coral Acropora palmata. 1–13. https://doi.org/10.1038/s41598-020-60864-z

Antúnez-Argüelles, E., Herrera-Bulnes, M., Torres-Ariño, A., Mirón-Enríquez, C., Soriano-García, M., & Robles-Gómez, E. (2020). Enzymatic-assisted polymerization of the lignin obtained from a macroalgae consortium, using an extracellular laccase-like enzyme (Tg-laccase) from Tetraselmis gracilis. *Journal of Environmental Science and Health - Part A Toxic/Hazardous Substances and Environmental Engineering*, *55*(6), 739–747. https://doi.org/10.1080/10934529.2020.1738171

Ardalan, Y., Jazini, M., & Karimi, K. (2018). Sargassum angustifolium brown macroalga as a high potential substrate for alginate and ethanol production with minimal nutrient requirement. *Algal Research*, *36*(February), 29–36. https://doi.org/10.1016/j.algal.2018.10.010

Bikker, P., van Krimpen, M. M., van Wikselaar, P., Houweling-Tan, B., Scaccia, N., van Hal, J. W., Huijgen, W. J. J., Cone, J. W., & López-Contreras, A. M. (2016). Biorefinery of the green seaweed Ulva lactuca to produce animal feed, chemicals and biofuels. *Journal of Applied Phycology*, *28*(6), 3511–3525. https://doi.org/10.1007/s10811-016-0842-3

Biswas, B., Singh, R., Krishna, B. B., Kumar, J., & Bhaskar, T. (2017). Pyrolysis of azolla, *Sargassum tenerrimum* and water hyacinth for production of bio-oil. *Bioresource Technology*, *242*, 139–145. https://doi.org/10.1016/j.biortech.2017.03.044

Bolger, A. M., Lohse, M., & Usadel, B. (2014). Trimmomatic: A flexible trimmer for Illumina sequence data. *Bioinformatics*, *30*(15), 2114–2120. https://doi.org/10.1093/bioinformatics/btu170

Borines, M. G., de Leon, R. L., & Cuello, J. L. (2013). Bioethanol production from the macroalgae *Sargassum* spp. *Bioresource Technology*, *138*, 22–29. https://doi.org/10.1016/j.biortech.2013.03.108

Chávez, V., Uribe-Martínez, A., Cuevas, E., Rodríguez-Martínez, R. E., van Tussenbroek, B. I., Francisco, V., Estévez, M., Celis, L. B., Monroy-Velázquez, L. V., Leal-Bautista, R., Álvarez-Filip, L., García-Sánchez, M., Masia, L., & Silva, R. (2020). Massive influx of pelagic *Sargassum* spp. On the coasts of the Mexican Caribbean 2014–2020: Challenges and opportunities. *Water (Switzerland)*, *12*(10), 1–24. https://doi.org/10.3390/w12102908

Devault, D. A., Pierre, R., Marfaing, H., Dolique, F., & Lopez, P. J. (2021). Sargassum contamination and consequences for downstream uses: a review. *Journal of Applied Phycology*, *33*(1), 567–602. https://doi.org/10.1007/s10811-020-02250-w

Egan, S., Kumar, V., Nappi, J., & Gardiner, M. (2017). Microbial Diversity and Symbiotic Interactions with Macroalgae. In and L. M. Martin Grube, Joseph Seckbach (Ed.), *Algal and Cyanobacteria Symbioses* (pp. 493–546). World Scientific.Estrada Medina, 2019. (2019). *El karst de Yucatán : su origen , morfología y biología The karst of Yucatan : its origin , morphology and biology Resumen*. 1–18.

Fenner, M. W. (2008). Genome sequence of Thermofilum pendens reveals an exceptional loss of biosynthetic pathways without genome reduction. *Lawrence Berkeley National Laboratory.*

García-Sánchez, M., Graham, C., Vera, E., Escalante-Mancera, E., Álvarez-Filip, L., & van Tussenbroek, B. I. (2020). Temporal changes in the composition and biomass of beached pelagic sargassum species in the Mexican Caribbean. *Aquatic Botany*, *167*. https://doi.org/10.1016/j.aquabot.2020.103275

Goecke, F., Labes, A., Wiese, J., & Imhoff, J. F. (2010). *Chemical interactions between marine macroalgae and bacteria*. *409*, 267–299. https://doi.org/10.3354/meps08607

Hervé, V., Lambourdière, J., René-Trouillefou, M., Devault, D. A., & Lopez, P. J. (2021). Sargassum differentially shapes the microbiota composition and diversity at coastal tide sites and inland storage sites on Caribbean Islands. *Frontiers in Microbiology*, *12*(October), 1–14. https://doi.org/10.3389/fmicb.2021.701155

Leal-Bautista, R. M., Rodríguez-García, J. C., Acosta-González, G., Chablé-Villacís, R., Tapia-Tussell, R., Bautista-García, J. E., Olguín-Maciel, E., Alzate-Gaviria, L., & González-López, G. (2024). Evaluation of leachates generated by *Sargassum spp*. in the Mexican Caribbean: Part 1 Spatial variations. *Water*, 16(9), 1251. https://doi.org/10.3390/w16091251

Lim, S. J., & Wan Aida, W. M. (2017). Extraction of Sulfated Polysaccharides (Fucoidan) From Brown Seaweed. In *Seaweed Polysaccharides: Isolation, Biological and*

Biomedical Applications. Elsevier Inc. https://doi.org/10.1016/B978-0-12-809816-5.00003-7

López-Contreras, A. M., Van Der Geest, M., Deetman, B., Van Den Burg, S., & Brust, H. (2021). Opportunities for valorisation of pelagic sargassum in the Dutch Caribbean. In *Wageningen Food & Biobased Research*. www.wur.eu/wfbr

Mei, X., Wu, C., Zhao, J., Yan, T., Jiang, P., & Walsh, D. A. (2019). *Community Structure of Bacteria Associated With Drifting Sargassum horneri, the Causative Species of Golden Tide in the Yellow Sea*. *10*(May). https://doi.org/10.3389/fmicb.2019.01192

Méndez, M. A. P., Hernández, R. S., Palma, D. J., & García, S. S. (2011). Caracterización química del compostaje de residuos de caña de azúcar en el sureste de México. *Interciencia*, *36*, 45–52.

Milledge, John J., & Harvey, P. J. (2016a). Ensilage and anaerobic digestion of *Sargassum muticum*. *Journal of Applied Phycology*, *28*(5), 3021–3030. https://doi.org/10.1007/s10811-016-0804-9

Milledge, John J., & Harvey, P. J. (2016b). Golden Tides: Problem or golden opportunity? The valorisation of sargassum from beach inundations. *Journal of Marine Science and Engineering*, *4*(3). https://doi.org/10.3390/jmse4030060

Milledge, John James, Maneein, S., Arribas, E., & Bartlett, D. (2020). *Sargassum Inundations in Turks and Caicos : Methane*.

Morrissey, K. L., Lopez, P. J., Hervé, V., Lambourdière, J., & René-trouillefou, M. (2021). *Sargassum Differentially Shapes the Microbiota Composition and Diversity at Coastal Tide Sites and Inland Storage Sites on Caribbean Islands*. *12*(October), 1–14. https://doi.org/10.3389/fmicb.2021.701155

Nielsen, B. V., Milledge, J. J., Hertler, H., Maneein, S., Al Farid, M. M., & Bartlett, D. (2021). Chemical characterisation of sargassum inundation from the Turks and Caicos: Seasonal and post stranding changes. *Phycology*, *1*(2), 143–162. https://doi.org/10.3390/phycology1020011

Olguin, E., Rosa, M., Leal, M., Liliana, B., Gaviria, A., & Domínguez, J. (2022). *Environmental impact of Sargassum spp . landings : an evaluation of leachate released from natural decomposition at Mexican Caribbean coast*. *0123456789*. https://doi.org/10.1007/s11356-022-22123-8

Oliveira, J. V., Alves, M. M., & Costa, J. C. (2015). Optimization of biogas production from *Sargassum* sp. using a design of experiments to assess the co-digestion with glycerol and waste frying oil. *Bioresource Technology*, *175*, 480–485. https://doi.org/10.1016/j.biortech.2014.10.121

Ponnusamy, V. K., Nguyen, D. D., Dharmaraja, J., Shobana, S., Banu, J. R., Saratale, R. G., Chang, S. W., & Kumar, G. (2019). A review on lignin structure, pretreatments, fermentation reactions and biorefinery potential. *Bioresource Technology*, *271*, 462–472. https://doi.org/10.1016/J.BIORTECH.2018.09.070

Rabemanolontsoa, H., & Saka, S. (2013). Comparative study on chemical composition of various biomass species. *RSC Advances*, *3*(12), 3946–3956. https://doi.org/10.1039/c3ra22958k

Resiere, D., Mehdaoui, H., Florentin, J., Gueye, P., Lebrun, T., Blateau, A., Viguier, J., Valentino, R., Brouste, Y., Kallel, H., Megarbane, B., Cabie, A., Banydeen, R., & Neviere, R. (2020). Sargassum seaweed health menace in the Caribbean: clinical characteristics of a population exposed to hydrogen sulfide during the 2018 massive stranding. *Clinical Toxicology*, 1–9. https://doi.org/10.1080/15563650.2020.1789162

Robledo, D., & Vázquez-Delfín, Er. (2019). Sargazo, conociendo al "enemigo." *Revista Avance y Perspectiva*, *5*(3). https://avanceyperspectiva.cinvestav.mx/sargazo-conociendo-al-enemigo/?print-posts=pdf

Rodríguez-Martínez, R. E., Gómez Reali, M. Á., Torres-Conde, E. G., & Bates, M. N. (2024). Temporal and spatial variation in hydrogen sulfide (H_2S) emissions during holopelagic *Sargassum* spp. decomposition on beaches. *Environmental Research*, *247*, 118235. https://doi.org/10.1016/J.ENVRES.2024.118235

Rodríguez-Martínez, R. E., Roy, P. D., Torrescano-Valle, N., Cabanillas-Terán, N., Carrillo-Domínguez, S., Collado-Vides, L., García-Sánchez, M., & van Tussenbroek, B. I. (2020a). Element concentrations in pelagic sargassum along the Mexican Caribbean coast in 2018-2019. *PeerJ*, *2020*(2), 1–19. https://doi.org/10.7717/peerj.8667

Rodríguez-Martínez, R. E., Roy, P. D., Torrescano-Valle, N., Cabanillas-Terán, N., Carrillo-Domínguez, S., Collado-Vides, L., García-Sánchez, M., & van Tussenbroek, B. I. (2020b). Element concentrations in pelagic sargassum along the Mexican Caribbean coast in 2018-2019. *PeerJ*, *8*, e8667. https://doi.org/10.7717/peerj.8667

Saldarriaga-Hernandez, S., Melchor-Martínez, E. M., Carrillo-Nieves, D., Parra-Saldívar, R., & Iqbal, H. M. N. (2021). Seasonal characterization and quantification of biomolecules from sargassum collected from Mexican Caribbean coast – A preliminary study as a step forward to blue economy. *Journal of Environmental Management*, *298*(August). https://doi.org/10.1016/j.jenvman.2021.113507

Serebryakova, A., Aires, T., Viard, F., Serrão, E. A., & Engelen, A. H. (2018). Summer shifts of bacterial communities associated with the invasive brown seaweed *Sargassum muticum* are location and tissue dependent. *PLoS ONE*, *13*(12), 1–18. https://doi.org/10.1371/journal.pone.0206734

Takagi, T., Kuroda, K., & Ueda, M. (2018). Platform construction of molecular breeding for utilization of brown macroalgae. *Journal of Bioscience and Bioengineering*, *125*(1), 1–7. https://doi.org/10.1016/j.jbiosc.2017.08.005

Thompson, T.M., Young, B. R., & Baroutian, S. (2020). Pelagic sargassum for energy and fertiliser production in the Caribbean: A case study on Barbados. *Renewable and Sustainable Energy Reviews*, *118*, 109564. https://doi.org/10.1016/j.rser.2019.109564

Thompson, Terrell M., Young, B. R., & Baroutian, S. (2019). Advances in the pretreatment of brown macroalgae for biogas production. *Fuel Processing Technology*, *195*. https://doi.org/10.1016/j.fuproc.2019.106151

Torralba, M. G., Franks, J. S., Gomez, A., Yooseph, S., Nelson, K. E., & Grimes, D. J. (2017). Effect of Macondo Prospect 252 Oil on microbiota associated with pelagic sargassum in the Northern Gulf of Mexico. *Microbial Ecology*, *73*(1), 91–100. https://doi.org/10.1007/s00248-016-0857-y

Vázquez-Delfín, E., Freile-Pelegrín, Y., Salazar-Garibay, A., Serviere-Zaragoza, E., Méndez-Rodríguez, L. C., & Robledo, D. (2021). Species composition and chemical characterization of sargassum influx at six different locations along the Mexican Caribbean coast. *Science of the Total Environment*, *795*. https://doi.org/10.1016/j.scitotenv.2021.148852

Wang, M., Hu, C., Barnes, B. B., Mitchum, G., Lapointe, B., & Montoya, J. P. (2019). The great Atlantic sargassum belt. *Science*, *364*(6448), 83–87. https://doi.org/10.1126/science.aaw7912

Wood, D. E., & Salzberg, S. L. (2014). Kraken: Ultrafast metagenomic sequence classification using exact alignments. *Genome Biology*, *15*(3). https://doi.org/10.1186/gb-2014-15-3-r46

Vol. 24, No. 3(2025) Bio25551
Revista Mexicana de Ingeniería Química

Biodegradation potential of thermophilic cellulolytic bacteria isolated from urban organic waste composting

Potencial de biodegradación de bacterias celulolíticas termófilas aisladas del compostaje de residuos orgánicos urbanos

A. Avila-Andrade[1], R. Beristain-Cardoso[2], D. García-Mondragón[1], S. Alcaraz-Ibarra[1], J. F. Aguirre-Garrido[3], G. González-Blanco*

[1] Instituto Interamericano de Tecnología y Ciencias del Agua, Universidad Autónoma del Estado de México, Carretera Toluca-Atlacomulco km 14.5, Unidad San Cayetano, Toluca C.P. 50295, México.

[2] Department of Environmental Sciences, Metropolitan Autonomous University-Lerma. Av. de las Garzas #10, El Panteón, 52005 Lerma de Villada, State of Mexico, Mexico.

[3] Department of Earth Resources, Metropolitan Autonomous University-Lerma. Av. de las Garzas #10, El Panteón, 52005 Lerma de Villada, State of Mexico, Mexico.

Sent date: March 17, 2025; Accepted: July 9, 2025

Abstract

The composting process of urban organic waste presents a microbial diversity depending on the phases of the process, which makes it a source of isolation of thermostable and hydrolytic bacteria of biotechnological importance due to their ability to degrade complex compounds such as cellulose, hemicellulose, and lignin. The objective of this study was to isolate and characterize thermophilic cellulolytic bacteria, as well as to determine their hydrolytic and degradation potential. Microbial isolation was performed from compost samples in the thermophile phase (47°C ± 2.25). Identification was performed by biochemical tests and massive amplicon sequencing. Hydrolytic capacity was determined by hydrolysis halos and kinetic activity in 0.1% CMC medium at 50°C. *Bacillus sp*. and *Bacillus licheniformis* strains were isolated from a thermophilic-phase composting system. These strains exhibited specific growth rates of 0.1051 h^{-1} and 0.0794 h^{-1}, doubling times of 6.5 h and 8.8 h, and hydrolysis halo diameters of 1.08 cm and 0.8 cm, respectively. The identification of bacteria of the Bacillus genus from the composting process highlights its importance as a source of thermophilic bacteria with hydrolytic capacity for biotechnological applications.

Keywords: Isolation, composting, thermophilic, bacilli, cellulose, residue.

Resumen

El proceso de compostaje de residuos orgánicos urbanos presenta una diversidad microbiana en función de las fases del proceso, lo que lo convierte en una fuente de aislamiento de bacterias termoestables e hidrolíticas de importancia biotecnológica debido a su capacidad para degradar compuestos complejos como celulosa, hemicelulosa y lignina. El objetivo de este estudio fue aislar y caracterizar bacterias celulolíticas termófilas, así como determinar su potencial hidrolítico y de degradación. El aislamiento microbiano se realizó a partir de muestras de compost en fase termófila (47 °C ± 2.5). La identificación se realizó mediante pruebas bioquímicas y secuenciación masiva de amplicones. La capacidad hidrolítica se determinó mediante halos de hidrólisis y actividad cinética en medio CMC al 0.1 % a 50°C. Las cepas de *Bacillus sp*. y *Bacillus licheniformis* se aislaron de un sistema de compostaje en fase termófila. Estas cepas presentaron tasas de crecimiento específicas de 0.1051 h^{-1} y 0.0794 h^{-1}, tiempos de duplicación de 6.5 h y 8.8 h, y diámetros de halo de hidrólisis de 1.08 cm y 0.8 cm, respectivamente. La identificación de bacterias del género Bacillus en el proceso de compostaje resalta su importancia como fuente de bacterias termófilas con capacidad hidrolítica para aplicaciones biotecnológicas.

Palabras clave: Aislamiento, compostaje, termófilo, bacilos, celulosa, residuo.

* *Corresponding author. E-mail*: gehovan25@yahoo.com.mx;
https://doi.org/10.24275/rmiq/Bio25551
ISSN:1665-2738, *issn-e*: 2395-8472

1 Introduction

Composting is an aerobic and exothermic process where a complex microbial community carries out the biotransformation of organic matter (Moreno *et al*., 2021; Firone *et al*., 2023). Globally, 19% of urban solid waste was recycled or composted (Cao *et al*., 2023). Babu *et al*. (2021) indicated that composting is the most applied biotechnology, due to its ease of implementation and low cost. However, it has the major disadvantage of requiring long operating times (from 4 to 6 months, attributed to the presence of lignocellulosic material, pruning and gardening remains) to obtain mature compost (Waqas *et al*., 2023).

In addition, due to the large volume of waste, strategies to improve the process are being sought (de Mendonça *et al*., 2021). In this sense, techniques have been implemented to shorten composting times by improving control parameters, such as aeration, turning frequency (Getahun *et al*., 2012), optimization of the C:N ratio (Guo *et al*., 2012; Nguyen *et al*., 2020), and the type of bulking agent (carbon source). These improvements aim to produce compost suitable for soil enhancement or use as a biofertilizer (de Mendonça *et al*., 2021).

Currently, one approach consists of the bioaugmentation of microorganisms isolated from the same process with specific metabolic characteristics that can be used to accelerate the degradation process (Babu *et al*., 2021), as well as in other production processes (Zhu et al., 2020). The metabolic reactions of the communities present in the composting process generate energy and cause an increase in temperature in the system leading to four phases: mesophilic (20-40 °C), thermophilic (40-60 °C), cooling (40-20 °C), and maturation (room temperature) (Moreno *et al*., 2021). The increase in temperature during the thermophilic phase provides favorable conditions for the isolation of thermotolerant microorganisms (Ince *et al*., 2020), capable of growing at temperatures between 40 – 120 °C (thermophilic microorganisms), which produce thermostable enzymes, proteins that retain their structure and function at high temperature (Kanekar & Kanekar, 2022). The ability of thermostable enzymes to operate at high temperature is essential for the transformation of organic waste, a process of great relevance in areas such as waste management and biofuel production (Banerje *et al*., 2020; Hussian & Leong, 2023).

Thermophilic cellulolytic bacteria can be found in various environments that present extreme temperature conditions such as: dry tropical forests, deep-sea hydrothermal vents, geothermal areas, and in artificial systems such as waste treatment plants and compost piles (Kanekar & Kanekar, 2022; Firone *et al*., 2023). Authors such as López *et al*. (2021) stated that the microbiota present in composting process includes thermophilic microorganisms capable of degrading lignocellulose-rich residues. These microorganisms are of great biotechnological interest due to their resistance to chemical denaturation, their wide optimal pH range, and their broad substrate specificity (Hussian & Leong, 2023). Additionally, bacteria have shorter doubling times measured in days, compared to fungi, which may take weeks to double (Wang & Kuzyakov, 2024); these characteristics make bacteria valuable in industrial and biotechnological applications (Banerjee *et al*., 2020) such as bioremediation, biorefinery and bioplastic production (Li & Huo 2025).

Authors such as Siu-Rodas (2018) reported the isolation of three thermophilic strains (optimal growth at 60 ° C) capable of growing in acidic pH (4-5) with endocellulase and exocellulase activity and mentioned that these strains have a potential application in the extraction and clarification of juices as well as paper bleaching. Anguiano (2019) has isolated compost bacteria from organic waste in the thermophilic phase (e.g., *Bacillus pumilus, Stenotrophomonas* and *Bacillus subtilis*) which showed growth in a selective carboxymethylcellulose medium. While Finore *et al*. (2023) reported the isolation of lignocellulosic bacteria from sawdust and bovine manure compost, associated with the thermophilic phase of the process (55°C). Although the isolation of lignocellulosic bacteria is reported in the literature, few reports are available regarding their metabolisms, kinetics and doubling times with carboxymethylcellulose as the sole carbon source. Therefore, this study evaluated the isolation and phenotypic, genotypic, and metabolic characterization of cellulolytic thermophilic bacteria from composting.

2 Materials and method

2.1 *Obtaining composting samples*

The compost used in this study was produced from urban organic waste (a heterogeneous mixture of fruit peels, raw and cooked vegetables, green leaves, and food scraps) combined with black soil at a 2:1 ratio. The mixture was placed in a sealed container measuring 32 cm in width, 53 cm in length, and 26.5 cm in depth, equipped with a hermetic lid and a leachate collection system.

Composting was performed in duplicate with daily turning to ensure proper aeration. Each compost bin was loaded with 2.9 kg of black soil as a bulking agent (initial moisture content: 30%) and 5.8 kg of urban organic waste (initial moisture content: 85%). The temperature and pH were monitored with an electronic soil meter (4 in 1 Soil Survey Instrument) and the moisture with a Tempo Disc ™ Bluetooth Sensor for temperature. Chemical oxygen demand (COD)

was measured using the closed reflux method with HACH® COD reagent vials (Method 8000), following the procedure outlined in the Mexican standard NMX-AA-52-1985 (SEMARNAT, 1985). Inorganic nitrogen species were measured using the HACH Kit 8039 for nitrate, the HACH Kit 8507 for nitrite, and an ammonium-selective electrode (Phoenix Electrode Company, USA) for NH_4^+ quantification. The samples for isolation were taken from the thermophilic phase of the composting system on day 80, when it presented an average temperature of 47°C ± 2, moisture of 67.8 ± 0.51%, and pH of 8.32 ± 0.13.

2.2 *Microbial isolation*

During the thermophilic phase, 5% of the compost was sampled. From this portion, a 5 g sample was taken to activate the microorganisms in 45 ml of sterile nutrient broth (DB BIOXON®). The sample was then incubated at 50°C for 24 hours. Subsequently, 1 ml of activated culture was inoculated into nutrient agar plates using the pour-plate technique and incubated for 48 hours at 50°C. Colonies with distinct morphologies were then re-streaked into nutrient agar plates using the cross-streak method to characterize their morphology. Additionally, the culture was plated on carboxymethylcellulose (CMC) agar to isolate bacteria with cellulolytic activity. These plates were incubated at 50°C for 48 hours (Lynd *et al*., 2022).

2.3 *Macroscopic and microscopic characterization*

The macroscopic morphological characterization of the strains was carried out following the guidelines provided in Bergey's Manual of Systematics of Archaea and Bacteria, which offers updated descriptions of prokaryotic taxa (Rainey, 2015). Microscopic morphology was observed through a Nikon Eclipse E200 optical microscope from a Gram-stained smear (Madigan *et al*., 2004).

2.4 *Metabolic characterization*

Strains isolated on 0.1% CMC agar plates, with less than 72 hours of growth, were sub-cultured on blood agar, MacConkey, and tryptic soy agar (TSA) and incubated for 24 hours at 37°C to assess their biochemical capacity for hemolysis and lactose hydrolysis. Following this, the strains underwent a series of biochemical tests, including triple sugar iron (TSI), citrate utilization, urea hydrolysis, motility-indole-ornithine (MIO), sulfate reduction-indole-mobility (SIM), nitrate reduction, sucrose, glucose, mannitol, lactose, gelatin liquefaction, hemolysis of bovine erythrocytes, and growth in 7.5% NaCl. Subculture and biochemical tests were carried out in duplicate and the results were interpreted based on Microbiological Diagnosis by Elmer W. Koneman (Koneman, 2012).

2.5 *Determination of cellulolytic activity*

Strains grown on 0.1% CMC agar were re-plated by puncturing onto CMC agar and incubated for 24 hours at 50°C. Congo red dye (1% w/v) was added and left to act for fifteen minutes. Excess dye was then removed and the plates were rinsed with a 0.1 M NaCl solution for 15 minutes. The plates were then left to rest for 24 hours at 4°C and the diameter of the cellulolytic activity ring was measured (Rodríguez & Llenque, 2016). The cellulolytic index (CI) was determined using Equation 1, as reported by Zainudin *et al*. (2022), based on the colony growth diameter and the diameter of the hydrolysis halo. Additionally, the efficiency of carboxymethylcellulose degradation was confirmed through COD measurements.

$$CI = \frac{(Total\ halo\ diameter - Growth\ colony\ diameter)}{Growth\ colony\ diameter} \quad (1)$$

2.6 *Genotypic characterization*

Bacterial DNA from strains with cellulolytic activity was extracted using the Wizard Genomic DNA Purification kit A1120. High-molecular weight DNA (approximately 20 000 bp) was separated by horizontal electrophoresis in 1% agarose gel, stained with SYBR safe (5 μg/mL) and visualized using a molecular weight marker (100 to 3000 bp).

For the amplification and purification of the 16S rRNA gene, a 10^{-1} dilution of the genomic DNA was prepared. PCR amplification was performed according to Aguirre-Garrido *et al*. (2012) using universal primers 27F (5'-AGAGTTTGATCCTGGCTCAG-3') and 1492R (5'-GGTTACCTTGTTACGACTT-3'). The PCR products were analyzed by electrophoresis on a 1% agarose gel stained with ethidium bromide (5 μg/mL) and compared to a molecular size marker (100 to 3000 bp).

The amplification was confirmed by electrophoresis and the PCR products were subsequently purified using the Wizard SV Gel and PCR Clean-Up kit (Promega; Ref: A9281). The purified DNA was quantified by electrophoresis on a 1% agarose gel. After amplification and purification of the 16S rRNA gene, the samples were sent to MACROGEN Inc. (South Korea) for sequencing.

Once the sequences were obtained, consensus sequences were generated using the BioEdit sequence alignment editor (Hall, 1999). Then, the sequences were compared with the sequences available in the NCBI GenBank database using the Basic Local Alignment Search Tool (BLAST) program (www.ncbi.

nlm.nih.gov/blast), as described by Aguirre-Garrido et al. (2012). The E value was considered, which is the measure used to estimate the degree of sequence similarity; the closer to 0, the better the alignment and the gaps that refer to the lack of a base in the alignment (Choudhuri, 2014).

The alignment of the sequences was performed using the software ClustalX (Larkin *et al*., 2007). The editing and trimming of the alignments were performed using the program SeaView (Gouy & Gascuel, 2010). Finally, the phylogeny was inferred using the maximum likelihood method and the HKY model (Hasegawa *et al*., 1985). The evolutionary analyses were carried out in MEGA version 12 (Kumar *et al*., 2024).

2.7 Microbial kinetics

Strains that showed halos of cellulose hydrolysis were re-inoculated in serological flasks containing 50 ml of 0.1% CMC broth and incubated at 50°C for 50 hours. For the kinetic study, serological flasks were used as experimental units, to which 60 ml of 0.1% CMC broth were added and inoculated with 10 ml of the previously cultured strain. The experimental units were incubated at 50°C and sampled at different times until reaching growth asymptote. Cell growth was measured indirectly by spectrophotometry (HACH-UV-vis Dr 6000) at a wavelength of 600 nm, using the non-inoculated culture medium as a blank. The microbial growth curve was constructed, the specific growth rate (μ) was determined using the exponential growth model and Gompertz model (Trinidad, 2014), and the doubling time (D_t) was calculated.

3 Results

3.1 Isolation, characterization and identification

The initial compost had a weight of 8.7 kg, a pH of 7.0, a moisture content of 75%, a temperature of 25°C, a COD of 2500 mg/L, and an inorganic nitrogen concentration of 2.5 mg/L. The composting process was successful in all phases and lasted 136 days, yielding 2.7 kg of stable compost. The mesophilic phase lasted 59 days, the thermophilic phase 40 days, the cooling phase 7 days, and the maturation phase 30 days. The results of parameters in the different phases of processing are presented in Table 1. According to the parameters established in the national (NMX-AA-180-SCFI-2018) and international standards such as the Test Methods for the Examination of Composting and Compost [U.S. Department of Agriculture (USDA), 2001] and the composting manual "European Compost Network-Quality Assurance Scheme (ECN-QAS) Manual for Compost and Digestate" [European Compost Network (ECN), 2018], the final compost presented a type 1 quality with a germination rate of 95%.

Among the compost samples in the thermolytic phase, two microbial strains with well-defined morphologies prevailed under the cultivation conditions (i.e., 50°C and CMC medium 0.1%). These strains were labeled as P11 and I12. Strain P11 (Figure 1A) formed punctate colonies with smooth, shiny, raised edges and a dry surface. Strain I12 (Figure 1B) exhibited irregular colonies with convex, filamentous, shiny edges and a dry surface. Regarding the microscopic characterization, both strains were bacillary and Gram positive (Figure 1C-D). Both strains underwent biochemical analysis, the results of which are summarized in Table 2. The results demonstrated the metabolic capability to assimilate glucose, sucrose, and mannitol as carbon sources, produce gas, and reduce nitrates. Additionally, they exhibited motility and growth in 7.5% NaCl (w/v) solution, proteolytic activity on collagen (gelatin), and alpha-hemolysis on bovine erythrocytes.

Based on the biochemical profiles and macro and microscopic morphology, both strains were presumptively identified as belonging to the genus *Bacillus*, following the identification and classification criteria outlined in Bergey's Manual (Vos *et al*., 2011; Koneman, 2012; Mac, 2003). According to the literature, bacteria of the genus *Bacillus* are Gram positive microorganisms capable of forming endospores, allowing them to survive in extreme environments (Beladjal *et al*., 2018). They are facultative aerobes and anaerobes (Harirchi *et al*., 2022) and produce various enzymes, including proteases, amylases, lipases, and cellulases (Yang *et al*., 2021a). Additionally, genus *Bacillus* can metabolize a broad range of carbon sources (e.g., glucose, sucrose, and mannitol) and nitrogen sources (e.g., amino acids, ammonium, nitrate, and nitrite) (Zaprasis et al., 2015).

Table 1. Physicochemical characteristics of the composting phases.

Phase	Phase duration (Day)	Temperature (°C)	pH	Moisture (%)	COD (mg/L)	Inorganic nitrogen (mg/L)
Mesophilic	1-59	29 ± 1	8.56 ± 0.14	67.91 ± 0.42	2450 ± 7.10	2.58 ± 0.20
Thermophilic	59-99	47 ± 2	8.32 ± 0.13	67.80 ± 0.51	1830 ± 14.11	13.58 ± 0.13
Cooling	99-106	30 ± 2	8.21 ± 0.12	80.00 ± 0.50	1013 ± 4.10	12.41 ± 0.21
Maturation	106-136	28 ± 1	7.4 ± 0.09	72.20 ± 0.46	689 ± 5.71	11.43± 0.14

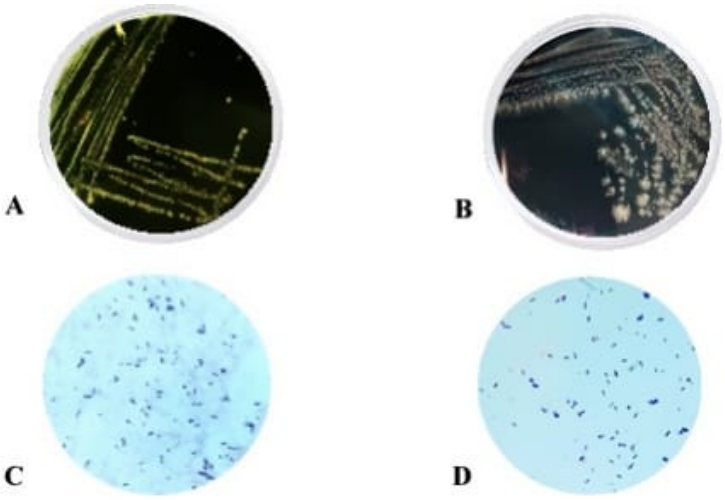

Figure 1. Colonial morphology on CMC 0.1% agar: A) strain P11 and B) strain I12; and Gram stain C) Strain P11 and D) Strain I12.

Table 2. Biochemical test of strains I12 and P11.

Biochemical test	Strain I12	Strain P11
*Glucose, sucrose and lactose	+	+
*Gas production	+	+
*Hydrogen sulfide production	-	-
**Motility	+	+
**Indole	-	-
**Ornitjine	-	-
***Sulfate reduction	-	-
***Indole	-	-
***Motility	+	+
Urea	-	-
Citrate	-	-
Nitrous Broth (nitrate reduction)	+	+
Glucose	+	+
Mannitol	+	+
Sucrose	+	+
Lactose	-	-
Growth in NaCl 7.5%	+	+
Gelatin liquefaction	+	+
Hemolysis of bovine erythrocytes	Alpha hemolysis	Alpha hemolysis

*TSI test, ** MIO test, *** SIM test

The ability of the strains to degrade a wide range of organic substrates suggests their capacity to ferment carbohydrates and adapt to low-oxygen environments by utilizing alternative electron acceptors such as nitrate and fumarate (Rey *et al*., 2004; Blanco *et al* 2024). Motility, likely mediated by flagella-like structures (Ni *et al*., 2024), along with the ability to grow in saline conditions, supports the halotolerant nature of the strains (James *et al*., 2023). Regarding their proteolytic activity on gelatin, this indicates that the bacteria might produce serine proteases and collagenase, which hydrolyze peptide bonds in collagen (Contesini *et al*., 2018; Al-Bedak *et al*., 2023). Additionally, their alpha-hemolytic activity suggests the production of hemolysins, which partially degrade red blood cell membranes (Muras *et al*., 2021).

Identification of strains P11 and I12 at the genus or species level was performed by PCR extraction and amplification of the 16S rRNA gene. For both strains, the Figure 2A shows the DNA extract obtained, with a weight of 20000 bp, and Figure 2B the amplified and purified 16s rRNA gene products a weight of 1500 bp. Sequence analysis in GenBank showed a 97.80% similarity percentage for strain P11 with *Bacillus sp*. and a 100% similarity percentage for strain I12 with *Bacillus licheniformis*. Figure 3 shows the phylogenetic tree where the clustering of *B. sp*. P11 and *B. licheniformis* I12 is shown in bold.

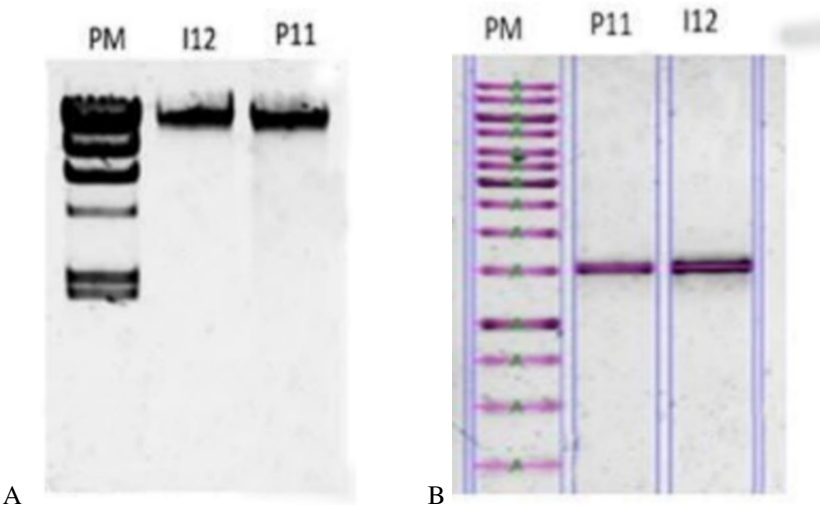

Figure 2. Electrophoresis gel: (A) bacterial DNA extraction, (B) 16s rRNA gene amplification and purification.

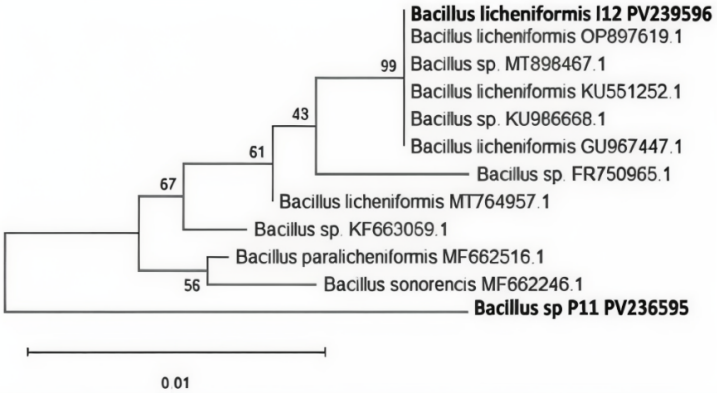

Figure 3. Phylogenetic tree for *Bacillus sp* P11 and *Bacillus licheniformis* I12 inferred by the Maximum Likelihood (ML) method using the nucleotide substitution model of Hasegawa-Kishino-Yano (1985). Twelve sequences with 1,363 positions were analyzed in the final data set. Numbers next to branches represent bootstrap support values, indicating statistical confidence in the clustering of strains within each clade. These values reflect the percentage of replicate trees in which associated taxa clustered (1,000 replicates).

The internal nodes of the phylogenetic tree indicate the proportion of sites where at least one unambiguous base is present in at least one sequence of each descendant clade. The phylogenetic tree suggests that both strains group into well-defined clades with high similarity with other strains within the genus *Bacillus*, although a separation in the tree is observed between the identified strains despite having similar metabolic characteristics. The genus *Bacillus* is highly diverse and includes species with significant genetic variability, even among those sharing similar physiological traits (Xu & Kovács, 2024). Phylogenetic analysis based on the 16S rRNA gene sequence can detect subtle differences that phenotypic tests may overlook, which explains the observed divergence between both genera (Blanco *et al*., 2024)

These results are consistent with the literature where the genus *Bacillus* is reported as the predominant microorganism in the thermophilic phase of composting (López *et al*., 2021; Yang *et al*., 2021b). López *et al*. (2021) identified 159 *Bacillus* and *Firmicutes* strains during composting process of pruning waste and tomato crops, with *Bacillus licheniformis* being one of the most abundant. In the present work, by correlating the molecular and morphological results of the strains, it was possible to corroborate that the characteristics obtained for the *Bacillus licheniformis* strain (I12), such as the lichen-like and cream-coloured colonial morphology, are consistent with the literature. However, it is important to note that the genus *Bacillus* presents a wide range of morphologies, which can vary between species (Logan & Vos, 2015).

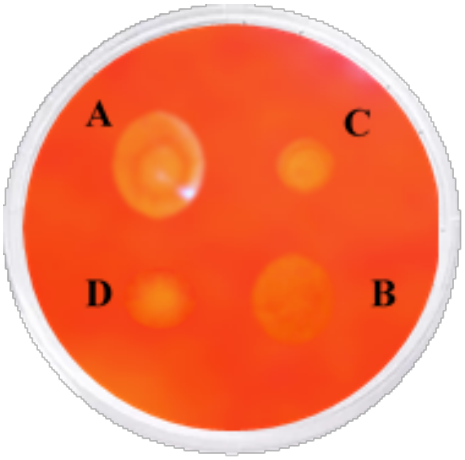

Figure 4. Hydrolysis halos. A and B: *Bacillus sp.,* (P11), C and D: *Bacillus licheniformis* (I12).

3.2 Enzymatic activity and microbial kinetics

Thermophilic microorganisms, such as *Bacillus licheniformis* and *Bacillus sp.,* play a crucial role in composting systems. Through the production of thermostable enzymes, particularly cellulases, they facilitate the efficient degradation of cellulose and other components of plant biomass (Kanekar & Kanekar, 2022; Zhu *et al*., 2020). In the present work, the isolated and characterized strains (i.e., *Bacillus licheniformis* and *Bacillus sp*.) showed their ability to degrade cellulose through a halo formation test using 1% CMC and Congo red agar plates. Both strains showed activity, presenting halos with an average diameter of 10.85 mm ± 0.7 (Figure 4 A-B) and 8 mm ± 0.7 (Figure 2 C-D) for *Bacillus sp.* (P11) and *Bacillus licheniformis* (I12), respectively. The cellulolytic index was determined by calculating the ratio between hydrolysis zone and the colony diameter. The strains *Bacillus sp.* (P11) and *Bacillus licheniformis* (I12) presented CI values of 9.9 ± 0.8 and 7 ± 0.7, respectively. These results highlight the cellulose-degrading ability of the isolated bacteria, which contrasts with the findings of López *et al*. (2021).

López *et al*. (2021) conducted a study during the thermophilic phase of composting (59.4°C ± 6), in which they isolated 159 bacterial strains. The majority belonged to the phylum *Firmicutes* (96%), including *Bacillus licheniformis*, with smaller proportions from *Actinobacteria* (2%) and *Proteobacteria* (2%). However, the isolates exhibited only xylanase activity, with no evidence of cellulolytic activity. Van (2009) documented that *Bacillus licheniformis* presents endoglucanase enzymes that cause the hydrolysis of the glycosidic bonds of cellulose. Medison *et al*. (2023) reported *Bacillus* hydrolysis halos of 5 to 20 mm in a medium with sodium carboxymethylcellulose through the Congo red test on CMC plates at culture temperatures of 28°C. Li *et al*. (2023) reported the isolation of *Bacillus subtilis* from silkworm excrement with a hydrolysis halo diameter of 1.75 mm and CI of 3.5, using sodium carboxymethylcellulose as a carbon source and cultivating it at 55°C with a pH of 6. Vásquez & Millones (2023) reported the isolation from the thermophilic phase of a compost with a temperature of 53.5°C, pH of 6.8 and moisture of 54.8% of *Bacillus subtilis* and *Bacillus safensis subsp. safensis* with a cellulose hydrolysis halo diameter of 7.5 to 8.6 mm and an CI of 0.33 to 0.9, respectively. The variations in hydrolysis halo diameters and cellulolytic index reflect the diversity of the strains and their adaptability to different isolation environments (Hemati et al., 2021; Jiang *et al*., 2021). In this context, the strains isolated in this study are particularly significant, as they exhibited a higher cellulolytic index, highlighting their potential for efficient cellulose degradation.

The CMC degradation efficiency was obtained from the initial and final COD of the strains grown in 0.1% CMC. The degradation percentages obtained for *Bacillus sp* (P11) and *Bacillus licheniformis* (I12) were 0.60% ± 0.01 and 0.49% ± 0.02, respectively. The role of *Bacillus* species in cellulose degradation during the thermophilic phase of composting has been previously reported (Ince *et al*., 2020). In this context, Table 3 presents recalculated cellulose degradation percentages based on enzymatic activity (U) values reported in the literature. These values were estimated using the conversion factor of 1U = 1.8016×10^4 g CMC hydrolyzed, which reflects the amount of substrate degraded per unit of enzyme activity.

Table 3. Comparison based on cellulose degradation percentage.

Reference	Substrate	Degradation (%)	Phase temperature (°C)	Bacteria associated with degradation
This work	CMC 0.1%	0.69 0.49	47	*Bacillus* sp *Bacillus licheniformis*
Ma *et al*. (2020)	*CMC	150 U 0.03**	57.6	*Bacillus*
Liu *et al*. (2020)		11.6 U 0.2**	55	*Bacillus*
Zhang *et al*. (2021)		144 U 2.5**	> 50	*Firmicutes*

U: amount of substrate consumed in μmol/min; *The use of CMC is indicated but not the concentration; **To compare the results obtained in this work, the units were changed to mass units, considering the equivalence of 1U = 1.8016×10^4 g CMC hydrolyzed.

Table 4. Comparison of the kinetic parameters obtained through the Gompertz model and the exponential growth model.

	Bacillus sp. (P11)			*Bacillus licheniformis* (I12)		
Model	μ (h^{-1})	D_t (h)	R^2	μ (h^{-1})	D_t (h)	R^2
Exponential	0.105 ± 0.010	6.5 ± 0.4	0.93	0.420 ± 0.005	1.6 ± 0.5	0.80
Gompertz	0.105 ± 0.005	6.5 ± 0.3	0.99	0.079 h^{-1} ± 0.010	8.8 ± 1.0	0.97

These results confirmed that the strains isolated in this work have a high potential for cellulose degradation. This capacity can be attributed to its enzymatic production and adaptation to composting conditions, reinforcing its applicability in environmental biotechnology, particularly in the treatment and valorization of organic waste through composting (López *et al*., 2021).

On the other hand, Figure 5 shows the microbial growth profiles of both strains, fitted to the Gompertz model. Both strains exhibited a lag phase of approximately 3 hours. Subsequently, *Bacillus sp.* entered the exponential phase, which lasted until hour 30, whereas *Bacillus licheniformis* maintained exponential growth until hour 40. Table 4 shows the specific growth rate (μ) and doubling time obtained using both the Gompertz and exponential growth models. For *Bacillus sp*., both models yielded similar values for growth rate and doubling time. In contrast, for *Bacillus licheniformis*, the Gompertz model provided a better fit to the experimental data, as indicated by a higher correlation coefficient (R^2 = 0.97).

Recent studies on the kinetic parameters of these strains are limited in the literature. Among the limited data available, the D_t varies based on culture conditions. Errington & Aart (2020) reported that *Bacillus* had a D_t of 0.33 hours at 35°C in a nutrient medium. Da Silva *et al*. (2021) reported a doubling time of 6.3 hours at 50°C when using glucose alone or in combination with casein as a carbon source. The influence of culture conditions, particularly the availability of carbon and nitrogen sources, on the growth of thermophilic bacteria is well documented. For instance, Da Silva *et al*. (2021) and O'Hair *et al*. (2020) reported doubling times of 11.5 hours and 0.43 hours, respectively, *for Bacillus licheniformis* grown on CMC and casein. Similarly, Hanlon & Hodges (1981) found that *Bacillus licheniformis* cultured at 37°C with glucose and ammonium chloride had a doubling time of 1 hour. However, when the nitrogen source was replaced with sodium nitrate, alanine, or glutamic acid, the doubling time increased to 1.65, 1.77, and 1.90 hours, respectively, demonstrating that both growth rate and doubling time are highly dependent on substrate availability. Liu *et al*. (2023) further emphasized that culture conditions significantly affect microbial kinetics, with *Bacillus* species maintaining their growth and degradation capacity at high temperatures, though their kinetic behavior varies depending on nutrient availability. Da Silva *et al*. (2021) highlights the importance of composting systems as valuable sources for isolating microorganisms, as the diversity of carbon sources in these environments influences microbial adaptation. In the case of lignocellulosic waste, bacteria degrade complex compounds such as cellulose, leading to shorter doubling times under similar culture conditions, particularly when using CMC as a carbon source (Zhu *et al*., 2021).

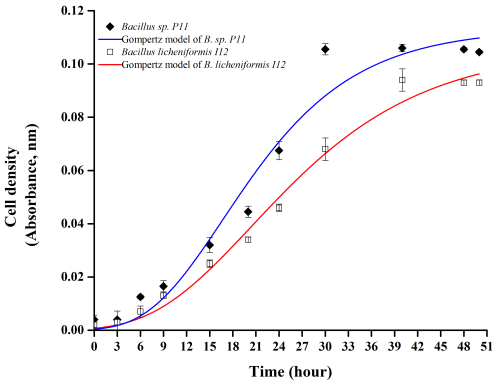

Figure 5. Cell growth curve and Gompertz model fitting of strain *B. sp* P11 and *B. licheniformis* I12.

Understanding key kinetic parameters, such as the specific growth rate and doubling time, provides deeper insights into microbial metabolism on different substrates. This knowledge enables better control of fermentation processes, the optimization of bioreactor design, and the development of strategies to enhance the production of valuable enzymes (Straathof, 2023). Currently, research is focused on exploring the applications of these bacterial enzymes in the biodegradation of lignocellulosic waste to obtain nanocellulose (Herrera-Basurto *et al*., 2024) and the production of biofuels or biomaterials such as polyhydroxyalkanoates (Castilla-Marroquín *et al*., 2024)

Conclusions

The two thermophilic bacterial strains isolated from the thermophilic phase of an urban organic waste compost were identified through macro and microscopic, metabolic, and genetic analyses as *Bacillus sp*. and *Bacillus licheniformis*. Their kinetic characterization

revealed growth rates and doubling times of 0.105 h^{-1} ± 0.005; 6.5 h ± 0.3 and 0.0794 h^{-1} ± 0.01; 8.8 h ± 1, respectively. Both strains exhibited significant cellulolytic activity, with hydrolysis halos of 10.85 mm ± 0.7 and 8 mm ± 0.7, and cellulolytic indexes of 9.9 ± 0.8 and 7 ± 0.7, respectively. These findings highlight the critical role of composting systems as reservoirs of thermostable cellulolytic microorganisms with valuable biotechnological applications. Furthermore, the metabolic and kinetic characterization of these strains provides a strong foundation for future research aimed at optimizing composting processes and enhancing the bioconversion of lignocellulosic waste into valuable products. Their potential application in sustainable waste management and bioresource recovery underscores their relevance in environmental biotechnology.

Acknowledgements

This work was part of a project financed by Secretaría de Investigación y Estudios Avanzados (SIEA) UAEMéx, México, code number: 7276/2025CIB.

References

Aguirre-Garrido, J. F., Montiel-Lugo, D., Hernández-Rodríguez, C., Torrescortes, G., Millán, V., Toro, N., Martínez-Abarca, F. and Ramírez-Saad, H. C. (2012). Bacterial community structure in the rhizosphere of three cactus species from semiarid highlands in central Mexico. *Antonie van Leeuwenhoek* 101, 891-904. https://doi.org/10.1007/s10482-012-9705-3

Al-Bedak, O. A.-H. M., Moharram, A. M., Hussein, N. A.-G., Taha, D. M., Stephenson, S. L., and Ameen, F. (2023). Microbial Exploitation of Feather Wastes for Sustainable Production of Keratinase and Collagenase Enzymes by Didymella keratinophila AUMC 15399 in Submerged Fermentation. *Fermentation*, 9(6), 507. https://doi.org/10.3390/fermentation9060507

Anguiano Aguilar, E. (2019). Aislamiento, selección y caracterización de bacterias con actividad celulolítica. Tesis de maestría, Universidad Michoacana de San Nicolás de Hidalgo, Morelia, México.

Babu, R., Veramendi, P. M. P. and Rene, E. R. (2021). Strategies for resource recovery from the organic fraction of municipal solid waste. *Case studies in chemical and environmental engineering 3*, 100098. https://doi.org/10.1016/j.cscee.2021.100098

Banerjee, A., Cornejo, J. and Bandopadhyay, R. (2020). Emergent climate change impact throughout the world: call for "Microbiome Conservation" before it's too late. *Biodiversity and Conservation* 29, 345-348. https://doi.org/10.1007/s10531-019-01886-6

Beladjal, L., Gheysens, T., Clegg, J. S., Amar, M. and Mertens, J. (2018). Life from the ashes: survival of dry bacterial spores after very high temperature exposure. *Extremophiles* 22, 751–759. https://doi.org/10.1007/s00792-018-1035-6

Blanco Crivelli, X., Cundon, C., Bonino, M. P., Sanin, M. S. and Bentancor, A. (2024). The Complex and Changing Genus Bacillus: A Diverse Bacterial Powerhouse for Many Applications. *Bacteria*, 3(3), 256-270. https://doi.org/10.3390/bacteria3030017

Cao, X., Williams, P. N., Zhan, Y., Coughlin, S. A., McGrath, J. W., Chin, J. P. and Xu, Y. (2023). Municipal solid waste compost: Global trends and biogeochemical cycling. *Soil & Environmental Health 1*, 100038. https://doi.org/10.1016/j.seh.2023.100038

Castilla-Marroquín, J. D., Pacheco, N., Herrera-Corredor, J. A., Hernández-Rosas, F., Jiménez-Morales, K., Benítez-Salamanca, M. J., and Hernández-Martínez, R. (2024). Polyhydroxyalkanoates Production by Bacillus thuringiensis HA1 Using Sugarcane Molasses as Carbon Source. *Revista Mexicana de Ingeniería Química* 23(3), 1-12. https://doi.org/10.24275/rmiq/Bio24352

Choudhuri, S. (2014). Sequence Alignment and Similarity Searching in Genomic Databases: BLAST and FASTA. *Bioinformatics for Beginners*, (Academic Press), Pp. 133-155. https://doi.org/10.1016/B978-0-12-410471-6.00006-2

Contesini, F. J., Melo, R. R. D. and Sato, H. H. (2018). An overview of Bacillus proteases: from production to application. *Critical reviews in biotechnology* 38, 321-334. https://doi.org/10.1080/07388551.2017.1354354

Da Silva, R. N., de Andrade Melo, L. F. and Finkler, C. L. L. (2021). Optimization of the cultivation conditions of *Bacillus licheniformis* BCLLNF-01 for cellulase production. *Biotechnology Reports*, 29. https://doi.org/10.1016/j.btre.2021.e00599

De Mendonça Costa, L. A., de Mendonça Costa, M. S. S., Damaceno, F. M., Chiarelotto,

M., Bofinger, J. and Gazzola, W. (2021). Bioaugmentation as a strategy to improve the compost quality in the composting process of agro-industrial wastes. *Environmental Technology & Innovation 22*, https://doi.org/10.1016/j.eti.2021.101478

Environmental Protection Agency. (2021). Standards for the Use or Disposal of Sewage Sludge https://www.federalregister.gov/documents/2001/12/21/01-31342/standards-for-the-use-or-disposal-of-sewage-sludge

Errington, J. and Aart, L. T. V. D. (2020). Microbe Profile: *Bacillus subtilis*: model organism for cellular development, and industrial workhorse. *Microbiology* 166, 425-427. https://doi.org/10.1099/mic.0.000922

European Compost Network. ECN – QAS Manual for Compost and Digestate. (2018) https://www.compostnetwork.info/ecn-qas/ecn-qas-manual/

Firone I., Feola A., Russo L., Cattaneo, A., Di Donato P., Nicolaus B. and Romano I. (2023). Thermophilic bacteria and their thermozymes in composting processes: a review. *Chemical and Biological Technologies in Agriculture 10*, 7. https://doi.org/10.1186/s40538-023-00381-z

Getahun, T., Nigusie, A., Entele, T., Van Gerven, T., and Van der Bruggen, B. (2012). Effect of turning frequencies on composting biodegradable municipal solid waste quality. *Resources, Conservation and Recycling 65*, 79-84. https://doi.org/10.1016/j.resconrec.2012.05.007

Gouy M., Guindon S., and Gascuel O. (2010) SeaView version 4 : a multiplatform graphical user interface for sequence alignment and phylogenetic tree building. Molecular Biology and Evolution 27(2):221-224. https://doi.org/10.1093/molbev/msp259

Guo, R., Li, G., Jiang, T., Schuchardt, F., Chen, T., Zhao, Y., and Shen, Y. (2012). Effect of aeration rate, C/N ratio and moisture content on the stability and maturity of compost. *Bioresource technology 112*, 171-178. https://doi.org/10.1016/j.biortech.2012.02.099

Hall, T. A. (1999, January). BioEdit: a user-friendly biological sequence alignment editor and analysis program for Windows 95/98/NT. *In Nucleic acids symposium series* 41, 95-98.

Hanlon, G. W. and Hodges, N. A. (1981). Bacitracin and protease production in relation to sporulation during exponential growth of *Bacillus licheniformis* on poorly utilized carbon and nitrogen sources. *Journal of bacteriology* 147, 427–431. https://doi.org/10.1128/jb.147.2.427-431.1981

Harirchi, S., Sar, T., Ramezani, M., Aliyu, H., Etemadifar, Z., Nojoumi, S. A., Yazdian, F., Awasthi, M. K. and Taherzadeh, M. J. (2022). Bacillales: From Taxonomy to Biotechnological and Industrial Perspectives. *Microorganisms* 10, 2355. https://doi.org/10.3390/microorganisms10122355

Hasegawa, M., Kishino, H., and Yano, T. (1985). Datinf the human-ape split by a molecular clock of mitochondrial DNA. Journal of Molecular Evolution 22, 160-174.

Hemati, A., Aliasgharzad, N., Khakvar, R., Khoshmanzar, E., Lajayer, B. A. and van Hullebusch, E. D. (2021). Role of lignin and thermophilic lignocellulolytic bacteria in the evolution of humification indices and enzymatic activities during compost production. *Waste Management*, 119, 122-134. https://doi.org/10.1016/j.wasman.2020.09.042

Herrera-Basurto, R., Ramos-López, E., Rodríguez-López, A., González-Olvera, J. C., Morales-Hernández, J., Hurtado-Macías, A., Vergara-Hernández, H. J., and Mercader-Trejo, F. (2024). Study on wild grasses as a potential source of cellulose nanofibers. *Revista Mexicana de Ingeniería Química* 23(3), 1-12. https://doi.org/10.24275/rmiq/Mat24245

Hussian, C. H. A. C., and Leong, W. Y. (2023). Thermostable enzyme research advances: a bibliometric analysis. *Journal of Genetic Engineering and Biotechnology* 21, 37. https://doi.org/10.1186/s43141-023-00494-w

Ince, O., Ozbayram, E. G., Akyol, Ç, Erdem, E. I, Gunel, G., and Ince, B. (2020). Bacterial succession in the thermophilic phase of composting of anaerobic digestates. *Waste and Biomass Valorization* 11, 841–849. https://doi.org/10.1007/s12649-018-0531-3

James, N., Umesh, M., Sarojini, S., Shanmugam, S., Nasif, O., Alharbi, S. A., Chi, L.T.N. and Brindhadevi, K. (2023). Unravelling the potential plant growth activity of halotolerant Bacillus licheniformis NJ04 isolated from soil and its possible use as a green bioinoculant on Solanum lycopersicum L. *Environmental Research*, *216*, 114620. https://doi.org/10.1016/j.envres.2022.114620

Jiang, J., Wang, Y., Yu, D., Yao, X., Han, J., Cheng, R., Cui, H., Yan, G., Zhang, X. and Zhu G. (2021). Garbage enzymes effectively regulated the succession of enzymatic activities and the bacterial community during sewage sludge composting. Bioresour Technology 327, 1–10. https://doi.org/10.1016/j. biort ech.2021.124792

Kanekar, P. P., and Kanekar, S. P. (2022). Thermophilic, thermotolerant microorganisms. *In Diversity and Biotechnology of Extremophilic Microorganisms from India* , Pp.117-153. Singapore: Springer Nature Singapore. https://doi.org/10.1007/978-981-19-1573-4_4

Koneman, E., Winn Jr, W., Allen, S., Janda, W., Procop, G., Schreckenberber, P. and Woods, G. (2012). Diagnóstico microbiológico: texto e atlas colorido. In *Diagnóstico microbiológico*: texto e atlas colorido (pp. xxxv-1565).

Kumar, S,. Stecher, G,. Suleski, M,. Sanderford, M,. Sharma, S., and Tamura, K. (2024). Molecular Evolutionary Genetics Analysis Version 12 for adaptive and green computing. *Molecular Biology and Evolution* 41, 1-9. https://doi.org/10.1093/molbev/msae263

Larkin, M. A., Blackshields, G., Brown, N. P., Chenna, R., McGettigan, P. A., McWilliam, H., Valentin, F., Wallace, I. M., Wilm, A., Lopez, R., Thompson, J. D., Gibson, T. J., and Higgins, D. G. (2007). Clustal W and Clustal X version 2.0. *Bioinformatics* 23, 2947-2948. https://doi.org/10.1093/bioinformatics/btm404

Li, H., Zhang, M., Zhang, Y., Xu, X., Zhao, Y., Jiang, X., Zhang, R., and Gui, Z. (2023). Chracterization of Cellulose-Degrading Bacteria Isolated from Silkworm Excrement and Optimization of Its Cellulase Production. *Polymers* 15, 4142. https://doi.org/10.3390/polym15204142

Li, J., Sun, L., and Huo, Y. X. (2025). High-Temperature Catalytic Platform Powered by Thermophilic Microorganisms and Thermozymes. *Synthetic Biology and Engineering*, 3(1), 10001. https://doi.org/10.70322/sbe.2025.10001

Liu, G., Zhang, K., Gong, H., Yang, K., Wang, X., Zhou, G., Cui, W., Chen, Y., and Yang, Y. (2023). Whole genome sequencing and the lignocellulose degradation potential of Bacillus subtilis RLI2019 isolated from the intestine of termites. *Biotechnol Biofuels* 16, 130. https://doi.org/10.1186/s13068-023-02375-3

Liu, H., Huang, Y., Wang, H., Shen, Z., Qiao, C., Li, R. and Shen, Q. (2020). Enzymatic activities triggered by the succession of microbiota steered fiber degradation and humification during co-composting of chicken manure and rice husk. *Journal of environmental management* 258, 110014. https://doi.org/10.1016/j.jenvman.2019.110014

Logan, N. A. and Vos, P. D. (2015). Bacillus. *Bergey's manual of systematics of archaea and bacteria*, Pp. 1-163.

López, M. J., Jurado, M. M., López-González, J. A., Estrella-González, M. J., Martínez-Gallardo, M. R., Toribio, A., and Suárez-Estrella, F. (2021). Characterization of thermophilic lignocellulolytic microorganisms in composting. *Frontiers in microbiology* 12, 697480. https://doi.org/10.3389/fmicb.2021.697480

Lynd, L., Weimer, P., Van Zyl, W. H. and Pretorius, I. S. (2022). Microbial Cellulose Utilization: Fundamentals and Biotechnology. *Microbiology and molecular biology reviews* 3, 506–577. https://doi.org/10.1128/mmbr.66.3.506-577.2002

Ma, C., Jin, H. J., Hu, B., Liu, N., Zhang, K., Zhao, J. H. and Zhang, H. Z. (2020). Changes in Enzyme Activity and Bacterial Succession During Sewage Sludge Composting. *Nature Environment & Pollution Technology* 19, 695-701. https://doi.org/10.46488/NEPT.2020.v19i02.024

Mac Faddin, J. (2003). Pruebas bioquimicas para la Identificacion de bacterias de Importancia Clinica. 3era Edicion. Editorial Médica Panamericana. Buenos Aires-Argentina.

Madigan, M. T., Martinko, J. M. and Parker, J. (2004). Brock. Biología de los microorganismos.

Medison, R. G., Jiang, J., Medison, M. B., Tan, L. T., Kayange, C. D., Sun, Z. and Zhou, Y. (2023). Evaluating the potential of *Bacillus licheniformis* YZCUO202005 isolated from lichens in maize growth promotion and biocontrol. *Heliyon 9* https://doi.org/10.1016/j.heliyon.2023.e20204

Moreno, J., López-González, J. A., Arcos-Nievas, M. A., Suárez-Estrella, F., Jurado, M. M., Estrella-González, M. J. and López, M. J. (2021). Revisiting the succession of microbial populations throughout composting: a matter of thermotolerance. Science of The Total Environment 773,145587. https://doi.org/10.1016/j.scitotenv.2021.145587

Muras, A., Romero, M., Mayer, C. and Otero, A. (2021). Biotechnological applications of *Bacillus licheniformis*. *Critical Reviews in Biotechnology* 41, 609-627. https://doi.org/10.1080/07388551.2021.1873239

Nguyen, V. T., Le, T. H., Bui, X. T., Nguyen, T. N., Vo, T. D. H., Lin, C., Vu, T. M. H., Nguyen, H. H., Nguyen, D. D., Senoro D. B. and Dang, B. T. (2020). Effects of C/N ratios and turning frequencies on the composting process of food waste and dry leaves. *Bioresource Technology Reports*, *11*, 100527. https://doi.org/10.1016/j.biteb.2020.100527

Ni, S., Wu, Y., Zhu, N., Leng, F. and Wang, Y. (2024). Bacillus licheniformis YB06: A Rhizosphere–Genome-Wide Analysis and Plant Growth-Promoting Analysis of a Plant Growth-Promoting Rhizobacterium Isolated from Codonopsis pilosula. *Microorganisms*, *12*(9), 1861. https://doi.org/10.3390/microorganisms12091861

O'Hair, J., Jin, Q., Yu, D., Poe, N., Li, H., Thapa, S., Zhou, S. and Huang, H. (2020). Thermophilic and alkaliphilic *Bacillus licheniformis* YNP5-TSU as an ideal candidate for 2, 3-butanediol production. *ACS Sustainable Chemistry & Engineering* 8, 11244-11252. https://doi.org/10.1021/acssuschemeng.0c02759

Rainey, F., Kämpfer, P., Trujillo, M., Chun, J., DeVos, P., Hedlund, B. and Dedysh, S. (2015). Bergey's manual of systematics of Archaea and Bacteria (Vol. 410). W. B. Whitman (Ed.). Hoboken, NJ.

Rey, M. W., Ramaiya, P., Nelson, B. A., Brody-Karpin, S. D., Zaretsky, E. J., Tang, M., Lopez de Leon, A., Xiang, H., Gusti, V., Clausen, I. G., Olsen, P. B., Rasmussen, M. D., Andersen, J. T., Jorgenses, P. L., Larsen, T. S., Sorokin, A., Bolotin, A., Lapidus, A., Galleron, N., Ehrlich, S. D., and Berka, R. M. (2004). Complete genome sequence of the industrial bacterium Bacillus licheniformis and comparisons with closely related *Bacillus* species. *Genome biology 5*, 1-12. https://doi.org/10.1186/gb-2004-5-10-r77

Rodríguez Silva, L. A., y Llenque Díaz, L. (2016). Aislamiento y selección de bacterias celulolíticas a partir de compost de residuos orgánicos. *REBIOL* 36, 19-28. https://revistas.unitru.edu.pe/index.php/facccbiol/article/view/1310

Secretaría de Economía. (2018). NMX-AA-180-SCFI-2018: Que establece los métodos y procedimientos para el tratamiento aerobio de la fracción orgánica de los residuos sólidos urbanos y de manejo especial, así como la información comercial y de sus parámetros de calidad de los productos finales. Diario Oficial de la Federación. https://dof.gob.mx/nota_detalle.php?codigo=5539165&fecha=26/09/2018#gsc.tab=0

Secretaría de Medio Ambiente y Recursos Naturales (SEMARNAT). (1985). NMX-AA-52-1985. Protección al ambiente- contaminación del suelo-residuos sólidos municipales-preparación de muestras en el laboratorio para su análisis. Diario Oficial de la Federación. http://legismex.mty.itesm.mx/normas/aa/aa052.pdf

Siu-Rodas, Y., de los Angeles Calixto-Romo, M., Guillén-Navarro, K., Sánchez, J. E., Zamora-Briseno, J. A. and Amaya-Delgado, L. (2018). *Bacillus subtilis* with endocellulase and exocellulase activities isolated in the thermophilic phase from composting with coffee residues. *Revista Argentina de Microbiología 50*, 234-243. https://doi.org/10.1016/j.ram.2017.08.005

Straathof, A. J. (2023). Modelling of end-product inhibition in fermentation. *Biochemical Engineering Journal* 191, 108796. https://doi.org/10.1016/j.bej.2022.108796

Trinidad Bello, A. (2014). Modelos de crecimiento en biología, su significado biológico y selección del modelo por su ajuste [Tesis de licenciatura, Universidad Autónoma Metropolitana - Iztapalapa]. Repositorio Institucional UAM. https://bindani.izt.uam.mx/concern/tesiuams/dj52w481t

Van Dyk, J. S. (2009). Characterization of the Cellulolytic and Hemicellulolytic System of *Bacillus Licheniformis SVD1* and the Isolation and Characterization of a Multi-enzyme Complex. Tesis de Doctorado, Rhodes University.

Vásquez, E. and Millones, C. (2023). Isolation and Identification of Bacteria of Genus Bacillus from Composting Urban Solid Waste and Palm Forest in Northern Peru. *Microorganisms*, 11, 751. https://doi.org/10.3390/microorganisms11030751

Vos, P., Garrity, G., Jones, D., Krieg, N. R., Ludwig, W., Rainey, F. A., ... & Whitman, W. B. (Eds.). (2011). Bergey's manual of systematic bacteriology: Volume 3: The Firmicutes (Vol. 3). Springer Science & Business Media.

Wang, C., & Kuzyakov, Y. (2024). Mechanisms and implications of bacterial-fungal competition

for soil resources. *The ISME journal*, 18(1), wrae073. https://doi.org/10.1093/ismejo/wrae073

Waqas, M., Hashim, S., Humphries, U. W., Ahmad, S., Noor, R., Shoaib, M., Naseem, A., Hlaing P. T. and Lin, H. A. (2023). Composting processes for agricultural waste management: a comprehensive review. *Processes 11*, 731. https://doi.org/10.3390/pr11030731

Xu, X., & Kovács, Á. T. (2024). How to identify and quantify the members of the Bacillus genus?. *Environmental Microbiology*, 26(2), e16593. https://doi.org/10.1111/1462-2920.16593

Yang, H., Qu, J., Zou, W., Shen, W. and Chen, X. (2021a). An overview and future prospects of recombinant protein production in *Bacillus subtilis*. *Applied Microbiology and Biotechnology* 105, 6607-6626. https://doi.org/10.1007/s00253-021-11533-2

Yang, J., Zhao, J., Jiang, J., Xu, H., Zhang, N., Xie, J. and Wei, M. (2021b). Isolation and characterization of *Bacillus sp*. capable of degradating alkali lignin. *Frontiers in Energy Research* 9, 807286. https://doi.org/10.3389/fenrg.2021.807286

Zainudin, M. H. M., Singam, J. T., Sazili, A. Q., Shirai, Y. and Hassan, M. A. (2022). Indigenous cellulolytic aerobic and facultative anaerobic bacterial community enhanced the composting of rice straw and chicken manure with biochar addition. Scientific Reports, 12(1), 5930. https://doi.org/10.1038/s41598-022-09789-3

Zaprasis, A., Bleisteiner, M., Kerres, A., Hoffmann, T. and Bremer, E. (2015). Uptake of amino acids and their metabolic conversion into the compatible solute proline confers osmoprotection to *Bacillus subtilis*. *Applied and Environmental Microbiology 81*, 250-259. https://doi.org/10.1128/AEM.02797-14

Zhang, S., Wang, J., Chen, X., Gui, J., Sun, Y. and Wu D. (2021). Industrial-scale food waste composting: effects of aeration frequencies on oxygen consumption, enzymatic activities, and bacterial community succession. *Bioresource Technology* 320, 1–10. https://doi.org/10.1016/j.biortech.2020.124357

Zhu, D., Adebisi, W. A., Ahmad, F., Sethupathy, S., Danso, B. and Sun, J. (2020). Recent development of extremophilic bacteria and their application in biorefinery. *Frontiers in Bioengineering and Biotechnology* 8, 483. https://doi.org/10.3389/fbioe.2020.00483

Zhu, N., Gao, J., Liang, D., Zhu, Y., Li, B,. and Jin, H. (2021). Thermal pretreatment enhances the degradation and humification of lignocellulose by stimulating thermophilic bacteria during dairy manure composting. *Bioresource Technology* 319, 1–9. https://doi.org/10.1016/j.biortech.2020.124149

Vol. 24, No. 3(2025) Bio25569
Revista Mexicana de Ingeniería Química

Thermoultrasonication as an emerging technology for raw cow's milk processing: A review of its impacts on food safety and physicochemical quality

La termoultrasonicación como tecnología emergente para la leche de vaca: Una revisión de su impacto sobre la inocuidad alimentaria y la calidad fisicoquímica

A. Monter-Arciniega[1], N. S. Cruz-Cansino[1], A. Castañeda-Ovando[2], A. S. Jiménez-Osorio[3], C. Jiménez-Pérez[4], S. R. Tello-Solís[5], G. M. Rodríguez-Serrano[4]*

[1]Área Académica de Nutrición, Universidad Autónoma del Estado de Hidalgo, Hidalgo 42160, México.
[2]Área Académica de Química, Universidad Autónoma del Estado de Hidalgo, Hidalgo 42184, México.
[3]Área Académica de Enfermería, Universidad Autónoma del Estado de Hidalgo, Hidalgo 42160, México.
[4]Departamento de Biotecnología, Universidad Autónoma Metropolitana, Cuidad de México 09340, México.
[5]Departamento de Química, Universidad Autónoma Metropolitana, Cuidad de México 09340, México.

Sent date: April 12, 2025; Accepted: August 30, 2025

Abstract

Ultrasonication combined with mild heating (TUS) has emerged as a promising alternative to conventional heat treatment (CHT) for the processing of raw cow's milk (RCM). Recent studies report significant microbial inactivation—typically around 2.5 log reductions—while preserving key nutritional and physicochemical properties. The majority of findings indicate minimal degradation of proteins and lipids, improved viscosity, enhanced stability of bioactive compounds, and a marked decrease in aflatoxin M1 (AFM1) levels. Although processing parameters such as amplitude, frequency, and duration vary across studies, there is a consistent emphasis on the synergistic effect of acoustic cavitation and moderate thermal input. This synergy not only contributes to microbial safety but also offers potential reductions in energy consumption compared to traditional thermal processing. Nevertheless, further efforts are required to scale up the technology and standardize operating protocols to facilitate regulatory acceptance. These findings collectively underscore the potential of TUS as an innovative and efficient approach for enhancing the safety and quality of dairy products.

Keywords: milk, thermoultrasonication, microbial inactivation, physicochemical properties, dairy processing.

Resumen

La ultrasonicación combinada con temperatura suave (TUS) ha surgido como una alternativa prometedora al tratamiento térmico convencional (CHT) para el procesamiento de leche cruda de vaca (RCM). Estudios recientes reportan una inactivación microbiana significativa —típicamente alrededor de 2.5 reducciones log—, mientras se preservan las propiedades nutritivas y fisicoquímicas clave. La mayoría de los hallazgos indican una degradación mínima de las proteínas y los lípidos, una mejor viscosidad, una mayor estabilidad de los compuestos bioactivos y una marcada disminución de los niveles de aflatoxina M1 (AFM1). Aunque los parámetros de procesamiento como la amplitud, la frecuencia y la duración varían entre los estudios, hay un énfasis constante en el efecto sinérgico de la cavitación acústica y la entrada térmica moderada. Esta sinergia no sólo contribuye a la seguridad microbiana, sino que también ofrece reducciones potenciales en el consumo de energía en comparación con el tratamiento térmico tradicional. Sin embargo, se requieren más esfuerzos para ampliar la tecnología y estandarizar los protocolos de funcionamiento a fin de facilitar la aceptación reglamentaria. Estos resultados subrayan colectivamente el potencial del TUS como un enfoque innovador y eficiente para mejorar la seguridad y calidad de los productos lácteos.

Palabras clave: leche, termoultrasonicación, inactivación microbiana, propiedades fisicoquímicas, procesamiento de leche.

*Corresponding author. *E-mail*: gmrs@xanum.uam.mx;
https://doi.org/10.24275/rmiq/Bio25569
ISSN:1665-2738, *issn-e*: 2395-8472

1 Introduction

Conventional heat treatments (CHT), such as pasteurization and ultra-high-temperature processing, are widely employed in the food industry to eliminate pathogenic microorganisms and extend shelf life. However, these methods often degrade heat-sensitive nutrients and alter the physical and sensory characteristics of food products (Albenzio *et al*. 2012; Cadwallader & Singh, 2009). In response to these drawbacks, alternative technologies have been proposed to ensure microbial safety while minimizing physical, chemical, and nutritional losses. Emerging food processing technologies such as pulsed electric fields, high hydrostatic pressure, microfiltration, ultrasonication (US), and thermoultrasonication (TUS) offer promising alternatives to reduce thermal damage in liquid matrices and potentially complement conventional methods in the dairy industry (Cregenzán *et al*. 2014; Hernandez-Falcón *et al*. 2018; Sharma *et al*. 2014; Stratakos *et al*. 2019).

Among these technologies, US has been reported to be used at low (<1 W/cm^2) or high (>1 W/cm^2) intensities, with frequencies ranging from 20 to 500 kHz (Karlović *et al*. 2014). The US has demonstrated considerable utility in food processing, improving meat texture and aging, modifying physicochemical properties, and regulating enzymatic activity in bovine muscle (Castillo-Andrade *et al*., 2025). Building on this, Loan *et al*. (2024) showed that US-assisted enzyme extraction of purple rice bran uses acoustic cavitation to accelerate mass transfer and alter plant cell structures, resulting in higher polyphenol recovery and faster reaction rates. Similarly, Obando-Galicia *et al*. (2024) reported that US or high-shear extraction with a food-grade soybean oil/lecithin system improves polyphenol recovery from the red pear shell of the cactus; the extracts were also tailored to match the rheology and microstructure of the oleo-gel. Additionally, Ramos-Villacob *et al*. demonstrated that complexing lauric acid with amylose in cassava starch promotes V-type inclusion complexes by enhancing diffusion and inducing transient disorder, enabling quicker kinetics and more precise control of functionality. Under specific conditions, however, this technology may degrade nutrients and produce undesirable flavor compounds due to the formation of peroxides and lipid oxidation products (Chandrapala *et al*. 2012; Marchesini *et al*. 2015). To minimize these effects, US has been combined with other treatments, such as pressure (manosonication), heat and pressure (manothermosonication), or heat alone (TUS). Although the temperature in TUS can be controlled, potential effects on thermolabile components such as proteins and vitamins cannot be ruled out (Mahmoud *et al*., 2022).

Compared to CHT, TUS has been shown to cause minimal changes in the nutritional properties, physical characteristics, antioxidant capacity, and enzymatic activity of fruits and vegetables and/or fermented beverages derived from blackberry, apple, strawberry, mango, carrot, beet, almond, cactus fruit, aguamiel, and milk (Cervantes-Elizarrarás *et al*., 2017; Cruz-Cansino *et al*., 2015; Hernández-Falcón *et al*., 2018; Parreiras *et al*., 2020; Zafra-Rojas *et al*., 2023). The consumption of liquid cow's milk remains an integral part of the human diet due to its content of high-biological-value proteins, calcium, essential fatty acids, amino acids, fats, water-soluble vitamins, and various bioactive compounds that play crucial roles in multiple biochemical and physiological processes (Albenzio *et al*., 2016).

In recent years, several studies have investigated TUS as a promising technique to improve the microbiological quality, rheological properties, and bioavailability of nutritional compounds in raw cow's milk (RCM), positioning it as a potential alternative for the dairy industry. This study aimed to evaluate the changes induced by TUS in raw milk intended for human consumption. Although some studies have reported temperatures exceeding the thermal threshold (>50 °C) during the US processing of RCM, none have surpassed the temperatures typically associated with CHT.

This review synthesizes current evidence from studies examining the application of TUS to RCM intended for direct human consumption. Only investigations that applied TUS directly to RCM were included, thereby ensuring that the analysis remains focused on the specific challenges and outcomes associated with unheated dairy matrices (Annandarajah *et al*., 2018; Bermúdez-Aguirre *et al*., 2008, 2009a, 2009b, 2011; Deshpande & Walsh, 2021; Dhiny *et al*., 2023; Herceg *et al*., 2012; Hernández-Falcón *et al*., 2018; Vijayakumar *et al*., 2015; Wang *et al*., 2022; Zhou *et al*., 2020). Focusing on RCM enhances comparability and industrial relevance for three main reasons: (1) cow's milk is the most widely consumed and processed worldwide, supported by standardized supply chains; (2) native microbial and enzymatic profiles differ among species, potentially affecting the comparability of microbial log reductions and product stability; and (3) from both regulatory and technological perspectives, parameters validated in bovine milk are directly applicable to the dominant dairy sector (Cimmino *et al*., 2023; Marangoni *et al*., 2019). Overall, this approach enables a more rigorous assessment of how TUS influences microbial safety and physicochemical quality in the most commercially significant dairy matrix. The objective of this review is to consolidate existing knowledge on the sensorial, functional, and microbiological implications of TUS, to evaluate its advantages relative to CHT, and to identify current research gaps and future directions in dairy

processing.

2 Conventional heat treatment of raw cow's milk

CHT, such as pasteurization and ultra-high-temperature (UHT) processing, are commonly used to eliminate pathogenic microorganisms and preserve food, although they often lead to nutrient losses (Cadwallader & Singh, 2009). Pasteurization, typically referred to as high-temperature short-time (HTST), raises the temperature of RCM to 72 °C for 15 seconds, effectively inactivating pathogens such as *Coxiella burnetii*, *Salmonella typhi, Streptococcus pyogenes*, and *Mycobacterium tuberculosis* (Bastam *et al*. 2021). In contrast, UHT treatments raise the temperature to 135 °C for 2–4 seconds, producing commercially sterile milk and extending shelf life for several months at ambient temperature (Bai *et al*. 2023). Although these thermal processes are effective for microbial inactivation, they often cause thermal damage to heat-sensitive components, thereby altering nutritional quality and affecting the sensory attributes of the final product (Lucey *et al*. 2022).

3 Principles and mechanisms of thermoultrasonication

TUS, also referred to as thermosonication, thermoultrasound, or thermosound, typically involves a control panel, an ultrasonic probe, and a temperature-controlled recirculating bath (Figure 1). This technology stands out as a sustainable alternative due to its energy efficiency, operational simplicity, and low environmental impact. Additionally, it reduces processing time while enhancing food quality and shelf life. Automated systems can further optimize labor and production costs (Akdeniz & Akalin, 2022; Arvanitoyannis *et al*. 2017).

TUS occurs when US is applied in combination with moderate temperatures (often <55 °C) (Bariya *et al*. 2023). The underlying principle of this technique is acoustic cavitation, in which sound waves oscillating at frequencies typically between 20 and 40 kHz generate microscopic vapor bubbles in the liquid medium (Asaithambi *et al*. 2022). These bubbles expand and grow during wave oscillations until they reach a resonant size, at which point they collapse due to alternating pressure cycles, releasing localized energy and generating shock waves (Crudo *et al*. 2014). This intense mechanism can disrupt cell membranes, facilitate the release of nutritionally

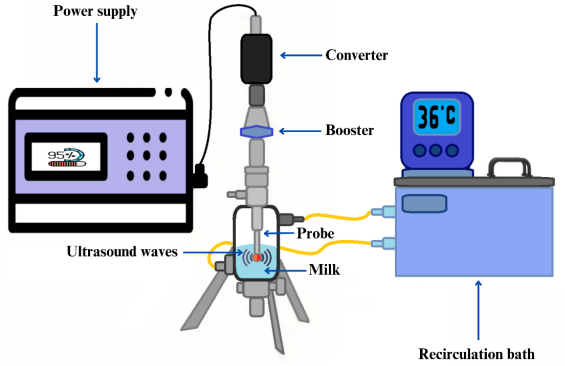

Figure 1. Equipment for thermoultrasonication.

relevant compounds, and promote the formation of stable emulsions (Shen *et al*. 2017).

The US mechanism relies on piezoelectric transducers that convert electrical energy into high-frequency sound waves. When applied to a liquid such as milk, these waves generate alternating compression and rarefaction cycles, leading to acoustic cavitation. With increasing sound intensity, microbubbles are formed and undergo oscillation, expansion, and subsequent collapse. The implosion of these bubbles produces highly localized extreme conditions, including transient temperatures approaching 4,700 °C, pressures exceeding 100 MPa, and intense shear forces (Zhang *et al*., 2018).

When US is combined with heat, as in TUS, the efficiency of acoustic cavitation is markedly enhanced. Elevated temperatures reduce the viscosity and surface tension of the liquid, thereby facilitating microbubble formation, expansion, and collapse. This thermal contribution amplifies cavitation intensity, resulting in greater molecular disruption, improved emulsification, and accelerated microbial inactivation. The synergistic interaction between thermal energy and US thus enables more effective modifications of food structure and functional properties, ultimately leading to optimized processing outcomes.

Other effects of TUS include enzyme inactivation, microbial reduction, and nutrient preservation due to lower processing temperatures (Villamiel & De Jong, 2000). These outcomes contribute to enhanced nutritional properties, minimized loss of heat-sensitive components, reduced development of cooked flavors, and minimal adverse effects on texture or appearance (Binti-Maklin *et al*. 2025). Additional studies on goat milk have shown increased solubility of calcium and phosphorus, while in camel milk cream, a reduction in fat globule size has been observed, positively affecting

product stability, viscosity, adhesiveness, and hardness (Kashaninejad & Razai, 2020; Ragab *et al*. 2019).

Despite these advantages, TUS may present some limitations, such as the potential generation of free radicals and modifications in the structure and texture of foods, which are matrix-dependent (Pérez-Andrés *et al*. 2018).

4 Thermoultrasonication of raw cow's milk

The studies published between 2008 and 2024 included in this review were conducted in various geographical regions: Canada (Wang *et al*., 2022), China (Zhou *et al*., 2021), Croatia (Herceg *et al*., 2012), Indonesia (Dhiny *et al*., 2023), Mexico (Hernández-Falcón *et al*., 2018), and the USA (Annandarajah *et al*., 2018; Bermúdez-Aguirre *et al*., 2008, 2009a, 2009b, 2011; Deshpande & Walsh, 2021; Vijayakumar *et al*., 2015). All studies applied high-intensity US simultaneously with heat, either in batch or continuous systems, using amplitudes between 30% and 100%, temperatures ranging from 15 °C to 72 °C, and treatment durations between 0.25 and 30 minutes. Most protocols adhered to the moderate temperature regime typically associated with TUS; increases beyond this range were only reported in two studies, which documented temperatures between 29–55 °C and 20–71 °C, respectively (Hernández-Falcón *et al*., 2018; Wang *et al*., 2022). The operating parameters are summarized in Table 1, which provides a comparative overview of US intensity, frequency, treatment duration, and thermal strategies, thereby illustrating the variability in TUS implementations and their potential effects on processing outcomes. While most studies included comparisons with CHT, Wang *et al*. (2022) and Herceg *et al*. (2012) did not report any direct comparative analyses. Table 2 summarizes the principal variables assessed across microbiological, physicochemical, and proximate composition domains, together with the changes associated with TUS application. Under certain conditions, TUS consistently reduced microbial counts, altered physicochemical properties, and modified techno-functional attributes (Table 3).

Table 1. TUS[1] conditions in the included studies.

Temperature (°C)			Time (min)	Amplitude (%)	kHz[2]	Watts	Reference
Water bath	Initial	Final					
72	15 – 75	15 – 75	1	100	20	140	Annandarajah *et al*. (2018)
65	63	63	10 – 30	100	24	400	Bermúdez-Aguirre *et al*. (2008)
65	63	63	30	100	24	400	Bermúdez-Aguirre *et al*. (2009a)
65	63	63	30	30 – 100	24	400	Bermúdez-Aguirre *et al*. (2009b)
57	63	63	10 – 30	100	24	400	Bermúdez-Aguirre *et al*. (2011)
72	20 – 25	67 – 72	0.11 – 0.19	90	–	168 – 180	Deshpande & Walsh, (2021)
55	–	60	5 – 20	–	20 – 22	365	Dhiny *et al*. (2023)
–	40 – 60	40 – 60	6 – 12	50 – 100	20	600	Herceg *et al*. (2012)
45	29 – 31	48 – 55	10 – 15	95	20	1500	Hernández-Falcón *et al*. (2018)
72	65	–	1 – 3	100	20	115	Vijayakumar *et al*. (2015)
90	63	–	1 – 9	–	25	400	Wang *et al*. (2022)
–	55 – 63	-	315 – 30	–	20	200 – 400	Zhou *et al*. (2021)

[1]TUS: termoultrasonication, [2]kHz: kilohertz.

Table 2. CHT1 conditions in the included studies.

Temperature (°C)	Time (min)	Reference
72	0.25	Annandarajah *et al*. (2018)
65	30	Bermúdez-Aguirre *et al*. (2008)
65	30	Bermúdez-Aguirre *et al*. (2009a)
63	30	Bermúdez-Aguirre *et al*. (2009b)
65	30	Bermúdez-Aguirre *et al*. (2011)
72	0.11 – 0.19	Deshpande & Walsh (2021)
65	30	Dhiny *et al*. (2023)
NI[2]	NI[2]	Herceg *et al*. (2012)
85	0.25	Hernández-Falcón *et al*. (2018)
72	1 – 3	Vijayakumar *et al*. (2015)
NI[2]	NI[2]	Wang *et al*. (2022)
63/121	30/0.25	Zhou *et al*. (2021)

[1]CHT: conventional heat treatment, [2]NI: not indicated.

Table 3. Summary of variables examined in the included studies and their observed changes.

Variables				
Microbiology	Physicochemical	Proximate analysis	Other	Reference
–	–	–	Plasmin (↓)	Annandarajah *et al.* (2018)
–	Color (↑), fat globule size (↓)	Fat (↑)	–	Bermúdez-Aguirre *et al.* (2008)
Mesophilic aerobic (↓)	pH (↓), color (↑), density (↓), acidity (↑),	Fat (↑), protein (↓), NFS[1] (↓)	–	Bermúdez-Aguirre *et al.* (2009a)
L. innocua (↓), mesophilic bacteria (↓)	Color (↑), pH (↓), acidity (↑)	Fat (↑), protein (↓)	–	Bermúdez-Aguirre *et al.* (2009b)
L. innocua (↓)	–	–	–	Bermúdez-Aguirre *et al.* (2011)
G. stearothermophilus (↓)	pH (↑)	–	FFAs[4] (↓)	Deshpande & Walsh, (2021)
E. coli (↓)	pH (↓), viscosity (↓)	Fat (↑), Protein (↓)	–	Dhiny *et al.* (2023)
E. coli (↓), *S. aureus* (↓)				Herceg *et al.* (2012)
Mesophilic aerobic (↓), enterobacteria (↓)	pH (↓), color (↑), density (↓), stability (↑), acidity (↑)	NFS (↑), TS (↑)	AFM1[3] (↓), antioxidants (↑)	Hernández-Falcón *et al.* (2018)
Total aerobic (↓), coliform count (↓)	Color (↑), fat globule size (↓), viscosity (↑)	–	Sensory evaluation, plasmin (↑),	Vijayakumar *et al.* (2015)
–	–	Protein (↑)	Enzymatic digestion (↑)	Wang *et al.* (2022)
S. aureus (↓)	pH (↓), color (↑), particle size (↓)	Protein (↓)		Zhou *et al.* (2021)

[1]NFS: nonfat solid. [2]TS: total solid. [3]AFM1: aflatoxin M1. [4]FFAs: free fatty acids. ↑: increase of the variable. ↓: decrease of the variable.

5 Impact of thermoultrasonication on milk microstructure and component functionality

TUS alters casein micelles and their spatial organization, two critical factors in firm gel formation and structural integrity of dairy matrices. It also enhances micellar interactions and promotes cross-linking, resulting in more stable and consistent gels that improve the texture of products such as yogurt and cheese (Ragab *et al.*, 2019; Song *et al.*, 2021). Silva, Zisu & Chandrapala (2018) refined this view by showing that the effect of US on micelles depends on the casein-to-whey protein ratio: in casein-dominant systems, sonication reduces particle size by promoting aggregate reorganization through exposure of hydrophobic regions, whereas in formulations with a higher serum fraction, primary aggregates are formed via disulfide bonds involving κ-casein and whey proteins, thereby altering micellar architecture and functional interactions.

TUS enhances interactions between casein micelles primarily by inducing conformational changes and rearrangements within the protein matrix, which promote greater connectivity and cohesion of the gelling network. Acoustic cavitation exposes hydrophobic regions and free sulfhydryl groups, favoring hydrophobic interactions and the formation of disulfide bonds between caseins and between caseins and whey proteins. These molecular events densify the network and increase gel firmness (Shanmugam *et al.*, 2012; Shen *et al.*, 2017; Meng *et al.*, 2021; Pérez-Andrés *et al.*, 2018). Such effects translate into functional improvements, including increased resistance to syneresis, shorter acid gelation times, and improved elasticity of fermented milk gels, attributable to a more interconnected and stable micellar network (Reiter *et al.*, 2023; Liu *et al.*, 2014). Hemar *et al.* (2020) further demonstrated that high-power US could moderately reduce the apparent size of reconstituted micelles without disrupting their internal structure, suggesting surface compaction that enhances structural density. In mixed protein systems, US facilitates complementary protein–protein interactions that further strengthen the network, as observed in combinations of casein with other proteins (Nascimento *et al.*, 2023; Yuno-Ohta *et al.*, 2020).

6 Microbiological effects of thermoultrasonication on raw cow's milk

In RCM, it is important to recognize that pathogenic microorganisms such as *Brucella abortus* and *Mycobacterium* sp may be present within the dairy chain and pose significant public health concerns

(Ninković *et al*., 2024; Ullah *et al*., 2024). Tavsanli *et al*. (2022) evaluated the effect of low-frequency US on the microbiota of raw goat milk inoculated with *Brucella melitensis*, reporting reductions exceeding 2 log CFU after 10 min of treatment at 20 kHz and 400 W. Similarly, Al Bsoul *et al*. (2010) investigated the effectiveness of US against *Mycobacterium* sp 6PY1, achieving >3 log reductions in cell density in aqueous suspension after 15 min of sonication at 20 kHz and 0.5 W/mL.

Under controlled conditions, TUS can achieve microbial reductions approaching sterilization. At US powers of 200–250 W, damage to the cell wall and membrane is intensified, leading to intracellular leakage. At 300 W, severe rupture occurs, with large cavities and fragmentation of the cell wall (Jiang *et al*., 2024). The extent of membrane disruption correlates positively with ultrasonic power density. Cavitation increases membrane permeability, allowing the entry of macromolecules and resulting in leakage of intracellular contents and damage to organelles, enzymes, and nucleic acids (Ahmad *et al*., 2023). In dairy matrices, multiple studies have demonstrated multilogarithmic microbial reductions consistent with these mechanisms. Under optimized conditions, no detectable growth has been observed following treatment and during refrigerated storage (Bermúdez-Aguirre *et al*., 2011; Hernández-Falcón *et al*., 2018; Dhiny *et al*., 2023). Nevertheless, sterilization efficacy is influenced by initial microbial load, reactor geometry, energy density, and matrix composition. Thus, pilot- and industrial-scale validations, along with regulatory frameworks defining process criteria and microbiological verification, are necessary.

Research summarized in Table 4 presents the application of TUS for microbial reduction, comparing pre- and post-treatment levels in RCM. For context, conventional HTST achieves >5 log reductions in indicator pathogens such as *Escherichia coli* and *Listeria* spp., while UHT treatment achieves commercial sterility levels (>6 log reductions) across a wide range of microorganisms (Cadwallader & Singh, 2009; Bai *et al*., 2023).

TUS treatments demonstrated effectiveness equal to or greater than that of traditional HTST in inactivating fecal contamination indicators and other pathogenic bacteria, including *E. coli*, *Listeria innocua*, *Staphylococcus aureus*, and Enterobacteriaceae (Bermúdez-Aguirre *et al*., 2008, 2009a, 2009b; Deshpande & Walsh *et al*., 2021, Dhiny *et al*., 2023; Herceg *et al*., 2012; Hernández-Falcón *et al*., 2018; Vijayakumar *et al*., 2015; Zhou *et al*., 2021).

Escherichia coli exhibited marked sensitivity to TUS, with reductions of up to 3.07 log CFU/mL, accompanied by pronounced structural damage to the cell envelope, including multiple cracks, fractures, and outward bulging, as well as alterations in milk viscosity and fat composition (Dhiny *et al*., 2023; Herceg *et al*., 2012). Mechanistic studies further demonstrate that cavitation induces severe membrane disruption, characterized by extensive cracking, fracturing, and outward deformation of the cell membrane, thereby confirming the destructive effects of acoustic cavitation on *E. coli* integrity (Lin *et al*., 2019). *Listeria innocua* was reduced by more than 5 log CFU/mL after 10 minutes of TUS at 63 °C, while CHT achieved only a 3 log CFU/mL reduction under similar conditions (Bermúdez-Aguirre *et al*. 2009b, 2001). *Staphylococcus aureus* was completely inactivated in milk subjected to TUS for 7.5 minutes at 63 °C highlighting the microbicidal potential of the combined treatment (Bastam *et al*. 2021; Arvanitoyannis *et al*., 2017). Additionally, mesophilic bacteria and the native microbiota experienced significant reductions, and in some cases, no microbial growth was detected after 15 days of refrigerated storage post- treatment (Hernández-Falcón *et al*., 2018, Bermúdez-Aguirre *et al*., 2009a, 2009b).

In a continuous-flow system, such as the one studied by Deshpande & Walsh (2020), the antimicrobial effect of TUS was consistent, showing reductions in both native microbiota and thermophilic bacteria. Although this study did not report detailed measurements of the initial pathogen loads, the findings suggest that, under optimized conditions, TUS can be as effective as CHT in microbial inactivation.

The effectiveness of TUS is strongly influenced by the structural characteristics of bacterial cell envelopes. In Gram-negative bacteria, the lipopolysaccharide-rich outer membrane combined with a thin peptidoglycan layer in the periplasmic space renders them particularly susceptible to shear forces, pressure pulses generated by cavitation, and oxidative stress caused by reactive oxygen species such as hydrogen peroxide produced during bubble collapse (Herceg *et al*., 2012; Li *et al*., 2019). By contrast, Gram-positive bacteria possess a thick (20–80 nm) peptidoglycan cell wall reinforced with peptide cross-bridges, which increases structural rigidity and provides greater resistance even against reactive species (Vadillo-Rodríguez & Dutcher, 2011; Zupanc *et al*., 2019). Under typical thermal conditions of TUS, increasing vapor pressure together with decreasing surface tension and viscosity of the medium enhances cavity formation and collapse, thereby intensifying microbial inactivation at temperatures approaching those of CHT, with Gram-negative bacteria displaying notably higher susceptibility (Ugarte-Romero *et al*., 2007).

For mesophilic aerobic microorganisms, higher ultrasonic amplitudes result in greater CFU reductions. Cavitation imposes a combination of mechanical, thermal, and chemical stresses. The implosion of microbubbles generates shear forces that disrupt cell membranes, alter permeability, and may lead to partial or complete lysis.

Table 4. Reducing microbial count (CFU/mL[1]) in RCM[2] after TUS[3] application.

Microorganism	CHT[4]	TUS[2]	Reference
Aerobics totals	1.86	1.86	Vijayakumar *et al*. (2015)
Aerobic mesophilic	~3.00	~0.30 - 2.20	Hernández-Falcón *et al*. (2018)
Coliforms	>3.60	>3.60	Vijayakumar *et al*. (2015)
Enterobacteriaceae	~4.3	~ 1.2 - 3.32	Hernández-Falcón *et al*. (2018)
Mesophilic bacteria	3.00 1.89- 3.75	3.00 0.53 – 4.25	Bermúdez-Aguirre *et al*. (2008)
			Bermúdez-Aguirre *et al*. (2009b)
E. coli	1.54 – 2.44 2.90	1.92 – 3.07 ~4.68	Herceg *et al*. (2012)
			Dhiny *et al*. (2023)
L. innocua	0.50 – 5.0 5.30	5.00 – 6.00 ~5.50	Bermúdez-Aguirre *et al*. (2011)
			Bermúdez-Aguirre *et al*. (2009b)
S. aereus	0.09 – 0.94 3.25	0.39 – 1.49 4.19	Herceg *et al*. (2012)
			Zhou *et al*. (2021)
Geobacillus stearothermophilus	0.05 – 0.37	0.26 – 0.54	Deshpande & Walsh (2021)

[1]CFU/mL: $\log_{10}$ colony-forming unit per milliliter. [2]RCM: raw cow´s milk. [3]TUS: thermoultrasonication [4]CHT: conventional heat treatment.

Simultaneously, the dissociation of water molecules produces hydrogen and hydroxyl radicals, while additional reactive oxygen and nitrogen species—including hydrogen peroxide, nitric oxide, and nitrous acid—are formed. These species induce oxidative stress, contributing to protein denaturation and the degradation of intracellular components (Furuta *et al*., 2004; Tsukamoto *et al*., 2004; Zhang *et al*., 2018). Moreover, TUS modifies surface electrostatic properties and destabilizes extracellular polymeric substances, thereby reducing adhesion and biofilm formation and diminishing microbial protection (Kentish & Feng, 2014; Ojha *et al*., 2017). These effects are further amplified by elevated temperatures, which accelerate bubble formation and pore development in membranes, ultimately causing rupture and leakage or accumulation of cytoplasmic material (Bermúdez-Aguirre *et al*., 2011).

7 Effects on physicochemical characteristics

Most authors reported a moderate pH decrease after treatments at 60–65 °C, without compromising colloidal stability or sensory properties; final pH values stayed within acceptable ranges for fluid milk products (Bermúdez-Aguirre *et al*. 2008, 2009b; Deshpande & Walsh, 2021; Hernández-Falcón *et al*. 2018; Zhou *et al*. 2021). Cavitation during TUS often raises the local temperature, likely contributing observed acidification. Additional pH changes during storage may come from acid metabolites produced surviving microorganisms, potentially linked to lipolysis (Bermúdez-Aguirre *et al*. 2009b) or from formation of carboxyl groups after TUS-induced molecular changes (Li *et al*. 2019). These processes can cause variations in the proximate composition reported in some studies (Bermúdez-Aguirre *et al*. 2008, 2009a).

Regarding color, multiple studies reported an increase in whiteness (L^*) and a reduction in particle size (Bermúdez-Aguirre *et al*. 2008, 2009a, Hernández-Falcón *et al*. 2018; Zhou *et al*. 2021 The color increase specifically refers to higher luminosity (L^*), not a change in hue (a^*) or yellowish/bluish (b^*). Color is a key factor in consumer acceptance of milk and is related to the dispersion of fat globules and casein micelles (Owen *et al*. 2001). Light reflection is enhanced by reduced fat globule size and protein denaturation caused by TUS-induced homogenization, making milk appear whiter (Gaucher *et al*. 2008; Li *et al*. 2019).

Protein denaturation under TUS predominantly affects membrane-associated proteins, particularly xanthine oxidase and butyrophilin, thereby weakening the integrity of the milk fat globule membrane (MFGM) (Zhao *et al*., 2024). Gregersen *et al*. (2019) reported that high-intensity US combined with moderate temperatures (50–70 °C) and intermediate power levels (30–50 W) can denature up to 40% of the major whey proteins β-lactoglobulin and α-lactalbumin, demonstrating that both acoustic energy and heat contribute significantly to protein destabilization. Cavitation also disrupts the fat globule membrane, promoting the adhesion of casein micelles and the formation of a granular interfacial network, which enhances emulsion stability and improves product texture (Gaucher *et al*., 2008; Li *et al*., 2019; Villamiel & De Jong, 2000).

TUS reorganizes protein–lipid interactions, thereby strengthening emulsion stability. Cavitation reduces the size of fat globules, increasing surface area and facilitating efficient adsorption of casein micelles and whey proteins. These proteins anchor to exposed lipid surfaces through hydrophobic and electrostatic interactions; polar residues such as lysine and glutamic acid interact with phospholipid head groups,

reinforcing the interfacial layer. The resulting network enhances colloidal stability, reduces creaming, and improves viscosity and uniformity—parameters critical for producing high-quality dairy products (Bermúdez-Aguirre *et al*., 2008; Ragab *et al*., 2019).

Conversely, studies assessing lipid fractions have not detected significant changes in free fatty acid concentration or total fat content following TUS treatment, confirming lipid stability under the evaluated conditions (Deshpande & Walsh, 2021; Hernández-Falcón *et al*., 2018). Nevertheless, disruption of the MFGM during TUS exposes the triglyceride core, enabling casein micelle adhesion and the development of a granular interfacial structure that contributes to improved emulsion stability (Villamiel & De Jong, 2000).

An increase in viscosity was observed in studies using higher amplitudes (100%) or extended treatment times (>10 min), attributed to interactions between protein and lipid fractions induced by localized shear forces (Dhiny *et al*. 2023). No signs of phase separation, gel formation, or sedimentation were reported, even after 15 days of storage (Annandarajah *et al*. 2018; Deshpande & Walsh, 2021; Hernández-Falcón *et al*. 2018; Vijayakumar *et al*. 2015). TUS also improved emulsion stability by reducing particle size through cavitation (Bermúdez-Aguirre *et al*. 2008; Hernández-Falcón *et al*. 2018). These results indicate that TUS enhances milk functionality without compromising its essential properties.

8 Proximate analysis after thermoultrasonication

Several studies assessed the proximate composition of RCM following TUS by measuring fat, total protein, non-fat solids (NFS), and total solids (TS) (Table 5) (Bermúdez-Aguirre *et al*. 2008, 2009a; Dhiny *et al*. 2023; Hernández-Falcón *et al*. 2018; Wang *et al*. 2022; Zhou *et al*. 2021). In most studies, protein content was not significantly affected, indicating that protein denaturation was not detectable under the evaluated conditions (Bermúdez-Aguirre *et al*., 2009a, 2009b; Zhou *et al*., 2021). For instance, total protein quantification by nitrogen determination (Kjeldahl or Dumas methods) is insensitive to conformational changes, and thus partial denaturation induced by cavitation may occur without affecting total protein values. The variations observed in some measurements likely reflect changes in solubility, recovery efficiency, or artefacts associated with colorimetric assays, rather than a true loss of protein mass.

Table 5. Effect of TUS[1] on the physicochemical and proximate analysis of RCM[2].

Physicochemical properties			
Parameter	CHT[3]	TUS[1]	Reference
pH	6.74± 0.06	6.67 ± 0.06 – 6.71 ± 0.06	Hernández-Falcón *et al*. (2018)
	6.74± 0.06	6.61 ± 0.01 – 6.66 ± 0.05	Bermúdez-Aguirre *et al*. (2009a)
	6.74± 0.06	6.61 ± 0.01 – 6.66 ± 0.05	Bermúdez-Aguirre *et al*. (2009b)
	6.82± 0.02	6.80 – 6.85	Deshpande & Walsh (2021)
	6.71± 0.04	6.66 ± 0.02	Zhou *et al*. (2021)
Acidity (%)	0.20± 0.05	0.19 ± 0.04 – 0.20 ± 0.05	Hernández-Falcón *et al*. (2018)
	0.126± 0.008	0.136 ± 0.012 – 0.14 ± 0.00	Bermúdez-Aguirre *et al*. (2009a)
	0.126± 0.008	0.136 ± 0.012 – 0.146 ± 0.00	Bermúdez-Aguirre *et al*. (2009b)
Density (g/mL)	1.032 ± 0.00	1.032 ± 0.00	Hernández-Falcón *et al*. (2018)
	1.0317 ± 0.0010	1.026 ± 0.001 – 1.026 ± 0.00	Bermúdez-Aguirre *et al*. (2009a)
Viscosity (mPa/s)	1.41 ± 0.14 – 1.42 ± 0.14	1.39 ± 0.00 – 1.60 ± 0.05	Vijayakumar *et al*. (2015)
Stability (%)	~ 96.2	~ 96.25–97.19	Hernández-Falcón *et al*. (2018)
Proximate analysis properties			
Fat (%)	4.22 ± 0.02	4.24 ± 0.02	Bermúdez-Aguirre *et al*. (2008)
	4.22 ± 0.02	4.21 ± 0.04 – 4.29 ± 0.05	Bermúdez-Aguirre *et al*. (2009a)
	4.22 ± 0.02	4.21 ± 0.04 – 4.29 ± 0.05	Bermúdez-Aguirre *et al*. (2009b)
Protein (%)	3.55 ± 0.01	3.00 ± 0.01 – 3.04 ± 0.03	Bermúdez-Aguirre *et al*. (2008, 2009a)
	2.53 ± 0.38 – 3.02 ± 0.16	3.22 ± 0.16	Zhou *et al*. (2021)
NFS[3] (%)	8.60 ± 0.40	8.63 ± 0.41 – 8.67 ± 0.54	Hernández-Falcón *et al*. (2018)
	9.50 ± 0.03	8.03 ± 0.04 – 8.36 ± 0.43	Bermúdez-Aguirre *et al*. (2009a)
TS[4] (%)	11.59 ± 0.40	11.62 ± 0.40 – 11.67 ± 0.54	Hernández-Falcón *et al*. (2018)

[1]TUS: thermoultrasonication. [2]RCM: raw cow´s milk. [3]CHT: conventional heat treatment. [3]NFS: nonfat solids. [4]TS: total solid.

Fat content, by contrast, was reported to increase by approximately 5%. In one study, TUS applied at 400 W, 24 kHz, and 100% amplitude for 30 min reduced the mean fat globule diameter to approximately 1 μm. Mechanistically, cavitation disrupts fat globule aggregates into triacylglycerol microdroplets, yielding a finer and more homogeneous lipid dispersion and thereby increasing the fraction of dispersed and analytically recoverable lipids (Bermúdez-Aguirre *et al*., 2008). Consequently, the altered size distribution of fat droplets results in a modestly higher measured fat content (~5%), even though the total lipid mass in the system remains unchanged (Bermúdez-Aguirre *et al*., 2008, 2009a, 2009b; Dhiny *et al*., 2023). TS and NFS values remained stable, showing no significant differences compared to CHT, indicating that TUS does not compromise the chemical integrity of RCM (Hernández-Falcón *et al*. 2018).

9 Functional and technological properties

TUS has also been shown to enhance the hydrolysis of soluble proteins when treated with pepsin and pancreatin (Wang *et al*., 2022). This effect is driven by significant conformational changes in milk proteins, including partial unfolding of tertiary structures, increased exposure of hydrophobic residues and peptide bonds, and disruption of intramolecular hydrogen and disulfide bonds. These structural modifications improve the accessibility of digestive enzymes to cleavage sites, thereby accelerating enzymatic hydrolysis. Fourier transform infrared (FTIR) spectroscopy revealed a decrease in α-helix content accompanied by an increase in β-sheet and random coil structures, consistent with enhanced enzymatic binding and fragmentation efficiency (Wang *et al*., 2022).

US -assisted enzymatic hydrolysis benefits from several mechanistic improvements, as reviewed by Qian *et al*. (2023). Cavitation enhances mass transfer by disrupting boundary layers, reducing particle size, and increasing surface area. US may also induce subtle conformational changes in enzyme molecules, improving flexibility and catalytic efficiency without compromising the integrity of active sites. Optimal US parameters (20–40 kHz, 100–500 W) have been reported to reduce hydrolysis times by up to 30%, increase the degree of hydrolysis by 10–20%, and generate bioactive peptides with enhanced functional properties (Yang *et al*., 2018; Balthazar *et al*., 2019; Qin *et al*., 2018; Magalhães *et al*., 2022). These findings suggest that integrating US into enzymatic protocols can significantly improve protein degradation and produce peptides with targeted bioactivities relevant to dairy applications.

The microstructural changes induced by TUS also result in techno-functional improvements, including increased protein solubility, higher emulsifying capacity, and improved gel stability in fermented products, with minimal differences in flavor, aroma, or mouthfeel compared with CHT (Abesinghe *et al*., 2019; Zlatev *et al*., 2018; Vijayakumar *et al*., 2015). In a sensory evaluation involving a trained panel (n = 8), participants used a triangle test to characterize odor attributes and quantify intensities on a 15-cm scale. Panelists generally rated TUS-treated milk as acceptable, with no significant sensory drawbacks (Vijayakumar *et al*., 2015). In addition, Vijayakumar *et al*. (2015) and Annadarajah *et al*. (2018) reported that TUS inactivated over 90% of plasmin, maintaining low activity through 49 days of storage. This inactivation is relevant for commercial shelf life, particularly in UHT milk, where plasmin degradation of caseins produces hydrophobic peptides associated with bitterness, viscosity changes, and protein destabilization. Controlling plasmin activity thus contributes to flavor and texture preservation during storage (7–14 days for HTST milk) (Bui *et al*., 2021). However, in cheese manufacture, plasmin plays a key role in proteolysis during ripening; therefore, its inactivation should be adjusted according to cheese type and ripening objectives (Vélez *et al*., 2016; France *et al*., 2021; Wang *et al*., 2024).

Beyond microbiological and physicochemical changes, TUS also affects sensory attributes and product stability through interconnected structural and molecular processes. Treated milk generally exhibits increased whiteness (L^*), smoother texture, and higher viscosity, primarily due to reduced fat globule size and enhanced protein–lipid interfacial stability (Zhou *et al*., 2021; Gou *et al*., 2023). Under moderate conditions, flavor remains comparable to HTST; however, high-intensity treatments (e.g., 200 W for 2 min) may produce subtle off-flavors described as gummy, burnt, or foreign, likely associated with whey protein unfolding and mild lipid oxidation (Pérez-Andrés *et al*., 2018). Overall, sensory panels have consistently rated TUS-treated milk as acceptable when processing parameters are properly optimized (Vijayakumar *et al*., 2015).

9.1 Shelf-life and stability under refrigeration

TUS extends the refrigerated shelf life of RCM by inhibiting microbial regrowth and maintaining physicochemical stability. Hernández-Falcón *et al*. (2018) observed stable microbial counts for up to 15 days at 4 °C without phase separation or sedimentation. Other studies reported that TUS-treated milk preserved its pH and fat quality over similar periods (Deshpande

& Walsh, 2021; Hernández-Falcón *et al*., 2018). At the molecular level, cavitation exposes hydrophobic amino acid residues and free sulfhydryl groups in proteins such as β-lactoglobulin and generates low levels of reactive species, including lipid hydroperoxides. These modifications enhance interfacial behavior and structural functionality; however, if TUS parameters are not properly controlled, mild oxidative reactions may occur, leading to subtle sensory changes (Astráin-Redín *et al*., 2023; Zhang *et al*., 2018). Nevertheless, oxidative stability is generally maintained under optimized conditions, with no significant increases in FFAs or off-flavor development (Shokri *et al*., 2022).

FTIR (post-treatment TUS) analysis of the Amide I band confirmed TUS-induced alterations in secondary protein structure, characterized by increased α-helix and random coil content at the expense of β-sheets and β-turns. While these spectra reflect the overall protein matrix rather than specific proteins, whey proteins such as β-lactoglobulin are particularly susceptible to denaturation. Such modifications may reduce immunoglobulin E binding and allergenicity, while also enhancing the digestibility of casein fractions (Ehn *et al*., 2004; Wang *et al*., 2022).

TUS has also been reported to reduce aflatoxin M1 (AFM1) content, potentially through structural modifications in the lactone or furan rings (Mortazavi *et al*. 2015). This reduction was associated with an increase in phenolic content and antioxidant activity (Hernández-Falcón *et al*. 2018). One study noted that the increase in antioxidant activity may result from weakened Van der Waals forces, hydrogen bonds, and hydrophobic interactions, leading to the release of phenolic compounds into the medium (Hassam *et al*. 2013).

10 Methodological limitations and experimental constraints

Although the overall evidence highlights the potential of TUS, the comparability and generalizability of findings are constrained by methodological heterogeneity among the reviewed studies. Key challenges for rigorous synthesis include variations in amplitude (30–100%), frequency (20–40 kHz), temperature (15–72 °C), sample volume, probe design, and treatment duration (0.25–30 min), as well as differences between batch and continuous applications, thermal control strategies, measurement of initial microbial loads, and inadequate characterization of the milk matrix. Several studies also lack sufficient replication or appropriate thermal controls, making it difficult to distinguish the specific contributions of TUS from temperature-related effects. Furthermore, few investigations report complete energy profiles, acoustic transfer efficiency, or scaling parameters, which hampers the assessment of industrial relevance. In addition, the absence of systematic analyses of oxidative by-products and markers of protein damage limits the capacity to balance potential risks against technological benefits. Most studies were conducted on a laboratory or pilot scale, with limited reproduction in industrial environments (Table 2). The survey by Deshpande & Walsh (2021) is a notable exception, as it assessed a continuous flow system on a small scale.

Further validation is necessary to translate these promising findings into industrial practice. Regulatory approval will also require reproducible data on microbial inactivation, enzyme activity reduction, and possible formation of toxic by-products. Additionally, new research into energy consumption and cost-effectiveness will help determine whether TUS offers economic advantages over traditional CHT.

11 Toward practical adoption in the dairy sector

The application of TUS to RCM aligns with current trends in the dairy industry, which seek to ensure microbial safety while preserving nutritional and sensory quality. The synergy between ultrasonic cavitation and moderate temperatures presents a promising option for processing raw milk and developing specialized dairy products that benefit from partial homogenization, extended shelf life, or reduced contaminants such as AFM1. However, practical adoption requires thorough pilot-scale experimentation, robust engineering for high-throughput systems, and full regulatory compliance. Integration into existing production lines, potentially before or after cream separation, must be carefully designed to avoid unwanted homogenization that could lead to rancidity if lipase activity remains high. Despite these challenges, the potential of TUS as an energy-efficient, environmentally friendly technology capable of improving final product quality highlights its promise in future dairy operations.

Although this review focuses on studies applying TUS directly to RCM, related research provides complementary insights. For example, Gautam *et al*. (2025) examined the effects of TUS on the plasmin system in buffalo milk, observing structural changes in proteolytic pathways that may also apply to cow's milk, albeit with species-specific matrix differences. Furthermore, recent work on US energy density and modulation modes (continuous versus pulsed) in fresh cow's milk without combined heating demonstrated significant effects on microbial, physicochemical, and techno-functional properties. While these findings fall outside the strict definition of TUS, they underscore

the importance of standardizing energy input and wave characteristics to improve reproducibility. Overall, structural and functional modifications induced by TUS enhance microbial safety and improve techno-functional properties of milk (emulsification, gelation, texture), positioning it as a promising tool for next-generation dairy products.

Building on the mechanisms described above, the advantages and limitations of TUS relative to CHT can be outlined. Comparative studies show that TUS achieves microbial reductions equal to or greater than those of HTST or UHT, while better preserving thermolabile compounds such as vitamins, bioactive peptides, and native enzymes, and maintaining the colloidal integrity of milk—attributes that support clean-label formulations (Wang *et al*., 2022; Shen *et al*., 2017). These features give TUS a clear advantage in final product quality without compromising safety. Nevertheless, several operational challenges persist precise control of parameters is required to avoid variability in cavitation distribution; prolonged treatments may increase energy consumption; and high intensities can generate undesirable flavors. To strengthen competitiveness against CHT, systematic comparisons under diverse raw milk conditions, harmonized regulatory criteria, and assessments of potential sub-lethal injury and microbial recovery are essential.

None of the included studies evaluated the effectiveness of TUS against *Brucella* sp. or *Mycobacterium* sp. in milk, highlighting a critical gap and an opportunity for future research to validate its capacity to inactivate these pathogens.

11.1 Scale-up and engineering considerations

Scaling TUS from laboratory to industrial systems presents several engineering challenges. Uniform cavitation distribution in larger volumes is hindered by acoustic attenuation, reflections, and dead zones; thus, reactor design must optimize transducer geometry, operating frequency, and sonication pattern (batch versus continuous flow) to ensure consistent energy densities. Thermal management must be integrated with US delivery to prevent hot spots and maintain synergy between acoustic and thermal effects. Real-time monitoring of acoustic energy density, effective temperature, and local intensity requires calibrated sensors or indirect methods (e.g., calorimetry, dissolution profiles), as the absence of robust metrics limits reproducibility and validation.

Continuous-flow systems offer advantages in scalability and uniformity compared to batch processes, but require balancing residence time, amplitude, and flow rate to ensure effective microbial inactivation while preserving product quality. Assessments of acoustic transfer efficiency and energy dissipation are essential at larger scales to optimize power usage and minimize energy losses from reflections or poor coupling. Integration into existing production lines also demands compatibility with upstream and downstream processes (e.g., cream separation, homogenization), while practical considerations such as maintenance, clean-in-place procedures, and noise-resistant materials must be addressed.

11.2 Regulatory and safety validation

For widespread adoption, TUS must undergo rigorous regulatory review to confirm its safety and consistency. Establishing critical control parameters and acceptance criteria for microbial inactivation, potential toxic by-products (e.g., aflatoxins), and preservation of functional compounds is essential. Validation should include inter-laboratory studies and benchmarking against HTST, with assessments of pathogen reduction, sub-lethal injury, and microbial recovery. Comprehensive analyses of acoustic energy transfer, thermal profiles, and oxidation products are also needed to identify hidden risks and balance potential drawbacks against benefits. Documentation should adhere to international standards (e.g., Codex Alimentarius, FDA, EFSA) to facilitate global market acceptance.

11.3 Economics and adoption roadmap

Adoption of TUS in dairy plants depends on both its technological benefits and economic feasibility. Initial cost–benefit analyses should compare energy use per liter with HTST/UHT, accounting for potential savings in refrigeration from extended shelf life and reduced product loss. Investments in specialized equipment, online monitoring, and operator training must be weighed against gains in waste reduction, quality retention, and product differentiation (e.g., clean-label marketing, longer shelf life). A phased implementation is recommended: beginning with pilot studies integrated into existing lines, followed by development of performance indicators that combine technical and economic metrics, and eventually scale-up to optimized continuous systems. Validation groups comprising academia, industry, and regulators should be established to share data, mitigate risks, and accelerate standardization.

*An adoption roadmap may include:

1. **Standardization and multi-centre validation** – development of consensus protocols for TUS parameters (acoustic energy density, temperature profiles, residence time) and inter-laboratory studies to ensure reproducibility.

2. **Industrial-scale pilot studies** – combining engineering optimization (reactor geometry, continuous-flow designs, real-time monitoring)

with techno-economic assessments of energy use, product quality retention, and process robustness.

3. **Safety and quality frameworks** – validation schemes covering microbial inactivation kinetics (including sub-lethal effects), oxidative and structural changes, and sensory stability under real storage conditions, aligned with international guidelines.

4. **Application-specific optimization** – tailoring TUS regimes for products such as yogurt or cheese, with endpoints including gel strength, emulsion stability, and flavor retention.

5. **Stakeholder integration** – creation of consortia involving academia, industry, and regulators to share data, develop certification standards, and establish labelling strategies*.

Conclusions

The evidence indicates that TUS is a viable technology for treating RCM, achieving microbial reductions comparable to CHT. In contrast to heat-based methods, TUS preserves heat-sensitive nutrients, bioactive compounds, and colloidal integrity, thereby supporting desirable techno-functional properties. By coupling temperature control with acoustic cavitation, TUS provides safety benefits with reduced thermal damage, positioning it as an innovation for "quality preservation" rather than a mere alternative to HTST. However, significant hurdles remain in methodological standardization, regulatory validation, and market integration. Addressing these challenges is essential to transition TUS from promising laboratory findings to widespread industrial adoption.

Although the antimicrobial potential of TUS has been consistently demonstrated under laboratory conditions, several critical limitations restrict its broader application. The variability in experimental setups, including reactor geometry, transducer configuration, and amplitude calibration, introduces substantial heterogeneity in reported microbial inactivation levels, complicating cross-study comparisons. Furthermore, most investigations have been performed at bench scale using model systems or artificially inoculated milk, which may not accurately replicate the microbial diversity and load present in commercial dairy chains. The lack of standardized reporting of acoustic parameters, energy densities, and thermal profiles further hampers reproducibility and limits the development of predictive models. Consequently, while TUS shows promise as a non-thermal or minimally thermal alternative to CHT, systematic pilot-scale evaluations, harmonized methodologies, and regulatory validation are essential before reliable industrial adoption can be achieved.

Acknowledgements

The author Monter-Arciniega acknowledges the Secretaría de Ciencia, Humanidades, Tecnología e Innovación (SECIHTI) from Mexico for its support through Fellowship No. 1077200.

References

Abesinghe, A., Islam, N., Vidanarachchi, J.K., Prakash, S., Silva, K. and Karim, M.A. (2019). Effects of ultrasound on the fermentation profile of fermented milk products incorporated with lactic acid bacteria. *International Dairy Journal* 90, 1–14. https://doi.org/10.1016/j.idairyj.2018.10.006

Ahmad, F., Mohammad, Z.H., Zaidi, S. and Ibrahim, S. A. (2023). A comprehensive review on the application of ultrasound for the preservation of fruits and vegetables. *Journal of Food Process Engineering* 46(6), e14291. https://doi.org/10.1111/jfpe.14291

Akdeniz, V. and Akalın, A.S. (2022). Recent advances in dual effect of power ultrasound to microorganisms in dairy industry: activation or inactivation. *Critical Reviews in Food Science and Nutrition 62*, 889–904. https://doi.org/10.1080/10408398.2020.1830027

Albenzio, M., Campanozzi, A., D'Apolito, M., Santillo, A., Mantovani, M.P. and Sevi, A. (2012). Differences in protein fraction from goat and cow milk and their role on cytokine production in children with cow's milk protein allergy. *Small Ruminant Research* 105*, 202–205*. https://doi.org/10.1016/j.smallrumres.2012.02.018

Albenzio, M., Santillo, A., Ciliberti, M.G., Figliola, L., Caroprese, M., Marino, R. and Polito, A. N. (2016). Milk from different species: Relationship between protein fractions and inflammatory response in infants affected by generalized epilepsy. *Journal of Dairy Science 99*(7), 5032–5038. https://doi.org/10.3168/jds.2015-10704

Al Bsoul, A., Magnin, J.P., Commenges-Bernole, N., Gondrexon, N., Willison, J. and Petrier, C. (2010). Effectiveness of ultrasound for the destruction of Mycobacterium sp. strain (6PY1). *Ultrasonics sonochemistry* 17(1), 106–110.

https://doi.org/10.1016/j.ultsonch.2009.04.005

Annandarajah, C., Grewell, D., Talbert, J. N., Raman, D. R. and Clark, S. (2018). Batch thermosonication for the reduction of plasmin activity in skim milk. *Journal of Food Processing and Preservation 42*, e13616. https://doi.org/10.1111/jfpp.13616

Arvanitoyannis, I.S., Kotsanopoulos, K. V. and Sava A.G. (2017). Use of ultrasounds in the food industry – Methods and effects on quality, safety, and organoleptic characteristics of foods. *Critical Reviews in Food Science and Nutrition* 57*,* 109–128. https://doi.org/10.1080/10408398.2013.860514

Asaithambi, N., Singha, P. and Singh, S.K. (2022). Comparison of the effect of hydrodynamic and acoustic cavitations on functional, rheological and structural properties of egg white proteins. *Innovative Food Science and Emerging Technologies* 82, 103166. https://doi.org/10.1016/j.ifset.2022.103166

Astráin-Redín, L., Skipnes, D., Cebrián, G., Álvarez-Lanzarote, I. and Rode, T.M. (2023). Effect of the application of ultrasound to homogenize milk and the subsequent pasteurization by pulsed electric field, high hydrostatic pressure, and microwaves. *Foods* 12(7), 1457. https://doi.org/10.3390/foods12071457

Bai, G., Cheng, L., Peng, L., Wu, B., Zhen, Y., Qin, G. and Wang, T. (2023). Effects of ultra-high-temperature processes on metabolite changes in milk. *Food Science and Nutrition* 11*,* 3601–3615. https://doi.org/10.1002/fsn3.3350

Balthazar, C.F., Santillo, A., Guimarães, J. T., Bevilacqua, A., Corbo, M. R., Caroprese, M. and Albenzio, M. (2019). Ultrasound processing of fresh and frozen semi-skimmed sheep milk and its effects on microbiological and physical-chemical quality. *Ultrasonics Sonochemistry* 51, 241-248. https://doi.org/10.1016/j.ultsonch.2018.10.017

Bariya, A.R., Rathod, N.B., Patel, A.S., Nayak, J.K.B., Ranveer, R. C., Hashem, A., Abd-Allah, E. F., Ozogul, F., Jambrak, A. R. and Rocha, J. M. (2023). Recent developments in ultrasound approach for preservation of animal origin foods. *Ultrasonics Sonochemistry* 101*,* 106676. https://doi.org/10.1016/j.ultsonch.2023.106676

Bastam, M.M., Jalili, M., Pakzad, I., Maleki, A. and Ghafourian, S. (2021). Pathogenic bacteria in cheese, raw and pasteurized milk. *Veterinary Medicine and Science* 7*,* 2445–2449. https://doi.org/10.1002/vms3.604

Bermúdez-Aguirre, D., Mawson, R. and Barbosa-Cánovas, G.V. (2008). Microstructure of fat globules in whole milk after thermo-sonication treatment. *Journal of Food Science* 73*,* E325–E332. https://doi.org/10.1111/j.1750-3841.2008.00875.x

Bermúdez-Aguirre, D., Mawson, R., Versteeg, K. and Barbosa-Cánovas, G.V. (2009a). Composition properties, physicochemical characteristics and shelf life of whole milk after thermal and thermo-sonication treatments. *Journal of Food Quality* 32*,* 283–302. https://doi.org/10.1111/j.1745-4557.2009.00250.x

Bermúdez-Aguirre, D., Corradini, M.G., Mawson, R. and Barbosa-Cánovas, G.V. (2009b). Modeling the inactivation of *Listeria innocua* in raw whole milk treated under thermo-sonication. *Innovative Food Science and Emerging Technologies 10*, 172–178. https://doi.org/10.1016/j.ifset.2008.11.005

Bermúdez-Aguirre, D., Mawson, R. and Barbosa-Cánovas, G.V. (2011). Study of possible mechanisms of inactivation of *Listeria innocua* in thermosonicated milk using scanning electron microscopy and transmission electron microscopy. *Journal of Food Processing and Preservation* 35*(6),* 767–777. https://doi.org/10.1111/j.1745-4549.2011.00527.x

Binti-Maklin, S. N., Binti-Julmohammad, N., Binti-Saallah, S., Mohd-Yaakub, N. B., Bin-Sintang, M. D., Binti-Abd-Rahman, S. N. and Binti-Julmohamad, N. (2025). Effect of sonication time on physical and foaming properties of pasteurized milk. *International Dairy Journal* 161, 106137. https://doi.org/10.1016/j.idairyj.2024.106137

Bui, A.T.H., Cozzolino, D., Zisu, B., and Chandrapala, J. (2021). Infrared analysis of ultrasound treated milk systems with different levels of caseins, whey proteins and fat. *International Dairy Journal* 117, 104983. https://doi.org/10.1016/j.idairyj.2021.104983

Castillo-Andrade, A.I., Ruiz-Cabrera, M. A., Rivera-Bautista, C., Gonzalez-Garcia, R., Abud-Archila, M. and Grajales-Lagunes, A. (2025). Effect of ultrasound on the aging process, physicochemical properties, and lysosomal enzyme activity of semitendinosus and semimembranosus bovine muscles. *Revista Mexicana de*

Ingenieria Química 24(1), Alim24358. https://doi.org/10.24275/rmiq/Alim24358

Cadwallader, K.R. and Singh, T.K. (2009). Flavors and off-flavors in milk and dairy products. In L. H. McSweeney P. F. Fox (Eds.), *Advanced Dairy Chemistry* (3rd ed., Vol. 3, pp. 5–14). Springer.

Cervantes-Elizarrarás, A., Piloni-Martini, J., Ramírez-Moreno, E., Alanís-García, E., Güemes-Vera, N., Gómez-Aldapa, C. A., Zafra-Rojas, Q. Y. and Cruz-Cansino, N. S. (2017). Enzymatic inactivation and antioxidant properties of blackberry juice after thermoultrasound: Optimization using response surface methodology. *Ultrasonics Sonochemistry* 34, 371–379. https://doi.org/10.1016/j.ultsonch.2016.06.009

Chandrapala, J., Oliver, C., Kentish, S., Ashokkumar, M. (2012). Ultrasonics in food processing. *Ultrasonics Sonochemistry 19*, 975–983. https://doi.org/10.1016/j.ultsonch.2012.01.010

Cimmino, F., Catapano, A., Villano, I., Di Maio, G., Petrella, L., Traina, G. and Cavaliere, G. (2023). Invited review: Human, cow, and donkey milk comparison: Focus on metabolic effects. *Journal of Dairy Science* 106(5), 3072-3085. https://doi.org/10.3168/jds.2022-22465

Cregenzán-Alberti, O., Halpin, R. M., Whyte, P., Lyng, J. and Noci, F. (2014). Suitability of ccRSM as a tool to predict inactivation and its kinetics for *Escherichia coli*, *Staphylococcus aureus* and *Pseudomonas fluorescens* in homogenized milk treated by manothermosonication (MTS). *Food Control* 39, 41–48. https://doi.org/10.1016/j.foodcont.2013.10.007

Crudo, D., Bosco, V., Cavaglià, G., Mantegna, S., Battaglia, L. and Cravotto, G. (2014). Process intensification in food industry: Hydrodynamic and acoustic cavitation for fresh milk treatment. *Agro Food Industry Hi-Tech* 25, 55–59

Cruz-Cansino, N.S., Ramírez-Moreno, E., León-Rivera, J.E., Delgado-Olivares, L., Alanís-García, E., Ariza-Ortega, J.A., Manríquez-Torres, J.J. and Jaramillo-Bustos, D.P. (2015). Shelf life, physicochemical, microbiological and antioxidant properties of purple cactus pear (*Opuntia ficus indica*) juice after thermoultrasound treatment. *Ultrasonics Sonochemistry* 27, 277–286. https://doi.org/10.1016/j.ultsonch.2015.05.040

Deshpande, V. K. and Walsh, M. K. (2020). Effect of thermosonication in a batch system on the survival of spore-forming bacteria. *International Journal of Dairy Technology 73*, 486–493. https://doi.org/10.1111/1471-0307.12685

Deshpande, V. K. and Walsh, M. K. (2021). Effect of thermosonication in a laboratory-scale continuous system on the survival of thermophilic bacteria and indigenous microbiota in milk. *International Food Research Journal* 28, 63–72. https://doi.org/10.47836/ifrj.28.1.06

Dhiny, A., Jariyah, J., Agung, L. and Dany, A. (2023). Effect of frequency and duration of thermosonication on the physical, chemical and microbiological quality of cow's milk. *Journal of Pure and Applied Agriculture* 11, 136–146. https://doi.org/10.21776/ub.jpa.2023.011.03.4

Ehn, B.M., Ekstrand, B., Bengtsson, U. and Ahlstedt, S. (2004). Modification of IgE binding during heat processing of the cow's milk allergen β-lactoglobulin. *Journal of Agricultural and Food Chemistry* 52, 1398–1403. https://doi.org/10.1021/jf0304371

France, T.C., O'Mahony, J.A. and Kelly, A.L. (2021). The plasmin system in milk and dairy products. In Agents of change: Enzymes in milk and dairy products. *Springer International Publishing*. 11–55. https://doi.org/10.1007/978-3-030-55482-8_2

Furuta, M., Yamaguchi, M., Tsukamoto, T., Yim, B., Stavarache, C.E., Hasiba, K. and Maeda, Y. (2004). Inactivation of *Escherichia coli* by ultrasonic irradiation. *Ultrasonics Sonochemistry* 11, 57–60. https://doi.org/10.1016/S1350-4177(03)00136-6

Gaucher, I., Mollé, D., Gagnaire, V. and Gaucheron, F. (2008). Effects of storage temperature on physico-chemical characteristics of semi-skimmed UHT milk. *Food Hydrocolloids* 22, 130–143. https://doi.org/10.1016/j.foodhyd.2007.04.007

Gautam, P.B., Sharma, R., Atbhaiya, Y., Gandhi, K. and Mann, B. (2024). Thermosonication: A technique to inactivate the plasmin system in milk. *International Dairy Journal* 157, 105997. https://doi.org/10.1016/j.idairyj.2024.105997

Gregersen, S. B., Wiking, L. and Hammershøj, M. (2019). Acceleration of acid gel formation by high intensity ultrasound is linked to whey protein denaturation and formation of functional

milk fat globule-protein complexes. *Journal of Food Engineering* 254, 17–24. https://doi.org/10.1016/j.jfoodeng.2019.03.004

Guo, Z. and Jayan, H. (2023). Fast nondestructive detection technology and equipment for food quality and safety. *Foods* 12(20), 3744. https://doi.org/10.3390/foods12203744

Hassan, Z.M.R., Fakhr, H.M., Din, E., Ali, A.A., Mehanna, N.S. and El-Messery, T. M. (2013). Interaction of some low molecular weight phenolics with milk proteins. *World Applied Sciences Journal* 23, 182–187. https://doi.org/10.5829/idosi.wasj.2013.23.02.13057

Herceg, Z., Režek-Jambrak, A., Lelas, V. and Mededovic-Thagard, S. (2012). The effect of high intensity ultrasound treatment on the amount of *Staphylococcus aureus* and *Escherichia coli* in milk. *Food Technology and Biotechnology* 50, 46–52. https://hrcak.srce.hr/78997

Hemar, Y., Xu, C., Wu, S. and Ashokkumar, M. (2020). Size reduction of "reformed casein micelles" by high-power ultrasound and high hydrostatic pressure. *Ultrasonics sonochemistry* 63, 104929. https://doi.org/10.1016/j.ultsonch.2019.104929

Hernández-Falcón, T.A., Monter-Arciniega, A., Cruz-Cansino, N.S., Alanís-García, E., Rodríguez-Serrano, G.M., Castañeda-Ovando, A., García-Garibay, M., Ramírez-Moreno, E. and Jaimez-Ordaz, J. (2018). Effect of thermoultrasound on aflatoxin M1 levels, physicochemical and microbiological properties of milk during storage. *Ultrasonics Sonochemistry* 48, 396–403. https://doi.org/10.1016/j.ultsonch.2018.06.018

Jiang, Z., Wang, Y., Bai, S., Bai, C., Tu, Z., Li, H. and Qiu, L. (2024). The viable but non-culturable (VBNC) status of Shewanella putrefaciens (*S. putrefaciens*) with thermosonication (TS) treatment. Ultrasonics *Sonochemistry* 109, 107008. https://doi.org/10.1016/j.ultsonch.2024.107008

Karlović, S., Bosiljkov, T., Brnčić, M., Semenski, D., Dujmić, F., Tripalo, B. and Ježek, D. (2014). Reducing fat globules particle-size in goat milk: Ultrasound and high hydrostatic pressures approach. *Chemical and Biochemical Engineering Quarterly* 28(4), 499–507. https://doi.org/10.15255/CABEQ.2014.19400

Kashaninejad, M. and Razai, S. M. A. (2020). Influence of thermosonication treatment on the average size of fat globules, emulsion stability, rheological properties and color of camel milk cream. *LWT – Food Science and Technology* 132, 109852. https://doi.org/10.1016/j.lwt.2020.109852

Kentish, S. and Feng, H. (2014). Applications of power ultrasound in food processing. *Annual review of food science and technology* 5(1), 263-284. https://doi.org/10.1146/annurev-food-030212-182537

Li, J., Wang, J., Zhao, X., Wang, W., Liu, D., Chen, S., Xingqian, Y. and Ding, T. (2019). Inactivation of *Staphylococcus aureus* and *Escherichia coli* in milk by different processing sequences of ultrasound and heat. *Journal of Food Safety* 39, e12614. https://doi.org/10.1111/jfs.12614

Lin, L., Wang, X., Li, C. and Cui, H. (2019). Inactivation mechanism of *E. coli* O157: H7 under ultrasonic sterilization. *Ultrasonics Sonochemistry* 59, 104751. https://doi.org/10.1016/j.ultsonch.2019.104751

Liu, X.T., Zhang, H., Wang, F., Luo, J., Guo, H. Y. and Ren, F.Z. (2014). Rheological and structural properties of differently acidified and renneted milk gels. *Journal of dairy science* 97(6), 3292–3299. https://doi.org/10.3168/jds.2013-7568

Loan, L.T.K., Vinh, B. T. and Tai, N.V. (2024). Impact of ultrasound-assisted process on enzymatic extraction of polyphenols from purple rice bran in Vietnam: Experimental kinetics and innovative artificial approach. *Revista Mexicana de Ingeniería Química* 23(3), 1. https://doi.org/10.24275/rmiq/Alim24310

Lucey, J. A., Wilbanks, D.J. and Horne, D.S. (2022). Impact of heat treatment of milk on acid gelation. *International Dairy Journal* 125, 105222. https://doi.org/10.1016/j.idairyj.2021.105222

Magalhães, I.S., Guimarães, A.D.B., Tribst, A.A.L., de Oliveira, E.B. and Júnior, B. R. D. C. L. (2022). Ultrasound-assisted enzymatic hydrolysis of goat milk casein: Effects on hydrolysis kinetics and on the solubility and antioxidant activity of hydrolysates. *Food Research International* 157, 111310. https://doi.org/10.1016/j.foodres.2022.111310

Mahmoud, M.Z., Fagiry, M.A., Davidson, R. and Abdelbasset, W.K. (2022). The benefits, drawbacks, and potential future challenges of the

most commonly used ultrasound-based hurdle combinations technologies in food preservation. *Journal of Radiation Research and Applied Sciences* 15, 206–212. https://doi.org/10.1016/j.jrras.2022.03.006

Mahmoud, M.Z., Davidson, R., Abdelbasset, W.K. and Fagiry, M.A. (2022). The new achievements in ultrasonic processing of milk and dairy products. *Journal of Radiation Research and Applied Sciences* 15(1), 199–205. https://doi.org/10.1016/j.jrras.2022.03.005

Marangoni, F., Pellegrino, L., Verduci, E., Ghiselli, A., Bernabei, R., Calvani, R. and Poli, A. (2019). Cow's milk consumption and health: a health professional's guide. *Journal of the American College of Nutrition* 38(3), 197–208. https://doi.org/10.1080/07315724.2018.1491016

Marchesini, G., Fasolato, L., Novelli, E., Balzan, S., Contiero, B., Montemurro, F., Andrighetto, I. and Segato, S. (2015). Ultrasonic inactivation of microorganisms: A compromise between lethal capacity and sensory quality of milk. *Innovative Food Science and Emerging Technologies* 29, 215–221. https://doi.org/10.1016/j.ifset.2015.03.015

Meng, Y., Liang, Z., Zhang, C., Hao, S., Han, H., Du, P. and Liu, L. (2021). Ultrasonic modification of whey protein isolate: Implications for the structural and functional properties. *LWT- Food Science and Technology* 152, 112272. https://doi.org/10.1016/j.lwt.2021.112272

Mortazavi, S.M., Sani, A.M. and Mohseni, S. (2015). Destruction of AFT by ultrasound treatment. *Journal of Applied Environmental and Biological Sciences* 4, 198–202.

Nascimento, J.C.N., Salgado, M.J.G., Gutierrez Alzate, K., de Alencar, J.C.G., Rosario, I.L. D.S., da Silva, J.G. and da Costa, M.P. (2023). Effect of Sonication Associated with Pasteurization on the Inactivation of Methicillin-Resistant *Staphylococcus aureus* in Milk Cream. *Applied Sciences* 13(22), 12093.

Ninković, M., Milićević, V., Radojičić, S., Bugarski, D. and Stević, N. (2024). Presence of *Mycoplasma bovis* in bulk tank milk and associated risk factor analysis in Serbian dairy farms. *Pathogens* 13(4), 302. https://doi.org/10.3390/pathogens13040302

Obando-Galicia, Y. T., Martínez-de Jesús, G. and Totosaus, A. (2024) Assisted (ultrasound or high shear impeller) soybean oil/lecithin extraction of polyphenolic compounds from red cactus pear peel. *Revista Mexicana de Ingeniería Química* **23**(2), Alim24237. https://doi.org/10.24275/rmiq/Alim24237

Ojha, K.S., Mason, T.J., O'Donnell, C.P., Kerry, J.P. and Tiwari, B. K. (2017). Ultrasound technology for food fermentation applications. *Ultrasonics sonochemistry* 34, 410–417. https://doi.org/10.1016/j.ultsonch.2016.06.001

Owens, S.L., Brewer, J.L. and Rankin, S.A. (2001). Influence of bacterial cell population and pH on the color of nonfat milk. *LWT – Food Science and Technology* 34, 329–333. https://doi.org/10.1006/fstl.2001.0781

Parreiras, P.M., Vieira-Nogueira, J.A., Rodrigues, L., Passos, M. C., Gomes, N.R., Breguez, G.S., Falco, T.S., Bearzoti, E. and Menezes, C.C. (2020). Effect of thermosonication on microorganisms, the antioxidant activity and the retinol level of human milk. *Food Control* 113, 107172. https://doi.org/10.1016/j.foodcont.2020.107172

Pérez-Andrés, J.M., Charoux, C.M.G., Cullen, P.J. and Tiwari, B.K. (2018). Chemical modifications of lipids and proteins by non-thermal food processing technologies. *Journal of Agricultural and Food Chemistry 66*, 5041–5054. https://doi.org/10.1021/acs.jafc.7b06055

Qin, X., Yang, R., Zhong, J., Shabani, K.I. and Liu, X. (2018). Ultrasound-assisted preparation of a human milk fat analog emulsion: Understanding factors affecting formation and stability. *Journal of Food Engineering* 238, 103-111. https://doi.org/10.1016/j.jfoodeng.2018.06.011

Qian, J., Chen, D., Zhang, Y., Gao, X., Xu, L., Guan, G. and Wang, F. (2023). Ultrasound-assisted enzymatic protein hydrolysis in food processing: Mechanism and parameters. *Foods* 12(21), 4027. https://doi.org/10.3390/foods12214027

Ragab, E.S., Lu, J., Pang, X.Y., Nassar, K.S., Yang, B.Y., Zhang, S.W. and Lv, J.P. (2019). Effect of thermosonication process on physicochemical properties and microbial load of goat's milk. *Journal of Food Science and Technology* 56, 5309–5316. https://doi.org/10.1007/s13197-019-03994-0

Ramos-Villacob, V., Figueroa-Flórez, J. A., Salcedo-Mendoza, J.G., Hernandez-Ruydíaz, J. E. and Romero-Verbel, L.A. (2024). Development of modified cassava starches by ultrasound-assisted

amylose/lauric acid complex formation. *Revista Mexicana de Ingeniería Química* 23(1) 1–15. https://doi.org/10.24275/rmiq/Alim24109

Reiter, M., Reitmaier, M., Haslbeck, A. and Kulozik, U. (2023). Acid gelation functionality of casein micelles in concentrated state: Influence of calcium supplementation or chelation combined with enzymatic stabilization. *Food Hydrocolloids* 143, 108927. https://doi.org/10.1016/j.foodhyd.2023.108927

Shanmugam, A., Chandrapala, J. and Ashokkumar, M. (2012). The effect of ultrasound on the physical and functional properties of skim milk. *Innovative Food Science and Emerging Technologies* 16, 251–258. https://doi.org/10.1016/j.ifset.2012.06.005

Sharma, P., Oey, I., Bremer, P. and Everett, D. W. (2014). Reduction of bacterial counts and inactivation of enzymes in bovine whole milk using pulsed electric fields. *International Dairy Journal* 39, 146–156. https://doi.org/10.1016/j.idairyj.2014.06.003

Shen, X., Shao, S. and Guo, M. (2017). Ultrasound-induced changes in physical and functional properties of whey proteins. *International Journal of Food Science and Technology* 52, 381–388. https://doi.org/10.1111/ijfs.13292

Shokri, S., Javanmardi, F., Mohammadi, M. and Khaneghah, A.M. (2022). Effects of ultrasound on the techno-functional properties of milk proteins: A systematic review. *Ultrasonics Sonochemistry* 83, 105938. https://doi.org/10.1016/j.ultsonch.2022.105938

Silva, M., Zisu, B. and Chandrapala, J. (2018). Influence of low-frequency ultrasound on the physico-chemical and structural characteristics of milk systems with varying casein to whey protein ratios. *Ultrasonics Sonochemistry 49*, 268–276. https://doi.org/10.1016/j.ultsonch.2018.08.015

Song, B., Zhang, Y., Yang, B., Zhu, P., Pang, X., Xie, N. and Lv, J. (2021). Effect of different temperature-controlled ultrasound on the physical and functional properties of micellar casein concentrate. *Foods* 10(11), 2673. https://doi.org/10.3390/foods10112673

Stratakos, A.C., Inguglia, E.S., Linton, M., Tollerton, J. and Murphy, L., Corcionivoschi, N., Tiwari, B. K. (2019). Effect of high-pressure processing on the safety, shelf life and quality of raw milk. *Innovative Food Science and Emerging Technologies* 52, 325–333. https://doi.org/10.1016/j.ifset.2019.01.009

Tavsanli, H., Aydin, M., Ede, Z.A. and Cibik, R. (2022). Influence of ultrasound application on the microbiota of raw goat milk and some food pathogens including *Brucella melitensis*. *Food Science and Technology International* 28(7), 634–640. https://doi.org/10.1177/10820132211049601

Tsukamoto, I., Constantinoiu, E., Furuta, M., Nishimura, R. and Maeda, Y. (2004). Inactivation effect of sonication and chlorination on *Saccharomyces cerevisiae*, calorimetric analysis. *Ultrasonics Sonochemistry* 11, 167–172. https://doi.org/10.1016/j.ultsonch.2004.01.014

Ugarte-Romero, E., Feng, H. and Martin, S.E. (2007). Inactivation of *Shigella boydii* 18 IDPH and *Listeria monocytogenes* Scott A with power ultrasound at different acoustic energy densities and temperatures. *Journal of Food Science* 72, M103–M107. https://doi.org/10.1111/j.1750-3841.2007.00340.x

Ullah, I., Naz, S., Khattak, U. S., Saeed, M., ul Akbar, N. and Rauf, S. (2024). Prevalence and associated risk factors of *Brucella abortus* and *Brucella melitensis* in humans and cattle populations: A comprehensive study. Comparative Immunology, *Microbiology and Infectious Diseases* 115, 102276. https://doi.org/10.1016/j.cimid.2024.102276

Vadillo-Rodríguez, V. and Dutcher, J.R. (2011). Viscoelasticity of the bacterial cell envelope. Soft Matter, 7(9), 4101-4110.

Vélez, M. A., Perotti, M.C., Candioti, M.C., Bergamini, C.V. and Hynes, E.R. (2016). Plasmin and coagulant activities in a minicurd model system: Study of technological parameters. *Journal of Dairy Science* 99(9), 7053-7062. https://doi.org/10.3168/jds.2015-10799

Vijayakumar, S., Grewell, D., Annandarajah, C., Benner, L. and Clark, S. (2015). Quality characteristics and plasmin activity of thermosonicated skim milk and cream. *Journal of Dairy Science* 98, 6678–6691. https://doi.org/10.3168/jds.2015-9429

Villamiel, M. and De Jong, P. (2000). Inactivation of *Pseudomonas fluorescens* and *Streptococcus thermophilus* in Trypticase® Soy Broth and total bacteria in milk by continuous-flow ultrasonic treatment and conventional heating. *Journal of*

Food Engineering 45, 171–179. https://doi.org/10.1016/S0260-8774(00)00059-5

Wang, Y., Guo, M., Wu, P., Fan, K., Zhang, W., Chen, C. and Yu, J. (2024). New insights into the destabilization of fat globules in ultra-instantaneous UHT milk induced by added plasmin: Molecular mechanisms and the effect of membrane structure on plasmin action. *Colloids and Surfaces B: Biointerfaces* 240, 113987. https://doi.org/10.1016/j.colsurfb.2024.113987

Wang, J., Saxena, R., Vanga, S.K. and Raghavan, V. (2022). Effects of microwaves, ultrasonication, and thermosonication on the secondary structure and digestibility of bovine milk protein. *Foods* 11, 138. https://doi.org/10.3390/foods11020138

Yang, Y., Wang, Z., Hu, D., Xiao, K. and Wu, J.Y. (2018). Efficient extraction of pectin from sisal waste by combined enzymatic and ultrasonic process. *Food Hydrocolloids* 79, 189–196. https://doi.org/10.1016/j.foodhyd.2017.11.051

Yuno-Ohta, N., Shimonomura, N., Hoshi, Y., Leocmach, M., Hori, K. and Ohta, H. (2021). Characterization of the gelation and resulting network of a mixed-protein gel derived from sodium caseinate and ovalbumin in the presence of glucono-δ-lactone. *Colloids and Surfaces B: Biointerfaces* 198, 111472. https://doi.org/10.1016/j.colsurfb.2020.111472

Zafra-Rojas, Q. Y., Jiménez-Hernández, J. L., Olloqui, E. J., Cruz-Cansino, N. S., Alanís-García, E., Ramírez-Moreno, E., Ariza-Ortega, J. A. and Moreno-Seceña, J. C. (2023). Optimization of thermoultrasound process of soursop (*Annona muricata*) nectar and comparison of its physicochemical properties and *in vitro* bioaccessibility of antioxidants with pasteurized sample. *Food Technology and Biotechnology* 61, 536–548. https://doi.org/10.17113/ftb.61.04.23.8180

Zhang, Y., Li, Y., Li, S., Zhang, H. and Ma, H. (2018). In situ monitoring of the effect of ultrasound on the sulfhydryl groups and disulfide bonds of wheat gluten. *Molecules* 23(6), 1376. https://doi.org/10.3390/molecules23061376

Zlatev, Z., Pehlivanova, T., Dimitrova, A., Baycheva, S., Taneva, I. and Keremidchieva, K. (2018). Development of an ultrasonic device for quality evaluation of yogurt. *Engineering Review* 38, 279–287. https://doi.org/10.30765/er.38.3.4

Zhao, Y., Ma, Q., Zhou, T., Liu, L., Wang, Y., Li, X. and Kouame, K. J. E. P. (2024). Ultrasound-induced structural changes of different milk fat globule membrane protein-phospholipids complexes and their effects on physicochemical and functional properties of emulsions. *Ultrasonics Sonochemistry* 103, 106799. https://doi.org/10.1016/j.ultsonch.2024.106799

Zhou, J., Sheng, L., Lv, R., Liu, D., Ding, T. and Liao, X. (2021). Application of a 360-degree radiation thermosonication technology for the inactivation of *Staphylococcus aureus* in milk. *Frontiers in Microbiology* 12, 771770. https://doi.org/10.3389/fmicb.2021.771770

Zupanc, M., Pandur, Ž., Perdih, T. S., Stopar, D., Petkovšek, M. and Dular, M. (2019). Effects of cavitation on different microorganisms: The current understanding of the mechanisms taking place behind the phenomenon. A review and proposals for further research. *Ultrasonics Sonochemistry* 57, 147–165. https://doi.org/10.1016/j.ultsonch.2019.05.009

Vol. 24, No. 3(2025) Bio25582
Revista Mexicana de Ingeniería Química

Dog feces with glucose-feed were the most effective to produce electricity in microbial fuel cells

Heces de perro y glucosa fueron las más efectivas para producir electricidad en celdas de combustible microbianas

N. Gómez-Flores[1], Y.S. Perea-Vélez[1], R. Carrillo-González[1], J.E. Corona-Sánchez[1], D. Tapia-Maruri[2], MCA González-Chávez[1]*

[1]Programa en Edafología, Colegio de Postgraduados, Carretera México-Texcoco, km 36.5. Texcoco estado de México. 56230.

[2]Laboratorio de Microscopia Avanzada. Centro de Productos Bióticos, Instituto Politécnico Nacional. CEPROBI # 8, San Isidro, Yautepec 62731, México.

Sent date: May 20, 2025; Accepted: September 23, 2025

Abstract

Microbial fuel cells (MFCs) generate electricity through microbial metabolism, which is an efficient, renewable, and sustainable biological alternative for domestic and potential commercial applications. Mine wastes and dog feces are common and abundant residues contributing to environmental pollution and human health concerns. This study analyzed the production of electricity by using mine waste, dog feces, and vermicompost as MFC feedstocks and tested two sources of carbon (saccharose and glucose) as co-substrates in the feeding solution. Dog feces produced the longest current output (41 days), the maximum voltage per day (0.33 V), and the highest cumulative power density (15 W $cm^{-3)}$. Dog feces with glucose generated the highest power density (5.6 to 15 W cm^{-3}), while saccharose and mine waste produced a maximum current output of 0.24 V day^{-1} and a cumulative power density of ~8 W cm^{-3}. There were changes in the mine waste-metal concentration. MFC can be a practical solution to the aged environmental concern of the disposal of wastes, especially dog feces. Moreover, it may participate in the removal of Zn present in mine wastes. It may help the worldwide energy crisis, but several aspects must be optimized to bring it to the commercial level.

Keywords: Bioelectrochemical hybrid technology, microbial electro-remediation, mine residues.

Resumen

Las celdas de combustible microbianas (CCM) generan electricidad a través del metabolismo microbiano y son una alternativa biológica renovable, sostenible y eficiente con diferentes aplicaciones. Los desechos mineros y las heces de perro son residuos comunes y abundantes que contribuyen a la contaminación ambiental y preocupan por sus efectos negativos en la salud humana. Esta investigación analizó la producción de electricidad utilizando desechos mineros, heces de perro y vermicompost como materias primas para CCM y dos fuentes de carbono (sacarosa y glucosa) como cosustratos en la solución de suplemento de celdas. Las heces de perro produjeron corriente duradera (41 días), voltaje máximo por día (0.33 V) y mayor densidad de potencia acumulada (15 W cm^{-3}). Las heces de perro con glucosa generaron la densidad de potencia más alta (5.6 a 15 W cm^{-3}). La sacarosa y los desechos mineros produjeron salida de corriente máxima de 0.24 V $día^{-1}$ y densidad de potencia acumulada de ~8 W cm^{-3}. Las CCM pueden ser solución práctica para la eliminación de residuos, especialmente las heces caninas. Lo cual auxilia en la crisis energética; pero es necesario optimizar varios aspectos para comercializarlas.

Palabras clave: Tecnología híbrida electroquímica, electro-remediación microbiana, residuos de mina.

*Corresponding author. *E-mail*: carmeng@colpos.mx;
https://doi.org/10.24275/rmiq/Bio25582
ISSN:1665-2738, *issn-e*: 2395-8472

1 Introduction

Global electricity demand continually increases, driven by growing industrial use, air conditioning, electrification, and data centers. According to the International Energy Agency, global power consumption increased by 4.3% in 2024, equivalent to 1,080 terawatt-hours. This number is nearly double the annual average of the preceding decade. Furthermore, the power energy demand is expected to increase by 4% until 2027 (IEA, 2025b, 2025a). Meanwhile, for global fossil fuel-based energy, a 33% increase in demand is projected by 2035, which will lead to an additional 87 gigatons of CO_2 equivalent by 2050, thereby accelerating the effects of the global climate change (Ray *et al*., 2025). Most of the electricity demand over the next three years will come from emerging and developing economies (IEA, 2025b, 2025a). In this regard, fuel-based energy sources need to be gradually replaced with cleaner energy sources to keep a balance between energy demand and sustainability (Choudhury *et al*., 2017; Chouler *et al*., 2016), and the principles of the circular economy could be a vital pillar to reach this energy transition (Boloy *et al*., 2021).

Waste-to-energy is an effective component of modern waste management strategy technology, and it may be a low-cost waste treatment approach for hazardous materials while simultaneously obtaining energy (Aznar-Sánchez *et al*., 2018; Choudhury *et al*., 2017; Elhenawy *et al*., 2022; Pandit *et al*., 2021; Yousefi *et al*., 2021). Among waste-to-energy technologies, microbial fuel cells (MFCs) are gaining attention for producing bioelectricity (Logan & Rabaey, 2012; Yousefi *et al*., 2021) because of their ability to generate energy directly from biodegradable waste and operate under low-energy conditions (Apollon *et al*., 2025). Moreover, in regions characterized by limited access to electricity, the implementation of MFCs can be a viable solution (Rajesh & Kumawat, 2023).

The MFCs are devices that convert chemical energy contained within organic compounds into electricity through electrochemical reactions. These reactions are generated by the metabolism of microorganisms involved in the system (Douma *et al*., 2025). In general, in anaerobic conditions, microorganisms near the anode oxidize organic compounds by releasing protons and electrons in the anode chamber. The electrons are then transferred to the cathode by an external circuit (Foudhaili *et al*., 2019; Rajesh & Kumawat, 2023). A typical MFC comprises two compartments, an anode and a cathode, separated by a membrane (Douma et al., 2025). However, several configurations (single chamber, double chamber, up-flow, or stacked) have been explored in order to enhance the energy efficiency of these devices and scalability (Apollon *et al*., 2025).

The large-scale implementation of MFCs technology faces several challenges, including the cell configuration type and shape of electrodes (Altın & Uyar, 2025), and the substrate used as a feedstock. Among those factors, the substrate is one of the key elements for the production of electricity because it provides microorganisms, nutrients, and electron donors. For many years, sugar-based wastes and wastewater have been used as feedstock for MFCs (Apollon *et al*., 2025). Nevertheless, some research work has been conducted on the use of non-conventional substrates, such as agro-residues (Rajesh & Kumawat, 2023) or animal and human feces (Douma *et al*., 2025; Memon *et al*., 2025) to feed MFCs. Under this frame, dog feces may also be a resource for electricity production, due to 95% of feces corresponding to organic matter content, the rest is related to elements such as N, P, K, Mg, Ca, Na, S, B, Ca, Fe, Cu, Mn, and Zn (Yavor *et al*., 2020). Moreover, it is estimated that 30% of households globally have a dog, resulting in between 0.7 and 1 billion dogs (Fiães *et al*., 2025), which leads to the production of more than 5 million tons of canine feces annually (Dróżdż *et al*., 2022).

Proper management of canine feces is essential for environmental and public health reasons. Improper disposal of dog feces can lead to contamination of landfills and water sources, the spread of pathogens, and air pollution (USDA, 2005). For example, Yavor *et al*. (2020), used a life cycle impact assessment, to analyze the environmental impact of dogs which have an average lifespan of 13 years. The authors related their food and excrement (urine and feces) to fifteen impact categories. These authors concluded that dog feces significantly contribute to the eutrophication and ecotoxicity of freshwater. According to these authors, this impact is comparable to 7% of the climate change impact that a European citizen makes annually. Furthermore, with low and inadequate feces disposal control, soil contamination occurs. These wastes are a social health risk because they can produce several diseases and human health effects (Penakalapati *et al*., 2017). On the other hand, nowadays, the use of dog feces bags is another environmental issue that contributes to 0.6% of the total plastic waste generated worldwide (Dróżdż *et al*., 2022). Despite the existence of alternative options for the management of dog waste, such as incineration and composting, in many countries, there are no guidelines for the proper management of canine feces. In addition, incineration and composting have limitations. The incineration process needs the establishment and maintenance of an incinerator, and the provision of energy, most commonly derived from fossil fuels. This methodology is exclusively feasible for large-scale facilities, as composting may not be effectively eliminated some pathogens present in the dog feces. Improper management of the composting process can lead to the generation of odors, attracting

flies and rodents (Fiães *et al*., 2025). Consequently, within this context, the MFC can be a potentially efficacious alternative for the treatment of canine feces.

Mining tailings, also known as mine wastes or mine residues, constitute an unconventional material that has gradually garnered interest for use as an MFC feed (Cui *et al*. 2025) because it is possible to recover energy and remove metals from low-value wastes. Mine wastes may be a feasible material for use as a final electron acceptor in MFC due to the presence of elements with a comparable or higher redox potential than oxygen (Gonzalez Olias *et al*., 2019). The sustainable management of mine waste continues to be a global concern, as well as its associated environmental and social costs (Damoah & Herat, 2022) For example, significant on-site storage problems, dust generation, and the potential release of heavy and toxic metals contained in the dust particles (Lim & Alorro, 2021). In addition, the worldwide annual generation of mine wastes is around 5-7 billion tons (Lorenzo-Tallafigo *et al*., 2022). Ideally, sustainable mine-waste management practices imply using techniques to reduce or prevent the mine waste before its generation. However, due to technical limitations and the nature of the mineral extraction process, it is almost impossible to reduce the production of mine wastes. Therefore, new approaches have been developed to address this issue, such as adding value to mine wastes through reprocessing, resource recovery, or repurposing (Calderon *et al*., 2020; Lim & Alorro, 2021). Through MFCs, the removal/recovery of some metals while generating energy is possible (Ghassemi, 2001; Mathuriya and Yakhmi 2014). However, the use of mine wastes to generate electricity is a relevant issue that has received little analysis and warrants further research.

As mentioned early, mine wastes and pet domestic waste, which pose a significant environmental and human health concern worldwide, may be suitable for producing electrical energy using MFCs and have received limited research attention. Therefore, the objectives of this research were: 1) To determine electricity production in MFC fed with non-conventional residues (mine wastes, dog feces), and one agricultural conventional transformed residue without environmental concern as vermicompost and two co-substrates functioning as extra-carbon sources (glucose and saccharose). 2) To morphologically identify the anode-bacteria of MFC by using scanning electron microscopy in the best treatments. This research addresses two alarming issues. On one hand, the mitigation of an environmental problem posed by excessive waste (from the mining industry and the most common domestic pets). On the other hand, an alternative cost-effective electricity generation is needed under an imminent energy crisis taking place in many countries.

2 Materials and methods

Mine wastes, dog feces, and vermicompost were used as feedstock materials. To start microorganisms' growth in the MFCs, glucose and saccharose were added separately, while tap water was used as a control. The treatments tested were the combination of substrates (3) and the nutrient solutions (2), plus the control (1 for each substrate involving the absence of nutrient solution). In total, nine treatments, three replicates of each treatment, were evaluated.

2.1 Chemical characterization of feedstock substrates

Electrical conductivity and pH of substrates were measured in a 1:2 slurry substrate: water solution using a conductimeter (Conductronic CL35), and a pH meter (Orion Research, Model 601, Beverly, MA) according to Rowell (1994) and Rhoades (1996). Organic carbon content (OC) was quantified using the method of Walkley-Black (1983); which measures oxidizable organic carbon. The chemical characterization was performed in the original substrates, and considering modifications in the MFCs, was also analyzed at the end of the experiment (42 days).

2.2 Configuration of MFC and experimental setup

H-type MFCs (two-chamber configuration) were constructed because they allow independent manipulation of electrodes (Rabaey *et al*., 2003). Briefly, sterile clinical bottles of 100 mL functioned as anode and cathode chambers. A saline bridge connected the anodic and cathodic chambers. The saline bridge consisted of a chlorinated polyvinyl chloride tube with a diameter of 1.27 cm and 2 cm long, containing 5 mL of 1 M KCl solution and 3% (w/v) agar-agar. The electrodes were circular pieces of aluminum (from soda cans) with a diameter of 4.6 cm (16.62 cm^2 surface area). Aluminum was chosen because it is a low-cost material that can be used as an alternative to carbon-based electrodes for oxygen reduction (Saad *et al*., 2025).

The electrodes' surface was rubbed using sandpaper to make it rough and allow biofilm adhesion. The electrodes were connected with a 13 AWG copper wire (11.5 cm long). A diagram of the configuration of MFC is provided in Fig. 1.

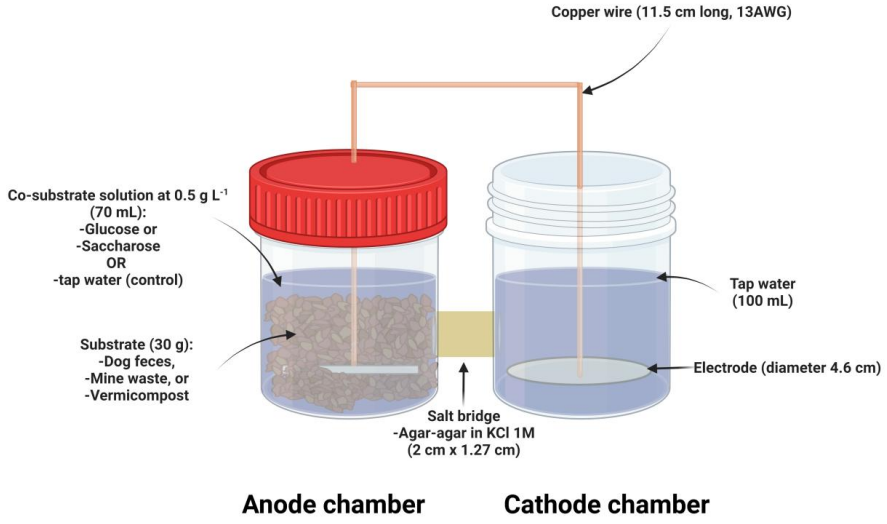

Figure 1. Design of microbial fuel cells used in this research

The anodic chamber was fed in all cases with 30 g of sieved (2 mm mesh) mine wastes (mining tailings), vermicompost, or dog feces, while the cathodic chamber was filled with 100 mL of tap water. Moreover, 70 mL of co-substrates (nutrient solutions), glucose or saccharose at 0.5 g L^{-1}, was added to the anodic chamber. In the case of the control treatment, tap water was added. The nutrient solutions or tap water were added at the beginning of the experiment establishment in a single addition. After immersing the electrodes, the anodic chamber was sealed with a plastic lid (to ensure anaerobic conditions), while the cathodic chamber was kept open. The MFCs operated for 42 days and were kept at room temperature. Room temperature was recorded daily (from 12 to 18 °C), and the voltage produced was measured daily at intervals of 24 hours using a multimeter (Steren Mul-005). The electrical resistance and the electrical power density were calculated according to Logan *et al.*(2006) and Luo *et al.* (2010). At the end of the operation the monitoring of MFCs, the electrodes, and substrates were separated for their analysis.

2.3 *Calculations*

The current was calculated based on the voltage and the resistance of the conducting wire used (7.55×10^{-4} Ω). The power density was calculated based on the volume of the anodic chamber and the surface area of the cathode as follows:

$$P_v = \frac{I \times V}{Volume\ of\ anodic\ chamber}$$ (Luo *et al.*, 2010)

where I is the current (A), V is the voltage (V). The volume of the anodic chamber was expressed in m^3. Normalizing the power output based on volume may be helpful to compare the economic feasibility of the system in terms of size and material cost (Logan *et al.*, 2006).

2.4 *Scanning electron microscopy analysis*

The anode-biofilm formation was examined by scanning electron microscopy. Anodes were separated from the MFC carefully, and a section of approximately 1 cm^2 was taken and fixed with 5 mL of phosphate-buffered saline solution (PBS 0.1 M pH 7.4) and 3% (v/v) glutaraldehyde. The samples were embedded for 12 hours at 4 °C with fixation solution, then washed three times with PBS solution, and kept at 4 °C until their imaging analyses. An environmental scanning electron microscope (ESEM) (Carl Zeiss EVO LS10, Jena, Germany) and an X-ray detector (EDX) (Bruker, Quantax 200, Germany) were used. The samples were placed in aluminum stubs with carbon conductive tape. A manometric pressure of 90 Pa of water vapor, an electron beam with a voltage of 30 kV, and backscattered electron detector (NTS BSD) were used. Photomicrographs were captured with the electron microscope. Elemental microanalysis of chemical elements was carried out with an EDX detector. For EDX analysis, three fields of view (each 20 mm^2) were analyzed for 240 s at an acceleration voltage of 30 kV.

2.5 Metal removal and recovery

The pseudo-total concentrations were analyzed in the original substrates and after finishing the experimental stage in both anode (metal removal) and cathode (metal recovery) chambers. The pseudo-total concentration was measured following the ISO 11466 method. Briefly, 500 mg of the sample were digested with 6 mL of HNO_3-$HClO_4$ (3:1 ratio). The samples were placed in a digestion block for 8 hours at 120 °C. After cooling, the digested samples were diluted to 25 mL and filtered through Whatman No. 42. The concentrations were analyzed using an atomic absorption spectrometer (PerkinElmer, model 3110).

2.6 Statistical analysis

Data compliance with normality assumptions (Shapiro-Wilks, $\alpha = 0.05$) and variance homogeneity (Bartlett, $\alpha = 0.05$) was corroborated. Data on pseudo-total metals and organic carbon did not satisfy the assumptions and were transformed with the Box-Cox power transformation. An analysis of the variance was carried out of cumulative voltage and power density output in the microbial fuel cells. The analysis was done with the Friedman test as repeated measures existed, but with no normality compliance. Similarly, the cumulative voltage and power density output by the same substrate with different co-substrates were compared. The statistical analyses were performed using Rstudio v. 4.2.1 software for Windows.

3 Results and discussion

The production of electricity through MFCs using dog feces, vermicompost, and mine wastes as substrates was explored. The first two materials may be a potential substrate feed in MFC and a renewable source of energy due to their high OC content (Table 1), microbial populations, and different nutrients contained in them, which are required for the growth and activity of microbes for electrochemical reactions (Nandy *et al*., 2015). In contrast, the MFC is a promising technology for the recovery/immobilization of metals contained in mine wastes, because the metal ions can be reduced and deposited in the electrodes. While simultaneously obtaining bioenergy. In addition, the metals contained in the mine waste (Zn, Cd, Fe, and Cu) may serve as direct electron acceptors or donors without any external power supply (Gonzalez Olias *et al*., 2019).

Table 1. Original chemical properties of substrates used in the microbial fuel cells and their modification by electron-donor substances at the end of the experiment (41 days).

Substrate	Treatments	pH			Electrical conductivity (mS/cm)			Organic carbon (%)		
		average	sd		average	sd		average	sd	
Mine waste	Original	2.3	0.01	b	7	0.05	a	0.7	0.08	b
	Saccharose	4.3	0.17	a	2.7	0.1	c	0.51	0.05	b
	Glucose	4.1	0.03	a	3.5	0.27	b	1.79	0.13	a
	Control	4.3	0.24	a	3.3	0.3	bc	0.62	0	b
Vermicompost	Original	7.8	0.03	b	11.4	0.29	a	10.4	0.56	a
	Saccharose	8.2	0.09	a	4.6	0.14	b	9.48	0.07	a
	Glucose	8.3	0.03	a	4.1	0.17	b	7.07	0.29	b
	Control	8.4	0.09	a	4.6	0.11	b	7.21	0.58	b
Dog feces	Original	7.4	0.06	c	4.8	0.07	a	19.59	1.02	a
	Saccharose	7.7	0.16	b	4.6	0.42	a	7.93	1.06	c
	Glucose	8.5	0.16	a	4.7	0.19	a	10.02	0.11	b
	Control	8.3	0.04	a	4.4	0.38	a	8.56	0.56	bc

Average and standard deviation are showed, $n = 3$. Different lower letters refer statistical significance when comparing treatments in the same substrate tested.

3.1 Electrochemical characterization of the MFC

The voltage generation profile was different among co-substrates (Figs. 2 and 3); however, a similar shape of the voltage generation time curve was observed between the treatments vermicompost and mine waste with saccharose and the control. In both treatments, saccharose, and control (tap water) the current production was observed from day 4 until 31; however, mine waste still produced a measurable voltage by day 35 (Fig. 2a). When using glucose, the electricity production was longer than, from day 4 to 37, with saccharose and the control treatment (Fig. 2b). Dog feces produced a low but detectable voltage by the end of the experiment (41 days).

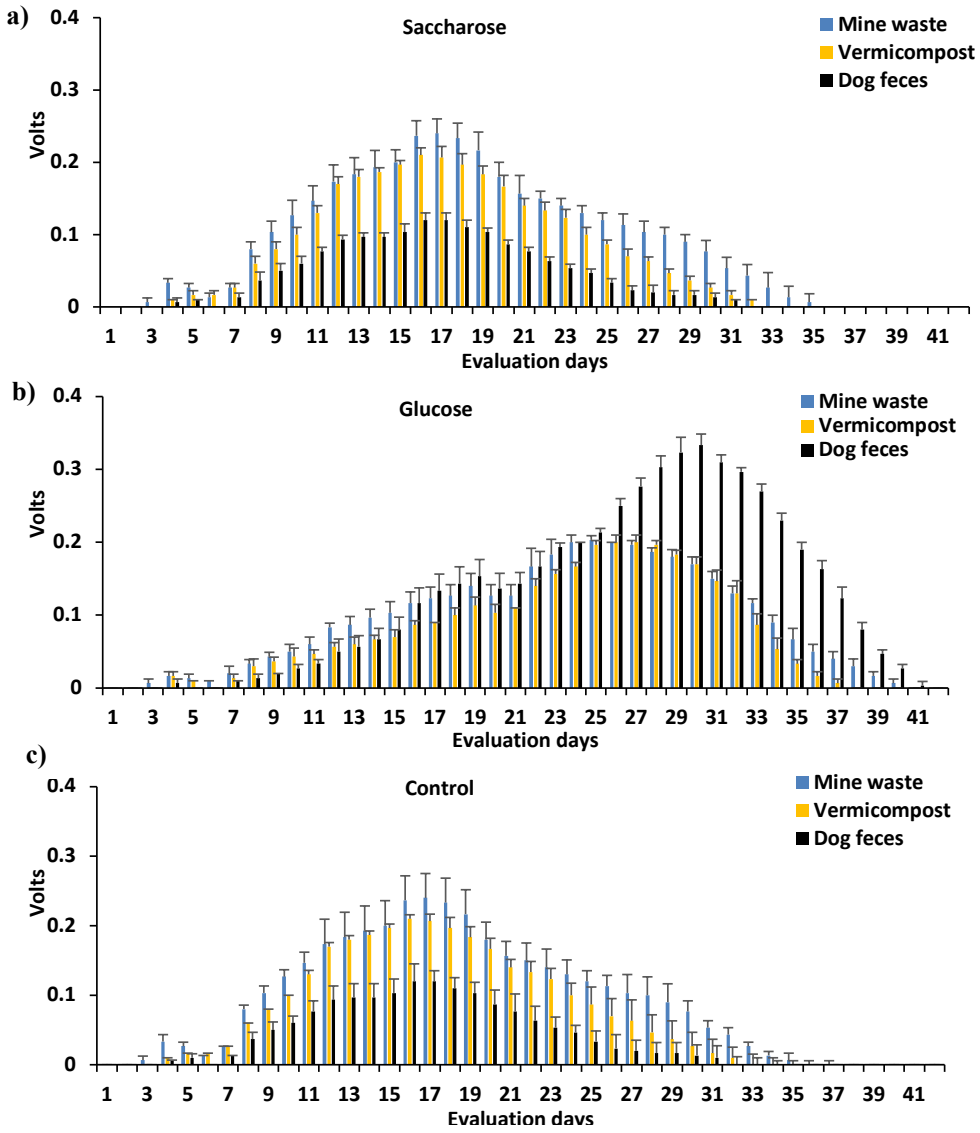

Figure 2. Kinetics of voltage output of microbial fuel cells in one operation cycle after addition of three substrates and three donor electrons sources. a) Saccharose, b) glucose, and c) tap water. Bars show average and standard deviation, n=3.

Borole *et al*. (2009) mentioned that MFC got starved before the voltage drops below 0.01 V. Aelterman *et al*. (2006) observed that the power output declined after 12 hours in MFC fed with three waste waters using hexacyanoferrate as an electron acceptor. The MFC used hexacyanoferrate as catholyte and was fed with industrial influent of an anaerobic digester from a potato-processing factory.

On the other hand, when comparing the voltage output by day, for treatments with saccharose the maximum energy production (from 0.16 to 0.24 V) was observed around days 16-17 in all substrates (Fig. 2a). In contrast, in treatments with glucose (Fig. 2b), the maximum voltage output was observed on day 30 in the case of dog feces (0.33 V), and by days 25 to 28 for the mine waste and vermicompost substrates. Logan et al. (2006) reviewed that theoretically, the maximum achievable MFC voltage in an open circuit, as used in this research, is around 0.8 V; however, during current generation, the voltages remain below 0.62 V. In the present research, using a rustic MFC, the greater voltage was half of the previously referred voltage. Therefore, making several adjustments to increase the efficiency of the MFC is needed. Also, different voltage generation profiles and the amount of energy produced can be explained by the differences in the substrate composition. Silva-Palacios *et al*. (2023) evaluated the use of mine residues as a substrate for the generation of energy through a single-chamber MFC with air cathode. After 30 days of operation of the MFC, a peak voltage value of 0.65 V was achieved. Meanwhile, Memon *et al*. (2025) developed a portable MFC feed with cow

manure. The authors reported an initial open-circuit voltage of 0.49 V and a stabilization at 0.31 V after 120 hours. Elhenawy *et al*. (2022) mentioned that the type and composition of waste influence the amount of energy produced. However, the performance of an MFC is dependent upon other variables, like the operating conditions, the nature of the electrolyte, the type of microorganisms, electrode materials, operation time, and cell configuration (Foudhaili *et al*., 2019).

The cumulative electricity production also varied according to the co-substrates and substrates (Fig. 3). The lag period for current production ranged between 11 and 15 days in all the treatments. In saccharose treatment, the dog feces reached the plateau by day 26, and the lowest electricity generation was observed (Fig. 3a). In contrast, approximately the highest cumulative electricity production (5.2 V) was detected in dog feces and glucose (Fig. 3b), and the plateau production was observed by day 37. When analyzing co-substrates, glucose was the most efficient in generating electricity, while saccharose behaved similarly to the control treatment. The different co-substrates function for the carbon enrichment of substrates in the MFC; consequently, they influence the growth of the microbial consortia involved in the current output; and the MFC efficiency. Borole *et al*., (2009) tested the use of glucose and lactate in combination with several factors to encourage biofilm of electrogenic microbes, but minimize the participation of non-electrogenic ones, to reach effective power production. In the present research, we did not know the type of microorganisms involved when using different substrates and co-substrates; however, molecular analysis will help elucidate this information, including the relationship between electrogenic/non-electrogenic microorganisms and power output and electricity production.

Results of the present research show that dog feces, referred to as environmental contaminants, are useful as feedstock and may provide the opportunity to produce energy and solve an aged environmental problem. Traditionally, dog feces have been mentioned as a source of pathogenic microorganisms and pollution to soil, water, and air. Recently, Pérez-Guevara *et al*. (2021) showed evidence that feces are also a source of contamination, transport, and dispersion of microplastics such as PET and polycarbonate. These authors highlight the possible ecological and environmental consequences of the association of microplastics to feces from dogs, other animals, and human beings. These potential concerns are: longer microplastic lifespan, an increase of microplastic bioavailability to organisms, feces as a route for microplastic dispersion, and microorganisms associated with plastic/feces. The findings from the present research open the opportunity to simultaneously analyze the electricity production and possible transformation of microplastics through MFC

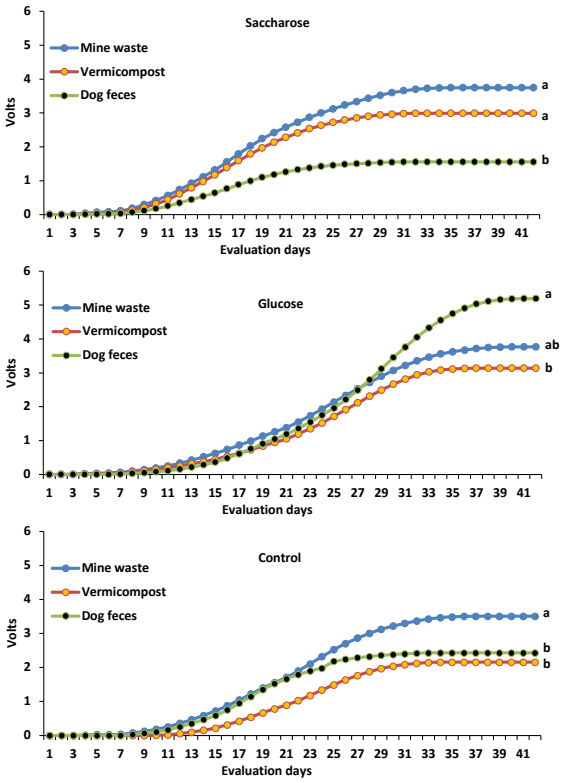

Figure 3. Cumulative voltage output in microbial fuel cells in one-operation cycle using three substrates and two donor electrons sources. Different lower letter shows statistical difference when comparing substrates in each donor electrons source (a) Saccharose, (b) glucose or (c) water.

This is a relevant and research issue to be urgently studied to give a solution to a dual environmental problem.

Although comparison of MFC devices on an equivalent basis is difficult (Logan *et al*., 2006), the power density obtained from the three substrates used in this research (Fig. 4) was detectable and comparable to some values observed in the literature. Gude (2016) reviewed the power outputs in lab-scale MFC using various wastewater sources as fuel in the anode. These authors mentioned that the power density for domestic waters was from 1.7 to 3.7 W m^{-3}, and for wastewater from hospital, it was from 8 to 14 W m^{-3}. Luo *et al*. (2010) obtained a power density from 2.1 to 3.3 W m^{-3}, within 18 hours and the operation period was up to 110 hours, in a batch-fed MFC (of an anode and a cathode, which were separated by a proton exchange membrane) using 250 mg L^{-1} of indole as the fuel. Zhang *et al*. (2009) obtained a maximum power density of 1.7 W m^{-3} from pyridine as a fuel in an MFC (two-chamber, separated by a proton exchange membrane and stocked with graphite).

In the present research, the cumulative power density by substrates is presented in Fig. 4. It was in the order dog feces > mine waste > vermicompost. By using MFC, the oxidation of OC from

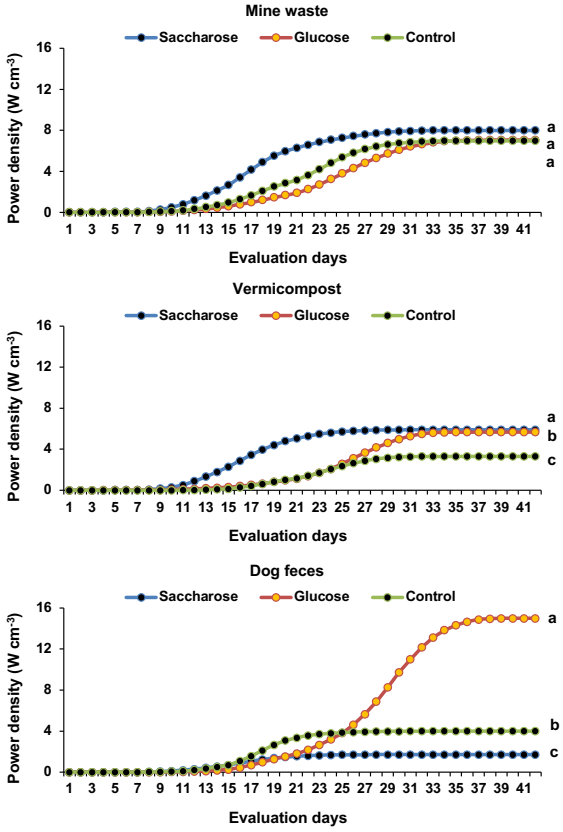

Figure 4. Cumulative power density output in microbial fuel cells in one operation cycle with the same substrate and different donor electrons sources. Different lower letters show statistical differences when comparing donor electrons in each substrate source. (a) Mine waste, (b) vermicompost, (c) dog feces.

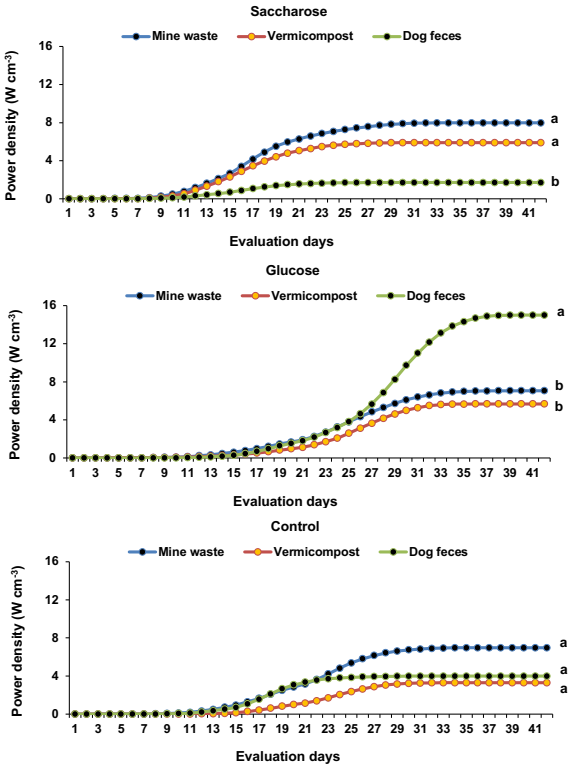

Figure 5. Cumulative power density output in microbial fuel cells in one operation cycle using three substrates and two donor electrons sources. Different lower letter show statistical difference when comparing substrates in each donor electrons source (a) saccharose, (b) glucose, (c) control.

dog feces and vermicompost was possible. Similarly, the oxidation of inorganic matter from mine wastes also produced electricity. However, the lower performance of MFC using vermicompost may be due to the higher recalcitrant OC of this source. Dunaj *et al*. (2012) observed 17 times lower performance of MFC using forest soil than agricultural. At the end of the experiment (42 days), the mine waste had a similar cumulative power density between the three co-substrates. The maximum power density was around 7.5 W cm^{-3} (Fig. 4a). Vermicompost (Fig. 4b) had the maximum accumulated power density with saccharose (5.8 W cm^{-3}), being different from this with glucose (5.5 W cm^{-3}) and this in the control (3.3 W cm^{-3}). The kinetics of cumulative power density for dog feces were different from those observed with mine waste or vermicompost (Fig. 4c). The maximum power density (15 W cm^{-3}) was nearly at the end of the experiment by glucose (day 40). In comparison, the lowest power density corresponded to saccharose as co-substrate (1.3 W cm^{-3}) and did not change from day 19 to 42. Douma *et al*. (2025) reported obtaining power densities of 0.352 W cm^{-3} by using cow dung as a feedstock for a single-chamber MFC.

When analyzing the effect of co-substrates on the production of power density (Fig. 5), the order of efficiency was glucose » saccharose > control treatments. Saccharose produced a power density between 1.8 and 7.9 W cm^{-3}. From day 15 to the end of the experiment propitiated a similar cumulative power density trend in the mine waste and vermicompost substrates used in the MFC (Fig. 5a). Glucose was the best promotor to produce the highest power density (5.6 to 15 W cm^{-3}) when compared to saccharose or control treatments, being dog feces the best substrate (Fig. 5b). Zhang *et al*. (2009) mentioned that higher power generation may be obtained when co-substrates are used. This is due to more electrons being generated in unit time due to the degradation of both contaminant and glucose. The maximum power density with no co-substrate was between 4 and 7 W cm^{-3} (Fig. 5c). Mine waste, even without any co-substrate, was able to produce a measurable power density at the end of the experiment without any co-substrate.

Luo *et al*. (2010) discussed that the combination of different substrates may result in differences in current output. For example, the combination of indole with glucose had stronger stimulation on bacterial activity in the electricity generation and recovered more electrons than those observed with glucose and

pyridine. In the present research, the combination of dog feces and glucose propitiates higher current output and power density. This result may be related to the greater coulombic numbers when there are fuel substrate combinations than individual components, as mentioned by Zhang *et al*. (2009). In this research, coulombic numbers were not quantified; however, these should be analyzed in a future investigation to gain an understanding of the mechanism involved that leads to increased bioelectricity.

The power density and efficiency depend on the anodic microbial catalyst. Moreover, power density provides a better measure of the MFC performance and maturity of biofilm (Borole *et al*., 2009). In this experiment, the native microorganisms from each substrate were involved in the efficiency of the electrochemical reactions in the MFC. Future research should elucidate and isolate these microorganisms involved in electricity generation to identify and select them based on their superior performance. Moreover, deeper research into the nutrient composition should be followed, as it also influences microbial activity. It is recognized that the type of microorganisms and the medium´s composition impact their electrochemical activity, as mentioned by Ríos-Guzman *et al*. (2024).

3.2 Electron microscopy analysis to visualize anode-microbial biofilms

Figs. 6-8 show general observations of the anode surface at the end of the experiment from the best treatments of each substrate. In the mine waste+saccharose, stronger colonization and a very diverse biofilm (Fig. 6e-h) were observed in comparison to the respective control treatment (Fig. 6a-d). The typical bacterial morphology and abundant actinomycetes are visualized. In dog feces, the control treatment has an abundant biofilm (Fig. 7); however, the microbial morphology is different from that observed in mine wastes. In comparison, in the anodes from dog feces+glucose (Fig. 7e-h), the biofilm looks more robust and more diverse than that observed in the control treatment (Fig. 7a-d). In the vermicompost-control treatment, in general, the biofilm formed is scarce (Fig. 8a-c), although a well-formed biofilm was observed (Fig. 8d). While in the vermicompost+saccharose treatment (Fig. 8e-h) the presence of bacteria, but peculiarly fungal structures were observed (Fig. 8f, g). Dunaj *et al*. (2012) referred to the assumption that MFCs with mixed microbes have high efficiency due to microbial interactions and *in situ* electrogenic production of intermediate metabolites. The molecular identification of these anode-microbes located is being investigated by our research group for a better understanding of biofilm composition. We hypothesize that higher bacterial activity and biomass

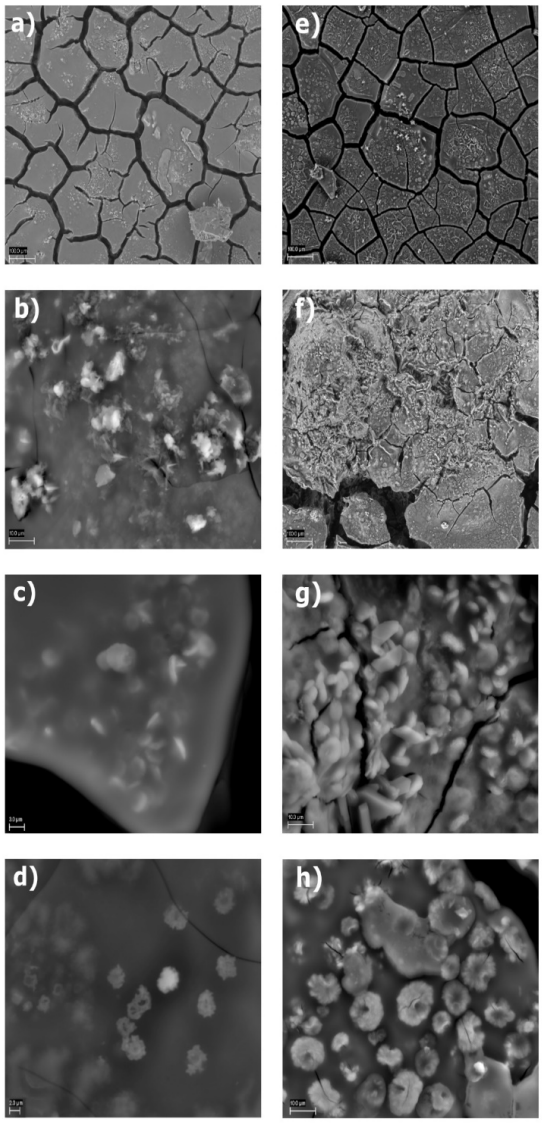

Figure 6. Scanning electron microscopy analysis of anode-surface from fuel microbial cell using mine waste as substrate. The control (a-d) and saccharose (e-h) as the best treatment producing power density are shown.

may be occurring in a diverse biofilm and then be more efficient in producing the higher power output. Dunaj *et al*. (2012) related the best MFC performance in agricultural soil (17 times more) than in forest soil to higher genomic DNA content in anodes (3-folds), which was used as a proxy for biomass. However, this hypothesis must be tested. The EDX analyses from the anode surfaces did not detect differences in elements observed (data not shown). The general elements identified were: P, S, K, and In. Interestingly, samples of anodes from mine waste treatments did not detect metals such as Pb, Cd, and others.

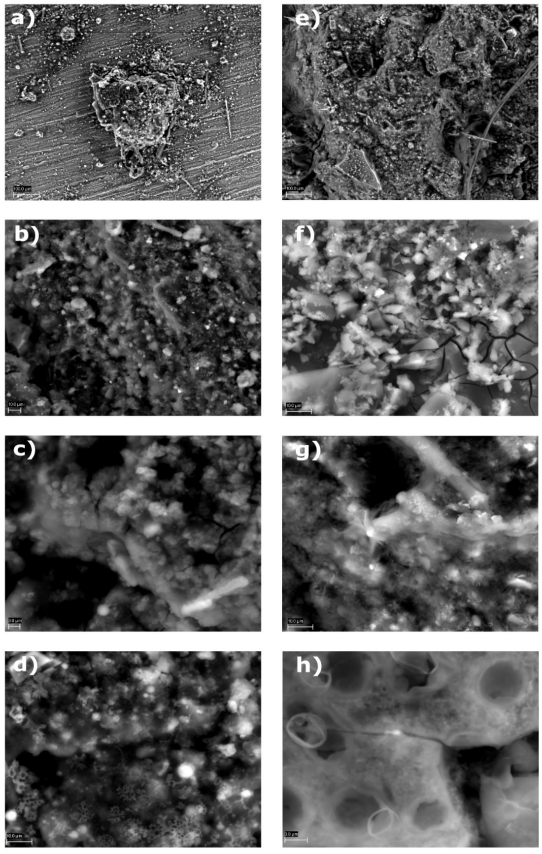

Figure 7. Morphological features observed in anodes of microbial fuel cells containing dog feces as substrate. The control (a-d) and glucose (e-h) as the best treatment producing power density are shown.

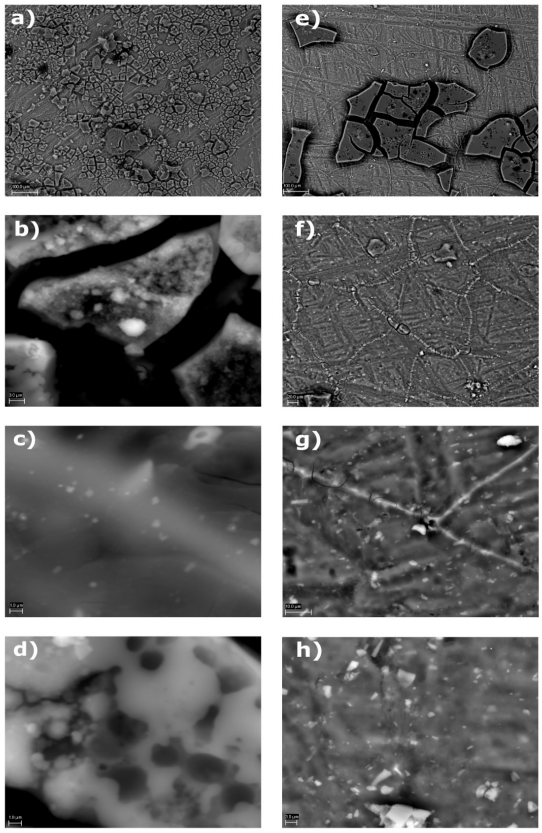

Figure 8. Scanning electron microscopy analysis of anode-surface from fuel microbial cell using vermicompost as substrate. The control (a-d) and saccharose (e-h) as the best treatment producing power density are shown.

3.3 Microbial electro-remediation of hazardous wastes

In the original mine waste, Zn, Pb, and Cd concentrations were high enough and are considered an environmental risk (Table 2). In dog feces, Pb and Cd were detected; which may be related to the dogs' diet and the environmental pollution to which they are exposed. The environmental impacts of feces will depend on how they are disposed of. In another scenario where the feces are not cleaned up, they emit Pb and Cd into the environment (Yavor *et al*., 2020). Hence, the treatment and valorization of these wastes through MFC are attractive. In the case of vermicompost, the concentration of Zn was higher than the average concentration of this element in non-contaminated soils. Concerning the potential redox of Pb (-0.126 V to 1.69 V), Cd (-0.4030 V to -0.943 V), Zn (-0.76 V to -1.47 V), Mn (-1.17 V to 1.70 V), and Fe (-0.44V to 0.771 V) (Bard, 1985), these metals may act as a source of electron donors. Therefore, mine waste was more efficient in producing electricity than vermicompost.

Reduction in the pseudo-total metal concentration in the substrates after the operation time of MFC was observed, and this is referred to as metal removal, which occurred at the anode chamber. In the mine waste, the original pseudo-total concentration of Fe and Cu decreased (16% and 12%, respectively) in the same magnitude as saccharose or glucose in relation to the concentration of these metals in the control treatment (6%). In the case of the concentration of Mn, no differences were found between treatments, and the reduction was 25% in relation to the original concentration. The Zn concentration decreased similarly in both the control and glucose treatments (68%), but with saccharose, a lower concentration was observed (78%). For Pb, the concentration did not change when using saccharose as a co-substrate, but decreased by 11% with glucose. Unexpectedly, in the control treatment (tap water) there was Pb solubilization (+13%) from the mine waste. The Cd concentration in the control treatment did not change from the original concentration in the mine waste, but the reduction was obtained by saccharose (31%) and glucose (19%). (Habibul *et al*., 2016) observed 44% Pb and 31% Cd removal from spiked soil treated within an MFC (double chamber air cathode separated by a proton exchange membrane and anode compartment filled with graphite granules). In accordance with this

information, in the present research, the Pb removal was lower, but a similar Cd removal was found. In the case of dog feces, relevant changes were observed. Cd concentration decreased by 46% in both the control and glucose treatments, but no modification was identified with saccharose. To explain the difference in these metal concentration changes after the incubation and electricity generation, microbial processes such as bioreduction, biosorption, bioaccumulation, and biomineralization may be suggested (Wu *et al*., 2017). The efficiency varies between metals and microbial cell composition since the standard electrode potential varies between metal ions (as referred earlier).

This wide response of differential metal concentration in the MFC makes it challenging to recover several metals from mine wastes and be successfully used in circular economy and electrochemical recycling methods, as mentioned by Pandit *et al*. (2021) and Petersen *et al*. (2021). The treatment of mine wastes and reduction of the initial Pb and Cd total concentrations by MFC represents an alternative technique to their direct disposal into the environment, which may be harmful to soil, water, air, and plants.

This primary treatment in MFC reduces the risk to ecosystems and human health by generating electricity while concurrently treating waste (Chandrasekaran *et al*., 2020). Although MFC has been proposed as an effective microbial electro-remediation method for heavy metals in groundwater, there are few reports supporting this on soil, sediments, or mine wastes. Some metallic inorganic pollutants treated in groundwater using microbial electro-remediation by MFC are Se, Cu, Cr (Pous *et al*., 2018), and Pb (Wang *et al*., 2021). Therefore, this is the first time MFC are tested for electro-remediation alternatives not only for mine wastes mainly polluted with Pb and Cd, but also for dog feces containing Cd as a contaminant. Unlike organic pollutants, heavy metals are not degraded. They are easily accumulated in different matrices. From this perspective, electrokinetic remediation is a technology that involves mobilizing metals using an electric potential generated by an external power source, resulting in excess energy costs. However, the electricity generated by MFC may achieve electrokinetic remediation effects without any additional energy cost (Wang *et al*., 2021).

Table 2. Original pseudototal metals concentration (mg kg^{-1}) in three substrates used and in the microbial cells with two electron acceptor-donor at the end of the experiment.

Treatments	Lead			Cadmium			Zinc			Copper			Manganese			Iron		
Treatments	Average	sd		Average	sd		Average	sd		Average	sd		Average	sd		Average	sd	
Mine waste																		
Original	1032	3	b	6	0.2	a	1332	33	a	386	5.9	a	245	6.7	a	128	1.3	a
Saccharose	1022	25	b	4	0.4	c	293	1	c	342	8.4	b	184	7.8	b	106	2.5	c
Glucose	914	24	c	5	0.4	bc	447	7	b	340	17.1	b	193	6.6	b	102	2.2	c
Control	1165	32	a	5	0	ab	420	11	b	385	10.4	a	191	3.4	b	119	2.2	b
SEMARNART†	22/260			37/450			400/800											
US-EPA††	400/1100			200														
†††	10-67			0.06-1			17-25			13-24			270-525			5,000-50,000		
Vermicompost																		
Original	Nd			nd			243	16	a	72	1.2	a	357	7.3	a	15	0.1	a
Saccharose	Nd			nd			198	6	b	60	1.9	c	301	14.9	b	14	0.1	a
Glucose	Nd			nd			116	5	c	41	1.5	d	220	8.2	c	14	0.0	a
Control	Nd			nd			191	10	b	66	0.1	b	302	5.9	b	15	0.3	a
Dog feces																		
Original	12	1	a	1.3	0	a	274	30	a	35	0.9	a	353	13.6	a	13	0.4	a
Saccharose	5	0.8	c	0.7	0.3	ab	266	21	a	32	3.4	a	352	22.9	a	11	0.9	bc
Glucose	6	1	bc	0.7	0.3	b	233	17	a	36	1.6	a	335	8.2	a	12	0.5	ab
Control	9	0.6	ab	1.0	0.3	b	177	14	b	32	2.9	a	252	17.4	b	10	0.5	c

Different letter shows statistical difference when comparing treatments in each substrate analyzed (n=3) by using Tukey test ($\alpha \leq 0.05$). sd=standard deviation (n=3), nd=under detection limits. †Maximum permissible limits in soils for agricultural and industrial use established by the Mexico´s environment ministry (The Secretariat of Environment and Natural Resources SEMARNAT, 2007). ††Limits of contaminants in soil and required intervention mentioned by United States Environmental Protection Agency (US-EPA, 2001). ††† Normal concentration in non-polluted soils according to Kabata-Pendias (2010)

Conclusions

MFC may be included in eco-friendly pet waste management to avoid contamination and dispersion pathways, and consequently, reduce human health impacts. The combination of glucose with the mine wastes produced a lower power density than glucose-dog feces, but, saccharose-mine wastes increased the power density produced by mine wastes (7.9 W cm^{-3}). In the absence of glucose or saccharose, the three substrates generated a power density in the range of 4 to 7 W cm^{-3}. This power density yield may still be functional in rural areas where mine wastes are abundantly disposed of. A lower concentration of Pb and Cd in the mine waste was observed in the MFC after 41 days of electricity production, but the response was co-substrate-dependent (glucose or saccharose). The highest removal of Zn, Pb, and Cd

was 78%, 31%, and 46%, respectively. Therefore, MFC represents a feasible alternative to electrochemically remediate mine wastes and, at the same time, produce electricity. These residues modify their energy and environmental value and occupy a place in the list of materials useful in waste-to-energy technology. MFC is a stand-alone power source, an electrochemical alternative, and more undesired residues should be tested under different conditions to increase the MFCs potential performance. Optimization concerning the analysis of power performance, system lifetimes, cost, and reliability is needed to afford clean energy, a healthier environment, and positive repercussions to social welfare.

References

Aelterman, P., Rabaey, K., Clauwaert, P. and Verstraete, W. (2006). Microbial fuel cells for wastewater treatment. *Water Science and Technology*, *54*(8), 9-15. https://doi.org/10.2166/wst.2006.702

Altin, N. and Uyar, B. (2025). Increasing power generation and energy efficiency with modified anodes in algae-supported microbial fuel cells. *Biomass Conversion and Biorefinery*. *15,*17203-17215. https://doi.org/10.1007/s13399-025-06536-2

Apollon, W., Rusyn, I., Paucar, N. E., Hibbert, M., Kamaraj, S. K. and Sato, C. (2025). Energy recovery from organic wastes using microbial fuel cells: Traditional and nonconventional organic substrates. *Resources 14*(3), 47. https://doi.org/10.3390/resources14030047

Aznar-Sánchez, J. A., García-Gómez, J. J., Velasco-Muñoz, J. F. and Carretero-Gómez, A. (2018). Mining waste and its sustainable management: Advances in worldwide research. *Minerals 8*(7), 284. https://doi.org/10.3390/min8070284

Bard, A. J. (1985). *Standard potentials in aqueous solutions*. Routledge, New York. https://doi.org/10.1201/9780203738764

Boloy, R. A. M., da Cunha Reis, A., Rios, E. M., de Araújo Santos Martins, J., Soares, L. O., de Sá Machado, V. A. and de Moraes, D. R. (2021). Waste-to-energy technologies towards circular economy: A systematic literature review and bibliometric analysis. *Water, Air, and Soil Pollution 232*(7), 306. https://doi.org/10.1007/s11270-021-05224-x

Borole, A. P., Hamilton, C. Y., Vishnivetskaya, T., Leak, D. and Andras, C. (2009). Improving power production in acetate-fed microbial fuel cells via enrichment of exoelectrogenic organisms in flow-through systems. *Biochemical Engineering Journal 48*(1), 71-80. https://doi.org/10.1016/j.bej.2009.08.008

Calderon, A. R. M., Alorro, R. D., Tadesse, B., Yoo, K. and Tabelin, C. B. (2020). Repurposing of nickeliferous pyrrhotite from mine tailings as magnetic adsorbent for the recovery of gold from chloride solution. *Resources, Conservation and Recycling 161*, 104971. https://doi.org/10.1016/j.resconrec.2020.104971

Chandrasekaran, U., Luo, X., Wang, Q. and Shu, K. (2020). Are there unidentified factors involved in the germination of nanoprimed seeds? *Frontiers in Plant Science 11,* https://doi.org/10.3389/fpls.2020.00832

Choudhury, P., Uday, U. S. P., Mahata, N., Nath Tiwari, O., Narayan Ray, R., Kanti Bandyopadhyay, T. and Bhunia, B. (2017). Performance improvement of microbial fuel cells for waste water treatment along with value addition: A review on past achievements and recent perspectives. *Renewable and Sustainable Energy Reviews 79*, 372-389. https://doi.org/10.1016/j.rser.2017.05.098

Chouler, J., Padgett, G. A., Cameron, P. J., Preuss, K., Titirici, M.-M., Ieropoulos, I. and Di Lorenzo, M. (2016). Towards effective small scale microbial fuel cells for energy generation from urine. *Electrochimica Acta 192*, 89-98. https://doi.org/10.1016/j.electacta.2016.01.112

Cui, W., Espley, S., Liang, W., Yin, S. and Dong, X. (2025). Microbial fuel cells for power generation by treating mine tailings: Recent advances and emerging trends. *Sustainability 17*(2), 466. https://doi.org/10.3390/su17020466

Damoah, E. and Herat, S. (2022). A review of sustainable management of mining waste. *International Journal of Environment and Waste Management 29*(3), 342. https://doi.org/10.1504/IJEWM.2022.122684

Douma, M. N. K., Ondel, O., Tsafack, P., Mieyeville, F. and Kengnou, N. A. (2025). Microbial fuel cell: Investigation of the electrical power production of cow dung and human faeces using 3D-printed reactors. *Bioresource Technology Reports 29*, 102036. https://doi.org/10.1016/j.biteb.2025.102036

Dróżdż, D., Malińska, K., Postawa, P., Stachowiak, T. and Nowak, D. (2022). End-of-life management

of biodegradable plastic dog poop bags through composting of green waste. *Materials 15*(8), 2869. https://doi.org/10.3390/ma15082869

Dunaj, S. J., Vallino, J. J., Hines, M. E., Gay, M., Kobyljanec, C. and Rooney-Varga, J. N. (2012). Relationships between soil organic matter, nutrients, bacterial community structure, and the performance of microbial fuel cells. *Environmental Science & Technology 46*(3), 1914-1922. https://doi.org/10.1021/es2032532

Elhenawy, S., Khraisheh, M., AlMomani, F., Al-Ghouti, M. and Hassan, M. K. (2022). From waste to watts: Updates on key applications of microbial fuel cells in wastewater treatment and energy production. *Sustainability 14*(2), 955. https://doi.org/10.3390/su14020955

Fiães, G. M. F., Rosa, A. P., Nascimento, L. A., Del Rei Passos, F. L. and Borges, A. C. (2025). Biodegradation of dog waste through anaerobic digestion at different temperatures. *Waste and Biomass Valorization 16*(4), 1973–1985. https://doi.org/10.1007/s12649-024-02761-4

Foudhaili, T., Rakotonimaro, T. V., Neculita, C. M., Coudert, L. and Lefebvre, O. (2019). Comparative efficiency of microbial fuel cells and electrocoagulation for the treatment of iron-rich acid mine drainage. *Journal of Environmental Chemical Engineering 7*(3), 103149. https://doi.org/10.1016/j.jece.2019.103149

Ghassemi, A. (2001). *Handbook of Pollution Control and Waste Minimization*. CRC Press. https://doi.org/10.1201/9780203907931

Gonzalez Olias, L., Cameron, P. J. and Di Lorenzo, M. (2019). Effect of electrode properties on the performance of a photosynthetic microbial fuel cell for atrazine detection. *Frontiers in Energy Research 7*. https://doi.org/10.3389/fenrg.2019.00105

Gude, V. G. (2016). Wastewater treatment in microbial fuel cells – an overview. *Journal of Cleaner Production 122*, 287-307. https://doi.org/10.1016/j.jclepro.2016.02.022

Habibul, N., Hu, Y. and Sheng, G.-P. (2016). Microbial fuel cell driving electrokinetic remediation of toxic metal contaminated soils. *Journal of Hazardous Materials*, *318*, 9–14. https://doi.org/10.1016/j.jhazmat.2016.06.041

IEA. (2025a). Electricity. Available at: https://www.iea.org/reports/electricity-2025.

IEA. (2025b). Growth in global electricity demand is set to accelerate in the coming years as power-hungry sectors expand. https://www.iea.org/news/growth-in-global-electricity-demand-is-set-to-accelerate-in-the-coming-years-as-power-hungry-sectors-expand

ISO 11466. (1995). *Soil quality. Extraction of trace elements soluble in aqua regia*. https://www.iso.org/standard/19418.html

Kabata-Pendias, A. (2010). *Trace elements in soils and plants*. CRC Press. Boca Raton. https://doi.org/10.1201/b10158

Lim, B. and Alorro, R. D. (2021). Technospheric mining of mine wastes: A review of applications and challenges. *Sustainable Chemistry 2*(4), 686-706. https://doi.org/10.3390/suschem2040038

Logan, B. E., Hamelers, B., Rozendal, R., Schröder, U., Keller, J., Freguia, S., Aelterman, P., Verstraete, W. and Rabaey, K. (2006). Microbial fuel cells: Methodology and technology. *Environmental Science & Technology 40*(17), 5181-5192. https://doi.org/10.1021/es0605016

Logan, B. E. and Rabaey, K. (2012). Conversion of wastes into bioelectricity and chemicals by using microbial electrochemical technologies. *Science 337*(6095), 686-690. https://doi.org/10.1126/science.1217412

Lorenzo-Tallafigo, J., Iglesias-González, N., Romero-García, A., Mazuelos, A., Ramírez del Amo, P., Romero, R. and Carranza, F. (2022). The reprocessing of hydrometallurgical sulphidic tailings by bioleaching: The extraction of metals and the use of biogenic liquors. *Minerals Engineering 176*, 107343. https://doi.org/10.1016/j.mineng.2021.107343

Luo, Y., Zhang, R., Liu, G., Li, J., Li, M. and Zhang, C. (2010). Electricity generation from indole and microbial community analysis in the microbial fuel cell. *Journal of Hazardous Materials 176*(1-3), 759-764. https://doi.org/10.1016/j.jhazmat.2009.11.100

Mathuriya, A.S. and Yakhmi, J. V. (2014). Microbial fuel cells to recover heavy metals. *Environmental Chemistry Letters* 12, 483-494. https://doi.org/10.1007/s10311-014-0474-2

Memon, M. F., Md Hasan, K. N. B. and Memon, Z. A. (2025). Sustainable energy generation from organic substrates using portable microbial fuel cells: Enhancing precision agriculture in rural regions of Malaysia. *Geological Journal*. https://doi.org/10.1002/gj.5199

Nandy, A., Kumar, V., Khamrai, M. and Kundu, P. P. (2015). MFC with vermicompost soil: power generation with additional importance of waste management. *RSC Advances 5*(51), 41300-41306. https://doi.org/10.1039/C5RA00870K

Nelson, D. and Sommers, L. E. (1983). Total carbon, organic carbon and organic matter. In *Methods of soil analysis: Part 2 chemical and microbiological properties* (2nd Edition, pp. 1-1159).

Pandit, S., Savla, N., Sonawane, J. M., Sani, A. M., Gupta, P. K., Mathuriya, A. S., Rai, A. K., Jadhav, D. A., Jung, S. P. and Prasad, R. (2021). Agricultural waste and wastewater as feedstock for bioelectricity generation using microbial fuel cells: Recent advances. *Fermentation 7*(3), 169. https://doi.org/10.3390/fermentation7030169

Penakalapati, G., Swarthout, J., Delahoy, M. J., McAliley, L., Wodnik, B., Levy, K. and Freeman, M. C. (2017). Exposure to animal feces and human health: A systematic review and proposed research priorities. *Environmental Science & Technology 51*(20), 11537-11552. https://doi.org/10.1021/acs.est.7b02811

Pérez-Guevara, F., Roy, P. D., Kutralam-Muniasamy, G. and Shruti, V. C. (2021). A central role for fecal matter in the transport of microplastics: An updated analysis of new findings and persisting questions. *Journal of Hazardous Materials Advances 4*, 100021. https://doi.org/10.1016/j.hazadv.2021.100021

Petersen, H. A., Myren, T. H. T., O'Sullivan, S. J. and Luca, O. R. (2021). Electrochemical methods for materials recycling. *Materials Advances 2*(4), 1113-1138. https://doi.org/10.1039/D0MA00689K

Pous, N., Balaguer, M. D., Colprim, J., and Puig, S. (2018). Opportunities for groundwater microbial electro-remediation. *Microbial Biotechnology 11*(1), 119-135. https://doi.org/10.1111/1751-7915.12866

Rabaey, K., Lissens, G., Siciliano, S. D. and Verstraete, W. (2003). A microbial fuel cell capable of converting glucose to electricity at high rate and efficiency. *Biotechnology Letters 25*(18), 1531-1535. https://doi.org/10.1023/A:1025484009367

Rajesh, S. and Kumawat, A. S. (2023). Opportunities for microbial fuel cells to utilize post-harvest agricultural residues. *Ionics*, *29*(11), 4417–4435. https://doi.org/10.1007/s11581-023-05175-9

Ray, A., Bhonsle, A. K., Singh, J., Trivedi, J. and Atray, N. (2025). Examining alternative carbon resources for sustainable energy generation: A comprehensive review. *Next Energy 6*, 100194. https://doi.org/10.1016/j.nxener.2024.100194

Rhoades, J. D. (1996). Salinity: Electrical conductivity and total dissolved solids. In: *Methods of Soil Analysis: Part 3. Chemical Methods*. Sparks D.L., Page, A.L., Helmke, R.J., Loeppert, R.H., Soltanpour, P. N., Tabatabai M.A., Johston, C. T., Summer, M. E. (eds.), Pp. 437-474. American Society of Agronomy.

Ríos-Guzmán, J.C., Alonso-Vargas, M., Cadena-Ramírez, A., Juárez López, K. and Portillo-Torres, L.A. (2024). Enhanced denitrification in *Paracoccus denitrificans* PD1222 by electrical field application. *Revista Mexicana de Ingeniería Química* 23(1):Bio24136. https://doi.org/10.24275/rmiq/Bio24136

Rowell, D. L. (1994). *Soil science: Methods and applications. Routledge, London.*

Saad, A., Ndiritu, H. and Hawi, M. (2025). Electricity generation from sewage wasterwater in a microbial fuel cell pilot power plant using aluminium cathodes. *Journal of Advance Research in Electrical & Electronics Engineering 10*(1), 1-9. https://doi.org/https://doi.org/10.53555/rae7bs08

SEMARNAT (2007). Norma Oficial Mexicana NOM-147.SEMARNAT-2004. Gobierno Federal. Mexico. Diario Oficial. 1–67. Mexico. Accessed June 21, 2023. https://www.profepa.gob.mx/innovaportal/file/1392/1/nom-147-semarnat_ssa1-2004.pdf

Silva-Palacios, F., Salvador-Salinas, A., Rojas-Flores, S., De La Cruz-Noriega, M., Nazario-Naveda, R., Gallozzo-Cardenas, M., Delfin-Narciso, D. and Díaz, F. (2023). En: Proceedings of the 5th International Conference on Clean Energy and Electrical Systems. Gaber, H. (eds), CEES 2023. Lecture Notes in Electrical Engineering 1058. Springer, Singapore. https://doi.org/10.1007/978-981-99-3888-9_24.

USEPA (2001). *Environmental Protection Agency. Risk Assessment Guidance for Superfund (RAGS) volume III: Part A*. Washington, DC: U.S. Environmental Protection Agency. https://www.epa.gov/risk/risk-assessment-guidance-superfund-rags-part

Wang, Y., Li, A. and Cui, C. (2021). Remediation of heavy metal-contaminated soils by electrokinetic technology: Mechanisms and applicability. *Chemosphere 265*, 129071. https://doi.org/10.1016/j.chemosphere.2020.129071

Wu, M. S., Xu, X., Zhao, Q. and Wang, Z. Y. (2017). Simultaneous removal of heavy metals and biodegradation of organic matter with sediment microbial fuel cells. *RSC Advances*, *7*(84), 53433-53438. https://doi.org/10.1039/C7RA11103G

Yavor, K. M., Lehmann, A. and Finkbeiner, M. (2020). Environmental impacts of a pet dog: An LCA case study. *Sustainability 12*(8), 3394. https://doi.org/10.3390/su12083394

Yousefi, R., Mardanpour, M. M. and Yaghmaei, S. (2021). Fabrication of the macro and micro-scale microbial fuel cells to monitor oxalate biodegradation in human urine. *Scientific Reports 11*(1), 14346. https://doi.org/10.1038/s41598-021-93844-y

Zhang, C., Li, M., Liu, G., Luo, H. and Zhang, R. (2009). Pyridine degradation in the microbial fuel cells. *Journal of Hazardous Materials 172*(1), 465-471. https://doi.org/10.1016/j.jhazmat.2009.07.027

Vol. 24, No. 3(2025) Bio25632
Revista Mexicana de Ingeniería Química

Kinetic and oxygen transfer assessment for Bikaverin production by *Gibberella fujikuroi*: Toward industrial scaling

Evaluación cinética y transferencia de oxígeno para la producción de bikaverina por *Gibberella fujikuroi:* Hacia el escalamiento industrial

D.B. Alanís-Gutiérrez[1], M.X. Negrete-Rodríguez[2], M.C. Chávez-Parga[3]*
[1,3]División de Estudios de Posgrado de la Facultad de Ingeniería Química, Universidad Michoacana de San Nicolás de Hidalgo, Santiago Tapia 403, Morelia Mich. 58000, México
[2]Tecnológico Nacional de México/Instituto Tecnológico de Celaya, García Cubas 600, Fovisste, Celaya, Gto., 38010, México
Sent date: July 16, 2025; Accepted: October 28, 2025

Abstract
Gibberella fujikuroi is a filamentous fungus that produces bikaverin, a pigment with pharmacological potential. Three strains (CDBB-H-972, CDBB-H-984 and CDBB-H-270) were evaluated in systems with forced aeration, analyzing the influence of pH and aeration rate. The CDBB-H-984 strain achieved the highest biomass concentration (15.73 ± 0.33 g/L at 48 h, pH 4, 0.5 vvm), while CDBB-H-972 presented the highest yield of bikaverin (0.134 ± 0.002 g bikaverin/g biomass at 96 h, pH 3, 0.75 vvm). The volumetric oxygen transfer coefficient (k_La) reached 169.90 ± 6.28 h^{-1} at 48 h and a maximum of 201.50 ± 2.42 h^{-1} at 72 h. The three-parameter Gompertz model described growth with high accuracy (R^2 = 0.999), while the Luedeking–Piret model confirmed that bikaverin is a metabolite not associated with growth. Bikaverin was purified and characterized by FT-IR, and morphology was evaluated by scanning electron microscopy. The Box–Behnken design indicated that the highest production of bikaverin was obtained with the CDBB-H-972 strain at pH 3 and an aeration rate of 1 vvm. Under these conditions, the oxygen consumption rate (OUR) exceeded the transfer rate (OTR), highlighting the need to increase aeration in larger-scale systems.
Keywords: Secondary metabolites, Bikaverin, Mass transfer, Biomass, Kinetic.

Resumen
Gibberella fujikuroi es un hongo filamentoso productor de bikaverina, un pigmento con potencial farmacológico. Se evaluaron tres cepas (CDBB-H-972, CDBB-H-984 y CDBB-H-270) en botellas con aireación forzada para estudiar la influencia del pH y la tasa de aireación. La cepa CDBB-H-984 alcanzó la mayor biomasa (15.73 ± 0.33 g/L a 48 h, pH 4, 0.5 vvm), mientras que CDBB-H-972 presentó el mayor rendimiento de bikaverina (0.134 ± 0.002 g/g biomasa a 96 h, pH 3, 0.75 vvm). El coeficiente volumétrico de transferencia de oxígeno (k_La) fue de 169.90 ± 6.28 h^{-1} a las 48 h y 201.50 ± 2.42 h^{-1} a las 72 h. El modelo de Gompertz de tres parámetros describió con precisión el crecimiento (R^2 = 0.999), y el modelo de Luedeking–Piret confirmó que la bikaverina es un metabolito no asociado al crecimiento. La bikaverina purificada se caracterizó por FT-IR, y la morfología se evaluó mediante microscopía electrónica de barrido. El diseño Box–Behnken indicó que la mayor producción es con la cepa CDBB-H-972 a pH 3 y 1 vvm. Bajo estas condiciones, la tasa de consumo de oxígeno (OUR) supera a la de transferencia (OTR), resaltando la necesidad de aumentar la aireación al escalar el proceso.
Palabras clave: Metabolitos secundarios, Bikaverina, Transferencia de masa, biomasa, Cinética.

*Corresponding author. *E-mail*: cparga@umich.mx;
https://doi.org/10.24275/rmiq/Bio25632
ISSN:1665-2738, *issn-e*: 2395-8472

1 Introduction

Bikaverin is a polyketide composed of 20 carbons, 14 hydrogens, and 8 oxygens. This compound exhibits a reddish pigment; therefore, its identification in submerged culture fermentation is immediate. In recent decades, several studies have reported its therapeutic properties, including antibiotic activity (Balan *et al*., 1970), antitumor activity (Hinojosa-Ventura *et al*., 2019), and neuroprotective activity (Nirmaladevi *et al.*, 2014).

Several authors have stated that bikaverin is widely found in fungal microorganisms of the genus *Gibberella fujikuroi*, which is known for producing secondary metabolites, primarily gibberellic acid (GA_3), including certain mycotoxins, including moniliformin, beauvericin, fusarins, fumonisins, fusaric acid, neurosporaxanthin, and bikaverin. However, the biosynthesis of bikaverin is strongly influenced by growth-related factors, such as the bioavailability of nutrients in the culture medium. Its production responds to nitrogen limitation and pH variations (Limón *et al*., 2010), as well as to a continuous air supply that promotes the biosynthesis of bikaverin (Giordano & Domenech, 1999).

Oxygen transfer often represents a major limitation in aerobic bioprocesses because of the inherently low solubility of oxygen in liquid media, making adequate aeration essential for fungal fermentations (Amaral *et al*., 2008). Industrial production of these secondary metabolites is typically carried out using mycelial cultures under submerged fermentation. Kinetic models describing fungal growth and secondary metabolite production, based on the physiological characteristics of the mycelium, have a significant influence on understanding, designing, and controlling industrial fermentation processes (Bailey & Ollis, 1977).

This study proposes the use of a fermentation system coupled with a forced-aeration mechanism to assess the influence of aeration rate (vvm) and pH on three different *G. fujikuroi* strains, applying the statistical criteria of a Box–Behnken experimental design and kinetic modeling of the fermentation process, with the aim of providing methodological bases to facilitate industrial scale-up of bikaverin production.

2 Materials and methods

2.1 Strains and inoculum preparation

In this study, *G. fujikuroi* strains CDBB-H-270, CDBB-H-972, and CDBB-H-984 (Colección de Cultivos del Departamento de Biotecnología y Bioingeniería, CINVESTAV-IPN, México) were used. The strains were maintained on Potato Dextrose Agar (Bioxon®) at 4 °C and subcultured monthly. The mycelium of *G. fujikuroi* was obtained from maintenance cultures grown on Potato Dextrose Agar (Bioxon®) incubated at 28 ± 1 °C for five days until full mycelial development. Subsequently, the fully developed mycelial material was recovered by adding 20 mL of sterile isotonic solution and homogenized using a sterilized serological pipette. The resulting homogenate was used as inoculum in 250 mL Erlenmeyer flasks containing 100 mL of liquid culture medium composed of dextrose (30 g/L) as the carbon source, NH_4NO_3 (1.2 g/L) as the nitrogen source, mineral salts KH_2PO_4 (5.09 g/L), $MgSO_4{\cdot}7H_2O$ (1.091 g/L), and trace elements (2 mL/L). Incubation was carried out on an orbital shaker using Erlenmeyer flasks (LabTech®) at 250 rpm and 28 ± 1 °C for 38 ± 2 h.

2.2 Culture medium and cultivation conditions

The maximum biomass formation and bikaverin production of the three *G. fujikuroi* strains were evaluated in a culture medium containing anhydrous dextrose (REPROQUIFIN®) as the carbon source, NH_4Cl (REPROFIQUIN®) as the nitrogen source, KH_2PO_4 (Golden Bell®) as the phosphate source, and a trace-element solution. Fermentations were conducted in GL45 Kimax® bottles equipped with a cylindrical stainless-steel diffuser (2 μm pore size). Each bottle was inoculated with 10 % (v/v) of a homogenized mycelial suspension (30 mL inoculum in 300 mL of medium) and incubated for 96 hours under orbital agitation at 100 rpm and 28 ± 1 °C.

The culture medium was freshly prepared prior to each fermentation experimental treatment, and all components were sterilized at 121 °C for 15 min in an autoclave (HMC EUROPE HV-50L©). The air supply was sterilized by passage through a 0.45 μm PVDF membrane prior to sparging. All glassware, tubing, and fittings were autoclaved before assembly, and the diffusers were disinfected with 70 % ethanol before each fermentation. These procedures ensured that aseptic conditions were maintained throughout the experimental process.

2.3 Experimental design (Box–Behnken)

A Box–Behnken response surface design was employed to simultaneously evaluate the effects of strain, pH, and aeration rate on biomass and bikaverin production (Table 1). The inclusion of the strain as a factor was based on the biosynthetic variability among *G. fujikuroi* isolates, which can influence their response to cultivation conditions. The coded values -1, 0, and 1 correspond to the low, medium, and high levels of each

Table 1. Parameters and levels used in the Box–Behnken experimental design.

Independent variables	Symbol	Coded levels		
		-1	0	1
Strain	C	CDBB-H-270	CDBB-H-972	CDBB-H-984
Aeration rate (vvm)	A	0.5	0.75	1
pH	pH	3	4	5

factor, respectively, as established in the experimental design.

The experimental setup followed a Box–Behnken design to assess the effects of pH, aeration rate, and fungal strain on bikaverin biosynthesis by *G. fujikuroi*. The experimental treatments were randomized using Minitab 19 ® software to minimize systematic errors and ensure statistical independence among treatments. Each treatment was performed in triplicate, and all data are reported as mean ± standard deviation.

The response variables were dry biomass (g/L) and bikaverin concentration (mg/L). The design included fifteen treatments with three replicates at the central point, randomized to minimize bias. The fitted quadratic model is expressed in Equation (1):

$$Y = \beta_0 + \beta_1 C_1 + \beta_2 pH_2 + \beta_3 A_3 + \beta_{11} C_1^2 + \beta_{22} pH_2^2 + \beta_{33} A_3^2 + \beta_{12} C_1 pH_2 + \beta_{13} C_1 A_3 + \beta_{23} pH_2 A_3 \quad (1)$$

where Y corresponds to the biomass or bikaverin concentration, C to the strain, A to the aeration rate (vvm), and pH to the coded pH values, the coefficients β represent the estimated regression parameters.

Statistical analysis was performed using Minitab 19® software through ANOVA ($\alpha = 0.05$). Based on the fitted models, response surface plots were constructed. The time course of biomass and bikaverin production was determined by measuring the samples at 0, 24, 48, 72, and 96 hours for each cultivation condition.

2.4 *Analysis of pH on biomass production*

To examine how variations in pH influence the growth behavior of *G. fujikuroi*, the experimental treatments corresponding to the three pH levels of the Box–Behnken design were analyzed using strain CDBB-H-972, selected for its intermediate and representative behavior compared to the other isolates. This approach allowed isolating the effect of pH as the variable of interest by reducing the variability attributable to genetic differences among strains and reinforcing its relevance under optimized cultivation conditions.

The medium pH was adjusted to 3, 4, and 5 using 1 N HCl or 1 N NaOH prior to inoculation. During cultivation, samples were taken at 0, 24, 48, 72, and 96 h. Aliquots of 1 mL were collected for pH measurement using a previously disinfected electrode (HANNA®) connected to a potentiometer (Thermo Fisher Scientific® Orion Star A2114). For biomass determination, 10 mL samples were taken, filtered under vacuum, and dried in an oven to constant weight. The statistical assessment of pH influence on biomass production involved a one-way ANOVA followed by Tukey's honestly significant difference (HSD) test at a confidence level of 95%.

2.5 *Analysis of aeration rate on* bikaverin production

To elucidate the relationship between aeration and bikaverin productivity in *G. fujikuroi*, experimental treatment 12 from the Box–Behnken design was selected, corresponding to the condition that yielded the highest pigment concentration. In this experimental treatment, the dynamic method described by Doran (2013) was applied, a widely used approach for estimating the volumetric oxygen transfer coefficient (k_La) and the oxygen transfer rate (OTR).

The dissolved oxygen (DO) concentration was measured using a digital probe (Smart Sensor AR8406®), which records data at 10-second intervals corresponding to the sensor's response time. A minimum of 30 data points per curve was obtained to ensure adequate statistical fitting. The OTR was defined according to Equation (2):

$$OTR = k_La\left(C^*_{0_2} - C_{O_2}\right) \quad (2)$$

where OTR is the oxygen transfer rate in the system ($mg\ O_2/Lh$), k_La is the mass transfer coefficient (h^{-1}), $C^*_{0_2}$ is the oxygen concentration at the gas–liquid interface (mg / L); and C_{O_2} is the oxygen concentration within the liquid phase (mg / L).

The oxygen uptake rate (OUR) was calculated according to Equation (3):

$$OUR = Q_{O_2}X \quad (3)$$

where OUR is the oxygen consumption by the microorganism ($mg\ O_2/Lh$), Q_{O_2} is the specific oxygen consumption rate per unit of biomass and time ($mg\ O_2/Lh$) and X is the biomass concentration (g/L). It is essential to note that the term aeration rate (vvm) refers to the supplied airflow, distinguishing it from the agitation speed (rpm) to avoid conceptual ambiguities.

2.6 Biomass production kinetics

The growth dynamics of *G. fujikuroi* were evaluated under the optimal pH and aeration rate conditions determined by the Box–Behnken design. To describe microbial growth, three kinetic models were used: the two-parameter Gompertz model, the modified three-parameter Gompertz model, and the Logistic model. The specific growth rate $\left(\mu,\ h^{-1}\right)$ was calculated from the slope of biomass values in 24-hour intervals according to Equation (4):

$$\mu = \frac{\ln\left(\frac{X_2}{X_1}\right)}{t_2 - t_1} \tag{4}$$

In this expression, X_1 and X_2 denote biomass concentrations (g/L) measured at times t_1 and t_2 (s) respectively. Generally, microbial growth models can be formulated with or without coupling to substrate consumption and usually include two or three adjustable parameters. The mathematical models considered here, which are independent of substrate consumption, are presented in Equations (5) – (7).

$$\frac{dX}{dt} = kXe^{-\mu t} \tag{5}$$

$$\frac{dX}{dt} = kXe^{-\mu t} - aX \tag{6}$$

$$\frac{dX}{dt} = kX - aX^2 \tag{7}$$

where X is the generated biomass (g/L), a and k are kinetic constants. Equation (5) corresponds to the two-parameter Gompertz model, Equation (6) to the three-parameter Gompertz model, and Equation (7) describes the Logistic model. Equations (5) – (7) were integrated using Python programming language.

Model comparison was performed using an F-test under the assumption that the three-parameter model predicts biomass precisely at each time point, as shown in Equation (8):

$$f = \frac{\frac{(RSS_2 - RSS_1)}{(DF_2 - DF_1)}}{\frac{RSS_1}{DF_1}} \tag{8}$$

where RSS_2 is the residual sum of squares of the Logistic model, RSS_1 is the residual sum of squares of the Gompertz model, DF_1 is the number of degrees of freedom of the Logistic model, and DF_2 is the number of degrees of freedom of the Gompertz model. The calculated f value was compared with the corresponding value from the F distribution table. Likewise, a comparison was made between the three-parameter Gompertz and Logistic models. If f is lower than F, no additional parameter is required; if f exceeds F, a different model must be selected. This analysis is an approximation due to the comparison of nonlinear models for model discrimination (Zwietering *et al.*, 1990).

2.6.1 Product formation kinetics

Bikaverin synthesis was evaluated using the Luedeking–Piret model, which describes product formation as the sum of a growth-associated and a non-growth-associated fraction, as defined in Equation (9):

$$\frac{dP}{dt} = \alpha\frac{dX}{dt} + \beta X \tag{9}$$

where P is the product concentration (g/L), X is the biomass concentration (g/L), α is the growth-associated formation coefficient, and β is the non-growth-associated formation coefficient. Thus, high α values indicate that bikaverin production depends mainly on cell growth, whereas high β values reflect a synthesis that is independent of growth.

2.7 Analytical determinations

Every 24 h, over a period of 96 h, subsamples of 11 mL were taken from the culture. From this volume, 10 mL were used for dry biomass determination by vacuum filtration using 0.45 μm membranes (Advantec®), followed by oven drying at 95 °C until constant weight was achieved. From the obtained filtrate, 1 mL was used for the analytical determination of medium components. Total reducing sugars (TRS) were quantified using the DNS method (Miller, 1959), and ammoniacal nitrogen was determined using the Berthelot method (Solórzano, 1969). Absorbance readings were performed on a UV–Vis spectrophotometer (Evolution 350, Thermo Fisher Scientific®).

The remaining 1 mL of each subsample was used to monitor mycelial growth by optical microscopy, allowing for the recording of morphological changes throughout the cultivation process.

2.8 Extraction and analysis of bikaverin production

An aliquot of the crude bikaverin extract was subjected to liquid–liquid partitioning with chloroform. Subsequently, separation was performed by glass column chromatography (36 cm height × 1.5 cm internal diameter), using silica gel 60 impregnated with oxalic acid (95:05, w/w) as the stationary phase. The mobile phase consisted of a mixture of chloroform:methanol:acetic acid (94:1:5, v/v/v). The collected fractions were monitored by normal-phase thin-layer chromatography (TLC) by comparing the obtained spots with a bikaverin standard (Sigma-Aldrich®). The positive fractions were concentrated and subsequently precipitated with methanol at –70 °C for 24 h, yielding pure bikaverin in crystalline form.

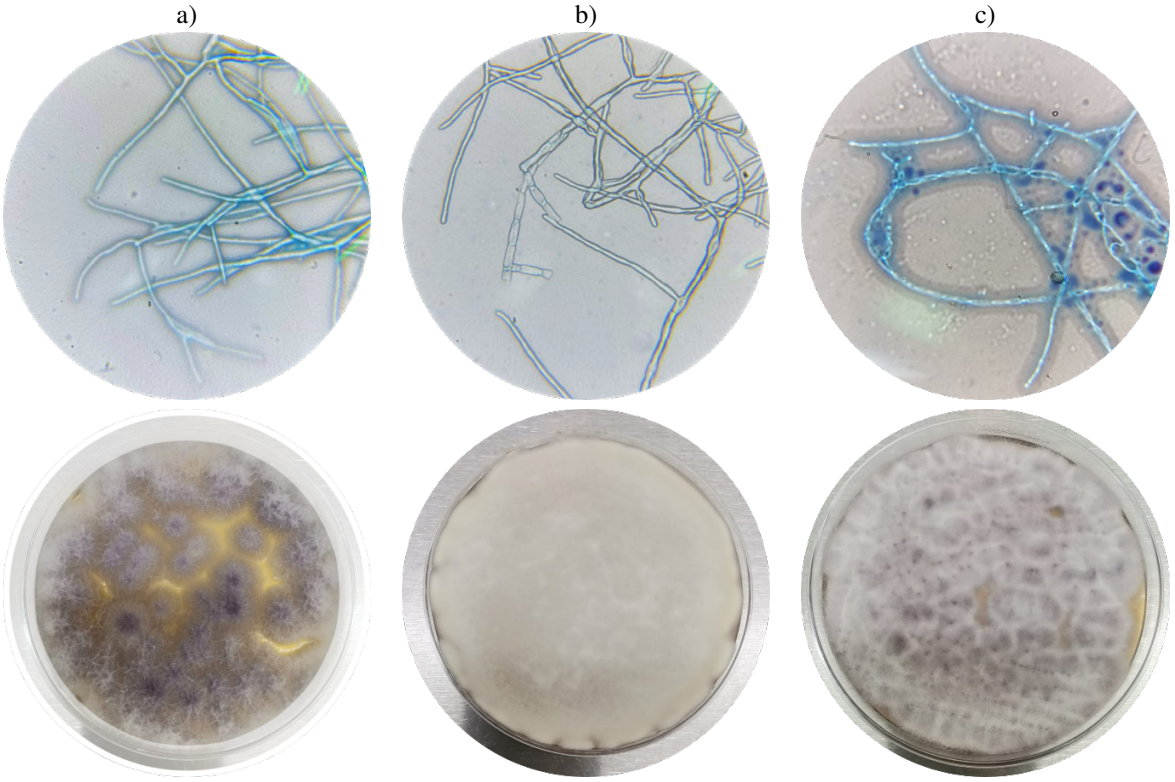

Figure 1. *G. fujikuroi* strains cultivated in liquid and solid media, stained with lactophenol blue. Submerged mycelium of strains a) CDBB-H-984, b) CDBB-H-972, and c) CDBB-H-270 grown in liquid medium and observed under an optical microscope at 100× magnification using an oil-immersion objective; the lower panels show the corresponding aerial mycelium of each strain grown on solid surfaces.

2.8.1 Structural and morphological characterization

The structural characterization of bikaverin was carried out by Fourier-transform infrared spectroscopy (FTIR) using a Spectrum 400 spectrometer (Perkin-Elmer®). Spectra were obtained in the range of 4000–800 cm^{-1} with a spectral resolution of 4 cm^{-1}, employing the MIR mode and four scans per sample.

For the morphological study, subsamples corresponding to different cultivation times were analyzed. Fresh material was observed using microscopy (LABOMED®) without staining, using a 100× objective lens. Additionally, the dehydrated material was examined by using scanning electron microscopy (SEM) with a JEOL JSM-7600F® instrument (Institute of Metallurgy and Materials, UMSNH).

3 Results and discussion

3.1 Strains

After five days of incubation at 28 ± 1 °C, a fully developed mycelium was observed in the three *G. fujikuroi* strains (Figure 1). In the optical micrographs (100×, stained with lactophenol blue), characteristic fungal structures such as conidia and chlamydospores were distinguished.

The CDBB-H-270 strain exhibited thicker hyphae and a more intense staining, associated with an advanced maturation state. In contrast, strains CDBB-H-972 and CDBB-H-984 showed thinner hyphae and cell walls with less pronounced thickening, characteristics of an actively growing mycelium. On solid medium, strain CDBB-H-984 displayed a more pronounced reddish pigmentation associated with bikaverin production, whereas CDBB-H-972 presented a predominantly white mycelium, and CDBB-H-270 exhibited a rough surface growth with lower homogeneity.

These morphological differences reflect the physiological variability among isolates, a phenomenon widely reported in species of the *Fusarium* genus, where genetic diversity has been documented to manifest in morphological changes, growth rate, and secondary metabolite production (Leslie & Summerell, 2006; Anama *et al*., 2021; Martínez-Moreno *et al*., 2021). However, these differences do not always correlate with productivity in submerged culture, as observed in this study with strain CDBB-H-270, which showed lower biomass and pigment yields. Overall, the observed variability justifies the inclusion of the strain as a factor in a comprehensive analysis such as the

Table 2. Bikaverin production (mg/L) by three *G. fujikuroi* strains under each experimental condition defined by the Box–Behnken response surface design. Values represent the mean ± standard deviation (n = 2).

Experimental treatment	Strain	Aeration rate (vvm)	pH	Bikaverin production (mg/L) 96 hours
1	972	0.75	4	331.25 ± 0.18
2	270	1.00	4	30.57 ± 0.77
3	270	0.75	5	86.75 ± 1.39
4	984	1.00	4	30.07 ± 0.92
5	972	0.50	3	483.58 ± 2.28
6	984	0.75	3	80.07 ± 6.30
7	270	0.75	3	88.65 ± 3.98
8	984	0.50	4	33.98 ± 1.61
9	972	0.75	4	345.45 ± 0.86
10	270	0.50	4	83.68 ± 2.56
11	984	0.75	5	73.53 ± 4.67
12	972	1.00	3	930.44 ± 6.95
13	972	1.00	5	40.59 ± 3.49
14	972	0.50	5	77.81 ± 5.85
15	972	0.75	4	339.90 ± 1.66

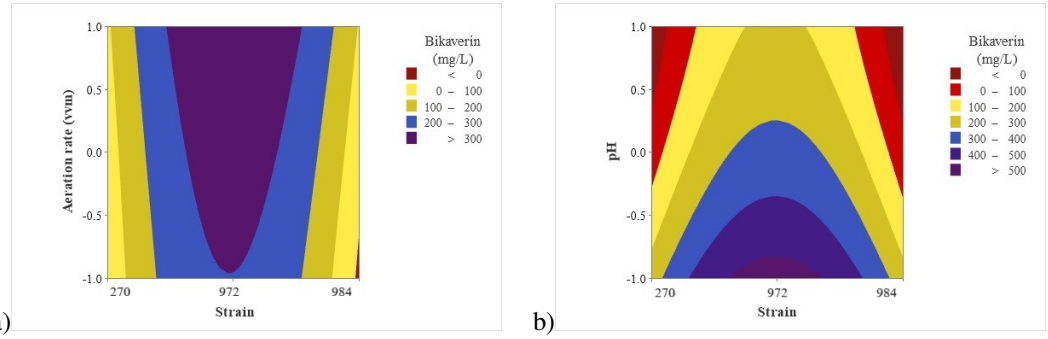

Figure 2. Response surface contour plots for bikaverin production: (a) strain × aeration interaction (pH fixed at 0; pH = 4); (b) strain × pH interaction (aeration fixed at 0; aeration = 0.75 vvm).

Box–Behnken design, reinforcing the influence of genetic factors on biomass and bikaverin production (Limón *et al*., 2010).

3.2 *Analysis of the Box–Behnken response surface design*

The Box–Behnken experimental design allowed the simultaneous evaluation of the effects of strain, pH, and aeration rate on bikaverin production. Fifteen experimental treatments were carried out according to the planned matrix (see Table 2). Under all experimental conditions, the highest bikaverin production was observed at 96 h of cultivation; therefore, this point was selected to fit the response surface model.

According to the Box–Behnken design results (Table 2), bikaverin production was markedly influenced by the strain factor, with *G. fujikuroi* CDBB-H-972 showing the highest pigment yields compared with isolates CDBB-H-270 and CDBB-H-984. The maximum concentration (930.44 ± 6.95 mg/L) was obtained with this strain at an aeration rate of 1.0 vvm and an initial pH of 3, suggesting that moderate aeration combined with acidic conditions favors secondary metabolite biosynthesis.

In contrast, the other isolates exhibited significantly lower production under similar conditions (< 100 mg/L), confirming the strain-dependent variability commonly reported for *G. fujikuroi* and other bikaverin-producing fungi. Aeration and pH also showed interactive effects, where higher oxygen transfer (1.0 vvm) at neutral to slightly acidic pH promoted growth but did not necessarily enhance pigment accumulation, consistent with the non-growth-associated nature of bikaverin synthesis.

The response surface plots (Figure 2) show that strain CDBB-H-972 is the most favorable for bikaverin production. In the strain × aeration interaction (Figure 2a), the highest pigment concentration was obtained with strain CDBB-H-972 even at low aeration rates (≥ 0.75 vvm).

Table 3. Analysis of variance (ANOVA) of the response surface model for biomass formation. F: Fisher's test; P: significance test. Significance levels: $\alpha = 0.05$ and $\alpha = 0.1$.

Source	DF	Adjusted SS	Adjusted MS	*F-value*	*p-value*
Model	9	631794	70199	1.50	0.342
Linear	3	228762	76254	1.63	0.296
Strain	1	648	648	0.01	0.911
Aeration rate	1	15543	15543	0.33	0.590
pH	1	212572	212572	4.53	**0.087**
Quadratic	3	343838	114613	2.44	0.179
Strain*Strain	1	326953	326953	6.97	**0.046**
Aeration rate*Aeration rate	1	40	40	0.00	0.978
pH*pH	1	6194	6194	0.13	0.731

In contrast, strains CDBB-H-270 and CDBB-H-984 did not reach high production levels under any aeration conditions. In the strain × pH interaction (Figure 2b), the optimum was observed with strain CDBB-H-972 at an approximate pH of 3, where bikaverin values above 400 mg/L were achieved; as the pH increased toward more neutral values (pH = 5), production decreased significantly.

Experimental treatment 12 (strain CDBB-H-972, pH 3, aeration 1.0 vvm) showed the highest concentration observed in this study (930.44 mg/L), confirming that this combination of conditions is favorable for maximizing pigment synthesis. This finding is consistent with optimizations reported in other polyketide-producing fungi, such as *Fusarium oxysporum*, where response surface methodology was used to optimize bikaverin production in flasks (Santos *et al.,* 2020). Furthermore, the ability of *G. fujikuroi* to modulate secondary metabolite biosynthesis under environmental variations has been recently documented, for example, in studies addressing nitrogen availability and its effect on the simultaneous production of bikaverin and gibberellins (Giordano, 1999).

The relevance of the strain factor is consistent with the notion that intrinsic physiological variability among isolates may exert a greater influence than minor operational factors, a phenomenon highlighted in recent works on the regulation of polyketide pigments in fungi (Lu *et al*., 2025). The analysis of variance (ANOVA) of the fitted model (Table 3) revealed that the linear pH term was statistically significant at a level of $\alpha = 0.05$ (*p-value* = 0.087, close to the threshold), indicating that pH variation affects bikaverin production. Moreover, the quadratic term associated with the strain (strain²) was significant (*p-value* = 0.046) when a significance level of $\alpha = 0.1$ was considered, suggesting that the effect of the strain is not linear and that there is an optimal response dependent on its intrinsic condition.

The analysis of variance (Table 3) indicates that the response surface model explained the observed variation in bikaverin production, although not all factors were significant at the $\alpha = 0.05$ level. The pH showed a near-significant effect ($p = 0.087$), confirming its critical influence on pigment biosynthesis. Likewise, the quadratic term associated with the strain was significant ($p = 0.046$), demonstrating that the variability among isolates does not follow a strict linear pattern but rather presents an optimum linked to the strain's physiology. In contrast, aeration did not show a statistically significant effect under the conditions evaluated ($p = 0.590$). However, graphical results suggest that an airflow higher than 0.5 vvm is required to maintain adequate pigment levels.

In summary, the results of the Box–Behnken design indicate that strain CDBB-H-972 and acidic conditions favor bikaverin production, justifying a more detailed analysis of the individual effects of pH and aeration, which is developed in the following sections.

3.3 Effect of pH on biomass production

Figure 3 shows the biomass generation in the *G. fujikuroi* CDBB-H-972 strain grown at three initial pH values (3, 4, and 5). It was observed that treatment at pH 5 promoted greater biomass accumulation compared to pH 3 and pH 4, which presented similar values.

The statistical analysis confirmed that pH had a significant effect on the final biomass at 96 hours of fermentation (ANOVA, F (2,3) = 31.93, p = 0.010). Tukey's multiple comparison test showed that pH 5 resulted in significantly higher biomass (12.66 ± 0.11 g/L) than pH 3 (8.65 ± 0.77 g/L) and pH 4 (8.08 ± 0.75 g/L), whereas no significant differences were found between pH 3 and pH 4 (Table 4).

These results suggest that a less acidic medium (pH = 5) favors biomass accumulation in *G. fujikuroi*. However, bikaverin synthesis is more closely associated with acidic values, since the bik genes responsible for its biosynthesis are only expressed under such conditions (Medentsev *et al*., 2005; Wiemann *et al*., 2009). Previous studies have shown that the progressive decrease in pH favors the bikaverin metabolic pathway: Giordano and Domenech (1999) reported that in

Table 4. Effect of pH on the biomass of *G. fujikuroi* CDBB-H-972 at 96 h. Values correspond to the mean ± standard deviation (n = 2). Significant differences between means were identified using Tukey's test (different letters indicate significant difference, $\alpha = 0.05$).

Source	DF	Adjusted SS	Adjusted MS	*F-value*	*p-value*
pH	2	24.841	12.421	31.930	0.010
Error	3	1.1670	0.389	-----	
Total	5	26.008	------	-----	
pH	Mean Biomass (g/L) ± DE		Tukey group		
3	8.65 ± 0.77		**a**		
4	8.08 ± 0.75		**a**		
5	12.66 ± 0.11		**b**		

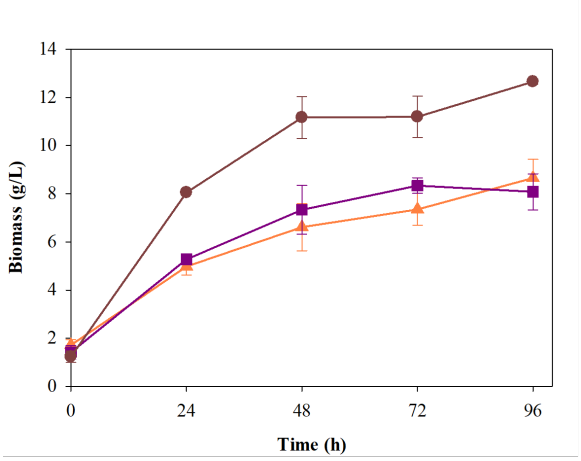

Figure 3. Effect of initial pH on biomass generation (g/L) of *G. fujikuroi* CDBB-H-972 during 96 hours of fermentation. Data represents mean values ± standard deviation (n = 2 biological replicates). [pH = 3 ▲, 0.5 vvm; pH = 4 ■, 0.75 vvm; pH = 5 ●, 1.00 vvm].

F. fujikuroi, an initial pH of 4.5 that decreased to 3.7 during fermentation promoted maximum pigment production. Similarly, Santiago (2013) described that in *Fusarium decemcellulare*, maximum pigmentation occurred between 48 and 72 hours, an interval consistent with the observations in this study.

Overall, these results confirm the dual role of pH in *G. fujikuroi*: neutral or slightly acidic values (pH 5) favor mycelial growth, whereas more acidic conditions (pH 3 – 4) are critical for the activation of bikaverin biosynthetic pathways.

In summary, the obtained results demonstrate that the initial pH is a crucial factor in determining biomass accumulation in *G. fujikuroi*, as it promotes mycelial growth under less acidic conditions. However, it does not necessarily promote pigment synthesis. Considering that bikaverin production depends not only on the physiological state of the fungus but also on the availability of dissolved oxygen in the medium, it becomes essential to evaluate the effect of aeration as a critical variable in the bioprocess. The following section presents the results of oxygen transfer analysis and its relationship with bikaverin accumulation, based on the experiments from the Box–Behnken design.

3.4 *Effect of aeration rate on bikaverin production*

Figure 4 shows the dissolved oxygen profiles during the fermentation of *G. fujikuroi* CDBB-H-972 at different cultivation times (0, 24, 48, 72, and 96 h), while Table 5 summarizes the calculated oxygen transfer and consumption parameters. At 0 h, the k_La value was 59.08 ± 4.75 h^{-1}, with a specific oxygen consumption rate (QO_2) of 79.02 ± 2.56 mg O_2/g*h and an OUR of 100.66 ± 2.87 mg O_2/g*h, reflecting a system not yet limited by oxygen due to the low biomass present.

At 24 h, the k_La increased to 79.55 ± 1.60 h^{-1}; however, the OUR (514.43 ± 41.07 mg O_2/L*h) exceeded the OTR (467.50 ± 42.92 mg O_2/L*h), indicating an imbalance between cellular demand and transfer capacity. This behavior intensified at 48 h, when a k_La of 169.90 ± 6.28 h^{-1} and an OUR of 1039.49 ± 25.59 mg O_2/L*h was recorded, confirming that the system was under oxygen-limiting conditions, coinciding with the phase of highest metabolic activity. Subsequently, at 72 h, the maximum k_La value (201.50 ± 4.22 h^{-1}) was reached, and the OUR also remained high (1287.94 ± 13.97 mg O_2/L*h).

Table 5. Correlation results of k_La, QO_2, OTR, OUR, and bikaverin production from the initial time (0 h) to 96 h of fermentation, during the fermentation of *G. fujikuroi* CDBB-H-972, pH = 3.

Time (h)	k_La (h^{-1})	Q_{O_2} (mg O_2)/(g*h)	OTR (mg O_2)/(L*h)	OUR (mg O_2/L*h)	Bikaverin (mg/L)	R^2
0	59.08 ± 4.75	79.02 ± 2.56	87.19 ± 0.41	100.66 ± 2.87	5.93 ± 1.09	0.867
24	79.55 ± 1.60	99.90 ± 1.15	467.50 ± 42.92	514.43 ± 41.07	30.69 ± 11.76	0.946
48	169.90 ± 6.28	135.56 ± 2.78	1003.95 ± 26.32	1039.49 ± 25.59	43.71 ± 15.74	0.944
72	201.50 ± 2.42	154.05 ± 1.99	1262.05 ± 14.01	1287.94 ± 13.97	180.81 ± 24.21	0.873
96	112.88 ± 2.03	85.12 ± 17.66	662.19 ± 12.08	690.37 ± 11.55	931.77 ± 22.13	0.935

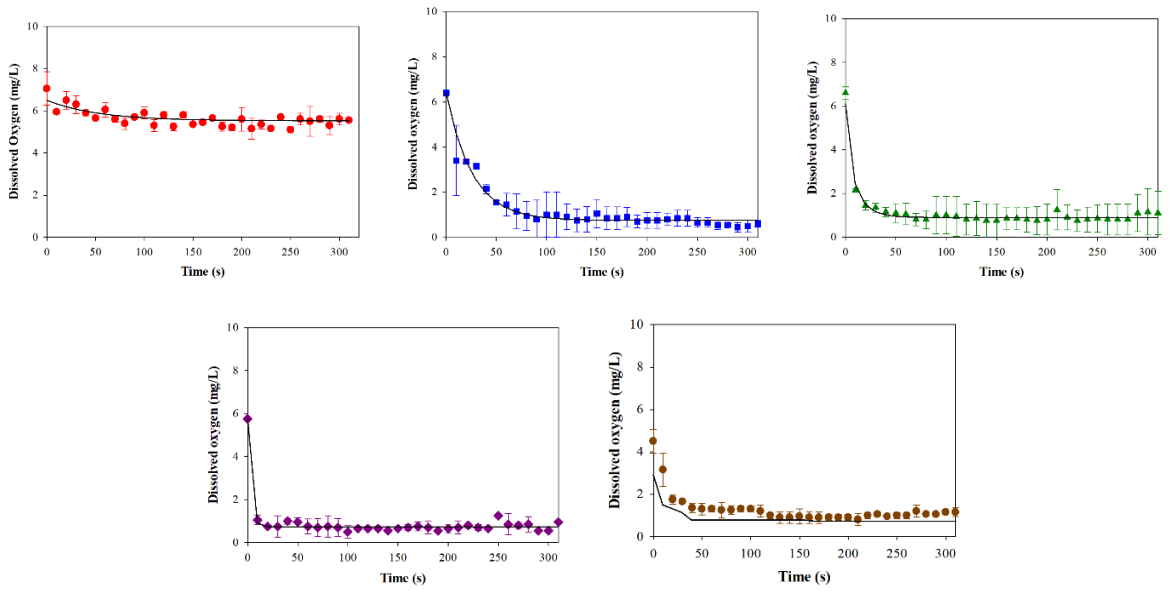

Figure 4. Dissolved oxygen (DO) profiles during the fermentation of *G. fujikuroi* CDBB-H-972, pH = 3 at different sampling times: 0 h (●), 24 h (■), 48 h (▲), 72 h (♦), and 96 h (⬟). The curves represent the fit obtained using the dynamic method for the calculation of k_La. A progressive decrease in dissolved oxygen concentration is observed as the culture proceeds, indicating that metabolic demand exceeds the transfer capacity during intermediate stages (24 - 48 h), generating oxygen-limiting conditions associated with bikaverin production.

However, bikaverin accumulation increased significantly (180.81 ± 24.21 mg/L), suggesting that oxygen limitation may have acted as a stimulus for the biosynthesis of this secondary metabolite. Finally, at 96 h, although the k_La decreased to 112.88 ± 2.03 h^{-1} and the OUR was reduced to 690.37 ± 11.55 mg O_2/L*h, bikaverin production reached its maximum (931.77 ± 22.13 mg/L). This suggests that pigment synthesis occurs preferentially under conditions of lower respiratory demand, a typical feature of intracellular metabolite accumulation (Giordano & Domenech, 1999; Wiemann *et al.,* 2009).

Overall, the results confirm that the OTR/OUR dynamics play a determining role in the fermentation process and that progressive oxygen limitation is a key factor in the induction of the bikaverin biosynthetic pathway.

In this study, it was observed that the relationship between the oxygen uptake rate (OUR) and the oxygen transfer rate (OTR) was strongly associated with bikaverin production. During the first 48 h, the OUR exceeded the OTR, indicating that the limiting conditions coincided with high metabolic activity. Subsequently, at 72–96 h, although k_La values fluctuated, bikaverin production increased significantly, supporting the hypothesis that oxygen limitation can act as a stimulus for secondary metabolite synthesis (Giordano & Domenech, 1999; Wiemann *et al.,* 2009).

Consistently, Chávez-Parga *et al.* (2014) reported that increasing aeration and agitation enhanced k_La values in an STR bioreactor, achieving favorable conditions for bikaverin production, although with a critical balance between oxygenation and mechanical stress on the mycelium. These findings align with recent reviews that recognize oxygen transfer as a primary challenge in the large-scale production of filamentous fungi, having a dual effect: promoting initial growth but inducing secondary pathways under limitation (Spraker *et al.*, 2018; Machado *et al.*, 2022). In this context, the results suggest that aeration strategies should not only aim to maximize k_La but also allow controlled limitation periods that favor intracellular bikaverin accumulation.

Comparable results have been recently reported in non-conventional biosaccharification and fermentation processes, where the selection of native strains and operational conditions were key to maximizing productivity (Garza-Garza *et al.*, 2025). This reinforces the importance of considering critical operational variables such as aeration and pH in the optimization of fungal bioprocesses. From a bioprocess perspective, the results obtained under forced aeration highlight the potential for process scale-up to industrial systems. The higher oxygen transfer coefficients (k_La) and bikaverin yields observed in aerated cultures suggest that similar performance could be achieved in external-loop airlift bioreactors. These systems offer efficient gas–liquid mass transfer and mixing with lower energy consumption compared to conventional stirred-tank reactors, which is a critical advantage for large-scale pigment production. Such scalability considerations are consistent with previous reports describing the influence of aeration and hydrodynamics on fungal secondary metabolism and bioreactor performance

(Limón *et al*., 2023; Chisti, 2016).

Taken together, the results obtained for the effects of pH and aeration on biomass and bikaverin production confirm that the cultivation conditions directly influence the activation of specific metabolic pathways. While pH determined the chemical environment favorable for *bik* gene expression, oxygen transfer modulated the balance between primary and secondary metabolism, acting as a key limiting factor in the critical stages of the process. Nevertheless, these factors alone do not fully explain the production dynamics. Therefore, it is essential to address the overall kinetics of growth and product formation, which not only allows the identification of the mathematical model that best describes biomass generation but also establishes the coupling relationship between cell growth and bikaverin synthesis through the Luedeking–Piret model.

3.5 Bikaverin production kinetics

The growth and bikaverin production kinetics were evaluated under experimental conditions defined from the optimal treatment of the Box–Behnken design (experiment 12). In this assay, *G. fujikuroi* strain CDBB-H-972 was cultivated in a medium composed of dextrose (50 g/L), NH_4Cl (0.75 g/L), KH_2PO_4 (1 g/L), and $MgSO_4$ (1 g/L). The initial pH was adjusted to 3.0 using 1 N HCl or 1 N NaOH; temperature was maintained at 28 ± 1 °C, and orbital agitation at 100 rpm. Aeration was set at 1 vvm (0.3 L/min in a working volume of 300 mL), and the inoculum corresponded to 10% (v/v) of a 36-h pre-culture.

These conditions were selected because they represented the scenario with the highest bikaverin production within the experimental matrix. The culture evolution showed a typical submerged fermentation profile, with progressive consumption of total reducing sugars (TRS) and ammoniacal nitrogen, accompanied by biomass increase and intracellular bikaverin accumulation (Figure 5).

The fitting of experimental data to mathematical growth models (two-parameter Gompertz, three-parameter Gompertz, and Logistic) showed that all three adequately described the system dynamics (Figure 6). However, the three-parameter Gompertz model exhibited the highest goodness of fit (R^2 = 0.999), capturing more accurately the transition toward the stationary phase. This suggests that this model is more sensitive to initial biomass variations and better represents the slight decrease observed at the end of the culture, attributed to reserve consumption under limiting conditions (Borketas *et al*., 2025). Similarly, Valle *et al*. (2024) applied nonlinear mathematical models to describe the fermentation of *Torulaspora delbrueckii* and found that the three-parameter Gompertz model provided a better representation of growth and substrate consumption, which is consistent with the strategy employed in this study for modeling the kinetics of *G. fujikuroi*.

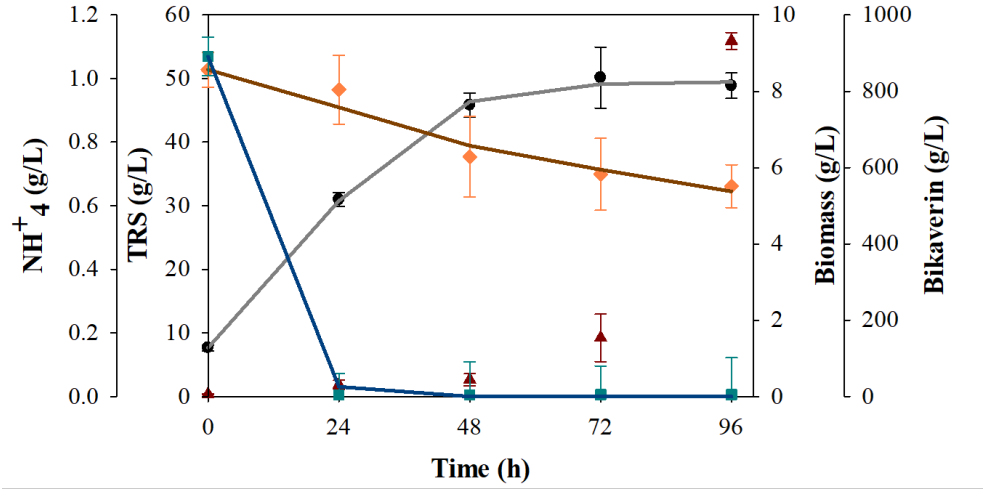

Figure 5. Fermentation kinetics of *G. fujikuroi* CDBB-H-972 under controlled conditions (dextrose 50 g/L, NH_4Cl 0.75 g/L, KH_2PO_4 1 g/L, $MgSO_4$ 1 g/L, initial pH 3, temperature 28 ± 1 °C, aeration 1 vvm, orbital agitation 100 rpm, inoculum 10% v/v). Evolution of biomass (•; fitted to the three-parameter Gompertz model), total reducing sugars, TRS (♦; fitted curve), ammoniacal nitrogen, NH_4^+ (■; fitted curve), and bikaverin concentration (▲) throughout 96 h of fermentation. Data represents the mean of two independent replicates ± standard deviation.

Table 6. Kinetic parameters obtained from biomass fitting to the Gompertz (two- and three-parameter) and Logistic models. Shown are the values of the growth constants (k, μ, and a), residual sum of squares (RSS), determination coefficient (R^2), and statistical model comparison using the F-test ($\alpha = 0.05$).

Model	Parameters			Yields	RSS	R^2	Comparison		
	k	μ	a	g/g					
Two-parameter Gompertz	0.110	0.058	-----	$Y_{\frac{X}{S}} = 0.3751 \pm 0.065$	0.114	0.996	**Models**	**F**	***p-value***
Three-parameter Gompertz	0.102	0.047	0.002	$Y_{\frac{P}{X}} = = 0.134 \pm 0.002$	0.003	0.999	Logistic vs G3P	29.840	0.031
Logistic	0.091	--------	0.011		0.049	0.998	G2P vs G3P	71.250	0.137

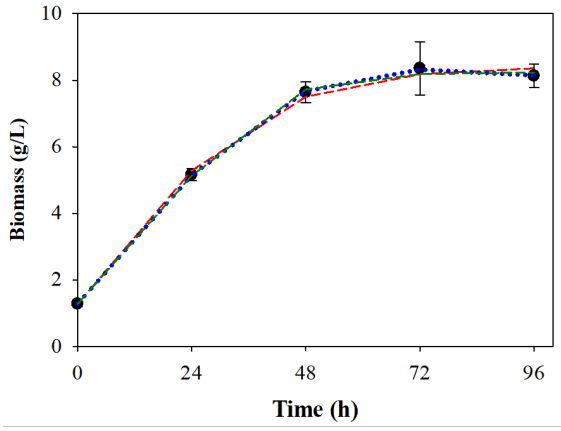

Figure. 6. Fitting of the growth kinetics of *G. fujikuroi* CDBB-H-972 during bikaverin production to three mathematical models: two-parameter Gompertz (- - -), three-parameter Gompertz (· · ·), and Logistic (- - -). Symbols represent the experimental data (●). Conditions: dextrose 50 g/L, NH_4Cl 0.75 g/L, KH_2PO_4 1 g/L, $MgSO_4$ 1 g/L, initial pH 3, 28 ± 1 °C, aeration 1 vvm, orbital agitation 100 rpm, inoculum 10% v/v.

Table 6 summarizes the kinetic parameters obtained and the statistical comparison between models using the F-test. Although both the Logistic and the two-parameter Gompertz models showed acceptable fits ($R^2 > 0.999$), the F-test indicated significant differences between the Logistic and the three-parameter Gompertz models ($F = 29.840$, $p = 0.031$).

In comparison, the kinetic parameters are consistent with those reported by Chávez-Parga *et al.* (2008) in an Airlift bioreactor, suggesting that when scaling up the system, the kinetic constants could remain within similar ranges. However, the magnitude of these parameters may vary depending on the air flow rate and the type of diffuser, factors that directly influence oxygen transfer and mycelial morphology.

Since bikaverin is secreted into the extracellular medium, it is reasonable to assume that during prolonged cultivation the fungus or secreted enzymes could metabolize or degrade the pigment, leading to a decline in its apparent concentration. In our experiments, the available nitrogen was depleted before 24 h, a condition known to trigger metabolic shifts and to regulate the onset of secondary metabolism in *G. fujikuroi* and other filamentous fungi. Nitrogen limitation has been widely reported as a key signal controlling secondary metabolite biosynthesis and degradation processes (Tudzynski *et al.,* 2014). Therefore, the cultivation time was limited to 96 h to avoid possible pigment reuptake or degradation, focusing the analysis on a reliable interval where bikaverin accumulation showed a consistent increasing trend.

Figure 6 shows the kinetics fitted to the three models, confirming that biomass reaches its maximum around 48 h, at which point the stationary phase begins. Finally, bikaverin production was analyzed using the Luedeking–Piret model, which describes product formation as the sum of a growth-associated fraction $\left(\alpha \frac{dX}{dt}\right)$ and a non-growth-associated fraction (βX). The obtained parameters ($\alpha = -72.28$; $\beta = 2.114$) indicate that bikaverin is a predominantly non-growth-associated metabolite. The negative value of α suggests that cell growth not only does not favor its synthesis but may even dilute the pigment concentration during the exponential phase. In contrast, the positive and high value of β confirms that bikaverin accumulates mainly during the stationary phase, consistent with the typical profile of secondary metabolites in filamentous fungi (Giordano & Domenech, 1999; Spraker *et al.,* 2018). These results are consistent with previous studies, which describe bikaverin as a secondary metabolite synthesized predominantly during the stationary phase and is strongly influenced by oxygen availability (Choi *et al*., 2020; Limón *et al*., 2023).

The obtained results show that the three-parameter Gompertz model more accurately describes the growth kinetics of *G. fujikuroi* under the evaluated experimental conditions, as it captures both the exponential phase and the stabilization, followed by a slight decrease in biomass at the end of the culture. This agrees with reports for other filamentous fungi producing secondary metabolites, where the stationary phase is associated with greater accumulation of polyketide products. The fitting capacity of the kinetic models, together with statistical verification through the F-test, reinforces the robustness of the analysis and provides a quantitative basis for interpreting the system dynamics. Nevertheless, since bikaverin is a secondary metabolite, its formation does not necessarily follow the same trend as biomass, making

it necessary to perform a specific analysis of the coupling between growth and production. In this sense, the Luedeking–Piret model was applied to evaluate the growth-associated or non-associated nature of bikaverin biosynthesis, which is presented in subsection 3.5.1.

3.5.1 Product formation kinetics (Luedeking-Piret model)

The relationship between cell growth and bikaverin synthesis was evaluated using the Luedeking–Piret model (Equation 8). This model differentiates the growth-associated production fraction (α) from the non-growth-associated fraction (β), providing a key tool to determine the nature of secondary metabolite biosynthesis in filamentous fungi.

From the data of experiment 12, conducted under controlled culture conditions (dextrose 50 g/L, NH_4Cl 0.75 g/L, KH_2PO_4 1 g/L, $MgSO_4$ 1 g/L, temperature 28 ± 1 °C, initial pH 3, aeration 1 vvm, orbital agitation 100 rpm, 10% inoculum), the parameters α and β were estimated by ordinary least squares, without intercept. The obtained values were α = –72.28 and β = 2.114, with an R^2 = 0.921 based on the dP/dt values. The negative α value indicates that biomass increase does not favor bikaverin production but exerts a diluting or inhibitory effect, In contrast, the positive and significant β value confirms that pigment formation occurs predominantly in a non-growth-associated manner.

This behavior is consistent with the typical profile of polyketide-type secondary metabolites, whose synthesis is activated during stationary or nutrient-stress phases rather than during active growth (Spraker *et al*., 2018; Medentsev & Akimenko, 1998). Similarly, Chávez-Parga *et al*. (2008) reported negative α values in bikaverin production within an Airlift bioreactor, which was interpreted as a clear indication that biosynthesis is triggered by regulatory mechanisms rather than biomass expansion. Likewise, Wiemann *et al*. (2009) demonstrated that the expression of *bik* genes responsible for the biosynthetic pathway is induced under acidic pH and nitrogen-limiting conditions, which is consistent with the conditions evaluated in this study.

Figure 7 shows the model fitting to the experimental bikaverin concentration data, where the prediction aligns with the experimental trend, although with slight deviations at early times, attributable to the negative α value. This effect reinforces the idea that bikaverin production intensifies once limiting nutrients are depleted, confirming its nature as a secondary metabolite independent of growth.

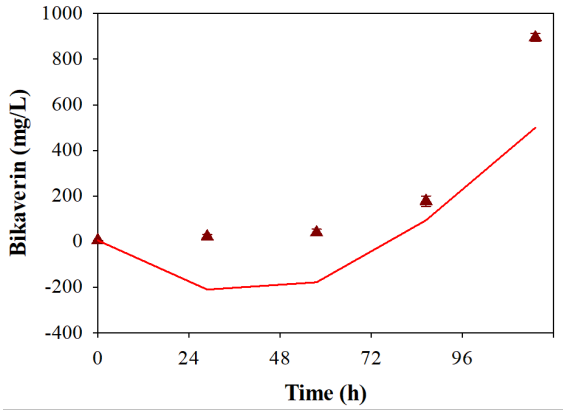

Figure 7. Bikaverin production profile by *G. fujikuroi* CDBB-H-972 under controlled conditions (initial pH 3, aeration 1 vvm, orbital agitation 100 rpm, temperature 28 ± 1 °C). (▲) Bikaverin concentration (mean ± SD, n = 2), while the solid line represents the fit of the Luedeking–Piret model (α = –72.28, β = 2.114).

Taken together, these results provide strong evidence that bikaverin in *G. fujikuroi* should be considered a strictly secondary metabolite, whose accumulation can be enhanced through culture-control strategies aimed at prolonging the stationary phase or intensifying stress conditions (e.g., dynamic pH control or variations in aeration rate). These findings are relevant for process scale-up design, as they enable the formulation of optimization strategies focus on maximizing pigment production beyond merely increasing biomass. The results confirm that bikaverin behaves as a non-growth-associated secondary metabolite, consistent with reports for other industrially relevant fungal polyketides. This result supports the applicability of the Luedeking–Piret model for describing production kinetics and emphasizes the relevance of regulating culture phases to enhance pigment accumulation. Once the formation kinetics were understood, the next key step involved the extraction and purification of the produced bikaverin to obtain the compound in crystalline form and proceed with its structural characterization, which confirmed its identity and allowed evaluation of the quality of the recovered metabolite.

3.6 Extraction and purification of produced bikaverin

Solid–liquid extractions were performed from the culture of *G. fujikuroi* CDBB-H-972, followed by concentration of the crude extract using a rotary evaporator. Subsequently, four successive washes with chloroform were performed, yielding extracts of varying color intensities depending on the cultivation time. Figure 8 shows the organic extracts collected from 0 to 96 hours, where a clear increase in pigment concentration is observed throughout the fermentation

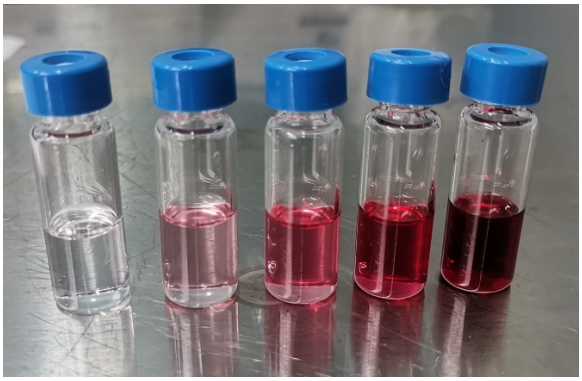

Figure 8. Organic phase extracts of *G. fujikuroi* CDBB-H-972 from 0 to 96 hours of cultivation.

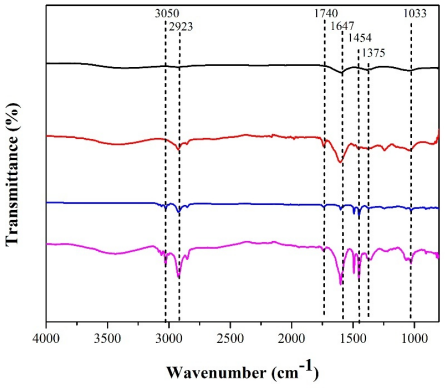

Figure 9. FTIR spectrum of (—) KBr pellet, (—) Bikaverin standard, (—) Chloroform, (—) Fraction 4 Bikaverin purified.

process. This gradient confirms that the highest proportion of bikaverin is associated with the biomass, validating its nature as an intracellular metabolite.

After purification of the crude extract, the characteristic red pigmentation allowed the visualization of distinct chromatographic bands. For the mobile phase employed, a retention factor (Rf) defined as the ratio between the distance traveled by the compound and that traveled by the solvent front of 0.85 was obtained, consistent with the association of bikaverin with cellular biomass and confirming its intracellular nature.

The crude fraction was purified by column chromatography on silica gel 60 acidified with oxalic acid (95:5, w/w), using a mobile phase consisting of a mixture of chloroform, methanol, and acetic acid (94:1:5, v/v/v). Thin-layer chromatography (TLC) analysis revealed an intense red band with an Rf value of 0.85, matching the commercial bikaverin standard (Sigma-Aldrich®). Structural characterization of the purified fraction was performed by FT-IR spectroscopy, and the results are shown in Figure 9.

The obtained spectra correspond to the characteristic peaks previously described for this polyketide, confirming the identity of the produced bikaverin.

A characteristic band was observed in the IR spectrum at 3050 cm^{-1}, characteristic of aromatic C–H stretching, 2923 cm^{-1} for unsaturated C–H groups, 1740 cm^{-1} for the C=O group, 1647 cm^{-1} for the C=C group, 1454 and 1375 cm^{-1} for C–H, and 1033 cm^{-1} for the C–O group. Studies conducted by Soumya *et al*. (2018) reported a similar IR spectrum; however, they characterized a red pigment produced by the fermentation of *Fusarium chlamydosporum*. Through SEM analysis, a more evident mycelial organization was observed, composed of loosely arranged hyphal filaments, hyphal aggregates forming mycelial strands, and some interconnections through anastomosis (Figure 10).

In the SEM micrographs, amorphous structures adhered to the mycelial surface were observed, showing morphology and distribution compatible with intracellular deposits. These aggregates could correspond to bikaverin accumulations, which have been previously reported as being either secreted or accumulated in specific regions of the mycelium. Cornforth *et al.* (1971) described bikaverin as a fungal vacuolization factor, owing to its possible role in inducing senescence-related morphological changes.

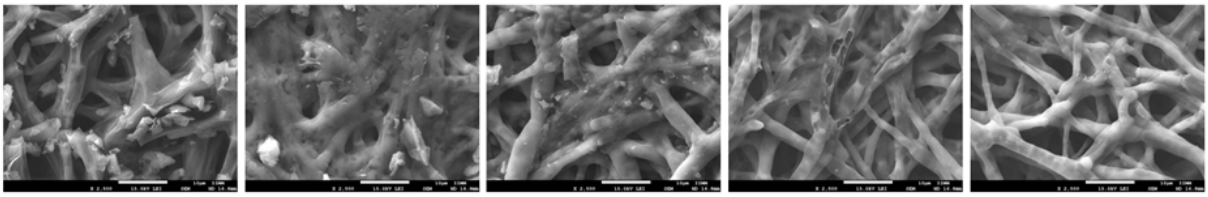

Figure 10. Scanning Electron Microscopy (SEM) analysis of *G. fujikuroi* CDBB-H-972 at 2500× magnification.

Conclusions

The results of this study provide clear evidence that *G. fujikuroi* efficiently produces bikaverin under controlled culture conditions, primarily influenced by the initial pH and aeration rate, with strain CDBB-H-972 exhibiting the best productive performance. The applied kinetic models confirmed that bikaverin production follows a non-growth-associated pattern, consistent with its classification as a secondary metabolite. Morphological analysis revealed structural alterations in the mycelium and intracellular pigment accumulation, in agreement with previous reports on fungal polyketides. Furthermore, the extraction, purification, and FT-IR characterization validated the identity of the metabolite, confirming the reliability of the experimental procedure. Overall, these findings provide valuable insights into the physiological and kinetic regulation of bikaverin biosynthesis, establishing a solid foundation for future optimization and scale-up efforts aimed at its biotechnological and pharmaceutical exploitation.

Acknowledgements

The authors acknowledge the financial support provided by the Secretaría de Ciencia, Humanidades, Tecnología e Innovación (SECIHTI) through the Doctoral Scholarship in Chemical Engineering Sciences (CVU No. 1081080). Appreciation is also extended to the Biotechnology and Bioengineering Laboratory of the Universidad Michoacana de San Nicolás de Hidalgo for the infrastructure and facilities that made this study possible.

Nomenclature

Y	Response variable of the experimental design
β_n	Estimated regression coefficients
OTR	Oxygen Transfer Rate, $mg\ O_2/Lh$
OUR	Oxygen Uptake Rate, $mg\ O_2/Lh$
Q_{O_2}	Oxygen Consumption rate, $mg\ O_2/Lh$
X	Biomass concentration, g/L
t_n	Time, s
a, k	Kinetics constants
f	Distribution coefficient
RSS_1	Residual sum of squares
DF_2	Degrees of freedom
P	Concentration of product, g/L.
α, β	Luedeking-Piret parameters
k_La	The mass transfer coefficient, h^{-1}
μ	Specific growth rate, h^{-1}
$Y_{\frac{X}{S}}$	Yield Biomass/substrate, $g\ biomass/g\ substrate$
$Y_{\frac{P}{X}}$	Yield Product/Biomass, $g\ product/g\ biomass$
vvm	Aeration rate, volume of air per volume of medium per minute
rpm	Orbital agitation, revolutions per minute

References

Amaral, P. F. F., Freire, M. G., Rocha-Leão, M. H. M., Marrucho, I. M., Coutinho, J. A. P., & Coelho, M. A. Z. (2008). Optimization of oxygen mass transfer in a multiphase bioreactor with perfluorodecalin as a second liquid phase. *Biotechnology and Bioengineering*, *99*(3), 588–598. https://doi.org/10.1002/bit.21640

Anama, Y. P., Díaz, R., Duarte-Alvarado, D. E., & Lagos-Burbano, T. C. (2021). Morphological and pathogenic characterization of *Fusarium oxysporum* in lulo (Solanum spp.). *Revista de Ciencias Agrícolas*, *38*(1), 20–37. https://doi.org/10.22267/rcia.213801.142

Bailey, J. E., & Ollis, D. F. (1977). *Biochemical Engineering Fundamentals*. Editorial McGraw-Hill, 2nd ed. United States

Balan, J., Fuska, J., Kuhr, I., & Kuhrová, V. (1970). Bikaverin, an antibiotic from *Gibberella fujikuroi*, effective against *Leishmania brasiliensis*. *Folia Microbiologica*, *15*(6), 479–484. https://doi.org/10.1007/BF02880192

Borkertas, S., Viskelis, J., Viskelis, P., Streimikyte, P., Gasiunaite, U., & Urbonaviciene, D. (2025). Fungal Biomass Fermentation: Valorizing the Food Industry's Waste. *Fermentation*, *11*(6), 351. https://doi.org/10.3390/fermentation11060351

Chávez-Parga, M. del C., González-Ortega, O., Negrete-Rodríguez, M. de la L. X., Vallarino, I. G., Alatorre, G. G., & Escamilla-Silva, E. M. (2008). Kinetic of the gibberellic acid and bikaverin production in an airlift bioreactor. *Process Biochemistry*, *43*(8), 855–860. https://doi.org/10.1016/J.PROCBIO.2008.04.007

Chávez-Parga, M. C., Hinojosa-Ventura, G., Maya-Yescas, R., & González-Hernández, J. C. (2014). Effect of rates of aeration and agitation on the volumetric coefficient of oxygen transfer in the production of bikaverin. *International Review Of Chemical Engineering (IRECHE)*, *6*(2), 100-107.

Chisti, Y. (2016). Airlift bioreactors: Principles, applications, and recent advances. *Chemical Engineering and Processing: Process Intensification*, 104, 1–21. https://doi.org/10.1016/j.cep.2016.03.007

Choi, S., Lee, S., Kim, J., & Park, Y. (2020). Regulation of bikaverin biosynthesis and oxidative metabolism in *Fusarium fujikuroi* under oxygen-limited fermentation. Journal of Biotechnology, 318, 45–53. https://doi.org/10.1016/j.jbiotec.2020.07.012

Cornforth, J. W., Ryback, G., Robinson, P. M., & Park, D. (1971). Isolation and characterization of a fungal vacuolation factor (bikaverin). *Journal of the Chemical Society C: Organic*, 2786. https://doi.org/10.1039/j39710002786

Doran, P. M. (2013). *Bioprocess engineering principles*. Academic Press. United Kingdom

Garza-Garza, C., Olguin-Maciel, E., Valdez-Ojeda, R., Huchin-Poot, E., Toledano-Thompson, T., Azcorra-May, K., Alzate-Gaviria, L., Dominguez-Maldonado, J., Lappe-Oliveras, P., & Tapia-Tussell, R. (2025). Bio-saccharification and fermentation process of a non-conventional starchy material with isolates of autochthonous strains. Revista Mexicana de Ingeniería Química, 24(2), 1-26. https://doi.org/10.24275/rmiq/bio25497

Giordano, W., & Domenech, C. E. (1999). Aeration affects acetate destination in *Gibberella fujikuroi*. *FEMS Microbiology Letters*, *180*(1), 111–116. https://doi.org/10.1111/j.1574-6968.1999.tb08784.x

Hinojosa Ventura, G., Puebla Pérez, A. M., Gallegos Arreola, M. P., Chávez Parga, M. del C., Romero Estrada, A., & Delgado Saucedo, J. I. (2019). Cytotoxic and Antitumoral Effects of Bikaverin from *Gibberella fujikuroi* on L5178Y Lymphoma Murine Model. *Journal of the Mexican Chemical Society*, *63*(4). https://doi.org/10.29356/jmcs.v63i4.729

Leslie, J. F., & Summerell, B. A. (2006). The Fusarium Laboratory Manual. En *Wiley eBooks*. https://doi.org/10.1002/9780470278376

Limón, M. C., Rodríguez-Ortiz, R., & Avalos, J. (2023). Oxygen availability modulates bikaverin production and fungal differentiation in *Fusarium fujikuroi*. *Applied Microbiology and Biotechnology*, 107(5), 1911–1924. https://doi.org/10.1007/s00253-023-12215-2

Limón, M. C., Rodríguez-Ortiz, R., & Avalos, J. (2010). Bikaverin production and applications. *Applied Microbiology and Biotechnology*, *87*(1), 21–29. https://doi.org/10.1007/s00253-010-2551-1

Lu, H., Guo, S., Yang, Y., Zhao, Z., Xie, Q., Wu, Q., Sun, C., Luo, H., An, B., & Wang, Q. (2025). Bikaverin as a molecular weapon: enhancing *Fusarium oxysporum* pathogenicity in bananas via rhizosphere microbiome manipulation. *Microbiome*, *13*(1). https://doi.org/10.1186/s40168-025-02109-7

Machado, S., Feitosa, V., Pillaca-Pullo, O., Lario, L., Sette, L., Pessoa, A., & Alves, H. (2022). Effects of oxygen transference on protease production by *Rhodotorula mucilaginosa* CBMAI 1528 in a stirred tank bioreactor. *Bioengineering*, *9*(11), 694. https://doi.org/10.3390/bioengineering9110694

Martínez-Moreno, F., Jofre y Garfias, A. E., Hernández-Orihuela, A. L., & Martínez-Antonio, A. (2021). Avocado seed hydrolysate as an alternative growth medium for fungi. *Revista Mexicana de Ingeniería Química*, *20*(2), 569–580. https://doi.org/10.24275/rmiq/Bio1951

Medentsev, A. G., Arinbasarova, A. Yu., & Akimenko, V. K. (2005). Biosynthesis of Naphthoquinone Pigments by Fungi of the Genus *Fusarium*. *Applied Biochemistry and Microbiology*, *41*(5), 503–507. https://doi.org/10.1007/s10438-005-0091-8

Medentsev, A., & Akimenko, V. (1998). Naphthoquinone metabolites of the fungi. Phytochemistry, 47(6), 935-959. https://doi.org/10.1016/s0031-9422(98)80053-8

Miller, G. L. (1959). Use of Dinitrosalicylic Acid Reagent for Determination of Reducing Sugar. *Analytical Chemistry*, *31*(3), 426–428. https://doi.org/10.1021/ac60147a030

Nirmaladevi, D., Venkataramana, M., Chandranayaka, S., Ramesha, A., Jameel, N. M., & Srinivas, C. (2014). Neuroprotective Effects of Bikaverin on H2O2-Induced Oxidative Stress Mediated Neuronal Damage in SH-SY5Y Cell Line. *Cellular and Molecular Neurobiology*, *34*(7), 973–985. https://doi.org/10.1007/s10571-014-0073-6

Santiago da Silva, W. (2013). *¨Produção de pigmentos fúngicos e seu uso no tingimento de tecidos* Tesis Maestre Dissertação apresentada ao programa de Pós Graduação em Tecnologias para

o Desenvolvimento Sustentável. Universidade Federal de São João Del-Rei (UFSJ). Brasil.

Santos, M. C. D., De Lima Mendonça, M., & Bicas, J. L. (2020). Modeling bikaverin production by *Fusarium oxysporum* CCT7620 in shake flask cultures. *Bioresources And Bioprocessing*, *7*(1). https://doi.org/10.1186/s40643-020-0301-5

Solórzano, L. (1969). Determination of Ammonia in natural waters by the Phenolhypochlorite Method 1 1 This research was fully supported by U.S. Atomic Energy Commission Contract No. ATS (11-1) GEN 10, P.A. 20. *Limnology and Oceanography*, *14*(5), 799–801. https://doi.org/10.4319/lo.1969.14.5.0799

Soumya, K., Narasimha Murthy, K., Sreelatha, G. L., & Tirumale, S. (2018). Characterization of a red pigment from *Fusarium chlamydosporum* exhibiting selective cytotoxicity against human breast cancer MCF-7 cell lines. *Journal of Applied Microbiology*, *125*(1), 148–158. https://doi.org/10.1111/jam.13756

Spraker, J. E., Wiemann, P., Baccile, J. A., Venkatesh, N., Schumacher, J., Schroeder, F. C., Sanchez, L. M., & Keller, N. P. (2018). Conserved Responses in a War of Small Molecules between a Plant-Pathogenic Bacterium and Fungi. *mBio*, *9*(3). https://doi.org/10.1128/mbio.00820-18

Tudzynski, B. (2014). Nitrogen regulation of fungal secondary metabolism in fungi. *Frontiers In Microbiology*, *5*. https://doi.org/10.3389/fmicb.2014.00656

Valle, P., Salazar, Y., Soto-Cruz, N., Páez-Lerma, J., Coria, L., Núñez-Guerrero, M., Rodríguez-Herrera, R., & Herrera, L. (2024). Modelling and analysis on the ethanol production by the *Torulaspora delbrueckii* yeast. *Revista Mexicana de Ingeniería Química*, *23*(3), 1-17. https://doi.org/10.24275/rmiq/sim24312

Wiemann, P., Willmann, A., Straeten, M., Kleigrewe, K., Beyer, M., Humpf, H., & Tudzynski, B. (2009). Biosynthesis of the red pigment bikaverin in *Fusarium fujikuroi*: genes, their function and regulation. *Molecular Microbiology*, *72*(4), 931–946. https://doi.org/10.1111/j.1365-2958.2009.06695.x

Zwietering, M. H., Jongenburger, I., Rombouts, F. M., & van 't Riet, K. (1990). Modeling of the Bacterial Growth Curve. *Applied and Environmental Microbiology*, *56*(6), 1875–1881. https://doi.org/10.1128/aem.56.6.1875-1881.1990

Vol. 24, No. 3(2025) IA25566
Revista Mexicana de Ingeniería Química

Variation in the bacterial and fungal communities over a three-year period at Mexico City's largest operational-capacity composting plant

Variación en las comunidades bacterianas y fúngicas durante un período de tres años en la planta de compostaje con mayor capacidad operativa de la Ciudad de México

L. Martínez-Montiel[1,3], F.J. Fernández[1*], L.R. Tovar-Gálvez[2], G. Saucedo-Castañeda[1*]

[1] Universidad Autónoma Metropolitana, Unidad Iztapalapa. Departamento de Biotecnología. Av. Ferrocarril San Rafael Atlixco 186, Col. Leyes de Reforma 1ª sección, Iztapalapa, C.P. 09310, Ciudad de México.

[2] Centro Interdisciplinario de Investigaciones y Estudios Sobre Medio Ambiente y Desarrollo. Instituto Politécnico Nacional. Calle 30 de Junio de 1520 S/N, Col. La Laguna Ticomán, Gustavo A. Madero, C.P. 07340, Ciudad de México.

[3] Universidad Anáhuac México Norte, Facultad de Ciencias de la Salud. Av. Universidad Anáhuac 46, Col. Lomas Anáhuac, Huixquilucan, C.P. 52786, Estado de México.

Sent date: April 10, 2025; Accepted: August 30, 2025

Abstract

In Mexico City, a daily generation of 12404 t of municipal solid waste was registered in 2022. Approximately 1374 t of organic matter are received at the Bordo Poniente Composting Plant (BPCP, West Rim Composting Plant) for transformation into compost. BPCP is likely the largest composting facility in Latin America. A total of 15 samples were collected over a three-year period after its opening in 2012. The samples were then subjected to analysis to ascertain their moisture content, pH, reducing sugar content, C/N ratio, and maximum CO_2 production rate. All the analyzed samples were found to meet the requisite criteria for stable compost. The polymerase chain reaction-denaturing gradient gel electrophoresis (PCR-DGGE) method was employed to identify the bacterial and fungal communities present in the samples. The descriptive analysis revealed the presence of seven bacteria and three fungi in all the compost samples coming from the rainy and dry seasons; thereby generating basic knowledge of the microbiota composition suitable for the composting process. Additionally, some of the identified microorganisms have biotechnological potential for application in different industrial sectors. The data obtained are highly relevant and remain so despite the time elapsed since the sampling. They shed light on the microbial dynamics during the composting process, with a broad approach (bacteria and fungi). Most of previous studies have only focused on one of these taxonomic categories, which misses a lot of information on the complex syntrophic relationships that may occur. The complexity and size of the composting plant studied is another element of great interest.

Keywords: Bacterial and fungal communities, compost, compost stability, DGGE-PCR, nested PCR.

Resumen

En 2022 se generaron diariamente 12404 t de residuos sólidos urbanos en la Ciudad de México. Aproximadamente 1374 t de materia orgánica se reciben en la Planta de Composta Bordo Poniente (BPCP) para su transformación en composta, siendo esta planta, muy probablemente, la mayor instalación de compostaje de toda América Latina. Un total de 15 muestras fueron recogidas durante un período de tres años después de su apertura en 2012. Las muestras se sometieron a análisis para determinar su contenido de humedad, pH, contenido de azúcares reductores, relación C/N y tasa máxima de producción de CO_2. Se comprobó que todas las muestras analizadas cumplían los criterios exigidos para una composta estable. Para identificar las comunidades bacterianas y fúngicas presentes en las muestras se empleó el método de reacción en cadena de la polimerasa-y electroforesis en gel de gradiente desnaturalizante (PCR-DGGE). El análisis descriptivo reveló la presencia de siete bacterias y tres hongos en todas las muestras de composta provenientes de las estaciones de lluvia y seca, generando así un conocimiento básico de la composición de la microbiota adecuada para el proceso de compostaje. Además, algunos de los microorganismos identificados tienen potencial biotecnológico para su aplicación en diferentes sectores industriales. Los datos obtenidos son altamente relevantes y siguen siéndolo a pesar del tiempo transcurrido desde el muestreo. Permiten comprende mejor la dinámica microbiana durante el proceso de compostaje, con un enfoque amplio (bacterias y hongos). La mayoría de los estudios previos sólo se han centrado en una de estas categorías taxonómicas, lo que hace que se pierda mucha información sobre las complejas relaciones sintróficas que pueden darse. La complejidad y el tamaño de la planta de compostaje estudiada es otro elemento de gran interés.

Palabras clave: composta, comunidades bacterianas y fúngicas, DGGE-PCR, estabilidad de la composta, PCR anidada.

*Corresponding authors. *E-mail*: fjfp@xanum.uam.mx, saucedo@xanum.uam.mx;
https://doi.org/10.24275/rmiq/IA25566
ISSN:1665-2738, *issn-e*: 2395-8472

1 Introduction

In Mexico City, the quantity of waste generated by anthropogenic activities has been on the rise in recent years, in parallel with the growth of the population. A daily generation of 12204 t of municipal solid waste was registered in 2013 (Noyola *et al*., 2014), increasing to 12893 t in 2014 and 12816 t in 2015. According to the latest data from the Mexico City Solid Waste Inventory, approximately 12404 t of municipal solid waste (MSW) were generated daily in Mexico City in 2022, equating to an estimated generation of 1.07 kg d^{-1} $inhabitant^{-1}$ (SEDEMA, 2022). Approximately 48% of this MSW is derived from households, 30% from services and businesses, 10% from markets, 5% from the Mexico City wholesale central market (Central de Abasto), 4% from various sources, and 3% is of controlled origin, including prisons, government offices, and medical units. The Ministry of Environment and Natural Resources (SEMARNAT, 2021) has reported that 38% of MSW is comprised of organic solid waste (OSW), which is classified into two major categories: pruning and gardening waste and food remains. The total quantity of organic solid waste generated per day is approximately 4676.3 t, with approximately 1374 t (over 30% of the MSW generated in Mexico City) received daily at the Bordo Poniente Composting Plant (BPCP, West Rim Composting Plant). The BPCP began its operation in 2012; the surface area of the facility is 370,000 m^2, with an installed capacity of 876000 t $year^{-1}$, and a compost production of 89717 t $year^{-1}$. Several works have been previously published regarding utilization of this Municipal Solid Organic Waste (MSOW) plant (Castilla-Hernández *et al*., 2016; Estrada-Martínez *et al*., 2021; Gan *et al*., 2013; Jimenez-Rodriguez *et al*., 2020). The facility comprises approximately 1000 piles, each measuring 200 m in length and 3 m in height. In consideration of the capacity of BPCP, it is the largest compost plant in Mexico and one of the largest in Latin America. In 2021, this composting plant received 449876 t of waste, which was transformed into 89702 t of compost. The quantity of organic solid waste (OSW) received daily (1374 t) for transformation into compost, along with the operational capacity of the plant (89 t d^{-1}) (SEDEMA, 2022), has led to the investigation of technologies that facilitate more efficient composting processes in recent years. In 2013, a waste separation program was established in Mexico City, where waste is collected from the source of generation (Programa General de Desarrollo Del Distrito Federal 2013-2018, 2013). Since a large portion of municipal solid waste (MSW) is generated in households, a segmented collection route was implemented where OSW is collected exclusively from households in Mexico City three days a week. After collection, the waste is weighed and transported directly to the BPCP. At the plant, the OSW is mixed with pruning and tree trimming waste from green areas. The composting process is carried out in open-air piles, which allows for the process to be aerobic (although BPCP is located at 2,250 msnm, with partial pressure of O_2 24% lower than at sea level, physiological processes are unaffected).The plant staff monitor the temperature to ensure the process reaches the thermophilic phase (60-70 °C). They also maintain the moisture of the piles by recirculating the leachate from the piles that have been processing for longer. The piles are periodically turned to prevent ignition zones and maintain homogeneity. Once the process is complete, the compost is screened to remove any remaining inorganic materials such as glass or plastic. After screening, the compost is placed in windrows for maturation.

Composting is defined as a biological process of aerobic degradation of organic matter through the succession of microbial communities of fungi and bacteria that have specific functions, resulting in the mineralization of easily degraded organic matter and the formation of a biologically stable end product (Noor *et al*., 2024; Xi *et al*., 2015; Yamamoto & Nakai, 2019). It is of great importance to understand the microorganisms present during the composting process. Nevertheless, technical challenges exist in conducting complex analyses based on direct isolation of microorganisms due to the potential for significant bias when selecting the culture media for isolation (Chen *et al*., 2023). Consequently, molecular tools and methods are employed to conduct microbial ecology studies in complex ecosystems or processes such as composting. Some of these tools include polymerase chain reaction (PCR) and denaturing gradient gel electrophoresis (DGGE), collectively known as PCR-DGGE. This is a molecular method for rapidly detecting changes in the microbial community or performing a comparative analysis of environmental samples, thereby providing information on the distribution and composition of the microbial species present (Tu Anh *et al*., 2018). Despite the fact that this technique has now been virtually displaced due to the cheapening of metagenomics studies by next generation sequencing (García-Uitz *et al*., 2024; Loreto-Muñoz *et al*., 2024), the DGGE technique remains in use for this purpose. Aydin *et al*. (Aydin et al., 2015) employed this technique to identify alterations in the microbial community present in compost bioreactors following the addition of varying antibiotic concentrations. In a study conducted by Xi *et al*. (Xi *et al*., 2015), the polymerase chain reaction-denaturing gradient gel electrophoresis (PCR-DGGE) method was employed to assess the influence of multistate inoculation on the composition and dynamics of the fungal and bacterial communities in a municipal solid waste composting process. Tu Anh *et al*. (Tu Anh *et al*., 2018) conducted a study to analyze and compare

Table 1. Identification codes and meteorological conditions during the sampling in BPCP in Mexico City.

Year	Month	Sample code	Season	Climate season	Precipitation* (mm*m^{-2})	Mean Temperature (°C)	Maximum Temperature (°C)	Minimum Temperature (°C)
2013	March	MAR13	Spring	dry	0.0	14.7	24.4	5.0
	May	MAY13	Spring	rainy	1.3	18.4	27.5	9.2
	September	SEP13	Autumn	rainy	4.6	17.2	22.4	12.0
	October	OCT13	Autumn	rainy	1.4	16.5	23.5	9.4
2014	February	FEB14	Winter	dry	1.8	14.1	24.7	3.4
	March	MAR14	Spring	dry	0.8	16.0	25.3	6.8
	May	MAY14	Spring	rainy	2.1	17.2	25.2	9.1
	July	JUL14	Summer	rainy	3.6	17.1	24.0	10.3
	September	SEP14	Autumn	rainy	2.8	17.3	24.0	10.7
	October	OCT14	Autumn	rainy	4.9	15.5	22.4	8.5
	November	NOV14	Autumn	dry	0.1	14.2	22.6	5.9
2015	February	FEB15	Winter	dry	0.1	12.8	22.2	3.5
	March	MAR15	Spring	dry	3.1	15.0	22.8	7.2
	May	MAY15	Spring	rainy	4.4	17.8	25.5	10.0
	September	SEP15	Autumn	rainy	2.0	17.2	23.7	10.8

* Average rainfall per month

the effectiveness of different sets of primers for the identification of fungi present in compost samples. Their findings indicated that, on certain occasions, DNA extractions may contain PCR inhibitors. Pandey *et al*. (Pandey *et al*., 2024) conducted a study in which they analyzed the evolution microbial communities and microbial shifts under anaerobic processes using DGGE. They applied this technique to analyze the dominant bacterial community in mesophilic and thermophilic anaerobic digestions of dairy manure in different temperatures (28-52 °C), examining the variable region V3 of the 16S rRNA gene of the present bacteria. The results showed that the bacterial community was affected by temperature and anaerobic incubation time, with significant changes in the microbial community.

To reduce the time required for composting processes, it is necessary to explore ways to modify the bioprocessing conditions to promote the specific activity of certain microorganisms. To achieve this, it is essential to have a comprehensive understanding of both the composting process conditions and the microorganisms involved. For this reason, the objective was to conduct a physicochemical and respirometric analysis of BPCP compost during the first three years of operation of the plant, period during both the dry and rainy seasons in Mexico City. The analysis was conducted to determine the stability of the compost and variation in the bacterial and fungal communities present, which was analyzed using the PCR-DGGE technique through the sequence of the predominant operational taxonomic units (OTUs).

2 Materials and methods

2.1 *Sampling*

A series of composting sampling procedures were conducted at the Bordo Poniente Composting Plant (BPCP) in Mexico City (19.461604451263426, -99.01750305249477), between 2013 and 2015. These procedures were conducted over several months during both the dry and rainy seasons, as detailed in Table 1. The sampling was conducted in accordance with the procedures outlined in the Test Methods for the Examination of Composting and Compost (TMECC), Method 02.01.(Thompson *et al*., 2001) All samples were obtained from the mature compost storage site at the BPCP and were maintained at a refrigerated temperature until analysis.

2.2 *Analytical techniques*

2.2.1 *Moisture determination*

The moisture content was determined in triplicate by gravimetry using the standard method TMECC 03.09-A (Thompson *et al*., 2001), as outlined in the Thermobalance OHAUS automatic moisture analyzer.

2.2.2 *pH determination*

The pH was determined using a calibrated potentiometer (Conductronic, model pH 120). In a beaker, 10 g of compost were weighed, and deionized water was added at a 1:5 ratio in accordance with the methodology outlined in section 04.11 of the TMECC

(Thompson *et al*., 2001). This standard establishes the requirements for compost production from the organic fraction of urban, agricultural, livestock, and forestry solid waste and the quality specifications for compost produced and distributed in Mexico City (SEDEMA, 2011).

2.2.3 Carbon/Nitrogen (C/N) ratio determination

The C/N ratio was determined using a CHN elemental analyzer (Model 2400, Series II, Perkin Elmer). Between 2 and 3 mg of dried and sieved (mesh No. 100) compost samples were weighed in a tin capsule for analysis, in accordance with the manufacturer's instructions (Perkin Elmer Company, 2005). All samples were kept desiccated, and the analyses were performed in triplicate.

2.2.4 Soluble reducing sugar determination

In an Erlenmeyer flask, 5 g of the sample was weighed, and 20 mL of distilled water was added. The flasks were agitated on an orbital shaker at 21 °C for 10 min at 300 rpm. The samples were then centrifuged for three min at 16000 × *g*. One mL of the supernatant was then extracted and analyzed for soluble reducing sugars (RS) using the DNS method (Miller *et al*., 1960). A volume of 1.5 mL of the DNS reagent was added to tubes containing 1 mL of the extract. The tubes were then placed in a boiling water bath for 10 min to develop color. Subsequently, the tubes were immersed in a cold-water bath, and the absorbance was read at 630 nm using a microplate reader (Elx808, BioTek).

2.2.5 Respirometric analysis

The compost samples were analyzed by respirometry in accordance with the procedure described by Martínez-Valdez *et al*. (2015) to quantify the production of CO_2 using a submerged system of packed-bed column bioreactors. The glass columns were filled with 30 g of compost, and the pH and humidity were not adjusted. During the analysis, a constant volumetric rate of 0.5 vkgm was maintained, and the analysis was performed over 48 h at 30 °C.

2.3 Molecular analysis techniques

The following techniques were used to perform PCR-DGGE analysis:

2.3.1 DNA extraction

DNA was extracted from biomass pellets (with a weight between 0.8 and 1.0 g) using a commercially available kit (PowerSoil® DNA Isolation Kit, MoBio Laboratories, Inc.). The integrity of the extracted DNA was evaluated through electrophoresis on a 1% agarose gel, which was run at 90 V for 40 min in 1X TAE buffer. The concentration and purity of the obtained DNA were determined spectrophotometrically (NanoDrop 2000, Thermo Scientific). Additionally, the A_{260}/A_{280} ratio was determined to assess its suitability for amplification reactions.

2.3.2 Nested PCR

Two distinct regions (for bacteria and fungi) were subjected to phylogenetic analysis. The 16S rDNA gene was amplified for the bacteria, followed by nested PCR of the V6-V8 region of the same gene. For fungi, the genomic region encoding the ribosomal RNA precursor, including the internal transcribed spacers ITS1 and ITS2, was initially amplified. Subsequently, the internal transcribed spacer 1 (ITS1) of this region was amplified by nested polymerase chain reaction (PCR).

To identify bacteria, 16S rDNA amplification was conducted in an endpoint thermocycler (Multigene, Labnet International, Inc.). The primers employed for the amplification process were 8F (5' AGA GTT TGA TCC TGG CTC AG 3') and 1492R (5' TAC GGT TAC CTT GTT ACG ACT T 3') (Forney *et al*., 2004). The reaction mixture included 1.5 mM $MgCl_2$, 200 μM of each dNTP (Promega Corporation USA), 10 pM of each primer, 1.5 U of GoTaq® Flexi DNA Polymerase (Promega Corporation USA) and 10-20 ng μL^{-1} of DNA template in 1X buffer. The amplification conditions were as follows: the initial denaturation phase was conducted for two min at 95 °C, followed by 25 cycles. Each cycle consisted of 30 s at 95 °C, 30 s at 50 °C for annealing, and one min at 72 °C for extension. A final extension step of five min at 72 °C was performed. The amplicons were subsequently subjected to analysis by 1% agarose gel electrophoresis (90 V, 45 min) stained with Texas Red® (Thermo Fisher Scientific). Following electrophoresis, the resulting bands were visualized under UV light using a transilluminator (Gel Logic 2200 Pro, Carestream Health, Inc.). Subsequent to the amplification of the 16S rDNA gene, nested PCR was performed to amplify the V6-V8 region with the previous product serving as the DNA template. The primers employed in this study were 1070F (5' ATG GCT GTC GTC AGC T 3') and 1392R+GC (5' GCC GCC CGC CCC GCG CCC GGC GCC GCC CCC GCC CCC C ACG GGC GGR GRG CT 3') (Burr *et al*., 2006) The amplification conditions followed those previously established for the amplification of the 16S rDNA gene, with the exception of the annealing temperature, which was elevated to 55 °C. As previously stated, the visualization of the amplicons was conducted. The purified products were obtained using a commercial kit in accordance with the protocol described by the supplier (Wizard® SV Gel and PCR Clean-Up System, Promega Corporation). Subsequently, the concentration of the products was determined through spectrophotometric analysis.

In order to identify the fungi present, a preliminary amplification reaction was conducted using the primers ITS1 (5' TCC GTA GGT GAA CCT GCG G 3') and ITS4 (5' TCC TCC GCT TAT TGA TAT GC 3') (White *et al*., 1990). The reaction mixture consisted of 1X PCR Super Master Mix (Biotools, B & M Labs, S.A.), 10 pM of each primer and 1-20 ng of template DNA. The amplification conditions were standardized as follows: an initial denaturation for 3 min at 95 °C, was followed by 30 cycles, each consisting of 30 s at 95 °C denaturation, 30 s at 60 °C annealing, 30 s at 72 °C extension, and a final extension for 2 min at 72 °C. The second amplification reaction was conducted using the previous products as template DNA with the primers ITS2 (5' GCT GCG TTC TTC ATC GAT GC 3') and ITS5+GC (5' CGC CCG CCG CGC GCG GCG GGC GGG GCG GGG GCA CGG GGG GAA GTA AAA GTC GTA ACA AGG 3'). The reaction mixture and amplification conditions were identical, with the exception of the annealing temperature, which was elevated to 65 °C.

2.3.3 DGGE analysis

The amplicon profiles were analyzed using a vertical electrophoresis chamber (DCode Universal Mutation Detection System, Bio-Rad Laboratories) on 7% acrylamide:bisacrylamide (37.5:1) with a parallel denaturing gradient, ranging from 30-65% for bacterial analysis and 25-55% for fungal analysis. The electrophoresis was conducted for 19 h at 60 °C and 80 V in 0.5X buffer (Neilson *et al*., 2013). Each gel lane was loaded with 100 ng of purified amplicons from nested-PCRs. Following electrophoresis, the acrylamide gels were silver stained using the technique described by Sanguinetti *et al*. (1994). The obtained gels were digitized using a photo documenter (MiniLumi, DNR Bio-Imaging Systems) and the band analysis was conducted using GelQuant software (DNR Bio-Imaging Systems). Subsequently, selected bands were excised and reamplified using the aforementioned primers, namely 1070F and 1392R for bacteria and ITS2 and ITS5 for fungi, respectively, in the absence of the –GC clamp. The amplification conditions were as previously described. The purified products were then subjected to further analysis using the Wizard® SV Gel and PCR Clean-Up System (Promega Corporation). After that, the samples were quantified and prepared for subsequent sequencing.

2.3.4 Sequencing and bioinformatic analysis

The purified samples were subsequently sent to Macrogen, Inc. (Seoul, Korea) for sequencing. Sequence analysis was conducted after the sequences were edited using the bioinformatics programs Clustal X V. 2.1 (http://www.clustal.org/clustal2/) and BioEdit V. 7.2 (https://thalljiscience.github.io/). The sequences were compared with the GenBank 16S rDNA and ITS1 gene databases using BLASTn, with uncultured/environmental sample sequences being excluded.

The nucleotide sequences included in this work were deposited under Bioproject PRJNA1047156 (accession numbers: KIDT00000000 for 16S rRNA and KIDU00000000 for ITS) as a Targeted Locus Study project in DDBJ/ENA/GenBank.

3 Results and discussion

3.1 Climatological conditions during compost sampling

The identification codes of the 15 samples and meteorological conditions during the sampling in BPCP in Mexico City are presented in Table 1. Four samples were collected in 2013, seven in 2014, and four in 2015. In terms of temporal distribution, samples were obtained from the four seasons of the year, with the highest frequency observed in summer and autumn. The average, maximum, and minimum temperatures, as well as the evaporation rate, were obtained from the database of the National Meteorological System of Mexico (SMN). The data were specifically extracted from the meteorological station of Nabor Carrillo Lake (Code C15383), situated in the Municipality of Texcoco de Mora (State of Mexico), approximately 5 km from the BPCP. The months with the highest rainfall were September 2013, October 2014, and May 2015, with 4.6, 4.9, and 4.4 mm m^{-2}, respectively. The minimum temperature for the months of sampling was maintained at intervals between 3.4 and 12 °C, the maximum temperature was between 22.2 °C (February 2015) and 27.5 °C (May 2013), and the average temperature recorded by the meteorological station was between 12.8 and 18.4 °C. It is noteworthy that in Mexico City, the period of lower rainfall occurs from December to April. During this period, precipitation levels decline, resulting in drier conditions (Table 1). In 2014, the BPCP implemented a modernization redesign in the composting process and a change in the location of the finished product for stabilization. Moreover, the final compost was placed in an open environment, which favored humidification due to rainfall during the rainy season and dehydration during the hot months. This resulted in differences in the final characteristics of the product. During the process of modifying the BPCP, a dome was constructed to maintain the maturity of the compost throughout the year.

3.2 Physicochemical and respirometric analysis of compost

The moisture content (in percent) of all compost samples ranged from 10.3 % ± 0.2 to 46.5 % ± 0.7, with notable fluctuations observed across different months of the year. The samples from March, May, and June of the three years (except for May 2014) exhibited lower moisture contents, while all the samples from September exhibited the highest moisture content. This high moisture content corresponded to the rainy season in Mexico City, as indicated in Table 1. According to the Mexican standard (NADF-020-AMBT-2011) (SEDEMA, 2011), the moisture content of the compost must be between 25 and 45 % by weight. Based on this parameter, it can be concluded that all the samples analyzed correspond to stable and good-quality compost. The concentration of soluble reducing sugars (RS) in the samples showed significant variations, regardless of the sampling month. The samples from March exhibited the highest concentration of reducing sugars, followed by those from May, which corresponded to the spring season. During this period, many of the organic residues found in the BPCP originated from fruits with high sugar contents.

Conversely, studies evaluate compost quality by determining maturity and stability, yet fail to clearly define the parameters to be used to determine these conditions (Azim *et al*., 2017; Olfa, 2013). Azim *et al*. (Azim *et al*., 2017) proposed a division into three categories, depending on the process stage. The initial category encompasses the proposed starting parameters, including the C/N ratio, moisture content, porosity, and particle size. The second category encompasses parameters that are monitored during the composting process, including temperature, oxygen consumption and CO_2 production, enzyme activities, and organic carbon. The third category assesses the quality of the final product by parameters such as the C/N ratio, humic substances, electrical conductivity (CEC), and salinity.

The effects of various factors, including pH, moisture content (%), the C/N ratio, reducing sugars, and CO_2 production rate, on the quality of the BPCP compost were analyzed (Table 2). The pH values of all samples were found to be between 8 and 9, indicating that all samples were obtained from composting piles that had reached an advanced stage of curing or stabilization (Barrena *et al*., 2009; Kumar Singh et al., 2009; Rastogi *et al*., 2020). The C/N ratio of each sample was less than 12, except for that of compost SEP14, which had a value of 13.6 ± 0.5. These results indicated that the compost in the sampled piles had already reached a stable stage, which corroborated with the findings of other authors (Guo *et al*., 2012; Xiao *et al*., 2009) and with the Mexican standard NADF-020-AMBT-2011 (SEDEMA, 2011).

Regarding the maximum CO_2 production rate (Table 2), all samples exhibited values within the range of 0.01 ± 0.001 and 3.48 ± 0.32 mg CO_2 g^{-1} IDM h^{-1}. The moisture content (%), pH, C/N ratio and CO_2 production rate of all the samples studied were within the limits for stable compost according to the local and international standards of the NADF-020-AMBT-2011 (SEDEMA, 2011) and US Composting Council (US Composting Council, 2023). Furthermore, no significant differences were found between the BPCP compost samples. The results presented indicate that the technical modifications implemented in the BPCP during 2014 were effective in maintaining the quality of the compost obtained.

Table 2. Physicochemical analysis and maximum CO_2 production rate of compost samples from BPCP in Mexico City.

Year	Sample code	Moisture (%)	pH	C/N ratio	Reducing sugars (mg g^{-1} IDM)	Maximum CO_2 production rate (mg CO_2 g^{-1} IDM h^{-1})
2013	May-13	12.6 ± 0.3	8.2 ± 0.1	9.5 ± 0.4	4.0 ± 0.2	0.03 ± 0.01
	Sep-13	38.9 ± 1.1	8.9 ± 0.0	11.7 ± 0.5	1.0 ± 0.2	2.92 ± 0.03
	Oct-13	36.0 ± 1.9	8.9 ± 0.1	8.5 ± 0.2	0.6 ± 0.1	0.09 ± 0.01
2014	Feb-14	18.5 ± 1.0	8.7 ± 0.2	9.8 ± 0.4	0.6 ± 0.1	0.51 ± 0.06
	Mar-14	11.2 ± 0.3	8.4 ± 0.2	9.7 ± 0.3	6.0 ± 0.1	0.05 ± 0.01
	May-14	30.5 ± 0.6	8.8 ± 0.2	8.1 ± 0.1	4.0 ± 0.3	0.02 ± 0.01
	Jul-14	10.5 ± 0.3	8.9 ± 0.1	8.9 ± 0.1	0.4 ± 0.0	0.02 ± 0.01
	Sep-14	46.5 ± 0.7	8.4 ± 0.0	13.6 ± 0.5	3.1 ± 0.1	3.48 ± 0.32
	Oct-14	16.3 ± 0.3	8.5 ± 0.1	9.4 ± 0.9	1.9 ± 0.1	0.01 ± 0.01
	Nov-14	18.3 ± 0.3	8.5 ± 0.1	9.2 ± 0.2	2.2 ± 0.2	1.20 ± 0.02
2015	Feb-15	15.0 ± 0.3	8.7 ± 0.0	9.1 ± 0.2	1.0 ± 0.1	0.04 ± 0.01
	Mar-15	12.0 ± 0.4	8.7 ± 0.2	9.3 ± 0.2	5.9 ± 0.6	0.01 ± 0.01
	May-15	11.3 ± 0.6	8.9 ± 0.0	10.4 ± 0.4	3.5 ± 0.4	0.03 ± 0.01
	SEP15	28.6 ± 1.0	8.9 ± 0.1	9.0 ± 0.2	0.6 ± 0.1	1.23 ± 0.02

Table 3. Bacteria identified from BPCP in Mexico City. The asterisk indicates the samples in which each of the bacteria was detected. The percentage of identity is expressed in comparison to the NCBI database.

Microorganism	Identity (%)	Sample code														
		2013					2014					2015				
		MAR	MAY	SEP	OCT	FEB	MAR	MAY	JUL	SEP	OCT	NOV	FEB	MAR	MAY	SEP
Acinetobacter albensis (2)	100	*	*		*	*	*					*	*	*	*	
Acinetobacter equi (2)	> 98.7	*	*	*	*	*	*									*
Acinetobacter johnsonii (12)	> 99.4	*	*	*	*	*	*	*	*	*	*	*	*	*	*	*
Acinetobacter sp. *(12)*	> 96.6	*	*	*	*	*	*	*	*	*	*	*	*	*	*	*
Bacillus benzevorans	99	*	*	*	*	*	*	*	*	*	*	*	*	*	*	*
Bacillus sp.	95.7	*	*	*	*	*	*	*	*	*	*	*	*	*	*	*
Cutibacterium sp.	97.7	*	*	*	*	*	*	*	*	*	*	*	*	*	*	*
Porticoccus sp.	96	*	*	*	*	*	*	*	*	*	*	*	*	*	*	*
Pseudomonas sp.	98.2	*	*	*	*	*	*	*	*	*	*	*	*	*	*	*
Saccharopolyspora sp.	97.1	*	*					*	*							
Variovorax sp.	95.1			*	*	*	*					*	*	*	*	*
Xanthomonas sp.	96	*														

3.3 Analysis of bacterial communities by PCR DGGE

High-molecular-weight DNA was successfully extracted from all samples, with an absorbance ratio (A_{260}/A_{280}) close to 1.8, indicating that the DNA was relatively pure (Wilfinger et al., 1997). According to the primers used, the fragments obtained via nested PCR had an approximate length of 300 bp (Piterina & Pembroke, 2013). The bacterial profiles of the different compost samples obtained during the three years were studied. Image analysis (Figure 1S, supplementary material) yielded 233 total bands distributed among the 15 compost samples. A total of 59 bands were selected and cut based on their ease of cutting, representativeness, and intensity as observed during the development of the gel (Figure 1S, supplementary material). Following the bioinformatic analysis, data was obtained from 36 operational taxonomic units (OTUs), corresponding to 61% of the selected bands.

One of the most crucial aspects of studying composting from a microbial perspective is the diversity of fungi and bacteria present in piles during the composting process. This diversity is crucial for the degradation of organic matter. Consequently, considerable effort has been invested in recent years to study these microorganisms with the objective of enhancing their degradation efficiency (Maeda *et al*., 2010; Rastogi *et al*., 2020).

Studies of microbial diversity constitute a sound experimental strategy. Nevertheless, diversity is frequently constrained by the quantity and quality of organic matter available for compost production. This in turn is influenced by the physicochemical characteristics of the compost at the end of the composting process (Francou *et al*., 2007; Rastogi *et al*., 2020). Table 3 presents the bacteria identified in this study. Some of the sequences analyzed exhibited a percentage of identity above 98.5 %, indicating that they could be assigned to the species level. In contrast, the remaining sequences exhibited a percentage of identity below the species level threshold, and thus could only be assigned to the genus level. The compost samples exhibited a similar diversity, except for those obtained in 2014, which exhibited a notable decline in the number of bacteria present. This decline can be attributed to the disturbances that occurred during the redesign of the BPCP, which affected the microbial diversity but not the final stability and maturity characteristics of the compost.

Some identified bacteria were intermittently present, including *Saccharopolyspora* sp. (previously known as *Streptomyces* sp.), which has an industrial application in the production of erythromycin and has frequently been found in soil (Saygin *et al*., 2021), and *Variovorax* sp., which produces octopin, a chemical compound related to the formation of tumors in the roots of some plants (Han *et al*., 2016) and to the degradation of phthalates, which are compounds added to plastics to increase their flexibility (Prasad & Suresh, 2012). This issue may be related to the presence of plastics of different types mixed with the organic matter that is destined for composting. During the separation of the municipal solid waste, the plastic materials are not completely removed from the organic fraction of the municipal solid waste. Seven of the 12 identified bacteria (*Acinetobacter johnsonii*, *Bacillus benzoevorans*, *Acinetobacter* sp., *Bacillus* sp., *Cutibacterium* sp., *Porticoccus* sp. and *Pseudomonas* sp.) were found in all the compost samples, which may suggest that these bacteria are very well adapted and established in the BPCP ecosystem and play an essential role in the degradation of the organic matter. The presence of these genera has also been reported in compost derived from a variety of materials (Aydin *et al*., 2015; Bouhia *et al*., 2022; Horisawa *et al*., 2008; Sundberg *et al*., 2011; Zhang *et al*., 2014). This is likely due to their ability to produce hydrolytic enzymes, including hemicellulases, cellulases, proteases, and lipases (Table 4), which are closely related to organic matter degradation.

Table 4. Major characteristics of the bacteria identified in the BPCP in Mexico City.

Microorganism	Origin and enzyme production	References
Acinetobacter albensis	Isolated from bodies of water, surfaces of stored fish, and commonly found in soil. Produce proteases.	Al Atrouni *et al*., 2016; Kaszab *et al*., 2021; Krizova *et al*., 2015
Acinetobacter equi	Horse faeces and soil. Bacteria capable of reducing nitrates, utilizing L-arabinose, caproate, malate, citrate and producing organic acids from D-glucose.	Al Atrouni *et al*., 2016; Poppel *et al*., 2016
Acinetobacter johnsonii	Isolated from activated sludge, bodies of water, . stored fish, wastewater, soils contaminated with pesticides, food and compost	Al Atrouni *et al*., 2016; Kaszab *et al*., 2021
Acinetobacer spp.	Water, soil, meat, fish, shrimp, sediments, plant nectar, animals, farms, biogas plants, aerobic digesters and contaminated soils.	Al Atrouni *et al*., 2016; Pulami *et al*., 2023
Bacillus benzoevorans	Isolated from soils, landfills. Degradation of phenolic compounds, hemicellulases, laccases, ammonium, and sulfate-reducing enzymes.	Madani *et al*., 2021
Bacillus sp.	Isolated from soil, water, decomposing plant material, industrial and extreme environments. Used in inoculum for the degradation of plant organic matter. Herbicide degrader produces α-amylases, alkaline proteases, lipases, cellulases.	Qian *et al*., 2023; G. Zhao *et al*., 2023
Cutibacterium sp.	Present in the rhizosphere of healthy soils. The presence of phytopathogenic fungi stimulates its presence in diseased soils.	T. Lin *et al*., 2023
Porticoccus sp.	Found in mangrove sediments, a phenanthrene and hydrocarbon-degrading microorganism.	Gao *et al*., 2022; Tiralerdpanich *et al*., 2021
Pseudomonas sp.	Degradation of aromatic hydrocarbons, phenols, plant growth-promoting rhizobacteria (PGPR), biocontrol, plant and animal pathogen, isolated from soil and compost. Cellulases and lipases.	Azhdarpoor *et al*., 2014
Saccharopolyspora sp.	Isolated from soil. Some species can degrade complex polymers such as starch and xylan. Antibiotic production.	Oliynyk *et al*., 2007; Saygin *et al*., 2021
Variovorax sp.	Isolated from soil. Capable of degrading phthalates, polylactic acid, polyhydroxyalkanoates. Produces cellulases, proteases.	Han *et al*., 2016; Prasad & Suresh, 2012
Xanthomonas sp.	Plant pathogen, soil isolates, insect gut isolates. Degradation and bioconversion of polyurethane (polyacrylic, polyester and polyether).	Kim *et al*., 2022; Rahman *et al*., 2014

Acinetobacter equi was present in all the samples collected between March 2013 and March 2014. It was subsequently identified in a sample collected in September. *Acinetobacter* spp. is worthy of particular attention, given that they have been isolated from a variety of compost samples (Sundberg *et al*., 2011). They have been reported to be a bacterium capable of degrading oils and acting as an adjuvant in the bioremediation of soils (C. Lin *et al*., 2022; Van Gestel *et al*., 2003). Additionally, they can partially degrade low-molecular-weight polyethylene oligomers, a precursor material for plastics. This genus has been identified in a considerable number of the different OTUs selected (27 in total), potentially due to the variable number of copies of the ribosomal operon per bacterial genome, which can range from one to 15 copies, with seven copies observed in the case of *Acinetobacter* sp. (del Rosario Rodicio & del Carmen Mendoza, 2004) as the copies differ in sequence, they can be detected as different OTUs.

Given the paucity of studies in this area, a comparison with the only available work in which the microbial diversity of the BPCP was analyzed is essential to contextualize our findings, despite the evident differences in terms of temporality and sample type (mature compost vs. leachates) and in the microbial groups analyzed (bacteria and fungi vs. bacteria and archaea). The finding that, in both cases,

the presence of bacteria of the genus *Acinetobacter* was found in higher proportion in all samples analyzed (Gállego Bravo *et al*., 2019) is of particular interest.

3.4 Analysis of fungal communities by PCR DGGE

Figure 2S (supplementary material) presents the DGGE profiles for fungi obtained for each of the compost samples under study. A total of 52 OTUs were selected from 250 bands identified by the GelQuant program. A total of 24 OTUs were identified, although in some instances, the same information was provided by different OTUs due to the DGGE technique detecting mutations that may result in changes to the position of the bands detected in comparison to wild types (Strathdee & Free, 2013). Table 5 presents the identified fungi in each compost sample, including the identity (%) for each of the sequences analyzed. Similarly, as in the analysis of bacteria, fungi could be assigned at the species level following the attainment of a percentage of identity exceeding 98.5 %. Conversely, those samples exhibiting lower values below the genus level were assigned. Three fungal species were consistently detected in all samples, namely *Botryotrichum* sp., *Metarhizium anisopliae* and *Peniophora* sp. In contrast, the remaining fungal species exhibited intermittent detection. Some fungi were detected at three consecutive sampling times, while others were not. This was the case for *Aspergillus niger* and *Thermomyces dupontii,* which appeared in the same samples. *Preussia* sp. was not detected in the initial samples. It was first observed in the NOV14 sample, after which it was consistently present in all subsequent samples. Its appearance may be associated with the modernization and standardization of the composting process that occurred in 2014, as previously mentioned. In the three samples collected in March, the following fungi were detected: *Aspergillus flavus, Botryotrichum* sp.*, Metharhizium anisopliae, Peniophora* sp., and *Scopulariopsis* sp. This indicates that some of the previously identified fungi persisted. Table 6 provides a detailed description of the major characteristics of the identified fungi. Regarding their provenance, numerous reports have indicated that a significant proportion of these fungi have been identified in soil, as part of the wider ecosystem, or as plant endophytes. Nevertheless, research has indicated that these fungi can cause disease in plant species, including *Aspergillus flavus*, *Exophiala* sp., *Fusarium* sp. and *Scopulariopsis* sp. All the fungi identified in this study have been extensively studied as producers of extracellular hydrolytic enzymes, which are related to organic matter degradation. This is because they are found in sites with abundant organic matter that can be used as a carbon and nitrogen source. Some fungal genera warrant particular attention, including *Aspergillus niger*, *Diutina rugosa* and *Thermomyces dupontii*. These have been extensively studied and present biotechnological potential for use in several industrial sectors (Christopher *et al*., 2005; C. Lin *et al*., 2022; Sonia *et al*., 2005).

Conclusions

Our results contribute to understand the dynamics of microbial communities in complex systems such as composting. It is important to note that the stability of microbial communities in plants or sites operated for long periods is a phenomenon that is influenced by different environmental factors and operational variables such as turning, aeration, humidity and temperature control, among other factors. This makes some of these sites subject to constant disturbances.

Table 5. Identified fungi in each of the samples obtained from the BPCP in Mexico City. An asterisk indicates the samples in which each of the fungi was detected. The percentage of identity is expressed in comparison to the NCBI database.

Microorganism	Identity (%)	Sample														
		2013					2014						2015			
		MAR	MAY	SEP	OCT	FEB	MAR	MAY	JUL	SEP	OCT	NOV	FEB	MAR	MAY	SEP
Aspergillus flavus (3)	> 98.8	*		*	*	*	*	*	*	*		*	*	*	*	*
Aspergillus niger (1)	100	*	*	*		*	*	*		*	*	*	*			*
Botryotrichum sp. (3)	> 97.6	*	*	*	*	*	*	*	*	*	*	*	*	*	*	*
Diutina rugosa (3)	> 98.5	*		*						*	*		*	*	*	
Exophiala sp.	95.2			*			*			*			*	*		*
Exserohilum rostratum	98.4			*								*	*		*	
Fusarium sp.	100	*			*	*				*						
Gymnascella aurantiaca	97.8		*				*	*	*						*	
Metarhizium anisopliae	100	*	*	*	*	*	*	*	*	*	*	*	*	*	*	*
Peniophora sp. (3)	>98.4	*	*	*	*	*	*	*	*	*	*	*	*	*	*	*
Pichia kudriavzevii	99.4	*		*						*	*					*
Preussia sp.	95.2											*	*	*	*	*
Scopulariopsis sp.	97.9	*	*	*	*	*	*			*		*	*	*	*	*
Thermomyces dupontii (2)	> 98.8	*	*	*		*	*	*		*	*	*	*			*
Thermomyces sp.	98.2		*				*	*	*						*	

Table 6. Major characteristics of the fungi identified in the BPCP of Mexico City in this study.

Microorganism	Origin and enzyme production	References
Aspergillus flavus	Isolated from soil. Plant pathogen. Produces aflatoxins, polygalacturonases, laccases and xylanases.	(de Alencar Guimaraes *et al*., 2013)
Aspergillus niger	Soil fungus used in second-generation biofuel production. Hemicellulases, pectinases and xylanases.	(Gomes *et al*., 2011)
Botryotrichum sp.	Isolated from pig manure compost, heavy metal passivation produces cellulases. Antibiotic synthesis in compost.	(Wu *et al*., 2022; B. Zhao *et al*., 2023)
Diutina rugosa	Production and immobilization of lipases; isolated from soil and oral cavities.	(Barton, 2011)
Exophiala sp.	Aquatic environments, pathogen of aquatic plants and animals. Chitinases and keratinases.	(do Nascimento *et al*., 2016)
Exserohilum rostratum	Endophyte of orchids, causing mycosis in humans.	(Chua *et al*., 2022)
Fusarium sp.	Isolated from plants and soil, plant pathogens and endophytes. Cellulases and hemicellulases.	(Chua *et al*., 2022; Kashiwa *et al*., 2017)
Gymnascella aurantiaca	Isolated from soil. Production of keratinases.	(Scott & Untereiner, 2004)
Metarhizium anisopliae	Entomopathogen of plants, found in soil. Produces lipases, hemicellulases.	(Aw & Hue, 2017)
Peniophora sp.	Isolated from wood, plant pathogen. Produces hemicellulases, cellulases.	(Lee *et al*., 2015)
Pichia kudriavzevii	Yeast isolated from fermented fruits. Used for second-generation bioethanol production.	(Hoppert *et al*., 2022)
Preussia sp.	Present in soil, activator of nitrogen variation inside cow manure compost. Producer of phytohormones, phosphatases and glucosidases.	(Khan *et al*., 2016; Sun *et al*., 2022)
Scopulariopsis sp.	Soil, plant material and insects; wheat cultivation fields and soil, plant pathogen. Produces cellulases, keratinases and chitinases.	(Sharaf & Khalil, 2011; Skóra *et al*., 2014)
Thermomyces dupontii	Soil, compost; plant pathogen. Produces chitinases, glucosidases and xylanases.	(Nisar *et al*., 2022)
Thermomyces sp.	Soil; production of xylanase, hemicellulases, lipases enzymes.	(Sun *et al*., 2022)

Furthermore, the composition of municipal solid waste in large cities such as Mexico City and its Metropolitan Zone is characterized by significant heterogeneity, resulting from a combination of socioeconomic, demographic and seasonal factors. All the samples collected were found to meet the criteria for classification as stable compost according to Mexican and international standards. A total of 111 operational taxonomic units (OTUs) were identified in 15 compost samples. Eight bacterial genera and 15 fungal genera were observed, suggesting a greater fungal diversity than bacterial diversity. Nine microorganisms (*Acinetobacter* spp., *Bacillus* sp., *Cutibacterium* sp., *Pseudomonas* sp., *Porticoccus* sp., *Botryotrichum* sp., *Metarhizium anisopliae* and *Peniophora* sp.) were present in all the samples, indicating that these microorganisms are adapted and distributed in that ecosystem. All the identified microorganisms exhibited enzymatic activities related to organic matter degradation, with a clear preference for plant-derived substrates.

Acknowledgements

The authors would like to express their gratitude to the National Council of Humanities, Science and Technology (CONAHCyT, Mexico) for scholarship number 280485 granted to LMM and for funding project number 215467. Special thanks to the staff of the Bordo Poniente Composting Plant (BPCP, West Rim Composting Plant) in Mexico City for providing facilities for sample collection and to Alejandra Serrato Ph.D. (†), from the Divisional Laboratory of Molecular Biology at UAM-I, for her invaluable contributions to the techniques employed. This work is dedicated to her memory.

Nomenclature

16S rDNA	Ribosomal 16S RNA gene
1X	Final stock concentration
A_{260}/A_{280}	Absorbance ratio
BLAST	Basic Local Alignment Search Tool

BPCP	Bordo Poniente Composting Plant (West Rim Composting Plant)
C/N	Carbon/Nitrogen ratio
DGGE	Denaturing gradient gel electrophoresis
DNA	Deoxyribonucleic acid
DNS	Dinitro salicylic acid
DM	Dry matter
$\times g$	Gravity
IDM	Initial dry matter
ITS	Internal transcribed spacer
NCBI	National Center for Biotechnology Information
OTU	Operational taxonomic unit
OSW	Organic solid waste
RS	Reducing sugars
t	Metric ton (1000 kg)
TAE	Tris-acetate-EDTA
TMECC	Test methods for the examination of composting and compost

References

Al Atrouni, A., Joly-Guillou, M.-L., Hamze, M., & Kempf, M. (2016). Reservoirs of non-*baumannii Acinetobacter* species. *Frontiers in Microbiology*, *7*. https://doi.org/10.3389/fmicb.2016.00049

Aw, K. M. S., & Hue, S. M. (2017). Mode of infection of *Metarhizium* spp. fungus and their potential as biological control agents. *Journal of Fungi*, *3*(2), 30. https://doi.org/10.3390/jof3020030

Aydin, S., Shahi, A., Ozbayram, E. G., Ince, B., & Ince, O. (2015). Use of PCR-DGGE based molecular methods to assessment of microbial diversity during anaerobic treatment of antibiotic combinations. *Bioresource Technology*, *192*, 735–740. https://doi.org/10.1016/j.biortech.2015.05.086

Azhdarpoor, A., Mortazavi, B., & Moussavi, G. (2014). Oily wastewaters treatment using *Pseudomonas* sp. isolated from the compost fertilizer. *Journal of Environmental Health Science and Engineering*, *12*(1). https://doi.org/10.1186/2052-336x-12-77

Azim, K., Soudi, B., Boukhari, S., Perissol, C., Roussos, S., & Thami Alami, I. (2017). Composting parameters and compost quality: a literature review. *Organic Agriculture*, *8*(2), 141–158. https://doi.org/10.1007/s13165-017-0180-z

Barrena, R., d'Imporzano, G., Ponsá, S., Gea, T., Artola, A., Vázquez, F., Sánchez, A., & Adani, F. (2009). In search of a reliable technique for the determination of the biological stability of the organic matter in the mechanical–biological treated waste. *Journal of Hazardous Materials*, *162*(2–3), 1065–1072. https://doi.org/10.1016/j.jhazmat.2008.05.141

Barton, R. C. (2011). *Candida rugosa*: a new fungal pathogen emerging, but from where? *Journal of Medical Microbiology*, *60*(3), 265–266. https://doi.org/10.1099/jmm.0.029199-0

Bouhia, Y., Hafidi, M., Ouhdouch, Y., El Boukhari, M. E. M., El Fels, L., Zeroual, Y., & Lyamlouli, K. (2022). Microbial community succession and organic pollutants removal during olive mill waste sludge and green waste co-composting. *Frontiers in Microbiology*, *12*. https://doi.org/10.3389/fmicb.2021.814553

Burr, M. D., Clark, S. J., Spear, C. R., & Camper, A. K. (2006). Denaturing gradient gel electrophoresis can rapidly display the bacterial diversity contained in 16S rDNA clone libraries. *Microbial Ecology*, *51*(4), 479–486. https://doi.org/10.1007/s00248-006-9050-z

Castilla-Hernández, P., Cárdenas-Medina, K., Hernández-Fydrych, V., Fajardo-Ortiz, C., & Meraz-Rodríguez, M. (2016). Compost leachates treatment in a two-phase acidogenic-methanogenic system for biofuels production. *Revista Mexicana de Ingeniería Química*, 15(1), 175–183.

Chen, M., Lan, X., Zhu, L., Ru, P., Liu, H., & Xu, W. (2023). Nucleic acid-aided molecular amplification techniques for food microorganism detection. *TrAC Trends in Analytical Chemistry*, *165*, 117116. https://doi.org/10.1016/j.trac.2023.117116

Christopher, L., Bissoon, S., Singh, S., Szendefy, J., & Szakacs, G. (2005). Bleach-enhancing abilities of *Thermomyces lanuginosus* xylanases produced by solid state fermentation. *Process Biochemistry*, *40*(10), 3230–3235. https://doi.org/10.1016/j.procbio.2005.03.027

Chua, R. W., Song, K. P., & Ting, A. S. Y. (2022). Antimicrobial activities and phytochemical screening of endophytic fungi isolated from *Cymbidium* and *Dendrobium* orchids. *South African Journal of Botany*, *151*, 909–918. https://doi.org/10.1016/j.sajb.2022.11.015

de Alencar Guimaraes, N. C., Sorgatto, M., Peixoto-Nogueira, S. de C., Betini, J. H.

A., Zanoelo, F. F., Marques, M. R., de Moraes Polizeli, M. de L. T., & Giannesi, G. C. (2013). Bioprocess and biotechnology: effect of xylanase from *Aspergillus niger* and *Aspergillus flavus* on pulp biobleaching and enzyme production using agroindustrial residues as substract. *SpringerPlus*, *2*(1). https://doi.org/10.1186/2193-1801-2-380

del Rosario Rodicio, M., & del Carmen Mendoza, M. (2004). Identificación bacteriana mediante secuenciación del ARNr 16S: fundamento, metodología y aplicaciones en microbiología clínica. *Enfermedades Infecciosas y Microbiología Clínica*, *22*(4), 238–245. https://doi.org/10.1016/s0213-005x(04)73073-6

do Nascimento, M. M. F., de Hoog, G. S., Gomes, R. R., Furuie, J. L., Gelinski, J. M. L., Najafzadeh, M. J., Boeger, W. A. P., & Vicente, V. A. (2016). Shared physiological traits of *Exophiala* species in cold-blooded vertebrates, as opportunistic black yeasts. *Mycopathologia*, *181*(5–6), 353–362. https://doi.org/10.1007/s11046-016-0001-z

Estrada-Martínez, R., Carrillo-Sancen, G., Cerón-Montes, G. I., Garrido-Hernández, A., & Martínez-Valdez, F. J. (2021). Mathematical modeling for monitoring and controlling aerobic degradation conditions of the organic fraction of urban solid waste. *Revista Mexicana de Ingeniería Química*, *20*(3), 1–20. https://doi.org/10.24275/rmiq/IA2479

Forney, L., Zhou, X., & Brown, C. (2004). Molecular microbial ecology: land of the one-eyed king. *Current Opinion in Microbiology*, *7*(3), 210–220. https://doi.org/10.1016/j.mib.2004.04.015

Francou, C., Le Villio-Poitrenaud, M., & Houot, S. (2007). Influence de la nature des déchets compostés sur la vitesse de stabilization de la matière organique au cours du compostage. *Techniques Sciences Méthodes*, *5*, 35–43. https://doi.org/10.1051/tsm/200705035

Gállego Bravo, A.K., Salcedo Serrano, D.A., López Jiménez, G., Nirmalkar, K., Murugesan, S., García-Mena, J., Gutiérrez Castillo, M.E., & Tovar Gálvez, L.R. (2019). Microbial profile of the leachate from Mexico City's Bordo Poniente Composting Plant: an inoculum to digest organic waste. *Energies,* 12, 2343. https://doi.org/10.3390/en12122343

Gan, J., Montaño, G., Fajardo, C., Meraz, M., & Castilla, P. (2013). Anaerobic co-treatment of leachates produced in a biodegradable urban solid waste composting plant in Mexico City. *Revista Mexicana de Ingeniería Química*, 12(3), 541–551.

Gao, Y., Yuan, L., Du, J., Wang, H., Yang, X., Duan, L., Zheng, L., Bahar, M. M., Zhao, Q., Zhang, W., Liu, Y., Fu, Z., Wang, W., & Naidu, R. (2022). Bacterial community profile of the crude oil-contaminated saline soil in the Yellow River Delta Natural Reserve, China. *Chemosphere*, *289*, 133207. https://doi.org/10.1016/j.chemosphere.2021.133207

García-Uitz, K., Cruz, J.C., León-Pech, M.G., Moreno-Andrade, I., Giácoman-Vallejos, G., & Ponce-Caballero, C. (2024). Isolation and characterization of microbial diversity in phenanthrene-degrading consortia in a pollution zone in Ciudad del Carmen, Mexico. *Revista Mexicana de Ingeniería Química*, 23(2), Bio24241. https://doi.org/10.24275/rmiq/Bio24241

Gomes, J., Zeni, J., Cence, K., Toniazzo, G., Treichel, H., & Valduga, E. (2011). Evaluation of production and characterization of polygalacturonase by *Aspergillus niger* ATCC 9642. *Food and Bioproducts Processing*, *89*(4), 281–287. https://doi.org/10.1016/j.fbp.2010.10.002

Guo, R., Li, G., Jiang, T., Schuchardt, F., Chen, T., Zhao, Y., & Shen, Y. (2012). Effect of aeration rate, C/N ratio and moisture content on the stability and maturity of compost. *Bioresource Technology*, *112*, 171–178. https://doi.org/10.1016/j.biortech.2012.02.099

Han, S.-R., Lee, J.-H., Kang, S., Park, H., & Oh, T.-J. (2016). Complete genome sequence of opine-utilizing *Variovorax* sp. strain PAMC28711 isolated from an Antarctic lichen. *Journal of Biotechnology*, *225*, 46–47. https://doi.org/10.1016/j.jbiotec.2016.03.042

Hoppert, L., Kölling, R., & Einfalt, D. (2022). Investigation of stress tolerance of *Pichia kudriavzevii* for high gravity bioethanol production from steam–exploded wheat straw hydrolysate. *Bioresource Technology*, *364*, 128079. https://doi.org/10.1016/j.biortech.2022.128079

Horisawa, S., Sakuma, Y., Nakamura, Y., & Doi, S. (2008). Profiling of a microbial community under confined conditions in a fed-batch garbage decomposer by denaturing gradient gel electrophoresis. *Bioresource Technology*, *99*(8), 3084–3093. https://doi.org/10.1016/j.biortech.2007.05.054

Jimenez-Rodriguez, J. E., Martínez-Valdez, F. J., Estrada-Martínez, R., Monrroy-Hermosillo, O., Saucedo-Castañeda, G., & Ramirez-Vives, F. (2020). Effect of incubation conditions on the aerobic pretreatment of the organic solid wastes and the volatile fatty acids production. *Revista Mexicana de Ingeniería Química, 19*(3), 1027–1040. https://doi.org/10.24275/rmiq/Bio849

Kashiwa, T., Kozaki, T., Ishii, K., Turgeon, B. G., Teraoka, T., Komatsu, K., & Arie, T. (2017). Sequencing of individual chromosomes of plant pathogenic *Fusarium oxysporum*. *Fungal Genetics and Biology*, *98*, 46–51. https://doi.org/10.1016/j.fgb.2016.12.001

Kaszab, E., Farkas, M., Radó, J., Micsinai, A., Nyírő-Fekete, B., Szabó, I., Kriszt, B., Urbányi, B., & Szoboszlay, S. (2021). Novel members of bacterial community during a short-term chilled storage of common carp (*Cyprinus carpio*). *Folia Microbiologica*, *67*(2), 299–310. https://doi.org/10.1007/s12223-021-00935-4

Khan, A. L., Asaf, S., Khan, A. R., Al-Harrasi, A., Al-Rawahi, A., & Lee, I.-J. (2016). First draft genome sequencing of indole acetic acid producing and plant growth promoting fungus *Preussia* sp. BSL10. *Journal of Biotechnology*, *225*, 44–45. https://doi.org/10.1016/j.jbiotec.2016.03.025

Kim, J.-H., Choi, S. H., Park, M. G., Park, D. H., Son, K.-H., & Park, H.-Y. (2022). Biodegradation of polyurethane by Japanese carpenter bee gut-associated symbionts *Xanthomonas* sp. HY-71, and its potential application on bioconversion. *Environmental Technology & Innovation*, *28*, 102822. https://doi.org/10.1016/j.eti.2022.102822

Krizova, L., Maixnerova, M., Sedo, O., & Nemec, A. (2015). *Acinetobacter albensis* sp. nov., isolated from natural soil and water ecosystems. *International Journal of Systematic and Evolutionary Microbiology*, *65*(Pt_11), 3905–3912. https://doi.org/10.1099/ijsem.0.000511

Kumar Singh, Y., Kalamdhad, A. S., Ali, M., & Kazmi, A. A. (2009). Maturation of primary stabilized compost from rotary drum composter. *Resources, Conservation and Recycling*, *53*(7), 386–392. https://doi.org/10.1016/j.resconrec.2009.02.004

Lee, H., Jang, Y., Lee, Y. M., Lee, H., Kim, G.-H., & Kim, J.-J. (2015). Enhanced removal of PAHs by *Peniophora incarnata* and ascertainment of its novel ligninolytic enzyme genes. *Journal of Environmental Management*, *164*, 10–18. https://doi.org/10.1016/j.jenvman.2015.08.036

Lin, C., Cheruiyot, N. K., Bui, X.-T., & Ngo, H. H. (2022). Composting and its application in bioremediation of organic contaminants. *Bioengineered*, *13*(1), 1073–1089. https://doi.org/10.1080/21655979.2021.2017624

Lin, T., Li, L., Gu, X., Owusu, A. M., Li, S., Han, S., Cao, G., Zhu, T., & Li, S. (2023). Seasonal variations in the composition and diversity of rhizosphere soil microbiome of bamboo plants as infected by soil-borne pathogen and screening of associated antagonistic strains. *Industrial Crops and Products*, *197*, 116641. https://doi.org/10.1016/j.indcrop.2023.116641

Loreto-Muñoz, C.D., López-Avilés, G., De la Cruz-Leyva, M.C., Martin-García, A.R., & Almendariz-Tapia F.J. (2024). Sulfidogenic activity related to microbial diversity in a biological system employed for sulfate-rich wastewater treatment. *Revista Mexicana de Ingeniería Química*, 23(1), IA24167. https://doi.org/10.24275/rmiq/IA24167

Madani, R. M., Liang, J., Cui, L., Zhang, D., Otitoju, T. A., Elsalahi, R. H., & Song, X. (2021). Novel simultaneous anaerobic ammonium and sulfate removal process: A review. *Environmental Technology & Innovation*, *23*, 101661. https://doi.org/10.1016/j.eti.2021.101661

Maeda, K., Hanajima, D., Morioka, R., & Osada, T. (2010). Characterization and spatial distribution of bacterial communities within passively aerated cattle manure composting piles. *Bioresource Technology*, *101*(24), 9631–9637. https://doi.org/10.1016/j.biortech.2010.07.057

Martínez-Valdez, F. J., Martínez-Ramírez, C., Martínez-Montiel, L., Favela-Torres, E., Soto-Cruz, N. O., Ramírez-Vives, F., & Saucedo-Castañeda, G. (2015). Rapid mineralisation of the organic fraction of municipal solid waste. *Bioresource Technology*, *180*, 112–118. https://doi.org/10.1016/j.biortech.2014.12.083

Miller, G. L., Blum, R., Glennon, W. E., & Burton, A. L. (1960). Measurement of carboxymethylcellulase activity. *Analytical Biochemistry*, *1*(2), 127–132. https://doi.org/10.1016/0003-2697(60)90004-x

Neilson, J. W., Jordan, F. L., & Maier, R. M. (2013). Analysis of artifacts suggests DGGE should not be used for quantitative diversity analysis. *Journal of Microbiological Methods*, *92*(3), 256–263. https://doi.org/10.1016/j.mimet.2012.12.021

Nisar, K., Abdullah, R., Kaleem, A., Iqtedar, M., Aftab, M., & Saleem, F. (2022). Purification, characterization and thermodynamic analysis of cellulases produced from *Thermomyces dupontii* and its industrial applications. *Saudi Journal of Biological Sciences*, *29*(12), 103483. https://doi.org/10.1016/j.sjbs.2022.103483

Noor, R. S., Shah, A. N., Tahir, M. B., Umair, M., Nawaz, M., Ali, A., Ercisli, S., Abdelsalam, N. R., Ali, H. M., Yang, S. H., Ullah, S., & Assiri, M. A. (2024). Recent trends and advances in additive-mediated composting technology for agricultural waste resources: A comprehensive review. *ACS Omega*, *9*(8), 8632–8653. https://doi.org/10.1021/acsomega.3c06516

Noyola, A., Hernández, B., Paredes, R., & Ayala, C. (2014). *Inventario de residuos sólidos de la Ciudad de México*.

Olfa, F. (2013). The maturity tests during the composting of municipal solid wastes. *Resources, Conservation and Recycling*, *72*, 43–49. https://doi.org/10.1016/j.resconrec.2012.12.001

Oliynyk, M., Samborskyy, M., Lester, J. B., Mironenko, T., Scott, N., Dickens, S., Haydock, S. F., & Leadlay, P. F. (2007). Complete genome sequence of the erythromycin-producing bacterium *Saccharopolyspora erythraea* NRRL23338. *Nature Biotechnology*, *25*(4), 447–453. https://doi.org/10.1038/nbt1297

Pandey, P., Chowdhury, D., & Wang, Y. (2024). Denaturing gradient gel electrophoresis approach for microbial shift analysis in thermophilic and mesophilic anaerobic digestions. *Gels*, *10*(5), 339. https://doi.org/10.3390/gels10050339

Perkin Elmer Company. (2005). *Protocol-OHHW CHNS/O Analyser 2400 Series II*. https://Resources.Perkinelmer.Com/Lab-Solutions/Resources/Docs/Bro_2400_seriesii_chnso_elemental_analysis.Pdf. Retrieved Date: 2024.05.01.

Piterina, A. V, & Pembroke, J. T. (2013). Use of PCR-DGGE based molecular methods to analyse microbial community diversity and stability during the thermophilic stages of an ATAD wastewater sludge treatment process as an aid to performance monitoring. *ISRN Biotechnology*, *2013*, 1–13. https://doi.org/10.5402/2013/162645

Poppel, M. T., Skiebe, E., Laue, M., Bergmann, H., Ebersberger, I., Garn, T., Fruth, A., Baumgardt, S., Busse, H.-J., & Wilharm, G. (2016). *Acinetobacter equi* sp. nov., isolated from horse faeces. *International Journal of Systematic and Evolutionary Microbiology*, *66*(2), 881–888. https://doi.org/10.1099/ijsem.0.000806

Prasad, B., & Suresh, S. (2012). Biodegradation of phthalate esters by *Variovorax* sp. *APCBEE Procedia*, *1*, 16–21. https://doi.org/10.1016/j.apcbee.2012.03.004

Programa General de Desarrollo del Distrito Federal 2013-2018, Gaceta Oficial del Distrito Federal (2013).

Pulami, D., Kämpfer, P., & Glaeser, S. P. (2023). High diversity of the emerging pathogen *Acinetobacter baumannii* and other *Acinetobacter* spp. in raw manure, biogas plants digestates, and rural and urban wastewater treatment plants with system specific antimicrobial resistance profiles. *Science of The Total Environment*, *859*, 160182. https://doi.org/10.1016/j.scitotenv.2022.160182

Qian, J., Wang, Y., Hu, Z., Shi, T., Wang, Y., Ye, C., & Huang, H. (2023). *Bacillus* sp. as a microbial cell factory: Advancements and future prospects. *Biotechnology Advances*, *69*, 108278. https://doi.org/10.1016/j.biotechadv.2023.108278

Rahman, A., Islam, R., Al-Reza, S. M., & Kang, S. C. (2014). In vitro control of plant pathogenic *Xanthomonas* spp. using *Poncirus trifoliata* Rafin. *EXCLI Journal*, *13*, 1104–1110.

Rastogi, M., Nandal, M., & Khosla, B. (2020). Microbes as vital additives for solid waste composting. *Heliyon*, *6*(2), e03343. https://doi.org/10.1016/j.heliyon.2020.e03343

Sanguinetti, C. J., Dias Neto, E., & Simpson, A. J. (1994). Rapid silver staining and recovery of PCR products separated on polyacrylamide gels. *BioTechniques*, *17*(5), 914–921.

Saygin, H., Ay, H., Guven, K., Inan-Bektas, K., Cetin, D., & Sahin, N. (2021). *Saccharopolyspora karakumensis* sp. nov., *Saccharopolyspora elongata* sp. nov., *Saccharopolyspora aridisoli* sp. nov., *Saccharopolyspora terrae* sp. nov.

and their biotechnological potential revealed by genome analysis. *Systematic and Applied Microbiology*, *44*(6), 126270. https://doi.org/10.1016/j.syapm.2021.126270

Scott, J. A., & Untereiner, W. A. (2004). Determination of keratin degradation by fungi using keratin azure. *Medical Mycology*, *42*(3), 239–246. https://doi.org/10.1080/13693780310001644680

SEDEMA. (2011). *). Secretaría del Medio Ambiente del Distrito Federal. Norma ambiental para el Distrito Federal NADF-020-AMBT-2011, que establece los requerimientos mínimos para la producción de composta a partir de la fracción orgánica de los residuos sólidos urbanos, agrícolas, pecuarios y forestales, así como las especificaciones mínimas de calidad de la composta producida y/o distribuida en el Distrito Federal*. http://Data.Sedema.Cdmx.Gob.Mx/Padla/Images/Stories/Normatividaddf/Nadf_020_ambt_2011.Pdf. Retrieved Date: 2024.05.01

SEDEMA. (2022). *Secretaría del Medio Ambiente del Distrito Federal. Inventario de Residuos Sólidos 2022*. https://Www.Sedema.Cdmx.Gob.Mx/Storage/App/Media/DGCPCA/Residuos/IRS_2022_Completo.Pdf. Retrieved Date: 2024.05.01.

SEMARNAT. (2021). *Basic diagnosis of the integral management of waste*. www.gob.mx/inecc

Sharaf, E. F., & Khalil, N. M. (2011). Keratinolytic activity of purified alkaline keratinase produced by *Scopulariopsis brevicaulis* (Sacc.) and its amino acids profile. *Saudi Journal of Biological Sciences*, *18*(2), 117–121. https://doi.org/10.1016/j.sjbs.2010.12.011

Skóra, M., Macura, A. B., & Bulanda, M. (2014). In vitro antifungal susceptibility of *Scopulariopsis brevicaulis* isolates. *Medical Mycology*, *52*(7), 723–727. https://doi.org/10.1093/mmy/myu039

Sonia, K., Chadha, B., & Saini, H. (2005). *Sorghum* straw for xylanase hyper-production by (DW) under solid-state fermentation. *Bioresource Technology*, *96*(14), 1561–1569. https://doi.org/10.1016/j.biortech.2004.12.037

Strathdee, F., & Free, A. (2013). Denaturing Gradient Gel Electrophoresis (DGGE). In *DNA Electrophoresis* (pp. 145–157). Humana Press. https://doi.org/10.1007/978-1-62703-565-1_9

Sun, Y., Liu, X., Sun, L., Men, M., Wang, B., Deng, L., Zhao, L., Han, Y., Jong, C., Bi, R., Zhao, M., Li, X., Liu, W., Shi, S., Gai, Z., & Xu, X. (2022). Microecological insight to fungal structure and key fungal communities regulating nitrogen transformation based on spatial heterogeneity during cow manure composting by multi-angle and multi-aspect analyses. *Waste Management*, *142*, 132–142. https://doi.org/10.1016/j.wasman.2022.02.013

Sundberg, C., Franke-Whittle, I. H., Kauppi, S., Yu, D., Romantschuk, M., Insam, H., & Jönsson, H. (2011). Characterisation of source-separated household waste intended for composting. *Bioresource Technology*, *102*(3), 2859–2867. https://doi.org/10.1016/j.biortech.2010.10.075

Thompson, W., Leege, P., Millner, P., & Watson, M. (2001). *Test methods for the examination of composting and compost (TMECC).*

Tiralerdpanich, P., Nasaree, S., Pinyakong, O., & Sonthiphand, P. (2021). Variation of the mangrove sediment microbiomes and their phenanthrene biodegradation rates during the dry and wet seasons. *Environmental Pollution*, *289*, 117849. https://doi.org/10.1016/j.envpol.2021.117849

Tu Anh, P. N., Thu Hang, P. T., Quynh Tram, L. T., Minh, N. T., & Dang Khoa, D. H. (2018). Comparison efficacy of its and 18s rdna primers for detection of fungal diversity in compost material by PCR-DGGE technique. *Vietnam Journal of Biotechnology*, *15*(4), 729–735. https://doi.org/10.15625/1811-4989/15/4/13416

US Composting Council. (2023). *Compost characteristics.* .https://www.Compostingcouncil.Org/Page/CompostCharacteristics?&hhsearchterms=%22compost+and+characteristics%22. Retrieved Date: 2024.05.01.

Van Gestel, K., Mergaert, J., Swings, J., Coosemans, J., & Ryckeboer, J. (2003). Bioremediation of diesel oil-contaminated soil by composting with biowaste. *Environmental Pollution*, *125*(3), 361–368. https://doi.org/10.1016/s0269-7491(03)00109-x

White, T. J., Bruns, T., Lee, S., & Taylor, J. (1990). Amplification and direct sequencing of fungal ribosomaL RNA genes for phylogenetics. In *PCR Protocols* (pp. 315–322). Elsevier. https://doi.org/10.1016/b978-0-12-372180-8.50042-1

Wilfinger, W. W., Mackey, K., & Chomczynski, P. (1997). Effect of pH and ionic strength on the spectrophotometric assessment of nucleic acid purity. *BioTechniques*, *22*(3), 474–481. https://doi.org/10.2144/97223st01

Wu, R., Long, M., Tai, X., Wang, J., Lu, Y., Sun, X., Tang, D., & Sun, L. (2022). Microbiological inoculation with and without biochar reduces the bioavailability of heavy metals by microbial correlation in pig manure composting. *Ecotoxicology and Environmental Safety*, *248*, 114294. https://doi.org/10.1016/j.ecoenv.2022.114294

Xi, B., He, X., Dang, Q., Yang, T., Li, M., Wang, X., Li, D., & Tang, J. (2015). Effect of multi-stage inoculation on the bacterial and fungal community structure during organic municipal solid wastes composting. *Bioresource Technology*, *196*, 399–405. https://doi.org/10.1016/j.biortech.2015.07.069

Xiao, Y., Zeng, G.-M., Yang, Z.-H., Shi, W.-J., Huang, C., Fan, C.-Z., & Xu, Z.-Y. (2009). Continuous thermophilic composting (CTC) for rapid biodegradation and maturation of organic municipal solid waste. *Bioresource Technology*, *100*(20), 4807–4813. https://doi.org/10.1016/j.biortech.2009.05.013

Yamamoto, N., & Nakai, Y. (2019). Microbial community dynamics during the composting process of animal manure as analyzed by molecular biological methods. In *Understanding Terrestrial Microbial Communities* (pp. 151–172). Springer International Publishing. https://doi.org/10.1007/978-3-030-10777-2_6

Zhang, X., Zhong, Y., Yang, S., Zhang, W., Xu, M., Ma, A., Zhuang, G., Chen, G., & Liu, W. (2014). Diversity and dynamics of the microbial community on decomposing wheat straw during mushroom compost production. *Bioresource Technology*, *170*, 183–195. https://doi.org/10.1016/j.biortech.2014.07.093

Zhao, B., Cao, X., Cai, Z., Zhang, L., Li, D., Zhang, H., Li, S., & Sun, X. (2023). Improving suppressive activity of compost on phytopathogenic microbes by inoculation of antagonistic microorganisms for secondary fermentation. *Bioresource Technology*, *367*, 128288. https://doi.org/10.1016/j.biortech.2022.128288

Zhao, G., Zhou, J., Tian, Y., Chen, Q., Mao, D., Zhu, J., & Huang, X. (2023). Remediation of fomesafen contaminated soil by *Bacillus* sp. Za: Degradation pathway, community structure and bioenhanced remediation. *Environmental Pollution*, *336*, 122460. https://doi.org/10.1016/j.envpol.2023.122460

Vol. 24, No. 3(2025) IA25570
Revista Mexicana de Ingeniería Química

Influence of chemical indicators on biogas production in a bioreactor from water hyacinth using canonical correlation analysis

Influencia de los indicadores químicos en la producción de biogás en un biorreactor a partir de lirio acuático mediante análisis de correlación canónico

D. B. Benitez-Suarez [1], H. Bautista-Zaragoza[1], J. P. Molina-Aguilar[2], J. Apolinar-Cortés[1], M. C. Chávez-Parga[1‡]
[1]Graduate Studies Division, Master of Science in Environmental Engineering, Chemical Engineering Faculty, Universidad Michoacana de San Nicolás de Hidalgo, Building V-1, Morelia, Michoacán, México.
[2]Civil Engineering Faculty, Universidad Michoacana de San Nicolás de Hidalgo, Building -C, Morelia Michoacán, México.
Sent date: April 14, 2025; Accepted: August 6, 2025

Abstract
The global energy crisis is currently a matter of great concern. With the rapid growth of the population, especially in emerging economies, energy supply often struggles to keep pace with demand. Biogas production from water hyacinth (*Eichhornia crassipes*) in an upflow anaerobic sludge blanket reactor offers a promising renewable energy alternative with multiple benefits. The anaerobic digestion of organic matter generates biogas, which holds significant potential for electricity and heat generation and can also be upgraded into a usable fuel. This study applied canonical correlation analysis to evaluate the relationship between sets of independent and dependent variables involved in the biogas production process. A 20 L anaerobic reactor upflow fed with water hyacinth pretreated with calcium oxide. Physicochemical variables were measured for the substrate, inoculum, effluent, and the biogas produced. The analysis yielded a canonical correlation coefficient of 0.8467 between the two variable sets, indicating a relatively strong relationship. Moreover, biogas production was estimated based on the input variables using the canonical variables derived from the analysis. These results demonstrate that canonical correlation analysis is a valuable tool for monitoring and optimizing the biogas production process, as it helps identify critical variables and their effects on reactor performance.
Keywords: anaerobic digestion, biogas, canonical correlation, canonical variables.

Resumen
La problemática energética mundial es un tema de gran relevancia en la actualidad. Con el rápido crecimiento de la población, especialmente en las economías emergentes, la oferta a menudo no puede mantener el ritmo de la demanda energética. La producción de biogás, a partir de lirio acuático (*Eichhornia crassipes*) en un reactor anaerobio de flujo ascendente es una alternativa para producir energía renovable que ofrece múltiples beneficios. La digestión anaerobia de la materia orgánica produce biogás, el cual tiene un gran potencial para su uso en la generación de energía eléctrica y calorífica, así como también puede ser transformado en combustible. El presente trabajo aplicó el análisis de correlación canónica para evaluar la relación entre los conjuntos de las variables independientes y dependientes del proceso de producción de biogás. Se utilizó un reactor anaerobio de flujo ascendente de 20 L alimentado con lirio acuático pretratado con óxido de calcio donde se midieron las variables fisicoquímicas del sustrato, el inóculo, el efluente y el biogás producido. Los resultados del análisis muestran un coeficiente de correlación canónica de 0.8467 entre ambos conjuntos, lo que indica una relación relativamente alta entre las variables, además se estimó la producción de biogás en función de las variables de entrada usando las variables canónicas obtenidas por el análisis. Estos resultados muestran que el análisis de correlación canónica es una herramienta útil para monitorear y optimizar el proceso de biogás, debido a que permite identificar las variables críticas y su efecto sobre el rendimiento del biorreactor.
Palabras clave: digestión anaerobia, biogás, correlación canónica, variables canónicas.

‡*Corresponding author. E-mail*: cparga@umich.mx;
https://doi.org/10.24275/rmiq/IA25570
ISSN:1665-2738, *issn-e*: 2395-8472

1 Introduction

Energy is essential for human well-being and daily life. Many countries, especially those in the developing world, face energy crises due to their heavy reliance on fossil fuels (Mohammed *et al.,* 2024). Approximately 80% of global energy is derived from fossil sources, such as oil, coal, and natural gas, which are the primary emitters of greenhouse gases, including carbon dioxide (CO_2) and methane (CH_4). These gases significantly contribute to global warming and environmental degradation (El-Araby, 2024; Gupta *et al.,* 2023; Hou *et al.,* 2023). In 2023, global natural gas consumption reached nearly four trillion cubic meters (Statista, 2024). Considering this demand, there is an urgent need to explore renewable energy alternatives, such as biogas, that could potentially replace natural gas in the future (Cisneros *et al.,* 2021).

Biogas is produced through the anaerobic degradation of organic matter and typically contains 55–70% CH_4, approximately 35–40% CO_2, and nitrogen (N_2) (Jameel *et al.,* 2024). It also includes trace amounts of other gases such as hydrogen sulfide (H_2S), hydrogen (H_2), ammonia (NH_3), oxygen (O_2), and carbon monoxide (CO) (Khan *et al.,* 2017). Biogas can be utilized for electricity generation, heating, and as a biofuel (Martínez-Gutiérrez, 2018).

Biowaste generated from commercial, industrial, and household activities can be broadly classified into two main fractions. The first is the *organic fraction of municipal solid waste (*OFMSW*)*, primarily consisting of food scraps and kitchen waste, and typically representing the largest share of the total waste stream. The second is the *lignocellulosic or vegetal fraction*, which comprises plant residues from public and private green areas. Proper separation and management of both fractions, particularly the OFMSW, is essential for enhancing waste valorization and minimizing landfill impacts, as evidenced in recent urban waste management studies (Rolewicz-Kalińska *et al*., 2020; Alves *et al*., 2023). Effective management of these waste streams is critical due to their environmental impact, including greenhouse gas emissions and contamination issues (Triviño-Pineda *et al.,* 2024). The anaerobic digestion of organic waste enables resource recovery by producing biogas and digestate, thereby closing the loops of energy and nutrient cycles (González *et al.,* 2024). This process is framed within the circular economy model, in which waste is reintegrated as a resource in productive systems, promoting more efficient and sustainable use of natural resources (Stylianou *et al.,* 2023).

In recent years, the use of lignocellulose-rich organic waste for anaerobic digestion aimed at producing biotechnologically valuable byproducts such as methane (CH_4) has become an increasingly complex challenge (Amiri & Karimi, 2018). Currently, the use of water hyacinth (*Eichhornia crassipes*) as a substrate to produce these byproducts has emerged as an efficient and cost-effective alternative for biogas generation. This invasive aquatic weed can double its biomass within 6 to 28 days, forming dense mats on the water's surface. These mats obstruct sunlight penetration, leading to eutrophication and the eventual degradation of aquatic ecosystems (Pottipati *et al.,* 2021). Biogas production is carried out through anaerobic digestion, a process composed of four sequential stages: hydrolysis, acidogenesis, acetogenesis, and methanogenesis. During this process, the substrate is degraded by a consortium of facultative and strict anaerobic microorganisms operating under controlled conditions, such as those provided by upflow anaerobic sludge blanket (UASB) reactors (Chiemchaisri & Visvanathan, 2018; Themelis & Uloa, 2007).

Optimizing process parameters, such as inoculum concentration and incubation temperature, significantly contributes to enhancing biogas production (Armah *et al.,* 2018). According to Kumar *et al*. (2019), mesophilic conditions (40°C) are more favorable for biogas generation compared to lower temperatures, such as 30 °C. Biogas production is closely linked to the diversity and dynamics of the anaerobic digestion process, which are strongly influenced by operational factors, including temperature, pH, hydraulic retention time, carbon-to-nitrogen (C/N) ratio, organic loading rate, substrate composition, and nutrient bioavailability (Nakasima-López *et al.,* 2017). Therefore, microbial community diversity and activity are critical variables that can be affected by environmental and biological factors (Rehman *et al.,* 2019). However, monitoring and analysis of these variables in anaerobic reactors remain limited.

In this context, multivariate analytical tools such as canonical correlation analysis (CCA) have gained importance, as they enable the simultaneous evaluation of multiple variables, facilitating the identification of those that most significantly influence the process (Badii & Castillo, 2017). CCA stands out as a powerful multivariate technique for assessing and optimizing the performance of anaerobic bioreactors, enabling the identification and interpretation of relationships between multiple input and output variables and offering a comprehensive view of process dynamics.

This study applied CCA to improve the control and management of the anaerobic digestion (AD) process. By examining both input and output variables, CCA enabled the identification of relationships between independent variables and the output variable (biogas), thereby clarifying their impact on biogas production. The findings highlight the potential of CCA to identify critical variables and enhance overall system performance (Rehman *et al.,* 2019; Zhuang *et al.,* 2020;

Hotelling, 1936; Molina *et al.,* 2019).

Therefore, this study contributes to current knowledge by applying CCA to identify the most relevant physicochemical predictors of biogas production in a mono-digestion system using lime-pretreated water hyacinth. Unlike traditional studies based on bivariate correlations or univariate models, the multivariate approach employed here enables a more comprehensive assessment of operational interactions under real-world conditions. This type of analysis has proven to be more robust and representative in anaerobic systems, as it simultaneously captures the complex dynamics between operational parameters and biological responses, as reported by Otto *et al.* (2024) in a comparative study of 80 full-scale digesters. The findings of this work support the development of predictive frameworks for process monitoring and control, particularly in systems that utilize invasive aquatic biomass under mesophilic conditions.

2 Materials and methods

The methodological framework employed in this study integrates the design and operation of a pilot-scale UASB bioreactor fed with water hyacinth pretreated with calcium hydroxide, along with standardized analytical procedures for measuring pH, electrical conductivity, and alkalinity across various system streams. Physicochemical characterization was complemented by a multivariate statistical approach based on CCA, which enabled the identification of optimal statistical projections between the sets of independent and dependent variables. The implementation of this methodological strategy ensures the statistical robustness and practical relevance of the findings under mesophilic conditions, which are representative of real-world operations.

2.1 Bioreactor characteristics

The system from which data were obtained for the canonical correlation analysis (CCA) was a pilot-scale upflow anaerobic sludge blanket (UASB) reactor (**Figure 1**), constructed from polymethylmethacrylate (acrylic) with a total volume of 33 L. A valve is located at the bottom of the reactor for purging sludge and effluent, connected to a diffuser that ensures even distribution of the feed within the reactor. At the top, the effluent outlet is equipped with a gas trap to prevent the loss of generated biogas. Additionally, a biogas outlet is located at the top and is connected to an external high-density polyethylene (HDPE) system with a 20 L capacity for biogas storage and quantification. Biogas volume is measured by liquid displacement.

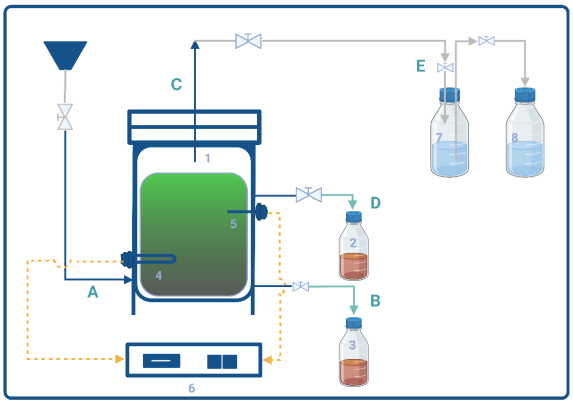

Figure 1. Schematic diagram of the pilot-scale UASB reactor. (**1**) UASB reactor; (**2**) Effluent outlet; (**3**) Sludge purge outlet; (**4**) Electric heating element; (**5**) Temperature sensor; (**6**) Temperature controller; (**7**) Biogas storage unit; (**8**) Displaced liquid collector; (**A**) Influent (feed); (**B**) Sludge purge; (**C**) Biogas outlet; (**D**) Effluent (discharge); (**E**) Liquid displacement.

The bioreactor is equipped with a temperature control system designed for automatic regulation, utilizing an I-Power Electronics STC-1000 controller. Two 60 W heating elements are installed inside the reactor to maintain a constant operating temperature of 35°C ± 1 °C.

2.2 Substrate characteristics

The water hyacinth used as a substrate in the bioreactor was collected from the "Grande" River, which runs through the city of Morelia, Michoacán, at coordinates 19.685611, -101.242114. After collection, the biomass underwent a pretreatment process that involved grinding the hyacinth in a disc mill (Estrella) to obtain particles with diameters ranging from 0.2 to 0.8 cm. Subsequently, a CaO solution heated to 60 °C was added to solubilize the organic matter. The mixture was then filtered to separate larger lignocellulosic fibers.

The preparation and feeding procedure of the substrate is illustrated in **Figure 2**. After harvesting, the water hyacinth was mechanically processed using a disc mill to reduce particle size and then filtered to eliminate coarse lignocellulosic residues. The resulting homogeneous slurry was transferred to the bioreactor using a peristaltic pump and combined with the inoculum before anaerobic digestion. The system incorporated temperature regulation at 35 °C and included dedicated outlets for biogas collection, effluent discharge, and sludge purging.

The filtered substrate was used to feed the UASB reactor, which had a total volume of 5 L. The volume of biogas produced was determined by measuring the volume of displaced liquid (Walker *et al.,* 2009).

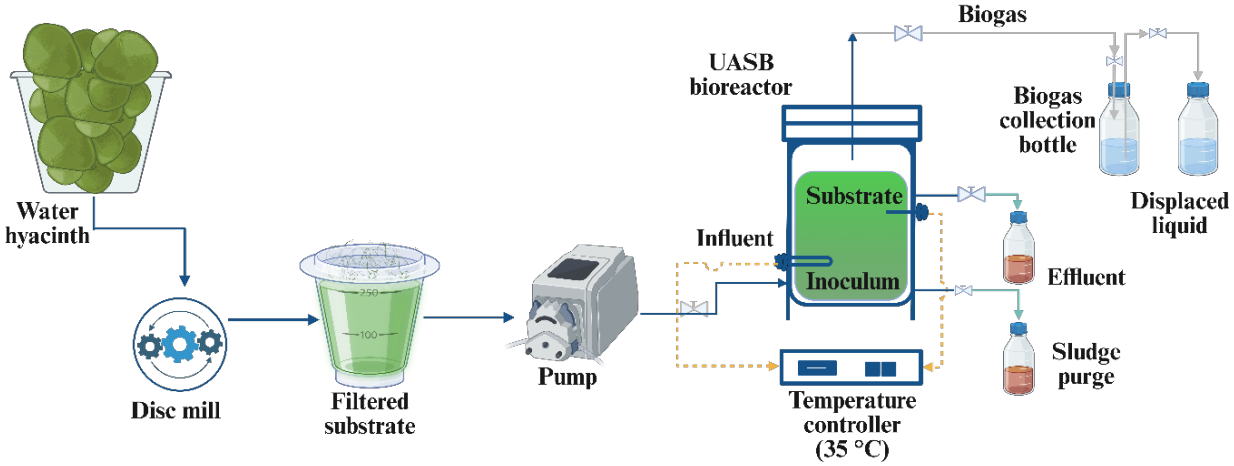

Figure 2. Schematic representation of the feeding and operation process of the UASB bioreactor. Water hyacinth is initially processed in a disc mill to reduce particle size, followed by filtration to remove coarse lignocellulosic fibers and obtain a homogeneous substrate. This filtered substrate is then pumped into the reactor and mixed with the inoculum. The bioreactor operates under mesophilic conditions (35 °C), maintained by an internal heating system and monitored via a temperature sensor. During anaerobic digestion, the generated biogas is collected and quantified by liquid displacement in an external gas collection and measurement system. The system also features separate outlets for sludge purge and effluent discharge, enabling operational monitoring and maintenance.

2.3 Analytical parameter determination

pH and conductivity measurements were conducted at the influent, effluent, and inoculum valves every 72 hours using a multiparameter instrument (Thermo Scientific Orion Star A325 portable pH/conductivity meter), by Mexican standards NMX-AA-008-SCFI-2016 and NMX-AA-093-SCFI-2000, respectively.

Alkalinity was determined in the influent, effluent, and inoculum of the reactor, following the NMX-AA-036-SCFI-2001 standard, with a frequency of every 72 hours, to calculate the total alkalinity as $CaCO_3$ in mg/L.

2.4 Canonical correlation analysis

Before conducting the canonical correlation analysis, the dataset, consisting of 22 paired observations collected over a 258-day monitoring period, was evaluated to ensure compliance with statistical assumptions. All variables were standardized using z-score transformation to eliminate the effect of differing measurement scales. Multicollinearity was assessed by analyzing the Pearson correlation matrix of the independent variable set. No correlation coefficients exceeded |r| = 0.9, indicating no significant redundancy among predictors (Hair *et al.*, 2009). Additionally, potential outliers were identified graphically using boxplots for all ten variables included in the model. Although some mild outliers were observed, particularly in inoculum alkalinity and effluent pH, no extreme values were detected. Consequently, all data points were retained in the canonical correlation analysis, as their presence did not compromise the robustness or validity of the model.

Despite the moderate sample size (22 paired cases), the model meets established statistical criteria for multivariate analysis. Recent findings by Helmer *et al.* (2024) suggest that canonical correlation can yield stable results in moderately sized datasets, particularly when strong relationships exist between variable sets. Furthermore, the widely accepted "one-in-ten" rule recommends a minimum of 10 observations per variable, a condition fulfilled in this study by including 10 variables and surpassing the 1:1 ratio. Therefore, the statistical model complies with the methodological requirements for its application.

All statistical analyses, including canonical correlation analysis, were performed using the Statistica® software.

The use of linear multivariate statistical analysis allows for the identification of optimal correlations between two sets of variables. According to Hair *et al.* (2009), this type of correlation simultaneously links p dependent variables with q independent variables by linearly combining both sets to establish two weight vectors that maximize the corresponding correlation coefficient.

The variables $x_1, x_2, \ldots, x_p$ are grouped to form an independent set (X), which generates the composite variable (U). Similarly, the variables $y_1, y_2, \ldots, y_q$ form the dependent set (Y), resulting in the composite variable(W). Both U and W are referred to as canonical variables.

These canonical variables are obtained by multiplying the transposed weight vectors $a = \left(a_1, a_2, \ldots, a_p\right)$ y $b = \left(b_1, b_2, \ldots, b_q\right)$ by the variable sets X and Y, respectively. The result defines their linear combinations with the maximum possible variance, based on the orthogonality between the canonical variables.

$$U = a^T X = \left(a_1, a_2, \ldots, a_p\right)\begin{pmatrix} x_1 \\ x_2 \\ \vdots \\ x_p \end{pmatrix}$$

$$= a_1 x_1 + a_2 x_2 + \ldots + a_p x_p \quad (1)$$

$$W = b^T Y = \left(b_1, b_2, \ldots, b_q\right)\begin{pmatrix} y_1 \\ y_2 \\ \vdots \\ y_q \end{pmatrix}$$

$$= b_1 y_1 + b_2 y_2 + \ldots + b_q y_q \quad (2)$$

Based on both results, the sample variance-covariance matrix (S), of order p x q, is established, noting that $C_{YX} = C_{XY}^T$

$$S = \begin{pmatrix} C_{XX} & C_{XY} \\ C_{YX} & C_{YY} \end{pmatrix} \quad (3)$$

Thus, the correlation coefficient between the canonical variables is referred to as the canonical correlation coefficient, and is defined as follows:

$$corr(U,W) = \frac{cov(U,W)}{\sqrt{var(U)}\sqrt{var(W)}} = \frac{a^T C_{XY} b}{\sqrt{a^T C_{XX} a}\sqrt{b^T C_{YY} b}} \quad (4)$$

In the above equation, the denominator imposes two normalization constraints, both of which determine the weight vectors that favor maximization (Khalil *et al.*, 2011).

$$var(U) = a^T C_{XX} a = 1 \quad (5)$$

$$var(W) = b^T C_{YY} b = 1 \quad (6)$$

Additionally, both constraints standardize the canonical variations, thereby establishing the solution to the canonical correlation problem as the maximization of the numerator.

$$corr(U,W) = a^T C_{XY} b \quad (7)$$

To achieve this, a two-parameter Lagrangian function is used, which enables the calculation of multivariate gradients by considering the solution weight vectors.

$$L(a,b) = a^T C_{XY} b - \tau_1\left(a^T C_{XX} a - 1\right) - \tau_2\left(b^T C_{YY} b - 1\right) \quad (8)$$

Each gradient requires the partial derivative of Equation (8) to be defined with respect to each vector, respectively.

$$\frac{\partial L(a,b)}{\partial a} = C_{XY} b - 2\tau_1 C_{XX} a = 0$$

$$C_{XY} b = 2\tau_1 C_{XX} a \quad (9)$$

$$\frac{\partial L(a,b)}{\partial b} = C_{XY}^T a - 2\tau_2 C_{YY} b = 0 \quad (10)$$

$$C_{XY}^T a = 2\tau_2 C_{YY} b \quad (11)$$

Both gradients yield a system of equations which, when solved, define the weight vectors a and b that maximize the numerator in Equation (7).

This solution is based on Equations (5) and (6), which are respectively multiplied by the transposed vectors from Equations (9) and (11) for simplification.

$$\left(C_{XY} b = 2\tau_1 C_{XX} a\right) a^T$$

$$a^T C_{XY} b = 2\tau_1 \quad (12)$$

$$\left(C_{XY}^T a = 2\tau_2 C_{YY} b\right) b^T$$

$$b^T C_{XY}^T a = 2\tau_2 \quad (13)$$

The algebraic simplification of the second term in Equations (12) and (13) defines the scalar of the solution, ensuring that the normalization constraints are satisfied

$$\left(a^T C_{XY} b\right)^T = b^T C_{XY}^T a = 1 \quad (14)$$

The equations are equivalent, defined as $2\tau_1 = 2\tau_2$, which represent the eigenvalue (λ). Therefore, Equations (9) and (11) can be rewritten in their simplified form

$$C_{XY} b = \lambda C_{XX} a \quad (15)$$

$$C_{XY}^T a = \lambda C_{YY} b \quad (16)$$

By solving for vector, a from Equation (15) and substituting it into Equation (16), the system is reduced as follows:

$$C_{XY}^T\left[\frac{1}{\lambda} C_{XX}^{-1} C_{XY} b\right] = \lambda C_{YY} b$$

$$C_{YY}^{-1} C_{XY}^T C_{XX}^{-1} C_{XY} b - \lambda^2 b = 0 \quad (17)$$

Analogously, we obtain:

$$C_{XX}^{-1} C_{XY} C_{YY}^{-1} C_{XY}^T a - \lambda^2 a = 0 \quad (18)$$

Finally, solving Equations (17) and (18) yields the vectors a and b, which represent the eigenvectors that maximize the correlation between the canonical variables for the given variable sets in the problem.

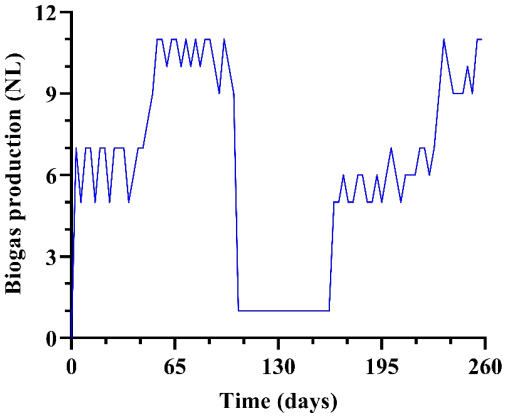

Figure 3. Normalized biogas production (NL) over a 258-day mono-digestion of calcium hydroxide pretreated water hyacinth. Biogas was measured every 72 h and standardized to 25 °C and 1 atm. Temporal fluctuations highlight periods of low production and recovery, corresponding to shifts in physicochemical parameters.

3 Results and discussion

The canonical correlation analysis enabled the identification of significant relationships between the input and output variables of the bioreactor over a 258-day monitoring period, with measurements taken every 72 hours (**Figure 3**).

The evaluated variables included pH, electrical conductivity, and alkalinity of the substrate and inoculum as input factors, while pH, electrical conductivity, alkalinity, and biogas production were considered as output variables (**Table 1** and **Table 2**). These variables were selected based on their operational relevance and their documented influence on anaerobic digestion performance (Ali *et al.*, 2021; Chen *et al.*, 2024). They serve as key indicators of buffering capacity, ionic strength, and microbial activity in anaerobic systems. They are easily measurable through routine monitoring, making them suitable for real-time decision-making and process control.

Table 1. Input variables used in the canonical correlation analysis.

Periods Days	Initial conditions					
	Substrate pH (S_{pH})	Inoculum pH (I_{pH})	Substrate electrical conductivity ($S_{E.C}$) μS/cm	Inoculum electrical conductivity ($I_{E.C}$) μS/cm	Substrate alkalinity (S_A) g $CaCO_3$/L	Inoculum alkalinity (I_A) g $CaCO_3$/L
0	10.60	8.01	4.96	3.52	4.30	11.00
12	11.21	8.08	3.13	4.97	5.50	36.00
24	9.47	7.62	8.37	6.66	1.80	12.00
36	9.13	7.63	8.56	8.33	2.00	15.00
48	9.85	7.36	4.32	7.68	2.00	26.00
60	9.16	7.62	6.47	6.22	2.00	13.00
72	9.24	7.53	7.18	7.86	2.50	17.00
84	9.32	7.54	9.32	7.54	2.00	15.00
96	9.81	7.52	5.01	8.21	2.70	18.00
108	9.09	7.35	8.32	8.09	2.70	17.00
120	9.04	7.50	8.12	12.24	2.90	10.00
132	8.19	7.19	9.33	10.65	2.50	28.00
144	7.88	7.70	12.93	9.66	3.40	20.00
156	7.74	7.69	11.94	10.18	3.10	20.00
168	7.37	7.73	4.76	9.00	1.60	19.00
180	7.73	7.47	12.59	10.66	3.10	26.00
192	7.73	7.56	14.09	10.90	3.60	16.00
204	7.62	7.71	16.60	13.46	3.20	15.00
216	7.85	7.60	10.83	10.88	4.60	16.00
228	8.02	7.62	10.97	11.25	3.70	10.00
240	7.61	7.59	12.05	11.64	2.80	13.00
252	7.73	7.43	9.99	10.57	4.10	15.00
258	7.91	7.46	13.79	11.59	3.80	18.00

Table 2. Response variables used in the canonical correlation analysis.

Periods Days	Response variable			
	Biogas produced NL	Effluent pH (E_{pH})	Effluent electrical conductivity ($E_{E.C}$) μS/cm	Effluent alkalinity (E_A) g $CaCO_3$/L
0	7.33	7.20	5.11	2.10
12	7.33	8.09	4.96	4.50
24	5.50	7.59	8.62	2.50
36	5.50	7.61	9.67	2.40
48	8.25	7.30	8.88	2.20
60	10.08	7.43	7.11	1.80
72	10.99	7.34	9.46	2.80
84	10.99	7.50	7.12	2.90
96	10.99	7.54	10.01	3.70
108	0.92	7.76	9.76	2.80
120	0.92	7.48	11.42	3.60
132	0.92	8.02	10.40	3.90
144	0.92	7.80	16.36	4.20
156	0.92	7.83	11.94	3.80
168	5.50	7.82	11.82	3.30
180	6.41	7.78	12.58	3.30
192	6.41	7.66	12.53	4.70
204	6.41	7.67	14.35	4.70
216	6.41	7.69	12.45	5.00
228	7.33	7.72	12.90	5.70
240	9.16	7.73	14.19	5.90
252	9.16	7.89	12.74	5.60
258	10.99	7.59	13.61	5.80

Their inclusion enabled a robust physicochemical characterization of the system, which is essential for developing multivariate statistical models, such as canonical correlation analysis, that require well-defined relationships between sets of independent and dependent variables.

Figure 4. Illustrates the relationship between the canonical variables **U** and **W**, obtained through canonical correlation analysis, which identifies the optimal linear combinations of input and output variables that maximize their mutual correlation. The linear fit between these variables resulted in a slope of **0.9202** and a correlation coefficient of $\mathbf{R^2 = 0.8467}$, indicating that approximately **84.67%** of the variability in the dependent variable **W** can be explained by the independent variable **U**. The canonical functions were defined by the Equations (19) and (20):

$$U = a_1 S_{pH} + a_2 I_{pH} + a_3 S_{C.E} + a_4 I_{C.E} + a_5 S_A + a_6 I_A \quad (19)$$

$$W = b_1 E_{pH} - b_2 E_{C.E} - b_3 E_A \quad (20)$$

Each coefficient represents the statistical weight assigned to the original variables within the canonical combination. These functions serve as new axes in a transformed space, analogous to a Cartesian coordinate system, allowing for a graphical representation of the observations projected onto these axes.

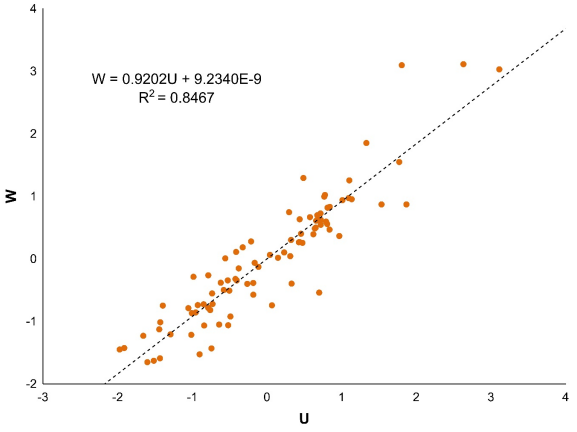

Figure 4. Canonical correlation analysis between the recorded values of the physicochemical variables in the bioreactor and the corresponding canonical variable values for estimating biogas production.

This transformation facilitates the visual interpretation of the multivariate relationship between the sets of predictor and response variables, providing a powerful tool for analyzing underlying structures in complex systems.

The eigenvalues obtained for the canonical functions were $\lambda_1 = 0.8467$, $\lambda_2 = 0.2996$, $\lambda_3 = 0.0973$, and $\lambda_4 = 0.0697$, with λ_1 representing the highest explained variance. These results highlight

the importance of the first canonical function, which accounts for the most significant portion of the relationship between the two variable sets. The coefficients of the first weight vectors were a = (-0.2211, 0.0801, 0.3313, 0.5170, 0.1056, -0.0717) and b = (-0.0327, 0.0064, 0.8338, 0.2094), indicating that substrate electrical conductivity and alkalinity are key factors influencing biogas production (Cao *et al.,* 2019). This finding is consistent with previous studies that have identified electrical conductivity as a potential indicator of microbial activity in anaerobic digestion systems (Callegari *et al.,* 2025). Additionally, Alvarado-Reyna *et al*. (2024) demonstrated that electrical conductivity displays greater sensitivity and earlier deviation compared to conventional indicators such as pH or methane content, reinforcing its value as a predictive variable within multivariate models such as canonical correlation analysis.

This finding suggests that the electrochemical characteristics of the environment, represented by electrical conductivity, may modulate nutrient availability and microbial performance in anaerobic systems. Similar associations have been reported by Callegari *et al*. (2025) and Hasani *et al*. (2025), who linked shifts in conductivity and alkalinity to microbial community adaptation and process efficiency under varying loading conditions. This reinforces the role of these variables not only as statistical predictors but also as functional indicators of biological responses.

These relationships show that increases in both electrical conductivity and alkalinity may reflect not only changes in buffering capacity and ion exchange but also shifts in microbial metabolic networks and community structure, which in turn impact biogas yield and system stability. For instance, empirical dynamic modeling of anaerobic digesters converting sucrose has revealed that temporal variations in microbial interaction networks (particularly among fermentative, syntrophic, and methanogenic functional groups) closely match performance dynamics, such as hydrogen concentrations and methane production, throughout operation (Chang *et al*., 2025; Goux *et al*., 2015). Highlighting similar mechanisms in lignocellulosic digestion, Al Hasani *et al*. (2025) reported that modifications in the electrochemical matrix enhance direct interspecies electron transfer (DIET), promoting microbial resilience and improving methane output (Negi *et al*., 2025). These findings validate that the observed statistical associations with conductivity and alkalinity are supported by functional microbial responses, reinforcing their usefulness for both process monitoring and mechanistic understanding.

Based on the canonical correlation equation derived from the analysis, a biogas production volume of 3.2579 L was estimated under the initial experimental conditions. However, by modifying the substrate's electrical conductivity and alkalinity values in Equation (21), the calculations suggest a potential biogas yield of up to 18.48 L. What suggests that proper regulation of these variables could optimize system performance, aligning with previous studies that highlight the importance of alkalinity in maintaining the stability of the anaerobic digestion process (Soto *et al.,* 2021).

$$Biogas = \frac{0.9202\left(a_1\ S_{pH} + a_2 I_{pH} + a_3 S_{C.E} + a_4 I_{C.E} + a_5 S_A + a_6 I_A\right) + 0.0000000092349\ \left(-b_1 E_{pH} - b_2 E_{C.E} - b_3 E_A\right)}{b_4} \tag{21}$$

Although the correlation values obtained suggest a strong association between the input variables and biogas production, it is essential to note that this relationship does not imply causation. The 15.33% variability in biogas production not explained by the model may be attributed to other unaccounted factors, such as substrate composition, temperature, the presence of inhibitors, or specific microbial activity within the bioreactor. This unexplained variance may also reflect the heterogeneous composition of the water hyacinth biomass or adaptive fluctuations in the inoculum´s microbial consortia, as suggested by Karouach *et al*. (2023). Recent studies have demonstrated that substrate composition, particularly the content of biodegradable organic matter, has a significant impact on biogas production efficiency (Chew *et al.,* 2021).

Despite the high correlation observed, it is important to recognize that biological systems exhibit inherent variability that is not always fully captured by mathematical models. Factors such as microbial dynamics, substrate composition, and operational conditions of the bioreactor remain sources of uncertainty in predicting biogas yield. Therefore, it is recommended that complementary studies be conducted with greater control over internal system variables to improve model accuracy and further optimize the anaerobic digestion process.

In the present study, electrical conductivity and alkalinity were identified as key predictors in the canonical model. These variables were also identified by Hernández-Eugenio *et al*. (2025) as being strongly associated with shifts in microbial community structure, particularly under varying organic loading rates and varying buffering capacities. While their study focused on microbial adaptation in co-digestion systems using metagenomic tools, our approach applied a statistical framework (canonical correlation analysis) to a mono-digestion system using lime-pretreated water hyacinth. This convergence reinforces the

idea that physicochemical indicators such as those measured in this study may also reflect microbial activity and resilience. Therefore, the observed statistical relationships gain biological relevance when interpreted in the context of known microbial responses to environmental conditions.

Another essential aspect to consider is the applicability of the canonical equation in closed biological systems. Although the predictions suggest an increase in biogas production with specific adjustments to the input variables, in practice, the ability to modify these variables is limited by the system's intrinsic conditions. Microbial dynamics within a bioreactor can be influenced by subtle changes in pH or ion concentration, which may result in adverse effects on the system's equilibrium (Martínez *et al.,* 2016).

Finally, it is recommended to conduct controlled experiments that evaluate not only the physical and chemical variables but also those related to the metabolism of the microorganisms present in the bioreactor. The integration of more complex mathematical models, incorporating factors such as organic loading rate and microbial kinetics, could provide a more accurate representation of the system and enhance the predictive capacity of the proposed canonical model. In this regard, future studies could focus on the inclusion of additional variables and the experimental validation of the predictions presented in this work.

4 Conclusions

4.1 General conclusions

This study demonstrated the influence of input and output physicochemical variables on biogas production in an Upflow anaerobic sludge blanket (UASB) reactor, using canonical correlation analysis as a multivariate statistical tool. The results indicated that substrate electrical conductivity and alkalinity are key factors in system efficiency, with a predictive model that accounted for 84.67% of the variability in biogas production. These findings demonstrate the potential of canonical correlation analysis as a valuable tool for analyzing and optimizing biotechnological processes.

From a practical perspective, the ability to adjust variables such as electrical conductivity and alkalinity represents a viable strategy for enhancing system performance. However, implementing these adjustments under real operating conditions requires controlled experimental trials to evaluate their impact on microbial dynamics, system stability, and the quality of the biogas produced.

Despite the model's high explanatory power, it is essential to acknowledge that biological systems exhibit inherent variability, which may limit the predictive capacity of purely statistical approaches. To strengthen the model's validity, factors such as substrate composition, specific microbial activity, temperature, and the presence of inhibitors should be considered in future studies.

4.2 Future research directions

It is recommended that this statistical approach be integrated with complementary tools such as metagenomic analysis, kinetic modeling, and real-time monitoring of critical parameters to develop more precise and robust control strategies. Such integration would facilitate the advancement toward more efficient, stable, and scalable anaerobic digestion systems for applications in organic waste treatment and renewable energy generation.

Additionally, future research should integrate the analysis of microbial consortium dynamics or functional metabolic monitoring to validate the statistical associations observed. What would strengthen the causal interpretation of physicochemical predictors, as proposed by Helmer *et al*. (2024).

Acknowledgements

We express our sincere gratitude to the SECIHTI for awarding the master's scholarship (No. 002528) and to the Graduate Studies Division of the Faculty of Chemical Engineering at the Universidad Michoacana de San Nicolás de Hidalgo (UMSNH) for providing the space and resources necessary for the completion of this work.

Nomenclature

$x_1, x_2, \ldots, x_p$	Independent variables
$y_1, y_2, \ldots, y_q$	Dependent variables
X	Vector grouping all independent variables
Y	Vector grouping all dependent variables
U	Canonical variate associated with the independent variable set X
W	Canonical variate associated with the dependent variable set Y
$a = (a_1, a_2, \ldots, a_p)^T$	Weight vector associated with the independent variable set
$b = (b_1, b_2, \ldots, b_q)^T$	Weight vector associated with the dependent variable set
λ	Eigenvalue representing the squared canonical correlation
τ_1, τ_2	Lagrange multipliers used in the optimization process

C_{XX}	Covariance matrix of the independent variables
C_{YY}	Covariance matrix of the dependent variables
C_{XY}	Cross-covariance matrix between independent and dependent variables
$C_{YX} = C_{XY}^T$	Transposed cross-covariance matrix
S	Combined covariance matrix (block matrix of order $p \times q$)
var(U), var(W)	Variance of canonical variables U and W
cov(U, W)	Covariance between the canonical variables
corr(U, W)	Canonical correlation coefficient
L(a, b)	Lagrangian function used to solve the canonical correlation maximization problem
$\partial L/\partial a$, $\partial L/\partial b$	Partial derivatives of the Lagrangian concerning a and b

References

Ali, H.A., Faraj, J.J., Hussien, F.M. (2021). Effect of pH on biogas production during anaerobic digestion. *Journal of University of Shanghai for Science and Technology*, *23*(8), 224–231. https://doi.org/10.51201/jusst/21/08369

Alvarado-Reyna, P., Albalate-Ramírez, A., García-Balandrán, E., Escamilla-Alvarado, C., Galván-Arzola, U., Miramontes-Martínez, L., & Rivas-García, P. (2024). Evaluation of the reaction capacity of early warning indicators to failures in biogas production systems. *Revista Mexicana de Ingeniería Química*, *23*(3), 1-30. https://doi.org/10.24275/rmiq/bio24313

Alves, D., Villar, I., Mato, S. (2023). Community composting strategies for biowaste treatment: methodology, bulking agent and compost quality. *Environmental science and pollution research*, *31*(7), 9873–9885. https://doi.org/10.1007/s11356-023-25564-x

Amiri, H., & Karimi, K. (2018). Pretreatment and hydrolysis of lignocellulosic wastes for butanol production: Challenges and perspectives. *Bioresource Technology*, *270*, 702-721. https://doi.org/10.1016/j.biortech.2018.08.117

Armah, E. K., Boamah, B. B., & Boakye, G. O. (2018). Impact of Water Hyacinth (Eicchornia crassipes) as a Feedstock for Biogas Production. *Chemical And Biomolecular Engineering*, *2*(4), 184. https://doi.org/10.11648/j.cbe.20170204.13

Badii, M. H., & Castillo, J. (2017). Análisis de correlación canónica (ACC) e investigación científica. *Revista Innovaciones de Negocios*, *4*(8). https://doi.org/10.29105/rinn4.8-9

Callegari, A., Tucci, M., Aulenta, F., Viggi, C. C., & Capodaglio, A. G. (2025). Anaerobic sludge digestion enhancement with bioelectrochemical and electrically conductive materials augmentation: A state of the art review. *Chemosphere*, *372*, 144101. https://doi.org/10.1016/j.chemosphere.2025.144101

Cao, Z., Jung, D., Olszewski, M. P., Arauzo, P. J., & Kruse, A. (2019). Hydrothermal carbonization of biogas digestate: Effect of digestate origin and process conditions. *Waste Management*, *100*, 138-150. https://doi.org/10.1016/j.wasman.2019.09.009

Chang, C., Chang, C., Lu, H., Hsieh, C., & Wu, J. (2025). Bioenergetically constrained dynamical microbial interactions govern the performance and stability of methane-producing bioreactors. *Npj Biofilms And Microbiomes*, *11*(1). https://doi.org/10.1038/s41522-025-00668-z

Chen, B., Azman, S., Crauwels, S., Dewil, R., & Appels, L. (2024). Mild alkaline conditions affect digester performance and community dynamics during long-term exposure. *Bioresource Technology*, *406*, 131009. https://doi.org/10.1016/j.biortech.2024.131009

Chew, K. R., Leong, H. Y., Khoo, K. S., Vo, D. N., Anjum, H., Chang, C., & Show, P. L. (2021). Effects of anaerobic digestion of food waste on biogas production and environmental impacts: a review. *Environmental Chemistry Letters*, *19*(4), 2921-2939. https://doi.org/10.1007/s10311-021-01220-z

Chiemchaisri, C., & Visvanathan, C. (2008). Greenhouse Gas Emission Potential of the Municipal Solid Waste Disposal Sites in Thailand. *Journal Of The Air & Waste Management Association*, ***58***(5), 629-635. https://doi.org/10.3155/1047-3289.58.5.629

El-Araby, R. (2024). Biofuel production: exploring renewable energy solutions for a greener future. *Biotechnology For Biofuels And Bioproducts*, *17*(1). https://doi.org/10.1186/s13068-024-02571-9

González, M. M. R., De León, E. M. D., Luque, L., Pitty, N., Arias, J., & Chen, A. (2024). Codigestión Anaeróbica de Lodos y Residuos Orgánicos Municipales en Clima Tropical. *I+D Tecnológico*, *20*(1), 82-93. https://doi.org/10.33412/idt.v20.1.3902

Goux, X., Calusinska, M., Lemaigre, S., Marynowska, M., Klocke, M., Udelhoven, T., Benizri, E., & Delfosse, P. (2015). Microbial community dynamics in replicate anaerobic digesters exposed sequentially to increasing organic loading rate, acidosis, and process recovery. *Biotechnology For Biofuels*, *8*(1). https://doi.org/10.1186/s13068-015-0309-9

Gupta, P., Kurien, C., & Mittal, M. (2022). Biogas (a promising bioenergy source): A critical review on the potential of biogas as a sustainable energy source for gaseous fuelled spark ignition engines. *International Journal Of Hydrogen Energy*, *48*(21), 7747-7769. https://doi.org/10.1016/j.ijhydene.2022.11.195

Hair, J.F., Anderson, R.E., Tatham, R.L., Black, W.C. (2009). *Multivariate data analysis* (7th ed.). Prentice Hall, Upper Saddle River, NJ.

Hasani, Z.A., Nayak, J.K., Balushi, N.J.A., Al-Mamun, A., Samal, K. (2025). Prospect of conductive materials in the anaerobic digester matrix for methane production: electron transfer and microbial communication. *Water*, *17*(9), 1321. https://doi.org/10.3390/w17091321

Helmer, M., Warrington, S., Mohammadi-Nejad, A., Ji, J.L., Howell, A., Rosand, B., Anticevic, A., Sotiropoulos, S.N., Murray, J.D. (2024). On the stability of canonical correlation analysis and partial least squares with application to brain-behavior associations. *Communications biology*, *7*(1). https://doi.org/10.1038/s42003-024-05869-4

Hernández-Eugenio, G., Espinosa-Solares, T., López-Ortiz, C., Meneses-Reyes, J.C., Ochoa-Bernal, T.G. (2025). Changes in microbial diversity and methane yield caused by overloading in systems of chicken litter, microalgae oil-free and glycerol in co-digestion. *Revista mexicana de ingeniería química*, *24*(2), IA25488. https://doi.org/10.24275/rmiq/IA25488

Hotelling, H. (1936). Relations between two sets of variants. *Biometrika*, *28*(3/4), 321–377.

Jameel, M. K., Mustafa, M. A., Ahmed, H. S., Mohammed, A. J., Ghazy, H., Shakir, M. N., Lawas, A. M., Mohammed, S. K., Idan, A. H., Mahmoud, Z. H., Sayadi, H., & Kianfar, E. (2024). Biogas: Production, properties, applications, economic and challenges: A review. *Results In Chemistry*, *7*, 101549. https://doi.org/10.1016/j.rechem.2024.101549

Karouach, F., Bakrim, W.B., Ezzariai, A., Mnaouer, I., Ibourki, M., Kibret, M., Sobeh, M., Hafidi, M., Kouisni, L. (2023). Valorization of water hyacinth to biomethane and biofertilizer through anaerobic digestion technology. *Fuel*, *358*, 130008. https://doi.org/10.1016/j.fuel.2023.130008

Khalil, B., Ouarda, T., & St-Hilaire, A. (2011). Estimation of water quality characteristics at ungauged sites using artificial neural networks and canonical correlation analysis. *Journal Of Hydrology*, *405*(3-4), 277-287. https://doi.org/10.1016/j.jhydrol.2011.05.024

Khan, I. U., Othman, M. H. D., Hashim, H., Matsuura, T., Ismail, A., Rezaei-DashtArzhandi, M., & Azelee, I. W. (2017). Biogas as a renewable energy fuel – A review of biogas upgrading, utilisation and storage. *Energy Conversion And Management*, *150*, 277-294. https://doi.org/10.1016/j.enconman.2017.08.035

Kumar, V., Singh, J., Nadeem, M., Kumar, P., & Pathak, V. V. (2018). Experimental and Kinetics Studies for Biogas Production Using Water Hyacinth (*Eichhornia crassipes* [Mart.] Solms) and Sugar Mill Effluent. *Waste And Biomass Valorization*, *11*(1), 109-119. https://doi.org/10.1007/s12649-018-0412-9

Martínez, E. J., Gil, M. V., Fernandez, C., Rosas, J. G., & Gómez, X. (2016). Anaerobic Codigestion of Sludge: Addition of Butcher's Fat Waste as a Cosubstrate for Increasing Biogas Production. *PLoS ONE*, *11*(4), e0153139. https://doi.org/10.1371/journal.pone.0153139

Mohammed, M., Belkair, A., Hamad, T., Jirhiman, I., Hassan, R., & Ahmeedah, A. (2022). Improving biogas production from animal manure by batch anaerobic digestion. *Algerian Journal of Engineering and Technology*, 6, 79–84. https://doi.org/10.5281/zenodo.6561086

Molina-Aguilar, J. P., Gutiérrez-López, A., & Cruz-Paz, I. M. (2019). Correlación canónica entre volúmenes de almacenamiento en presas e intensidades de precipitación durante huracanes. *Tecnología y Ciencias del Agua*, *10*(6), 25-56. https://doi.org/10.24850/j-tyca-2019-06-02

Nakasima-López, M., Taboada-González, P., Aguilar-Virgen, Q., & Velázquez-Limón, N. (2017).

Adaptación de Inóculos Durante el Arranque de la Digestión Anaerobia con Residuos Sólidos Orgánicos. *Información Tecnológica*, *28*(1), 199-208. https://doi.org/10.4067/s0718-07642017000100020

Negi, S., Chai, J., Tjhin, A. C. T., & Pan, S. (2025). Electro-anaerobic digestion as carbon–neutral solutions. *Chemical And Biological Technologies In Agriculture*, *12*(1). https://doi.org/10.1186/s40538-025-00776-0

Otto, P., Puchol-Royo, R., Ortega-Legarreta, A., Tanner, K., Tideman, J., De Vries, S., Pascual, J., Porcar, M., Latorre-Pérez, A., & Abendroth, C. (2024). Multivariate comparison of taxonomic, chemical and operational data from 80 different full-scale anaerobic digester-related systems. *Biotechnology For Biofuels And Bioproducts*, *17*(1). https://doi.org/10.1186/s13068-024-02525-1

Pottipati, S., Yadav, K. D., & Kalamdhad, A. S. (2021). The Potential of Biogas Production from Water Hyacinth by Using a Floating Drum Biogas Reactor. *Springer eBooks*, pp. 215-223. https://doi.org/10.1007/978-3-030-70463-6_20

Rolewicz-Kalińska, A., Lelicińska-Serafin, K., Manczarski, P. (2020). The circular economy and organic fraction of municipal solid waste recycling strategies. *Energies*, *13*(17), 4366. https://doi.org/10.3390/en13174366

Soto, M., Ruiz, I. (2021). Co-digestión anaerobia para la obtención de biogás a partir de residuos forestales. Tesis de doctorado, *Universidad de A Coruña*. https://ruc.udc.es/dspace/handle/2183/29172

Statista. (2024). Global natural gas consumption 1998–2023. *Statista*. Disponible en: https://www.statista.com/statistics/282717/global-natural-gas-consumption/

Stylianou, M., Laifi, T., Bennici, S., Dutournie, P., Limousy, L., Agapiou, A., Papamichael, I., Khiari, B., Jeguirim, M., & Zorpas, A. A. (2023). Tomato waste biochar in the framework of circular economy. *The Science Of The Total Environment*, *871*, 161959. https://doi.org/10.1016/j.scitotenv.2023.161959

Themelis N.J. y Ulloa P.A. (2007). Methane generation in landfills. Renew. *Energy*, *32* (7), 1243-1257. https://doi.org/10.1016/j.renene.2006.04.020

Triviño-Pineda, J., Sanchez-Rodriguez, A., & Peláez, N. P. (2024). Biogas production from organic solid waste through anaerobic digestion: A meta-analysis. *Case Studies In Chemical And Environmental Engineering*, *9*, 100618. https://doi.org/10.1016/j.cscee.2024.100618

Walker, M., Zhang, Y., Heaven, S., & Banks, C. (2009). Potential errors in the quantitative evaluation of biogas production in anaerobic digestion processes. *Bioresource Technology, 100*(24), 6339-6346. https://doi.org/10.1016/j.biortech.2009.07.018

Zhuang, X., Yang, Z., & Cordes, D. (2020). A technical review of canonical correlation analysis for neuroscience applications. *Human Brain Mapping, 41*(13), 3807-3833. https://doi.org/10.1002/hbm.25090

Vol. 24, No. 3(2025) IA25620
Revista Mexicana de Ingeniería Química

Treatment of brackish sardine processing wastewater employing an integrated anaerobic/anoxic/aerobic fixed-bed reactor

Tratamiento de aguas salobres de la industria sardinera en un reactor integrado anaerobio/anoxico/aerobio de lecho fijo

C. D. Loreto-Muñoz [1], C. Gastelum-Rosas[1], G. López-Avilés[1], M. Plascencia-Jatomea[2], F.J. Almendariz-Tapia[1‡]
[1]Department of Chemical Engineering and Metallurgy, University of Sonora.
[2]Department of Research and Postgraduate Studies in Food, University of Sonora.
Sent date: June 30, 2025; Accepted: September 23, 2025

Abstract
Marine product processing of sardines, shrimp, and squid generates large quantities of wastewater with high organic matter, protein, nitrogen, and salts. Biological wastewater treatment for brackish sardine processing wastewater (SPW) requires the combination of anaerobic, anoxic, and aerobic stages and microorganisms that can tolerate brackish conditions. This study evaluates the treatment of brackish sardine processing wastewater in an integrated anaerobic/anoxic/aerobic fixed-bed reactor. Anaerobic and aerobic consortia were adapted to denitrifying and nitrifying conditions with synthetic influents. The treatment of a synthetic influent mimicking a brackish sardine processing wastewater was evaluated in the integrated anaerobic/anoxic/aerobic up-flow reactor once both reactors reached steady state. The reactor operated with gradual salinity increases from 1 – 14 g NaCl/L, 2 d HRT, 7.5 pH, and 35°C. The increase to 14 g NaCl/L, pH control, and nitrate recirculation (Stage VI) favored the performance of the IAAB, attaining an overall 94.1% COD removal, 99.70% protein removal, 92.86% protein hydrolysis, and 21.93% nitrate yield. This study shows the feasibility of employing an integrated anaerobic/anoxic/aerobic reactor to treat industrial sardine effluents containing carbon and nitrogen compounds.
Keywords: brackish wastewater, sardine processing wastewater, integrated anaerobic/anoxic/aerobic reactor, salinity, protein hydrolysis.

Resumen
El procesamiento de productos marinos como sardinas, camarones y calamares genera grandes cantidades de agua residual, con un alto contenido de materia orgánica, proteínas, nitrógeno y sales. El tratamiento biológico de aguas residuales pesqueras requiere de la combinación de una etapa anaerobia, anóxica y aerobia, y microorganismos que puedan tolerar alta salinidad. Este estudio evalúa el tratamiento de un agua residual pesquera en un reactor de lecho fijo integrado anaerobio/anóxico/aerobio. Los consorcios anaerobios y aerobios se adaptaron a condiciones desnitrificantes y nitrificantes con efluentes sintéticos. Una vez que ambos reactores se estabilizaron, se evaluó el tratamiento de un efluente sintético simulando un agua residual pesquera salobre en un reactor integrado anaerobio/anoxico/aerobio (IAAB) de flujo ascendente. El reactor operó con un incremento gradual de salinidad de 1 – 14 g NaCl/L, 2 d TRH, pH de 7.5 y 35 °C. El incremento a 14 g NaCl/L, control de pH y reflujo de nitrato (Etapa VI) favoreció el rendimiento del reactor integrado alcanzando una remoción global de DQO del 94.1%, 99.70% de remoción de proteínas, 92.86% de hidrólisis de proteínas y 21.93% de conversión de nitrato. Este estudio demuestra la viabilidad de emplear un reactor anaerobio/anóxico/aerobio integrado para tratar efluentes industriales del procesamiento de sardinas que contienen compuestos de carbono y nitrógeno.
Palabras clave: aguas residuales salobres, aguas residuales de la industria sardinera, reactor integrado anaerobio/anóxico/aerobio, salinidad, hidrólisis de proteínas.

‡*Corresponding author. E-mail*: javier.almendariz@unison.mx;
https://doi.org/10.24275/rmiq/IA25620
ISSN:1665-2738, *issn-e*: 2395-8472

1 Introduction

The seafood processing industry of sardines, shrimp, and squid, amongst others, consumes 2% of the freshwater consumed by the food and beverage industry. Water is used throughout processing, including cleaning, cooking, and cooling, resulting in high-strength wastewater containing salts, lipids, and proteins (Pereira *et al.*, 2022). Fish canning, sardine processing, and seafood processing wastewater commonly contain high salinity, suspended solids, organic matter, proteins, and nitrogen concentrations (Val del Rio *et al*., 2018; Chen *et al*., 2021; Ismail *et al*., 2022). Volume and pollutant concentration depend on the fish type, processing methods, region, production, and season. For example, the fish canning industry generates wastewater with a pH ranging between 5.6 and 9.6, 1.14 – 90 g COD/L, 20 – 2000 mg TN/L, 156 – 26,816 mg/L of oil and grease, and 2 -36 g NaCl/L (Casero-Díaz *et al*., 2024; Feizi *et al*., 2024). Canned sardine wastewater (CSW) is protein-rich and contains 100 – 3,000 mg BOD_5/L, 1,000 – 18,000 mg COD/L, and 80 – 1,000 mg N/L (Srimachai *et al.*, 2024).

Although nitrogen is an essential component of living organisms, nitrate (NO_3^-) and nitrite (NO_2^-) can lead to health problems and eutrophication (Lanzagorta-Cortes *et al.*, 2025). Sardine processing wastewater (SPW) is usually untreated and discharged into the sea or estuaries, leading to eutrophication (Chowdhury *et al*., 2010; Sanjaya *et al*., 2020). Additionally, the high organic load in SPW causes a decrease in dissolved oxygen concentrations in water, decreasing water organisms and producing odorous gases (Prihandrijanti *et al.*, 2021).

Chemical, physical, and biological treatment technologies can be applied for FPW removal from wastewater, including hydrolysis, bioremediation, methane fermentation, and filtration (Sanjaya *et al.*, 2020). Due to low cost and energy consumption, as well as the capacity of bacteria to adapt to high salinity levels and high organic loading, biological systems are an alternative for treatment (Jemli *et al.*, 2015). Some studies have focused on wastewater treatment designs for fish cannery wastewater, including physical and biological stages, both anaerobic and aerobic processes (Prihandrijanti *et al.*, 2021). For example, anaerobic digestion is economical, sustainable, and environmentally friendly, and is usually used by fish processing industries for chemical oxygen demand and protein treatment (Chen *et al.*, 2021). High nitrogen levels, likely due to lipid and protein content in fish processing wastewater (FPW), can be suitable for anaerobic digestion and biogas production; nonetheless, salinity can cause inhibition in the process (Choudhury *et al.*, 2022). SPW contains proteins that decompose into ammonia nitrogen during anaerobic digestion (Panpong *et al.*, 2017). Treatment of fish waste, FPW, SPW, and recirculating aquaculture systems (RAS) have employed anaerobic batch and continuous fed, UASB, and fixed bed reactors under brackish and saline conditions. Fixed-bed anaerobic reactors have been used to treat high wastewater loads (Choudhury *et al.*, 2022).

High ammonium concentrations can harm microorganisms (Val del Rio *et al.*, 2018; Huiliñir *et al.*, 2012). Denitrification is the process that produces nitrogen gas (N_2) due to biological nitrate removal. In anoxic denitrification, organic carbon sources become electron donors, while nitrate is used as an electron acceptor (Negari, 2023). In aerobic conditions, through nitrification, ammonia nitrogen converts to nitrate, a less toxic compound (Medellín-Castillo *et al.*, 2024). The coupling of nitrification to denitrification allows molecular nitrogen as an end product (Hernández-Fydrych *et al.*, 2018). Combining both anaerobic and aerobic processes for SPW treatment is a promising solution, using the anaerobic stage as a pre-treatment (Paulo *et al.*, 2021).

Biological wastewater treatment for brackish sardine industrial wastewater requires denitrifying and nitrifying stages, and microorganisms that can tolerate high salinity. Brackish wastewaters contain 0.5 to 30 g/L of salinity concentrations. High salinity and concentrated organic matter can inhibit microbial activity. Salinity can cause cell lysis, dehydration, and intracellular and extracellular enzyme reduction in unacclimated microbes, causing metabolism inhibition (Choudhury *et al.*, 2022). Recent interest has been shown in SPW treatment. Still, infrastructure, digestate management, process efficiency, and reactor design challenges require attention. Integrated anaerobic/aerobic systems allow higher chemical oxygen demand (COD) removal efficiencies, reduce space, eliminate odors, and allow lower solid production (Chan *et al.*, 2009).

This study evaluates brackish sardine industrial wastewater in an integrated anaerobic/anoxic/aerobic fixed-bed reactor. The proposed treatment consists of an anaerobic-anoxic-aerobic treatment train for simultaneous nitrogen and organic pollutant removal in FPW in a single reactor.

2 Materials and methods

2.1 Sardine processing wastewater (SPW)

A brackish sardine processing wastewater from Guaymas, Sonora, Mexico, was collected and characterized based on physicochemical parameters. Characterization included chemical oxygen demand (COD), biological oxygen demand in five days (BOD_5), conductivity, ammoniacal and organic nitrogen, total

(TS), volatile (VS), fixed solids (FS), and salt concentration.

COD was determined by open reflux digestion, with a dilution factor of 40. BOD_5 was determined in Wheaton vials. Grease and oil were quantified by Soxhlet extraction; quantification includes substances with similar physicochemical properties that can be extracted with hexane, such as fatty acids, grease, waxes, hydrocarbons, and lubricating oils. Total dissolved solids (TDS), salt concentration, and conductivity were measured by HACH SESION 5. The Kjeldahl method was employed for ammoniacal and organic nitrogen, while total Kjeldahl nitrogen (TKN) was determined using equation 1:

$$N_{TKN} = N_{NH_3} + N_{organic} \quad (1)$$

where: N_{TKN} = total Kjendahl nitrogen (mg/L), N_{NH_3} = ammoniacal nitrogen (mg/L), and $N_{organic}$ = organic nitrogen (mg/L) (Rice and Bridgewater, 2012).

2.2 Culture media

The culture media employed for the anaerobic denitrifying reactor (ADR) contained (in mg/L): NH_4Cl (475), K_2HPO_4 (580), KH_2PO_4 (230), $MgSO_4{\cdot}7H_20$ (90), $CaCl_2$ (53), $NaHCO_3$ (2000), $NaNO_3$ (2276.7), NaCl (1000), Glucose (1876), and 1 mL/L of trace element solution.

The culture media employed for the aerobic nitrifying reactor (ANR) contained (in mg/L): NH_4Cl (320.9), KH_2PO_4 (109.8), $CaCl_2$ (66.48), $MgSO_4{\cdot}7H_2O$ (318.6), $NaHCO_3$ (1000), sucrose (1000), NaCl (1000), and 1 mL/L of trace element solution.

The synthetic inlet of the integrated anaerobic/anoxic/aerobic reactor (IAAB) contained (in mg/L): peptone from casein (3000), $CaCl_2$ (0.5), $MgSO_4{\cdot}7H_2O$ (5), $NaHCO_3$ (400), NaCl (1000), yeast extract (50), and 1 mL/L of trace element solution.

The trace element solution contained (in mg/L): $FeCl_2{\cdot}4H_2O$ (2000), $MnCl_2$ (500), EDTA (500), Na_2SeO_3 (100), H_2BO_3 (50), $ZnCl_2$ (50), $(NH_4)_6Mo_7O_{24}{\cdot}4H_2O$ (50), $AlCl_3$ (50), $NiCl_3{\cdot}6H_2O$ (50), $NiCl_3{\cdot}6H_2O$ (50), $CoCl_2{\cdot}2H_2O$ (50), $CuCl_2{\cdot}2H_2O$ (50), and 36% HCl (1 mL/L).

2.3 Biomass immobilization

An anaerobic sludge was collected from a bioreactor employed for brewery effluent treatment, from Ciudad Obregon, Sonora. The anaerobic biomass was immobilized in a 1.75 L acrylic reactor with recirculation, packed with 300 g of clinoptilolite zeolite (0.5 – 0.8 mm) and 300 g of anaerobic sludge, using 2 g COD/L, with glucose as substrate. The aerobic sludge was collected from a municipal wastewater treatment plant, "Los Arroyos" from Hermosillo, Sonora. The aerobic biomass was immobilized in a 1.23 L glass bioreactor with recirculation, packed with 1 kg of clinoptilolite zeolite (1 – 3 mm), and inoculated with 500 mL of aerobic sludge. During the start-up phase, the reactor was fed glucose with 1 g COD/L·d, followed by an increase to 5 g COD/L·d to favor biomass adherence to the support. Both reactors operated at pH 7 and 35 °C in a temperature-controlled chamber. The immobilization process was assessed for 30 days using the gravimetric method. Both consortia were immobilized within 17 and 21 days of operation, respectively. Once the immobilization phase ended, both consortia were adapted to denitrifying (anaerobic) and nitrifying (aerobic) conditions.

2.4 Anaerobic Denitrifying (ADR) and Aerobic Nitrifying (ANR) Reactors

The anaerobic consortium was adapted to denitrifying conditions with a nitrate-rich synthetic inlet with 1660 mg NO_3^-/L, hydraulic residence time (HRT) of 1 d, pH of 7, and 35°C, and glucose as carbon source (2 g COD/L·d). The aerobic consortium was adapted to nitrifying conditions with an ammonium-rich synthetic inlet, containing 17.833 mmol NH_3/L, using an HRT of 1 d, pH of 7, and 35°C. The organic loading rate (OLR) was decreased from 5 to 3 g COD/L·d to allow autotrophic conditions. COD, pH, protein, and ammonium concentration were determined in the inlet and outlet of both reactors. Additionally, methane was determined in the anaerobic reactor. Nitrate was only determined in the aerobic reactor. The adaptation period concluded once both reactors reached a COD removal efficiency above 90%. Denitrifying and nitrifying conditions were supposed once nitrate and ammonium removal efficiencies reached a steady state.

2.5 Integrated Anaerobic/Anoxic/Aerobic Biological Fixed Bed Reactor (IAAB)

Once both consortia were adapted, the treatment of a synthetic inlet, mimicking brackish sardine processing wastewater, was evaluated in the integrated anaerobic/anoxic/aerobic (IAAB) fixed bed reactor (Figure 1). An anaerobic denitrifying (ADR), anoxic region (AO), and aerobic nitrifying (ANR) reactor formed the integrated system. Both the anaerobic and aerobic regions were separated by an aerobic chamber containing four air diffusers connected to an external air pump. The integrated system had a 3.5 L operating volume, 1 m height, and 7 cm i.d. The operating conditions of the reactor were HRT = 2 d, 7.5 pH, and 35 °C, as described in Table 1.

The synthetic inlet of the reactor was prepared based on brackish sardine processing wastewater characterization, where casein peptone was used as the protein source.

Table 1. Operational parameters in the integrated anaerobic/anoxic/aerobic fixed-bed reactor.

Stage	Units	I	II	III	IV	V	VI
HRT_G	h	48	48	48	48	48	48
HRT_{ADR}	h	24	24	24	24	24	24
HRT_{ANR}	h	24	24	24	24	24	24
T	°C	35	35	35	35	35	35
pH	-	7 - 8	7 - 8	7 - 8	7 - 8	7 - 8	7 - 8
COD Inlet	gCOD/L·d	5	5	5	5	5	5
Protein Inlet	g/L·d	2.30	2.30	2.30	2.30	2.30	2.30
NaCl	g/L	1	5	10	14	14	14
$NaHCO_3$	g/L	-	-	-	-	4.15	4.15
NO_3^- Recirculation Stream	g/L	-	-	-	-	-	0.16

First, the integrated system operated with gradual salinity increases from 1 – 14 g NaCl/L (S_1 = 1 g/L; S_2 = 5 g/L; S_3 = 10 g/L; S_4 = 14 g/L), with a 2 C/N ratio. Afterward, sodium bicarbonate was fed to the reactor through the air chamber as an alkalinity buffer to ensure a 1.67 C/N ratio in the aerobic region (Stage V). Protein, ammonium, nitrate, nitrite, COD, and pH were measured in the inlet and outlet of the IAAB reactor.

The synthetic SPW was fed to the anaerobic chamber (ADR) or ammonifying stage. In this stage, hydrolyzed proteins and nitrates transform into ammonium. Additionally, anaerobic digestion produces biogas, which was not quantified. Afterward, the produced ammonium enters the aerobic chamber (ANR) or nitrifying stage and transforms to nitrate again. To generate an anoxic (AO) region where nitrates are denitrified, an additional recirculation stream from the nitrifying to the ammonifying chamber was added (Stage VI). This final step assures the removal of both the carbon and nitrogen source.

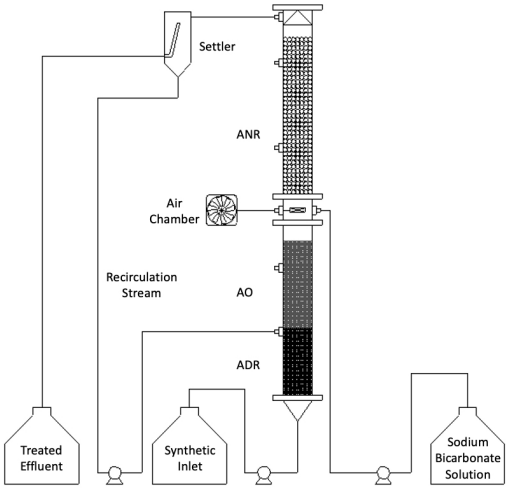

Figure 1. Schematic representation of the integrated anaerobic/anoxic/aerobic fixed bed reactor, formed by the anaerobic denitrifying reactor (ADR), anoxic region (AO), and the aerobic nitrifying reactor (ANR); operating volume of 3.5 L, 1 m height, 7 cm internal diameter.

2.6 Analytical methods

Chemical oxygen demand (COD) was determined by closed reflux digestion using a DR/890 HACH kit. Proteins were measured by the Lowry-Peterson Method (Peterson, 1977). TS, SS, and FS were determined using techniques established in the Standard Methods for the Examination of Water and Wastewater (Rice and Bridgewater, 2012). Ammonium was measured by the salicylate method and an ammonium-specific ion electrode (Cole-Palmer K-27504-00). Nitrate was quantified with a high-range Nitra-Ver5 Hach kit and an ion-specific electrode (Cole-Palmer K-27504-22). Back-titration determined carbonates as described by Powell and Archer (1989). pH was measured with an Orion 266s (Thermo Electron Corporation) potentiometer and an HI 1230B electrode. Displacement of a 3% NaOH solution was used for methane determination.

2.7 Calculations

COD removal efficiency was calculated using equation 2:

$$\%COD_i = 100\ x \left(\frac{I_{COD,i} - E_{COD,i}}{I_{COD,i}} \right) \qquad (2)$$

where: $I_{COD,i}$ = organic matter concentration in the inlet of the *"i"* reactor, $E_{COD,i}$ = organic matter concentration in the effluent of the *"i"* reactor, and *"i"* represents the stage in the reactor.

The protein removal efficiency in the integrated anaerobic/anoxic/aerobic reactor ($\%P_{IAAB}$, Eq. 3) and anaerobic denitrifying reactor ($\%P_{ADR}$, *Eq.* 4) was determined using the following equations:

$$\%P_i = 100\ x \left(\frac{I_{P,i} - E_{P,i}}{I_{P,i}} \right) \qquad (3)$$

where: $I_{P,i}$ = protein concentration in the inlet of the *"i"* reactor, $E_{P,\,i}$ = protein concentration in the effluent of the *"i"* reactor, $E_{P,i}$ = protein concentration in the *"i"* reactor, and *"i"* represents the stage in the reactor.

Theoretical ammonium production (mg NH_4^+/L) was estimated by considering that proteins have 16% of

nitrogen and a complete protein hydrolysis, as follows:

$$NH_{4,\ Theoretical}^{+} = 1000 \cdot \left(\frac{P_{R,\ ADR} \cdot F_N}{M_N} \right) M_{NH_4^+} \quad (4)$$

where: $P_{R,\ ADR}$ = protein removal in the ADR (g/L), F_N = 0.16 g N/g protein, M_N = 14 g N/mol, $M_{NH_4^+}$ = 18 g $NH_4{}^+$/mol.

Protein hydrolysis was determined using the theoretical ammonium concentration according to stoichiometry, as follows:

$$\%H_{ADR} = 100\ x \left(\frac{NH_{4,\ ADR}^{+}}{NH_{4,\ Theoretical}^{+}} \right) \quad (5)$$

where: $NH_{4,\ ADR}^{+}$= ammonium concentration in mg/L in the ADR effluent.

Ammonium removal efficiency was only determined in the ANR using equation 6:

$$\%NH_{4,\ ANR}^{+} = 100\ x \left(\frac{E_{NH_4^+,ADR} - E_{NH_4^+,ANR}}{E_{NH_4^+,ADR}} \right) \quad (6)$$

where: $E_{NH_4^+,ADR}$ = ammonium concentration in the outlet of the ADR, and $E_{NH_4^+,ANR}$ = ammonium concentration in the outlet of the ANR.

Theoretical nitrate and nitrate yield were determined using a stoichiometric ratio, as follows:

$$NO_{3,\ Theoretical}^{-} = NH_{4,\ R}^{+} \cdot 3.45 \quad (7)$$

$$\%NO_{3,\ Yield}^{-} = 100\ x \left(\frac{E_{NO_3^-,\ ANR}}{NO_{3,\ Theoretical}^{-}} \right) \quad (8)$$

where: $NO_{3,\ Theoretical}^{-}$ = theoretical nitrate production based on ammonium removal in the ANR, $NH_{4,\ R}^{+}$ = ammonium removal in the ANR, and $E_{NO_3^-,\ ANR}$ = nitrate concentration in the outlet of the ANR.

3 Results and discussion

3.1 Sardine Processing Wastewater (SPW)

Typical brackish sardine processing wastewater (SPW) contains organic matter that is easily degraded, except for grease and oil. Table 2 shows the physicochemical properties of the collected sardine industrial wastewater sample from the region. Sample characterization results are similar to the canned sardine wastewater characterized by Panpong, *et al.* (2017), containing pH 6.8, 14.4 g COD/L, 0.87 g/L of total nitrogen, 3.90 g/L of protein, and 0.13 g/L of grease. COD content compares to the sardine cooking wastewater reported by Pereira, *et al.* (2022) with 28.08 g COD/L. SPW composition varies depending on the industrial origin and overall fish output. The sample contains considerable amounts of grease, oil, and solids. High quantities of these components occlude pipes, decrease organic matter degradation, and compromise biodegradability (Paulo *et al.*, 2021). The BOD_5/COD ratio indicates that the wastewater sample can be easily biodegraded (Feizi *et al.*, 2024). The high conductivity and salt content indicate that microorganisms with high salinity tolerance are required to avoid cellular lysis (Choudhury *et al.*, 2022). The synthetic wastewater fed to the integrated system was prepared based on the characterization of the collected wastewater.

3.2 Anaerobic and aerobic biomass immobilization

Biomass immobilization was conducted in a batch system with recirculation to favor biomass adherence to the zeolite. Maximum immobilization of the anaerobic bioreactor was attained within 15 days of operation with a 0.036 g IVS/g zeolite, reaching high removal efficiencies for COD (94±3%) and nitrate (82±11%). The aerobic reactor lasted 21 days, reaching its maximum immobilization on the eleventh day (0.038 g IVS/g zeolite). The removal efficiencies attained for COD and nitrate yield were 94±4% and 54±11%, respectively.

3.3 Anaerobic Denitrifying (ADR) and Aerobic Nitrifying (ANR) Reactors

Following the immobilization of the anaerobic and aerobic biomass, both reactors were acclimated to ammonifying (anaerobic) and nitrifying (aerobic) conditions.

Table 2. Physicochemical characterization of the brackish sardine processing wastewater.

Parameter		g/L	Parameter		g/L
	pH	6.38	Ammoniacal	Total	0.21
	COD	29.21	Nitrogen	Soluble	0.14
	BOD_5	17.14	Organic	Total	1.94
	BOD_5/COD	0.59	Nitrogen	Soluble	1.72
Grease	Total (TS)	13.00	N_{TKN}	Total	2.15
and oil	Fixed (FS)	2.72		Soluble	1.87
(as solids)	Volatile (VS)	10.28	Salts %	%	15.90
	Total Dissolved (TDS)	15.13	Conductivity	mS/cm	18.58

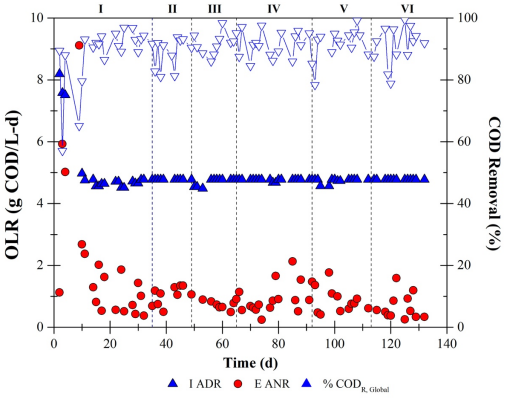

Figure 2. Organic loading rates and removal efficiency in the integrated anaerobic/anoxic/aerobic reactor.

Nitrate concentration and the OLR remained constant during the anaerobic denitrifying reactor (ADR) operation. After 35 days, COD removal efficiency ranged between 81 and 90%, while nitrate removal reached 76±12%. The results indicate a rapid and efficient microorganism adaptation to high nitrate concentrations. Nitrate removal in anaerobic digestion can be attributed the nitrate conversion to ammonium in the ADR.

The aerobic nitrifying reactor (ANR) was acclimated with a high OLR (5 g COD/L·d) followed by a decrease in the OLR (1 g COD/L·d) and ammonium addition. During the 30 d of operation, the aerobic biomass efficiently removed the organic matter fed to the reactor (92±3%). Nonetheless, ammonium conversion to nitrate stabilized at 41±14%, with a decrease in the OLR. The inhibition in nitrate production can be attributed to heterotrophic and nitrifying bacteria competing for oxygen.

3.4 Integrated Anaerobic/Anoxic/Aerobic Biological Fixed Bed Reactor (IAAB)

3.4.1 Organic matter degradation

The IAAB salinity increase (Stages I-IV) began once the ADR and ANR reactors were coupled. Figure 2 shows the COD removal efficiency in the integrated anaerobic/anoxic/aerobic reactor. After coupling the anaerobic and aerobic reactors and salt increase, the ADR reached a 76% COD removal (Stages II-IV), indicating that microorganisms adapted to high salinity. Increase to 14 g NaCl/L and the addition of the NO_3^- recirculation stream increased COD removal to 86.4±7.95%.

Due to the configuration of the integrated system, the COD concentration in the inlet of the ANR was variable. COD removal efficiency in the ANR decreased significantly with salinity increase, from 64.20±2.28 (Stage I) to 40.80±2.7% (Stage VI). An additional bicarbonate solution was fed to increase the amount of inorganic carbon available to the autotrophic nitrifying bacteria, causing an increase of 54.4±3.1% in COD removal. The recirculation stream added in the final stage of operation favored carbon matter removal in both regions. Global organic matter removal showed no adverse effect with salt increase, reaching efficiencies above 85% for all stages (Table 3).

3.4.2 Protein hydrolysis

Table 3 shows the overall protein hydrolysis and nitrate yield efficiencies in the integrated anaerobic/anoxic/aerobic reactor under salt increase (Stages I-VI). Protein hydrolysis was carried out in the ADR, as shown in Figure 3a. Results indicate high protein hydrolysis regardless of salinity increase. Peak hydrolysis was attained at Stage IV (14 g NaCl/L), with a 98.95±6.66%. Adding the anoxic region also favored protein hydrolysis, reaching 92.86±7.89% (Stage VI). In anoxic conditions, hydrolysis rates increase due to nitrate increase (Huiliñir *et al.*, 2012).

Although aerobic conditions prevailed in the ANR, the remaining protein was gradually degraded, with final stages reaching efficiencies above 85%. Protein degradation can be attributed to anaerobic regions in the ANR due to incomplete aeration, allowing protein hydrolysis. Additionally, heterotrophic bacteria can consume proteins to produce smaller molecules that can enter the Krebs cycle or glycolysis pathways.

3.4.3 Nitrogen compounds

Ammonium production in the ADR remained constant for lower salt concentrations (1 – 10 g NaCl/L), reaching 373.98±44.64, 3567.95±58.84, and 337.92 mg NH_4^+/L for Stages I, II, and III, respectively. Nonetheless, salinity increase to 14 g NaCl/L increased ammonium production, with the highest production attained during Stage V (454.7±33.04 mg NH_4^+/L). Therefore, salinity increase favored ammonium production in the ADR. Salt increase can favor protein hydrolysis, increasing ammonium production (Shi *et al.*, 2014). Ammonium production remained constant with the nitrate recirculation stream (Stage VI).

Ammonium inlet concentration in the ANR was variable; therefore, ammonium removal varied in each stage. At least 60% of the fed ammonium was removed in the early stages of the reactor (Stages I-III). The increase to 10 and 14 g NaCl/L caused instability in the ANR operation and a negatively impacted ammonium removal, decreasing to 109.58 mg NH_4^+/L (24.10%) in Stage IV. Adding the bicarbonate solution (Stage V) favored nitrifying bacteria and reactor stability, increasing ammonium removal to 53.83% and 56.34%, for Stages V and VI. Additionally, the overall ammonium removal increased to 56±16.4%.

The average ammonium removed through nitrification in the ANR was 30.83±0.33%, 77±1.63, and 43.05±0.29% for Stages I, II, and III, respectively. The highest nitrate yield was attained at 5 g NaCl/L (Stage II), reaching 1,089.02±284.90 g NO_3^-/L ($\%NO_{3,\ Yield}^-$=77±1.63%). The increase in salt concentration to 10 (Stage III) and 14 g NaCl/L (Stage IV) affected nitrification, as shown in Figure 3c. Low alkalinity (< 50 mg $CaCO_3$/L) in water leads to unstable pH, inhibiting nitrification. A ratio between 6.5 - 7.14 g of alkalinity is consumed for each gram of produced nitrate (Medellín-Castillo *et al.*, 2024). Adding bicarbonate (Stage V-VI) improved nitrifying bacteria development, causing a gradual increase in ammonium conversion to nitrate, reaching 21.93±6.70% in Stage VI. Maintaining pH between 6.8 and 7.2 can prevent ammonia toxicity, improving nitrification (Mahat *et al.*, 2021). Nitrification, biomass generation, and cellular regeneration are responsible for ammonium removal, allowing a simultaneous treatment of contaminants.

Protein hydrolysis and COD removal showed a positive effect with increased salt concentration up to 14 g NaCl/L, favoring ammonification in the ADR. Nonetheless, as shown by ammonium removal and nitrate yield, higher salt concentrations inhibited nitrification. In a multi-stage anoxic-oxic (AO) system, proposed by Shi, *et al*. (2025), COD, nitrogen, and ammonium removal efficiencies remained stable under 0 – 10 g NaCl/L; nonetheless, the initial addition of salt impacted microorganisms. Nitrifying and denitrifying bacteria are impacted by salinity but can eventually adapt and reach stability, allowing high nitrogen removal efficiencies.

Overall attained efficiencies were 94.1% COD removal, 99.70% protein removal, 92.86% protein hydrolysis, and 21.93% nitrate yield, as shown in Table 3. These results indicate that although high salinity inhibited nitrification and denitrification, COD removal increased. The increase up to 14 g NaCl/L alongside the addition of bicarbonate and NO_3^- recirculation stream (Stage V-VI) improved the performance of the reactor, including nitrification and denitrification processes. Integrated anaerobic/anoxic/aerobic sequential batch reactors can reach COD removal efficiencies above 90% and high nitrogen removal. Combining anaerobic-aerobic fixed bioreactors allows simultaneous organic matter and nitrogen removal efficiencies from wastewater with steady performance even at high loading (Rajab *et al.*, 2017). Denitrification decreases sludge production and can remove up to 69% of nitrogen, resulting in low operational costs; the remaining nitrogen can be converted via nitrification. Therefore, the coupling of denitrification and nitrification presents a solution for the simultaneous removal of organic matter and nitrogen from wastewater (Khan *et al.*, 2023). This study shows the feasibility of employing an integrated anaerobic/anoxic/aerobic reactor to treat industrial brackish sardine wastewater containing carbon and nitrogen compounds.

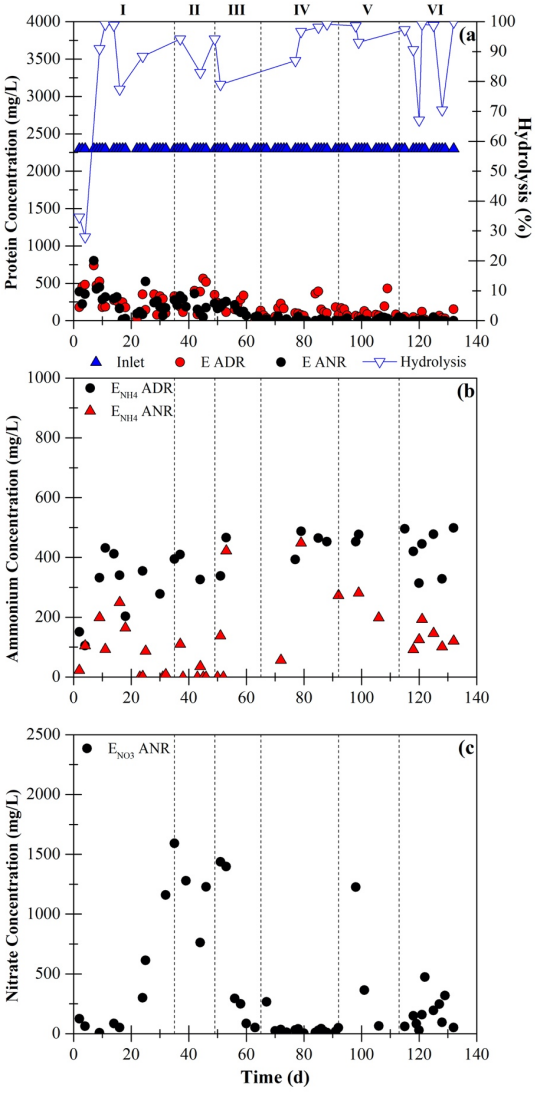

Figure 3. a) Protein hydrolysis, b) ammonium, and c) nitrite concentrations in the integrated anaerobic/anoxic/aerobic reactor.

Conclusions

The anaerobic and aerobic consortia were adapted to denitrifying and nitrifying conditions, reaching COD removal efficiencies above 90%, 76±12% nitrate removal, and 41±14% nitrate yield.

Global COD removal efficiencies remained above 85% for all stages, showing no inhibition to salinity increase up to 14 g NaCl/L. The COD was mainly removed by the ADR.

Table 3. Overall efficiencies in the integrated anaerobic/anoxic/aerobic reactor.

Stage		**Units**	**I**	**II**	**III**	**IV**	**V**	**VI**
Conditions			1 gNaCl/L	5 gNaCl/L	10 gNaCl/L	14 gNaCl/L	$NaHCO_3$	NO_3 Recirculation
ADR	COD removal	mg/L	2,925.8	2,937.2	3,025.9	2,968.3		3,351.2
		%COD	75.4	75.7	78.0	76.5		86.4
	Protein Inlet	mg/L	2300	2300	2300	2300		2300
	Protein Effluent	mg/L	288.16	319.24	195.75	129.44		49.77
	Protein Removal	mg/L	2,024.36	2009.78	2,119.30	2,117.95		2,250.23
		%	88.02	87.38	92.14	94.69		97.84
	NH_4^+ Inlet	mg/L	0	0	0	0		0
	NH_4^+ Effluent	mg/L	373.98	367.95	337.92	454.7		425.63
	Protein Hydrolysis	%	90.95	88.60	79.42	98.95		92.86
ANR	COD removal	mg/L	612	468.8	380.6	371.8	527.4	298
		%	64.2	49.8	44.6	40.8	54.4	56.5
	Protein Effluent	mg/L	264.29	207.71	132.82	10.21	16.65	6.901
	Protein Removal	mg/L	23.88	111.53	62.94	119.23	112.79	42.87
		%	8.29	34.94	32.15	92.11	87.13	86.14
	NH_4^+ Effluent	mg/L	95.74	74.08	190.08	259.18	250.60	162.96
	NH_4^+ Removal	mg/L	248.10	321.06	196.45	109.58	244.77	252.56
		%	66.34	87.26	58.14	24.10	53.83	56.34
	NO_3^- Inlet	mg/L	0	0	0	0	0	0
	NO_3^- Effluent	mg/L	376.43	1089.02	586.17	39.87	551.86	169.22
	NO_3^- Yield	%	30.83	77.00	43.05	9.08	15.70	21.93
IAAB	COD removal	mg/L	3,537.8	3,406	3,406.5	3,340.1	3,437.2	3,649.2
		%	91.2	87.8	87.8	86.1	88.6	94.1
	Protein Removal	mg/L	2035.71	20992	2167.18	2289.79	2283.35	2293.10
		%	88.51	90.97	94.23	99.56	99.28	99.70

Protein hydrolysis was gradually affected by salinity increase in early stages (I-III); nonetheless, it improved, reaching 98.95% (Stage V) and 92.86% (Stage VI) at 14 g NaCl/L. Also, salinity increases benefited ammonium production, with the highest production attained at 14 g NaCl/L (454.7±33.04 mg NH_4^+/L). After the salinity increase in the IAAB, results indicate adaptation to brackish conditions, showing efficient organic matter removal and protein hydrolysis.

Nitrification was affected at higher salt concentrations, reaching peak nitrate production at 5 g NaCl/L, and the lowest production at 14 g NaCl/L. pH increase through bicarbonate addition improved nitrification even at high salinity, reaching a 21.93±6.70% nitrate yield.

The increase to 14 g NaCl/L, pH control, and nitrate recirculation (Stage VI) favored the performance of the IAAB, attaining an overall 94.1% COD removal, 99.70% protein removal, 92.86% protein hydrolysis, and 21.93% nitrate yield.

Therefore, this study shows the feasibility of employing an integrated anaerobic/anoxic/aerobic reactor to treat brackish sardine processing wastewater containing carbon and nitrogen compounds in a single reactor.

Acknowledgements

The authors would like to acknowledge the support of the Department of Chemical Engineering and Metallurgy of the University of Sonora and the Secretariat of Science, Humanities, Technology, and Innovation (Secretaría de Ciencia, Humanidades, Tecnología e Innovación - SECIHTI).

Nomenclature

ADR	Anaerobic Denitrifying Reactor
ANR	Aerobic Nitrifying Reactor
AOR	Anoxic Region

BOD_5	Biological Oxygen Demand
COD	Chemical Oxygen Demand
FPW	Fish Processing Wastewater
FS	Fixed Solids
HRT	Hydraulic Retention Time
IAAB	Integrated Anaerobic/Anoxic/Aerobic Biological Reactor
N_{NH3}	Ammoniacal Nitrogen
$N_{organic}$	Organic Nitrogen
N_{TKN}	Total Kjendahl Nitrogen
OLR	Organic Loading Rate
RAS	Recirculating Aquaculture Systems
SPW	Sardine Processing Wastewater
TDS	Total Dissolved Solids
TS	Total Solids
VS	Volatile Solids
IVS	Immobilized Volatile Solids
UASB	Up-flow Anaerobic Sludge Red Reactor
E_{ADR}	Anaerobic Denitrifying Reactor Effluent
E_{ANR}	Aerobic Nitrifying Reactor Effluent
%CODi	Chemical Oxygen Demand Removal Efficiency of the *"i"* Reactor
$I_{COD,i}$	Chemical Oxygen Demand in the Inlet of the *"i"* Reactor
$E_{COD,i}$	Chemical Oxygen Demand in the Effluent of the *"i"* Reactor
%Pi	Protein Removal Efficiency of the *"i"* Reactor
$\%P_{IAAB}$	Protein Removal Efficiency of the IAAB Reactor
$\%P_{ADR}$	Protein Removal Efficiency of the ADR Reactor
$I_{P,I}$	Protein Inlet in the *"i"* Reactor
$E_{P,I}$	Protein Effluent in the *"i"* Reactor
$P_{R,ADR}$	Protein Removal in the ADR
$NH^+_{4,\ Theoretical}$	Theoretical Ammonium Production in the ADR
$\%H_{ADR}$	Protein Hydrolysis
$NH^+_{4,\ ADR}$	Ammonium Concentration in the ADR effluent
$\%NH^+_{4,\ ANR}$	Ammonium Removal Efficiency
$E_{NH^+_4,ADR}$	Ammonium Concentration in the ADR Effluent
$E_{NH^+_4,ANR}$	Ammonium Concentration in the ANR Effluent
$NH^+_{4,\ R}$	Ammonium Removal in the ANR
$\%NO^-_{3,\ Yield}$	Nitrate Yield
$E_{NO^-_3,\ ANR}$	Nitrate Concentration in the ANR Effluent
i	Reactor stage (ADR, ANR, or IAAB)

References

Casero-Díaz, T., Castro-Barros, C., Taboada-Santos, A., Rodríguez-Hernández, L., Mauricio-Iglesias, M., and Carballa, M. (2024). Turning fish canning wastewater into resources: Effluents and operational conditions selection for volatile fatty acids production. *Journal of Water Process Engineering. 64*, 2–9. https://doi.org/10.1016/j.jwpe.2024.105738.

Chan, Y. J., Chong, M. F., Law, C. L., and Hassell, D. G. (2009). A review on anaerobic-aerobic treatment of industrial and municipal wastewater. *Chemical Engineering Journal. 155*(*1–2*), 1–18. https://doi.org/10.1016/j.cej.2009.06.041.

Chen, Y., Sanjaya, E. H., Guo, G., and Li, Y. Y. (2021). High nitrogen removal performance of anaerobically treated fish processing wastewater by one-stage partial nitritation and anammox process with hydroxyapatite (HAP)-based syntrophic granules and granule structure. *Bioresource Technology. 338*(*May*), 125526. https://doi.org/10.1016/j.biortech.2021.125526.

Choudhury, A., Lepine, C., Witarsa, F., and Good, C. (2022). Anaerobic digestion challenges and resource recovery opportunities from land-based aquaculture waste and seafood processing byproducts: A review. *Bioresource Technology. 354*, 127144. https://doi.org/10.1016/j.biortech.2022.127144.

Chowdhury, P., Viraraghavan, T., and Srinivasan, A. (2010). Biological treatment processes for fish processing wastewater. *Bioresource Technology. 101*, 439–449.

Feizi, R., Kazemi, Zohre, Kazemi, Zahra, Jorfi, S., Reshadatian, N., and Jaafarzadeh, N. (2024). A review on efficient technologies for fish canning wastewater treatment. *Desalination and Water Treatment. 317*, 100220. https://doi.org/10.1016/j.dwt.2024.100220.

Hernández-Fydrych, V. C., Castilla-Hernández, P., Beristain-Cardoso, R., Trejo-Aguilar, G. M., and Fajardo-Ortiz, C. (2018). COD and ammonium removal in SBR operated under different combinations using pre-treated slaughterhouse wastewater. *Revista Mexicana de Ingeniería Química. 17*(2), 621–631. https://doi.org/10.24275/10.24275/uam/izt/revmexingquim/2018v17n2/Hernandez.

Huiliñir, C., Hernández, S., Aspé, E., and Roeckel, M. (2012). Simultaneous nitrate and organic matter removal from salmon industry wastewater: The effect of C/N ratio, nitrate concentration and organic load rate on batch and continuous process. *Journal of Environmental Management. 101*(*82–91*).

Ismail, I. N., Taufik, M., Umor, N. A., Norulhuda, M. R., Zulkarnaini, Z., and Ismail, S. (2022). Anammox process for aquaculture wastewater treatment: operational condition, mechanism, and future prospective. *Water Science and Technology. 86*(*12*), 3093–3112. https://doi.org/10.2166/wst.2022.403.

Jemli, M., Karray, F., Feki, F., Loukil, S., Mhiri, N., Aloui, F., and Sayadi, S. (2015). Biological treatment of fish processing wastewater: A case study from Sfax City (Southeastern Tunisia). *Journal of Environmental Sciences. 30*, 102–112. http://dx.doi.org/10.1016/j.jes.2014.11.002.

Khan, A., Khan, S. J., Miran, W., Zaman, W. Q., Aslam, A., and Shahzad, H. M. A. (2023). Feasibility Study of Anaerobic Baffled Reactor Coupled with Anaerobic Filter Followed by Membrane Filtration for Wastewater Treatment. *Membranes. 13*(*1*). https://doi.org/10.3390/membranes13010079.

Lanzagorta-Cortes, R., Romo-Gómez, C., Camacho-López, C., Aceedo-Sandoval, O. ., González-Ramírez, C. ., and Leyva-Morales, J. (2025). Efficiency of a denitrifying sludge in a UASB reactor fed with whey. *Revista Mexicana de Ingeniería Química. 24*(*1*). https://doi.org/10.24275/rmiq/IA24384.

Mahat, S. B., Omar, R., Che Man, H., Mohamad Idris, A. I., Mustapa Kamal, S. M., Idris, A., Shreeshivadasan, C., Jamali, N. S., and Abdullah, L. C. (2021). Performance of dynamic anaerobic membrane bioreactor (DAnMBR) with phase separation in treating high strength food processing wastewater. *Journal of Environmental Chemical Engineering. 9*(*3*), 105245. https://doi.org/10.1016/j.jece.2021.105245.

Medellín-Castillo, N. ., Arvizu-Vázquez, S., Gallegos-García, M., Hidalgo-Millán, A., and Espinoza-Rodríguez, M. A. (2024). Evaluation of nitrification and denitrification in an activated sludge process through mass balance using GPS-X software. *Revista Mexicana de Ingeniería Química. 23*(*3*). https://doi.org/10.24275/rmiq/IA24268.

Negari, M. S. (2023). Denitrification of recirculated aquaculture system effluents using fish sludge as primary substrate. Masters Thesis Environmental Engineering, Offshore Environmental Technology, University of Stavenger, Norway.

Panpong, K., Srimachai, T., Nuithitikul, K., Kongjan, P., O-thong, S., Imai, T., and Kaewthong, N. (2017). Anaerobic co-digestion between canned sardine wastewater and glycerol waste forbiogas production: Effect of different operating processes. *Energy Procedia. 138*, 260–266. https://doi.org/10.1016/j.egypro.2017.10.050.

Paulo, A. M. S., Amorim, C. L., Costa, J., Mesquita, D. P., Ferreira, E. C., and Castro, P. M. L. (2021). Long-term stability of a non-adapted aerobic granular sludge process treating fish canning wastewater associated to EPS producers in the core microbiome. *Science of the Total Environment. 756*, 144007. https://doi.org/10.1016/j.scitotenv.2020.144007.

Pereira, M. J., Grosjean, O., Pintado, M., Brazinha, C., and Crespo, J. (2022). Clean Technologies for Production of Valuable Fractions from Sardine Cooking Wastewaters: An Integrated Process of Flocculation and Reverse Osmosis. *Clean Tecnologies.4*, 276–295. https://doi.org/10.3390/cleantechnol14020016.

Peterson, G. L. (1977). A Simplification of the Protein Assay Method of Lowry et al. Which is More Generally Applicable. *Anal. Biochem. 83*, 346–356.

Powell, G. E. and Archer, D. B. (1989). On-line titration method for monitoring buffer capacity and total volatile fatty acid levels in anaerobic digesters. *Biotechnology and Bioengineering. 33*(*5*), 570–577.

Prihandrijanti, M., Marcos, K. J., and Salim, C. (2021). Integrated anaerobic-aerobic and wetland system for wastewater treatment and recycling in fish canning industry. *Chemical Engineering Transactions. 83*, 127–132. https://doi.org/10.3303/CET2183022.

Rajab, A. R., Salim, M. R., Sohaili, J., Anuar, A. N., Salmiati, and Lakkaboyana, S. K. (2017). Performance of integrated anaerobic/aerobic sequencing batch reactor treating poultry slaughterhouse wastewater. *Chemical Engineering Journal. 313*, 967–974. http://dx.doi.org/10.1016/j.cej.2016.10.144.

Rice, E. and Bridgewater, L. (2012). *Standard Methods for the Examination of Water and*

Wastewater (22nd ed). American Public Health Association, Washington, DC.

Sanjaya, E. H., Cheng, H., and Li, Y. Y. (2020). Mesophilic methane fermentation performance and ammonia inhibition of fish processing wastewater treatment using a self-agitated anaerobic baffled reactor. *Bioresource Technology. 313*, 123644. https://doi.org/10.1016/j.biortech.2020.123644.

Shi, S., Cui, P., Wang, S., Long, J., and Yang, X. (2025). Effects of High Salinity on Nitrogen Removal Efficiency and Microbial Community Structure in a Three-Stage AO System. *Water. 17*(*8*), 1–17. https://doi.org/10.3390/w17081112.

Shi, X., Lefevre, O., Kwang, K., and Yong, H. (2014). Sequential anaerobic-aerobic treatment of pharmaceutical wastewater with high salinity. *Bioresource Technology. 153*, 79–86.

Srimachai, T., Imai, T., and Rattanadilok Na Phuket, K. (2024). Biogas and Biohythane Production from Anaerobic Codigestion of Canned Sardine Wastewater with Glycerol Waste. *Journal of Scientific and Technological Reports*. *27*(*2*), 1–13. https://doi.org/10.55164/ajstr.v27i2.249551.

Val del Rio, A., Pichel, A., Fernandez-Gonzalez, N., Pedrouso, A., Fra-Vázquez, A., Morales, N., Mendez, R., Campos, J. L., and Mosquera-Corral, A. (2018). Performance and microbial features of the partial nitritation-anammox process treating fish canning wastewater with variable salt concentrations. *Journal of Environmental Management. 208*, 112–121. https://doi.org/10.1016/j.jenvman.2017.12.007.

Vol. 24, No. 3(2025) IA25621
Revista Mexicana de Ingeniería Química

Effect of operational parameters in electrocoagulation for the removal of phosphorus, nitrates, and ammoniacal nitrogen from water

Efecto de los parámetros operativos en la electrocoagulación para la remoción de fósforo, nitratos y nitrógeno amoniacal en agua

G. A. Tamayo-Roman, S. Enciso-Sáenz, J.H. Castañon-González, J.J. Villalobos-Maldonado*
Tecnológico Nacional de México/I. T. Tuxtla Gutiérrez. División de Estudios de Posgrado e Investigación. Carretera Panamericana km 1080. Col. Juan Crispin. C.P. 29050. Tuxtla Gutiérrez, Chiapas, México.
Sent date: June 13, 2025; Accepted: September 23, 2025

Abstract
Electrocoagulation represents an efficient and low-cost alternative for the removal of contaminants present in water bodies affected by domestic discharges and agricultural activities. In this study, the application of an electrocoagulation reactor equipped with aluminum anodes and graphite cathodes was evaluated for the removal of phosphorus, nitrates, and ammoniacal nitrogen in a synthetic water matrix similar to that of the Garrido Canabal River, Bochil, Chiapas, Mexico. The effects of electrode distance, applied voltage, operating time, and initial pH were analyzed. The best results were obtained with a 1 cm electrode distance, 9 V voltage, 20 minutes of operation time, and an initial pH of 7, achieving removal efficiencies of 81% for phosphorus, 82% for nitrates, and 76% for ammoniacal nitrogen. The results confirm the direct influence of operational variables on process efficiency, highlighting its potential as a sustainable alternative for water treatment in rural communities, while complying with the limits established in the NOM-127-SSA1-2021 regulation.
Keywords: Electrocoagulation, phosphorus, nitrates, ammoniacal nitrogen, water treatment.

Resumen
La electrocoagulación representa una alternativa eficiente y de bajo costo para la remoción de contaminantes presentes en cuerpos de agua afectados por descargas domésticas y actividades agrícolas. En este estudio se evaluó la aplicación de un reactor de electrocoagulación equipado con ánodos de aluminio y cátodos de grafito para la remoción de fósforo, nitratos y nitrógeno amoniacal en un agua sintética similar a la del río Garrido Canabal, Bochil, Chiapas, México. Se analizaron los efectos de la distancia entre electrodos, voltaje aplicado, tiempo de operación y pH inicial. Los mejores resultados se obtuvieron con una distancia de 1 cm, voltaje de 9 V, tiempo de 20 minutos y pH de 7, alcanzando remociones de 81% para fósforo, 82% para nitratos y 76% para nitrógeno amoniacal. Los resultados confirman la influencia directa de las variables operativas en la eficiencia del proceso, destacando su potencial como alternativa sustentable para el tratamiento de aguas en comunidades rurales, cumpliendo los límites establecidos en la NOM-127-SSA1-2021.
Palabras clave: Electrocoagulación, fósforo, nitratos, nitrógeno amoniacal, tratamiento de agua.

* *Corresponding author. E-mail*: juan.vm@tuxtla.tecnm.mx;
https://doi.org/10.24275/rmiq/IA25621
ISSN:1665-2738, *issn-e*: 2395-8472

1 Introduction

The contamination of water bodies by nitrates, phosphates, and ammoniacal nitrogen originates mainly from anthropogenic sources, particularly the discharge of wastewater from nearby populations (Reilly *et al*., 2019), as well as the intensive use of nitrogen fertilizers and organophosphorus pesticides in agricultural activities. The fractions of these inputs that are not absorbed by crops eventually leach into surface or groundwater bodies due to the effects of irrigation and rainfall (Isiuku & Enyoh, 2020). These contaminants, which are highly soluble in water, promote the eutrophication of aquatic ecosystems, thereby affecting their balance and biodiversity (Yazici Karabulut *et al*., 2021).

This issue is critical since various rural communities depend directly on these water sources for human consumption, usually applying only disinfection techniques such as boiling or chlorination. However, such methods are not capable of removing these contaminants, despite the fact that prolonged ingestion is associated with gastrointestinal and urinary system disorders, including diarrhea, vomiting, kidney problems, and hypertension (Hameed *et al*., 2021). Moreover, in infants it may induce methemoglobinemia, and there is evidence of its association with colorectal and bladder cancer (Wang *et al*., 2008).

Electrocoagulation emerges as a viable alternative for water treatment in rural, low-resource areas, as this technology has demonstrated a strong capacity to remove dissolved ionic contaminants, presenting several advantages over conventional technologies, such as lower costs, shorter treatment times, and reduced sludge generation (Aguilar-Ascon, 2020). Furthermore, its operation can be implemented using solar energy through photovoltaic cells (Medrano-Hurtado *et al*., 2022) or combined with other systems, such as functionalized membranes (Bastida-Vázquez et al., 2024), making it an efficient and sustainable method. This process is based on the principles of conventional coagulation, which has been studied and compared with the use of natural coagulants, both showing good results in turbidity removal (Cadena-Álava *et al*., 2024). In both cases, the coagulant destabilizes the superficial layer of the electrical double layer of colloids, which usually carry a negative charge that allows them to remain stable and suspended by forming dipolar interactions with surrounding molecules, thus generating repulsive forces that prevent agglomeration (Kosmulski *et al*., 1999).

In electrocoagulation, however, the coagulant agent is formed by applying an electric current that promotes the oxidation of a sacrificial anode plate, leading to the formation of metal hydroxides, whose specific species depend on the electrode material. The efficiency of the process is determined by several factors, including the supplied current density (Zhu *et al*., 2021), reactor geometry, electrode material and spacing (Sahu *et al*., 2014), circuit configuration, and the initial pH of the solution (Vepsäläinen & Sillanpää, 2020). Different materials and operational conditions yield varying contaminant removal efficiencies. For instance, the use of aluminum and iron electrodes has achieved removal rates of up to 80% for dissolved nitrates in water (Yazici Karabulut *et al*., 2021), while the application of graphite electrodes has enabled removal rates above 70% for heavy metals such as manganese, zinc, and iron, in addition to removal efficiencies greater than 90% for suspended solids, turbidity, color, oils, and greases (Ismail *et al*., 2024). The redox reactions that occur when using a combination of aluminum and graphite electrodes (Chen, 2004) are presented below.

Reactions at the anode plate:

$$Al - 3e^- \longrightarrow Al^{3+} \tag{1}$$

Water electrolysis reaction:

$$2H_2O + 2e^- \longrightarrow H_2 + 2OH^- \tag{2}$$

Formation of aluminum hydroxide:

$$Al^{3+} + 3H_2O \longrightarrow Al(OH)_3 + 3H^+ \tag{3}$$

Therefore, this study focused on investigating the removal efficiency of phosphorus, nitrates, and ammoniacal nitrogen dissolved in water using an electrocoagulation reactor with aluminum anodes and graphite cathodes, analyzing the effect of the operating conditions governing this system, such as the applied voltage, initial solution pH, and reaction time.

2 Materials and methods

2.1 *Sampling and characterization of surface water body*

Sampling was carried out in the "Santo Domingo" river, which is used for domestic consumption by the community of Garrido Canabal, Bochil, Chiapas, located at the geographic coordinates N 17.0435, W 93.0129. Three sampling points were selected (Figure 1), and at each point four simple samples of 250 mL were collected at 1-hour intervals using sterilized glass containers. A composite sample was obtained for each sampling point, which were then unified into an integral sample. Additionally, one sample was collected for microbiological analysis using a sterile polyethylene bag from the LaMotte® coliform test kit, following the guidelines of the Mexican Official Standard NOM-230-SSA1-2002. Sampling was carried out during the dry season and the rainy season, corresponding to March

Fig 1. Sampling sites of the Santo Domingo River, located in the town of Garrido Canabal, Bochil, Chiapas. The river flow goes from the 1st to the 2nd sampling site. Image obtained through Google Earth©, 2025.

and August of 2024, respectively. The integral water sample from both seasons was characterized according to the following parameters: electrical conductivity, pH, temperature, turbidity, total suspended solids (TSS), color, total nitrogen, total phosphorus, nitrates, nitrites, ammoniacal nitrogen, and presence/absence of total coliforms and *E. coli*.

Electrical conductivity and pH were determined using a portable multiparameter meter HQ30d HACH® following the manufacturer's specifications. A mercury thermometer was used for temperature measurement, and turbidity and total suspended solids (TSS) were measured with the HACH DR/900 colorimeter. Total nitrogen, total phosphorus, and ammoniacal nitrogen were measured with HACH® kits TNT 870, TNT 845, and TNT 832, respectively, according to the manufacturer's protocols. Nitrate and nitrite quantification followed the Mexican Standards NMX-AA-079-SCFI-2001 (brucine sulfate method) and NMX-AA-099-SCFI-2021 (sulfanilamide method), respectively, with absorbance measured using a HACH® DR-5000 spectrophotometer at 410 and 543 nm. Finally, the presence or absence of total coliforms and *E. coli* was determined with the LaMotte® coliform test kit, following the manufacturer's specifications.

2.2 *Construction of the electrocoagulation reactor*

A batch electrocoagulation reactor was constructed from transparent acrylic with dimensions of 10 × 10 × 17 cm and a capacity of 1 L. The electrode support was designed in SketchUP® software (Figure 2) and 3D-printed in polyethylene terephthalate glycol (PETG) with a height of 3 cm. The reactor employed a pair of aluminum plates as anodes and a pair of graphite plates as cathodes (Figure 3), each measuring 10 × 5 cm, fully submerged in the solution throughout the process. Electrodes were connected in series to a variable DC power supply HYELEC® (0–30 V, 0–5 A).

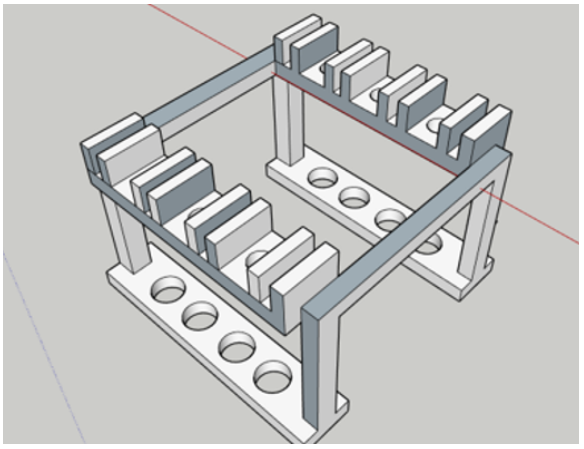

Fig 2. Supports of the electrodes of the electrocoagulation reactor designed in SketchUp ®, printed in polyethylene terephthalate glycol (PETG).

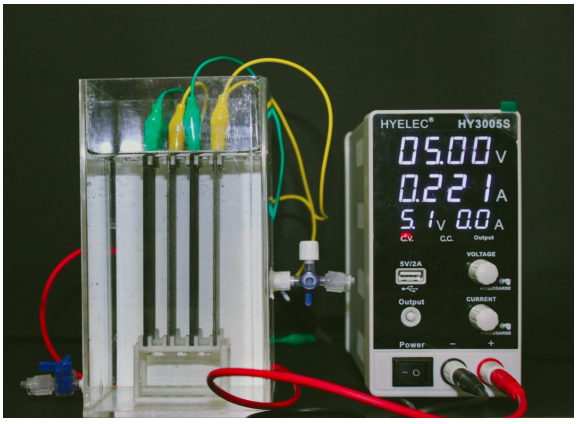

Fig 3. Electrocoagulation reactor made of transparent acrylic, with a capacity of 1 L, using a pair of aluminum anodes and graphite cathodes connected in series, fully submerged with a contact area with the medium of 104.5 cm2 and 106 cm2 per plate, respectively. The system is connected to a HYELEC ® variable DC power supply.

2.3 *Experimental tests*

A completely randomized triplicate design was used to evaluate the effect of electrode distance inside the laboratory-scale electrocoagulation reactor, based on the recommendation of several authors that it should exceed 0.1 cm (Deveci *et al.*, 2019), and limited by the 1 L capacity of the reactor. Fixed electrode distances of 0.5, 1.0, 1.5, and 2.0 cm were tested for the individual removal of phosphorus, ammoniacal nitrogen, and nitrates dissolved in water with initial concentrations of 10 mg/L. Each experimental unit was operated for 20 minutes at 5 V, after which samples were taken for analysis of the response variables. Phosphorus and ammoniacal nitrogen concentrations were measured with HACH® kits TNT 845 and TNT 832, respectively, following the manufacturer's protocols. Nitrate quantification followed the Mexican Standard NMX-AA-079-SCFI-2001 (brucine sulfate

method). Statistical analysis was performed through analysis of variance (ANOVA) using Statgraphics® Centurion XVI software with a 95% confidence level.

The efficiency of the electrocoagulation reactor was evaluated based on the removal percentages of phosphorus, nitrates, and ammoniacal nitrogen, applying Eq. 4:

$$\% \, Removal = \frac{Ci - Cf}{Ci} \, x \, 100 \qquad (4)$$

Where: Ci: Initial concentration; Cf: Final concentration.

Subsequently, the effects of three operational conditions were evaluated through a full 3^3 factorial design, as presented in Table 1: the initial pH of the water to be treated, with values close to neutrality, since the literature reports the highest formation of aluminum hydroxide under certain conditions, acting as a coagulant agent (Yehya *et al*., 2014), with levels of 6, 7, and 8; the applied voltage, selecting low and medium levels to limit energy consumption and excessive bubble formation (Omwene *et al*., 2018), with values of 5, 7, and 9 V; and finally, the operation time, established according to the kinetics of floc formation reported in the literature, where other authors have achieved higher removal efficiencies of ionic pollutants (Ano *et al*., 2020; Dehghani *et al*., 2016), with values of 10, 20, and 30 min. These factors were evaluated with respect to the removal of phosphorus, nitrate, and ammoniacal nitrogen from synthetic water with concentrations similar to those found in the river located in the community of Garrido Canabal, Bochil, Chiapas. For this purpose, a sample was collected at the outlet of the reactor at the end of each treatment for the analysis of each response variable. Adjustment of the pH in the solution was performed using 1 M sulfuric acid and sodium hydroxide solutions, while the synthetic water was prepared according to the concentrations obtained from river sampling, following the methodologies established in the "reagents and standards" section of the corresponding Mexican Standards for phosphorus (NMX-AA-029-SCFI-2001), nitrates (NMX-AA-079-SCFI-2001), and ammoniacal nitrogen (NMX-AA-026-SCFI-2010). Statistical analysis of the factorial design was carried out using Statgraphics® Centurion XVI software with a 95% confidence level.

Table 1. 3^3 factorial design for the electrocoagulation reactor.

Factors	Levels		
Voltage (Volts)	5	7	9
Operation time (min)	10	20	30
pH	6	7	8

3 Results and discussion

3.1 Sampling and characterization of surface water body

The results obtained from the sampling are presented in Table 2, showing the average concentrations for the characterization of the river water from the locality of Garrido Canabal, Bochil, Chiapas, during both the dry and rainy seasons.

Table 2. Sampling results during dry and rainy seasons of the river located in the town of Garrido Canabal, Bochil, Chiapas.

Parameter	Dry season	Rainy season	Concentration range
Flow rate (L/s)	2892.65 ± 114	8056.23 ±86	N/A
Temperature (°C)	20 ± 0.2	23 ± 0.3	N/A
Electrical conductivity (μS/cm)	433 ± 11	359 ± 9	N/A
pH	7.21 ± 0.05	7.52 ± 0.08	6.5 – 8.5
Turbidity (FAU)	2 ± 0.02	12 ± 0.01	3
Total suspended solids (mg/L)	2 ± 0.07	13 ± 0.1	N/A
Settleable solids (mg/L)	0.5 ± 0.002	1.2 ± 0.002	N/A
Color (Pt – Co)	11 ± 0.01	14 ± 0.4	15
Total nitrogen (mg/L)	<LMD	19 ± 0.5	NA
Ammoniacal nitrogen (mg/L)	<LMD	2 ± 0.1	0.5
Total Phosphorus (mg/L)	1.9 ± 0.1	2.7 ± 0.2	0.1
Nitrates (mg/L)	0.1 ± 0.04	13.9 ± 0.17	11
Nitrites (mg/L)	<LMD	0.14 ± 0.01	0.9
COD (mg/L)	–	26 ± 0.75	N/A
Total coliforms	Present	Present	Absence
E. coli	Present	Present	Absence

Table 3. Removal of phosphorus, nitrates, and ammoniacal nitrogen at different electrode distances. Means within the same column with different lowercase letters are significantly different ($p \leq 0.5$) according to Tukey's test.

Electrode distance (cm)	Phosphorus	Nitrates	Ammoniacal nitrogen
2	57 ± 1.6 c	61.53 ± 1.10 c	47.3 ± 1.31 c
1.5	62.23 ± 1.47 b	64.03 ± 0.85 c	55.73 ± 0.46 b
1	71.5 ± 0.86 a	77.23 ± 1.46 a	67.87 ± 2.68 a
0.5	64.87 ± 0.9 b	71.47 ± 0.42 b	55.37 ± 2.51 b
Tukey	3.2751	2.6953	5.1369

Turbidity values during the dry season remained within normal ranges; however, during the rainy season, concentrations above the maximum permissible limits established in NOM-127-SSA1-2021 were recorded. This may be attributed to sediment drag and landslides from the riverbanks caused by the increase in flow (Elazzouzi *et al*., 2017). In conventional treatment systems, such suspended solids can be efficiently removed through sedimentation processes in primary tanks (Sahu *et al*., 2014). Likewise, the presence of total coliforms and *Escherichia coli* was detected in both seasons, which is characteristic of surface water bodies (Govindan *et al*., 2015).

Phosphorus concentrations were recorded above the maximum permissible limits during both the dry and rainy seasons. Additionally, during the rainy season, ammoniacal nitrogen and nitrate concentrations were detected above the limits established in NOM-127-SSA1-2021. The presence of phosphorus during the dry season may be associated with wastewater discharges from upstream rural areas, mainly consisting of gray waters with high concentrations of phosphate detergents (Reilly *et al*., 2019). Meanwhile, the simultaneous detection of phosphorus, nitrates, and ammoniacal nitrogen during the rainy season may be attributed to the use of organophosphorus pesticides and nitrogen fertilizers in adjacent corn crops, whose residual fractions, when applied in excess, are carried into the river during rainfall events (Isiuku & Enyoh, 2020; Yazici Karabulut *et al*., 2021).

3.2 Effect of electrode distance

The results of the analysis of variance (ANOVA) corresponding to the effect of electrode distance in the electrocoagulation reactor on the removal percentage of phosphorus, nitrates, and ammoniacal nitrogen, along with their respective standard deviations, are presented in Table 3.

Treatments using electrode distances of 2, 1.5, and 1 cm showed statistically significant differences at a significance level of $p < 0.05$. Increasing electrode separation to 2 cm resulted in a notable decrease in removal percentages of phosphates, nitrates, and ammoniacal nitrogen. This behavior can be attributed to the reduction of electrostatic interactions among the charged species present in the solution, which decreases the efficiency of coagulant formation (Yazici Karabulut *et al*., 2021).

Conversely, reducing the electrode distance to 1 cm yielded the highest removal values, indicating a more efficient operating condition for the evaluated system. This improvement can be explained by the fact that shorter spacing significantly reduces the electrical resistance of the medium, allowing the applied current to be distributed more uniformly with lower energy loss. As a result, the effective current density on the aluminum anode surface increases, favoring its electrolytic dissolution and, consequently, a greater release of active coagulant species such as aluminum hydroxide. These species contribute to the neutralization of the surface charges of ions present (e.g., phosphates and nitrates), which in turn promotes the formation of more stable flocs through adsorption mechanisms. Consequently, particle agglomeration and subsequent sedimentation are enhanced, explaining the significant increase in removal efficiency under these conditions (Elabbas *et al*., 2016; Ismail *et al*., 2024; Omwene *et al*., 2018).

Finally, it was observed that when the electrode distance was reduced below 1 cm, removal efficiency decreased. Although shorter spacing decreases the medium's electrical resistance and increases current density, excessively small spacing generates an intense electric field that induces undesirable phenomena in the solution. These include rapid formation and premature agglomeration of gas bubbles, as well as excessive collisions among ions and suspended particles, which can destabilize the formed metal hydroxides. Once destabilized, these hydroxides have a lower capacity to adsorb and coagulate contaminants, thus limiting overall efficiency. Previous studies have reported similar behaviors, where excessively short electrode distances negatively affect contaminant sedimentation and retention, recommending that electrode spacing should not be less than 10 mm (Deveci *et al*., 2019; Elabbas *et al*., 2016).

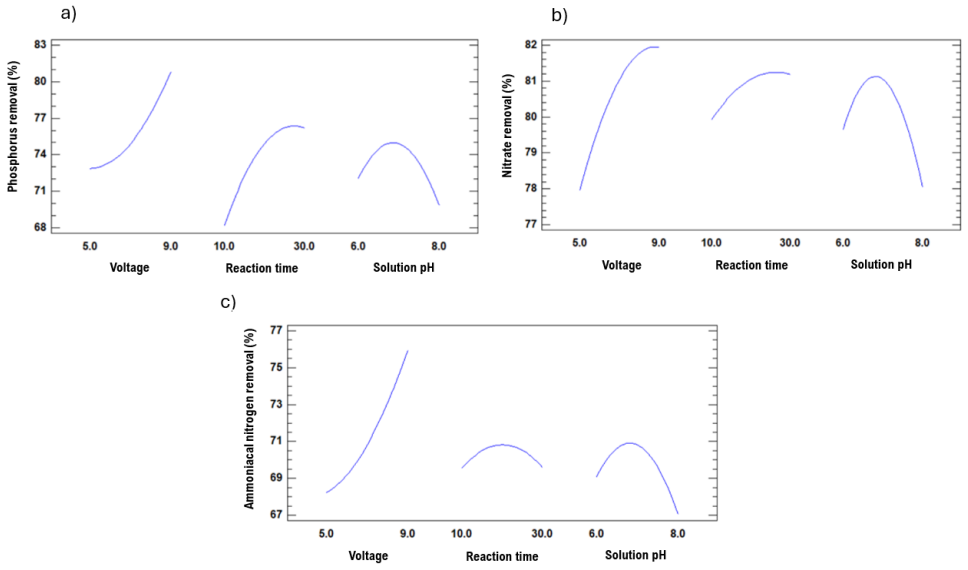

Fig 4. Main effects plots for the removal percentage of a) phosphorus, b) nitrate, and c) ammoniacal nitrogen, showing nearly linear increasing trends with applied voltage, and a quadratic response with respect to reaction time and solution pH, with the identification of operating conditions of maximum efficiency.

3.3 Effect of operating conditions of the electrocoagulation reactor

3.3.1 Influence of applied voltage

The applied voltage exerts a direct effect on the removal of phosphorus, nitrates, and ammoniacal nitrogen from synthetic water, as shown in the main effects plots for removal percentage (Figure 4). As the voltage supplied by the power source increases, removal percentages also increase, reaching maximum values when operating at 9 V. This behavior is related to the dosage of the coagulant agent produced within the system, since higher voltage enhances anodic plate oxidation, resulting in a higher concentration of dissolved metal ions in the water. This, in turn, increases the formation of the coagulant agent, aluminum hydroxide, which captures colloidal particles present in the solution, including phosphate, nitrate, and ammoniacal nitrogen molecules. This process leads to the formation of agglomerates that settle at the bottom of the container due to their weight, facilitating removal. Nitrates, in particular, may also be removed by formation or by adhering to the precipitated metal hydroxides (Rodziewicz *et al*., 2020). Although alternative pathways may lead to their reduction to nitrites or ammonia and subsequently to N_2 formation (Abdel-Aziz *et al*., 2020), it has been reported that these are only formed at the beginning of the process before being removed (Govindan *et al*., 2015). It is worth noting that no electrode passivation due to oxide layer formation was observed during experiments, a phenomenon that occurs when the system operates at very high voltage values (Aguilar-Ascon, 2020).

On the other hand, since the system operated with fixed voltages supplied by the power source, it was observed that the current intensity fluctuated within a specific range for each treatment, conditioned by the different operational variables. According to Ohm's Law, this behavior reflects changes in the resistance of the medium, which tends to decrease as metallic ions and dissolved salts gradually precipitate in the solution (Elabbas *et al*., 2016; Omwene *et al*., 2018). Considering the contact area of the aluminum electrodes, fully submerged with 104.5 cm² (Figure 3), in the most efficient treatment operating at 9 V a current density of 0.0047 A/cm² was calculated. This value is relatively low compared to those reported in other studies, where current densities between 0.1 and 0.5 A/cm² have been applied to optimize the formation of metal hydroxides (Dehghani *et al*., 2016). Nevertheless, the low density applied favored a more gradual release of coagulant, resulting in a slow but effective aggregation process, which may represent an advantage by reducing energy consumption and electrode passivation (Elazzouzi *et al*., 2016).

The highest removal percentages achieved were 81% for phosphorus, 82% for nitrates, and 76% for ammoniacal nitrogen, which are comparable to studies such as Aguilar (2020), who reported 99% phosphorus removal. This differential affinity in the removal of these contaminants is associated with the negative charge of these ions in solution, behaving as colloidal particles that become destabilized in the presence of metallic hydroxides (Chellam & Sari, 2016).

3.3.2 Influence of operation time

The electrocoagulation reactor's operation time showed variable effects on the removal of each contaminant

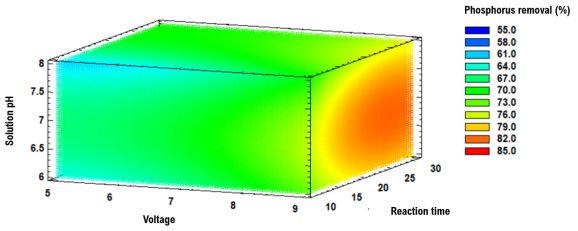

Fig 5. Estimated response surface mesh plots for the removal percentage of phosphorus, with respect to the interaction of operating conditions: voltage, reaction time, and solution pH. Higher efficiency is observed in regions with red color shades.

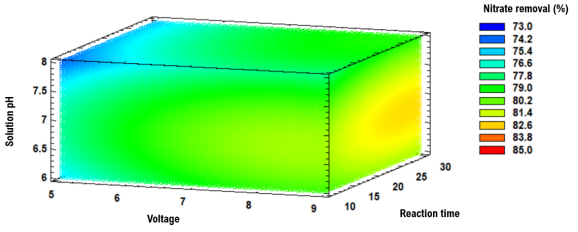

Fig 6. Estimated response surface mesh plots for the removal percentage of nitrate, with respect to the interaction of operating conditions: voltage, reaction time, and solution pH. Higher efficiency is observed in regions with yellow color shades.

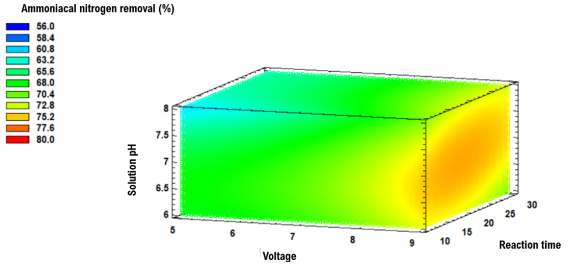

Fig 7. Estimated response surface mesh plots for the removal percentage of ammoniacal nitrogen, with respect to the interaction of operating conditions: voltage, reaction time, and solution pH. Higher efficiency is observed in regions with orange color shades.

(Figure 4). For phosphorus, 75% removal was achieved after 20 minutes, slightly increasing to 76% at 30 minutes (Figure 5). In the case of nitrates, removal reached 81% at 20 minutes and remained constant at longer times (Figure 6). Similar results have been reported in previous studies, with nitrate removal efficiencies of 73.8% at 33 minutes using aluminum and iron electrodes (Ano *et al*., 2020), and 63% at 30 minutes (Dehghani *et al*., 2016). For ammoniacal nitrogen, removal efficiencies of up to 71% were obtained, gradually decreasing as operation time increased (Figure 7).

These results suggest that an operation time of 20 minutes is sufficient to maximize the removal efficiency of the three contaminants. Continuing the process beyond this point yields only marginal improvements, constant values, or even decreases in phosphorus, nitrate, and ammoniacal nitrogen removal percentages, respectively. This phenomenon occurs because, as operation time progresses, contaminant concentrations decrease due to removal by agglomerate formation and sedimentation. Therefore, the rate of new floc formation declines, meaning extended operation only increases energy consumption. Beyond the time of greatest removal efficiency, current supply should be stopped, since removal improvements beyond this point are not significant compared to energy costs (Deveci *et al*., 2019). It is more cost-effective to achieve high removal efficiencies with low energy consumption by modifying other reactor-influencing variables (Bashir *et al*., 2019).

3.3.3 Influence of initial solution pH

The pH value of the water to be treated significantly influences the efficiency of the electrocoagulation process, as it partially determines the electrical conductivity of the electrolyte. This value fluctuates during operation due to hydroxyl ion formation at the cathode, which explains why treated water often exhibits a slightly alkaline pH (Vepsäläinen & Sillanpää, 2020). It has been observed that relatively alkaline pH values yield higher removal percentages (Deveci *et al*., 2019), though neutral pH values can also be effective (Elazzouzi *et al*., 2017).

pH also determines the type of metal hydroxide species formed depending on the anode material. For instance, at pH ranges of 4 to 10 under low voltages, aluminum hydroxide formation is favored. Response surface plots show that the highest removal percentages for phosphorus, nitrates, and ammoniacal nitrogen were obtained at pH 7, reaching 75%, 82%, and 71%, respectively (Figures 5, 6, and 7), describing a quadratic effect. At pH 8, removal efficiency decreased, as higher hydroxyl ion concentrations at alkaline pH generate repulsion forces with the anionic contaminants in solution, preventing their adsorption onto coagulant agglomerates, even though metallic hydroxides are being formed (Ismail *et al*., 2024).

Moreover, pH affects the solubility of the metal hydroxides formed; at neutral pH, the formation of $Al(OH)_3$, which is insoluble in water, is facilitated, enhancing its effectiveness in contaminant removal (Yehya *et al*., 2014).

Conclusions

This study demonstrated the technical feasibility of the electrocoagulation process for the efficient removal of phosphorus, nitrates, and ammoniacal nitrogen in surface water from the river in the locality of Garrido

Canabal, Bochil, Chiapas, Mexico. The evaluation of the operational variables allowed the identification of conditions that achieved maximum operating efficiency, reaching removal rates of 81% for phosphorus, 82% for nitrates, and 76% for ammoniacal nitrogen.

The most efficient electrode distance was determined to be 1 cm, maximizing current density without generating destabilization phenomena due to intense electromagnetic fields. In addition, a voltage of 9 V promoted efficient metallic hydroxide generation without inducing electrode passivation. Furthermore, an operation time of 20 minutes was sufficient to achieve maximum removal efficiencies, avoiding unnecessary energy consumption. Finally, an initial pH of 7 favored the precipitation of $Al(OH)_3$ and maximized the capture of ionic species through colloidal destabilization and sedimentation mechanisms.

These results confirm the potential of electrocoagulation as an accessible and effective alternative for water treatment in rural communities, where combined domestic, agricultural, and pluvial pollution threatens water quality. The development of such technologies can significantly contribute to compliance with the limits established in NOM-127-SSA1-2021 and to the protection of public health in vulnerable regions.

Acknowledgements

The authors thank the availability of laboratory No. 5 of the Technological Hub at the National Technological Institute of Mexico (TecNM), Tuxtla Gutiérrez campus, and the scholarship granted to student Gustavo Alonso Tamayo-Román by the Secretariat of Science, Humanities, Technology and Innovation (SECIHTI) for his master´s degree studies.

References

Abdel-Aziz, M. H., El-Ashtoukhy, E. S. Z., Sh. Zoromba, M., Bassyouni, M., & Sedahmed, G. H. (2020). Removal of nitrates from water by electrocoagulation using a cell with horizontally oriented Al serpentine tube anode. *Journal of Industrial and Engineering Chemistry*, *82*, 105–112. https://doi.org/10.1016/j.jiec.2019.10.001

Aguilar-Ascon, E. (2020). Removal of nitrogen and phosphorus from domestic wastewater by electrocoagulation: Application of multilevel factorial design. *Journal of Ecological Engineering*, *21*(7), 124–133. https://doi.org/10.12911/22998993/125439

Ano, J., Henri Briton, B. G., Kouassi, K. E., & Adouby, K. (2020). Nitrate removal by electrocoagulation process using experimental design methodology: A techno-economic optimization. *Journal of Environmental Chemical Engineering*, *8*(5). https://doi.org/10.1016/j.jece.2020.104292

Bashir, M. J., Lim, J. H., Abu Amr, S. S., Wong, L. P., & Sim, Y. L. (2019). Post treatment of palm oil mill effluent using electro-coagulation-peroxidation (ECP) technique. *Journal of Cleaner Production*, *208*, 716–727. https://doi.org/10.1016/j.jclepro.2018.10.073

Bastida-Vázquez, J., Roa-Morales, G., Gómez-Espinosa, R. M., Balderas-Hernández, P., & Natividad-Rangel, R. (2024). Water treatment applying electrocoagulation and filtration processes with a functionalized membrane of a contaminated water body from San Cayetano de Morelos, Toluca. *Revista Mexicana de Ingeniera Quimica*, *23*(1). https://doi.org/10.24275/rmiq/IA24164

Cadena-Álava, A. P., Cevallos-Cedeño, R. E., & García-Muentes, S. A. (2024). Evaluation of the coagulant property of carica papaya seeds in surface water treatment. *Revista Mexicana de Ingeniera Quimica*, *23*(3). https://doi.org/10.24275/rmiq/IA24301

Chellam, S., & Sari, M. A. (2016). Aluminum electrocoagulation as pretreatment during microfiltration of surface water containing NOM: A review of fouling, NOM, DBP, and virus control. In *Journal of Hazardous Materials* (Vol. 304, pp. 490–501). Elsevier. https://doi.org/10.1016/j.jhazmat.2015.10.054

Chen, G. (2004). Electrochemical technologies in wastewater treatment. *Separation and Purification Technology*, *38*(1), 11–41. https://doi.org/10.1016/j.seppur.2003.10.006

Dehghani, M., Hoseini, M., Fathi Fath-Aabaadi, M.-K., Elhamiyan, Z., Shamsedini, N., Ghanbarian, M., Shahsavani, S., & Nourozian Baghani, A. (2016). Optimizing Electrocoagulation Process for the Removal of Nitrate From Aqueous Solution. *Jundishapur Journal of Health Sciences*, *8*(1). https://doi.org/10.17795/jjhs-31095

Deveci, E. Ü., Akarsu, C., Gönen, Ç., & Özay, Y. (2019). Enhancing treatability of tannery wastewater by integrated process of electrocoagulation and fungal via using RSM in

an economic perspective. *Process Biochemistry*, *84*, 124–133. https://doi.org/10.1016/j.procbio.2019.06.016

Elabbas, S., Ouazzani, N., Mandi, L., Berrekhis, F., Perdicakis, M., Pontvianne, S., Pons, M. N., Lapicque, F., & Leclerc, J. P. (2016). Treatment of highly concentrated tannery wastewater using electrocoagulation: Influence of the quality of aluminium used for the electrode. *Journal of Hazardous Materials*, *319*, 69–77. https://doi.org/10.1016/j.jhazmat.2015.12.067

Elazzouzi, M., Haboubi, K., & Elyoubi, M. S. (2017). Electrocoagulation flocculation as a low-cost process for pollutants removal from urban wastewater. *Chemical Engineering Research and Design*, *117*, 614–626. https://doi.org/10.1016/j.cherd.2016.11.011

Govindan, K., Noel, M., & Mohan, R. (2015). Removal of nitrate ion from water by electrochemical approaches. *Journal of Water Process Engineering*, *6*, 58–63. https://doi.org/10.1016/j.jwpe.2015.02.008

Hameed, A., Nazir, S., Rehman, J. U., Ahmad, N., Hussain, A., Alam, I., Nazir, A., & Tahir, M. B. (2021). Assessment of health hazards related to contaminations of fluorides, nitrates, and nitrites in drinking water of Vehari, Punjab, Pakistan. *Human and Ecological Risk Assessment*, *27*(6), 1509–1522. https://doi.org/10.1080/10807039.2020.1858021

Isiuku, B. O., & Enyoh, C. E. (2020). Pollution and health risks assessment of nitrate and phosphate concentrations in water bodies in South Eastern, Nigeria. *Environmental Advances*, *2*. https://doi.org/10.1016/j.envadv.2020.100018

Ismail, M. D. E., Oiza, J. H., Pelumi, K. D., & Agnes, T. I. (2024). Purification of Heavy Metals Contaminated Groundwater by Electro-Coagulation Process Using Graphite Electrodes. *Pollution*, *10*(1), 32–44. https://doi.org/10.22059/POLL.2023.360784.1949

Kosmulski, M., Gustafsson, J., & Rosenholm, J. B. (1999). *Correlation between the Zeta Potential and Rheological Properties of Anatase Dispersions*. http://www.idealibrary.com

NMX-AA-026-SCFI-2010. Análisis de agua. Determinación de amoníaco en aguas naturales, potables, residuales y residuales tratadas.

NMX-AA-029-SCFI-2001. Análisis de agua. Determinación de fósforo total en aguas naturales, potables, residuales y residuales tratadas.

NMX-AA-079-SCFI-2001. Análisis de agua. Determinación de nitratos en aguas naturales, potables, residuales y residuales tratadas.

NMX-AA-099-SCFI-2021. Análisis de agua. Determinación de nitritos en aguas naturales, potables, residuales y residuales tratadas.

NOM-127-SSA1-2021. Agua para uso y consumo humano. Límites permisibles de la calidad del agua y tratamientos a que debe someterse el agua para su potabilización. https://www.dof.gob.mx/nota_detalle.php?codigo=5629525&fecha=22/03/2021

NOM-230-SSA1-2002. Salud ambiental. Agua para uso y consumo humano. Procedimientos sanitarios para el muestreo. https://www.dof.gob.mx/normasOficiales/230SSA12002.pdf

Medrano-Hurtado, Z. Y., Medina-Aguirre, J. C., Marcelo-Medrano, H., Castillón-Barraza, A., Zamora-Alarcón, R., Casillas-Lamadrid, M. E., Jumilla-Corral, A. A., & Mayorga-Ortiz, P. (2022). Domestic wastewater treatment by electrocoagulation system using photovoltaic solar energy. *Revista Mexicana de Ingeniera Quimica*, *21*(2). https://doi.org/10.24275/rmiq/IA2809

Omwene, P. I., Kobya, M., & Can, O. T. (2018). Phosphorus removal from domestic wastewater in electrocoagulation reactor using aluminium and iron plate hybrid anodes. *Ecological Engineering*, *123*, 65–73. https://doi.org/10.1016/j.ecoleng.2018.08.025

Reilly, M., Cooley, A. P., Tito, D., Tassou, S. A., & Theodorou, M. K. (2019). Electrocoagulation treatment of dairy processing and slaughterhouse wastewaters. *Energy Procedia*, *161*, 343–351. https://doi.org/10.1016/j.egypro.2019.02.106

Rodziewicz, J., Mielcarek, A., Janczukowicz, W., & Bryszewski, K. (2020). Electric power consumption and current efficiency of electrochemical and electrobiological rotating disk contactors removing nutrients fromwastewater generated in soil-less plant cultivation systems. *Water (Switzerland)*, *12*(1). https://doi.org/10.3390/w12010213

Sahu, O., Mazumdar, B., & Chaudhari, P. K. (2014). Treatment of wastewater by electrocoagulation: A review. In *Environmental Science and Pollution Research* (Vol. 21, Issue 4, pp. 2397–2413). https://doi.org/10.1007/s11356-013-2208-6

Vepsäläinen, M., & Sillanpää, M. (2020). Electrocoagulation in the treatment of industrial waters and wastewaters. In *Advanced Water Treatment: Electrochemical Methods* (pp. 1–78). Elsevier Inc. https://doi.org/10.1016/B978-0-12-819227-6.00001-2

Wang, W. X., Rajeev, B. W., Stromberg, A. J., Ren, N., Tang, G., Huang, Q., Rigoutsos, I., & Nelson, P. T. (2008). The expression of microRNA miR-107 decreases early in Alzheimer's disease and may accelerate disease progression through regulation of β-site amyloid precursor protein-cleaving enzyme 1. *Journal of Neuroscience*, *28*(5), 1213–1223. https://doi.org/10.1523/JNEUROSCI.5065-07.2008

Yazici Karabulut, B., Atasoy, A. D., Can, O. T., & Yesilnacar, M. I. (2021). Electrocoagulation for nitrate removal in groundwater of intensive agricultural region: a case study of Harran plain, Turkey. *Environmental Earth Sciences*, *80*(5). https://doi.org/10.1007/s12665-021-09488-8

Yehya, T., Chafi, M., Balla, W., Vial, C., Essadki, A., & Gourich, B. (2014). Experimental analysis and modeling of denitrification using electrocoagulation process. *Separation and Purification Technology*, *132*, 644–654. https://doi.org/10.1016/j.seppur.2014.05.022

Zhu, M., Fan, J., Zhang, M., Li, Z., Yang, J., Liu, X., & Wang, X. (2021). Current intensities altered the performance and microbial community structure of a bio-electrochemical system. *Chemosphere*, *265*. https://doi.org/10.1016/j.chemosphere.2020.129069

Vol. 24, No. 3(2025) IA25642
Revista Mexicana de Ingeniería Química

Aromatic hydrocarbons in mangrove areas in Tabasco: Preliminary studies

Hidrocarburos aromáticos en zonas de manglares de Tabasco: Estudios preliminares

I. Fuentes-Domínguez, L. L. Vázquez-Vázquez, C. M. Morales-Bautista*, Y. Y. Solís-Pérez, J. A. González-Garrido, M. E. Ojeda-Morales

Red de Investigación Multidisciplinaria en Materia Ambiental desde Perspectiva de la Química Aplicada. Universidad Juárez Autónoma de Tabasco. Av. Universidad s/n, Zona de la Cultura, Col. Magisterial, Villahermosa, Centro, Tabasco, Mex. C.P. 86040.

Sent date: August 8, 2025; Accepted: November 5, 2025

Abstract

This preliminary study evaluates the presence of total petroleum hydrocarbons (TPH) and aromatic fractions (HA) in mangrove soils in the municipality of Jalpa de Méndez, Tabasco, near the Laguna Mecoacán, Natural Protected Area, a strategic area due to its proximity to the Dos Bocas maritime terminal and the Olmeca refinery. Seventeen sites with varying degrees of disturbance were analyzed, also measuring pH and electrical conductivity (EC) parameters as geochemical indicators of environmental status. The results showed that, although TPH and HA levels do not exceed the limits established by NOM-138-SEMARNAT-SSA1-2012, several samples exceed ecological risk thresholds 500 mg/kg for HA), which could represent a danger to biota and local communities. A positive correlation was identified between TPH and HA ($R^2 = 0.8846$ when urban areas were excluded), and a trend toward decreasing pH and increasing EC was observed in soils with greater contamination, suggesting hydrocarbon-induced salinization and acidification processes. The observed spatial variability reflects the ecological complexity of the system and suggests cumulative impacts of petroleum activities. Continued monitoring, evaluation of bioindicators, and consideration of ecological restoration strategies are recommended to mitigate the effects on these vulnerable ecosystems.

Keywords: mangrove, petroleum, pollution, refinery, soil.

Resumen

Este estudio preliminar evalúa la presencia de hidrocarburos totales de petróleo (HTP) y fracciones aromáticas (HA) en suelos de manglar en el municipio de Jalpa de Méndez, Tabasco, cerca del Área Natural Protegida Laguna Mecoacán, una zona estratégica debido a su proximidad a la terminal marítima Dos Bocas y la refinería Olmeca. Se analizaron diecisiete sitios con diferentes grados de perturbación, midiendo también los parámetros de pH y conductividad eléctrica (CE) como indicadores geoquímicos del estado ambiental. Los resultados mostraron que, si bien los niveles de HTP y HA no superan los límites establecidos por la NOM-138-SEMARNAT-SSA1-2012, varias muestras superan los umbrales de riesgo ecológico (500 mg/kg para HA), lo que podría representar un peligro para la biota y las comunidades locales. Se identificó una correlación positiva entre HTP y HA ($R^2 = 0.8846$ al excluir las zonas urbanas), y se observó una tendencia a la disminución del pH y al aumento de la CE en los suelos con mayor contaminación, lo que sugiere procesos de salinización y acidificación inducidos por hidrocarburos. La variabilidad espacial observada refleja la complejidad ecológica del sistema y sugiere impactos acumulativos de las actividades petroleras. Se recomienda el monitoreo continuo, la evaluación de bioindicadores y la consideración de estrategias de restauración ecológica para mitigar los efectos en estos ecosistemas vulnerables.

Palabras clave: manglar, petróleo, contaminación, refinería, suelo.

*Corresponding author. *E-mail*: carlos.morales@ujat.mx;
https://doi.org/10.24275/rmiq/IA25642
ISSN:1665-2738, *issn-e*: 2395-8472

1 Introduction

Mangroves are highly productive coastal ecosystems that provide essential ecological functions such as carbon sequestration, sediment retention, water regulation, and coastal storm protection (Alongi, 2002). Mexico ranks fourth worldwide in mangrove area (~905,000 ha), of which approximately 50% is in the Gulf of Mexico region, which encompasses the states of Tamaulipas, Veracruz, and Tabasco (Velázquez-Salazar *et al.,* 2021). This region also concentrates strategic industrial activities related to the extraction, transportation, and refining of hydrocarbons, generating a critical overlap between areas of high biodiversity and energy development hubs. This spatial coincidence poses relevant environmental challenges due to the accumulation of persistent organic pollutants, especially polycyclic aromatic hydrocarbons (PAHs) (Davis, 2017; Velázquez-Vázquez *et al.,* 2022; Billah *et al.,* 2022).

Aromatic hydrocarbons are characterized by their toxicity, persistence, and bioaccumulation capacity, affecting both benthic organisms and human health through the food chain (Dönmez, 2023). Have documented the presence of PAHs in sediments and plant tissues of mangroves and estuaries in the Gulf of Mexico, particularly in the Tonalá River basin and other coastal areas of Tabasco (Godoy-Lozano *et al.,* 2018). However, there are information gaps in areas adjacent to the Laguna Mecoacán Natural Protected Area (PNA), which is under increasing pressure due to its proximity to the Dos Bocas maritime terminal and the Olmeca Refinery, two national-scale energy infrastructures. In particular, the municipalities of Paraíso, Jalpa de Méndez and Comalcalco, have active wells that supply raw materials to these facilities, and recent studies indicate that the cumulative impacts on these fragile ecosystems could intensify in the coming decades (Méndez-Moreno *et al.,* 2021).

Despite the ecological and social importance of this region, environmental monitoring programs are still incipient, and long-term impacts on soil, a key receptor medium in mangroves, have been poorly assessed (Rivera-Arriaga *et al.,* 2020). In this context, this study carries out a preliminary characterization of total petroleum hydrocarbons (TPH) and aromatic compounds (HA), as well as their pH and salinity, in mangrove soils in the municipality of Jalpa de Méndez, Tabasco. This information seeks to provide a useful environmental baseline for identifying areas at ecological and human risk. The pH and electrical conductivity (EC), as both represent key indicators of the geochemical status of saline and marine-influenced soils, such as mangroves. For sample, pH determines the solubility and availability of metals and organic contaminants, while EC allows estimating the accumulation of soluble salts, a factor that influences the distribution of plant species and the retention or mobility of aromatic compounds (Pil-Gon *et al.,* 2023; Dhara & Dutta,2025).

Due to logistical limitations and the exploratory nature of the study, other soil or biological parameters were not included; however, the results obtained offer a useful initial diagnosis to guide future monitoring, ecological restoration, and environmental remediation strategies in the region, especially in highly marginalized communities that depend on the direct use of ecosystem services, such as the consumption of transportation products or the collection of natural resource.

2 Methodology

In 2021, targeted sampling was carried out in the area adjacent to the Laguna Mecoacán National Park, within the mangrove zone belonging to Jalpa de Méndez (Table 1). Sample collection and pretreatment were carried out following the guidelines established in NOM-021-SEMARNAT-2000 (SEMARNAT, 2002). In addition, pH and electrical conductivity (EC) analyses were performed following these same regulations. Likewise, total petroleum hydrocarbons (TPH) were quantified according to the methodology described in NOM-138-SEMARNAT-SSA1-2012 (SEMARNAT, 2013). The HTP extract was treated on a chromatographic column to determine aromatic hydrocarbons (AH) (Marín-García *et al.,* 2016). In all cases, the tests were performed in triplicate.

Statistical analysis of the data was performed using R Project software (4.5.1), applying normality tests using the Shapiro-Wilk test to determine data distribution. In cases where data heterogeneity was detected, nonparametric Kruskal-Wallis analyses were performed to compare differences between sites. An analysis of variance (ANOVA) followed by the Tukey HSD post hoc test was also applied to identify homogeneous groups and determine which sites presented significant differences in the evaluated parameters. Statistical results were presented with a significant level of 0.05, ensuring the robustness and reliability of the analysis (Maestre, 2008).

3 Results and discussions

For TPH, the Shapiro-Wilk normality test showed that several samples did not follow a normal distribution, and that there was heterogeneity in the variances between groups ($W = 0.855$ with a p-value =

0.00015). For these reasons, a non-parametric Kruskal-Walli's test was chosen, which yielded a p-value < 0.05, indicating statistically significant differences between the samples. To identify the specific groups that presented differences, Dunn's post-hoc test with Bonferroni correction for multiple comparisons was applied.

The results showed that samples with concentrations close to zero (2, 9, 13, and 17) did not differ statistically from each other, forming a hydrocarbon-free group (Table 2). Likewise, samples with intermediate concentrations, such as samples 1, 3, 5, and 6, showed statistically significant differences compared to the extreme groups (values close to zero and high values), but not among themselves, suggesting a classification in an intermediate contamination group. This group is statistically different from samples with high concentrations, such as samples 8 and 14, whose medians approach values that represent a high level of contamination. However, these values do not exceed the Maximum Permissible Limit (MPL) of the Mexican Standard NOM-138-SEMARNAT-SSA1-2012 (SEMARNAT, 2013) of 5500 mg/kg for agricultural and conservation use. It is important to highlight that the extraction was carried out with hexane, a solvent that, according to the literature, extracts up to 85–87% of the hydrocarbons present in the soil (Morales-Bautista *et al.,* 2020). Therefore, the actual concentrations could be higher, approaching or even exceeding the MLP, implying that the values observed in samples 8, 14, 15, and 16 suggest a significant environmental risk.

The Shapiro-Wilk normality test applied to the complete set of individual aromatic hydrocarbon (HA) data that yielded a statistic $W = 0.885$ with a p-value $= 0.00014$, indicating deviation from normality. This deviation is likely due to the presence of multiple zero values (i.e., samples with undetectable HA levels), combined with a wide dispersion of concentrations ranging from 0 to over 1000 mg/kg, resulting in a right-skewed distribution. To assess significant differences in HA concentrations among the 17 samples, a Kruskal-Walli's test was conducted, revealing a significant difference ($p < 0.05$) among the sample groups. Subsequently, a post-hoc Dunn's test with Bonferroni correction was applied to identify specific group differences.

Table 1. Location of samples in the study area.

Sample	UTM 15 Q	Characteristics
1	15Q0495034/2027327	Urban
2	15Q0495029/2027302	Urban
3	15Q0493617/2031753	Urban/ agricultural-livestock
4	15Q0493563/2031730	Conservation of wetlands with human invasion (white mangrove)
5	15Q0493477/2026909	Conservation of wetlands with human invasion (white mangrove)
6	15Q0494555/2027159	Conservation of anthropogenic wetlands due to land use change due to agricultural activities (black mangrove)
7	15Q0497601/2031046	Conservation of anthropogenic wetlands due to land use changes due to agricultural activities (black mangrove)
8	15Q0494928/2029737	Wetland conservation (white and black mangrove reforestation)
9	15Q495547/2027113	Urban (community pier)
10	15Q495518/2027181	Urban/ discharge wastewater
11	15Q495157/2027277	Conservation of wetlands with human invasion (white mangrove)
12	15Q494837/2027246	Urban (cooperative pier)
13	15Q495179/2027311	Wetland conservation (white mangrove)
14	15Q496863/2025990	Wetland conservation (white mangrove)
15	15Q496843/2025992	Wetland conservation (white mangrove)
16	15Q497088/2025869	Wetland conservation (white mangrove)
17	15Q496267/2026305	Wetland conservation (white mangrove)

Table 2. Concentration of hydrocarbons and properties of analyzed soils.

Sample	TPH	HA	pH	E.C.
	mg/Kg			dS/m
1	1190.01 ± 3.82	595.02 ± 1.23	7.90 ±0.01	1.100 ± 0.002
2	0 ± 0	0 ± 0	7.30 ± 0.04	0.960 ± 0.001
3	1000.10 ± 3.21	800.01 ± 1.66	7.13 ± 0.01	1.260 ± 0.003
4	1400. 02 ± 4.500	280.01 ± 0.58	5.70 ± 0.02	4.030 ± 0.008
5	1000.05 ± 3.21	100.01 ± 0.20	7.16 ± 0.01	0.640 ± 0.001
6	1300.02 ± 4.17	312.02 ± 0.64	6.86 ± 0.01	0.570 ± 0.002
7	1800.05 ± 5.78	414.05 ± 0.86	5.05 ± 0.01	3.180 ± 0.006
8	4900.03 ± 15.75	1078.08 ± 2.24	3.80 ± 0.06	3.570 ± 0.007
9	0 ± 0	0 ± 0	6.46 ± 0.02	0.880 ± 0.003
10	630 .01 ± 2.02	63.01 ± 0.13	6.13 ± 0.06	0.570 ± 0.001
11	200.01 ± 0.64	20.01 ± 0.04	6.26 ± 0.02	0.950 ± 0.009
12	2500.09 ± 8.03	875.03 ± 1.82	6.50 ± 0.01	1.500 ± 0.003
13	0 ± 0	0 ± 0	6.00 ± 0.02	1.200 ± 0.002
14	4700.03 ± 15.11	564.01 ± 1.17	4.86 ± 0.01	5.170 ± 0.010
15	3300.02 ± 10.61	495.03 ± 1.03	5.30 ±0.01	3.450 ± 0.007
16	4100.04 ± 13.17	697.02 ± 1.45	5.70 ± 0.01	1.600 ± 0.003
17	0 ± 0	0 ± 0	5.93 ± 0.01	2.150 ± 0.004

Where: TPH is the total petroleum hydrocarbons, HA is the concentration of aromatic fractions in the soil sample, pH is the hydrogen potential, and EC is the electrical conductivity.

Samples with zero values (2, 9, 13, and 17) formed a homogeneous group with no significant differences among them but differed significantly from groups with higher concentrations. The group of samples with intermediate concentrations (5, 6, 7, 10, and 11) was homogeneous internally and differed statistically from both the zero-concentration group and the highest concentration group. Samples 8 (1078 mg/kg), 12 (875 mg/kg), and 3 (800 mg/kg) were identified as having the highest concentrations. While samples 12 and 3 did not differ significantly from each other, sample 8 did not differ statistically from either 12 or 3, indicating these three form a homogeneous group of the highest HA concentrations.

In the analysis of the evaluated samples, an initial moderate relationship between total petroleum hydrocarbons (TPH) and aromatic hydrocarbons (HA) concentrations was observed, with a coefficient of determination $R^2 = 0.6186$. This value indicates a moderate positive association rather than a lack of clear relationship.

However, when excluding samples highly influenced by urban sources (samples 1, 2, 3, 10, and 12), which are subject to more mobile, variable, and transient pollutants due to factors such as boat traffic, wastewater discharges, and proximity to point sources like the Olmeca Refinery and the Dos Bocas Terminal, where controlled hydrocarbon flaring occurs, the correlation improved significantly. A linear correlation coefficient of $R^2 = 0.8846$ was obtained (Figure 1), indicating a strong and significant association between TPH and HA concentrations in areas impacted

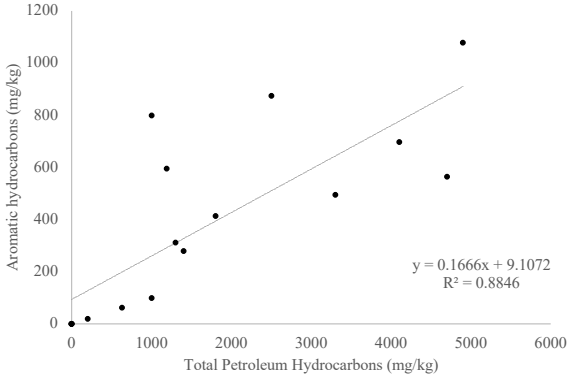

Figure 1. Relation between TPH and aromatic hydrocarbons (excluding urban use).

primarily by more persistent and soil-bound pollutants (Chen *et al.,* 2019).

The exclusion of these urban samples was necessary because episodic contamination events and transient pollutant inputs related to these industrial and maritime activities introduce variability that can obscure the underlying relationship in sediments less affected by direct urban and industrial disturbances. Therefore, when these disturbances are removed, aromatic hydrocarbons behave proportionally with respect to petroleum hydrocarbons present in the sediments (Pinheiro *et al.,* 2017; Seo *et al.,* 2020).

Furthermore, the observed relationship is moderate (Figure 1), suggesting that the accumulation of aromatic hydrocarbons is associated with slow and continuous input processes, such as atmospheric deposition, diffuse runoff, historical pollution events, or subsurface leaching. This behavior has been associated

with aromatic hydrocarbons (AH), which tend to absorb onto the fine soil fraction and accumulate stably over a long period (Abdel-Shafy and Mansour, 2016). In contrast, polycyclic aromatic hydrocarbons (PAHs) have been linked to maritime traffic and other activities, which are mostly recurrent due to events that generate nonlinear distribution gradients and asymptotes (Egardt *et al.,* 2018; Houbron *et al.,* 2021).These patterns reflect transient pollution inputs such as fuel spills, exhaust emissions, and flaring events, differentiating PAHs dynamics from the more gradual accumulation of HA from diffuse sources.

Some studies in estuarine environments have shown that two-stroke engines emit compounds such as naphthalene, chrysene, and benzo[a]pyrene, which exhibit irregular and spatially localized accumulation patterns (Terence & Masni, 2021). By excluding these mobile sources from the analysis, the dynamics of emission factors (EFs) tend to fit linear or zero-order models, like those observed in wetlands contaminated by historical spills, where degradation occurs slowly and in a controlled manner (Nguyen *et al.,* 2021). This distinction is key to interpreting pollution sources, as it allows differentiation between recent and intermittent inputs, such as those from marine engines, and more persistent, diffuse inputs linked to cumulative impacts or historical legacies.

These results indicate that wetlands have a limited capacity for self-remediation, gradually accumulating aromatic compounds that can persist over time and pose long-term ecological risks, even in the absence of an evident point source (Yu *et al.,* 2019; Saunders *et al.,* 2022). However, it is necessary to analyze a larger number of urban samples and include them in the analysis to determine whether pollutant source dynamics influence the detection of consistent patterns.

In the context of mangroves ecosystems with a high capacity to accumulate pollutants due to their characteristics and abundant organic matter the medium to high concentrations of aromatic hydrocarbons reported in the samples represent a significant environmental and ecological risk (Iwegbue *et al.,* 2016; Wu *et al.,* 2021). The capacity of these ecosystems to accumulate toxic compounds, along with their crucial role in conserving biodiversity and ecosystem services, makes them highly vulnerable to persistent pollutants. This slow degradation process can lead to bioaccumulation and biomagnification in aquatic and terrestrial species inhabiting wetlands such as mangroves. This risk is greater in local communities that depend on fishing and the exploitation of natural resources (Wang *et al.,* 2024).

In this regard, some studies indicate that aromatic hydrocarbon concentrations exceeding 500 mg/kg in soils and sediments pose a significant risk to biota and public health (Kim et al., 2013; Yu et al., 2019; Saunders et al., 2022). Therefore, samples with elevated levels of aromatic hydrocarbons (e.g., those near or above 800 mg/kg, such as samples 3, 8, and 12) may represent a direct risk due to the transfer of hydrocarbons along the food chain through bioaccumulation and biomagnification (Billah *et al*., 2022; Wang *et al.,* 2024).

Although these concentrations do not exceed the permissible limits established in the Mexican standard NOM-138-SEMARNAT-SSA1-2012 (5500 mg/kg), some reports suggest that values greater than 500 mg/kg may pose risks to the environment and public health (Kim *et al.,* 2013; Yu *et al.,* 2019; Saunders *et al.,* 2022). In this regard, samples with concentrations greater than 800 mg/kg (e.g., samples 3, 8, and 12) could present risks due to bioaccumulation and transfer between different matrices. It is documented that these risks are greater due to the biomagnification of contaminants, since the population relies on the ecosystem services of wetlands such as mangroves (Billah *et al.,* 2022; Wang *et al.,* 2024).

The pH analysis at these sites reveals not only significant statistical differentiation but also a significant ecological gradient that can influence the productivity, resilience, and ecosystem services of the wetland. Systematic evaluation of this parameter, along with other physicochemical and biological variables, is essential for establishing conservation, management, or restoration strategies tailored to each are

In this regard, a study of pH at 17 sites within a wetland revealed marked variability in soil acidity, possibly related to the specific characteristics of each site and the processes of input and retention of organic and inorganic materials. Data were collected at each site (Table 2), and a Shapiro-Wilk normality test confirmed that the pH values at all sites met the assumption of normality ($p > 0.05$), unlike the hydrocarbon data which did not meet this assumption. Therefore, an independent parametric analysis of variance (ANOVA) was applied to the pH data, yielding highly significant differences between sites ($F = 20419.83$; $p < 0.001$). Likewise, a post-hoc Tukey test revealed significant differences between several pairs of sites. The minimum significant difference (HSD) value was 0.082, indicating meaningful differences; for example, between sites 1 and 8 (difference = 4.11), while other pairs such as 4 and 16, or 9 and 12, did not show statistically significant differences.

These results indicate that, although the sites are located within the same humid ecosystem, the soils exhibit distinct chemical characteristics in terms of pH. Some studies indicate that this behavior may be related to various specific phenomena such as atypical rainfall, microbiological activity (which depends on the macrobiotic and soil type), the deposition of organic matter, and anthropogenic activities (Aguirre Forero *et al.,* 2022). These changes are common in wetlands and pose a challenge for environmental assessments, since

small differences can significantly alter soil conditions (Bruland & Richardson, 2005).

A poorly understood phenomenon related to flooding is the redissolution and transport of sediments, whose pH varies, thus favoring the proliferation of microbiota in the water. In this regard, the pH of the samples was analyzed and compared with the classification of the Mexican Official Standard NOM-021-SEMARNAT-2000 (SEMARNAT, 2002). The observed ranges showed that the sites present conditions varying from strongly acidic (site 8) to moderately alkaline (site 1). These ranges indicate anaerobic activity, common in gleysol soils of wetlands. In these units, organic matter under reducing conditions favors the release of organic acids and the presence of hydrogen ions, resulting in a low pH compared to other more aerated areas where channels and dikes are present (Ma *et al.,* 2020).

It is important to note that some studies indicate that hydrocarbon spills cause increased acidity in wetland soils and that this reduces the availability of nutrients such as phosphorus, calcium and magnesium, in addition to increasing the solubility of potentially toxic metals such as aluminium and iron (Sparks, 2003; Cisneros *et al.,* 2025). Decreased pH affects emergent and submerged vegetation, as well as microorganisms involved in key ecosystem cycles, such as denitrification or carbon mineralization. Conversely, near neutral or slightly alkaline soils can favour greater availability of essential nutrients and allow greater floral diversity, although they may also reflect salinization processes or calcareous sediment inputs (Reddy & Delaune, 2008).

Linear regression analysis between pH and total petroleum hydrocarbon (TPH) levels in the wetland soils showed a negative relationship, described by the equation y = -0.0004x + 6.7928, with a coefficient of determination R^2 = 0.4417. This indicates that, as TPH concentration increases, pH tends to decrease slightly; however, the relationship explains less than 45% of the observed variability, and its statistical significance should be interpreted with caution. In contrast, the relationship between pH and aromatic hydrocarbons (HA) was also negative, with the equation y = -0.001x + 6.4812, but with a much lower coefficient of determination (R^2 = 0.1125). No statistically significant correlation was detected for this relationship, suggesting that other environmental factors are likely govern pH variability beyond HA concentrations.

The decrease in pH and the increase in hydrocarbon concentration has been widely reported. Degradation processes have been observed to favor the acidification of primarily organic soils and sediments. This is due to the generation of organic acids and oxidation processes during microbial degradation (Abdel-Shafy & Mansour, 2016; García *et al.,* 2019). Strongly acidic pH levels affect soil fertility by altering nutrient availability and modifying the microbial community, thus disrupting natural soil processes (Kakde & Sharma, 2024).

However, other studies indicate that pH regulation may also be related to factors such as soil buffering capacity, organic matter, texture, and biological activity (Reddy and Delaune, 2008). Furthermore, while the relationship between hydrocarbons and pH is strong, this is not the case with aromatic hydrocarbons. Aromatic compounds have been reported to tend to adsorb strongly onto soil particles, which reduces their availability and degradation, thus limiting their direct effect on soil properties.These results underscore the importance of considering the combined impact of hydrocarbon contaminants and intrinsic soil characteristics to understand pH variations and their effect on the environmental quality of wetlands affected by industrial activities or water transport.

The electrical conductivity (EC) of soils sampled at 17 mangrove sites varied widely, ranging from 0.57 to 5.17 dS/m, reflecting substantial differences in ecosystem salinity gradients. The Shapiro-Wilk normality test applied by site did not detect significant deviations from normality (W = 0.9214; p = 0.4572); however, given the small sample size (n = 3 per site), these results should be interpreted with caution due to limited statistical power. Therefore, both parametric (ANOVA) and non-parametric (Kruskal-Wallis) analyses were conducted to ensure robustness. The Kruskal-Walli's test revealed significant differences in EC among sites (H = 49.63, p < 0.00003), while ANOVA was used exploratorily and indicated significant differences (F = 259.879, p < 0.001).

Subsequent multiple comparisons using Tukey's HSD test, with a minimum significant difference (HSD) estimated at approximately 0.02 dS/m, identified 136 pairs of sites showing statistically significant differences in EC. Based on these results, homogeneous groups of sites with similar EC values were defined:

1. Group A (low CE): sites 6, 7, 11 (≈ 0.57 dS/m).
2. Group B (moderate-low EC): sites 1, 2, 5, 10, 12 (≈ 0.88–1.10 dS/m).
3. Group C (moderate EC): sites 3, 13, 16 (≈ 1.26–1.60 dS/m).
4. Group D (medium-high EC): sites 17 (≈ 2.15 dS/m).
5. Group E (high EC): sites 4, 8, 9, 14, 15 (≈ 3.18–5.17 dS/m).

From a regulatory perspective, NOM-021-SEMARNAT-2000 (SEMARNAT, 2002) classifies soils with EC > 4 dS/m as severely saline. In this study, several sites exceeded these thresholds, particularly site 14 with a value of 5.17 dS/m, representing a potential ecological risk (Zheng *et al.,* 2016). Furthermore, a

correlation between EC and soil hydrocarbons was observed. EC showed a moderate relationship with TPH (y = 0.0006x + 0.9926 with R^2 = 0.4513) and a weaker relationship with HA (y = 0.0016x + 1.3424 with R^2 = 0.1575).

These trends suggest that hydrocarbons promote increased soil salinity in mangrove ecosystems. This behavior has been reported as a "salting-out" effect, which describes the decreased solubility of nonpolar organic compounds in aqueous solutions with high salt concentrations. In this context, aromatic hydrocarbons and heavy fractions (resins and asphaltenes) tend to precipitate or adsorb onto the solid soil matrix when exposed to saline environments, rather than remaining in solution (forming aggregates, although it is unknown whether these aggregates are of low or high density, as this depends on the soil's textural fractions). This process not only favors the retention of organic compounds in the soil but also conditions the cation exchange capacity of the system, as it buffers the available salts and limits their availability for other biochemical processes (Zheng *et al.,* 2016).

Furthermore, some studies mention that the microbial biodegradation of hydrocarbons in saline environments can release acidic or charged intermediates, such as organic acids or sulfate anions, which modify both the electrical conductivity and acidity of the substrate (Li et al., 2022). Similarly, the accumulation of hydrocarbons in soils can decrease cation exchange capacity (CEC) by coating the active sites of clays and organic matter with hydrophobic films, thus reducing the availability of essential cations such as Ca^{2+}, Mg^{2+}, and K^{+}. This loss affects field capacity and contributes to the accumulation of salts in the liquid fraction, increasing electrical conductivity. Under normal conditions, gleyic units can become solonchaks, which alters the ecosystem dynamics (Naidoo & Naidoo, 2021). However, hydrocarbons can accelerate salinization, exacerbating environmental stress in plant communities such as mangroves and thereby reducing their capacity to capture carbon and the reproduction of the species that thrive there.

From an ecological perspective, these changes in salinity can significantly alter the vegetation composition of the mangrove. For example, the white mangrove (*Laguncularia racemosa*) shows greater tolerance to variable saline conditions and hydrocarbon pollution, while the black mangrove (*Avicennia germinans*), although halophilic, requires more stable salinities for adequate osmotic function. The literature suggests that pollution-induced salinity fluctuations limit the growth of plants with low tolerance to these changes. Some studies mention that the combination of hydrocarbons and high salinity generates synergistic and cumulative effects that, in the long term, cause osmotic stress (Velázquez-Vázquez *et al.,* 2022). Furthermore, the observed variability in soil pH, which ranges from strongly acidic to moderately alkaline conditions, can intensify these impacts. Under these conditions, a decrease in photosynthetic activity, height, and biomass of mangrove seedlings has been documented, accompanied by an alteration in the internal ionic balance, with a reduction in the uptake of K^{+}, Ca^{2+}, and Mg^{2+}, and an increase in the uptake of Na^{+}. (Wang *et al.,* 2021; Vieira *et al.,* 2023).

Conclusions

The study yielded preliminary conclusions about the state of the mangrove ecosystem near the Olmeca refinery. Its importance as an indicator of the accumulation and potential impacts of anthropogenic and industrial activities in the region is particularly noteworthy. On the one hand, soil acidity significantly influences the solubility and mobility of nutrients and contaminants, increasing toxicity and affecting the availability of essential elements for plant development. These physiological alterations can compromise the adaptive capacity of certain species and favour more tolerant ones, which can modify the structure and dynamics of the mangrove in the medium term. Clear statistical differences in electrical conductivity were observed at the sampled sites, allowing them to be grouped into five homogeneous categories. Some of these sites exceeded the regulatory limits established by Mexican legislation, posing an environmental risk to the integrity of the ecosystem.

Although total petroleum hydrocarbons and aromatic hydrocarbons were found at values below regulatory limits, they showed a positive association with salinity, likely mediated by physicochemical and microbiological mechanisms that affect the adsorption and mobility of these compounds in the soil. This evidence suggests that current conditions reflect a direct or cumulative influence of the nearby refinery's oil activities, affecting soil quality and the health of the mangrove ecosystem. Therefore, it is recommended to implement continuous environmental monitoring that includes physicochemical parameters, bioindicators, and specific hydrocarbon analyses to detect temporal trends and assess potential long-term impacts. Furthermore, it is necessary to further investigate the toxicity and physiological response of the dominant plant species, as well as develop remediation and ecological restoration strategies tailored to these specific conditions. Consequently, combined changes in salinity and pH can favour more tolerant species such as *Laguncularia racemosa* and negatively affect sensitive species such as *Avicennia germinans*, modifying the resilience and ecological dynamics of the mangrove.

Acknowledgements

To the Secretaría de Ciencia, Humanidades, Tecnología e Innovación for the scholarships awarded to graduate students IFD, LLVV, and YYSP. To the Academic Division of Basic Sciences (DACB-UJAT) for the university infrastructure provided for the development of this research.

References

Abdel-Shafy, H. I., and Mansour, M. S. M. (2016). A review on polycyclic aromatic hydrocarbons: Source, environmental impact, effect on human health and remediation. *Egyptian Journal of Petroleum 25*(1), 107-123. https://doi.org/10.1016/j.ejpe.2015.03.011

Aguirre Forero, S. E., Piraneque Gambasica, N. V., and Mercado Fernández, T. (2022). *Suelo y cambio climático: Incluye estudio de casos*. Editorial Unimagdalena, Colombia.

Alongi, D. M. (2002). Present state and future of the world's mangrove forests. *Environmental Conservation 29*(3), 331-349. https://doi.org/10.1017/S0376892902000231

Billah, M. M., Bhuiyan, M. K. A., Amran, M. I. U. A., Cabral, A. C., and Garcia, M. R. D. (2022). Polycyclic aromatic hydrocarbons (PAHs) pollution in mangrove ecosystems: global synthesis and future research directions. *Reviews in Environmental Science and Bio/Technology 21*(3), 747-770. https://doi.org/10.1007/s11157-022-09625-0

Bruland, G. L., and Richardson, C. J. (2005). Hydrologic, edaphic, and vegetative responses to fire and hydrologic manipulation in the Everglades. *Ecological Applications 15*(4), 1379-1395. https://doi.org/10.1890/04-1206

Chen, Y., Li, X., Zhao, L., and Liu, C. (2019). Distribution and risk assessment of petroleum hydrocarbons in sediments of a coastal bay in China. *Environmental Science and Pollution Research 26*(22), 22957-22967. https://doi.org/10.1007/s11356-019-05969-2

Cisneros-de la Cueva, S., Martínez-Prado, M. A., Rojas-Contreras, J. A., & López-Miranda, J. (2024). Effect of surfactants on the removal of total petroleum hydrocarbons and microbial communities during bioremediation of a contaminated mining soil. *Revista Mexicana de Ingeniería Química 23*(2), 1-17. https://doi.org/10.24275/rmiq/Bio2417

Davis Jr, R. A. (2017). Sediments of the Gulf of Mexico. In: *Habitats and Biota of the Gulf of Mexico: Before the Deepwater Horizon Oil Spill: Volume 1: Water Quality, Sediments, Sediment Contaminants, Oil and Gas Seeps, Coastal Habitats, Offshore Plankton and Benthos, and Shellfish*, (Ward, C. https://doi.org/10.1007/978-1-4939-3447-8_3, eds), Pp. 165-215 Springer, New York, NY.

Dhara, A., and Dutta, R. (2025). A review on sources and distribution of polycyclic aromatic hydrocarbons (PAHs) in wetland ecosystem: Focusing on plant-biomonitoring and phytoremediation. *Environmental Science and Pollution Research 32*, 1-23. https://doi.org/10.1007/s11356-025-36240-7

Dönmez, A. E. (2023). Sucul Ortamların İzlenmesinde Biyobelirteç Olarak Histopatoloji. *Journal of Anatolian Environmental and Animal Sciences 8*(2), 183-190. https://doi.org/10.35229/jaes.1245431

Egardt, J., Larsen, M. M., Lassen, P., and Dahllöf, I. (2018). Release of PAHs and heavy metals in coastal environments linked to leisure boats. *Marine pollution bulletin 127*, 664-671.https://doi.org/10.1016/j.chemosphere.2024.143910

García, M. E., Pérez, R. A., and Torres, J. L. (2019). Impacto de hidrocarburos en propiedades fisicoquímicas de suelos agrícolas: una revisión. *Revista de Ciencias Ambientales*, *11*(2), 143-156 https://doi.org/10.22201/icat.16656423e.2019.2.173

García-Rodríguez, M. J., and Delgado-Mendoza, J. A. (2020). Changes in mangrove vegetation caused by long-term exposure to petroleum hydrocarbons. *Marine Pollution Bulletin* 150, 110748. https://doi.org/10.1016/j.marpolbul.2019.110748

Godoy-Lozano, E. E., Escobar-Zepeda, A., Raggi, L., Merino, E., Gutierrez-Rios, R. M., Juarez, K., and Pardo-López, L. (2018). Bacterial diversity and the geochemical landscape in the southwestern Gulf of Mexico. *Frontiers in microbiology 9*, 1-15. https://doi.org/10.3389/fmicb.2018.02528

Houbron, E., Cruz-Carmona, E., Ponciano-Rosas, A., Rustrián-Portilla, E., and Canul-Chan, M. (2021). Motor oil wastewater treatment in a packed bed bioreactor using immobilized native microbial consortium. *Revista Mexicana de Ingeniería Química 20*(2), 761-773. https://doi.org/10.24275/rmiq/IA2271

Iwegbue, C. M., Obi, G., Aganbi, E., Ogala, J. E., Omo-Irabor, O. O., and Martincigh, B. S. (2016). Concentrations and health risk assessment of polycyclic aromatic hydrocarbons in soils of an urban environment in the Niger Delta, Nigeria. *Toxicology and Environmental Health Sciences 8*(3), 221-233. https://doi.org/10.1007/s13530-016-0279-8

Kakde, P., and Sharma, J. (2024). Microbial Bioremediation of Petroleum Contaminated Soil: Structural Complexity, Degradation Dynamics and Advanced Remediation Techniques. *Journal of Pure & Applied Microbiology 18*(4), 22-44. https://doi.org/10.22207/JPAM.18.4.28

Kim, K.-H., Jahan, S. A., Kabir, E., and Brown, R. J. C. (2013). A review of airborne polycyclic aromatic hydrocarbons (PAHs) and their human health effects. *Environment International 60*, 71-80. https://doi.org/10.1016/j.envint.2013.07.019

Li, Y., Li, W., Ji, L., Song, F., Li, T., Fu, X., and Wang, J. (2022). Effects of salinity on the biodegradation of polycyclic aromatic hydrocarbons in oilfield soils emphasizing degradation genes and soil enzymes. *Frontiers in microbiology 12*, 1-12. https://doi.org/10.3389/fmicb.2021.824319

Ma, J., Zhou, T., Xu, C., Shen, D., Xu, S., and Lin, C. (2020). Spatial and temporal variation in microbial diversity and community structure in a contaminated mangrove wetland. *Applied Sciences 10*(17), 1-15. https://doi.org/10.3390/app10175850

Maestre, F. T., Escudero, A., and Bonet, A. (Eds.). (2008). *Introducción al análisis espacial de datos en ecología y ciencias ambientales: métodos y aplicaciones*. Editorial Dykinson, España.

Marín-García, D. C., Adams, R. H., and Hernández-Barajas, R. (2016). Effect of crude petroleum on water repellency in a clayey alluvial soil. *International journal of environmental science and technology 13*(1), 55-64. https://doi.org/10.1007/s13762-015-0838-6

Méndez-Moreno, J. D. C., Garza-Rodríguez, I. M., Torres-Sánchez, S. A., Jiménez-Pérez, N. D. C., Sánchez-Lombardo, I., López-Martínez, S., and Morales-Bautista, C. M. (2021). Changes in restored soils subject to weathering and their implication in Mexican environmental regulations. *Terra Latinoamericana 39*. 1-21. https://doi.org/10.28940/terra.v39i0.798

Morales-Bautista, C. M., Méndez-Olán, C., López-Martínez, S., and Ojeda-Morales, M. E. (2020). Design of experiments to optimize soxhlet-HTP method to establish environmental diagnostics of polluted soil: Optimization of the soxhlet-HTP method by DOE. In *Design of experiments for chemical, pharmaceutical, food, and industrial applications* (E.G. Carrillo-Cedillo. J.A. Rodríguez-Avila, K.A. Arredondo-Soto and, J.M. Cornejo-Bravo. https://doi.org/10.4018/978-1-7998-1518-1 , eds.). P.p. 33-52. IGI Global Scientific Publishing.

Nguyen, T. N. T., Park, M. K., Son, J. M., and Choi, S. D. (2021). Spatial distribution and temporal variation of polycyclic aromatic hydrocarbons in runoff and surface water. *Science of the Total Environment 793*, 148339. https://doi.org/10.1016/j.scitotenv.2021.148339

Pil-Gon, K. I. M., Tarafdar, A., and Jung-Hwan, K. W. O. N. (2023). Effect of soil pH on the sorption capacity of soil organic matter for polycyclic aromatic hydrocarbons in unsaturated soils. *Pedosphere 33*(2), 365-371. https://doi.org/10.1016/j.pedsph.2022.06.049

Piñeiro, P. P., Massone, C. G., and Carreira, R. S. (2017). Distribution, sources and toxicity potential of hydrocarbons in harbor sediments: A regional assessment in SE Brazil. *Marine pollution bulletin 120*(1-2), 6-17. https://doi.org/10.1016/j.marpolbul.2017.04.049

Reddy, K. R., and Delaune, R. D. (2008). *Biogeochemistry of wetlands: Science and applications*. CRC Press, Taylor & Francis, UK. https://doi.org/10.1201/9781420017626

Rivera-Arriaga, E., I. Azuz-Adeath, O. D. Cervantes Rosas, A. Espinoza-Tenorio, R. Silva Casarín, A. Ortega-Rubio, A. V. Botello y B. E. Vega-Serratos (2020). *Gobernanza y Manejo de las Costas y Mares ante la Incertidumbre. Una Guía para Tomadores de Decisiones*. Editorial Ricomar, Universidad Autónoma de Campeche, México

Saunders, D., Carrillo, J. C., Gundlach, E. R., Iroakasi, O., Visigah, K., Zabbey, N., and Bonte, M. (2022). Analysis of polycyclic aromatic hydrocarbons (PAHs) in surface sediments and edible aquatic species in an oil-contaminated mangrove ecosystem in Bodo, Niger Delta, Nigeria: Bioaccumulation and human health risk assessment. *Science of the Total Environment 832*, 154802. https://doi.org/10.1016/j.scitotenv.2022.154802

Sparks, D. L., Singh, B., and Siebecker, M.G. (2003). *Environmental Soil Chemistry*. Academic Press, United Kingdom. https://doi.org/10.1016/B978-012656446-4/50000-9

SEMARNAT (2002). Secretaría de Medio Ambiente y Recursos Naturales Norma Oficial Mexicana NOM-021-SEMARNAT-2000. Que establece las especificaciones de fertilidad, salinidad y clasificación de suelos. Estudio, muestreo y análisis. Diario Oficial de la Federación, 31 de diciembre de 2002. Available at: https://www.dof.gob.mx/nota_detalle.php?codigo=698211&fecha=31/12/2002 Accessed: August 2, 2022.

SEMARNAT. (2013). Secretaría del Medio de Ambiente y Recursos Naturales. Norma Oficial Mexicana NOM-138-SEMARNAT/SSA1-2012 que establece los límites máximos permisibles de hidrocarburos en suelos y las especificaciones para su caracterización y remediación. Recuperado de: www.profepa.gob.mx/innovaportal/file/6646/1/nom-138-semarnat.ssa1-2012.pdf Accessed: August 5, 2022.

Seo, S. H., Kwon, H. O., Park, M. K., Lee, I. S., and Choi, S. D. (2020). Contamination characteristics of polycyclic aromatic hydrocarbons in river and coastal sediments collected from the multi-industrial city of Ulsan, South Korea. *Marine Pollution Bulletin 160*, 111666. https://doi.org/10.1016/j.marpolbul.2020.111666

Terence, R. C., and Masni, M. A. (2021). Vertical profile of polycyclic aromatic hydrocarbons in the core sediment found in Langkawi, Kedah. *Journal of Environmental Biology 42*, 849-856. http://doi.org/10.22438/jeb/42/3(SI)/JEB-17

Velázquez-Salazar S., Rodríguez-Zúñiga M.T., Alcántara-Maya J.A., Villeda-Chávez E., Valderrama-Landeros L., Troche-Souza C., Vázquez-Balderas B., Pérez-Espinosa I., Cruz-López M. I., Ressl R., De la Borbolla D. V. G., Paz O., Aguilar-Sierra V., Hruby F. y Muñoa-Coutiño J. H. (2021). Manglares de México. Actualización y análisis de los datos 2020. Editorial Comisión Nacional para el Conocimiento y Uso de la Biodiversidad, México.

Velázquez-Vázquez, V. W., Gómez, S. A., Gutiérrez-Rojas, M., Díaz-Ramírez, I., and Volke-Sepúlveda, T. (2022). Estimation of hydrocarbon sequestration in soils: influence of the chemical characteristics of humic substances. *Revista Mexicana de Ingeniería Química 21*(1), 1-16. https://doi.org/10.24275/rmiq/IA2660

Naidoo, G., and Naidoo, K. (2021). Salinity exacerbates oil contamination effects in mangroves. *Environmental Science and Pollution Research 28*(48), 68398-68406. https://doi.org/10.1007/s11356-021-15450-9

Wang, Z., Meng, Q., Sun, K., and Wen, Z. (2024). Spatiotemporal distribution, bioaccumulation, and ecological and human health risks of polycyclic aromatic hydrocarbons in surface water: a comprehensive review. *Sustainability 16*(23), 1-32. https://doi.org/10.3390/su162310346

Yu, Z., Lin, Q., Gu, Y., Du, F., Wang, X., Shi, F., and Yu, Y. (2019). Bioaccumulation of polycyclic aromatic hydrocarbons (PAHs) in wild marine fish from the coastal waters of the northern South China Sea: risk assessment for human health. *Ecotoxicology and environmental safety 180*, 742-748. https://doi.org/10.1016/j.ecoenv.2019.05.065

Zheng, W., Wang, Y., and Zhang, M. (2016). Influence of salinity on the sorption and mobility of petroleum hydrocarbons in estuarine soils. Chemosphere, 144, 1635–1642. https://doi.org/10.1016/j.chemosphere.2015.10.071

Vol. 24, No. 3(2025) IA25694
Revista Mexicana de Ingeniería Química

Chemical, physical, and energetic characterization of biochar produced via sugarcane bagasse pyrolysis

Caracterización química, física y energética del biochar producido por la pirólisis de bagazo de caña de azúcar

O. Sánchez-Castillo, M.G. Vizcarra-Mendoza, C. Martínez-Vera, S.A. Gómez-Torres*, E. Rojas-García
Departamento de Ingeniería de Procesos e Hidráulica, Universidad Autónoma Metropolitana-Iztapalapa, Ciudad de México, 09340, México.
Sent date: October 14, 2025; Accepted: November 6, 2025

Abstract
The objective of this work is to study the production of biochar from the pyrolysis of sugar cane bagasse with the purpose of determining the effect of pyrolysis temperature on the biochar properties. The results could be relevant for choosing the operation conditions according to the purpose for which the biochar is produced. For this study, a pyrolizer was designed and constructed for carrying out the experiments. The parameters analyzed were the inert gas flow (N_2), the effect of the bagasse particle size, and the temperature. Biochar was produced at four temperatures: 300, 400, 500, and 600°C. The morphological and physical-chemical characteristics of the biochar produced were determined by several analytical techniques: elemental chemical analysis, N_2 adsorption, scanning electronic microscopy, X-ray diffraction, and infrared and Raman spectroscopies. The effect of the operation temperature on the mass, energetic, and fixed carbon yields, as well as on the lower heating value of the biochar obtained is analyzed. In addition, the present study reports the relationship between the order degree of the carbon structures in biochar and the pyrolysis temperature.
Keywords: Sugarcane bagasse; pyrolysis; biochar; energy yield; low heating value.

Resumen
El objetivo de este trabajo es estudiar la producción de biochar a partir de la pirólisis de bagaso de caña de azúcar y determinar el efecto de la temperatura de pirólisis en las propiedades del biochar. Los resultados pueden ser relevantes para la selección de las condiciones de operación adecuadas de acuerdo al propósito para el cual se desea utilizar el biochar. Para éste estudio se diseñó y construyó un pirolizador. Los parámetros de operación analizados fueron: el flujo de gas inerte (N_2), el tamaño de partícula de bagazo y la temperatura. Los experimentos de llevaron a cabo a 300, 400, 500 y 600 °C. Las características físico-químicas y morfológicas del biochar se determinaron mediante: análisis químico elemental, adsorción de N_2, microscopía electrónica de barrido, difracción de Rayos X y espectroscopía infrarroja y Raman. Se analizó el efecto de la temperatura en los rendimentos másico, energético y a carbon fijo, así como en el poder calorífico inferior del biochar producido. Se reporta el incremento en el orden de las estructuras de carbón en el biochar en función de la temperatura de pirólisis.
Palabras clave: *Bagazo de caña*; *pirólisis*; *biochar,* rendimiento energético, valor bajo de calentamiento.

*Corresponding author. *E-mail*: sgomez@xanum.uam.mx;
https://doi.org/10.24275/rmiq/IA25694
ISSN:1665-2738, *issn-e*: 2395-8472

1 Introduction

The necessity for sustainable energy sources, driven by growing global demand and the limitations of fossil resources, has highlighted the use of biomass (BM) as a promising energy alternative due to its abundance and characteristics (Karp *et al.* 2013; Zafranet, 2025). Biomass is defined as a renewable resource that is derived from living organisms. A wide range of sources can be utilized for this purpose, including agricultural residues. A significant amount of research attention has been focused on residual biomass (RBM) since it can be transformed into valuable products such as biofuels and biochar (Karp *et al.* 2013; Iwuozor *et al.* 2022).

It is estimated that Mexico produces between 18 and 58 Mt of agricultural waste annually. This waste comprises notable quantities of residues, with 95.8% of the total available residues originating from maize (43.3%), sorghum (25.5%), and sugarcane bagasse (SCB) (18.1%), followed by wheat (6.3%), barley (1.6%) and beans (1.0%) (Honorato-Salazar and Sadhukhan 2022). This waste constitutes a substantial potential bioenergy resource, though a significant portion is currently burned or left in the fields (Marín Apolo *et al.* 2025). The total energy potential was estimated at 670 PJ/yr (Honorato-Salazar and Sadhukhan 2022). Then, the proper management of this waste is crucial to addressing environmental challenges and capitalizing on its energy potential (Honorato-Salazar and Sadhukhan 2022; Marín Apolo *et al.* 2025).

SCB is an abundant byproduct of the Mexican sugar industry. On average, between 0.1 and 0.15 tons of dry SCB are produced for every ton of processed sugar. In Mexico, it is estimated that the 2024/25 harvest will yield around 4.6 million tons of processed sugar (Zafranet, 2025). Based on this data, the amount of dry bagasse is approximately 460 thousand tons of dry SCB, which is mostly used as a thermal energy source in sugar mills. On average, SCB is composed of 45 to 50% cellulose, 25 to 30% hemicellulose, 25% lignin, and 2 to 9% ash (Karp *et al.* 2013, Honorato-Salazar and Sadhukhan 2022; Marín Apolo *et al.* 2025). Due to its cellulose content, SCB can be used for bioenergy production, such as electricity generation, in the paper industry, or as a solar energy reserve (Karp *et al.* 2013, Honorato-Salazar and Sadhukhan 2022). Additionally, it can be used to produce bio-oil, combustible gases, and biochar through pyrolysis, a thermochemical process that converts residual biomass into useful products for energy, agricultural, and environmental applications (Karp *et al.* 2013, Iwuozor *et al*. 2022; Honorato-Salazar and Sadhukhan 2022; Marín Apolo *et al.* 2025). The pyrolysis process can be performed in a fluidized bed or in a batch reactor. For example, Ahumada et al. (2022) investigated the pyrolysis of various biomass types, including SCB, in a fluidized bed using N_2 as the carrier gas. In contrast, the present study focuses on the pyrolysis of SCB in a batch reactor, allowing for different temperature profiles and residence times compared to fluidized bed systems.

The process of pyrolysis is initiated by the drying of biomass, which is then subjected to additional heating. This results in the release of volatile matter, including carbon dioxide (CO_2), carbon monoxide (CO), methane (CH_4), water vapor (H_2O), hydrogen (H_2) condensable organic compounds including methanol (CH_3OH) and acetic acid (CH_3COOH). The occurrence of subsequent reaction, such as polymerization and cracking, is facilitated by the high temperature in the gas phase (Weber and Quicker 2018). The solid present within the reactor undergoes a transformation dependent upon the pyrolysis conditions, resulting in a high carbon content and its conversion into biochar (Parihar *et al.* 2007; Weber and Quicker 2018; Toscano *et al*. 2021).

Biochar can be defined as a solid product containing carbon and mineral elements. It is valued for its textural and acidic surface properties, which support soil improvement as a biofertilizer, water treatment, its use as a selective adsorbent for harmful gases, and as a precursor of active carbons. As pointed out by Romero-Bonilla (2025), biochar can enhance soil structure and improve nutrient retention in agricultural systems, and it can also be utilized for the adsorption of pollutants in waterways and agricultural soils. It has been used as an adsorbent to reduce the CO_2 concentration and other greenhouse gases from the environment. Nevertheless, the quality of biochar, including its yield, structural and surface characteristics, and textural properties, is dependent upon the critical variables employed during the pyrolysis process of SCB. These critical variables include the temperature, the flow rate of inert gas, and the particle size (Weber and Quicker 2018; Rambhatla *et al.* 2025). Therefore, the aim of this work is to utilize SCB to optimize the operation of our pyrolysis system for biochar production using SCB, through the characterization of the resulting biochar. Additionally, the effect of process variables on the yield and properties of the biochar was probed again those reported in the literature and focused on specific operational variables such as N_2 flow, temperature, and particle size. This approach enables the SCB utilization and the promotion of biochar production and their use in Mexico, which possesses specific characteristics that have the potential for agricultural and environmental applications.

2 Methodology

Sugarcane was bought in the Central Market of Mexico City ("*Central de Abastos*", the main wholesale market for foodstuffs in the country). The canes were peeled off and cut in small cylindrical pieces of approximately

0.8 cm x 3.3 cm. The pieces were pressed with a pressing force of 4 Ton/cm^2 for extracting the juice. To determine the required time for reducing the moisture content of the pressed SCB to 10% (db), a series of drying experiments were conducted in a thermobalance (OHAUS MB200, USA) at temperatures of 40, 60, and 80°C for 180 min. The bone-dry mass was determined by heating the SCB at 120°C for 180 min in the thermobalance (Sánchez *et al.* 2025). The moisture content (db) was calculated by using Eq. (1).

$$X = \frac{m(t) - m(ss)}{m(ss)} \quad (1)$$

Where *m(t)* denotes the mass of the samples at time t, whereas *m(ss)* signifies the dry mass.

To ensure the suitability of the SCB for the pyrolysis experiments, it was cut into cubes of approximately 1 cm x 1.5 cm x 1.2 cm. These were then oven-dried (Riossa, HCF-48, Mexico) at 70°C for 20 h prior to introduction into the pyrolytic reactor.

A stainless-steel pyrolytic reactor was designed and built according to the measures indicated in Fig. (1a). The pyrolizer is equipped with a heating system comprising 4 kW electrical resistances, a ceramic insulating system, and a stainless-steel coating. The resistances and two Type K thermocouples are connected to control system that includes two temperature controls (Novus N48OD, China) for defining the heating rate and the pyrolysis temperature. The pyrolizer was designed in such a way that the material to be pyrolyzed is loaded into a cartridge, which can be easily introduced into the reactor and, upon completion of the reaction, can also be easily removed to extract the produced biochar (Fig. 1a). This facilitates the loading and cleaning operations. Inside the reactor, the cartridge is supported on a bed of 5 mm diameter stainless steel spheres, the purpose of which is to ensure a homogeneous distribution of the N_2 flow that is fed at the bottom of the reactor. The gas-phase products exit via the upper part section of the reactor, where they are condensed to obtain bio-oils (Fig. 1b).

Preliminary experiments were conducted to study how the size of SCB particles affects the homogeneity and carbonization degree of the resulting biochar. Considering the findings, the dried samples of SCB were subjected to grinding to achieve a size of 60 mesh (0.25 mm). This size was determined to be optimal for carrying out the pyrolysis experiments, as it has been shown to yield biochar of consistent quality. Sifting through a 60 mesh, the biomass prior to processing has been reported by Romero-Bonilla (2025).

The pyrolytic reactor was operated at four temperatures (300, 400, 500, and 600°C) for 1 h. These temperatures were selected because the preliminary experiments indicate that the amount of biochar decrease as the pyrolysis temperature increase and, also, they lie within the range reported by other researchers, for example, Romero-Bonilla (2025) obtained biochar from cocoa shells by calcinating them for 2 h at 400 and 600°C. In each one of these experimental runs, the flow rate of N_2 was varied from 500 to 3000 cm^3/min. This was done to ensure an inert atmosphere and facilitate the removal of volatile compounds (Parihar *et al.* 2007; Toscano *et al.* 2021). In the preliminary proofs, it was also established that the flow of N_2 did not affect the biochar yield or its physical characteristics. Consequently, a N_2 flow rate of 500 cm^3/min was selected for the subsequent tests. The spatial velocity (SV) was calculated based on the selected N_2 flow and the mass of dried SCB having an average particle size of 0.25 mm. In all subsequent experiments, the SV was maintained at a constant value of 28 h^{-1}. The resultant vapours were then directed through two condensers, the first one operated at 60°C and the second at -5°C, where the bio-oils were collected (Fig. 1b).

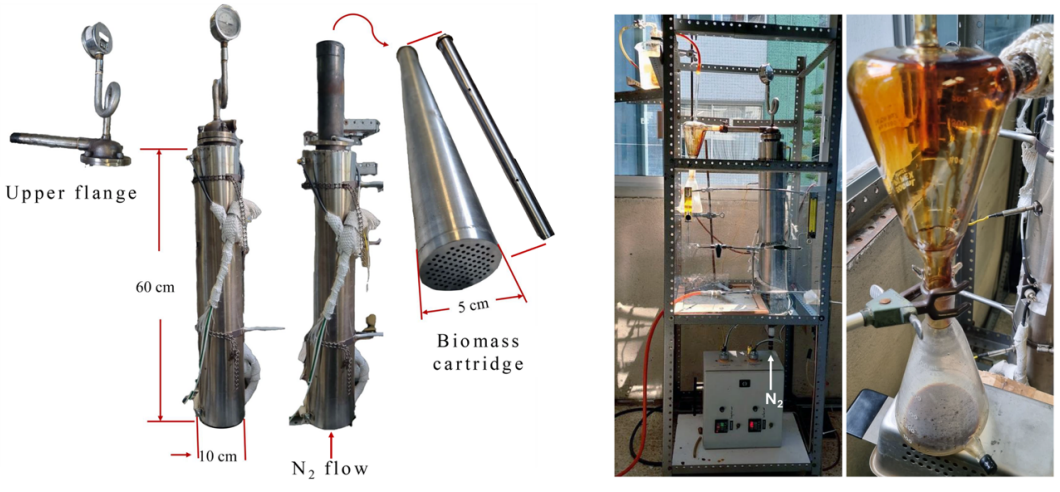

a) b)

Figure 1. Pyrolysis reactor with heating system and biomass container cartridge (a), and pyrolysis reactor and bio-oil condensers in operation (b).

The biochar obtained in the reactor was characterised by means of a range of analytical techniques, including scanning electron microscopy (SEM) (JEOL JSM-7600F, Field emission source 30kV with a 5120X3840 pixel scanning generator, resolution of 1 nm at 15kV, Japan), X-ray diffraction (XRD) (Bruker D8 Advance with $\lambda_{Cu\kappa\alpha} = 0.15406\ nm$), BET analysis ($N_2$ adsorption) (Quantachrome ASiQwin, USA, previous to analysis, the samples were treatment to 120ºC by 12 h), Fourier transform infrared (FTIR Thermo Nicolet Nexus 4700, USA, in the range of 400-4000 cm^{-1}), and Raman spectroscopies (Renishaw In Via with a Green Laser λ = 532 nm, 10 accumulations of 10 seconds, and 1% power laser).

The biochar mass yield (Y_m) was calculated using Eq. (2) (Parihar *et al.* 2007; Weber and Quicker 2018), the energetic yield (Y_e) was obtained by means of Eq. (3), and the yield to fixed carbon (Y_{cf}) is given by Eq. (4) (Weber and Quicker 2018).

$$Y_m = \frac{m_{Biochar}}{m_{SCB}}(100) \tag{2}$$

$$Y_e = Y_m \frac{LHV_{Biochar}}{LHV_{SCB}} \tag{3}$$

$$Y_{cf} = Y_m \frac{m_{cf\ biochar}}{m_{cf\ SCB}} \tag{4}$$

In Eq. (3), *LHV* denotes low heating value for biochar or SCB, they were calculated using the methodology proposed by Weber and Quicker (2018) and by the modified Dulong equation (Tillman D.A. 1978) which is a function of the C, H, O, S results from the elemental analysis results. The LHV values obtained using both methods agree very well (+/- 3%) so we use the average values, they range between 23 and 37 MJ/kg, depending on the temperature. The quantity of fixed carbon (m_{cf}) in both the biochar and SCB was determined also from the elemental chemical analysis (CA) of the samples. The elemental content of carbon (C), hydrogen (H), and nitrogen (N) in all samples was determined based on ASTM D5373-21, using a Thermo Scientific™ Flash 2000 CHNS elemental analyzer. To do this, the samples were first ground (< 250 μm) and dried at 105°C for 24 h. Subsequently, 2-3 mg of dry sample was weighed into high-purity tin capsules using an analytical balance with an accuracy of ±0.1 mg. The capsules containing the sample were placed in the equipment's combustion furnace, operating at 950–1000 °C in an oxygen-rich atmosphere (99.99%). Vanadium oxide (V_2O_5) was used as an oxidation catalyst, followed by a reduction column with metallic copper at 650 °C. The gases formed (CO_2, H_2O, N_2) were separated chromatographically and quantified by a thermal conductivity detector (TCD). Methionine (Thermo Fisher Scientific Certified Reference Material; C: 40.30%, H: 7.45%, N: 9.39%, S: 21.95%, O: 21.45%) was used as the calibration standard. The samples were analyzed in triplicate, achieving an error < 0.3% w/w.

3 Results and discussion

As mentioned above, before the SCB was loaded in the pyrolytic reactor, it was dried, and, to find the appropriate temperature and the corresponding necessary drying time for reducing the SCB moisture content to the desired value (10% db), drying experiments were carried out to obtain the drying curves at 40, 60, and 80°C. These curves are presented in Fig. 2. It can be seen that in the three curves, there is a constant drying period (in which the moisture transfer is controlled by convection) followed by a decreasing drying period (controlled by diffusion). This information is required for designing the dryer and allows the calculation of the heat and mass convective transfer coefficients needed for resolving the energy and mass balances.

Based on these results, a temperature of 70°C was chosen for drying the SCB for 20 h before being loaded in the reactor. This is consistent with what has been reported in the literature (Kumar *et al.* 2022).

The quantity of biochar produced depends on the operation conditions under which the pyrolytic reactor is operated, in particular, the particle size and the temperature (Parihar *et al*. 2007; Iwuozor *et al.* 2022; Sánchez *et al.* 2025), because these parameters affect the decomposition processes of the SCB (as was said above, the flow of N_2, from 500 to 3000 cm^3/min, has no effect on the characteristics and quantity of the biochar obtained).

In Fig. 3, the photograph of biochar obtained at each temperature is presented alongside the corresponding SEM images.

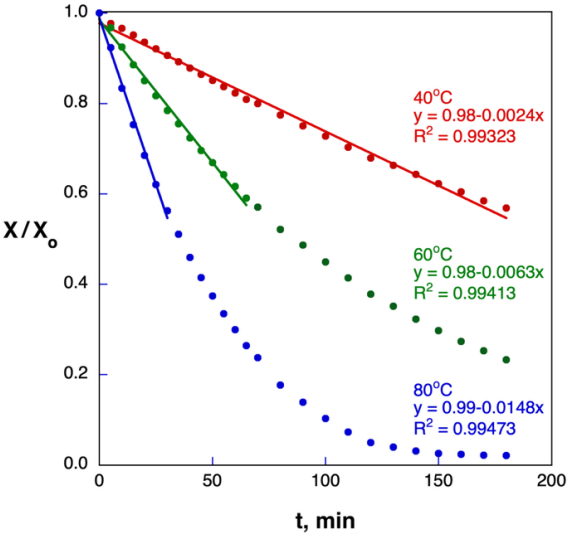

Figure 2. Drying curves of sugar cane bagasse at 40, 60, and 80°C. The continuous lines stress the constant drying period in each curve.

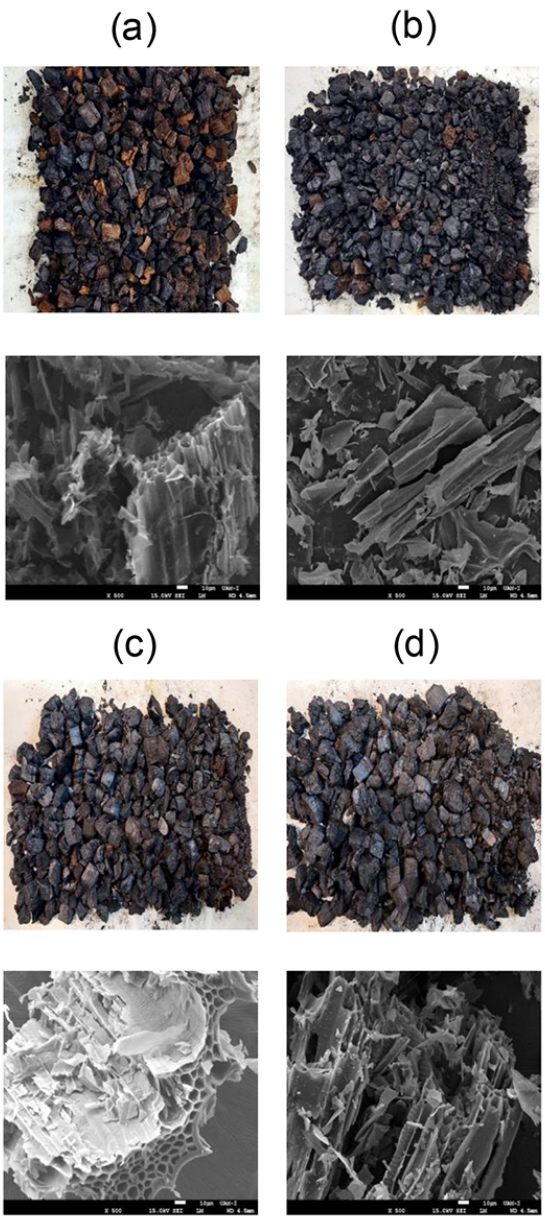

Figure 3. Photographs and SEM images of biochar obtained at 300 (a), 400 (b), 500 (c), and 600 °C (d).

In the low temperature photographs (300-400 ºC), the presence of uncarbonized sugarcane bagasse particles is evident. This suggests a partial decomposition of the lignocellulosic components. Their degree of carbonization increases as the temperature rises. All the SEM images were obtained with a 500x field of view. The SEM image of biochar obtained at 300 °C reveals an irregular and fractured surface morphology. Laminar structures with jagged edges and rough textures are evident, indicating partial decomposition of lignocellulosic components. The presence of broken plates and cavities suggests early porosity development, attributable to the initial stages of carbonization. These details are consistent with low-temperature pyrolysis, in which organic residues remain and the carbonaceous matrix begins to consolidate (Kumar et al. 2019). The 10 µm scale bar highlights the heterogeneous distribution of cracks and voids, influencing the material's adsorption capacity and physicochemical properties. As the pyrolysis temperature increases, collapsed structures with irregular edges, well-defined cavities, and an open texture emerge, indicating advanced carbonization (Fig. 3b-d). These morphological features result from extensive thermal degradation of lignocellulosic components, leading to a more stable carbonaceous matrix with increased surface area. The presence of microfractures and interconnected pores suggests enhanced adsorption potential, relevant for environmental remediation, nutrient retention, or catalytic support.

In this work, the pyrolytic reactor was operated at four temperatures: 300, 400, 500 and 600°C. In Table 1 are reported the results at each of the operation temperatures. In particular, it can be appreciated that the mass of biochar obtained, and the yield of biochar diminish as the operation temperature increases. It can also be seen that the density and volume of bio-oil obtained in the first condenser (operating at 60°C) are always greater than those obtained in the second condenser (which operates at -5°C). This indicates that the heavier compounds are separated in the first condenser, and the lighter ones are obtained in the second condenser. It can also be observed that as the yield to biochar goes down as the temperature goes up, the yield to bio-gas increases.

Table 1. Results from the pyrolysis of SCB (particle size of 0.25 mm) at SV of 28 h^{-1}.

T ºC	MBCH g	VBO1 mL	ρ_{BO1} g/mL	V_{BO2} mL	ρ_{BO2} g/mL	Y_m %	Y_{BO1} %	Y_{BO2} %	Y_{BG} %
300	46	15	1.16	22	1.13	42	19	23	19
400	33	15	1.22	25	1.15	31	17	26	26
500	29	10	1.22	22	1.17	26	11	24	39
600	26	10	1.20	21	1.15	25	11	23	42

* M_{BCH}: biochar mass; V_{BO1}: bio-oil 1 volume; ρ_{BO1}: bio-oil 1 density; V_{BO2}: bio-oil 2 volume; ρ_{BO2}: bio-oil 2 density; Y_m: biochar yield; Y_{BO1}: bio-oil 1 yield; Y_{BO2}: bio-oil 2 yield; and Y_{BG}: biogas yield.

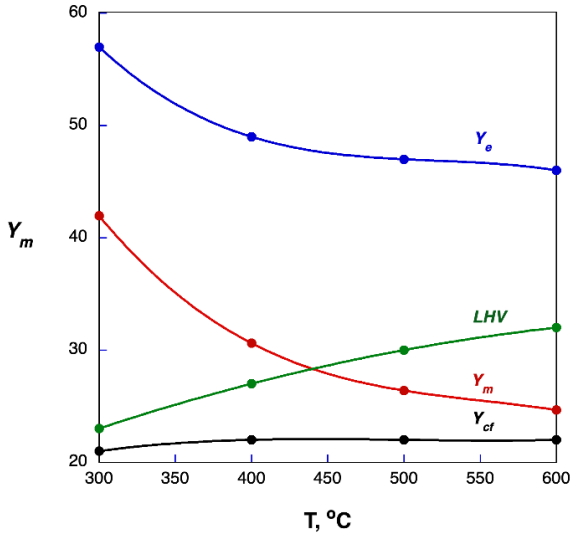

Figure 4. Mass (Y_m), energy (Y_e), and fixed carbon (Y_{cf}) yields, and *LHV* as a function of pyrolysis temperature.

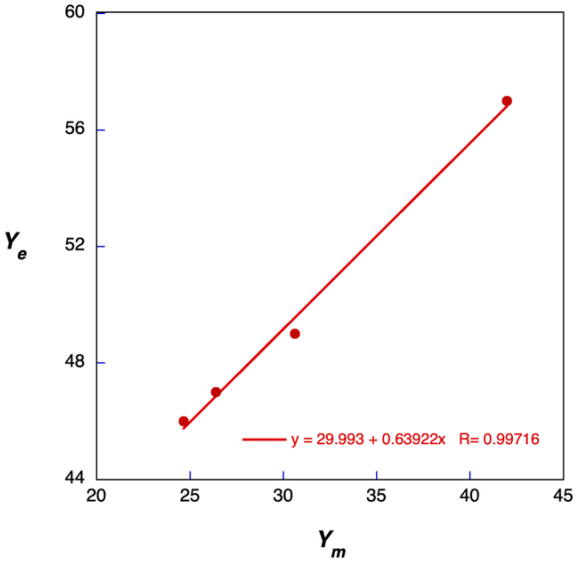

Figure 5. Correlation between energy (Y_e) and mass (Y_m) yields for the biochar of SCB.

In Fig. 4, it is evident that an increase in the operating temperature of the pyrolytic reactor correlates with a decrease in both, mass yield (Y_m) and energetic yield (Y_e). Notably, Y_m decreases by approximately 40% within the studied temperature range of 300 to 600°C. Notably, mass yield decreases by approximately 40% within the studied temperature range of 300 to 600°C. This finding aligns with previous literature (Parihar *et al.* 2007; Iwuozor *et al.* 2022, Sánchez *et al.* 2025) and suggests that the quality of biochar improves due to enhanced biomass decomposition at elevated operating temperatures. The energetic yield (Y_e) reflects the proportion of energetic content from the SCB that remains in the biochar produced during the pyrolytic process. According to Eq. 2, the relationship between Y_e and Y_m is linear, with the slope determined

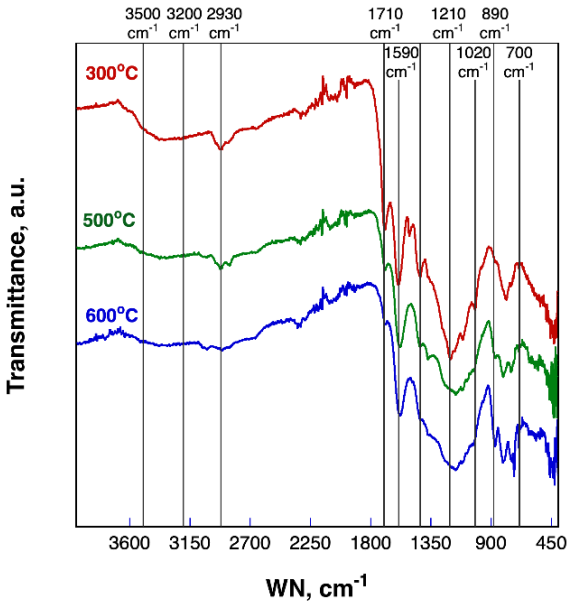

Figure 6. FTIR spectra of biochar samples obtained between 300 and 600°C.

by the *LHV*s of the materials as well as the operating temperature (Fig. 5).

The *LHV* of the biochar increases with the operational temperature of the pyrolytic reactor, consistent with the concentration of fixed carbon in the solid product. Literature indicates that the specific energy content of biochar can increase from 15-20 MJ/kg to 25-30 MJ/kg when carbonized at temperatures between 250-350°C, reaching *LHV* values of 30-35 MJ/kg at higher temperatures (Weber and Quicker 2018; Xu *et al.* 2020). Our biochar samples demonstrate this trend; for instance, the *LHV* of the biochar produced at 300°C is 23 MJ/kg, whereas the *LHV* at 600°C is 32 MJ/kg. The most significant increase in *LHV* values occurs between 300°C and 400°C, a temperature range where the significant reduction of oxygenated compounds enhances the energetic content of the biochar substantially. Above 400°C, the *LHV* value rises moderately as the biochar composition approaches that of the mineral carbon (33 MJ/kg).

To sustain the assertions mentioned above, the biochar obtained at each of the operation temperatures considered in this work was characterized by several techniques: BET analysis (N_2 adsorption), scanning electronic microscopy (SEM), x-ray diffraction (XRD), infrared (IR) and Raman spectroscopies. According to the N_2 adsorption isotherms and the BET analysis, the biochar obtained in our laboratory have low specific areas that go from 30 to 80 m^2/g depending on the pyrolytic reactor operation conditions, particularly the temperature. This indicates that the biochar porous structure also depends on the operation temperature.

The results of the Fourier transform infrared spectroscopy (FTIR) presented in Fig. 6 show the evolution that the functional groups undergo in the

biochar structure as the temperature at which they were produced increases.

The intensity of the hydroxyl groups, presented between 3600 - 3200 cm^{-1}, goes down as the temperature goes up, which is an indication of thermal degradation. The stretching of the alkyl groups, located between 3000-2800 cm^{-1}, reduce their intensity, which reflects the degradation of the aliphatic chains. The band between 1750-1650 cm^{-1}, characteristic of the carbonyl groups, decreases progressively as the temperature increases which suggest the formation of aromatic structures. The increment in the intensity of the band between 1600-1400 cm^{-1}, corresponding to the double bond C=C, is congruent with a mayor structural stability of the biochar's produced at the higher temperatures. Also, the bands C-O located in 1300-1000 cm^{-1}, decrease as the temperature increases which corresponds to the formation of more carbonized compounds (Parihar *et al*. 2007; Toscano *et al.* 2021; Rambhatla *et al.* 2025). Finally, the presence of signals in the range 900-700 cm^{-1} is evidence of the formation of a more ordered graphitic structure at higher temperatures (Parihar *et al*. 2007; Toscano *et al.* 2021).

The biochar Raman spectra present the D band around 1350 cm^{-1}, that corresponds to the mode A_{1g} of sp^3 carbon atoms activated by defects disorder structures, and the G band in ~1590 cm^{-1}, of the vibrational mode E_{2g} that indicates sp^2 carbon atoms in graphitic structures. In Fig. (7a) can be clearly observed that, as the temperature increases the G band becomes more intense and lightly defined, which suggest a greater structural order in the biochar. Also, the relative intensity of the D band decreases as the temperature increases, especially in the spectra at 600°C. To prove this, the intensity relation of the bands D and G (I_D/I_G) was calculated at each of the experimental temperatures, and, in Table 2, it can be observed how this relation decreases with temperature. According to the literature (Parihar *et al*. 2007; Xu *et al*. 2020), a decrease in the relation I_D/I_G indicates an increase in the biochar carbon structural order degree that corresponds to fewer defects and more graphitic domains (Parihar *et al*. 2007; Xu *et al*. 2020). These results are consistent with the DRX patterns (Parihar *et al*. 2007) (Fig. 7b). These results not only facilitate the identification of phases and defects in the material but also provide relevant information for optimizing the pyrolysis process and guaranteeing the quality of the produced biochar from SCB.

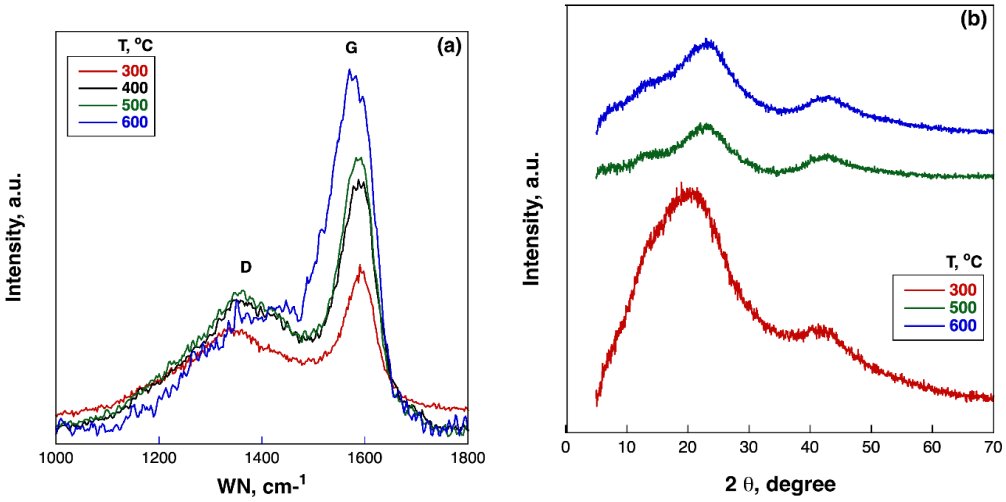

Figure 7. Raman spectra (a) and XRD patterns (b) for biochar obtained at different temperatures.

Table 2. Determination of parameters for the van Krevelen diagram of Biochar [6].

T (°C)	C_{CA}	H_{CA}	O_{CA}	I_D/I_G	V_{daf}	H/C_{CA}	H/C_{Eq6}	O/C_{CA}	O/C_{Eq7}	O/C_{SEM}
300	71.02	4.42	21.83	0.63	51.26	0.75	0.89	0.23	0.35	0.32
400	75.62	3.75	19.89	0.53	30.31	0.60	0.52	0.20	0.20	0.30
500	81.46	3.35	14.04	0.52	17.93	0.49	0.30	0.13	0.11	0.12
600	83.47	2.71	12.47	0.33	11.62	0.39	0.19	0.11	0.07	0.10

C_{CA}, H_{CA}, and O_{CA} in wt %; CA: Chemical Analysis; Eq6: Calculated from Equation 6; O/C_{SEM}: Obtained from EDX – SEM; H/C and O/C ratios in mol/mol.

Xu *et al.* (2020) studied the biochar production from three different biomass sources: rice husk, rice straw, and pinewood. Their results indicate that the more than the biomass type, the pyrolysis temperature is the determining factor in the yield to biochar. Based on their experimental results, they report correlations for the residual volatile content (RV), dry basis volatile content free of ashes (V_{daf}), molar ratio hydrogen/carbon (H/C), the molar ratio oxygen/carbon (O/C), and Y_e as functions of Y_m at different pyrolysis temperatures. Their correlations are valid for the three types of biomasses studied by them, rice husk, rice straw, and pinewood. To verify if their correlations could be applied to the SCB, with the Y_m data reported in Table 1 and the correlations of Xu *et al.* the H/C, and O/C relations were obtained and compared with the data obtained with elemental chemical analysis (CA), H/C_{CA} and O/C_{CA}, and $O/C_{EDX\text{-}SEM}$ from the SEM results, and the van Krevelen's diagram (van Krevelen 1950) reported by Weber and Quicker (2018) that includes results for woody and herbaceous biomass types. The correlations are presented below, and in Table 2 are shown the values obtained from Y_m for the biochar obtained from SCB and C, H and O in wt% obtained from the elemental chemical analysis (CA) and the mol/mol ratios H/C_{CA} and O/C_{CA}.

$$RV = -23.70 + 1.07735 y_m \tag{5}$$

$$V_{daf} = \frac{RV}{y_m} \tag{6}$$

$$\frac{H}{C} = -0.0144 + 0.0177 V_{daf} \tag{7}$$

$$\frac{O}{C} = 0.077 + 0.3253\frac{H}{C} + 0.0647\left(\frac{H}{C}\right)^2 \tag{8}$$

Diverse effects can be observed as the temperature increases: the residual volatiles decrease, which suggests an increase in the carbonization degree and in the biochar order; H/C decreases, which is related to an increment in the aromatization and in the condensation of the carbonated net; O/C decreases, which indicates the progressive elimination of oxygenated functional groups. These observations are concordant with the results of the IR and Raman spectra. We consider that it is important to emphasise the agreement between the O/C obtained from EDX-SEM analysis, H/C_{CA} and O/C_{CA}, and those calculated from the Xu *et al.* (2020) correlation's (Table 2).

In Figs. 9a and 9b is shown the form in which the position and the amplitude of the bands D and G change with V_{daf}. As can be seen, when the dry basis volatile content free of ashes decreases, the position of the D band goes down while the position of the G band goes up, which indicates an increment in the order degree of the carbon structures in the biochar as the pyrolysis temperature increases. Additionally, according to the literature (Xu *et al.* 2020), a lesser content of volatiles in the biochar corresponds to a more ordered carbon structure, as can be seen in Table 2. The band Full Width at Half Medium (FWHM) for the D band decrease when V_{daf} decreases, which can be due to the progressive liberation of alkanic and C-O structures as the pyrolysis temperature increases. In Fig. 7c can be observed that when V_{daf} decreases, the FWHM of the G band firstly decreases until a 500°C pyrolysis temperature is reached, and, later, increases with temperature. This is because the aromatic rings are converted to small graphite crystals at higher temperatures, making the G band become dominant and its FWHM increase.

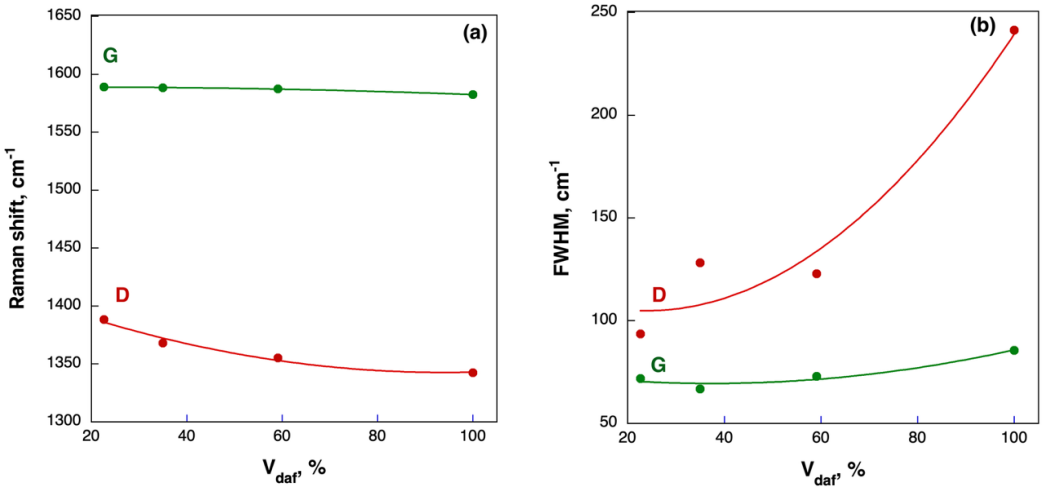

Figure 8. Raman shift (a) and FWHM (b) of the D and G bands of the spectra of biochar.

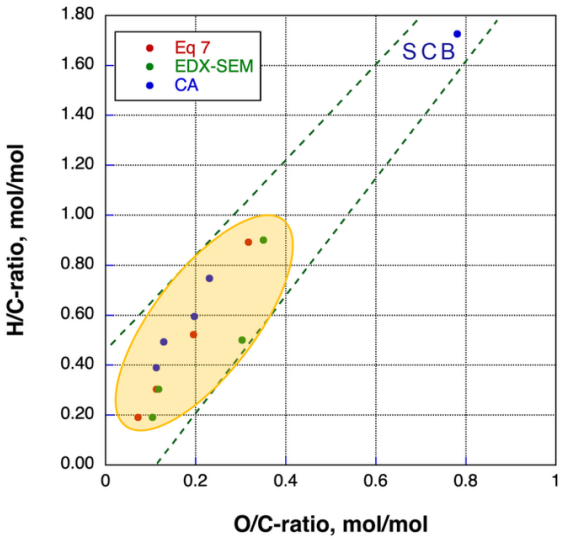

Figure 9. van Krevelen diagram, H/C_{CA} and H/C (Eq. 6) as a function of O/C_{CA}, O/C (Eq. 7), and O/C (EDX-SEM) mol/mol ratio for biochar samples. The dotted lines show the limits of the van Krevelen diagram reported by Weber and Quicker for herbaceous biomass, and the yellow ellipse indicates the limits for temperatures between 300 and 600°C.

From the values reported in Table 2 and the van Krevelen diagram (Fig. 9) (van Krevelen, 1950), it can be appreciated that as the H/C values decrease, also the O/C ones decrease, which is indicative of an increase in the aromatization and condensation of the carbonaceous net and is correlated with an elimination of oxygenated functional groups during the process. H/C and O/C experimentally determined and calculated by the correlations found in literature.

It should be noted, in Table 2, the good agreement of the results obtained with the EDX-SEM and the elemental chemical analysis of our biochar samples with those obtained with the reported correlations (Xu *et al.* 2020). It should be noted that the dotted green lines in Fig. 9 illustrate the limits of the van Krevelen diagram reported by Weber and Quicker (2018) for herbaceous types of biomasses, and the yellow ellipse denotes the limits for temperatures between 300 and 600°C. This finding serves to substantiate the outcomes observed in the present study and underscores the paramount role of temperature in the pyrolysis of SCB, a finding that aligns with previous research (Weber and Quicker 2018; Xu *et al.* 2020). Our preliminary results indicates that when the biochar samples obtained at 500 and 600°C were activated by using KOH we obtained activated carbons having 1200 m^2/g and that they could be applied to the adsorption of CO_2 from a mixture of 15% CO_2 in N_2.

Conclusions

Key findings of this work include the following: The grinding the biomass to 60 mesh is critical to ensure the production of homogeneous biochar. The inert gas flow rate exerts a negligible influence on biochar characteristics. The pyrolysis temperature has the most significant impact on the properties of biochar. As indicated by IR and Raman spectra, the H/C and O/C molar ratios decrease with higher pyrolysis temperatures, reflecting the removal of oxygenated functional groups. Spectroscopic and SEM analyses demonstrate that elevated temperatures decrease volatile content by releasing alkanic and C-O structures. These alterations are associated with the development of a more structured carbon configuration, as substantiated by SEM, FTIR and Raman analyses. The biochar samples from SCB could be applied in the adsorption of CO_2.

References

Ahumada C.D., Hinojosa- Palafox J.F., Maytorena V.M., Pérez-Rábago, C. (2022). Computational study of biomass fast pyrolysis in a fluidized bed reactor. Revista Mexicana de Ingeniería Química Vol. 21, No. 2. ISSN:1665-2738. issn-e: 2395-8472 https://doi.org/10.24275/rmiq/Cat2744

Antonangelo, J.A., Zhang, H., Sun, X. Kumar A., Physicochemical properties and morphology of biochars as affected by feedstock sources and pyrolysis temperatures. Biochar **1**, 325–336 (2019). https://doi.org/10.1007/s42773-019-00028-z

Honorato-Salazar, J.A., Sadhukhan, J. (2020). Annual biomass variation of agriculture crops and forestry residues, and seasonality of crop residues for energy production in Mexico. *Food and Biomass Processing 119*, 1-19. https://doi.org/10.1016/j.fbp.2019.10.005.

Iwuozor, K.O., Emenike, E.Ch., Ighalo, J.O., Omoaruke, F.O., Omuku, P.E., Adeniyi, A. G. (2022). *Cleaner Materials* 6 100162. https://doi.org/10.1016/j.clema.2022.100162

Karp, S.G., Woiciechowski, A.L., Soccol V.T., Soccol R. (2013). Pretreatment strategies for delignification of sugarcane bagasse: A review. *Brazilian Archives of Biology and Technology* 56, 679-689. https://doi.org/10.1590/S1516-89132013000400019

Kumar, M., Upadhyay, S.N., Mishra, P.K. (2022). Pyrolysis of sugarcane (Saccharum officinarum L.) Leaves and Characterization Products, *ACS Omega*, *7*, 28052-28064. https://doi.org/10.1021/acsomega.2c02076

Marín Apolo, Y.C., Vega Iñiguez, M.E., Ochoa-Correa D. (2025). Aprovechamiento de residuos agrícolas para producción de electricidad en Latinoamérica: Revisión literaria de casos exitosos en México, Colombia y Brasil. *InGenio Journal 8*(1) 46-68. https://doi.org/10.18779/ingenio.v8il.901

Parihar, M.F., Kamil, M., Goyal, H.B., Gupta, A.K., Bhatnagar, A.K. (2007). An experimental study on pyrolysis of biomass. *Trans I Chem. E., Part B. Process Safety and Environmental Protection 85*, B5, 458-465. https://doi.org/10.1205/psep07035

Rambhatla, N., Panicker, T., Mishra, R.K., Manjeshwar, S.K., Sharma, A. (2025). Biomass pyrolysis for biochar production: Study of kinetics parameters and effect of temperature on biochar yield its physicochemical properties. *Results in engineering 25*, 103679 1-12. https://doi.org/10.1016/j.rineng.2024.103679

Romero-Bonilla, H. I., Jaramillo-Guanolique, A., Zambrano, C., Rios-Hidalgo, M., Solano-Maza, L., Choez-Tobo, C. (2025). Cocoa shell biochars for sustainable biodiesel production in Ecuador. *Revista Mexicana de Ingeniería Química 24*, No. 1, IE24221. https://doi.org/10.24275/rmiq/IE24221 ISSN:1665-2738, issn-e: 2395-8472

Sánchez Castillo, O., Vizcarra-Mendoza, M.G., Martínez Vera, C., Gómez Torres, S.A., Rojas García, E. (2025). Producción de biochar a partir de la pirólisis de bagazo de caña de azúcar. *Avances en IQ 4*(1), AMB 343-AMB348. ISSN: 2683-2925.

Tillman, D.A. (1978). Fuels and Combustion Handbook. Mc Graw-Hill, NY, p.65.

Toscano Miranda, N., Lopes Motta, I., Maciel Filho, R., Wolf Maciel, M.R. (2021). Sugarcane bagasse pyrolysis: A review of operating conditions and products properties. *Renew. Sustain. Energy Rev. 149*, 111394. https://doi.org/10.1016/j.rser.2021.111394

van Krevelen, D. W. (1950). Graphical-statistical method for the study of structure and reaction processes of coal. *Fuel 29*, 269-284.

Weber, K., Quicker, P. (2018). Properties of biochar. *Fuel 217*, 240-261. https://doi.org/10.1016/j.fuel.2017.12.054

Xu, J., Liu, J., Ling, P., Zhang, X., Xu, K., He, L., Wang, Y., Su, S., Hu, S., Xiang, J. (2020). Raman spectroscopy of biochar from the pyrolysis of three typical Chinese biomasses: A novel method for rapidly evaluating the biochar property. *Results in Energy 202*(1-10) 117644. https://doi.org/10.1016/j.energy.2020.117644

Zafranet (2025). Available at: https://www.zafranet.com/noticias/zafra-2024-25-produccion-de-azucar-acumulada-supera-los-4-6-millones-de-toneladas/ Accessed: June 24, 2025.

Vol. 24, No. 3(2025) IE25590
Revista Mexicana de Ingeniería Química

Using a composite coating ($Cu/(TiO_2) + (SiO_2)/Al_2O_2$)to increase the efficiency of photovoltaic panels

Usando un recubrimiento compuesto($Cu/(TiO_2) + (SiO_2) / Al_2O_2$)para aumentar la eficiencia de los paneles fotovoltaicos

R. khatir[1], K. kessairi[2], N. sellami[3], A. fidjah[4]*
[1.2.3]Laboratory of Electrical Engineering and Materials (LGEM), Oran, 31000, Algeria.
[4] Faculty of Science and Technology University of Djelfa Algeria.
Sent date: May 11, 2025; Accepted: August 31, 2025

Abstract
This research analyzes the effect of applying a heat-reflective coating to a 270W polycrystalline panel. Solar panels suffer reduced efficiency due to high temperatures, negatively impacting their performance, especially in high solar irradiance conditions. This is a fundamental step toward promoting solar energy as an economical source. The research aims to evaluate the effect of a heat-reflective coating technique (using a multilayer system (copper, a titanium dioxide/silicon dioxide middle layer, and an aluminum oxide protective layer), on improving panel efficiency by increasing energy production. The researchers followed an exploratory, experimental approach, comparing the performance of a standard panel to a coated panel by estimating irradiance, temperature, and power generation under varying climatic conditions. The results showed increased photovoltaic efficiency, approaching the panel's maximum power with an increase of 8% to 9%. The study highlights the practical potential of this technology in improving the efficiency of solar systems and expanding their application in environments with high temperatures and radiation, supporting the long-term development of clean energy solutions. It is an effective method for improving panel efficiency, paving the way for advanced solar energy technologies.
Keywords: Solar energy, Heat-reflective coating , Polycrystalline panel, Photovoltaic efficiency , Multilayer design.

Resumen
Esta investigación analiza el efecto de aplicar un revestimiento termorreflectante a un panel policristalino de 270W. Los paneles solares sufren una eficiencia reducida debido a las altas temperaturas, lo que afecta negativamente a su rendimiento, especialmente en condiciones de alta irradiación solar. Este es un paso fundamental para promover la energía solar como fuente económica. La investigación tiene como objetivo evaluar el efecto de una técnica de recubrimiento reflectante del calor (utilizando un sistema multicapa (cobre, una capa intermedia de dióxido de titanio/dióxido de silicio y una capa protectora de óxido de aluminio), en la mejora de la eficiencia del panel al aumentar la producción de energía. Los investigadores siguieron un enfoque exploratorio y experimental, comparando el rendimiento de un panel estándar con un panel recubierto estimando la irradiancia, la temperatura y la generación de energía en condiciones climáticas variables. Los resultados mostraron una mayor eficiencia fotovoltaica, acercándose a la potencia máxima del panel con un aumento del 8% al 9%. El estudio destaca el potencial práctico de esta tecnología para mejorar la eficiencia de los sistemas solares y expandir su aplicación en entornos con altas temperaturas y radiación, apoyando el desarrollo a largo plazo de soluciones de energía limpia. Es un método eficaz para mejorar la eficiencia de los paneles, allanando el camino para tecnologías avanzadas de energía solar.
Palabras clave: Energía solar, Revestimiento termorreflectante, Panel policristalino, Eficiencia fotovoltaica, Diseño multicapa.

* *Corresponding author. E-mail*: fidjah.abdelkader@gmail.com;
https://doi.org/10.24275/rmiq/IE25590
ISSN:1665-2738, *issn-e*: 2395-8472

1 Introduction

Solar energy is becoming one of the most prominent environmentally friendly renewable sources (Maka & Alabid, 2022). It provides practical solutions to address the world's environmental and economic challenges. Solar panels play a key role in converting solar energy into electrical energy (El Hammoumi *et al*., 2022). With the advancement of technology and the growing interest in renewable energy sources, it has become necessary to understand the impact of the nature of these materials on the performance of solar panels, especially under different natural conditions such as high temperatures. This challenge affects the efficiency of solar panels in hot regions (Agyekum *et al*. 2021). High temperatures decrease the efficiency of these panels due to the negative impact of heat on their photovoltaic efficiency (Li *et al*. 2023). Solar panels must be made of materials that allow the free movement of electrons to convert light into electricity (Dambhare et al,2021). When light falls on the solar panel, the material absorbs some of it. This excites the electrons, which in turn move, triggering chemical reactions that generate electricity. However, if the material becomes too hot, the electrons stop functioning properly, and the energy production system collapses (Vaillon *et al*.,2018). Cell efficiency declines almost linearly with temperatures above 25°C (~0.3%/°C for silicon and ~0.5%/°C for cadmium telluride) (McCandless *et al*., 2011), (Sachenko *et al*., 2019). Consequently, standard test conditions are set at 25°C, the cell temperature, and the module's open-circuit voltage (the cell voltage when no current is drawn from the module) (Mavromatakis et al, 2014). However, solar panel temperatures on sloping residential roofs can significantly exceed standard test conditions. Solar photovoltaic modules lose their efficiency due to unwanted heating. Part of the solar spectrum is absorbed, causing them to heat up (Santhosh et al,2016) . Standard single-junction crystalline silicon panels reach operating temperatures between 45°C and 62°C. This thermal effect degrades output and can lead to cell cracking as large temperature gradients develop within the device. There are models and experimental correlations linking increased temperature to efficiency loss. Several past studies have addressed the effect of temperature on the efficiency of photovoltaic cells (Sun *et al*.,20222),(Murtadha *et al*.,2022),(Jathar et al,2023).Given the threat of global warming, scientists are proposing chemically treating solar panels to increase their efficiency, allowing them to avoid overheating and efficiency loss (Xu *et al*.,2022) . One option is to use copper, abundant in the Earth, to manufacture the solar cells in the panels. Copper absorbs sunlight better than the more expensive and widely used silicon. Unfortunately, the Earth is also rich in heat, which weakens copper's ability to absorb sunlight. By adding a thin, inexpensive, heat-reflecting layer to solar cells, sunlight is absorbed, and heat is reflected (Wette *et al*.,2019). As a result, the panel can generate more electricity from the absorbed sunlight. Copper is one of the few materials that best meets the theoretical limits for light absorption. A drawback of copper is that it is not cheap compared to the price of materials like silicon, which is commonly used in solar panels (Dias *et al*.,2022). Although it does not absorb sunlight as efficiently as copper, it is cheap. Reducing the use of cheaper materials in commercial panels means producing less electricity for the same amount of sunlight. On the other hand, this would mean using more hazardous chemicals to manufacture silicon solar panels. In this context, using heat-reflective coatings is a promising innovation that contributes to reducing the surface temperature of solar panels, enhancing their performance, and extending their lifespan (Sarkın *et al*.,2020). Heat-reflective coatings are advanced materials used to reduce heat absorption by reflecting a large portion of the sun's radiation, especially infrared radiation, which is the primary support for surface heating (Shanmugam *et al*.,2020). This coating has optical properties allow it to reflect harmful radiation while allowing visible light to pass through to the solar cells. It does not negatively affect the amount of light needed for energy generation (El-Khozondar *et al*.,2021). In hot regions such as Algeria, solar radiation is high year-round, ranging from 800 W/m^2 to 1200W/m^2. Significant increases in electrical output can be achieved (Nia *et al*.,2013). Furthermore, using smart coatings improves performance and reduces the need for dynamic cooling systems, saving operating costs and making systems more maintainable and naturally attractive (Kausar,2018). Smart coatings are more practical and wise than other technical solutions, such as water-cooling systems or dynamic-mechanical technologies. Heat-reflective coatings are an innovative solution to address solar panel efficiency challenges in hot climates (Adak *et al*.,2022). Some studies have shown that heat-reflective coatings improve solar panel efficiency by reflecting infrared radiation and sunlight, reducing heat absorption. This has improved solar panel efficiency, as high temperatures negatively impact energy generation (Law *et al*.,2023),(Adak *et al*.,2020),(Ji *et al*.,2022). In a study conducted by Yu *et al*.., aspects of coating design, process control, and scientific characterization (regarding microstructure and spectral properties) were addressed (Yu *et al*.,2020). In another study, novel copper ferrite and polyaniline (PANI) nanocomposites were studied using state-of-the-art chemical and experimental methods to use in solar collector applications. The results showed a strong solar absorption of 95% within the apparent range and a 1% reduction in thermal emissivity, giving them an ultrahigh solar selectivity of up to 96.28%

(Mostafa et al,2024). Various types of coatings are applied in this field, such as ceramic coatings deposited by vacuum evaporation or spraying. The absorption of solar radiation in ceramic coatings originates from the metallic component, typically nickel and chromium. At the same time, an insulating material such as alumina controls the reflectance of infrared radiation (Winnicki *et al*.,2021). Black chrome absorbers are typically deposited on a stainless steel substrate and generally have an absorptivity of 95% or more and a low thermal emissivity of between 5% and 12%. Paint coatings, also known as organic or composite coatings, are widely used commercially. Various companies are developing various paint coating technologies (Nazari *et al*.,2020). The technology developed specifically for solar collectors involves complex equipment and processes that can apply a nanocomposite coating of heat-resistant metal oxide nanoparticles embedded in an electrochemically bonded polymeric material (Khan *et al*.,2023). Not all of these technologies have been sufficiently proven for large-scale solar collector projects. This new technology can manufacture highly selective Cr-Ni-Steel sheets with a solar absorption of 95.57 ± 1.20% and a low thermal emittance of 4.94 ± 0.91%.

This study used a three-layer experimental copper, titanium dioxide, and aluminum oxide coating. These coatings were deposited using a magnetic sputtering technique. This produced thin, homogeneous layers that ensured high stability on the target surface, significantly increasing the panel's efficiency. The results demonstrated that this coordinated formulation could lower the panel temperature, representing a breakthrough in improving panel production efficiency and extending its operational life. It embodies a futuristic vision in materials construction and mechanical innovations. It contributes to the sustainability of energy projects and electronic systems by improving thermal performance and reducing reliance on traditional cooling methods.

2 Materials and tests

Solar panels are an efficient form of renewable energy, using sunlight as a natural energy source to produce electricity (Deshmukh *et al*.,2023). Due to the increasing use of solar panels, research, and development of their efficiency through nano-coating is constantly being conducted. The global acceptance and commercialization of solar panels have expanded the market size and encouraged the rapid growth of the panel industry. Solar panels are primarily made of glass or plastic, 0.3 to 0.5 mm thick, and are reinforced or coated with an anti-reflective (AR) coating. This coating is known as UV-visible cutting technology (Belançon *et al*.,2023).

Heat-reflective coatings are typically arranged in layers consisting of three main components (Mara *et al*.,2023):

2.1 Reflective metal layer

This is the basic fabric and typically uses metals such as aluminum (Al), copper (Cu), and silver (Ag). These metals have high reflectivity in the infrared range. They reflect this thermal radiation and reduce heat transfer to the inner layers or the surface used for photo conversion.In this research, a 120-nm-thick copper metal is used.

2.2 Intermediate layer

This insulating fabric with a high refractive index creates an impedance effect that improves the system's reflectivity in the infrared range without affecting the transmittance of visible light. In this work, we add titanium dioxide (TiO_2) and silicon dioxide (SiO_2) with a thickness of 90 nm.

2.3 Protective outer layer

The materials used in this layer are thin polymeric or ceramic materials or even some oxides. Within this layer, aluminum oxide (Al_2O_2) is used with a thickness of 90 nanometers.Figure 1 shows a cross-section of the coating used.

Magnetic sputter coating is an advanced technique for depositing thin layers of materials on various surfaces. It relies on a technique known as physical vapor deposition (PVD), where a magnetic field generates plasma in a vacuum chamber. The plasma ionizes the target material, causing it to disperse or vaporize and be deposited on the substrate (Pošković *et al*., 2021).

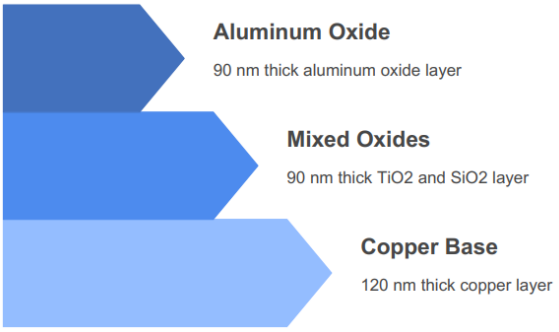

Figure 1 . Structure of the paint components.

Table 1. Polycrystalline solar panel characteristics.

Electrical Data		Thermal Characteristics	
Power	270W	Nominal Operating Cell Temperature (NOCT)	45°C±2°C
Maximum Power Voltage-Vmp(V)	30.7V	Temperature Coefficient of Voc	-0.32%/°C
Maximum power current-Imp(A)	8.79A	Temperature Coefficient of Isc	0.05%°C
Open Circuit Voltage-Voc(V)	37.9V	Temperature Coefficient of Pmax	-0.39%/°C
Short Circuit Current-Isc(A)	9.76A	Operational Temperature	-40~+85°C

2.4 *Polycrystalline solar panel*

The thermal and electrical characteristics of this panel are shown in Table 1.

Summary of the solar panel's electrical and thermal characteristics:

Electrical characteristics:

- The maximum control power (Pmax) is 270 W, the highest output of the panel.
- The maximum control voltage (Vmp) is 30.7 volts, designed for optimal performance.
- The maximum control current (Pixie) is 8.79 amps when operating at full power.
- The maximum open-circuit voltage (Voc) is 37.9 volts, the maximum voltage when no charge is present.
- The short-circuit current (Isc) is 9.76 amps when the circuit is fully connected.

Thermal characteristics:

Apparent operating temperature (NOCT): 45°C ± 2°C, representing the panel's temperature under normal conditions.

Thermal voltage coefficient (Voc): indicating a decrease in voltage with increasing temperature. Efficiency decreases by 0.32% at a temperature of 25°C.

The thermal voltage coefficient (Isc) is 0.05%/°C, indicating a decrease in current with temperature. The Pmax temperature coefficient is -0.39%/°C, demonstrating a decrease in control as the temperature increases. The operating temperature range is between -40 and +85°C, demonstrating the board's ability to withstand harsh conditions. Performance Testing: Efficiency is negatively affected by temperature. The board is designed for medium-performance systems that can withstand harsh operating conditions.

2.5 *Mathematical equations used*

2.5.1 *Calculating the electrical power output of a solar panel (P)*

$$P = V \times I \tag{1}$$

P: Electrical power output (Watts).V: Electrical voltage (Volts). I: Electrical current (Amperes).

$$P_{actual} = P_{stc} \times \left(\frac{G}{1000}\right) \times [1 - \gamma \times (T - 25)] \tag{2}$$

$\mathbf{P_{actual}}$: Actual power produced by the solar panel (watts).$\mathbf{P_{stc}}$: Rated power under standard test conditions (STC), typically at 1000 W/m^2 irradiance and 25°C.$\mathbf{G}$: Solar irradiance incident on the solar panel (W/m^2). γ: Temperature effect coefficient on power, a constant that determines the change in performance per degree of temperature increase (usually a negative value).$\mathbf{T}$: Actual solar panel temperature (°C).**25**: Standard temperature under standard test conditions (°C).

This equation is important because it takes into account the true impact of natural conditions on the solar panel, which makes a difference in design optimization and performance prediction in many situations (Pervez *et al*.,2023).

2.5.2 *The effect of temperature on efficiency*

Efficiency is affected by temperature according to the following equation:

$$\eta = \eta_{STC} \times (1 - \beta \times (T - T_{STC}) \tag{3}$$

Where:

$\eta_{\mathbf{STC}}$: Efficiency at Standard Test Conditions. β: Temperature effect coefficient on efficiency (%/°C).$\boldsymbol{T}$: Solar panel operating temperature (°C).$\boldsymbol{T_{STC}}$: Standard temperature (typically 25°C).

2.5.3 *Calculating the current and voltage generated by the panel*

The resulting current depends on solar radiation:

$$I = I_{sc} \times \frac{G}{G_{stc}} \tag{4}$$

The output voltage is affected by temperature:

$$V = V_{oc} \times (1 - \gamma \times (T - T_{STC}) \tag{5}$$

Where:

$\mathbf{I_{SC}}$: Maximum current at standard conditions.$\mathbf{G_{stc}}$: Irradiance at standard conditions.$\mathbf{V_{OC}}$: Open-circuit voltage at standard conditions. γ: Temperature coefficient on voltage (%/°C).

2.6 Tests

To comprehensively evaluate the performance and effectiveness of the heat-reflective coated panel, we conducted tests that included thermal aspects.

2.6.1 Surface temperature measurement

Thermal sensors are used to monitor the temperature of the coated panel compared to the uncoated panel. Figure 2(a) shows the apparatus used to measure air temperature using an HTC-1 thermo-hygrometer conforming to ASTM E1251 standard (Immanuel & Panigrahi,2015). Figure 2(b) shows the irradiance value measured using a Fluke 572-2 infrared thermometer conforming to ASTM E220 (Dillingh *et al*.,2021). The researchers conducted the measurement on March 17, 2025. The measurement period lasted 8 hours, from 11:00 a.m. to 6:00 p.m. This study aimed to investigate the effect of exposure time on the efficiency of the coated solar panel. A Fluke FLK-IRR1-SOL solar radiometer was used to measure the solar radiation. The device was connected to a precision sensor conforming to ASTM E892 (Gueymard *et al*.,2002). Figure 3 illustrates the device used for the measurement. The temperature was measured on the sun-exposed side and the unexposed back side. The measurement results for both panels are shown in Figure 4.

The HT M70 is used to measure various electrical variables, such as DC and AC voltage, frequency, resistance, and solar radiation, making it suitable for electrical engineers and professionals in the fields of solar energy and electrical systems.

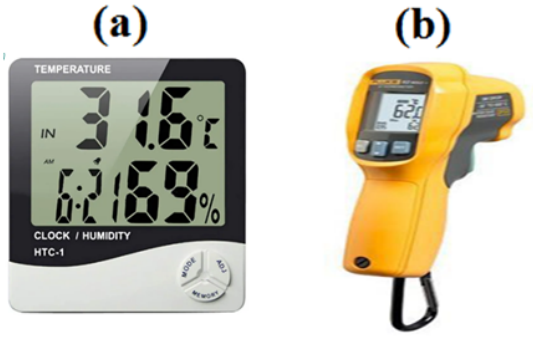

Figure 2.(a) digital thermometer, (b) infrared thermometer.

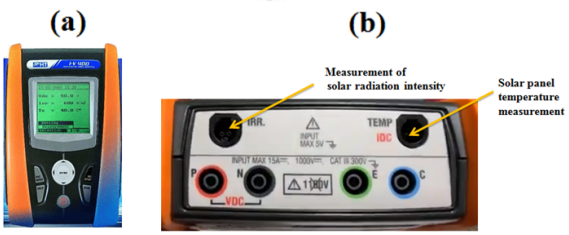

Figure 3. Solar panel-connected solar radiation meter.

Figure 4(a) shows the temperature difference between the coated panel's ambient and front and back surfaces. Figure 4(b) shows the temperature difference between the uncoated panel's ambient and front and back surfaces. Figure 5 represents the change in solar radiation value during the experiment. The initial analysis shows that the amount of solar radiation is low at the beginning of the day and then increases with the increase in temperature until it reaches its peak at 14:00 PM. Then it decreases.

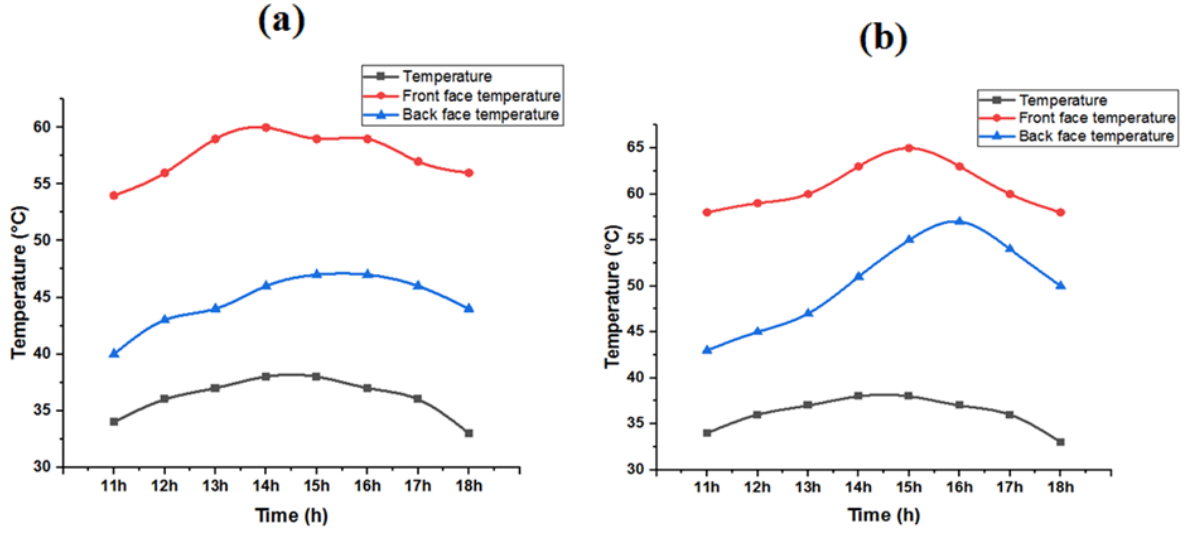

Figure 4. (a) Coated solar panel, (b) Uncoated solar panel.

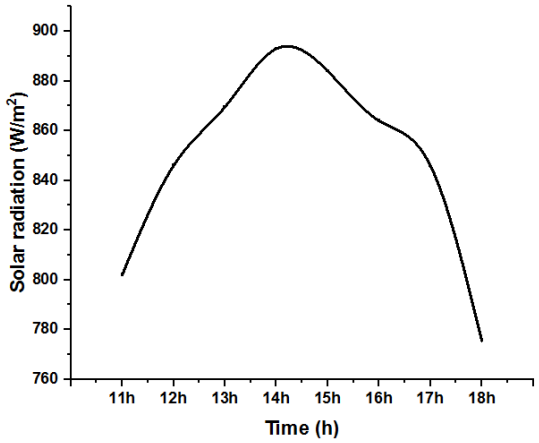

Figure 5. Change in solar radiation value during the experiment.

Meters play a pivotal role in evaluating the performance of photovoltaic cells. These devices help determine solar radiation levels and quantify solar energy changes, enabling researchers to evaluate cell performance under various conditions. Measuring cell temperature also enables us to monitor the effects of thermal energy on efficiency, as high temperatures lead to lower voltage and conversion yield. Measuring current and voltage also contributes to analyzing the electrical performance curve, enabling us to determine optimal operating points. These devices provide accurate data that can be used to analyze energy loss due to shade, dust, or weather changes, contributing to the development of plans and improved maintenance.

Analyzing the two figures,(Figure 4(a),4(b)) the effect of the coating can be seen by comparing the temperatures recorded for the coated panel with those of the uncoated panel. A closer examination follows:

2.6.2 Coated panel

The difference between the ambient and front surface temperatures ranged from 20 to 27 degrees, while the temperature between the front and back surfaces ranged from 11 to 15 degrees.

2.6.3 Uncoated panel

The difference between the ambient and front surface temperatures ranged from 6 to 17 degrees, while the temperature between the front and back surfaces ranged from 6 to 14 degrees.

For example, at 2:00 PM, the coated panel recorded a front temperature of 59°C, compared to 65°C .for the uncoated panel, representing a discrepancy of 6 degrees Celsius. At most hours, the difference between the two panels is approximately 1 to 6 degrees on the front side, with the uncoated panel tending to record higher temperatures as solar radiation increases. However, the difference on the back surface ranges from 2 to 10 degrees. From this, the coating reduces heat exchange from the front to the back surface, as the coating maintains lower temperatures than the uncoated panel. This is consistent with previous research examining the effect of coatings on reducing heat transfer (Mozumder *et al*.,2019),(Sharma & Chandra,2025),(Atkinson *et al*.,2015).

Reflective coatings play a vital role through their high reflectivity toward the sun, reducing the total radiation the panel absorbs the panel absorbs (Alshammari *et al*.,2024). When a large amount of incident radiation is reflected, the thermal mass on the front surface decreases, thus reducing the total heat exchanged to the back surface through thermal conduction(Alshammari *et al*.,2024). This effect is most pronounced during peak heat hours (such as 3:00 PM - 4:00 PM) when solar radiation is high, leading to greater temperature differences.

2.6.4 Thermal productivity

Using coatings on solar panels, or even in building materials, contributes to lower surface temperatures, significantly impacting operational efficiency and component life (Fang *et al*.,2024). Lower temperatures reduce thermal stress, which can lead to fabric damage over time. Reference data show that reflective coatings positively reduce the temperatures of solar panels' front and back surfaces compared to uncoated panels. The higher the solar radiation level, the greater the differences between panels, confirming that reflecting more radiation reduces heat absorption and transfer within the panel. This effect makes smart coatings a preferred option for improving thermal performance and preventing overheating, which can affect the efficiency of panels and materials used in engineering and energy applications (Balal *et al*.,2024). We are conducting further experiments to understand the effects of temperature, radiation, and panel productivity.

Tests will be conducted on March 19, 20, and 21, 2025. A study was conducted at the Materials Research Facility at the University of Ghardaia, southern Algeria, to test the performance of two polycrystalline solar panels. The first panel was unmodified, while the second panel was coated with a 390-nanometer layer of this coating within the concentrated spectral range and left to dry for 72 hours. Figure 6 shows the temperature changes in the external medium. Both panels were exposed to direct sunlight. Solar radiation and temperature were recorded at the test site from 9 a.m. to 6 p.m. throughout the three days. The power of both panels was also measured during the study. Figures 7 and 8 illustrate the power changes for both panels. Table 2 represents the change in solar radiation value during the experimental days.

Table 2. Change in solar radiation value during the experimental days.

Time (h)	March 19, 2025	March 20, 2025	March 21, 2025
	Solar radiation (W/m^2)		
9h	723,85	653,8	677,15
10h	747,2	677,15	700,5
11h	793,9	723,85	770,55
12h	863,95	770,55	840,6
13h	910,65	793,9	887,3
14h	957,35	863,95	980,7
15h	934	910,65	957,35
16h	910,65	863,95	934
17h	887,3	840,6	863,95
18h	840,6	817,25	793,9

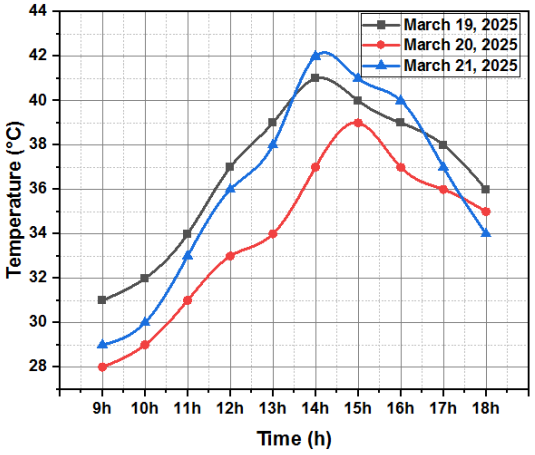

Figure 6. Temperature changes in the external environment.

Table 2 represents the variation in solar radiation throughout the experiment. It is noted that radiation increases throughout the day from 11 AM to 2 PM, reaching its highest levels between 1 PM and 2 PM. Radiation steadily declines from 2 PM to 6 PM, with values declining completely with sunset.

Examining the daily peak radiation, we find that the peak occurs between 1 PM and 3 PM when the temperature is at its highest. For example, on March 21, the radiation reaches 980.7 W/m^2 at 2 PM, the highest recorded estimate.

Some variations can be observed between days, with radiation being higher on March 21 than on the 19th and 20th. This is related to climatic conditions and the sun's altitude. Despite the slight variations, the prevailing solar radiation curve follows the same behavior: it rises in the morning, peaks in the evening, and gradually decreases until evening. This information can be used to evaluate the performance of solar systems during these periods. For example, the best time to take measurements is between 12:00 and 3:00 PM, when the radiation concentration is at its highest.

Figure 6 represents the change in air temperature during the experiments. Temperatures typically start low in the early morning and rise steadily due to increased solar radiation from 12 noon to 3 PM: Solar radiation peaks, accompanied by the highest temperatures of the day. The post-peak period is from 3 PM to 6 PM when temperatures slowly decline as solar radiation decreases. From 6 PM to nightfall: Temperatures drop primarily due to the loss of radiant heat from the ground and the lack of a consistent heating source such as daylight.

On March 19, temperatures ranged between 31°C and 41°C, while on March 20, temperatures ranged between 28°C and 39°C. On March 21, temperatures ranged between 29°C and 42°C, making this the hottest day of the experiments.

2.7 *The effect of solar radiation and temperature on the power decrease of a polycrystalline panel (270W)*

2.7.1 *Solar radiation*

Radiation is the primary energy source, with the amount of power generated increasing with increasing radiance (for example, on the 21st, at 2:00 p.m., the radiance was 980 W/m^2, with a power of 256.48 W). When the radiance value decreases (for example, on the 20th, at 9:00 a.m., the power was 653.8W/m^2, with a power of 183.77W), A decrease in energy production is observed due to a decrease in solar radiation value. These results are consistent with previous studies that examined the effect of solar radiation on the ability to control panel power (Kurpaska *et al.*, 2018),(Chikate *et al.*, 2015).

2.7.2 *Temperature*

Temperature negatively affects the efficiency of solar panels. According to the criteria specified in Table 1, the efficiency decreases by approximately 0.32% for each degree Celsius above 25°C. This is typically observed on the 21st, at 2:00 p.m., with a temperature of 42°C (17 degrees larger). The decrease in productivity was between 5.1% and 8.5%, and the power loss was between 13.77W and 22.95W.We can conclude that high temperature affects the efficiency of the solar

panel.This is consistent with previous research in this field (Abdel-Aziz *et al*., 2025),(Libra *et al*., 2021).

2.7.3 Comparison of energy yield with maximum power (270 W)

During periods of high irradiance (980.7W/m^2) and high temperatures (42°C), the efficiency reaches 95% of the maximum power (256.48/270) W. During periods of low irradiance (653.8W/m^2) and moderate temperatures (28°C), energy yield drops to 68% (183.77W/270 W), underscoring the dominance of radiation and temperature in controlling energy production (Hasan *et al*.,2022),(Mohammad & Mahjabeen, 2025). Solar radiation is a determining factor in the total energy output, while high temperatures cause a slight decrease in yield (3-9% depending on conditions). To improve yield, optimizing the placement of panels to absorb maximum radiation and providing the necessary ventilation to reduce the heat impact is recommended.

3 Discussion and analysis

Figures 7 and 8 show the changes in the energy yield of the two solar panels(normal and coated)over the three test days.

Figure 7 shows the changes in the energy yield of the uncoated polycrystalline solar panel. On March 19, 2025, the temperature changed from 31°C to 41°C, and the solar irradiance ranged between 724 W/m^2 and 957 W/m^2. The panel's energy yield decreased between 6.5% and 29%, with the power output starting at 191.47 W and reaching a maximum of 252 W.

During the morning, the efficiency decreases (191.47W at 9:00 a.m.) due to the decreasing sun angle and solar irradiance.

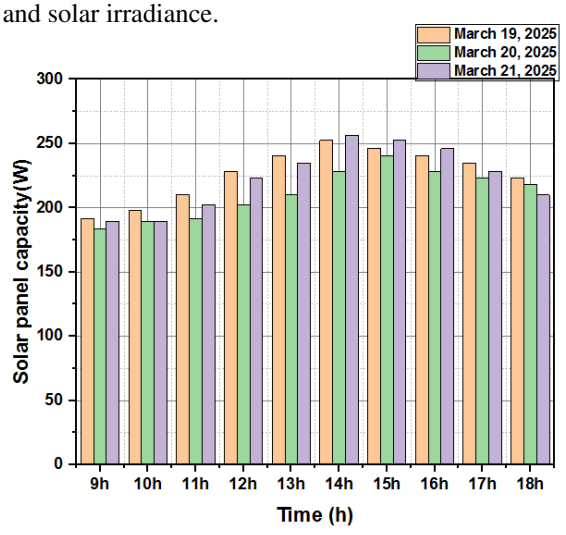

Figure 7. Change in the energy production value of the coated solar panel.

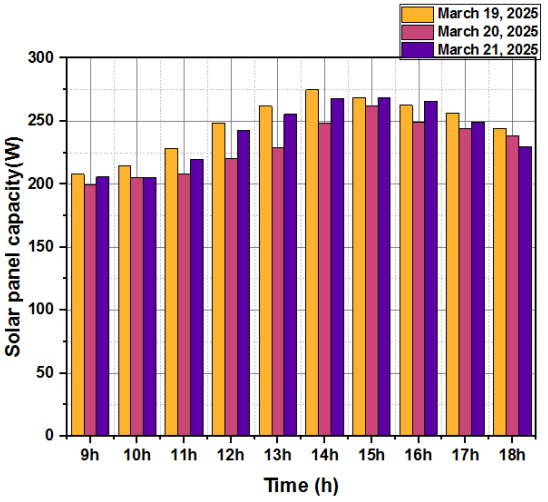

Figure 8. Change in energy production value of uncoated solar panel.

As the day progresses, the output gradually increases, reaching its peak at noon12:00 p.m. (252W at 2 p.m.), when the sun is high in the sky, and the irradiance is at its highest. After that, performance gradually declines (246W at 3:00 p.m. and 223.28W at 6:00 p.m.) due to the decreasing sun angle and the effect of shadows.

On March 20, 2025, the temperature changed from 28°C to 39°C, and solar radiation ranged between 653W/m^2 and 911W/m^2. The decrease in panel power ranged between 11% and 32%, with power output starting at 183W and reaching a peak of 241W.

The same pattern was observed: the lowest panel power output was at 9:00 a.m. (183W), peaking at 3:00 p.m. (241W) and then declining at 6:00 p.m. (218W).

On March 21, 2025, the temperature changed from 29°C to 42°C, and solar radiation ranged between 677W/m^2 and 980W/m^2. The decrease in panel power ranged between 5% and 30%, with power output ranging from 189 watts to a peak of 256 watts.

Figure 8 represents the change in power output of a coated polycrystalline solar panel.

On March 19, 2025, the temperature changed from 31°C to 41°C, and the solar radiation ranged between 724W/m^2 and 957 W/m^2. The decrease in panel power ranged between 0.6% and 23%, with power output starting at 207W and reaching a peak of 268 W.

On March 20, 2025, the temperature changed from 28°C to 39°C, and the solar radiation ranged between 653 W and 911 W/m^2. The panel power decreased between 2.9% and 26%, with power output starting at 199W and reaching a peak of 262W.

On March 21, 2025, the temperature changed from 29°C to 42°C, and the solar radiation ranged between 677 W/m^2 and 980 W/m^2. The panel power decreased between 0.7% and 24%, with power output starting at 206W and reaching a peak of 268W.

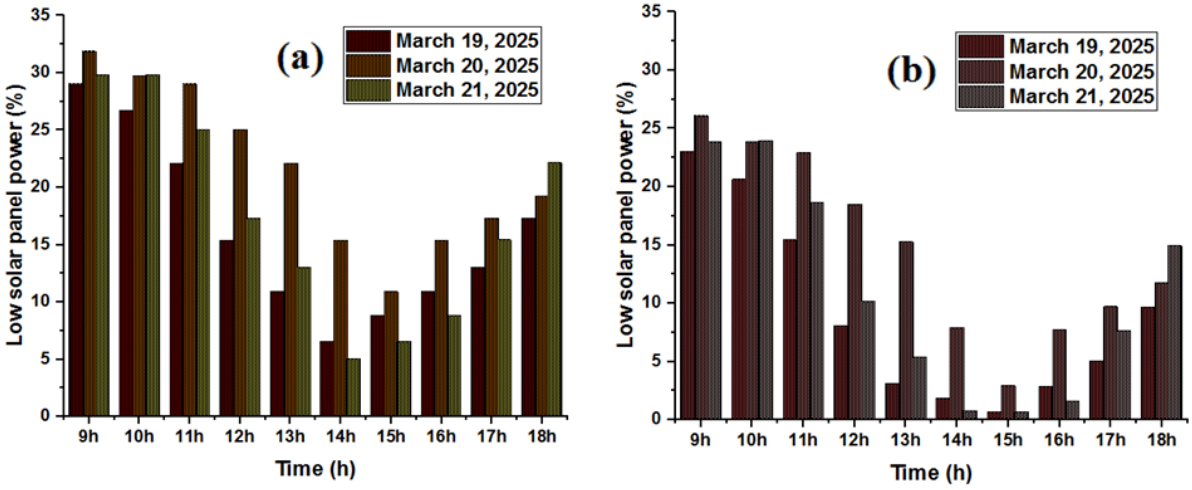

Figure 9. Energy loss in solar panels.

3.1 Energy loss in solar panels

Analyzing Figure 9(a), which shows the power loss on the uncoated panel during the test days, it is noted that the power loss rate is greatest during the early morning hours. For example, at 9:00 a.m., a 29% decrease is observed on March 19, 31% on March 20, and 29.8% on March 21. This is typically explained by the lower solar radiation at sunrise. Over time, the power loss decreases with increased power generation until the peak hours between 2 p.m. and 3:00 p.m. Then, a rise in power loss is observed until sunset. On March 19, power generation on the uncoated panel started at 71% at 9:00 a.m., then increased to 93.5% at 2:00 p.m. The power loss increased from 6.5% to 29%, then decreased to 82.3%, a decrease of 17.7%. On March 20, the power loss increased from 6.5% to 29%, then decreased to 82.3%, a decrease of 17.7%. The productivity drop ranged from 32% to 11% between 9:00 a.m. and 2:00 p.m., then increased from 11% to 17.3%. On March 21, the same situation recurred, with the solar panel's efficiency ranging from 70% to 95%, with an average power loss of 5% to 30%. A change in productivity was observed after 2:00 p.m. Analyzing Figure 9(b), which represents the power loss within the reflective-coated panel during the test days, it is noted that the power loss rate is higher during the morning hours due to the lower solar radiation. In the experiment on March 19, power generation within the coated panel started at 77% at 9:00 a.m. and then increased to 99.4% at 2:00 p.m. The power loss ranged from 0.6% to 23%. In the experiment on March 20, the power loss ranged between 2.8% and 26% between 9:00 a.m. and 2:00 p.m., then increased from 7.7% to 11%. In the experiment on March 21, the same pattern was observed, with solar panel efficiency ranging between 76% and 99.4%, with power loss ranging from 0.6% to 24%. A change in efficiency was observed after 2:00 PM.

Coated panels have lower output loss than uncoated panels. At all times, the efficiency loss (%) for coated panels is lower than for uncoated panels. For example, on March 19, at 12:00 p.m., the uncoated panel lost 15.40%, while the coated panel lost only 8.04%. At 3:00 p.m., the uncoated panel lost 8.81%, while the coated panel lost only 0.60%.

The highest efficiency loss values are recorded in the early afternoon (9:00 a.m. to 2:00 p.m.) for both types, but the difference between them is clear. In the morning (9:00 a.m. to 11:00 a.m.), the uncoated panel loses approximately 22–29%, while the coated panel loses 15–23%. The values for both types decrease during the evening (1 p.m. to 6 p.m.), but the coated panel maintains its superiority. From this, it can be concluded that smart coatings reduce sunlight reflection from the panel surface, increasing solar energy retention and improving efficiency (Thongsuwan *et al*.,2022),(Alhodaib *et al*.,2024).

Furthermore, the materials used in the coatings help retain heat more effectively, reducing energy loss and providing additional protection against moisture or corrosion, maintaining panel performance over time (Oni *et al*., 2024), Smart coatings transfer heat evenly across the panel surface, reducing heat concentrations that lead to efficiency loss (Elnozahy *et al*., 2024).

3.2 The relationship between temperature, irradiance, and solar energy generation

3.2.1 Effect of solar irradiance

It is observed that the higher the sun's brightness, the more energy is produced, and this is reflected in increased solar energy generation up to the peak. For example, March 21st saw the highest irradiance (980 W/m^2), which was expected to increase energy generation. However, high temperatures (up to 42°C) negatively impacted conversion efficiency, keeping solar energy generation at 268 watts.

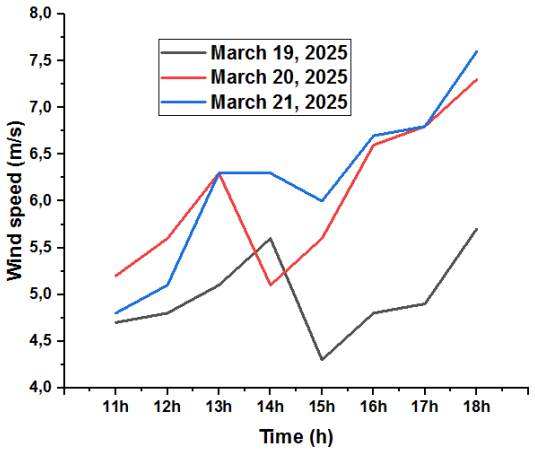

Figure 10. Wind speed change during testing.

3.2.2 *Variation in solar energy generation*

Compared to the uncoated panel, the coated panel produced approximately 15W-22 W more energy, or 5% to 7.4%, despite the variation in irradiance and temperature over the three days. The effects of temperature and irradiance were observed to be different on each day; increased irradiance pushed production to the higher end, while high temperatures negatively impacted efficiency. The coated panel achieved record output (268 W on March 19 and 21, with a slight decrease on the 20th).

Figure 10 represents the variation in wind speed during the three-day experiment.

It is noted that wind speed did not significantly affect the output of the two panels, as the speed generally ranged between 4 m/s and 8 m/s.The nature of the hot region explains this.

3.2.3 *Variation of decrease rates*

The lowest decrease rate (0.6%- 0.7%) reflects ideal conditions in terms of radiation point and energy use without significant thermal impact, while the highest rate (23%- 26%) shows periods when increasing temperature or other factors (such as partial shade or changes in surface point) could significantly decrease energy conversion output.

3.2.4 *Notes on overall performance*

Despite the variability of daily conditions, the ability of the coated panel to achieve maximum output remains constant.

- Increased irradiance leads to increased output. - On March 21 at 2:00 p.m., the solar irradiance was 980.7 W/m^2, resulting in a power output of 268W (99.2% of maximum power) for the coated panel.

This is typically 9% higher than for the uncoated panel. - Compared to the uncoated panel, an improvement in efficiency (from 95% to 99%) was observed, which may reflect improvements in operating conditions or panel quality. Decreased irradiance reduces power output: On March 20 at 9:00 a.m., the solar irradiance was 653.8 W/m^2, resulting in a power output of 199.39 W (73.8% of maximum power).

3.2.5 *Effect of temperature on efficiency*

The panel efficiency decrease ranged between 5.1% and 8.5%, with an estimated power loss ranging from 13.77W to 22.95W. For the coated panel, at 2:00 p.m. on March 21, output increased from 256.48Wto 268.02 W(an increase of 4.5%). It is noted that solar radiation remains the most important factor in output, as its increase is closely related to the increase in generated power. This is generally consistent with previous studies that examined the effect of solar radiation on solar panel efficiency (Akhlaghi *et al.*, 2025);(Darjay *et al.*,2025). High temperatures cause a decrease in output, but this effect is limited for both panels (3%-9%, depending on the conditions). It is noted that the coated panel provides greater power output than the uncoated panel at different times of the day.

3.3 *Explanation of the effect of heat-reflective coating*

3.3.1 *Reducing panel temperature rise*

It is well known that solar panels are negatively affected by high temperatures. High temperatures lead to a decrease in voltage and conversion efficiency due to the negative temperature coefficient. Heat-reflective coatings reflect a portion of the thermal radiation (especially in the infrared range) and trap it for some time, reducing the heating of the panel surface. As a result, the coated panel maintains a relatively low operating temperature, minimizing the impact of heat loss on photovoltaic performance.

3.3.2 *Stability of performance over time*

Over a day, and with changes in irradiance, temperature, and wind speed, the coated panel provides consistent performance, showing a positive difference from the conventional panel most of the time. This indicates that the coating technology is beneficial at high temperatures and operates in low irradiance conditions, maintaining consistent system efficiency.

3.4 *Natural factors and their combined effect*

3.4.1 *Solar radiation*

As solar irradiance increases, power output increases; however, a coated panel benefits from the radiation

while reducing the effect of rising temperatures, resulting in increased power generation.

3.4.2 Temperature

A conventional panel is subjected to greater thermal stress, decreasing efficiency. Instead, the coating reduces this effect by reducing heat absorption. This can be demonstrated in relative variations; as the temperature difference increases, the energy output remains approximately constant, demonstrating the effective portion of the coating.

4 The importance of coating materials

Coating additives significantly improve solar panel efficiency by reducing the effect of temperature rise, bringing the panel closer to achieving its maximum potential under harsh operating conditions. Our experimental results indicate that the relative variation in efficiency typically ranges between 8% and 9% over most periods, demonstrating the coating's effectiveness in maintaining consistent and extended performance under high irradiance, high temperatures, and moderate wind speeds.

5 Future development

Future research in this area includes examining the temperature coefficient and its effect on the coating. Temperature variations on the panel surface (rather than the ambient temperature) can be measured to obtain more accurate information about the coating's effect. Conversely, testing coating efficiency with different solar panel models can reveal options that may increase system performance under certain climatic conditions. The thickness and nature of coatings can also be varied because they reflect thermal radiation, reducing heat penetration into the inner layers or surface that converts light into energy. This significantly reduces the temperature of the photovoltaic cells, maintaining their efficiency, as high temperatures often lead to decreased performance. Coating thickness is important in determining the efficiency of a solar panel. The thickness in experiments is the value chosen to achieve a homogeneous band with high infrared reflection efficiency. The thinner coating may not form a consistent layer; therefore, it is believed that a thicker coating can lead to increased radiation diffusion. The type of coatings can also be varied because each layer has a specific role in radiation diffusion. Metal reflects infrared radiation while insulating layers form useful barriers that improve the reflection of unwanted spectra while maintaining light transmittance. Therefore, precisely varying the thickness and composition of these layers directly affects the efficiency of the solar panel.

6 Conclusions

This study investigated the effect of applying a heat-reflective coating to two 270W polycrystalline panels and observed improvements in the performance of the coated PV panels. Comparing the plain and coated panels, the study showed that the application of the coating reduced heat absorption, thus lowering operating temperatures. This improved the PV energy conversion efficiency, increasing by approximately 8% to 9%. With an increase in power output of 16W to 22W, this research demonstrates that the multilayer design (120nm-thick copper as an infrared smart layer, in addition to middle and outer layers of titanium dioxide/silicon dioxide and aluminum), improves the stability and performance of PV systems under changing climatic conditions. The research also highlights the importance of controlling thermal and radiative factors to balance low temperatures and essential visible light transmittance in electrical exchange. Based on the experimental results, the heat-reflective coating technology can be considered an effective tool for improving the efficiency of solar panels, opening up prospects for its application in environments with high temperatures and strong solar radiation. Furthermore, this technology serves as a foundation for creating a modern advancement to improve reliance on solar-based energy as a sustainable and successful solution to future energy challenges.

References

Abdel-Aziz, M. M., Khelifa, A., Attia, M. E. H., & Bady, M. (2025). A numerical investigation on improving the thermal efficiency of PV panels through integration with solar water collectors. Solar Energy, 287, 113259. https://doi.org/10.1016/j.solener.2024.113259

Adak, D., Bhattacharyya, R., & Barshilia, H. C. (2022). A state-of-the-art review on the multifunctional self-cleaning nanostructured coatings for PV panels, CSP mirrors and related solar devices. Renewable and Sustainable Energy Reviews, 159, 112145. https://doi.org/10.1016/j.rser.2022.112145

Adak, D., Bhattacharyya, R., & Barshilia, H. C. (2022). A state-of-the-art review on the

multifunctional self-cleaning nanostructured coatings for PV panels, CSP mirrors and related solar devices. Renewable and Sustainable Energy Reviews, 159, 112145. https://doi.org/10.1016/j.rser.2022.112145

Agyekum, E. B., PraveenKumar, S., Alwan, N. T., Velkin, V. I., & Shcheklein, S. E. (2021). Effect of dual surface cooling of solar photovoltaic panel on the efficiency of the module: experimental investigation. Heliyon, 7(9). https://doi.org/10.1016/j.heliyon.2021.e07920

Akhlaghi, M. M., Alavijeh, A. S., Hosseinalizadeh, R., Nasri, S., & Ghazinoory, S. (2025). Systematic failures in the development of photovoltaic systems: The case study of Iran's solar energy. Energy Strategy Reviews, 57, 101637. https://doi.org/10.1016/j.esr.2025.101637

Alhodaib, A., Yahya, Z., Khan, O., Equbal, A., Equbal, M. S., Parvez, M., ... & Idrisi, M. J. (2024). Sustainable coatings for green solar photovoltaic cells: performance and environmental impact of recyclable biomass digestate polymers. Scientific Reports, 14(1), 11221. https://doi.org/10.1038/s41598-024-61432-5

Alshammari, A. A., Salilih, E. M., Almatrafi, E., & Rady, M. (2024). Polymeric coatings for passive radiative cooling of PV modules in hot and humid weather: Design, optimization, and performance evaluation. Case Studies in Thermal Engineering, 57, 104341. https://doi.org/10.1016/j.csite.2024.104341

Alshammari, A., Almatrafi, E., & Rady, M. (2024). Radiative coatings for solar cell cooling: Materials, and applications. Solar Energy, 273, 112545. https://doi.org/10.1016/j.solener.2024.112545

Atkinson, C., Sansom, C. L., Almond, H. J., & Shaw, C. P. (2015). Coatings for concentrating solar systems–A review. Renewable and Sustainable Energy Reviews, 45, 113-122. https://doi.org/10.1016/j.rser.2015.01.050

Balal, A., Sheikhzadeh, G. A., & Fattahi, A. (2024). Experimental evaluation of the hybrid-bifacial cooling of a PV panel in arid weather using channel heat exchanger and impingement flow nozzles. Journal of Heat and Mass Transfer Research, 11(2), 195-210. https://doi.org/10.48369/JHMR.2024.2102

Belançon, M. P., Sandrini, M., Zanuto, V. S., & Muniz, R. F. (2023). Glassy materials for Silicon-based solar panels: Present and future. Journal of Non-Crystalline Solids, 619, 122548. https://doi.org/10.1016/j.jnoncrysol.2023.122548

Chikate, B. V., Sadawarte, Y., & Sewagram, B. D. C. O. E. (2015). The factors affecting the performance of solar cell. International Journal of Computer Applications, 1(1), 0975-8887. https://doi.org/10.5120/ijca2015905713

Dambhare, M. V., Butey, B., & Moharil, S. V. (2021, May). Solar photovoltaic technology: A review of different types of solar cells and its future trends. In Journal of Physics: Conference Series (Vol. 1913, No. 1, p. 012053). IOP Publishing. https://doi.org/10.1088/1742-6596/1913/1/012053

Darjay, S., & Agyekum, E. B. (2025). Assessment of solar energy generation potential in Western Bhutan–A case study of 12 kWp grid-tied rooftop solar photovoltaic system. International Journal of Thermofluids, 26, 101142. https://doi.org/10.1016/j.ijft.2024.101142

Deshmukh, M. K. G., Sameeroddin, M., Abdul, D., & Sattar, M. A. (2023). Renewable energy in the 21st century: A review. Materials Today: Proceedings, 80, 1756-1759. https://doi.org/10.1016/j.matpr.2023.02.161

Dias, P. R., Schmidt, L., Chang, N. L., Lunardi, M. M., Deng, R., Trigger, B., ... & Veit, H. (2022). High yield, low cost, environmentally friendly process to recycle silicon solar panels: Technical, economic and environmental feasibility assessment. Renewable and Sustainable Energy Reviews, 169, 112900. https://doi.org/10.1016/j.rser.2022.112900

Dillingh, B., Kaldal, G. S., Thorbjornsson, I., Wollenweber, J., & Vercauteren, F. (2021). Tensile testing of casing material at elevated temperatures up to 550° C. In Proceedings of the World Geothermal Congress. https://doi.org/10.5281/zenodo.5115497

El Hammoumi, A., Chtita, S., Motahhir, S., & El Ghzizal, A. (2022). Solar PV energy: From material to use, and the most commonly used techniques to maximize the power output of PV systems: A focus on solar trackers and floating solar panels. Energy Reports, 8, 11992-12010. https://doi.org/10.1016/j.egyr.2022.09.058

El-Khozondar, H. J., El-Khozondar, R. J., Al Afif, R., & Pfeifer, C. (2021). Modified solar cells with antireflection coatings. International Journal of Thermofluids, 11, 100103. https://doi.org/10.1016/j.ijft.2021.100103

Elnozahy, A., Abd-Elbary, H., & Abo-Elyousr, F. K. (2024). Efficient energy harvesting from PV Panel with reinforced hydrophilic nano-materials for eco-buildings. Energy and Built Environment, 5(3), 393-403. https://doi.org/10.1016/j.enbenv.2023.10.003

Fang, H., Zhou, L., Xu, L., Dang, S., De Wolf, S., & Gan, Q. (2024). Radiative cooling for vertical solar panels. Iscience, 27(2). https://doi.org/10.1016/j.isci.2024.109029

Gueymard, C. A., Myers, D., & Emery, K. (2002). Proposed reference irradiance spectra for solar energy systems testing. Solar energy, 73(6), 443-467. https://doi.org/10.1016/S0038-092X(02)00074-5

Hasan, K., Yousuf, S. B., Tushar, M. S. H. K., Das, B. K., Das, P., & Islam, M. S. (2022). Effects of different environmental and operational factors on the PV performance: A comprehensive review. Energy Science & Engineering, 10(2), 656-675. https://doi.org/10.1002/ese3.1043

Immanuel, R. J., & Panigrahi, S. K. (2015). Influence of cryorolling on microstructure and mechanical properties of a cast hypoeutectic Al–Si alloy. Materials Science and Engineering: A, 640, 424-435. https://doi.org/10.1016/j.msea.2015.07.079

Jathar, L. D., Ganesan, S., Awasarmol, U., Nikam, K., Shahapurkar, K., Soudagar, M. E. M., ... & Rehan, M. (2023). Comprehensive review of environmental factors influencing the performance of photovoltaic panels: Concern over emissions at various phases throughout the lifecycle. Environmental Pollution, 326, 121474. https://doi.org/10.1016/j.envpol.2023.121474

Ji, C., Liu, W., Bao, Y., Chen, X., Yang, G., Wei, B., ... & Wang, X. (2022, November). Recent applications of antireflection coatings in solar cells. In Photonics (Vol. 9, No. 12, p. 906). MDPI. https://doi.org/10.3390/photonics9120906

Kausar, A. (2018). Polymer coating technology for high performance applications: Fundamentals and advances. Journal of Macromolecular Science, Part A, 55(5), 440-448. https://doi.org/10.1080/10601325.2018.1470472

Khan, M. E., Aslam, J., & Verma, C. (Eds.). (2023). Nanocomposites-Advanced Materials for Energy and Environmental Aspects. Elsevier. https://doi.org/10.1016/B978-0-323-95177-7.00001-5

Kurpaska, S., Knaga, J., Latała, H., Sikora, J., & Tomczyk, W. (2018). Efficiency of solar radiation conversion in photovoltaic panels. In BIO web of conferences (Vol. 10, p. 02014). EDP Sciences. https://doi.org/10.1051/bioconf/20181002014

Law, A. M., Jones, L. O., & Walls, J. M. (2023). The performance and durability of Anti-reflection coatings for solar module cover glass–a review. Solar Energy, 261, 85-95. https://doi.org/10.1016/j.solener.2023.05.023

Li, G., Su, Z., Canil, L., Hughes, D., Aldamasy, M. H., Dagar, J., ... & Abate, A. (2023). Highly efficient pin perovskite solar cells that endure temperature variations. Science, 379(6630), 399-403. https://doi.org/10.1126/science.ade9877

Libra, M., Petrík, T., Poulek, V., Tyukhov, I. I., & Kouřím, P. (2021). Changes in the efficiency of photovoltaic energy conversion in temperature range with extreme limits. IEEE Journal of Photovoltaics, 11(6), 1479-1484. https://doi.org/10.1109/JPHOTOV.2021.3110540

Maka, A. O., & Alabid, J. M. (2022). Solar energy technology and its roles in sustainable development. Clean Energy, 6(3), 476-483. https://doi.org/10.1093/ce/zkac039

Mara, J., Bodnár, A. E., Trif, L., & Telegdi, J. (2023). Development of Effective Infrared Reflective Coatings. Applied Sciences, 13(23), 12903. https://doi.org/10.3390/app132312903

Mavromatakis, F., Kavoussanaki, E., Vignola, F., & Franghiadakis, Y. (2014). Measuring and estimating the temperature of photovoltaic modules. Solar Energy, 110, 656-666. https://doi.org/10.1016/j.solener.2014.10.020

McCandless, B. E., & Sites, J. R. (2011). Cadmium telluride solar cells. Handbook of photovoltaic science and engineering, 600-641. https://doi.org/10.1002/9780470974704.ch15

Mohammad, A., & Mahjabeen, F. (2025). From silicon to sunlight: exploring the evolution of solar cell materials. Authorea Preprints. https://doi.org/10.22541/au.170845011.17624504/v1

Mostafa, E. M., & Hammam, R. E. (2024). Tailored solar collector coatings: Synthesis and characterization of CuFe2O4/PANI nanocomposites. Optical Materials, 156, 115879. https://doi.org/10.1016/j.optmat.2024.115879

Mozumder, M. S., Mourad, A. H. I., Pervez, H., & Surkatti, R. (2019). Recent developments in multifunctional coatings for solar panel applications: A review. Solar Energy Materials and Solar Cells, 189, 75-102. https://doi.org/10.1016/j.solmat.2018.12.020

Murtadha, T. K., dil Hussein, A. A., Alalwany, A. A., Alrwashdeh, S. S., & Al-Falahat, A. A. M. (2022). Improving the cooling performance of photovoltaic panels by using two passes circulation of titanium dioxide nanofluid. Case Studies in Thermal Engineering, 36, 102191. https://doi.org/10.1016/j.csite.2022.102191

Nazari, M. H., Zhang, Y., Mahmoodi, A., Xu, G., Yu, J., Wu, J., & Shi, X. (2022). Nanocomposite organic coatings for corrosion protection of metals: A review of recent advances. Progress in Organic Coatings, 162, 106573. https://doi.org/10.1016/j.porgcoat.2021.106573

Nia, M., Chegaar, M., Benatallah, M. F., & Aillerie, M. (2013). Contribution to the quantification of solar radiation in Algeria. Energy Procedia, 36, 730-737. https://doi.org/10.1016/j.egypro.2013.07.085

Oni, A. M., Mohsin, A. S., Rahman, M. M., & Bhuian, M. B. H. (2024). A comprehensive evaluation of solar cell technologies, associated loss mechanisms, and efficiency enhancement strategies for photovoltaic cells. Energy Reports, 11, 3345-3366. https://doi.org/10.1016/j.egyr.2024.03.042

Pervez, I., Shi, J., Ghazzai, H., & Massoud, Y. (2023, May). NeuralPV: a neural network algorithm for PV power forecasting. In 2023 IEEE international symposium on circuits and systems (ISCAS) (pp. 1-5). IEEE. https://doi.org/10.1109/ISCAS46773.2023.10181373

Pošković, E., Franchini, F., Ferraris, L., Fracchia, E., Bidulska, J., Carosio, F., ... & Actis Grande, M. (2021). Recent advances in multi-functional coatings for soft magnetic composites. Materials, 14(22), 6844. https://doi.org/10.3390/ma14226844

Sachenko, A., Kostylyov, V., Sokolovskyi, I., & Evstigneev, M. (2019). Effect of temperature on limit photoconversion efficiency in silicon solar cells. IEEE Journal of Photovoltaics, 10(1), 63-69. https://doi.org/10.1109/JPHOTOV.2019.2949807

Santhosh, N., & Prasad, B. (2016, March). Efficiency improvement of a solar PV-panel through spectral sharing by combination of different panels. In 2016 IEEE Students' Conference on Electrical, Electronics and Computer Science (SCEECS) (pp. 1-4). IEEE. https://doi.org/10.1109/SCEECS.2016.7509316

Sarkın, A. S., Ekren, N., & Sağlam, Ş. (2020). A review of anti-reflection and self-cleaning coatings on photovoltaic panels. Solar energy, 199, 63-73. https://doi.org/10.1016/j.solener.2020.03.085

Shanmugam, N., Pugazhendhi, R., Madurai Elavarasan, R., Kasiviswanathan, P., & Das, N. (2020). Anti-reflective coating materials: A holistic review from PV perspective. Energies, 13(10), 2631. https://doi.org/10.3390/en13102631

Sharma, K. K., & Chandra, P. (2025). Selective response surface methodology for Anti Reflective Coated Nano-film filter thickness optimization in hybrid PVT system. Engineering Applications of Computational Fluid Mechanics, 19(1), 2443119. https://doi.org/10.1080/19942060.2024.2443119

Sun, C., Zou, Y., Qin, C., Zhang, B., & Wu, X. (2022). Temperature effect of photovoltaic cells: a review. Advanced Composites and Hybrid Materials, 5(4), 2675-2699. https://doi.org/10.1007/s42114-022-00567-3

Thongsuwan, W., Sroila, W., Kumpika, T., Kantarak, E., & Singjai, P. (2022). Antireflective, photocatalytic, and superhydrophilic coating prepared by facile sparking process for photovoltaic panels. Scientific Reports, 12(1), 1675. https://doi.org/10.1038/s41598-022-05704-y

Vaillon, R., Dupré, O., Cal, R. B., & Calaf, M. (2018). Pathways for mitigating thermal losses in solar photovoltaics. Scientific reports, 8(1), 13163. https://doi.org/10.1038/s41598-018-31597-x

Wette, J., Sutter, F., & Fernández-García, A. (2019). Evaluation of anti-soiling coatings for CSP reflectors under realistic outdoor conditions. Solar Energy, 191, 574-584. https://doi.org/10.1016/j.solener.2019.06.023

Winnicki, M. (2021). Advanced functional metal-ceramic and ceramic coatings deposited by low-pressure cold spraying: A review. Coatings, 11(9), 1044. https://doi.org/10.3390/coatings11091044

Xu, Y., Lin, Z., Wei, W., Hao, Y., Liu, S., Ouyang, J., & Chang, J. (2022). Recent progress of electrode

materials for flexible perovskite solar cells. Nano-Micro Letters, 14(1), 117. https://doi.org/10.1007/s40820-022-00856-y

Yu, H., Zhang, Y., Zhang, Q., Pang, W., Yan, H., & Li, G. (2020). Microstructure and thermal stability of Cu/TixSiyN/AlSiN solar selective absorbing coating. Materials, 13(4), 882. https://doi.org/10.3390/ma13040882

Vol. 24, No. 3(2025) Mat25638
Revista Mexicana de Ingeniería Química

Influence of the retardant additive on the compressive strength of concrete

Influencia del aditivo retardante en la resistencia a la compresión del hormigón

S. Vishkulli*, M. Hoxhaj, S. Vito, I. Boci
Department of Industrial Chemistry, Faculty of Natural Sciences, University of Tirana, Blv. Zogu I, 1001, Tirana, Albania

Received: July 30, 2025; Accepted: September 15, 2025

Abstract

Concrete is the most widely used construction material globally, and its performance can be tailored through the incorporation of various admixtures. Chemical additives for concrete preparation have achieved great success in recent decades. Proper use of admixtures can improve the quality and properties of concrete mixes. This experimental study investigates the effect of a retardant additive on the compressive strength of the concrete. The water and aggregates used were characterized and their accordance with standard requirements was confirmed before their use in concrete mixtures. Standard cubic specimens of 15x15x15cm were prepared in accordance with relevant specifications to achieve the desired concrete grade (C20/25). A comparative analysis was conducted using concrete samples with and without additive. Compressive strength tests were performed at 3, 7 and 28 days. The results indicate that the use of the retardant additive contributes positively to the enhancement of the compressive strength of the concrete over time.

Keywords: concrete, retardant additive, compressive strength, aggregate, PSD.

Resumen

El hormigón es el material de construcción más utilizado a nivel mundial, y su rendimiento puede ajustarse mediante la incorporación de diversos aditivos. Los aditivos químicos para la preparación del hormigón han alcanzado un gran éxito en las últimas décadas. El uso adecuado de aditivos puede mejorar la calidad y las propiedades de las mezclas de hormigón. Este estudio experimental investiga el efecto de un aditivo retardante en la resistencia a la compresión del hormigón. El agua y los agregados utilizados se caracterizaron y su conformidad con los requisitos estándar se confirmó antes de su uso en mezclas de hormigón. Se prepararon muestras cúbicas estándar de 15x15x15cm de acuerdo con las especificaciones pertinentes para lograr el grado de hormigón deseado (C20/25). Se realizó un análisis comparativo utilizando muestras de hormigón con y sin aditivo. Se realizaron pruebas de resistencia a la compresión a los 3, 7 y 28 días. Los resultados indican que el uso del aditivo retardante contribuye positivamente a la mejora de la resistencia a la compresión del hormigón a lo largo del tiempo.

Palabras clave: hormigón, aditivo retardante, resistencia a la compresión, agregado, PSD.

*Corresponding author. *E-mail*: sidorela.vishkulli@fshn.edu.al ;
https://doi.org/10.24275/rmiq/Mat25638
ISSN:1665-2738, *issn-e*: 2395-8472

1 Introduction

Currently, there is an increasing demand for building new homes, buildings and public spaces. Thus, the construction industry requires resources and raw materials to satisfy these requirements, leading to high demand for concrete, steel, glass, red brick, geopolymers, and other materials (Torres-Ochoa *et al*., 2019). Among them, concrete is the most widely used construction material in the world due to its durability and low cost (Al-Adili, 2009). It offers several advantages, including high compressive strength, long-term durability, and ease of application (Jonbi *et al*., 2022). Concrete is produced by mixing water, cement, aggregates and admixtures (Al-Adili, 2009). With the rise in building activities across both developing and developed countries, the demand for concrete continues to grow (Fayadh *et al*., 2020). The total amount of concrete used globally, by weight, is more than twice the combined usage of aluminum, steel, wood, and plastics. Consequently, the concrete industry has evolved into a massive commercial enterprise (Jawad *et al*., 2023). Concrete structures are expected to fulfill their intended functions throughout their entire service life. In this context, economic and environmental considerations play a critical role in ensuring long-term durability. Durability is a key factor not only in the design and construction of new structures but also in assessing the condition and performance of existing ones. The ability of concrete to resist chemical attack, abrasion, weathering action and other forms of deterioration is crucial throughout the service life of a structure. The materials used in its composition play a key role in determining this resistance. Among the primary components of concrete, chemical admixtures are particularly important, as they significantly influence the performance and durability of the final product (Liu *et al*., 2019).

Admixtures are additional ingredients introduced into concrete beyond the conventional wet-mixed components of water, cement and aggregate (Mohammed & Nariman, 2023). They play a vital role in enabling the production and application of high-performance, ready-mix and precast concretes (Liu *et al*., 2019). Chemical admixtures are commonly used to impart specific durability characteristics to concrete, tailoring it to meet particular performance requirements (Liu *et al*., 2019). Today, it is widely recognized that achieving concrete with specialized properties is only possible through the inclusion of carefully selected chemical additives. As a result, nearly every modern concrete production facility incorporates various admixtures into their mixes, significantly enhancing quality characteristics while also influencing the setting and hardening behavior of the concrete. Depending on the intended performance, experts typically classify concrete additives into six main categories: superplasticizers, strength accelerators (which reduce hardening time), sealants, mobility regulators, antifreeze agents and modifiers (Bekturganova & Kolesnikova, 2025). The effectiveness of a given admixture is influenced by several variables, including the type and quantity of cement, water content, mixing time, slump and ambient temperature during placement (Mohammed & Nariman, 2023). The use of admixtures arises complex relationship between the performance demands placed on modern concrete and the limitations of its basic components. As construction techniques advance and technical standards become more demanding, the need for specialized concrete formulations continues to grow – driving both research and the adoption of a wide variety of additives. Ramirez-Arreola *et al*., 2020 have studied the effect of sugar cane bagasse ash addition as partial replacement of Portland cement in the concrete recipe toward the corrosion behavior of steel reinforcement bars embedded in concrete. They concluded that the addition of 15% sugar cane bagasse ash as partial replacement of Portland cement in the concrete mix inhibes the corrosion of the steel rebar, thus prolonging the life of the concrete structure. Ungsson-Nieblas *et al*., 2023 have studied the effect of polycarboxylate-based superplasticizer with added silica sub-microspheres in Portland cement materials. They concluded that the hydration process of Portland cement modified with additives slowed down significantly and the compressive strength of the mortars for each cuing age was increased.

This study aims to investigate the effect of the Mapetard admixture on the compressive strength of concrete produced by using locally sourced aggregates.

2 Materials and methods

2.1 Materials

2.1.1 Aggregates

In this experimental work, three coarse aggregates with different particle size distributions were used, respectively 12.5-25mm, 5-12.5mm and 2-10mm. As fine aggregate was used sand with a granulometry of 0-5mm.

2.1.2 Cement

The cement used in this study was CEM II 42.5R, sourced from the Kruja-Cem factory. It was stored in a dry environment, well-protected from dampness to prevent any premature hydration and hardening.

Table 1.Technical data of the Mapetard additive used in concrete mix.

PRODUCT IDENTITY/ TECHNICAL DATA	
Consistency	Liquid
Colour	Brown
Density according to ISO 758 (g/cm^3)	1.08±0.02 at +20ºC
Main action	Retarding of initial hydration; retention of workability
Collateral action	High range water reduction and/or increased workability
Classification according to EN 934-2	Set retarding admixture
Classification according to ASTM C494	Type B
Chlorides soluble in water according to EN 480-10 (%)	<0.1 (absent according to EN 934-2)
Alkali content (Na_2O equivalent) according to EN 480-12 (%)	<3.0
pH	6.0±1.0

2.1.3 Water

The water used in this study was tap water. Prior to its use, the water was tested to ensure its suitability for concrete mixing. The water was tested in accordance with the standard BS EN 1008:2002 requirements.

2.1.4 Additive

The additive chosen for this experimental work was Mapetard, a liquid admixture used as a retardant for concrete and mortar with a plasticizing effect. In addition to its retarding effect, Mapetard helps maintain the workability of the concrete mix, making it easier to handle and place, especially during extended work periods.The technical data of the mapetard used in this experimental work are given in table 1. The product is produced from Mapei company, Milan, Italy.

2.2 Methodology

2.2.1 Grain size distribution analysis

The grain size distribution analysis for the aggregates was conducted using the sieve analysis method in accordance with the standard BS EN 933-2:1996. The sample for each aggregate was prepared according to standard BS EN 932-1:1997.

2.2.2 Density test

The density of the aggregates was tested in accordance with the standard requirements outlined in BS EN 1097-6:2013.

2.2.3 Water absorption test

The water absorption test for the aggregates was carried out in accordance with the standard BS EN 1097-6:2013.

2.2.4 Sulphate and chloride test

The tests on the sulphate and chloride content for all the aggregates used in this study were performed according to BS EN 1744-1:2009+A1:2012 standard requirements.

2.2.5 Preparation of the mixes, casting and curing

The mix design involves the calculation of the required materials to produce a specific volume of concrete. In this research, the goal was to achieve a concrete grade C20/25 using a mix proportion that ensures the desired strength and durability. Three cubes with dimensions 15x15x15cm were used to cast the concrete samples for compressive strength testing. The details of the concrete mix proportion required to achieve the desired concrete grade are shown in table 2. The concrete mix was prepared according to the standard BS EN 206-2013 +A1:2016.

After one day of casting, the concrete cubes were carefully removed from the moulds. To ensure proper curing and strength development, the cubes were then transferred to a water tank for continuous curing under water until they were ready for compressive strength testing.

Table 2. Mix design of the concrete.

Component	Unit	Amount
Cement	kg/m^3	310
Water	lt/m^3	178
Additive	kg/m^3	2.48
Aggregate 12.5-25mm	kg/m^3	663.6
Aggregate 5-12.5mm	kg/m^3	94.8
Aggregate 2-10mm	kg/m^3	189.6
Aggregate 0-5mm	kg/m^3	948
Total weight of fresh concrete	kg/m^3	2386

2.2.6 *Compressive strength testing*

The concrete cubes were cured under standard conditions, and compressive strength testing was conducted at 3, 7 and 28 days. Three cubes were tested at each curing age and the average value of the three tested cubes was taken as the final compressive strength. The tests were carried out according to the standard BS EN 12390-3.

3 Results and discussion

3.1 *Properties of water used in this experimental work*

The properties of water that was used in this experimental work are presented in table 3. The table includes key parameters such as pH, impurities and other relevant characteristics of the water that could impact the quality of concrete mix. According to the standard requirements and the obtained experimental results, the water properties fell within the acceptance range. This confirmed that the water was suitable for use in the concrete mix.

Table 3. Results of water tests used in experiments.

Parameters	Unit	Results	Standard requirements
Source		Tap water	
Color		Transparent	
Density at 19ºC	kg/l	1.0026	0.9982
Hardness ($CaCO_3$)	mg/l	2.83	
Sedimentation at 180ºC	mg/l	2.16	≤ 4
pH		7.91	≥ 4
Cl^- content	mg/l	632.3	≤1000
SO_4^{2-} content	mg/l	1212.1	≤2000
NaCl content	mg/l	62.5	≤100

3.2 *Properties of the aggregates*

The sieve analysis results for all the aggregates are shown in figure 1. All the aggregates fell within the standard requirements, indicating that their particle size distribution was in accordance with the standard grading criteria.

To create a dense concrete with the required grade, the aggregates were proportioned according to the standard using the advanced computer software ED TOP MIX from Mapei company. The software takes the upper and lower limits of the standard as input and calculates the necessary percentage for each aggregate to be included in the mix.

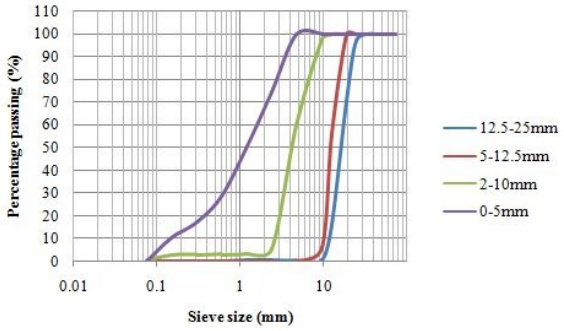

Figure 1. Particle size distribution curves for the aggregates used in this experimental work.

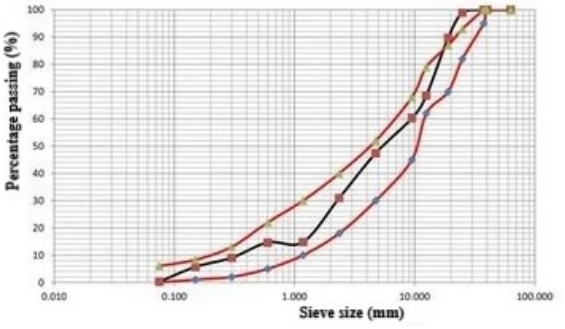

Figure 2. Gradation curve for concrete mix.

The software's recommendation led to the formulation of the concrete mix, which is presented in table 2. In figure 2, the optimal mixing combination of the aggregates is presented, as suggested by the software. In abscise are set the sieve size (mm) and in the ordinate are set the percentage passing (%) values.

The figure shows the grading curve, which is crucial for determining the proper distribution of aggregate sizes in the concrete mix. Green triangle curve represents the upper limit of the standard grading requirements, blue square curve represents the lower limit of the standard grading requirements. The black line illustrates the actual blending of aggregates that will be used in the concrete mix. This line is positioned within the bounds of the upper and lower limits, indicating that the selected aggregate blend complies with the standard grading requirements. This ensures that the aggregates are well-suited for the concrete mix, meeting the expected performance characteristics, such as strength and durability. If the black line were positioned outside the upper or lower limits, it would be a signal a potential issue with the aggregate mix. In that case, adjustments would need to be made to the proportions of the different aggregates in the blend to bring it within the acceptable range.

3.3 *Density test*

The results of the density testing for all the aggregates indicated that the aggregates fell within the standard range requirements. The standard limit for the density of aggregates is set at 3g/cm^3 and the tested aggregates

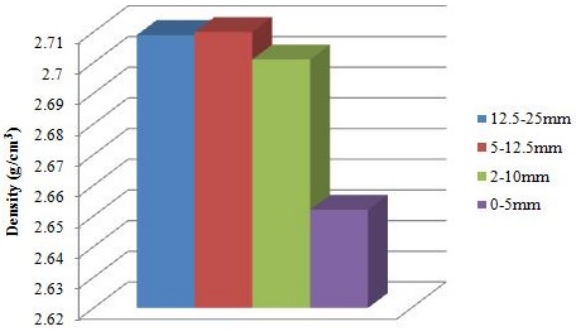

Figure 3. Density values for aggregates used in this experimental work.

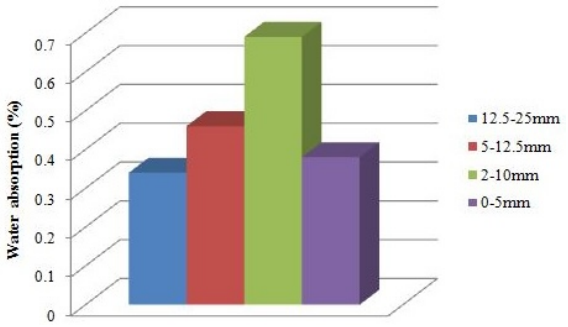

Figure 4. Water absorption values for aggregates used in this experimental work.

met this requirement. The results are presented in figure 3.

3.4 Water absorption

The results of the water absorption test for all the aggregates are presented in figure 4. The standard limit for water absorption is up to 1.5%.

The results of the water absorption tests for all the aggregates indicated that the absorption values fell within the standard limit, confirming that the aggregates were suitable for the concrete mix.

3.5 Chloride and sulphate content

The experimental results for the chloride and sulphate content of the aggregates used in this study are presented in table 4.

Table 4. Chloride and sulphate content of the aggregates.

Aggregate	Unit	Result for sulphate	Result for chloride
12.5-25mm	%	0.015	0.003
5-12.5mm	%	0.019	0.005
2-10mm	%	0.011	0.002
0-5mm	%	0.021	0.0043

The results of the chloride and sulphate content tests were in accordance with the standard requirements. According to the standard, the sulphate content should be less than 0.2% and the chloride content should be less than 0.01%. All aggregates used in this study met these standards and were therefore suitable for use in the concrete mix.

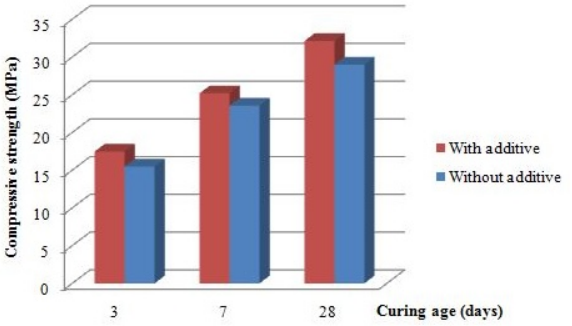

Figure 5. Compressive strength results of the concrete with and without additive.

Table 5. Results of the compressive strength in MPa, for concrete C20/25 with and without additive.

Curing age (days)	3	7	28
No additive	15.49	23.56	28.98
With additive	17.48	25.19	32.12

3.6 Compressive strength

The results of the compressive strength tests for concrete samples with and without the retardant additive are presented in figure 5 and in table 5.

In general, it was observed that the compressive strength of the concrete samples was increased with the age of curing. Additionally, the compressive strength values of the samples containing the additive were consistently higher than those without additive. This indicates that the retardant additive has a positive effect on enhancing the compressive strength of concrete over time.

Conclusions

Based on the results of this experimental study, the following conclusions can be drawn:

- The water used for concrete preparation met the standard requirements and was suitable for use.
- Both the coarse and fine aggregates fulfilled the standard requirements and were appropriate for use in concrete mixes.
- The compressive strength of the samples was increased with curing time, reaching its highest value at 28 days.
- The inclusion of the retardant additive extended the setting time of the concrete and significantly improved its compressive strength.

- Therefore, the same concrete mix, incorporating the retardant additive, can be recommended for producing more durable and workable concrete, particularly in high-temperature conditions where rapid cement hydration is a concern.

References

Akindahunsi, A. A. and Uzoegbo, H. C. (2015). Strength and durability properties of concrete with starch admixture. *International Journal of Concrete Structures and Materials*, 9, 323-335, https://doi.org/10.1007/s40069-015-0103-x

Al-Adili, A. S. (2009). Effect of different wastes additives on compression strength of concrete. *HBRC Journal*, vol.5, no.1, pp. 8-17.

Bekturganova, N. Y. and Kolesnikova, I. V. (2025). Effect of polymer additives on improvement of concrete properties. *Advances in Polymer Technology*, https://doi.org/10.1155/adv/6235216

BS EN 1008: 2002 Mixing Water for Concrete. Specification for sampling, testing and assessing the suitability of water, including water recovered from processes in the concrete industry, as mixing water for concrete.

BS EN 932-1: 1997 Tests for general properties of aggregates. Methods for sampling.

BS EN 933-2:1996 Tests for geometrical properties of aggregates. Determination of particle size distribution. Test sieves, nominal size of apertures.

BS EN 1097-6:2013 Tests for mechanical and physical properties of aggregates. Determination of particle density and water absorption.

BS EN 1744-1:2009 + A1:2012 Tests for chemical properties of aggregates. Chemical analysis.

BS EN 206:2013 +A1:2016 Concrete. Specification, performance, production and conformity.

BS EN 12390-3 Compressive strength of test specimens for testing hardened concrete.

Fayadh, O. K., Qasim, O. A., Farhan, O. S. (2020). Experimental comparative study of effect of different additive materials on concrete mix alkalinity and heat generation. *3rd International Conference on Sustainable Engineering Techniques*, 881, https://doi.org/10.1088/1757-899X/881/1/012041

Jonbi, Meutia, W., Tinumbia, N., Rafliansyah, F. (2022). Effect of using different types of additives against the compressive strength of cement paste. *Journal Infrastruktur*, 8(2):79-84

Jawad, R. K. M., Kadhim, M. J., Kamal, H. M. (2023). A review of the effect of additives on the mechanical properties of lightweight concrete. *Journal of Engineering and Sustainable Development*, vol. 27, no. 6, ISSN 2520-0917, https://doi.org/10.31272/jeasd.27.6.4

Liu, J., Yu, C., Shu, X., Ran, Q., Yang, Y. (2019). Recent advance of chemical admixtures in concrete. *Cement and Concrete Research*, vol. 124, https://doi.org/10.1016/j.cemconres.2019.105834

Mohammed, I. I. and Nariman, N. A. (2023). Natural and chemical admixtures in concrete – A review. *Eurasian Journal of Science and Engineering*, vol. 9, no. 3, 108-123, https://doi.org/10.23918/eajse.v9i3p11

Ramírez-Arreola, D. E., Aranda-García, F. J., Sedano-de la Rosa, Camacho-Vidrio A. M., Silva, R. V. (2020). Corrosion behavior of steel reinforcement bars embedded in concrete with sugar cane bagasse ash. *Revista Mexicana de Ingeniería Química*, vol. 19, sup.1, 469-481, ISSN: 1665-2738, issn-e: 2395-8472, https://doi.org/10.24275/rmiq/Mat1651

Torres-Ochoa, J. A., Osornio-Rubio, N. R., Jiménez-Islas, H., Navarrete-Bolaños, J. L., Martínez-Gonzáles, G. M. (2019). Synthesis of a geopolymer and use of response surface methodology to optimize the bond strength to red brick for improving the internal coating in burner kilns. *Revista Mexicana de Ingeniería Química*, vol. 18, No. 1, 361-373, issn-e: 2395-8472, https://doi.org/10.24275/uam/izt/dcbi/revmexingquim/2019v18n1/TorresO

Ungsson-Nieblas, M. J., Rubio-Rosas, E., Vargas-Ortíz, R. A., Bórquez-Mendivil, A., Cabrera-Covarrubias, F. G., Castro-Beltran, A., García-Grajeda, B. A., Almaral-Sánchez, J. L. (2023). Polycarboxylate-based superplasticizer with added silica sub-microspheres for use in Portland cement materials. *Revista Mexicana de Ingeniería Química*, vol. 22, No. 3, Proc2348, ISSN: 1665-2738, issn-e: 2395-8472, https://doi.org/10.24275/rmiq/Proc2348

Vol. 24, No. 3(2025) Proc25626

Revista Mexicana de Ingeniería Química

Alternative activated carbon method for recovery of gold from thiosulfate solutions

Método alternativo de carbón activado para la recuperación de oro a partir de soluciones de tiosulfato

J. Bautista-Hernández[1*], J. L. Valenzuela-García[1*], J. R. Parga-Torres[2], M. A. Encinas-Romero[1], G. Tiburcio-Munive[1], G. Martínez-Ballesteros[1]

[1]Department of Chemical Engineering and Metallurgy, Universidad de Sonora, Hermosillo, Sonora 83000, México.
[2]Department of Materials and Metallurgy, Instituto Tecnológico de Saltillo, Tecnológico Nacional de México, Saltillo, Coahuila 25280, México

Received: July 7, 2025; Accepted: September 26, 2025

Abstract

The activated carbon adsorption (CIP) process used for the gold recovery stage has proven to be highly effective and efficient in being able to recover complexes formed from cyanide leaching solutions. However, the recovery of the gold-thiosulfate complex from leaching solutions has been difficult due to the low recoveries obtained in this process; This is due to the diameter of the complex ion formed from thiosulfate solutions. The present work seeks to carry out the adsorption of the gold-thiosulfate complex; carrying out a pre-treatment to activated carbon washing (AC-PW) it with sodium cyanide and sodium thiosulfate solution to impregnate the activated carbon with the cuprocyanide complex (AC-PW-Cu) to obtain the aurocyanide complex by ion exchange, in addition to obtaining the adsorption of the gold thiosulfate complex. Evaluating the impregnation of activated carbon with cuprocyanide complex, as well as contact with the gold-thiosulfate complex, in discontinuous assays. Using concentrations of 5 to 20 mg/L of gold, 0.2 mol/L of sodium thiosulfate and 12.5 g of activated carbon, obtaining results in adsorption assays of 97 to 99% recovery, expanding the possibilities of being able to recover the gold complex formed from leaching with sodium thiosulfate.

Keywords: activated carbon, adsorption, cuprocyanide, thiosulfate, gold.

Resumen

El proceso de adsorción en carbón activado (CIP) utilizado para la etapa de recuperación de oro ha demostrado ser altamente efectivo y eficiente para poder recuperar complejos formados a partir de soluciones de lixiviación con cianuro. Sin embargo, la recuperación del complejo oro-tiosulfato a partir de soluciones de lixiviación ha sido difícil debido a las bajas recuperaciones obtenidas en este proceso. Esto se debe al diámetro del ion complejo formado a partir de soluciones de tiosulfato. El presente trabajo busca llevar a cabo la adsorción del complejo oro-tiosulfato; realizando un pretratamiento de lavado al carbón activado (AC-PW) con cianuro de sodio y solución de tiosulfato de sodio para impregnar el carbón activado con el complejo cuprocianuro (AC-PW-Cu) para obtener el complejo aurocianuro por intercambio iónico, además de obtener la adsorción del complejo de tiosulfato de oro. Evaluando la impregnación de carbón activado con el complejo de cuprocianuro, así como el contacto con el complejo oro-tiosulfato, en ensayos discontinuos. Utilizando concentraciones de 5 a 20 mg/L de oro, 0.2 mol/L de tiosulfato de sodio y 12.5 g de carbón activado, obteniendo resultados en ensayos de adsorción de 97 a 99% de recuperación, ampliando las posibilidades de poder recuperar el complejo aurífero formado a partir de la lixiviación con tiosulfato de sodio.

Palabras clave: carbón activado, adsorción, cuprocianuro, tiosulfato, oro.

*Corresponding author. *E-mail*: jose_bautistah@hotmail.com; jesusleobardo.valenzuela@unison.mx ;
https://doi.org/10.24275/rmiq/Proc25626
ISSN:1665-2738, *issn-e*: 2395-8472

1 Introduction

Sodium cyanide is widely used in the leaching of gold-containing ore. The resulting pregnant leach solution is typically subjected to gold recovery through processes such as Merrill-Crowe or carbon adsorption. However, due to environmental and regulatory restrictions, cyanide-based leaching is banned in several regions around the world. Therefore, it is growing interest in developing alternative lixiviants that not only demonstrate high gold dissolution efficiency but also offer a reduced environmental impact. Sodium thiosulfate has emerged as a promising alternative owing to its high selectivity for gold, lower affinity for base metals such as copper, and its relatively benign environmental profile (Gallagher *et al*., 1990; Marsden & House, 2006; McDougall & Copperthwaite, 1980; Young *et al*., 2012). Extensive studies have demonstrated its effectiveness even in the presence of cyanide-consuming minerals and preg-robbing carbonaceous materials (Abbruzzese *et al*., 1995; Edwards *et al*., 2013; Fleming & Nicol, 1984; Grosse *et al*., 2003).

Using thiosulfate leaching, the stability range for the gold-thiosulfate complex lies within a wide pH range of 8.5 to 10.5—much broader than that of the cyanide complex, which requires a pH of 10.5 to 11.5 for safety and efficiency. Operating below pH = 10 in cyanide systems risks the formation of toxic hydrogen cyanide gas and reduced leaching yield (Abbruzzese *et al*., 1995; Fleming *et al*., 2003; Jiang *et al*., 2022).

Activated carbon remains one of the most effective media for the recovery of gold complexes from leach solutions due to its large surface area (1,005–1,565 m^2/g), high mechanical strength, favorable adsorption kinetics, suitable particle size, and the potential for thermal reactivation (Andrade *et al*., 2018; Marsden & House, 2006; Streat et al., 1987; Zadra *et al*., 1952). The carbon adsorption process has largely supplanted the Merrill-Crowe method in the recovery of gold from low-concentration leachates (Arima *et al*., 2002; Fleming *et al*., 2003; Xia *et al*., 2022).

Desorption of gold from loaded carbon can be achieved via conventional elution techniques, typically involving elevated temperatures (>100 °C), pressures (~500 kPa), and a stripping solution containing 1.0% NaOH and 0.1% NaCN at a pH of 11–12 over a 48-hour cycle (Marsden & House, 2006). In contrast, for thiosulfate-loaded carbon, desorption requires different conditions—often involving ammonia or ammonium hydroxide combined with thiosulfate at temperatures exceeding 75 °C (Vargas *et al*., 2006). Given the potential of sodium thiosulfate as a viable alternative for cyanide in gold leaching, recent studies have explored strategies to enhance the adsorption of the gold-thiosulfate complex onto activated carbon. One effective approach involves pre-treatment or impregnation of carbon to improve its selectivity and adsorption capacity.

For instance, Young *et al*. (2012) impregnated activated carbon with potassium cuprocyanide (K_2CuCN) in alkaline media (pH = 9, using NaOH) under stirring at 300 rpm for one hour at 20 °C. By adjusting the Cu:Au molar ratio below 80%, they achieved over 99% adsorption of the gold-thiosulfate complex from a 20 mg/L solution. Similarly, Yu *et al*. (2015) impregnated activated carbon with $CuCl_2$, followed by thermal treatment at 900 °C and subsequent exposure to potassium ferrocyanide ($K_4Fe(CN)_6$) for four hours, yielding gold complex adsorption efficiencies above 98%. In another study, Hon *et al*. (2018) used silver nitrate for pre-treatment, obtaining 70% adsorption. Chen *et al*. (2020) demonstrated that nitrogen-rich activated carbon could achieve up to 95% recovery, while Escobar-Ledesma *et al*. (2020) used thioglycolic acid pretreatment, achieving 90% adsorption. Jiang *et al*. (2022) explored thiosemicarbazide-modified carbon, successfully adsorbing $Au(S_2O_3)_2^{-3}$ from thiosulfate solutions while minimizing copper interference (de la Torre-Miranda *et al*., 2023).

The present study aims to further enhance the adsorption of the gold-thiosulfate complex ($Au(S_2O_3)_2^{-3}$) by employing a novel pre-treatment method involving sequential washing of activated carbon with sodium cyanide and sodium thiosulfate, followed by impregnation with the cuprocyanide complex. The purpose is to improve the ion exchange capacity for forming the aurocyanide complex while simultaneously increasing the adsorption efficiency of the gold-thiosulfate species and reducing non-specific adsorption of the cuprocyanide complex. Batch adsorption tests were conducted to evaluate the performance of the activated carbon treated under varying concentrations of cuprocyanide during impregnation and sodium thiosulfate in the leaching solution. This study contributes to the growing body of research supporting the industrial implementation of thiosulfate-based gold leaching and recovery systems, offering an environmentally safer and technically viable alternative to cyanide.

2 Methodology

2.1 Activated carbon impregnated with cuprocyanide complex

To carry out the experimentation of the present investigation, Figure 1, commercial grade activated carbon mesh N° 6-8 was used (brand CALGON), washed with deionized water to remove all impurities and unclog pores. Laboratory grade reagents such as

sodium cyanide (Meyer) and standard copper were used to prepare the cuprocyanide complex (HYCEL), equation 1.

$$Cu(CN)_2^{-1} + C_{site} \longrightarrow Cu(CN)_{ads}^{-2} \quad (1)$$

For the experimental work, a Batch system was used, to carry out the adsorption process, synthetic solutions of cuprocyanide complex were prepared at different concentrations of cuprocyanide complex (1, 5 and 10 mg/L). Once the solutions were prepared, the activated carbon was impregnated, according to equation 1, with the cuprocyanide complex solution (AC-Cu) through mechanical stirring at 300 rpm, for 30 minutes using 12.5 g of activated carbon. Once the carbon impregnation was completed, solid-liquid separation was carried out. Afterwards, the impregnated activated carbon was put in contact with the solution of the gold-thiosulfate complex through mechanical stirring at 300 rpm for 30 minutes. Solutions of the sodium gold-thiosulfate complex were prepared by varying the concentrations of $Na_2S_2O_3$ (0.03, 0.06, 0.1 and 0.2 mol/L) and a gold concentration of 5 mg/L. The atomic absorption spectroscopy technique (PerkinElmer AAnalyst 400 AA) was used to determine the concentration of copper and gold in the solution; metallurgical balances were used to determine the concentration adsorbed on the activated carbon.

The exchange reaction is considered to occur on the surface of the activated carbon, as described by the chemical equation 2, (Young *et al*., 2012):

$$Au(S_2O_3)_2^{-3} + Cu(CN)_{ads}^{-2} \longrightarrow Au(CN)_{ads}^{-1} + Cu(S_2O_3)_2^{-3} \quad (2)$$

2.2 *Activated carbon impregnated with cuprocyanide complex and treated with sodium thiosulphate and sodium cyanide solution*

To obtain better adsorption of the gold-thiosulfate complex, 12.5 g of the activated carbon was treated with sodium thiosulfate solution 0.2 mol/L, for 30 minutes, then with sodium cyanide solution 150 mg/L, for 30 minutes. Afterwards, the activated carbon passed through the impregnation with cuprocyanide complex at 10 mg/L, using a gold-thiosulfate complex solution of 5 mg/L for 30 minutes.

2.3 *Adsorption isotherms*

The adsorption isotherm is a model that is represented with a curve, in which the experimental data are sought to fit this curve to obtain the theory that describes the adsorption phenomenon. Freundlich's Isothermal Model, Ec. 3, describes the formation of a heterogeneous multilayer surface on the surface of the adsorbent, (Foo & Hameed, 2010; Pinzón-Bedoya & Vera Villamizar, 2009; Tejada-Tovar *et al*., 2020):

$$q_e = K_F C_e^{\frac{1}{n}} \quad (3)$$

Where K_F is the Freundlich constant, n is the intensity of the adsorption, which is the adsorption capacity at equilibrium (mg/g) and Ce is the concentration at equilibrium (mg/L). Eq. 4 expresses its linear form:

$$\log q_e = \log K_F + \frac{1}{n} \log C_e \quad (4)$$

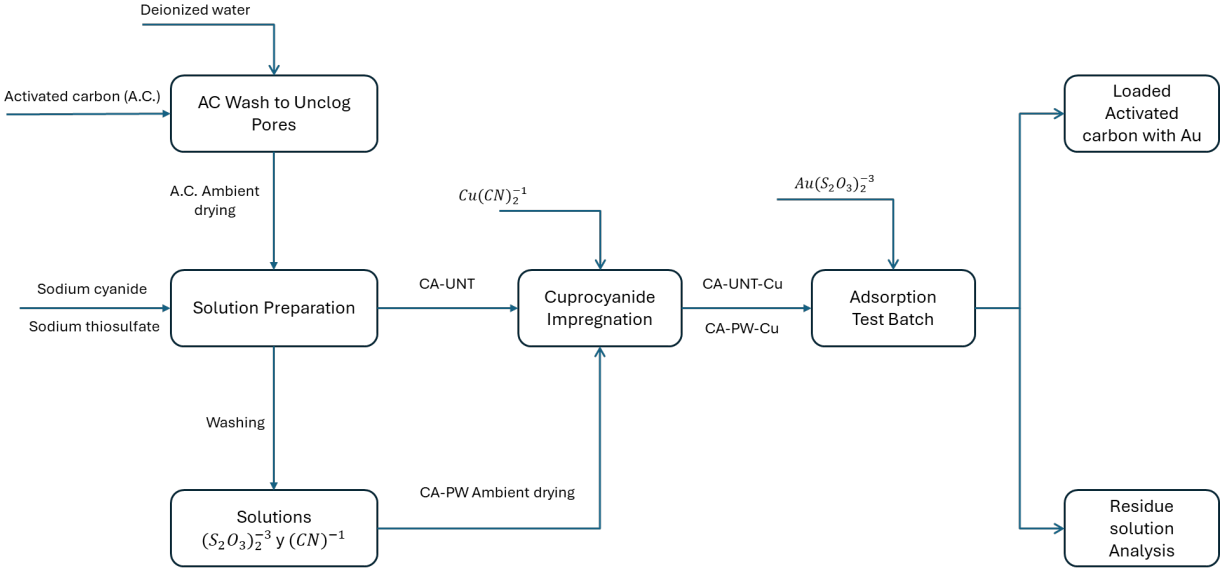

Figure 1. Flowchart for the adsorption of the thiosulfate gold complex.

The Langmuir Isotherm Model describes the formation of a homogeneous uniform layer on the surface of the solid, which is expressed:

$$q_e = \frac{Q_0 K_L C_e}{1 + K_L C_e} \tag{5}$$

Where q_e is the adsorption capacity at equilibrium (mg/g), Q_o is the maximum adsorption capacity, monolayer (mg/g), K_L is Langmuir's constant that defines the affinity of the adsorbate for the adsorbent and C_e is the concentration at equilibrium (mg/L), K_L also associated with the adsorption energy (L/mg). Its expressed linear form is as follows:

$$\frac{1}{q_e} = \frac{1}{Q_0} + \frac{1}{K_L Q_0 C_e} \tag{6}$$

Maintaining the amount of activated carbon, washing solutions, impregnation concentration, thiosulfate concentration, temperature, time and varying the gold concentrations in the adsorption batch tests, the experimental data are evaluated.

3 Results and discussion

3.1 Adsorption of the gold-thiosulfate complex without impregnating the activated carbon

Figure 2 shows the gold-thiosulfate complex adsorption in relation with the activated carbon used. It can be observed that the adsorption of the gold-thiosulfate complex is increased by having a higher quantity of activated carbon, the best adsorption was obtained with 12 g of activated carbon at 50%.

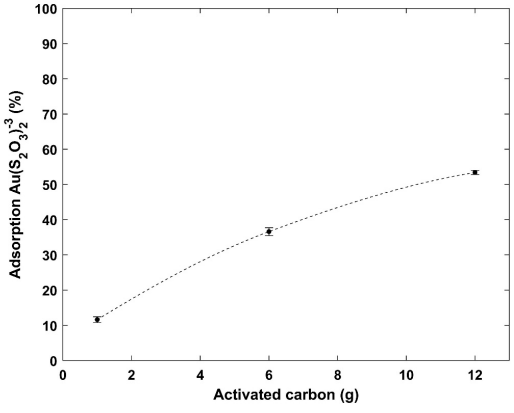

Figure 2. Adsorption of the gold-thiosulfate complex (%) in function to the untreated activated carbon without impregnating (g) at 300 rpm, [$Na_2S_2O_3$] = 0.03 M, [Au]= 5 mg/L, volume 100 mL, t=30 min., during 30 min of contact.

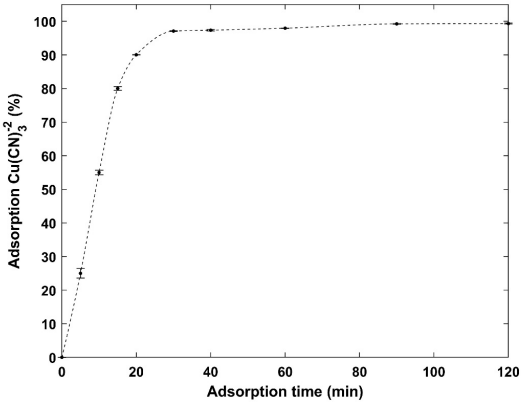

Figure 3. Adsorption of cuprocyanide complex (%) as a function of the time, in 12.5 g of activated carbon [Cu]= 10 mg/L, [CN]= 150 mg/L, volume of 100 mL and room temperature.

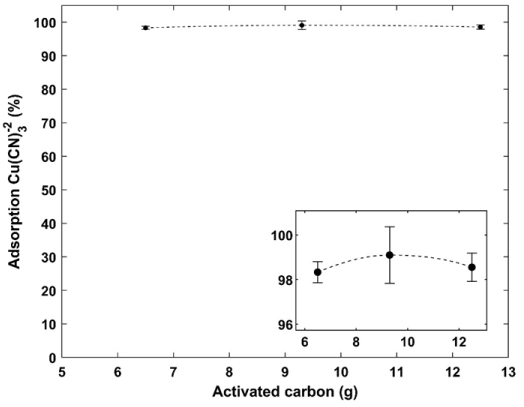

Figure 4. Adsorption of cuprocyanide complex (%) as a function of activated carbon (g), [Cu]= 10 mg/L, [CN]= 150 mg/L, 300 rpm, volume 100 mL, room temperature and t=30 min.

3.2 Cuprocyanide complex impregnation of activated carbon

To determine the contact time of the cuprocyanide complex with the activated carbon, placed in contact at different times, as shown in Figure 3, 30 minutes onwards the adsorption curve of cuprocyanide complex remains, that is, the adsorption percentage does not increase after 30 minutes.

Figure 4 shows the adsorption of cuprocyanide complex in relation to the activated carbon used during this investigation. The adsorption of the cuprocyanide complex remains above 98%.

Figure 5 shows the adsorption of the gold-thiosulfate complex as a function of the concentration of sodium thiosulfate in the leaching solution, using different concentrations of the cuprocyanide complex adsorbed during the impregnation of the activated carbon (AC-Cu). The adsorption of the gold-thiosulfate complex reached percentages above 90%

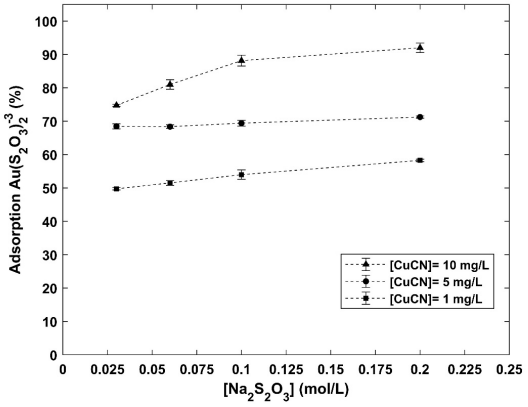

Figure 5. Adsorption of the gold-thiosulfate complex (%) as a function of sodium thiosulfate concentration (mol/L), at different concentrations of CuCN, [Au] = 5 mg/L, 12.5 g activated carbon, 300 rpm, volume of 100 mL and room temperature.

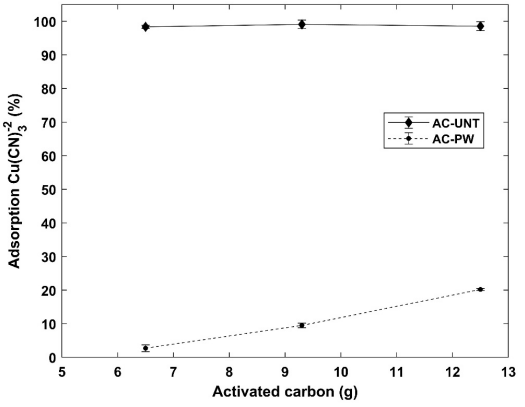

Figure 6. Cuprocyanide complex adsorption (%) with activated carbon (g) treated with $[Na_2S_2O_3]$ = 0.2 mol/L, [CN]= 150 mg/L, 300 rpm, volume 100 mL, and impregnation time = 30 minutes, with [Cu]= 10 mg/L.

when using 0.2 mol/L of sodium thiosulfate and 10 mg/L of the cuprocyanide complex to impregnate the activated carbon.

3.2.1 Sodium thiosulfate and sodium cyanide prewash activated carbon impregnation

The sodium thiosulfate and sodium cyanide were used to prewash activated carbon (AC-PW). To compare the effect of this treatment, untreated activated carbon was used (AC-UNT) and both samples were impregnated with cuprocyanide complex solutions. The cuprocyanide complex adsorption (%) in relation to the activated carbon used (g) for untreated (AC-UNT) and prewashed activated carbon (AC-PW) is shown in Figure 6, where the adsorption is greater than 98% for AC-UNT and less than 30% for AC-PW.

The adsorption of the gold-thiosulfate complex was greater than 90% when prewashed and impregnated activated carbon (AC-PW-Cu) was used. Increasing AC-PW-Cu it was obtained higher the adsorption rate. Figure 7 shows the adsorption % in relation to the AC-PW-Cu used.

3.2.2 Cu concentration reduction in the cuprocyanide complex impregnation solutions

The copper concentration does not affect the adsorption rate of the gold-thiosulfate complex. When 5 or 10 mg/L were used the adsorption was greater than 98% for both concentrations. Table 1 shows the results obtained when copper concentration varied in the impregnation solution, 12.5 g of AC-PW and a 5 mg/L gold-thiosulfate complex concentration were used.

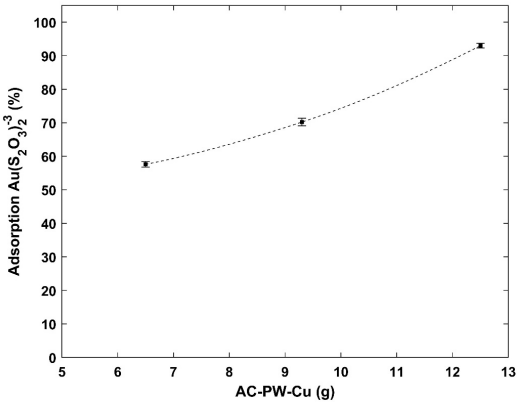

Figure 7. Adsorption of the gold-thiosulfate complex (%) as a function of activated carbon prewashed and impregnated (g) with cuprocyanide complex, $[Na_2S_2O_3]$ = 0.2 mol / L, [Au] = 5mg / L, volume of 100 mL, for 30 minutes.

Table 1. Cuprocyanide complex concentration in impregnation tests using AC-PW.

[Cu] (mg/L)	Cu_{ads} (%)	Au_{ads} (%)
0	0	60.0
5	23	99.4
10	63	99.4

The adsorption of the gold-thiosulfate complex is related to the gold concentration; the adsorption rate does not decrease significantly to the gold concentrations used in this research. The adsorption rate of washed and impregnated activated carbon (AC-PW-Cu) the gold concentration in the sodium thiosulfate was varied and shown in Figure 8.

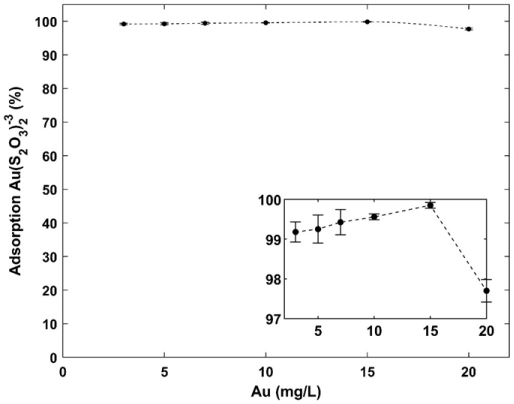

Figure 8. Adsorption of the gold-thiosulfate complex (%) with activated carbon (g) prewashed and impregnated with cuprocyanide complex, 12.5 g of activated carbon, [$Na_2S_2O_3$] = 0.2 mol / L, volume of 100 mL, t=30 min.

3.2.3 Adsorption isotherms

Applying the Freundlich and Langmuir models to the results of the tests expressed in Figure 8, the graphs are obtained in which there is a better fit to the Freundlich model compared to the Langmuir model (Figure 9). The parameters of the models are shown in Table 2. This confirms that the model that best fits the experimental data is the Freundlich isotherm model, which describes the formation of heterogeneous multilayers on the surface of the solid.

Table 2. Parameters for Langmuir and Freundlich models.

Freundlich			Langmuir		
K_F (mg/g)(dm^3/g)^n	n ads ints	R^2	Q_o mg/g	K_L L/mg	R^2
0.2171	1.7699	0.9616	0.1509	7.6848	0.9742

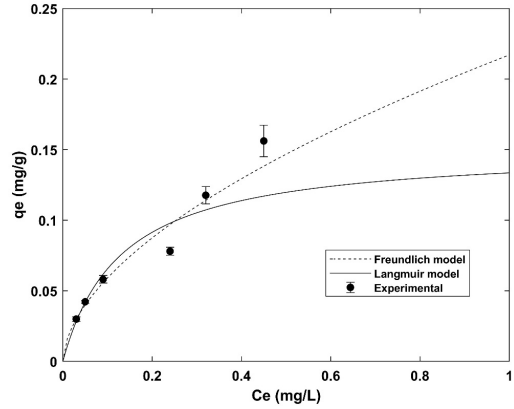

Figure 9. Isotherms models.

Conclusions

In this study, an alternative for the adsorption of gold from thiosulfate solutions was investigated. According to the type of exchange reactions in the copper-thiosulfate and aurocyanide complexes, the activated carbon must first be impregnated with cuprocyanide complex for the adsorption of the gold-thiosulfate complex.

The best conditions for the adsorption of the gold thiosulfate complex in activated carbon were obtained by impregnating the carbon with a concentration of 10 mg/L of cuprocyanide complex (AC-Cu) and 0.2 mol/L of sodium thiosulfate. Under these conditions, the adsorption of gold thiosulfate was greater than 98%. It was shown that the experimental results fit the Freundlich model, which describes that the adsorption phenomenon occurs by chemisorption, forming a chemical bond between the surface of the activated carbon and the gold-thiosulfate.

Activated charcoal treated with sodium cyanide and sodium thiosulfate prior to impregnation (AC-PW) with cuprocyanide results in less adsorption of $Cu(CN)_3^{-2}$ than the results obtained; however, it does not affect the adsorption of the gold-thiosulfate complex. Whereas activated carbon, when impregnated with a lower concentration of $Cu(CN)_3^{-2}$, has the possibility of adsorbing Au in thiosulfate solution as a aurocyanide, due to the exchange reaction that occurs between the gold-thiosulfate complex.

The use of thiosulfate in leaching, unlike cyanide, would have the advantage of storing cyanide in vessels that would provide greater safety to the environment and to personal handling.

References

Abbruzzese, C., Fornari, P., Massidda, R., Veglio, F., & Ubaldini, S. (1995). Thiosulphate leaching for gold hydrometallurgy. *Hydrometallurgy*, *39*(1-3), 265-276.

Andrade, S. N., Veloso, C. M., Fontan, R. C. I., Bonomo, R. C. F., Santos, L. S., Brito, M. J. P., & Diniz, G. A. (2018). Chemical-activated carbon from coconut (Cocos nucifera) endocarp waste and its application in the adsorption of ß-lactoglobulin protein. *Revista Mexicana de Ingeniería Química*, *17*(2), 463-475.

Arima, H., Fujita, T., & Yen, W.-T. (2002). Gold cementation from ammonium thiosulfate solution by zinc, copper and aluminium powders. *Materials transactions*, *43*(3), 485-493.

Chen, Y., Zi, F., Hu, X., Yang, P., Ma, Y., Cheng, H.,... Chen, S. (2020). The use of new modified activated carbon in thiosulfate solution: A green gold recovery technology. *Separation and Purification Technology*, *230*, 115834.

de la Torre-Miranda, N., Reilly, L., Eloy, P., Poleunis, C., & Hermans, S. (2023). Thiol functionalized activated carbon for gold thiosulfate recovery, an analysis of the interactions between gold and sulfur functions. *Carbon*, *204*, 254-267.

Edwards, I. A. S., Marsh, H., & Menendez, R. (2013). *Introduction to carbon science*. Butterworth-Heinemann. Escobar-Ledesma, F. R., Aragón-Tobar, C. F., Espinoza-Montero, P. J., & Torre-Chauvin, E. d. l. (2020). Increased Recovery of Gold Thiosulfate Alkaline Solutions by Adding Thiol Groups in the Porous Structure of Activated Carbon. *Molecules*, *25*(12), 2902.

Fleming, C. A., McMullen, J., Thomas, K. G., & Wells, J. A. (2003). Recent advances in the development of an alternative to the cyanidation process: Thiosulfate leaching and resin in pulp. *Mining, Metallurgy & Exploration*, *20*, 1-9.

Fleming, C. A., & Nicol, M. J. (1984). The absorption of gold cyanide onto activated carbon. III. Factors influencing the rate of loading and the equilibrium capacity. *Journal of the Southern African Institute of Mining and Metallurgy*, *84*(4), 85-93.

Foo, K. Y., & Hameed, B. H. (2010). Insights into the modeling of adsorption isotherm systems. *Chemical engineering journal*, *156*(1), 2-10.

Gallagher, N. P., Hendrix, J. L., Milosavljevic, E. B., Nelson, J. H., & Solujic, L. (1990). Affinity of activated carbon towards some gold (I) complexes. *Hydrometallurgy*, *25*(3), 305-316.

Grosse, A. C., Dicinoski, G. W., Shaw, M. J., & Haddad, P. R. (2003). Leaching and recovery of gold using ammoniacal thiosulfate leach liquors (a review). *Hydrometallurgy*, *69*(1-3), 1-21.

Jiang, Y., Chen, Y., Zi, F., Hu, X., Chen, S., He, P.,... Lin, Y. (2022). Making untreated carbon effective in cleaner thiosulfate system: A new and high-efficiency method including gold adsorption and desorption. *Journal of Cleaner Production*, *334*, 130185.

Marsden, J., & House, I. (2006). *The chemistry of gold extraction*. SME. McDougall, G. J. H. R. D. N. M. J. W. O. L., & Copperthwaite, R. G. (1980). The mechanism of the adsorption of gold cyanide on activated carbon. *Journal of the Southern African Institute of Mining and Metallurgy*, *80*(9), 344-356.

Pinzón-Bedoya, M. L., & Vera Villamizar, L. E. (2009). Modelamiento de la cinética de bioadsorción de Cr (III) usando cáscara de naranja. *Dyna*, *76*(160), 95-106.

Streat, M., Naden, D., & Society of Chemical, I. (1987). *Ion Exchange and Sorption Processes in Hydrometallurgy*. Wiley.

Tejada-Tovar, C., Mancilla, H. B., Moreyra, J. D. P., & Toro, R. O. (2020). Effect of the adsorbent dose in Pb (II) removal by using sugar cane bagasse: Kinetics and isotherms. *Revista Mexicana de Ingeniería Química*, *19*(3), 1413-1423.

Xia, J., Marthi, R., Twinney, J., & Ghahreman, A. (2022). A review on adsorption mechanism of gold cyanide complex onto activation carbon. *Journal of Industrial and Engineering Chemistry*.

Young, C., Gow, N., Melashvili, M., & LeVier, M. (2012). Impregnated activated carbon for gold extraction from thiosulfate solutions. *Separation Technologies for Minerals, Coal, and Earth Resources*, 391.

Yu, H., Zi, F., Hu, X., Nie, Y., Chen, Y., & Cheng, H. (2018). Adsorption of gold from thiosulfate solutions with chemically modified activated carbon. *Adsorption Science & Technology*, *36*(1-2), 408-428.

Yu, H., Zi, F., Hu, X., Nie, Y., Xiang, P., Xu, J., & Chi, H. (2015). Adsorption of the gold–thiosulfate complex ion onto cupric ferrocyanide (CuFC)-impregnated activated carbon in aqueous solutions. *Hydrometallurgy*, *154*, 111-117.

Zadra, J. B., Engel, A. L., & Heinen, H. J. (1952). *Process for recovering gold and silver from activated carbon by leaching and electrolysis* (Vol. 4843). US Department of the Interior, Bureau of Mines.

Vol. 24, No. 3(2025) Proc25627

Revista Mexicana de Ingeniería Química

Zinc solvent extraction from waste electronic card leaching solutions

Extracción de zinc por solventes a partir de soluciones de lixiviación de tarjetas electrónicas de desecho

E.G. Sustaita-Martínez[1*], J. L. Valenzuela-García[1*], G. Martínez-Ballesteros[1], B. Valdez-Salas[2], M.M. Salazar-Campoy[1], G. López-Aviles[1]

[1]Department of Chemical Engineering and Metallurgy, University of Sonora, Blvd Luis Encinas y Rosales s/n, Col. Centro, Hermosillo, Son., 83000, México.

[2]Institute of Engineering, Autonomous University of Baja California, Avenida Álvaro Obregón s/n, Nueva, 21100 Mexicali, Baja California.

Received: July 7, 2025; Accepted: October 29, 2025

Abstract

In this study, the purification of a leach solution obtained from waste electronic cards was investigated to separate zinc from base metals (Cu, Fe, and Ni) and to produce a purified $ZnSO_4$ solution through solvent extraction. A comparative evaluation was performed using Cyanex 272 and D2EHPA as extractants at 15% v/v in the organic phase, achieving zinc extraction efficiencies of 94% and 90%, respectively, at pH 3.0 and an O/A phase ratio of 1.2:1. McCabe–Thiele diagrams indicated that two theoretical extraction stages are required for Cyanex 272, whereas three stages were needed for D2EHPA. During the stripping stage, sulfuric acid (H_2SO_4) solutions at concentrations of 180 and 200 g/L were tested under varying phase ratios. Under optimal conditions, a stripping efficiency of 95% was obtained for the organic phase loaded with Cyanex 272 (O/A = 1:1), while 94% was achieved for D2EHPA under the same phase ratio.

Keywords: Zinc, Solvent Extraction, Cyanex 272, D2EHPA, Secondary Resources.

Resumen

En esta investigación, se estudió la purificación de una solución de lixiviación de tarjetas electrónicas de desecho para separar zinc de los metales base (Cu, Fe y Ni) y obtener una solución purificada de $ZnSO_4$, mediante el proceso de extracción por solventes, realizando un estudio comparativo de los extractantes Cyanex 272 y D2EHPA con una concentración al 15 % v/v en la fase orgánica, obteniendo extracciones del 94% y 90% respectivamente, a un pH 3.0 y una relación de fases ORG/AQ 1.2:1. Los diagramas de McCabe-Thiele muestran que son necesarias 2 etapas de extracción teóricas para Cyanex 272 y 3 etapas teóricas para D2EHPA. En la etapa de despojamiento se utilizó una solución de ácido sulfúrico (H_2SO_4) a una concentración de 180g/L y 200 g/L, variando las relaciones de fases, obteniendo un despojamiento arriba del 95 % para la fase orgánica con Cyanex 272, con una relación de fases de 1:1 y del 94% para la solución con D2EHPA, con una relación de fases de 1:1.

Palabras clave: Zinc, Extracción por Solventes, Cyanex 272, D2EHPA, Recursos Secundarios.

*Corresponding author. *E-mail*: a207215699@unison.mx; jesusleobardo.valenzuela@unison.mx ;
https://doi.org/10.24275/rmiq/Proc25627
ISSN:1665-2738, *issn-e*: 2395-8472

1 Introduction

Green or circular mining has experienced notable growth in its current application, focusing on the recovery and recirculation of metals of high industrial interest. The main objective is to recover strategic metals that, due to their high demand and exploitation, are currently considered critical or difficult to access. This has opened a wide range of possibilities for the recovery of these metals through secondary raw materials, such as waste electrical and electronic equipment (WEEE) (Schaeffer *et al*. 2018). This waste has been rapidly increasing worldwide (Cayumil *et al*. 2016), becoming one of the most critical pollution problems due to the fast evolution of electronic devices, which causes electronic appliances to become obsolete for users and to end up in landfills, causing adverse environmental effects (Kiddee et al. 2013). Therefore, their recovery, recycling, and reincorporation into the supply chain seeks to have a positive environmental impact and, at the same time, it aims at mitigating the environmental effects associated with the exploitation and extraction of key minerals for the industry, such as zinc, which is fundamental in processes such as galvanization and has multiple applications in sectors such as electronics, energy, and food (Zhang *et al*. 2014).

To optimize the extraction of zinc from secondary resources, metallurgical routes that offer more efficient and sustainable recovery methods, primarily from waste, continue to be explored; one example is the waste generated by the steel industry, where research has focused on the leaching of electric arc furnace dust (EAFD) (Borda & Torres, 2021; Zhu Xiao-lin, 2019). Another area for zinc recovery from waste is the recycling of printed circuit boards (PCBs), which are essential components in the operation of electrical and electronic equipment. Their polymetallic composition makes them highly valuable for recovering base, precious, or critical metals (Rao *et al*. 2020). However, the extraction process can be complex, which is why selective methodologies and/or pretreatments for the recovery of base and precious metals must be developed in order to achieve effective extractions (Martinez-Ballesteros *et al*. 2023; Segura-Bailón & Lapidus-Lavine, 2023). For this reason, the focus of this research is on obtaining a purified zinc electrolyte solution from a pressure acid leaching solution of printed circuit boards (PCBs), aiming at recovering base metals (Cu, Ni, Zn, and Fe) in the initial stage (Martinez-Ballesteros *et al*. 2024; Martinez-Ballesteros *et al*. 2023).

To obtain this purified zinc electrolyte solution, a solvent extraction process has been chosen. This is a widely studied technique for base metals such as copper, yielding favorable results due to its selectivity for metal ions of interest, in addition to being very economical. The solvent extraction process involves two phases: an aqueous phase and an organic phase. The aqueous phase is the leach solution, while the organic phase consists of an extractant with an affinity for the target metal and a modifier in a diluent, commonly kerosene. This process is attractive due to its high efficiency and low cost (Aguayo *et al*. 2007). The selection of the extractant depends on the chemical composition of the leach solution, the metals to be extracted, and the impurities present, which constitutes a real challenge in the development of liquid–liquid extraction processes. This is especially necessary for the treatment of complex minerals or secondary resources to be carried out more efficiently and economically (Chagnes & Cote, 2010; Omelchuk *et al*. 2018).

In this work, two acidic organophosphorus extractants were used, which have been extensively studied for zinc extraction (Sun *et al*. 2019) as separating zinc from other metals has become an important industrial resource. One of them is di-2ethylhexyl phosphoric acid (D2EHPA), which exhibits high selectivity for zinc due to its cation exchange mechanism (Xie *et al*., 2019). Some authors propose the saponification of D2EHPA to improve zinc extraction percentages, increasing recovery by up to 25% compared to unmodified D2EHPA (Tahmasebizadeh & Javanshir, 2021). Other researchers have also widely used bis(2,4,4-trimethypentyl) phosphinic acid (Cyanex 272) for zinc extraction due to its high selectivity (Li et al. 2016; Lupi & Pilone, 2020; Sun *et al*. 2019). Ahmadipour *et al*. studied the synergistic effects of these extractants combined for zinc recovery from other metals, obtaining favorable results (Ahmadipour et al. 2011). For this reason, the solvent extraction process, combined with a meticulous adjustment of the operational parameters, including solution pH, reagent concentration, and the aqueous-to-organic phase ratio (AQ: ORG; AQ refers to the aqueous phase, and ORG corresponds to the organic phase), was used to achieve optimal selectivity during metal extraction from leach solutions (Habashi, 2003). This is crucial because these solutions often contain metal ions with similar chemical behaviors, making the precise configuration of the operational conditions essential for efficient and selective separation (Sun *et al*. 2019).

The extraction (Eq. 1) and re-extraction (Eq. 2) reactions expected for zinc using an organophosphorus extractant are as follows, where R will be $(C_8H_{17})PO_2H$ (Cyanex 272) or $C_{16}H_{35}O_4P$ (D2EHPA).

$$ZnSO_{4(AQ)} + 2RH_{(ORG)} \longleftrightarrow ZnR_{2(ORG)} + H_2SO_{4(AQ)} \quad (1)$$

$$ZnR_{2(ORG)} + H_2SO_{4(AQ)} \longleftrightarrow ZnSO_{4(AQ)} + 2RH_{(ORG)} \quad (2)$$

2 Methodology

The solution obtained from the pressure acid leaching of waste electronic circuit boards (PCBs) was subjected to analysis and a purification process for the selective recovery of metals. To achieve this, the procedure was structured in four key stages.

2.1 Pre-treatment and initial analysis

The solution obtained from the acid leaching of electronic circuit boards to separate base metals was analyzed using an AAS instrument to determine the concentrations of Zn, Cu, Fe, and Ni (Table 1). After obtaining these data, a pretreatment was carried out. Initially, the leaching liquor was treated with magnesium oxide until it reached a pH of 4, which precipitated the iron present in the solution (Bolin & Sundkvist, 2008). This optimizes the removal of this impurity because the extractants used in this work have a high selectivity for iron (Cognis, 2008). The initial solution, with a pH of 1.30, was gradually neutralized by the addition of powdered MgO under continuous stirring to ensure uniform dispersion. The process was maintained until the pH stabilized at 4, after which the suspension was allowed to rest to promote the precipitation of solid phases. The clarified supernatant was subsequently separated and reserved for the solvent extraction experiments, while the precipitated solid was collected and stored for further characterization. Removing iron from the solution is essential. The resulting aqueous phase was analyzed by AAS, and the metal concentrations are presented in Table 1, which shows that iron was not detected.

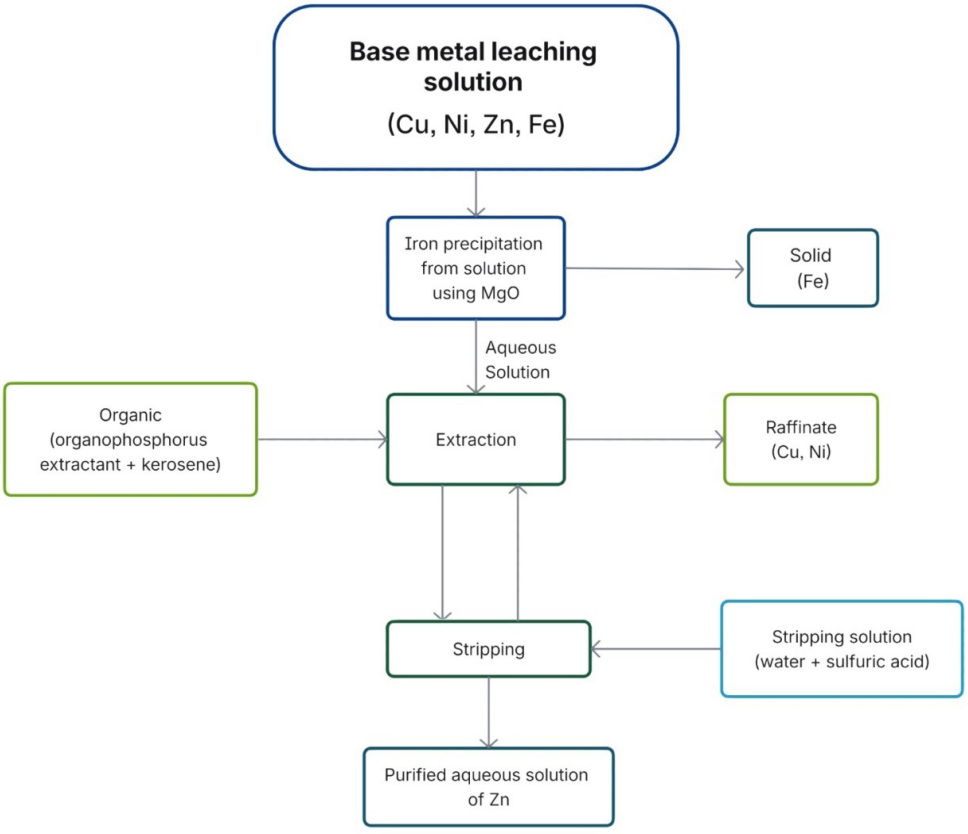

Figure 1. Experimental diagram for the solvent extraction process for a base metal leaching solution.

Table 1. Concentration of metals in solution.

Metals	Zn (mg/L)	Cu (g/L)	Ni (g/L)	Fe (g/L)
Solution before pretreatment	107.3	33.15	3.92	3.66
Solution after pretreatment	107.3	14.86	3.35	ND

Table 2. Properties characters of solvents.

Characteristic	D2EHPA	Cyanex 272	Kerosene
Molecular Formula	$C_{16}H_{35}O_4P$	$(C_8H_{17})_2PO_2H$	$C_{12}H_{26}$
Molecular Weight	322.4	290.42	170.132
Solubility in water (g/L)	<0.01	0.016	0.02
Density (g/cm^3)	0.97	0.92	0.82
Appearance	Colorless or yellowish, oily liquid	Colorless to light, amber liquid	Colorless

2.2 *Solvent extraction*

The solution obtained after iron precipitation was concentrated by applying the solvent extraction process in a 125 mL separatory funnel; the organic and aqueous phases were brought into contact and subjected to vigorous agitation to promote efficient mass transfer. The zinc concentration in the aqueous phase was analyzed to determine the optimal contact time for the process, aiming at maximizing extraction and stripping efficiency. The initial time point (t = 0) was defined as the moment when both phases were introduced into the separatory funnel, before vigorous stirring. In this funnel, the leach solution (aqueous phase) and the solvent (organic phase) were combined; the solvents used, Cyanex 272 and D2EHPA, shown in Table 2 (Ahmadipour *et al*. 2011), were added to the separatory funnel. This was followed by vigorous stirring for a fixed time of 3 minutes. Once the time had elapsed and the two phases were separated, the raffinate solution was separated from the loaded organic phase.

The experimental parameters were established as follows: the extractant concentration in the organic phase was set at 15% v/v for both extractants. The pH of the leach solution varied between 1.5, 2, 2.5, 3, and 3.5 for Cyanex 272, and between 1, 1.5, 2, 2.5, and 3 when using D2EHPA. The pH of the solution was controlled with a 1 N sodium hydroxide and 1M sulfuric acid. The AQ: ORG phase ratio varied between 0.8:1, 1:1, and 1.2:1. The concentration in the aqueous phase was determined by AAS. In contrast, the concentration in the organic phase was calculated by metallurgical balance.

The concentration of ions in the organic phase was calculated by means of a mass balance using Equation 3:

$$V_{AQ}([M]_i - [M]_f)_{AQ} = V_{ORG}([M]_f - [M]_i)_{ORG} \quad (3)$$

where V_{AQ} is the volume in the aqueous phase, V_{ORG} is the volume in the organic phase, $[M_i]_{AQ}$ represents the initial concentration of metal ions in the solution before extraction in the aqueous phase, $\left[M_f\right]_{AQ}$denotes the final concentration of metal ions after phase separation (AQ: ORG), $[M_i]_{ORG}$ represents the initial concentration of metal ions in the organic phase before extraction, and $\left[M_f\right]_{ORG}$ denotes the final concentration of metal ions after phase separation (AQ: ORG).

In Equation 3, the concentration [M] is expressed in mg/L, which is valid at any given time as well as under steady-state conditions. This mass balance was used to determine zinc concentrations in each phase during the batch experiments. Since no accumulation occurs in the system, the mass balance is also applicable under steady-state conditions. Moreover, since the system does not involve flow rates and is not continuous, this formulation is appropriate for the experimental conditions.

2.3 *Stripping*

Zinc was transferred from the loaded organic phase to the aqueous phase using sulfuric acid, with varying concentrations (180 g/L and 200 g/L). Experimentally, contact times between phases of 0.5, 1, 2, 3, 4, 5, 6, 7, and 8 minutes were tested to determine the optimal stripping time. The aqueous phase obtained was analyzed by AAS to measure the metal concentration in solution through a mass balance of the organic phase concentration (Eq. 3). The contact time for each system studied in this research was determined. The AQ: ORG phase ratio varied between 1:1, 2:1, and 5:1. This approach enabled the establishment of optimal operational parameters to maximize metal recovery during the stripping stage, ensuring the efficient transfer of metals from the organic to the aqueous phase.

2.4 *McCabe–Thiele diagram analysis*

For the generation of equilibrium isotherms, the load capacity for both organic extractants (Cyanex 272 and D2EHPA) was evaluated during the extraction and stripping stages to determine the maximum amount of zinc that can be removed from the pregnant leach solution (PLS) of PCBs in the extraction stage for each aqueous-to-organic phase ratio (AQ: ORG). The organic phase (consisting of reagent, diluent, and extracted zinc) was mixed with the PLS at various AQ: ORG phase ratios (10:1, 5:1, 2:1, 1:1, 1:2, 1:5, and 1:10) until equilibrium was reached. Each phase was then analyzed: the aqueous phase by AAS, and the organic phase concentration was

calculated by mass balance (Eq. 3) (Cytec, 2010). During the stripping stage, the maximum amount of zinc that can be recovered from the organic phase was defined by mixing it with an aqueous phase containing sulfuric acid at concentrations of 180 and 200 g/L. After the AQ: ORG phase separation, the zinc concentration in each phase was analyzed. The data obtained were plotted, and McCabe–Thiele diagrams were constructed for both extraction and stripping systems. For the extraction system, zinc concentration in the organic phase was plotted on the Y-axis and zinc concentration in the aqueous phase on the X-axis. For the stripping system, zinc concentration in the organic phase was plotted on the X-axis and zinc concentration in the aqueous phase on the Y-axis.

3 Results and discussion

3.1 *Extraction kinetics*

Figure 2 illustrates the extraction kinetics of zinc, copper, and nickel using the extractants Cyanex 272 and D2EHPA. The data demonstrate that zinc sulfate ($ZnSO_4$) extraction efficiencies exceeded 90% for both extractants, achieving peak values of 97% with Cyanex 272 and 93% with D2EHPA at a contact time of 3 minutes. This time corresponds to the attainment of the extraction equilibrium, indicating that 3 minutes was sufficient to reach the equilibrium state under the experimental conditions.

For the extraction of $CuSO_4$ and $NiSO_4$, less than 10% extraction was achieved in both cases, with the extraction efficiency stabilizing after 2 minutes when using Cyanex 272 and after 1 minute with D2 EHPA.

3.2 *Zinc extraction vs. pH*

Figure 3 compares the influence of pH on the extraction behavior of zinc, copper, and nickel using Cyanex 272 (Figure 3a) and D2EHPA (Figure 3b), both at 15% v/v with an aqueous-to-organic (AQ: ORG) phase ratio of 0.8:1. With Cyanex 272, zinc extraction reached a maximum efficiency of 98% at pH 4, while copper and nickel showed limited extraction, with maximum values of 24% and 27%, respectively, both at pH 2.

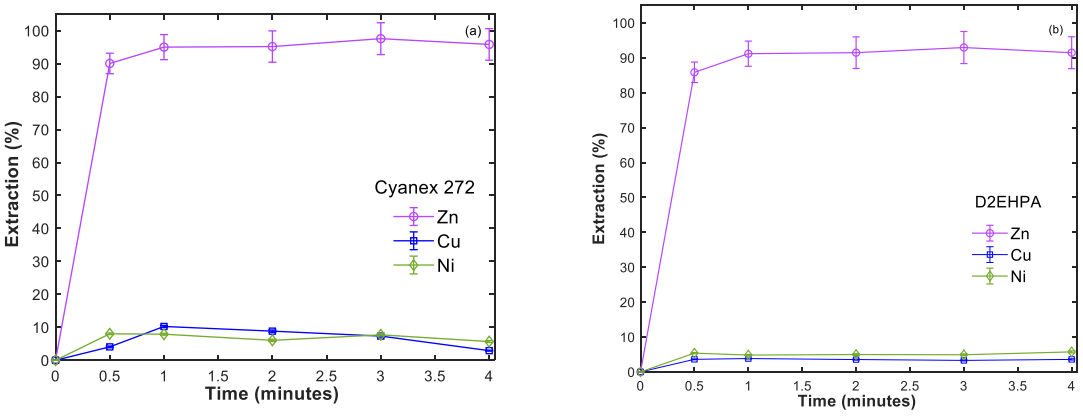

Figure 2. Extraction kinetics for zinc, copper, and nickel using (a) Cyanex 272 15% v/v AQ:ORG 1:1, pH 3; (b) D2EHPA 15% v/v AQ:ORG 1:1, pH 3.

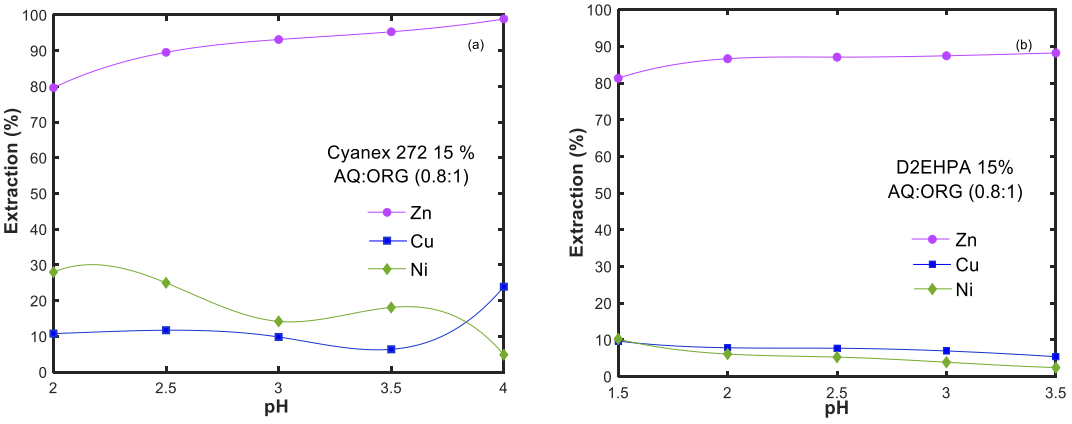

Figure 3. Zinc extraction (%) as a function of pH using (a) 15% v/v Cyanex 272 with an AQ: ORG ratio of 0.8:1 and (b) 15% v/v D2EHPA with an AQ: ORG ratio of 0.8:1.

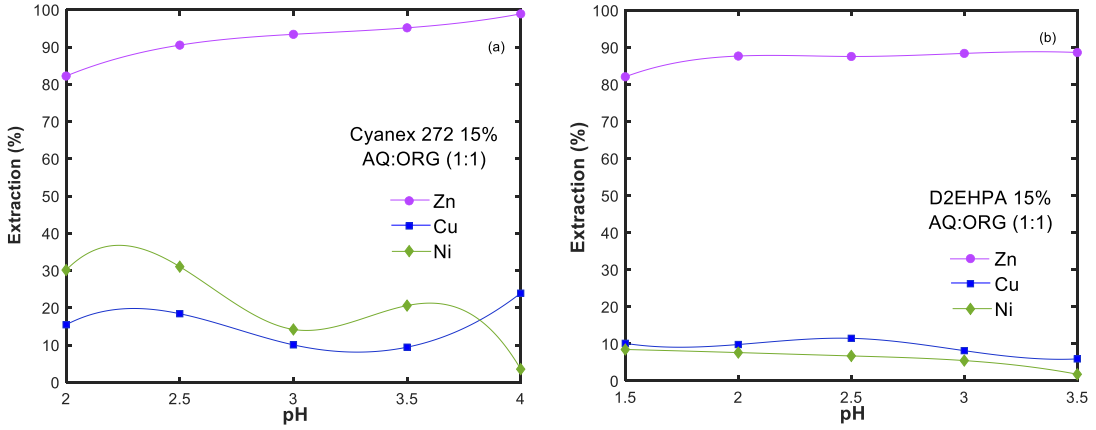

Figure 4. Zinc extraction (%) as a function of pH using (a) 15% v/v Cyanex 272 with an AQ: ORG (1:1) and (b) 15% v/v D2EHPA with AQ: ORG (1:1).

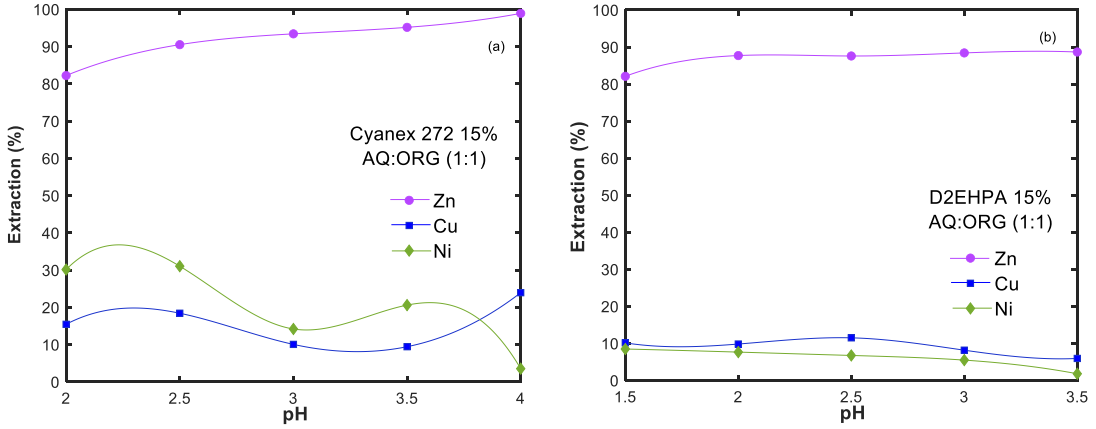

Figure 5. Zinc extraction (%) as a function of pH using (a) 15% v/v Cyanex 272 with an AQ:ORG ratio of 1.2:1 and (b) 15% v/v D2EHPA with an AQ: ORG ratio of 1.2:1.

In contrast, when D2EHPA was used under the same conditions, the maximum zinc extraction was lower, reaching 88% at pH 3.5. Copper and nickel extractions were significantly lower, with maximum values of 10% at pH 2 and 7% at pH 1.5, respectively. These results indicate that Cyanex 272 exhibits higher selectivity and efficiency for zinc than for the other base metals in the studied pH range, compared with D2EHPA.

Figure 4(a) shows the influence of pH on zinc extraction with Cyanex 272 at 15% v/v, with an AQ: ORG ratio of 1:1, achieving a maximum efficiency of 99% at pH 4. The maximum copper extraction occurred at a pH of 4, with 24% extraction, and for nickel, at a pH of 2, with 30% extraction. Figure 4(b) presents the behavior of the extractant D2EHPA 15% v/v at an AQ: ORG ratio of 1:1, where the maximum zinc extraction, 88%, was obtained at a pH of 3.5, copper extraction reached 12% at a pH of 2.5, and nickel showed its highest extraction, 8%, at a pH of 1.5.

Figure 5(a) shows the influence of pH on zinc extraction using 15% v/v Cyanex 272 at an aqueous-to-organic phase ratio (AQ: ORG) of 1.2:1, achieving a maximum efficiency of 99% at pH 4. The maximum copper extraction, 24%, occurred at a pH of 4, and nickel extraction reached 30% at a pH of 2.5. Figure 5(b) presents the behavior of 15%v/v D2EHPA at an AQ: ORG ratio of 1.2:1, where the maximum zinc extraction was 90% at a pH of 3, copper extraction reached 10% at pH 2.5%, and nickel extraction 7% at pH 2.5.

During the experimental work, it was observed that, above pH 3.5, a third interfacial phase formed for both extractants, compromising the stability of the extraction system and thus limiting its practical applicability. The optimal conditions were found at a pH of 3 for both extractants, obtaining a zinc extraction of 94 % with Cyanex 272 at AQ: ORG 1.2:1 (Fig. 5a) and 90% with D2EHPA at the same phase ratio (Fig. 5b).

According to the literature, the extractants Cyanex 272 and D2EHPA exhibit a strong affinity for divalent cations in acidic media. In agreement with these reports, it was observed that when Cyanex 272 was applied at pH values above 3, third-phase formation

tended to occur, as shown in Figures 3a, 4a, and 5a. This phenomenon can be attributed to the generation of hydroxide species such as $Ni(OH)^+$, $Ni(OH)_2$, $Cu(OH)^+$, and $Cu(OH)_2$, which destabilize the organic phase. Additionally, protonation of the solution within this pH range appears to favor the occurrence of third phases, further limiting the applicability of Cyanex 272 under such conditions.

3.3 Extraction isotherms and McCabe-Thiele diagrams

Based on the optimal conditions obtained from the batch experimentation, isotherms and McCabe–Thiele diagrams were developed to evaluate the theoretical extraction stages. The AQ: ORG ratios were varied (1:0.8, 1:1, and 1:1.2), and the data derived guided the scaling of the experiments to a continuous system once the required extraction stages had been determined. Experimentally, the optimal conditions were found at pH 3 and an AQ: ORG phase ratio of 1.2:1 for both extractants. Figure 6(a) shows the McCabe–Thiele diagram for Cyanex 272, where theoretically two stages were required for zinc extraction. Figure 6(b) presents the McCabe–Thiele diagram for D2EHPA, indicating that three theoretical stages were needed for zinc extraction using this reagent. The theoretical stages indicated by the McCabe–Thiele diagrams, when the phase ratio was varied (AQ: ORG) to 0.8:1 or 1:1, showed no significant difference.

3.4 Selectivity of Cyanex 272 and D2EHPA extractants

For the calculation of the distribution coefficient and selectivity of metals (Zn, Cu, and Ni) in the aqueous solution using the extractants Cyanex 272 and D2EHPA, both at a concentration of 15% v/v, the distribution coefficient is defined as a function that depends on parameters such as temperature, pH, and the composition of the organic phase. The calculation was based on Equation (4):

$$D_M = \frac{[M]_{ORG}}{[M]_{AQ}} \tag{4}$$

where $[M]_{ORG}$ is the concentration of the metal in the organic phase and $[M]_{AQ}$ the concentration of the metal in the aqueous phase.

The selectivity factor for zinc was calculated following Equation 5:

$$S_M^{Zn} = \frac{D_{Zn}}{D_M} \tag{5}$$

where D_{Zn} is the distribution coefficient corresponding to zinc and D_M is the distribution coefficient corresponding to the other metals (copper and nickel) that were compared to zinc. From these calculations, Table 3 summarizes the distribution coefficients of the extractant Cyanex 272.

The extractant exhibited the following selectivity order:

Zn>Cu>Ni

Table 4 summarizes the distribution coefficients of the extractant D2EHPA.

The extractant exhibited the following selectivity order:

Zn>Ni>Cu.

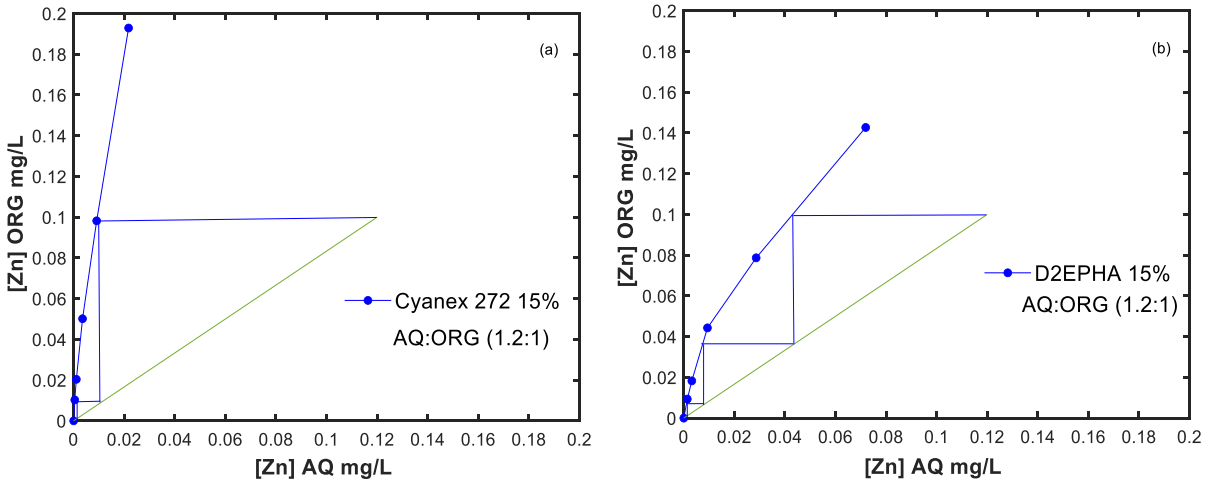

Figure 6. McCabe–Thiele diagrams using (a) Cyanex 272 at 15% v/v, AQ:ORG (1.2:1), and (b) D2EHPA at 15% v/v, AQ:ORG (1.2:1).

Table 3. Distribution coefficients and selectivity for Cyanex 272.

Metal	AQ:ORG	Extractant	$[M]_{AQ}$ (mg/L)	$[M]_{ORG}$ (mg/L)	D_M	S_M^{Zn}
Zn	1.2:1	Cyanex 272	6.6	100.6	15.2	1
Cu	1.2:1		13562	1357.7	0.10	200
Ni	1.2:1		2928	661.6	0.23	67

Table 4. Distribution coefficients and selectivity for D2EHPA

Metal	AQ:ORG	Extractant	$[M]_{AQ}$ (mg/L)	$[M]_{ORG}$ (mg/L)	D_M	S_M^{Zn}
Zn	1.2:1	D2EHPA	11.6	95.7	8.4	1
Cu	1.2:1		14016	904.3	0.06	125
Ni	1.2:1		3467	122.7	0.04	241

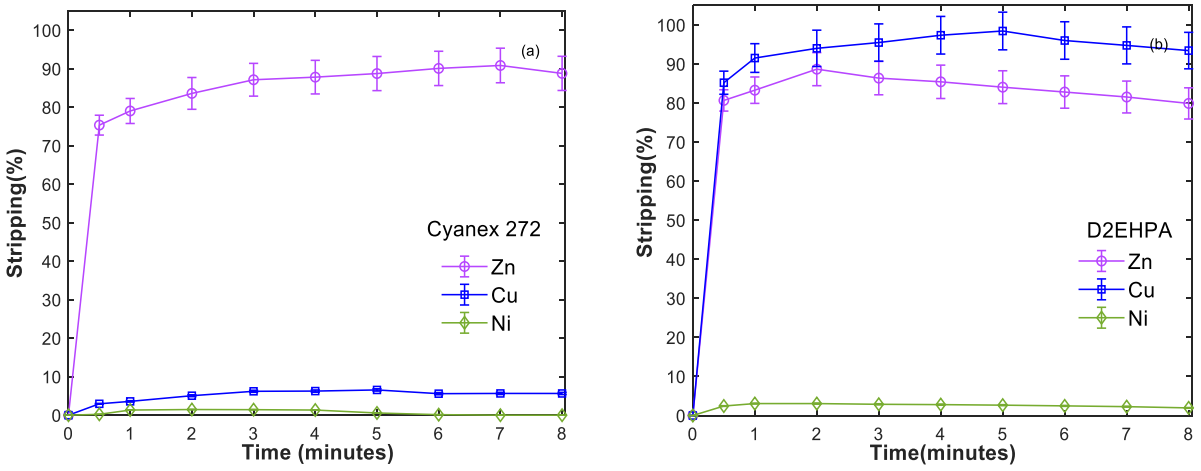

Figure 7. Stripping kinetics for zinc, copper, and nickel using H_2SO_4 at 180g/L, AQ/ORG phase ratio 1:1, extractant 15% v/v: (a) [Zn] in Cyanex 272; (b) [Zn] in D2EHPA.

3.5 Stripping kinetics

For the stripping tests, a sulfuric acid concentration of 180 g/L was used, and the contact time between phases during re-extraction was varied (0.5, 1, 2, 3, 4, 5, 6, 7, and 8 minutes). As shown in Figure 7(a), the stripping efficiency reached a maximum at 7 minutes, achieving 91% recovery of zinc contained in the solution with Cyanex 272, followed by a maximum copper recovery of 6.5% and nickel at a lower percentage of 3.8%. The latter becomes undetectable in the aqueous solution after 5 minutes. In Figure 7(b), a maximum zinc re-extraction of 88% was observed at 2 minutes. For copper, the highest re-extraction occurs after 5 minutes, reaching 98%. In contrast, nickel shows a lower percentage of 3% at 1 minute, remaining stable over time.

3.6 McCabe–Thiele analysis for stripping

McCabe–Thiele diagrams were constructed to determine the number of theoretical stages required for zinc stripping from the organic phase, examining two sulfuric acid concentrations in the aqueous phase, namely, 180 and 200g/L, and varying aqueous-to-organic phase ratios (AQ: ORG), namely, 1:1, 2:1 and 5:1. Figure 8(a) shows the steps required for stripping, when the aqueous solution has a sulfuric acid concentration of 180g/L and is put in contact with the organic phase at a 1:1 phase ratio with Cyanex 272 15%. This suggests that three theoretical stages were necessary to achieve complete zinc stripping. Figure 8(b) shows the theoretical stages required for stripping when the phase ratio was AQ: ORG of 1:1, with a concentration in the aqueous phase of sulfuric acid of 180 g/L, and the organic phase with D2EHPA 15%, where, under these established conditions, only one theoretical stage was required in the zinc stripping process.

Figure 9(a) shows the theoretical stages required for zinc stripping from the organic phase containing Cyanex 272, when in contact with an aqueous phase of H_2SO_4 at 200g/L concentration, indicating that three theoretical stages are necessary for zinc re-extraction. Figure 9(b) illustrates that for zinc stripping from the organic phase with D2EHPA under the same aqueous sulfuric acid concentration (200 g/L), only one theoretical stage is required for re-extraction. It is observed that increasing the sulfuric

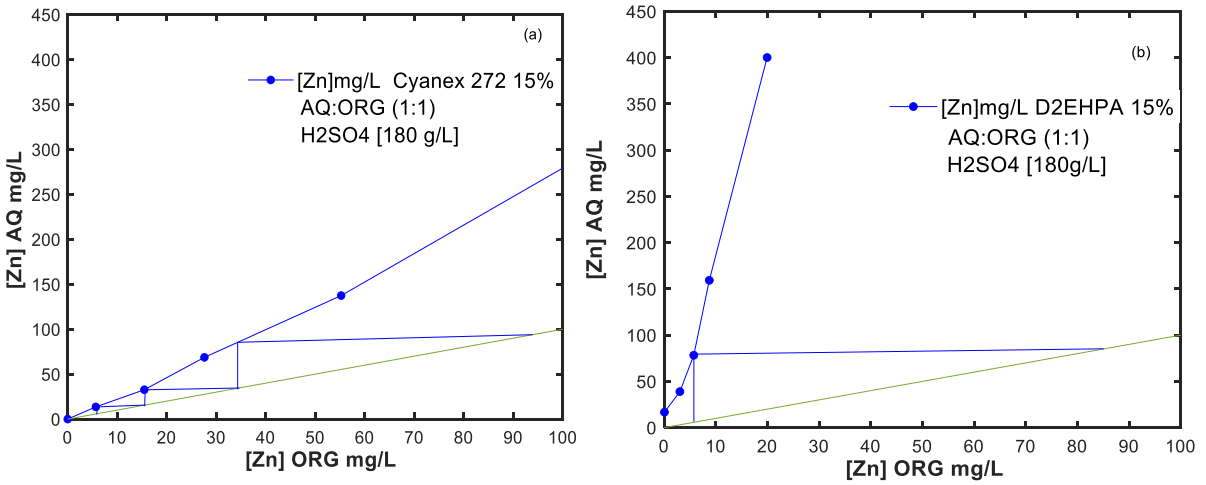

Figure 8. McCabe–Thiele diagrams for Zn stripping, AQ: ORG phase ratio (1:1), [H_2SO_4] 180g/L, 15% v/v extractant: (a) Cyanex 272; (b) D2EHPA.

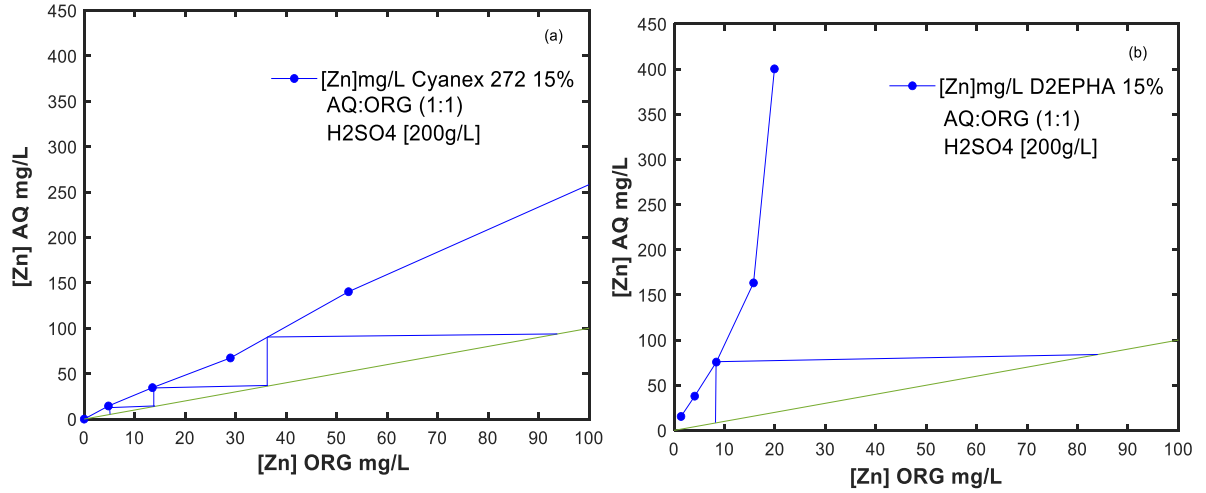

Figure 9. McCabe–Thiele diagrams for Zn stripping, AQ: ORG phase ratio (1:1), [H_2SO_4] 200g/L, 15% v/v extractant: (a) Cyanex 272; (b) D2EHPA.

acid concentration from 180 to 200 g/L does not affect the number of theoretical stages needed for zinc stripping. The optimal conditions were found at an aqueous-to-organic phase ratio of 1:1 for both Cyanex 272 and D2EHPA, as this ratio exhibited better phase separation compared to 2:1 and 5:1 for both extractants.

Conclusions

The use of organophosphate extractants, such as Cyanex 272 and D2EHPA, proved effective for the selective extraction of zinc ions from sulfuric acid solutions. Cyanex 272 exhibited higher zinc extraction efficiencies; however, its performance at elevated pH values was limited by the formation of colloidal solutions and third phases, which resulted in organic phase entrainment into the aqueous phase. This instability highlights a practical drawback of Cyanex 272 under operational conditions above pH 3. Under optimized conditions at pH 3, zinc extraction efficiency reached 94%, while copper extraction was 10% and nickel extraction was 15%, revealing the challenge of achieving complete selectivity. In comparison, D2EHPA demonstrated more stable behavior across the tested pH range, reaching a maximum zinc extraction of 90%. Copper and nickel extractions remained around 10% or less, confirming a higher selectivity for zinc under acidic conditions, despite the slightly lower overall extraction efficiency.

Once the optimal parameters were defined, namely, 3 minutes of contact time, an AQ: ORG phase ratio of 1.2:1, and a pH of 3, Cyanex 272 achieved 94% zinc extraction, with copper extraction at 8% and nickel extraction at 18%. In the subsequent stripping step, performed with 180 g/L H_2SO_4 for 7 minutes, zinc recovery from the organic phase reached 91%, while that of copper decreased to 6%

and nickel was not detectable by AAS, confirming the high efficiency of the re-extraction stage. Under similar extraction conditions, D2EHPA extracted 90% zinc, 6% copper, and 4% nickel. During stripping with 180 g/L H_2SO_4 and a contact time of 2 minutes, the zinc recovery reached 88%, underscoring the faster kinetics of D2EHPA despite its slightly lower overall efficiency.

McCabe–Thiele diagrams provided additional insight into stage requirements. At optimal conditions of pH 3 and an AQ: ORG phase ratio of 1.2:1, zinc extraction with Cyanex 272 required two theoretical stages, whereas D2EHPA required three stages. In the stripping step, increasing the sulfuric acid concentration from 180 to 200 g/L did not significantly influence the number of stages, indicating that 180 g/L was sufficient for efficient operation. Under these conditions, stripping with Cyanex 272 required three theoretical stages, while D2EHPA required only one stage to achieve zinc recoveries above 90%. These findings suggest that Cyanex 272 offers higher extraction efficiency, but with the drawback of co-extraction and potential third-phase formation. In contrast, D2EHPA provides greater operational stability and faster stripping performance, albeit with a slightly lower zinc loading capacity.

References

Aguayo, S., Valenzuela, J. L., Parga, J. R., Lewis, R. G., & Cruz, M. (2007). Continuous Laboratory Gold Solvent Extraction from Cyanide Solutions using LIX 79 Reagent. *Chemical Engineering & Technology: Industrial Chemestry-Plant Equipment-Process Engineering-Biotechnology*, *30*(11), 1532-1536. https://doi.org/https://doi.org/10.1002/ceat.200700202

Ahmadipour, M., Rashchi, F., Ghafarizadeh, B., & Mostoufi, N. (2011). Synergistic Effect of D2EHPA and Cyanex 272 on Separation of Zinc and Manganese by Solvent Extraction. *Separation Science and Technology - SEPAR SCI TECHNOL*, *46*. https://doi.org/https://doi.org/10.1080/01496395.2011.594848

Bolin, N. J., & Sundkvist, J. E. (2008). Two-stage precipitation process of iron and arsenic from acid leaching solutions. *Transactions of Nonferrous Metals Society of China*, *18*, 1513-1517. https://doi.org/https://doi.org/10.1016/S1003-6326(09)60034-0

Borda, J., & Torres, R. (2021). Compartive study of selective zinc leaching from EAFD using carboxylic agents. *Revista Mexicana de Ingeniería Química*, *20*, 389-398. https://doi.org/https://doi.org/10.24275/rmiq/IA2022

Cayumil, R., Khanna, R., Rajarao, R., Mukherjee, P. S., & Sahajwalla, V. (2016). Concentration of precious metals during their recovery from electronic waste. *Waste Management*, 121-130. https://doi.org/https://doi.org/10.1016/j.wasman.2015.12.004

Chagnes, A., & Cote, G. (2010). Séparation du cobalt et du nickel à l'aide du Cyanex® 272 par extraction liquide-liquide. *L'Actualité chimique*(346), 29-34.

Cognis, G. (2008). *MCT Redbook: Reactivos de Extracción por Solvente y sus Aplicaciones*.

Cytec. (2010). *Mining Chemicals Handbook*.

Habashi, F. (2003). *Metals from Ores. An Introducction to Extractive Metallurgy*.

Kiddee, P., Naidu, R., & Wong, M. H. (2013). Electronic waste management approaches: An overview. *Waste Management*, *33*, 1237-1250. https://doi.org/https://doi.org/10.1016/j.wasman.2013.01.006

Li, Y., Hu, J., Fu, M., Tang, J., Dong, L., & Liu, S. (2016). Investigation of intermolecular interactions of mixed extractants of quaternary phosphonium or ammonium chlorides and bis(2,4,4-ethylhexyl)phosphoric acid for metal separation [10.1039/C6RA07813C]. *RSC Advances*, *6*(62), 56772-56779. https://doi.org/10.1039/C6RA07813C

Lupi, C., & Pilone, D. (2020). Effectiveness of saponified D2EHPA in Zn(II) selective extraction from concentrated sulphuric solutions. *Minerals Engineering*, *150*, 106278. https://doi.org/https://doi.org/10.1016/j.mineng.2020.106278

Martinez-Ballesteros, G., Valenzuela- Garcia, J. L., Guerrero- Germán, P., Valdez-Salas, B., & Gómez-Álvarez, A. (2024). Separation of palladium from waste electronic card leaching solutions by solvent extraction using a tertiary amine. *Revista Mexicana de Ingenieria Química*, *3*. https://doi.org/https://doi.org/10.24275/rmiq/Proc24380

Martinez-Ballesteros, G., Valenzuela-Garcia, J. L., Gomez-Alvarez, A., Encinas-Romero, M. A., Mejia-Zamudio, F. A., & Rosas-Durazo, A. d. J. (2023). Base Metals Extraction from Printed Circuit Boards by Pressure Acid Leaching.

Minerals. https://doi.org/https://doi.org/10.3390/min13010098

Omelchuk, K., Stambouli, M., & Chagnes, A. (2018). Investigation of aggregation and acid dissociation of new cationic exchangers for liquid-liquid extraction. *Journal of Molecular Liquids*, *262*, 111-118. https://doi.org/https://doi.org/10.1016/j.molliq.2018.04.082

Rao, M. D., Singh, K. K., Morrison, C. A., & Love, J. B. (2020). Challenges and opportunities in the recovery of gold from electronic waste. *RSC Adv.*, *10*(8), 4300-4309. https://doi.org/https://doi.org/10.1039/C9RA07607G

Schaeffer, N., Passos, H., Billard, I., Papaiconomou, N., & Coutinho, J. A. P. (2018). Recovery of metalsfrom waste electrical and electronic equipment (WEEE) using unconventionalsolvents based on ionic liquids. *Critical Reviews in Environmental Science and Technology*, *48*(13-15), 859-922. https://doi.org/https://doi.org/10.1080/10643389.2018.1477417

Segura-Bailón, B., & Lapidus-Lavine, G. (2023). Importance of chemical pretreatment for base metals remotion and its effect on theselective extraction of gold from Printed Circuits Boards (PCBs). *Revista Mexicana de Ingeniería Química*, *22*. https://doi.org/https://doi.org/10.24275/rmiq/IA2335

Sun, M., Liu, S. Y., Zhang, Y., Liu, M., Yi, X., & Hu, J. (2019). Insights into the saponification process of di(2-ethylhexyl) phosphoric acid extractant: Thermodynamics and structural aspects. *Journal of Molecular Liquids*, *280*, 252-258. https://doi.org/https://doi.org/10.1016/j.molliq.2019.02.025

Tahmasebizadeh, P., & Javanshir, S. (2021). Solvent Extraction of Zinc from a Bioleaching Solution by Modification of D2EHPA: Optimization and Thermodynamic Studies. *Journal of Mining and Environment*, *12*, 253-269. https://doi.org/https://doi.org/10.22044/jme.2021.10324.1979

Xie, W., Zhang, L., Yang, J., Zhang, L., & Ju, S. (2019). Separation of Zn(II) from Zn-Ni-Co sulphate solution by di-(2-ethylhexyl)phosphoric acid (D2EHPA) using a slug flow microreactor. *Chemical Engineering and Processing - Process Intensification*, *123*, 107562. https://doi.org/https://doi.org/10.1016/j.cep.2019.107562

Zhang, Y., Deng, J., Chen, J., Yu, R., & Xing, X. (2014). The electrowinning of zinc from sodium hydroxide solutions. *Hydrometallurgy*, *146*, 59-63. https://doi.org/https://doi.org/10.1016/j.hydromet.2014.03.006.

Zhu Xiao-lin, X. C.-y., Tang Jie, Hua Yi-xin, Zhang Qi-bo, Liu Hai, Wang Xiang, Huang Meng-ting. (2019). Selective recovery of zinc from zinc oxide dust using choline chloride based deep eutectic solvents. *29*(10), 2222-2228. https://www.sciencedirect.com/science/article/pii/S1003632619651289

Casa abierta al tiempo

UNIVERSIDAD AUTÓNOMA METROPOLITANA

Coordinador del Posgrado

Dr. Guadalupe Ramos Sánchez

piq@xanum.uam.mx; pdiv@xanum.uam.mx

http://piq.izt.uam.mx

Ejemplos de algunos temas de investigación actuales y trascendentes en el escenario nacional e internacional:

- Ciencia de datos aplicadas al diseño de procesos químicos.
- Síntesis de productos de alto valor agregado mediante catalizadores heterogéneos, biocatalizadores y microorganismos.
- Potabilización de agua mediante tratamientos fisicoquímicos.
- Materiales, prototipos y análisis de Baterías Ion-Li con aplicaciones en autos eléctricos y almacenamiento de energía a gran escala.
- Hidrotratamiento de combustibles convencionales y provenientes de energías renovables.
- Captura de CO_2 y valorización mediante catálisis para la producción de combustibles sintéticos y otros productos de alto valor agregado.
- Cultivo y utilización de micro algas para la producción de biocombustibles
- Eliminación de contaminantes orgánicos e inorgánicos en el tratamiento de agua.
- Ciencia de alimentos aplicada a la estabilización de sistemas

Doctorado: ingreso cada trimestre
Próxima convocatoria: julio 2024
Recepción de Documentos: agosto-septiembre 2024
Inicio de Clases: octubre 2024

Maestría: ingreso a inicios de cada año
Próxima convocatoria: octubre 2024
Propedéutico: noviembre-diciembre 2024
Ingreso: febrero 2025

Universidad Autónoma Metropolitana Unidad Iztapalapa, Av. Ferrocarril San Rafael Atlixco 186, Colonia Leyes de Reforma 1a. Sección Iztapalapa, C. P. 09310 Ciudad de México. Tel. 5804 4600

Investigación y docencia

Posgrados

ciencia tecnología arte humanismo

uam

Maestría y Doctorado en Ciencias (Ingeniería Química)

CBI Unidad Iztapalapa

División de Ciencias Básicas e Ingeniería

Líneas de Investigación:

- *Ingeniería de reactores catalíticos*
- *Fenómenos de transporte en sistemas multifásicos*
- *Ingeniería de sistemas en procesos químicos*
- *Catálisis y nuevos materiales*
- *Bioprocesos y tecnología de alimentos*

Casa abierta al tiempo
UNIVERSIDAD AUTÓNOMA METROPOLITANA